

Yu Sun
Xian Wang
Jiangfan Yu *Editors*

Field-Driven Micro and Nanorobots for Biology and Medicine



Springer

Field-Driven Micro and Nanorobots for Biology and Medicine

Yu Sun • Xian Wang • Jiangfan Yu
Editors

Field-Driven Micro and Nanorobots for Biology and Medicine

 Springer

Editors

Yu Sun 

Robotics Institute
University of Toronto
Toronto, ON, Canada

Jiangfan Yu 

Shenzhen Institute of Artificial Intelligence
and Robotics for Society, The Chinese
University of Hong Kong, Shenzhen
Shenzhen, Guangdong, China

Xian Wang 

Program in Developmental and Stem Cell
Biology, Arthur and Sonia Labatt Brain
Tumour Research Centre
The Hospital for Sick Children
Toronto, ON, Canada

ISBN 978-3-030-80196-0

ISBN 978-3-030-80197-7 (eBook)

<https://doi.org/10.1007/978-3-030-80197-7>

© Springer Nature Switzerland AG 2022

This work is subject to copyright. All rights are reserved by the Publisher, whether the whole or part of the material is concerned, specifically the rights of translation, reprinting, reuse of illustrations, recitation, broadcasting, reproduction on microfilms or in any other physical way, and transmission or information storage and retrieval, electronic adaptation, computer software, or by similar or dissimilar methodology now known or hereafter developed.

The use of general descriptive names, registered names, trademarks, service marks, etc. in this publication does not imply, even in the absence of a specific statement, that such names are exempt from the relevant protective laws and regulations and therefore free for general use.

The publisher, the authors, and the editors are safe to assume that the advice and information in this book are believed to be true and accurate at the date of publication. Neither the publisher nor the authors or the editors give a warranty, expressed or implied, with respect to the material contained herein or for any errors or omissions that may have been made. The publisher remains neutral with regard to jurisdictional claims in published maps and institutional affiliations.

This Springer imprint is published by the registered company Springer Nature Switzerland AG
The registered company address is: Gewerbestrasse 11, 6330 Cham, Switzerland

Book Description

Micro and nanorobotics is a booming interdisciplinary field, which holds significant potential for healthcare and other applications. *Field-Driven Micro and Nanorobots for Biology and Medicine* is a comprehensive resource for students and researchers in robotics and related areas.

Contents

1	Fundamentals and Field-Driven Control of Micro-/Nanorobots	1
	Antoine Ferreira	
2	Ultrasound-Powered Micro-/Nanorobots: Fundamentals and Biomedical Applications	29
	Liqiang Ren, Fernando Soto, Luyang Huang, and Wei Wang	
3	Manipulation and Patterning of Micro-objects Using Acoustic Waves	61
	Citsabehsan Devendran and Adrian Neild	
4	Light-Driven Microrobots: Mechanisms and Applications.	91
	Shuailong Zhang, Fan Nan, and Steven L. Neale	
5	Electric-Field-Driven Micro/Nanomachines for Biological Applications	113
	Hyungmok Joh and Donglei (Emma) Fan	
6	Electrophoresis-Based Manipulation of Micro- and Nanoparticles in Fluid Suspensions	133
	Kaiyan Yu	
7	Magneto-Acoustic Hybrid Micro-/Nanorobot	165
	Simon W. Sanchez and Jinxing Li	
8	Colloidal Microrobotic Swarms.	179
	Qian Zou, Yibin Wang, and Jiangfan Yu	
9	Shape-Programmable Magnetic Miniature Robots: A Critical Review	211
	Chelsea Shan Xian Ng, Changyu Xu, Zilin Yang, and Guo Zhan Lum	
10	In Vitro Biosensing Using Micro-/Nanomachines	243
	Jinhong Gao, Ke Yuan, and Li Zhang	

11	Biophysical Measurement of Cellular and Intracellular Structures Using Magnetic Tweezers	269
	Xian Wang, Tiancong Wang, Zhuoran Zhang, and Yu Sun	
12	Hepatic Vascular Network Construction Using Magnetic Fields	285
	Eunhye Kim, Masaru Takeuchi, and Toshio Fukuda	
13	Biohybrid Microrobots	305
	Federica Iberite, Lorenzo Vannozzi, and Leonardo Ricotti	
14	Microrobots in the Gastrointestinal Tract	349
	Ming You, Daniel Mukasa, and Wei Gao	
15	Polymer-Based Swimming Nanorobots Driven by Chemical Fuels	369
	Zhiguang Wu, Tingxin Yang, and Qiang He	
16	Magnetic Micro-/Nanopropellers for Biomedicine	389
	Tian Qiu, Moonkwang Jeong, Rahul Goyal, Vincent M. Kadiri, Johannes Sachs, and Peer Fischer	
	Index	413

About the Editors

Yu Sun is a member of two national academies of Canada (Canadian Academy of Engineering; Academy of Science of the Royal Society of Canada). He is a Tier I Canada Research Chair and the director of the University of Toronto's Robotics Institute. His Advanced Micro and Nanosystems Laboratory specializes in developing innovative technologies and instruments for manipulating and characterizing cells, molecules, and nanomaterials. He was elected Fellow of the ASME (American Society of Mechanical Engineers), IEEE, AAAS (American Association for the Advancement of Science), National Academy of Inventors (USA), and AIMBE (American Institute of Medicine and Biomedical Engineering) for his work on micro-nano devices and robotic systems. Among the awards he received were an NSERC E.W.R. Steacie Memorial Fellowship, an NSERC Synergy Award for Innovation, the McLean Award, and the IEEE C.C. Gotlieb Computer Award.

Xian Wang is a research fellow at the Hospital for Sick Children in Toronto. He received a B.Eng. degree from Tianjin University in 2015 and his Ph.D. degree from the University of Toronto in the collaborative Ph.D. program in mechanical engineering and biomedical engineering in 2020. He has published more than 20 peer-reviewed papers in international journals, including *Science Robotics*, *Nature Communications*, *PNAS*, *IEEE Transactions on Robotics*, *Biophysical Journal*, and *Journal of Cell Science*. He received the Best Paper Award on Automation at the 2019 IEEE International Conference on Robotics and Automation (ICRA), and the Best Poster Presentation at the 2018 and 2019 University of Toronto MIE Symposiums. He has been awarded a Lap-Chee Tsui Fellowship, Ontario Graduate Fellowship and Mitacs Graduate Fellowship in Canada, a National Scholarship in China, and Milligan Graduate Fellowship at the University of Toronto.

Jiangfan Yu is an assistant professor at the Chinese University of Hong Kong, Shenzhen. He received his B.Eng. degree from Harbin Institute of Technology (2014) and his Ph.D. degree from the Chinese University of Hong Kong (2018). He worked as a postdoctoral fellow at the Chinese University of Hong Kong (2018–2019) and at the University of Toronto (2019–2020). Dr. Yu's research interests lie in

micro/nanorobotics and medical robotics. He has made contributions to swarm control of micro/nanorobots, including their fundamental modeling, actuation strategy, motion and reconfiguration control, and biomedical applications. Since 2017, he has published more than 30 papers in international journals, including *Science Robotics*, *Nature Communications*, *The International Journal of Robotics Research* (IJRR), *IEEE Transactions on Robotics* (T-RO), *IEEE/ASME Transactions on Mechatronics* (TMECH), and *ACS Nano*. Several of his journal papers have been indexed as ISI highly cited papers and have been highlighted in science, nature, and international press reports, such as CNN. Dr. Yu has won several awards, including Nature Communications Top 50 Physics Articles (2018), TMECH Best Paper Award finalist (2020), CUHK Postgraduate Research Output Award (2018), Hong Kong Young Scientist Award shortlist (2018), and the First Prize of the International Bionic Innovation Competition (2019). He served as a guest editor for *Frontiers in Robotics and AI* and *Micromachines*, and an associate editor for the International Conference on Ubiquitous Robots 2019.

Chapter 1

Fundamentals and Field-Driven Control of Micro-/Nanorobots



Antoine Ferreira

1.1 Introduction

When microdevices are propelled in the body fluids, especially in the blood circulatory system, a very large number of remote locations in the human body become accessible. However, since the diameters of the blood vessels in the human body may vary from approximately 25 mm (aorta) down to 0.006–0.010 mm (capillaries) with diameters of 1.0–4.0 mm in large arteries, it is obvious that propelling such wireless microdevices in the human cardiovascular system with existing technologies represents a great technical challenge. Because the method of propulsion should allow such a microdevice to navigate through the cardiovascular system, the use of the normal blood flow itself must be considered only as a complementary means of propulsion when the travel path is in the direction of the blood flow. As such, it is essential to develop a mean of propulsion that could also steer such a microdevice independently from the direction of the blood flow. Generally, micro-robot propulsion consists of applying magnetic gradients generated by a magnetic resonance imaging (MRI) system to exert a displacement force on a ferromagnetic core embedded onto a miniature untethered device. Since MRI systems generate magnetic gradients and also provide the imaging modality, interfaces, and control within an infrastructure already accessible in clinics and hospitals, the technique is referred here to as magnetic resonance propulsion. Although the methods of propulsion using magnetic gradients are not new, the use of a MRI to propel such microcapsules is new. Although constrained by the characteristics of clinical MRI systems, this approach offers significant advantages at the system level when compared to other methods. As a matter of fact, MRI systems are already implanted in hospitals and provide imaging, tracking, computation, analysis, human interface, gradient

A. Ferreira (✉)

INSA Centre Val de Loire – Université d’Orléans, PRISME, Bourges, France

e-mail: antoine.ferreira@insa-cvl.fr

© Springer Nature Switzerland AG 2022

Y. Sun et al. (eds.), *Field-Driven Micro and Nanorobots for Biology and Medicine*, https://doi.org/10.1007/978-3-030-80197-7_1

coils, cooling systems, and real-time navigational control, and several more aspects are tightly linked to the method of propulsion in order to realize a complete and effective system.

1.2 General Architecture of MRI-Guided Nanorobotic Systems

MRI-guided nanorobotic systems aim at diagnosing and treating diseases in cells, organs, or tissues. Their proper function relies on providing engineering and scientific solutions in three technical challenges [1]:

- (i) *Enhanced diagnostics*: The clinical magnetic resonance imaging (MRI) is an advanced imaging system that provides 3D visualization, offering the radiologists a detailed three-dimensional view of the tissue or organ of interest. Nanorobotic systems are detectable by MRI without creating artifacts.
- (ii) *In vivo propulsion and navigation*: The MRI system is employed for propulsion and navigation of the nanocapsules. The propulsion of a micro- or nanocapsule with magnetic properties in the cardiovascular system is realized through the induction of forces and torques by magnetic gradients and magnetic fields, respectively, generated by the MRI coils. The nanocapsules are guided in vivo to the targeted organs or are accumulated to the tumors' capillary networks. Also, the MRI forces retain the nanocapsules at the target site. Table 1.1 demonstrates a list of commercial clinical and preclinical MRI machines [2].
- (iii) *Drug delivery and release*: The magnetic nanocapsules are loaded with drug molecules. Also their surface is chemically processed (coated with polymers and bioconjugated with specific antibodies) so that on the one hand they are not detected by the immune system and on the other hand they have increased chances to bind to the receptors of malignant cells. When inside the cell or at its vicinity, the release mechanism of the drug is triggered. The architecture for implementing the MRI-based nanorobotic system is depicted in Fig. 1.1. Four main *subsystems* can be identified:
 - *The graphical user interface module*, which comprises input command prompt, 3D visualization, and process supervision tools.
 - *The control module*, which comprises (a) the high-level controller responsible for the nanocapsule navigation tasks and for the generation of the corresponding field gradients and (b) the low-level controller (manufacturer MRI controller) responsible for implementing the actuation commands for the generation of the desired field gradients and for the image acquisition tasks.
 - *The hardware module: MRI and the nanocapsules*. This is the controlled hardware, which comprises (a) the MRI hardware and software systems and

Table 1.1 List of clinical and preclinical MRI machines

MRI devices						
Model	Type	Company	Field	Gradient	Bore (cm)	Slew rate
BioSpec 94/30	Preclinical	Bruker Biospin	9.4 T	200 mT/m	ID 200.5 - OD 301.5	640 T/m/s
BioSpec 94/20	Preclinical	Bruker Biospin	9.4 T	440 mT/m	ID 116 - OD 205	3440 T/m/s
BioSpec 70/30	Preclinical	Bruker Biospin	7 T	200 mT/m	ID 200.5 - OD 301.5	640 T/m/s
BioSpec 70/31	Preclinical	Bruker Biospin	8 T	440 mT/m	ID 116 - OD 205	3440 T/m/s
BioSpec 47/40	Preclinical	Bruker Biospin	4.7 T			
ClinScan	Preclinical	Bruker Biospin	7 T	290 mT/m	ID 200.5 - OD 301.5	1160 T/m/s
ClinScan S line	Preclinical	Bruker Biospin	7 T	630 mT/m	ID 114 - OD 198	6300 T/m/s
Achiva 3.0T X-series	Clinical	Philips	3 T	80 mT/m (dual mode)		
Discovery MR750 3.0T	Clinical	GE	3 T	50 mT/m		200 T/m/s
Echelon		Hitachi	3 T	30 mT/m		
MAGNETOM 7T*	Clinical	Siemens	7 T	45 mT/m - 80 mT/m (Head)		400 mT/m/s
MAGNETOM! Verio 3T	Clinical	Siemens	3 T	45 mT/m		200 mT/m/s

(b) the nanocapsules that have been injected within the vasculature and are navigated by the field gradients.

- *The tracking module*, which comprises the (a) MRI image generation and (b) the image processing software that estimates the position and accumulation of the nanocapsules within the vasculature, the tissues, and organs of the human.

1.3 Propulsion and Navigation Limitations at Microscales

Three components are necessary for real-time controlled navigation of untethered nanocapsules in the human vasculature, namely, (i) propulsion, (ii) tracking, and (iii) closed-loop control. These untethered devices have been mainly developed according to three different designs: magnetic bead pulling, biomimetic flagellated robot, and magnetotactic bacteria. Navigation requires observation of the scene in order either to plan the trajectory by off-line mapping or to correct online the nanocapsule's pose error between the planned and the observed trajectory.

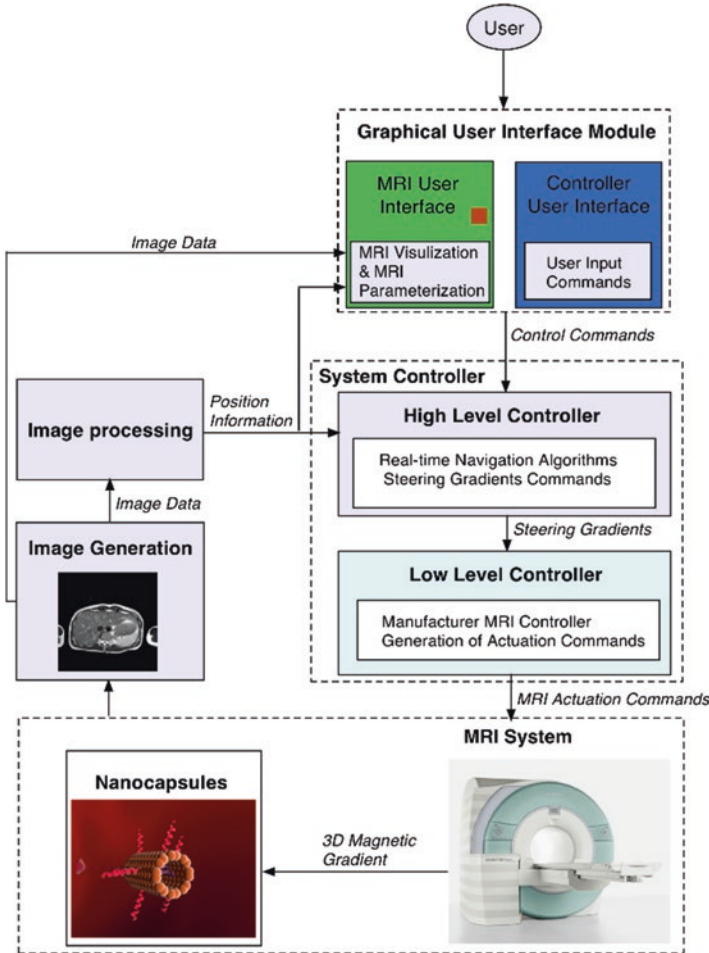


Fig. 1.1 MRI-guided nanorobotic system architecture

The first propulsion scheme is referred to as magnetic bead: thrust is ensured by pulling the magnetic bead using the magnetic force related to gradients of the external field. This concept was first studied in the 1980s using magnets [3] or superconducting magnets [4, 5].

The last innovation in this domain has been provided by the Ecole Polytechnique de Montréal, Canada, where the basic idea is the use of magnetic gradients provided by a clinical MRI device to pull the beads [6]. Such a system combines several advantages: the MRI device provides both fine observation of the scene (thanks to the MRI imager) and actuation of the bead; besides, it makes the implementation easier, since MRI devices are widely implanted in hospitals. This approach is well developed at milli- and microscale, since low-level multiplexed controllers and observers have been developed [7, 8], and in vivo experiments have been trialed on

a living animal [8] (though the blood flow had been stopped using a balloon catheter).

The main drawback of this approach results from strong limitations on the magnetic gradient amplitude in available MRI devices. As magnetic forces used for propelling are volumetric, whereas the drag force is – at best – dependant on the bead’s area, the smaller the bead, the higher the required control forces with respect to hydrodynamic perturbations. Consequently, this approach is well-conditioned for beads whose radius is up to a few dozen micrometers with actual MRI devices. At lower scales, it is necessary either to use additional coils to supply higher gradients [9], or to consider other approaches. MRI system upgraded with additional gradient steering coils in order to increase standard MRI gradient amplitudes (100–500 mT) is currently investigated by the authors in [10]. Another issue is referred to as biomimetic robots using flagella: a red blood cell is fixed to beating flagella [11] imitating the motion of eukaryotic bacteria, or a magnetic bead is attached to a helical nanocoil [12], like prokaryotic bacteria. In the first case, the flagellum is an elastic rod consisting of magnetic particles that a periodic transverse magnetic field causes to bend and pivot, inducing a backward motion. In the second case, conversely, the nanocoil is not subjected to any deformation: propulsion is provided by the torque induced by a rotating magnetic field on the bead. In a Stokes flow, swimming is thus obtained through a corkscrew effect in the fluid [13]: the higher the rotation frequency of the magnetic field, the higher the thrust. Even if these two swimming methods result from different motions, they are both based on converting mechanical power from the magnetic torque to produce the motion. Recent results suggest that, under a given size, helical propelling is better than pulling [14] at low Reynolds number. The comparison is still at the benefit of biomimetic robots as the distance to the magnetic coils increases, which is likely to occur when navigating in the body. However, the assumption of navigating at low Reynolds number can be violated if the rotation frequency becomes too high. Reversing direction can also get complicated because of the rigid rod. Furthermore, this actuation approach is limited in practice due to the difficulty of using it within an MRI device. In fact additional coils providing a rotational magnetic field in an MRI device is a delicate matter, since the precision of an MRI observer relies on a constant magnetic field. This implies the need for an additional imaging system so as to estimate the nanocapsule’s pose; otherwise no closed-loop control will be achievable. Recently, a third approach has been proposed: magnetotactic bacteria. Such bacteria are actuated thanks to embedded or attached ferromagnetic material. The concept had already been studied [15] in the field of nanofactory, though not for actuation purpose. Propulsion is supplied directly by the bacteria’s flagella, and the magnetic field is used in order to steer the bacteria toward the targeted point [16]. This technique can also be used in addition to the classic magnetic pulling. The bacteria are too small to be directly visible by the MRI scanner; however the local magnetic perturbation caused by a swarm of bacteria can be used to locate them, provided that their concentration is sufficient. This raises a crucial issue: the need to control a cloud of robots in order to keep the system observable, which is more difficult than controlling a single robot, since interactions between parts of this multi-agent

Functionalized Nanoparticle

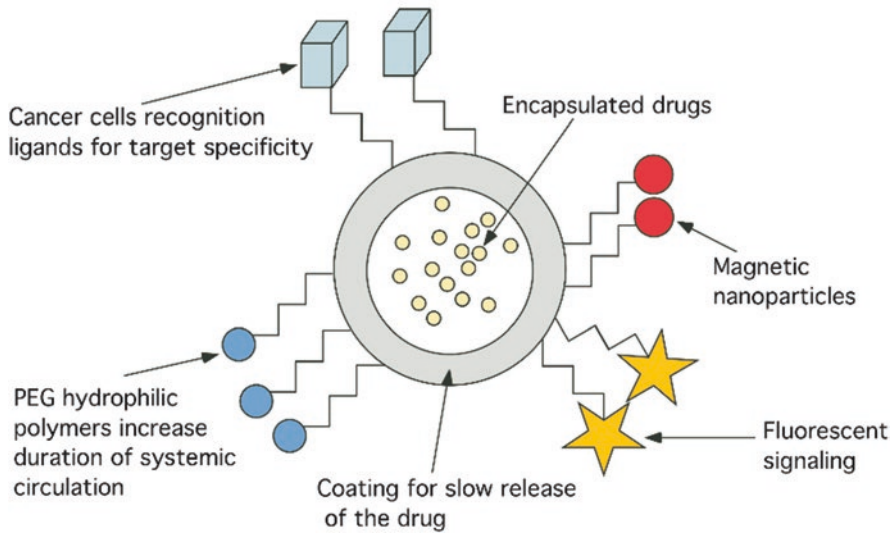


Fig. 1.2 Multi-functionalized drug-loaded magnetic microrobot [1]

system have to be modeled. Despite this technique being promising, since velocities reached by such systems are about ten times higher than velocities of biomimetic robots of similar dimensions, it still has to be improved. In fact, some problems are not solved yet [17], such as side effects of the fixation of the magnetic material on or in the bacteria [18], or Joule heating that reduces the bacteria's efficiency and velocity.

Most of magnetic field-driven microrobots used in drug delivery microrobots are microcapsules composed of components that function as actuators, sensors, drug delivery mechanism, and drug release mechanisms (as shown in Fig. 1.2). In terms of robotics, the components integrated on a microrobotic capsule can be classified into the following: (i) *actuation module* such as iron oxides magnetic nanoparticles, which together with the MRI field gradients serve as the propulsion mechanism; (ii) *sensor module*, such as proteins and other biomolecules that respond to external stimuli, to release drug or to detect and bind to the receptors of malignant cells; and (iii) *carrier module*, which constitutes the main body of the microcapsule and is responsible for carrying (by encapsulation or surface conjugation) drug molecules, sensing biomolecules, and polymer decorations that are needed for biocompatibility and sustained circulation of the nanorobotic capsules.

At this stage, a dedicated control strategy requires a physical model based on analytical equations to derive state-space representation for control purposes.

1.4 Theoretical Modeling of Steering and Navigation of Microrobots in a Fluid

This section proposes a model taking into account the preponderant forces acting on a magnetic spherical microrobot, i.e., magnetic forces generated by the MRI system and the drag force applied by the blood flow.

1.4.1 Modeling of Physical Forces on Magnetic Microrobots

The microrobot is a polymer-bonded aggregate of ferromagnetic particles immersed in blood vessels. A 2D nonlinear model of the robot will be established. This model encompasses the different forces that affect the robot's motion. Assuming the microcapsule spherical, with a radius of some hundred micrometers $r = D/2$, we now detail the forces acting on it (as shown in Fig. 1.3a).

The translational and rotational motions of the robot are expressed by:

$$\begin{cases} m_i \frac{d\mathbf{V}_i}{dt} = \mathbf{F}_{mi} + \mathbf{F}_{di} + \mathbf{W}_{ai} + \mathbf{F}_{ci} + \mathbf{F}_{vdwi} + \mathbf{F}_{eleci} + \mathbf{F}_{bi} \\ J_i \frac{d\mathbf{W}_i}{dt} = \mathbf{T}_{di} + \mathbf{M}_{ci} + \mathbf{T}_{mi} \end{cases} \quad (1.1)$$

where \mathbf{V}_i and \mathbf{W}_i are, respectively, the translational and rotational velocity of the robot and m_i and J_i its mass and moment of inertia. \mathbf{F}_{mi} , \mathbf{F}_{di} , \mathbf{W}_{ai} , \mathbf{F}_{ci} , \mathbf{F}_{vdwi} , and \mathbf{F}_{ei} , respectively, denote the magnetic force produced by the MRI gradient coils (\mathbf{F}_{mi}), blood hydrodynamic drag force (\mathbf{F}_{di}), apparent weight (\mathbf{W}_{ai}), the robot-to-wall contact force ($\mathbf{F}_c = \mathbf{F}_{c_{ni}} \cdot \mathbf{n}_i + \mathbf{F}_{c_{ti}} \cdot \mathbf{t}_{ji}$) with normal $\mathbf{F}_{c_{ni}} \cdot \mathbf{n}_i$ and tangential $\mathbf{F}_{c_{ti}} \cdot \mathbf{t}_{ji}$ contact components, the van der Waals force (\mathbf{F}_{vdw}), and the electrostatic force (\mathbf{F}_{ei}). \mathbf{T}_{mi} , \mathbf{T}_{di} , and \mathbf{M}_{ci} denote, respectively, the magnetic torque, hydrodynamic drag torque, and the robot-to-wall contact moment. In the rest of this chapter, we assume that the orientation of the robot does not change due to the magnetic torque which tends to align the magnetization of the robot along the external field. \mathbf{T}_{di} and \mathbf{M}_{ci} are much smaller order than \mathbf{T}_{mi} .

Hydrodynamics

The hydrodynamic drag force \mathbf{F}_{di} exerting on a spherical body is expressed as:

$$\mathbf{F}_{di} = -\frac{1}{2} \rho_f \left(\frac{(\mathbf{v} - \mathbf{v}_f)^2}{\beta} AC_d \frac{(\mathbf{v} - \mathbf{v}_f)}{(\mathbf{v} - \mathbf{v}_f)} \right) \quad (1.2)$$

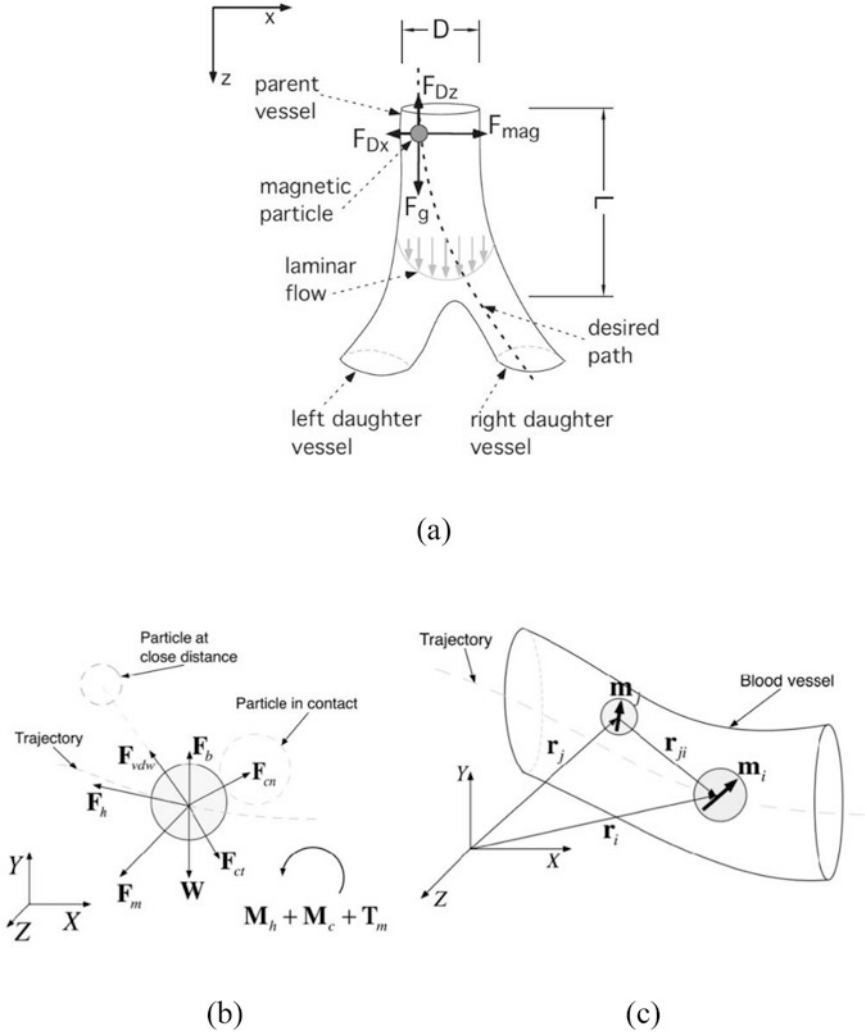


Fig. 1.3 Forces exerted on the magnetic capsule navigating in the vessel. (a) Vessel configuration, (b) free body diagram of a single microcapsule, and (c) configuration of magnetic interaction [25]

where $\mathbf{v}-\mathbf{v}_f$ is the relative velocity of the microrobot with respect to the fluid, A is the frontal area of the core, C_d is the drag coefficient, ρ_f is the density of the fluid, and β is a dimensionless ratio related to wall effect caused by the vessel's occlusion by the robot [19]:

$$\beta = \frac{1 + \left(\frac{\lambda}{\lambda_0}\right)^{\alpha_0}}{1 - \alpha^0} \quad (1.3)$$

with ratio $\lambda = 2r/D$ and D denoting the vessel's diameter (in meter). Parameters α_0 and λ_0 are functions of the Reynolds number but are commonly set to 1.5 and 0.29, respectively. The drag coefficient, C_d , is a function of the Reynolds number. $Re = 2rp f |\mathbf{v} - \mathbf{v}_f|/\beta\eta$. In our study case, we assume the flow to be laminar, i.e., we neglect the turbulences generated in arteries by heart pumping. This assumption is not too restrictive if we consider a blood vessel quite far from the heart. In a low Reynolds number ($Re < 1$), the drag coefficient can be approximated by $C_d = 24/Re$. For higher Reynolds numbers, a more precise drag coefficient in laminar flow for a spherical core is expressed as [20]:

$$C_d = \frac{24}{Re} + \frac{6}{1 + \sqrt{Re}} + 0.4 \quad (1.4)$$

Let r_v denote the radius of the blood vessel the microcapsule evolves in. Previous expressions have assumed that the system evolves in an infinite fluid, i.e., that the boundaries of the blood vessel are far enough from the capsule that their influence has no effect. However the presence of walls has an important effect when the ratio $\lambda = r/r_v$ increases, causing the relative velocity of the microcapsule in the fluid to be no longer zero at equilibrium as it would be in an infinite extent of fluid. To take into account this wall effect, a wall correction factor $f_w(\lambda) = \frac{u}{u_\infty}$ is used to modify the

drag force, where u and u_∞ , respectively, denote the terminal velocity in a finite and in an infinite vessel. A variety of correcting factors have been proposed in the literature [21, 22], a quite simple expression is given by Munroe [23]:

$$f_w(\lambda) = (1 - \lambda^{1.5}) \quad (1.5)$$

Apparent Height

In addition to the drag force, apparent weight (combined action of weight and buoyancy) is acting on the microrobot:

$$\mathbf{W}_a = V(\rho - \rho_f) \cdot \mathbf{g} \quad (1.6)$$

where $\rho = \tau_m \rho_m + (1 - \tau_m) \rho_{poly}$ with ρ_m and ρ_{poly} the magnetic material's and polymer's densities, τ_m ratio of magnetic material, V the volume, and \mathbf{g} the gravitational acceleration. The magnetic gradient required to reach the equilibrium between magnetic force and apparent weight, referred as levitating, is obtained by:

$$\nabla B = \frac{(\rho_m - \rho)}{\tau_m M} \cdot \mathbf{g} \quad (1.7a)$$

Table 1.2 Effect of apparent weight of a ferromagnetic core on the magnetic force required for displacement: magnetic gradient $\nabla \mathbf{B}$ required for levitating assuming that the embedded material has a density $\rho_{emb} = 1300 \text{kg/m}^3$ (density of carbon nanotube). Physical data for ferromagnetic materials from [24]

Ferromagnetic material	$\tau_m = 1$	$\tau_m = 0.9$	$\tau_m = 0.5$
Carbon steel 1010/1020	48.5 mT/m	48.7 mT/m	50.3 mT/m
Permendur	35.9 mT/m	36.1 mT/m	37.1 mT/m
Fe ₃ O ₄	113.4 mT/m	114.1 mT/m	120.0 mT/m
FeSi 6%	44.1 mT/m	44.3 mT/m	45.7 mT/m
Alfenol 16	83.8 mT/m	84.2 mT/m	87.5 mT/m
Superalloy	120.7 mT/m	121.2 mT/m	124.5 mT/m

Since ρ_m is always close to iron's density, if $\rho_{poly} > \rho$, the minimal value for the magnetic gradient is obtained for $\tau_m = 1$, *that is, no drug embedded*. Table 1.2 shows effects of τ_m and influence of the magnetic material on the gradient required to levitate. Table 1.2 clearly shows that few materials can provide levitation, even for a non-loaded microcapsule: Carbon steel, permendur, and FeSi are the best fitted types of ferromagnetic material to use for microcapsule manufacturing – permendur, since its high density is counterbalanced by the highest magnetization saturation value reached at ambient temperature, and FeSi due to its low magnetization at saturation which is counterbalanced by a low density. However, the magnetic force with a FeSi core is about 1.33 times lower than the one with a Permendur core, for a same applied gradient: that is why iron/cobalt or carbon steel alloys are more likely to be used for propulsion purpose.

Magnetic Force

The permanent magnet of a clinical MRI device commonly generates a strong and uniform magnetic field ($B_0 \geq 1.5 \text{T}$), so that we can assume the capsule's magnetization reaches the saturation magnetization. This magnetic field induces a torque which tends to align the magnetization of the capsule along the field.

$$\mathbf{F}_{mi} = (\mathbf{m}_i \cdot \nabla) \mathbf{B}_i \quad (1.7b)$$

$$\mathbf{T}_{mi} = \mathbf{m}_i \times \mathbf{B}_i \quad (1.8)$$

where \mathbf{m}_i is the magnetic moment of particle i and ∇ is the gradient operator. \mathbf{B}_i is the total magnetic field at particle i and is given by:

$$\mathbf{B}_i = \mathbf{B}_{0i} + \sum_{j \neq i}^N \mathbf{B}_{ji} \quad (1.9)$$

where \mathbf{B}_0 is the external magnetic field applied at particle i and \mathbf{B}_{ji} is the field at the i^{th} particle due to the magnetic moment of particle j placed at position \mathbf{r}_j . N is the total number of particles. Then \mathbf{B}_{ji} is given by:

$$\mathbf{B}_{ij} = \frac{\mu_0}{4\pi} \left[\frac{3(\mathbf{m}_j \cdot \mathbf{r}_{ji})}{|\mathbf{r}_{ji}^5|} - \frac{\mathbf{m}_j}{|\mathbf{r}_{ji}^3|} \right] \quad (1.10)$$

where \mathbf{r}_{ji} is as demonstrated in Fig. 1.3c. The particles exhibit superparamagnetic properties, i.e., they are hysteresis-free and zero applied magnetic field they exhibit zero magnetization.

Taking into account that a number of magnetic nanoparticles might be embedded into the capsule, Eq. (1.7a and 1.7b) becomes:

$$\mathbf{F}_{mi} = N_{mp} V_{mp} (\mathbf{m}_i \cdot \nabla) \mathbf{B}_i \quad (1.11)$$

where N_{mp} is the number of magnetic particles that are embedded into the microcapsule and V_{mp} is the volume of each magnetic particle.

Contact Forces

Contact force models are critical for predicting the formation and the size of the agglomerations and also for predicting their breakup processes due to the shear flow. The modeling method used in this paper is the Discrete Element Modeling (DEM). This method exploits the viscoelastic properties of spheres and provides an excellent tool for moderate-size problems (up to $\sim 10^4$). The general modeling method is described in detail in [24]. What follows is a brief presentation of the basic modeling elements used in the nanoparticle system model (Fig. 1.4). Particles in a DEM problem are physically approximated as rigid bodies and the contacts between them, as contact points. The contact takes place if and only if the following condition holds:

$$(a_i - a_j) - r_i - r_j > 0 \quad (1.12)$$

where a_i and a_j are the radii of the spheres i and j . \mathbf{F}_{cni} and \mathbf{F}_{cti} are represented by a Voigt model comprising a nonlinear spring and a linear damper (see Fig. 1.3b, c). Dry friction was being neglected.

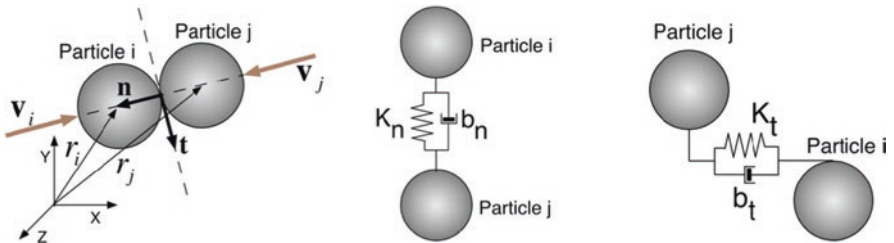


Fig. 1.4 Contact interaction forces: (a) collision, (b) normal forces, and (c) tangential forces [25]

The normal contact force is given by:

$$\mathbf{F}_{c_ni} = \left(k_{ni} \xi_i^{3/2} + b_{ni} \dot{\xi}_i \right) \mathbf{n}_i \quad (1.13)$$

where the first term is the elastic force – based on the Hertz contact law for spherical particles – and the second is the viscous force. The variable ξ_i represents the elastic deformation of sphere i at the contact point of spheres i and j .

The tangential contact force on sphere i is given by:

$$\mathbf{F}_{\tau i} = \left(k_{\tau i} \zeta_i + b_{\tau i} \dot{\zeta}_i \right) \mathbf{t}_{ji} \quad (1.14)$$

where ζ_i is the displacement in the tangential direction that took place since the instant of contact. Slight modification of the aforementioned elements allows modeling also the interaction between particles and the vessel walls. In this case the wall is considered rigid body along the tangential direction and deformable along the normal direction. Further details are given in [25].

Gravitational Forces

These include the force due to gravity and the force due to buoyancy. Although of limited effect at the nanoscale, they might become important when micron-size aggregates are formulated. The gravitational force is given by:

$$\mathbf{F}_{gi} = \mathbf{W}_i + \mathbf{F}_{bi} = \frac{4}{3} \pi a_i^3 (\rho_i - \rho_b) \mathbf{g} \quad (1.15)$$

where ρ_i and ρ_b are the density of the particle i and of the blood, respectively.

Van der Waals Forces

van der Waals forces act among the particles when they are not in contact. The van der Waals potential between spheres of equal radius a is given by:

$$V_{ji} = -\frac{A}{6} \left(\frac{2a^2}{|r_{ji}|^2 - 4a^2} + \frac{2a^2}{|r_{ji}|^2} + \ln \left(\frac{|r_{ji}|^2 - 4a^2}{|r_{ji}|^2} \right) \right) \quad (1.16)$$

where A is the Hamaker constant and $|r_{ji}|^2 \geq 2a + \delta$. The minimum distance δ to which the two surfaces can approach is assumed to be $4A$. The force is given by:

$$\mathbf{F}_{vdwij} = -\nabla V_{ji} \quad (1.17)$$

The electrostatic force between the robot and the wall considered as an uncharged surface is given by [26]:

$$\mathbf{F}_{elij} = \frac{q^2}{4\pi\epsilon\epsilon_0(r+h)^2} \mathbf{n} \quad (1.18)$$

with q the robot's charge, ϵ the dielectric density of the medium in which the interaction occurs, and ϵ_0 the vacuum permittivity. [27] gives the expression of the maximum allowable charge for a spherical body of radius r :

$$q(\mu\text{C}) = S \times Q = 4\pi r^2 \times 30(100r)^{-0.3} \quad (1.19)$$

1.4.2 State-Space Representation

Let (x, z) denote the position of the microrobot in the blood vessel with respect to a given frame $F(O, \mathbf{i}, \mathbf{k})$. The state model is established from differential Eq. (1.1) defining the robot's dynamic behavior, projected on \mathbf{i} and \mathbf{k} axes: If we consider that the drag force is distributed linearly between the \mathbf{i} axis and the \mathbf{k} axis, applying Newton's third law leads to:

$$\begin{cases} \ddot{m}_i x = F_{di_x} + F_{vdwij_x} + F_{elij_x} + F_{ci_x} + F_{mi_x} \\ \ddot{m}_i z = F_{di_z} + F_{vdwij_z} + F_{elij_z} + F_{ci_z} + F_{mi_z} + W_{ai_z} \end{cases} \quad (1.20)$$

where $m = \frac{4}{3}\pi r^3 \rho_r$ is the mass of the microrobot and indexes x and z , respectively, denote projections on \mathbf{i} and \mathbf{k} .

Let x_1, x_2 and x_3, x_4 denote, respectively, the particle's position and velocity along \mathbf{i} axis and \mathbf{k} axis. Assuming that positions x_1 and x_3 can be measured thanks to the MRI system, let y denote the state's measure. Using expressions of forces given by (1.11), (1.13), (1.14), (1.15), (1.17), (1.19), and adequate projection of local frame along the geometry of the vessel, system (1.20) can be written in the form:

$$(\mathbb{C}) \left\{ \begin{array}{l} \dot{x}_1 = x_2 \\ \dot{x}_2 = f_2(x_1, x_2, x_3) + au_1 \\ \dot{x}_3 = x_4 \\ \dot{x}_4 = f_4(x_1, x_3, x_4) + au_2 \\ y = (x_1, x_3)^T \end{array} \right. \quad (1.21)$$

where control inputs $u_1 = \nabla B_x$ and $u_2 = \nabla B_z$ are the magnetic gradients, parameter $a = \tau_m M / \rho$, and functions f_i are given by:

$$\begin{cases} f_2(\cdot) = F_{din_x} + F_{vdwijn_x} + F_{elijn_x} + F_{cin_x} + F_{mni_x} \\ f_4(\cdot) = F_{din_z} + F_{vdwijn_z} + F_{elijn_z} + F_{cin_z} + F_{min_z} + W_{ain_z} \end{cases} \quad (1.22)$$

The index n indicates that the forces are normalized with respect to the robot's mass m .

$$\left\{ \begin{aligned} F_{din_x} &= \frac{9\eta \cos \theta}{2r^2 \beta \rho} (x_2 - v_{fx}) + \frac{3\rho_f \cos \theta}{20r\beta^2 \rho} (x_2 - v_{fx})^2 + \frac{9\rho_f \cos \theta}{4r\beta^2 \rho} \bullet \frac{(x_2 - v_{fx})^2}{1 + \sqrt{\frac{2\rho_f r}{\beta\eta} (x_2 - v_{fx})}} \\ F_{elijn_x} &= \frac{3q^2 \cos \theta}{8\pi^2 r^3 \rho \epsilon \epsilon_0} \left[\frac{1}{(r+h_1)^2} - \frac{1}{(r+h_2)^2} \right] \\ F_{vdwijn_x} &= \frac{A_h \cos \theta}{8\pi r^2} \left[\begin{aligned} &\left(\frac{1}{h_1^2} + \frac{1}{(2r+h_1)^2} - \frac{2}{h_1(2r+h_1)} \right) \\ &- \left(\frac{1}{h_2^2} + \frac{1}{(2r+h_2)^2} - \frac{2}{h_2(2r+h_2)} \right) \end{aligned} \right] \\ F_{cin_x} &= \frac{3k \cos \theta}{4\pi r^3 \rho} \times \delta^{\frac{3}{2}} \\ F_{mni_x} &= \frac{M}{\rho} \times \nabla B_x \end{aligned} \right.$$

where h_1 and h_2 are the robot to the upper and lower walls distances.

1.5 Control Strategies

We review in the following sections different control strategies for microrobot trajectory following in fluidic vascular vessels in MRI-based microrobotic systems:

1.5.1 MRI-Based Backstepping Control Approach

Control law Lyapunov-stabilizing trajectories for system (C) are now presented. The determination of Lyapunov functions is generically a challenging issue. According to [30], it is preferable to use control Lyapunov functions (CLF) in a backstepping control approach. Since this design requires a triangular form for the control system, we propose the following change of variables:

$$X = \begin{pmatrix} x_1 \\ x_3 \end{pmatrix}; Z = \begin{pmatrix} x_2 \\ x_4 \end{pmatrix}; u = \begin{pmatrix} u_1 \\ u_2 \end{pmatrix}; U = au \tag{1.23}$$

As shown in the force balance, the model has many parameters highly variable from one person to another. An adaptive nonlinear control [30] based on a backstepping approach can be developed (as shown in Fig. 1.5). The update law must ensure convergence of the estimated parameter to its real value, while the control inputs must stabilize the tracking error between the actual and reference trajectory to zero. To apply the adaptive control and assuming the parameter q^2/ϵ to be unknown, we set the new system from (1.21) and (1.23):

$$(C') \begin{cases} \dot{X} = Z \\ \dot{Z} = F_0(X,Z) + \varphi(X)\theta + U \\ Y = X \end{cases} \tag{1.24}$$

where $\varphi(X)$ is the electrostatic force without the parameter q^2/ϵ and θ the vector of unknown constant parameter and with:

$$F_0(X,Z) = \begin{pmatrix} F_{di_x} + F_{ci_x} + F_{vdwi_x} \\ F_{di_z} + F_{ci_z} + F_{vdwi_z} + W_a \end{pmatrix} \tag{1.25}$$

Using the change of variables given in (1.23), we construct the control law in two steps.

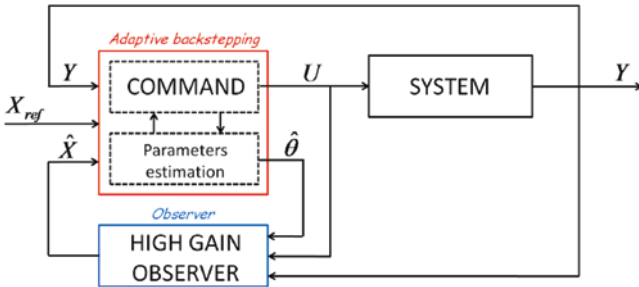


Fig. 1.5 MRI-based adaptive backstepping control with high-gain observer [30]

Step 1: Let

$$\begin{cases} \tilde{X} = X - X_r \\ \tilde{Z} = Z - Z_r - \alpha \end{cases} \quad (1.26)$$

denote the position and velocity error, respectively. X_r , $\dot{X}_r = Z_r$, and \ddot{X}_r are the desired reference trajectory, velocity, and acceleration, respectively. α is a stabilizing function.

A control Lyapunov function (CLF) candidate is:

$$V_1 = \frac{1}{2} \tilde{X}^T \tilde{X} + \frac{1}{2} (\hat{\theta} - \theta)^T \Gamma^{-1} (\hat{\theta} - \theta) \geq 0 \quad (1.27)$$

where $\hat{\theta}$ is the estimated parameter and Γ a positive-definite matrix. Calculating the derivative of V_1 along system (1.24), we obtain:

$$\dot{V}_1 = \tilde{X}^T (\dot{\tilde{Z}} + \alpha) + (\hat{\theta} - \theta)^T \Gamma^{-1} \dot{\hat{\theta}} \quad (1.28)$$

Setting $\alpha = -k_1 \tilde{X}$, we obtain

$$\dot{V}_1 = -k_1 \tilde{X}^T \tilde{X} + \tilde{X}^T \dot{\tilde{Z}} + (\hat{\theta} - \theta)^T \Gamma^{-1} \dot{\hat{\theta}} \quad (1.29)$$

The second term $\tilde{X}^T \dot{\tilde{Z}}$ will be cancelled at the next step. One can notice from the previous expressions that:

$$\dot{\tilde{X}} = \dot{X} - \dot{X}_r = \dot{\tilde{Z}} + \alpha = \dot{\tilde{Z}} - k_1 \tilde{X} \quad (1.30)$$

Step 2: From (1.26) and (1.30), we have:

$$\dot{\tilde{Z}} = F_0 + \varphi\theta + U - \dot{Z}_r + k_1 (\tilde{Z} - k_1 \tilde{X}) \quad (1.31)$$

In this step, the CLF is given by:

$$V_2 = V_1 + \frac{1}{2} \tilde{Z}^T \tilde{Z} \geq 0 \quad (1.32)$$

The derivative of V_2 along system (1.24) is expressed as:

$$\begin{aligned} \dot{V}_2 &= \dot{V}_1 + \tilde{Z}^T [F_0 + \varphi\theta + U + k_1 \tilde{Z} - k_1^2 \tilde{X} - \dot{Z}_r] \\ &= -k_1 \tilde{X}^T \tilde{X} + (\hat{\theta} - \theta)^T \Gamma^{-1} \dot{\hat{\theta}} + \tilde{Z}^T [(1 - k_1^2) \tilde{X} + F_0 + \varphi\theta + U + k_1 \tilde{Z} - \dot{Z}_r] \end{aligned} \quad (1.33)$$

Since we have $\theta = \hat{\theta} + (\theta - \hat{\theta})$, the derivative of V_2 along system (1.24) is expressed as:

$$\dot{V}_2 = -k_1 \tilde{X}^T \tilde{X} + \tilde{Z}^T \left[(1 - k_1^2) \tilde{X} + F_0 + \varphi \hat{\theta} + U + k_1 \tilde{Z} - \dot{Z}_r \right] + (\hat{\theta} - \theta)^T \Gamma^{-1} \left(\hat{\theta} - \Gamma \varphi^T \tilde{Z} \right) \quad (1.34)$$

To cancel the last term in (1.34), we set $\dot{\hat{\theta}} = \Gamma \varphi^T \tilde{Z}$ and to ensure \dot{V}_2 is negative definite, we set:

$$(1 - k_1^2) \tilde{X} + F_0 + \varphi \hat{\theta} + U + k_1 \tilde{Z} - \dot{Z}_r = -k_2 \tilde{Z} \quad (1.35)$$

To summarize, from (1.29), (1.34), and (1.35), the control law U and the update law for the parameter estimate $\hat{\theta}$ can be expressed as:

$$\begin{cases} U = \ddot{X}_r - (k_1 + k_2)(Z - \dot{X}_r) - (1 + k_1 k_2)(X - X_r) - F_0 - \varphi \hat{\theta} \\ \dot{\hat{\theta}} = \varphi^T [Z - \dot{X}_r + k_1(X - X_r)] \end{cases} \quad (1.36)$$

Considering the magnetization M to be unknown, the control law and the update law $\hat{\theta}$ are given by:

$$\begin{cases} u = \varphi^{-1} \left(\ddot{X}_r - (k_1 + k_2)(Z - \dot{X}_r) - (1 + k_1 k_2)(X - X_r) - F_0 - \varphi \hat{\theta} \right) \frac{1}{\hat{\theta}} \\ \dot{\hat{\theta}} = u^T \varphi^T [Z - \dot{X}_r + k_1(X - X_r)] \end{cases} \quad (1.37)$$

The backstepping control laws (1.36) and (1.37) require the knowledge of the robot's velocity in addition to its position, measured by the MRI system. Among the different observers cited in the literature, our attention was drawn to the high-gain observer. Unlike other observers, locally Lipschitzian state's functions ensure the convergence of the observer. This one requires the system to have canonical form which can be obtained using the change of variables of Eq. (1.23). From the force expressions, one can notice that only the drag force depends on the robot's position and velocity. Hence, only drag force has to be locally Lipschitzian to ensure the convergence of the observer given for the backstepping control law by [31]:

$$\begin{cases} \dot{\hat{X}} = \hat{Z} + L G_x (\hat{X} - Y) \\ \dot{\hat{Z}} = F_0(\hat{X}, \hat{Z}) + \varphi(\hat{X}) \hat{\theta} + U + L^2 G_z (\hat{X} - Y) \end{cases} \quad (1.38)$$

where L is the high gain and $G_x = \begin{pmatrix} g_1 & 0 \\ 0 & g_3 \end{pmatrix}$ and $G_z = \begin{pmatrix} g_2 & 0 \\ 0 & g_4 \end{pmatrix}$ are defined from the Hurwitz matrix Hu :

$$Hu = \begin{pmatrix} g_1 & 0 & 1 & 0 \\ 0 & g_3 & 0 & 1 \\ g_2 & 0 & 0 & 0 \\ 0 & g_4 & 0 & 0 \end{pmatrix}$$

1.5.2 MRI-Based Predictive Control Approach

Model predictive control (MPC) has become an area of significant research interest over the last 20 years. This interest has been powered by a stream of successful industrial applications. When focusing on linear (and unconstrained) discrete time transfer function models and quadratic cost functions, some of the best known approaches include the generalized predictive control (GPC) introduced by Clarke et al. [32] and the inner loop stabilizing stable predictive control.

MPC refers to a class of computer control algorithms which use an explicit process model to predict the future response of system. One way to design MPC is to use an extended state-space representation, which is given by:

$$\begin{cases} \dot{X}_{k+1} = AX_k + B \bullet u_k \\ Y_k = CX_k \end{cases} \quad (1.39)$$

where $\Delta u_k = u_k - u_{k-1}$ is the discrete difference operator. The predicted state vector at time $k + i$ is then computed from [33]:

$$\hat{X}_{(k+ik)} = A^i X_{(klk-1)} + \sum_{j=0}^{i-1} A^j B u_{k-j-1} \quad (1.40)$$

Then, the future outputs $Y_{(k+jk)}$ can be computed based on the plant for future times starting at time k using a recursion procedure, that is:

$$\hat{Y}_{(k+ik)} = C(A^i X_k) + \sum_{j=1}^i A^{i-j-1} B u_{k+i-jk} \quad (1.41)$$

Design criterion is defined for certain interval of predictions (several steps to future). It includes the part of control error, in which the model of system is covered (insertion of equations of prediction (1.7a and 1.7b)), and part of control actions, where the input energy (control actions) is weighted. This part redistributes control errors to individual steps of predictions and provides coupling within interval of predictions. Usual form of the criterion for predictive design is written as follows:

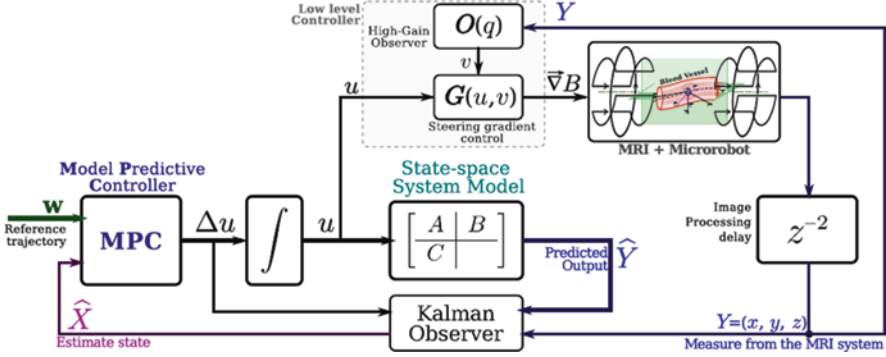


Fig. 1.6 MRI-based predictive control with Kalman observer [34]

$$J_k = \sum_{j=N_1+1}^{N_2} \left[Y_{k+j} W_{k+j}^T Q_Y Y_{k+j} W_{k+j} \right] + \sum_{j=1}^{N_u} \left[u_{k+j-1}^T Q_u u_{k+j-1} \right] \quad (1.42)$$

The criterion is expressed in step k . $N = N_2 - N_1$ is a horizon of prediction, and N_u is the control horizon. Q_Y and Q_u are output and input penalizations. Y_{k+j} and u_{k+j-1} are output and input (full or incremental) values. Finally, let us note how to construct real control actions at incremental algorithm: after computing a vector for whole horizon, only first control u_k is used; then to obtain the full control actions, the second line of Eq. (1.5) is applied. When using MPC in the state-space formulation and generally at the use of whichever state-space control, it is necessary to solve the question of availability of the state of the system (state vector). If it is not available and only system output from the measurement is known, then some state-space estimation has to be considered. Suitable, well-known solution of such estimation is the state-space observer based on Kalman filter (as shown in Fig. 1.6) [7, 34].

1.5.3 MRI-Based Optimal Control Approach

This section proposes to use the linear quadratic integral (LQI) controller. LQI control scheme is simple to implement and has been applied in a wide range of robotic applications [35, 36]. Basically, LQI computes an optimal state-feedback control law, like linear quadratic regulator (LQR), with an additional integral-action. Let's consider the linear system (1.13), in which the “integral state” is added on the state feedback [37].

$$w(t) = \int_0^t (y^*(t) - y(\tau)) d\tau \quad (1.43a)$$

and the following new dynamics:

$$\dot{w} = y^* - y = y^* - \mathbf{C}x \quad (1.43b)$$

where y^* is the reference input. Thus, the LQI control design addresses the augmented state $\chi = (x, w)^T$, that is, the new system:

$$\begin{aligned} \dot{\chi} &= \tilde{\mathbf{A}}\chi + \tilde{\mathbf{B}}u \\ y &= \tilde{\mathbf{C}}\chi \end{aligned} \quad (1.44)$$

with the matrices:

$$\tilde{\mathbf{A}} = \begin{bmatrix} \mathbf{A} & \mathbf{0} \\ \mathbf{C} & \mathbf{0} \end{bmatrix}; \tilde{\mathbf{B}} = \begin{bmatrix} \mathbf{B} \\ \mathbf{0} \end{bmatrix}; \tilde{\mathbf{C}} = [\mathbf{C} \ \mathbf{0}] \quad (1.45)$$

Thus, the objective is to determine an optimal control law minimizing the cost functional:

$$J(\mathbf{u}) = \int_0^{\infty} \left\{ \chi^T \mathbf{Q} \chi + u^T \mathbf{R} u + 2\chi^T \mathbf{N} u \right\} dt \quad (1.46)$$

where \mathbf{Q} , \mathbf{R} , and \mathbf{N} are symmetric, positive (semi-)definite weighting matrices, that is, the LQI design parameters. This is the LQI problem, and, considering a stabilizable and detectable system, its solution yields the linear state-feedback control law:

$$u = -\left(\mathbf{R}^{-1} \tilde{\mathbf{B}} \mathbf{P} + \mathbf{N}^T \right) \chi \quad (1.47)$$

where $\left(\mathbf{R}^{-1} \tilde{\mathbf{B}} \mathbf{P} + \mathbf{N}^T \right)$ is the optimal gain matrix, with \mathbf{P} the solution of the well-known continuous time algebraic Riccati equation (CARE):

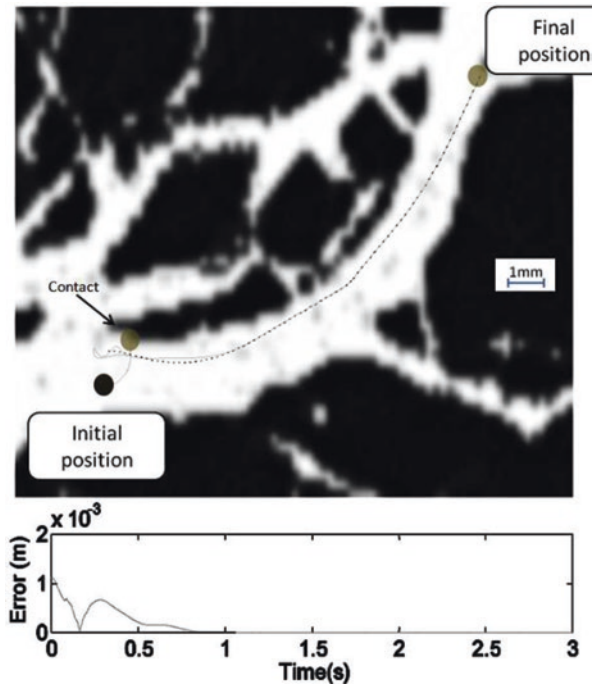
$$\mathbf{P} \tilde{\mathbf{A}} + \tilde{\mathbf{A}}^T \mathbf{P} - \left(\mathbf{P} \tilde{\mathbf{B}} + \mathbf{N} \right) \mathbf{R}^{-1} \left(\tilde{\mathbf{B}}^T \mathbf{P} + \mathbf{N}^T \right) + \mathbf{Q} = 0 \quad (1.48)$$

1.6 Results

Simulations are performed by taking into account the limitations of a clinical MRI system [38]. The magnetic field of $3T$ is strong enough to assume that the particles reach their saturation magnetization. The magnetic field gradients are used to control the microrobot's motion in the human body. As stated, these MRI devices can provide a maximum magnetic field gradient of $80mT.m^{-1}$. In order not to exceed the capacity of MRI systems, the applied control law is now corrected as:

$$U_a(t) = \frac{U(t)}{k(t)} \text{ with } k(t) = \max \left[1; \frac{U(t)}{U_{sat}} \right] \quad (1.49)$$

Fig. 1.7 Reference (black dash line) and simulated (gray solid line) trajectories and tracking error [28]



Furthermore, the pulsative blood's velocity is modeled by an affine combination of a time-varying periodic flow with a spatial parabolic shape. So as to simplify the analytical expression, but with no loss of generality, we only consider the first terms in the time-varying Fourier series of the physiological pulse. We demonstrate in the following some results that have been obtained using the different MRI-based control approaches developed in Sect. 1.4.

First, Figs. 1.7, 1.8, 1.9 and 1.10 show the robustness gains model uncertainties of the backstepping approach developed in Sect. 1.4.1 [30, 38]. As example, the magnetization of the NdFeB microrobot is chosen as the one of the most sensitive parameters of the model, as it appears in factor of the control inputs. This second simulation is performed assuming an error of 5% from the nominal magnetization value. Figure 1.7 illustrates that the closed-loop system is stable and the tracking is efficient. The magnetization of the microrobot is underestimated, so the commands will be higher during this transient phase. This phase is critical since the control inputs reach the actuator saturation and the parameter is not updated. One can notice that the microrobot is moving rapidly toward the reference trajectory and the collision with the blood vessel's wall is inevitable by twice. The estimated position of the microrobot (Fig. 1.8) and the estimated velocity (Fig. 1.9) are highly disturbed during this phase. The estimation of the parameter (Fig. 1.10) drops after the collision before converging. At time $t = 1$ s, one can notice that the parameter has converged to zero and the robot is stabilized along the reference trajectory. However, when the blood flow is too high, the adaptive controller/observer demonstrates some

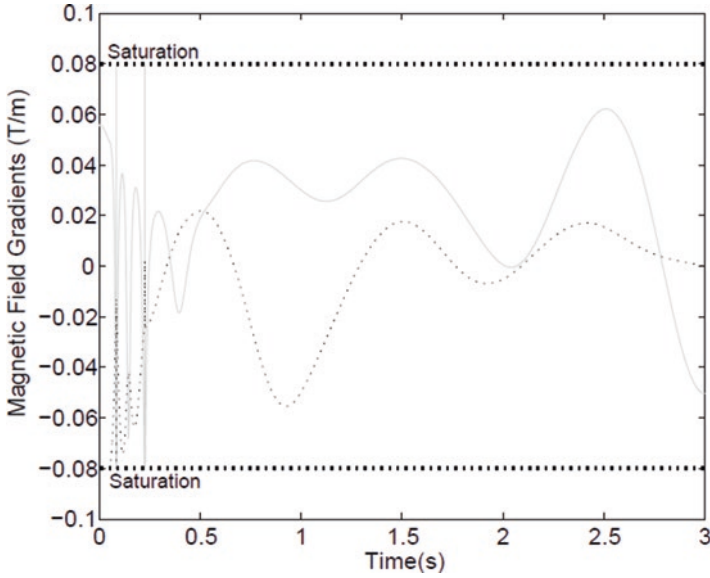
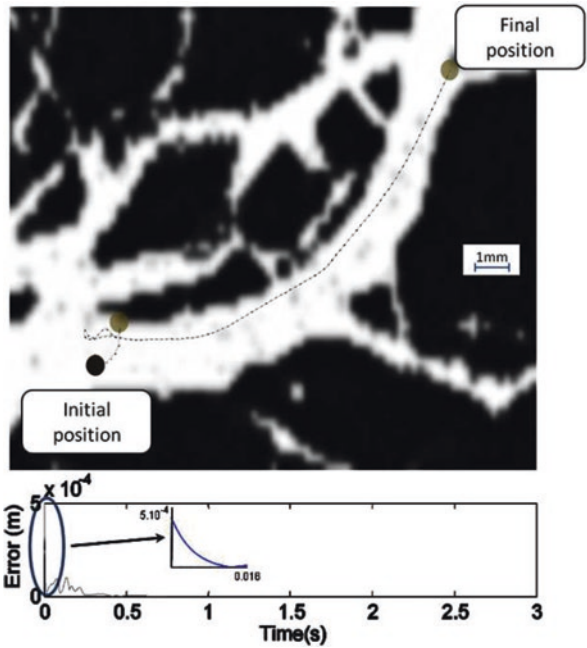


Fig. 1.8 Control input: magnetic field gradients on i axis (black dash line) and on k axis (gray solid line) [28]

Fig. 1.9 Simulated (gray solid line) and estimated (black dash line) trajectories and estimation error [28]



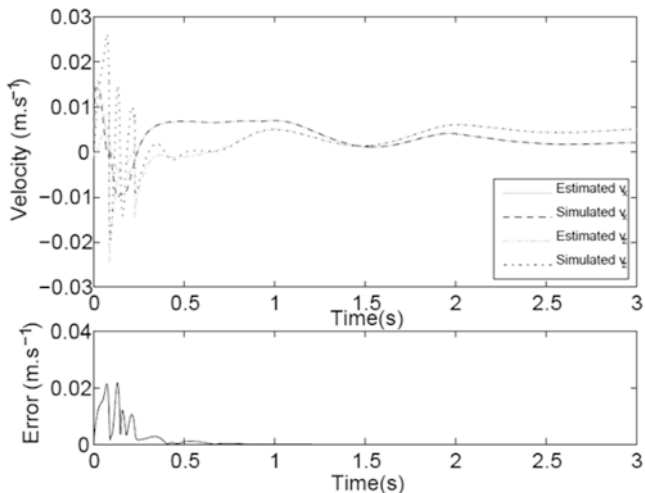


Fig. 1.10 Simulated and estimated velocities along i and k axes and velocity estimation error [28]

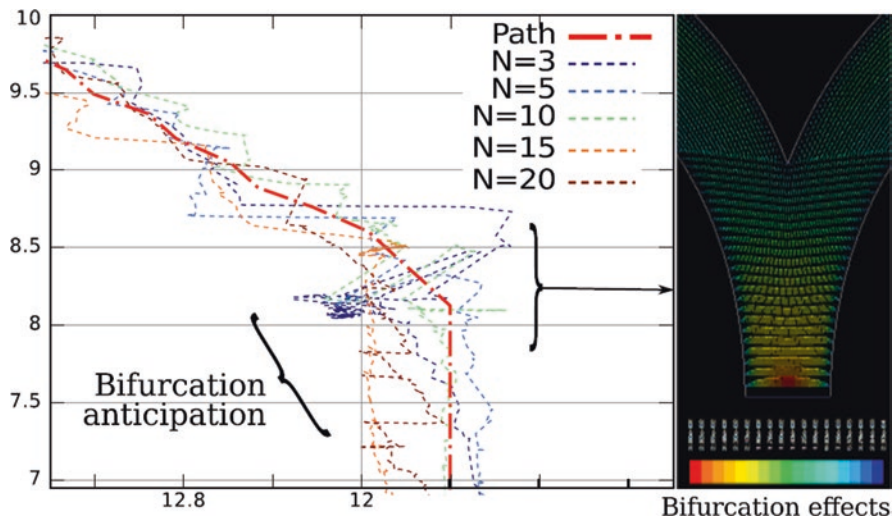


Fig. 1.11 Path tracking with generalized predictive controller (GPC) with a varying horizon N and blood flow conditions with pulsatile flow [33]

limitations in the navigation control strategy. Experiments are also conducted considering pulsatile flow to validate the proposed predictive navigation control strategy. Figure 1.11 depicts the overall tracking error for different the GPC horizon values N within a biological fluid [33]. As previously stated, increasing the prediction horizon increases the anticipatory behavior of the predictive navigation scheme. Comparing to the static flow experiments, one can see that the presence of the

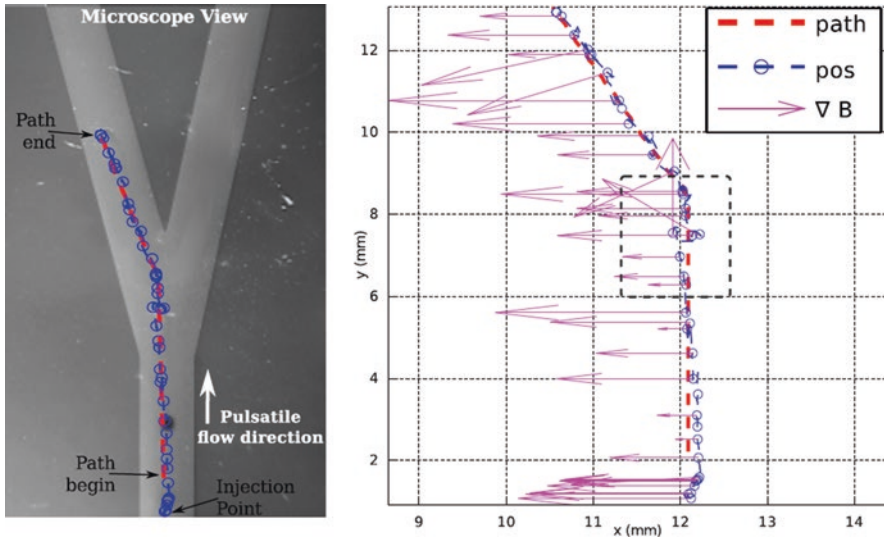


Fig. 1.12 Path tracking with generalized predictive controller (GPC) horizon $N = 10$ and blood flow conditions with pulsatile flow [33]

pulsatile flow, the amplitude value of the applied gradients increases greatly. It can be explained by the need to counterbalance the antagonistic pulsatile flow during navigation. Figure 1.12 shows the case where the $N = 10$ using a biological fluid of 50% water–50% glycerol mixture. The experimental results illustrate that the controller remains robust even in the presence of pulsatile flow for different mixtures. The analysis of the results points out several remarks on the proposed model given in Sect. 1.3. First, the proposed predictive navigation strategy considers linear assumptions on the Stokes' drag force, neglects the electrostatic force, and assumes a Newtonian flow. The GPC proved to be sufficiently robust against modeling uncertainties such as those at the bifurcation area where non-Newtonian model applies and at the injection point that produces flow turbulences [34]. In both cases, the microrobot follows the trajectory in a robust way. The main drawback of the predictive navigation approach remains on its anticipatory behavior observed when the time horizon N increases. For high prediction horizon values, the microrobot tends to leave the reference path (increasing the tracking error) by anticipating the bifurcation branch. For low prediction horizon values, the bifurcation effects influence the microsphere behavior.

1.7 Conclusion

This chapter focuses on an innovative method to perform targeted therapy by navigating in the cardiovascular system using a MRI system. The idea is the use of the magnetic gradient coils of a clinical MRI to pull a therapeutic microrobot to the

desired area as well as providing fine observation of its motion in vasculature. To perform this task, a precise and highly nonlinear model is presented for a MRI-guided microrobot in blood vessels. The microrobot is a polymer-bonded aggregate of nanoscale ferromagnetic particles which is subjected to numerous external forces. This model takes into account the non-Newtonian behavior of the blood and the properties of blood vessels such as electrostatic, van der Waals, and contact forces. An optimal trajectory is then derived from this precise model, so as to minimize the control efforts. Since the modeling describes both physical and physiological forces, it has affected many biological parameter uncertainties. To robustify the tracking with respect to these uncertainties, an adaptive backstepping law has been developed and exposed in this chapter. The aim of the reviewed controllers is twofold. First is to ensure the stability of the system. Second is to perform an online estimation of some key parameters. As these control design requires the velocity of the microrobot, which cannot be measured by the MRI system, different observers are proposed to reconstruct the full state. The challenges related to targeted therapy through MRI-guided nanorobots are wide, and this chapter cannot address all the connected research topics: experimental setups designs, increased precision of the agglomerate's position using its magnetic properties, physical properties of self-assembly structures, path planning, etc. A crucial hindrance of MRI-based navigation stems from the strong limitations on the magnetic gradient coils in clinical MRI devices. Since propulsion is provided by the volumetric magnetic forces, whereas the drag force is mainly surfacic, the smaller the aggregate, the higher the required control forces with respect to hydrodynamic perturbations. At the nanoscale, magnetic forces induced by available MRI devices are not sufficient to steer the agglomerate within the smallest blood vessels, which reduces the accuracy of the drug delivery. Current research aims to overcome this limitation by upgrading the MRI systems with additional gradient steering coils in order to increase their amplitude and, in turn, provide a more precise delivery of the drugs in the vicinity of the diseased cells.

References

1. Vartholomeos, P., Fruchard, M., Ferreira, A., & Mavroidis, C. (2011). MRI-guided Nanorobotic Systems for Therapeutic and Diagnostic Applications. *Annual Review of Biomedical Engineering*, 13, 157–184.
2. Folio, D., & Ferreira, A. (2017). 2D robust magnetic resonance navigation of a ferromagnetic microrobot using Pareto optimality. *IEEE-Transactions on Robotics*, 33(3), 583–593.
3. Gillies, G. T., Ritter, R. C., Broaddus, W. C., et al. (1994). Magnetic manipulation instrumentation for medical physics research. *Review of Scientific Instruments*, 65(3), 533–562.
4. Quate, E. G., Wika, K. G., Lawson, M. A., et al. (1991). Goniometric motion controller for the superconducting coil in a magnetic stereoaxis system. *IEEE Transactions on Biomedical Engineering*, 38, 899–905.
5. Takeda, S.-I., Mishima, F., Fujimoto, S., Izumi, Y., & Nishijima, S. (2006). Development of magnetically targeted drug delivery system using superconducting magnet. *Journal of Magnetism and Magnetic Materials*, 311, 367–371.

6. Mathieu, J., Beaudoin, G., & Martel, S. (2006). Method of propulsion of a ferromagnetic Core in the cardiovascular system through magnetic gradients generated by an MRI system. *IEEE Transactions on Biomedical Engineering*, 53(2), 292–299.
7. Mathieu, J.-B., & Martel, S. (2007). Magnetic microparticle steering within the constraints of an MRI system: Proof of concept of a novel targeting approach. *Biomedical Microdevices*, 9, 801–808.
8. Tamaz, S., Gourdeau, R., Chanu, A., Mathieu, J.-B., & Martel, S. (2008). Real-time MRI-based control of a ferromagnetic Core for endovascular navigation. *IEEE Transactions on Biomedical Engineering*, 55(7), 1854–1863.
9. Martel, S., Mathieu, J.-B., Felfoul, O., et al. (2007). Automatic navigation of an untethered device in the artery of a living animal using a conventional clinical magnetic resonance imaging system. *Applied Physics Letters*, 90(11), 114105.
10. Yesin, K. B., Vollmers, K., & Nelson, B. J. (2006). Modeling and control of untethered bio-microbots in a fluidic environment using electromagnetic fields. *International Journal of Robotics Research*, 25, 527–536.
11. Jun, Y.-W., Seo, J.-W., & Cheon, J. (2007). Nanoscaling laws of magnetic nanoparticles and their applicabilities in biomedical sciences. *Accounts of Chemical Research*, 41(2), 179–189.
12. Dreyfus, R., Beaudry, J., Roper, M. L., et al. (2005). Microscopic artificial swimmers. *Nature*, 437(6), 862–865.
13. Behkam, B., & Sitti, M. (2006). Design methodology for biomimetic propulsion of miniature swimming robots. *ASME Journal of Dynamic Systems, Measurement and Control*, 128, 36–43.
14. Yesin, K. B., Vollmers, K., & Nelson, B. J. (2004). Analysis and design of wireless magnetically guided microrobots in body fluids. In *Proceedings of the IEEE international conference on robotics and automation, New Orleans, USA* (pp. 1333–1338).
15. Abbott, J. J., Peyer, K. E., Lagomarsino, M. C., et al. (2007). How should microrobots swim? In *International symposium on robotics research*.
16. Lee, H., Purdon, A. M., Chu, V., & Westervelt, R. M. (2004). Controlled assembly of magnetic nanoparticles from magnetotactic bacteria using microelectromagnets arrays. *Nano Letters*, 4(5), 995–998.
17. Martel, S., Mohammadi, M., Felfoul, O., Lu, Z., & Pouponneau, P. (2009). Flagellated magnetotactic bacteria as controlled MRI-trackable propulsion and steering systems for medical nanorobots operating in the human microvasculature. *The International Journal of Robotics Research*, 28(4), 571–582.
18. Martel, S., Tremblay, C. C., Ngakeng, S., & Langois, G. (2006). Controlled manipulation and actuation of micro-objects with magnetotactic bacteria. *Applied Physics Letters*, 89(23), 233904.
19. Plowman, S. A., & Smith, D. L. (1997). *Exercise physiology*. Needham Heights: Allyn and Bacon.
20. White, F. (1991). *Viscous fluid flow*. New York: McGraw Hill.
21. Kehlenbeck, R., & Di Felice, R. (1999). Empirical relationships for the terminal settling velocity of spheres in cylindrical columns. *Chemical Engineering & Technology*, 21, 303–308.
22. Francis, A. W. (1933). Wall effect in falling ball method for viscosity. *Physics*, 4, 403–406.
23. Munroe, H. S. (1888). The English versus the continental system of jiggling is close sizing advantageous? *Transactions of the American Institute of Mining, Metallurgical, and Petroleum Engineers*, 17.
24. Tijskens, E., Ramon, H., & De Baerdemaeker, J. (2003). Discrete element for process simulation in agriculture. *Journal of Sound and Vibration*, 266, 493–514.
25. Varthomoleos, P., & Mavroidis, C. (2020). Magnetic targeting of aggregated nanoparticles for advanced lung therapies: A robotics approach. In: *3rd IEEE International Conference on Biomedical Robotics and Biomechatronics*, 26–29 September 2010, Tokyo, Japan.
26. Hays, D. (1991). Electrostatic adhesion of non-uniformly charged dielectric sphere. *International Physics Conference Series*, 118, 223–228.

27. Hays, D. (1991). Role of electrostatics in adhesion, in fundamentals of adhesion. *PLENUMPRESS*.
28. Arcese, L., Fruchard, M., & Ferreira, A. (2012). Endovascular magnetically-guided robots: Navigation modeling and optimization. *IEEE-Transactions on Biomedical Engineering*, 59(4), 977–987.
29. Belharet, K., Folio, D., & Ferreira, A. (2013, April). Simulation and planning of a magnetically actuated microrobot navigating in the arteries. *IEEE-Transactions on Biomedical Engineering*, 60(4), 993–1001.
30. Arcese, L., Fruchard, M., & Ferreira, A. (2013). Adaptive controller and observer for a magnetic microrobot. *IEEE-Transactions on Robotics*, 29(4), 1060–1067.
31. Sadelli, L., Fruchard, M., & Ferreira, A. (May 2017). 2D observer-based control of a vascular microrobot. *IEEE-Transactions on Automatic Control*, 62(5), 2194–2206.
32. Clarke, D., Mohtadi, C., & Tuffs, P. (1987). Generalized predictive control – part I & II. *Automatica*, 23, 137–160.
33. Belharet, K., Folio, D., & Ferreira, A. (2011, May). 3D controlled motion of a microrobot using magnetic gradients. *Advanced Robotics*, 25(8), 1069–1083.
34. Belharet, K., Folio, D., & Ferreira, A. (2020) Endovascular Navigation of Ferromagnetic Microrobot using MRI-based Predictive Control. In *IEEE International Conference on Intelligent Robots and Systems (IROS'10)*, Taipei, Taiwan, October 18–22, 2010, pp. 2804–2809.
35. Shin, J., Nonami, K., Fujiwara, D., & Hazawa, K. (2005). Model-based optimal attitude and positioning control of small-scale unmanned helicopter. *Robotica*, 23(01), 51–63.
36. Seto, K., Fuji, D., Hiramathu, H., & Watanabe, T. (2002). Motion and vibration control of three dimensional flexible shaking table using LQI control approach. In *Proceedings of American control conference* (Vol. 4, pp. 3040–3045). IEEE.
37. Mellal, L., Folio, D., Belharet, K., & Ferreira, A. (2016). Optimal Control of Multiple Magnetic Microbeads Navigating in Microfluidic Channels. In *IEEE International Conference on Robotics and Automation (ICRA16)*, Stockholm, Sweden, May 16–21, 2016.
38. Arcese, L., Fruchard, M., & Ferreira, A. (2009). *Nonlinear modeling and robust controller-observer for a magnetic microrobot in a fluidic environment using MRI gradients*. IROS.

Chapter 2

Ultrasound-Powered Micro-/Nanorobots: Fundamentals and Biomedical Applications



Liqiang Ren, Fernando Soto, Luyang Huang, and Wei Wang

2.1 Introduction

A micro-/nanorobot is a small, functional device that moves, senses, and operates at a micro- or nanoscale. As this book aptly illustrates, plenty of approaches have been developed to synthesize and power micro-/nanorobots, each with a unique strategy and emphasis. Prominent examples include, on the small side, molecular machines that change configurations under external cues [1, 2], and, on the large side, MEMS/NMES devices that trap cells and inject chemicals [3, 4]. The current chapter, however, deals with the type that is more commonly referred to as micro-/nanomotors, synthetic microswimmers, or colloidal motors that are untethered and swim autonomously in a liquid environment [5, 6]. They do so by harvesting energy stored in their environments, in the form of chemical, electromagnetic, light, heat, and sound energy, the last of which will be the focus of this chapter.

However, before we expand on ultrasound-powered micro-/nanorobots, let us first provide a brief background to set the stage. Micro-/nanorobots, or micro-/nanomotors to be more specific, have been around for roughly two decades, starting from the pioneering discoveries in the early twenty-first century by groups at Penn State and University of Toronto [7, 8], which reported that bimetallic microrods are able to self-propel in aqueous solutions of hydrogen peroxide (H_2O_2). This was the first discovery of synthetic materials that move like living microorganisms and has thus

L. Ren

Department of Engineering Science and Mechanics, The Pennsylvania State University,
University Park, PA, USA

F. Soto

School of Medicine, Stanford University, Palo Alto, CA, USA

L. Huang · W. Wang (✉)

School of Materials Science and Engineering, Harbin Institute of Technology (Shenzhen),
Shenzhen, Guangdong, China

e-mail: weiwangsz@hit.edu.cn

sparked wide interests and intense research efforts in the years that followed (reviewed by other chapters in this book). Ever since this early discovery, the research interest has been in two directions. On the one hand, micro-/nanomotors are envisioned as prototype microrobots for a variety of fascinating operations, such as minimally invasive surgeries [9, 10], biomedical sensing [11, 12], environmental remediation [13–15], and micro-assembly [16–18]. On the other hand, soft matter physicists see micro-/nanomotors as useful model systems in the studies of active matter [19, 20], a physical concept that encompasses anything that self-propels and exhibits collective behaviors. It is these two branches of research, one practical and one fundamental, that drive most of micro-/nanomotor research today.

For either purpose, the power source is one of the key elements in the design of a micro/nanomotor, together with the capability to control, and the integration of useful functionalities. Limited by the physics operating at micro- and nanoscale, in particular Brownian motion and a viscous medium (i.e., low Reynolds number) [21], many classical, inertia-based methods to power macroscopic objects fail for micro-/nanomotors, where surface effects dominate [22]. As a result, the majority of propulsion mechanisms for micro-/nanomotors circumvent the so-called scallop theorem by exploiting the interesting chemistry and physics at the particle-liquid interface. For example, a major category of micro-/nanomotors is powered by surface chemistry. They move by ejecting bubbles [8, 23, 24], or by a slip flow arising from chemical gradients (i.e., self-electrophoresis or self-diffusiophoresis) [25–27]. However, all chemically powered micro-/nanomotors require some kind of fuel in their environment, or on board, or both, which to say the least causes inconvenience. Alternatively, fuel-free micro-/nanomotors are gaining popularity in practical scenarios where the presence of chemicals or chemical reactions is not desirable [28, 29]. These micro-/nanomotors can be powered by an external magnetic field, by a DC or AC electric field, by light of various wavelengths and intensity, and by ultrasound.

Ultrasound, sound waves of a frequency beyond human hearing (>20 kHz), has long been used in manipulating microscopic or even nanoscopic objects [30]. More recently, the discovery of ultrasound-powered micro-/nanomotors opens a new chapter in its usefulness [31] and ushered in new possibilities of functional micro-machines in biologically relevant environments. In the remainder of this book chapter, we give an extensive review of the progress made in micro-/nanomotors powered by ultrasound, with an emphasis in their operating principles and their usefulness and limitations in biomedical applications.

This book chapter is organized as follows. In Sect. 2.2, we briefly review the fundamentals of ultrasound physics, in particular acoustic radiation forces and acoustic streaming, two concepts that are often encountered in the literature of micro-/nanomotors and critical in their designs. Ultrasound micro-/nanomotors of four types, namely, microrod streamers, bubble streamers, flagella streamers, and acoustic jets, are then thoroughly described and discussed in Sect. 2.3. Finally, in Sect. 2.4, we comment on the future prospects of ultrasound-powered micro-/nanomotors. Throughout this book chapter, we connect the underlying principles of ultrasound-related physical effects to the propulsion of a micro-/nanomotor, and

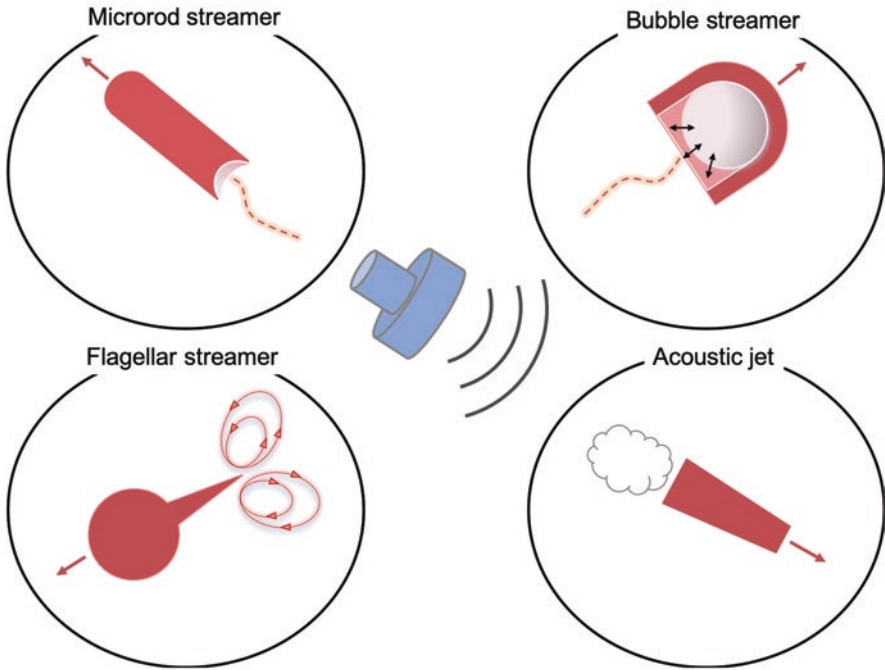






Fig. 2.1 A general scheme of the four types of ultrasound micro-/nanomotors discussed in this book chapter

highlight the various challenges that needed to be addressed before these micro-/nanomotors can be translated into clinical scenarios. It is our sincere hope that this book chapter will serve as an access point for scientists and engineers interested in the development of micro-/nanomachines (Fig. 2.1; Table 2.1).

2.2 Fundamentals of Ultrasound Physics

Before we discuss the various types of nanomotors powered by ultrasound, it is instrumental to give a brief introduction to how ultrasound affects a colloidal particle suspended in water. In particular, we focus on two acoustic effects—acoustic radiation forces and acoustic streaming—that are most relevant for micro-/nanomotors in ultrasound. Readers interested in the details of these effects are directed to more comprehensive reviews on acoustic radiation forces [30, 32] and acoustic streaming [33, 34] (Fig. 2.2).

Table 2.1 Four types of ultrasound-powered micro-/nanomotors

Motor type	Operating principles	Main features	Operating frequencies	Limitations
 <p>Microrod streamers</p>	Steady fluid streaming around an asymmetrically shaped colloidal particle	<ul style="list-style-type: none"> Operates on a levitational plane 3 modes of motion Most popular for biological applications 	<ul style="list-style-type: none"> Depends on the size of the acoustic chamber 3–4 MHz for a chamber of 200 μm tall 	<ul style="list-style-type: none"> Requires a standing wave Doesn't work for polymeric or symmetrically shaped particles
 <p>Bubble streamers</p>	Cavitation microstreaming near an oscillating, trapped microbubble	<ul style="list-style-type: none"> Only requires traveling waves Strong Bjerknes force leads to motor-motor and motor-structure attraction Able to manipulate colloidal particles, such as cells, and to move in 2D or 3D space Can be fabricated by lithography, 3D printing, or chemical/physical deposition + etching 	<ul style="list-style-type: none"> Related to the resonance frequency of the bubble, which is further governed by the bubble size MHz for bubbles of μm in sizes 	<ul style="list-style-type: none"> Fabrication can be complicated and resource-heavy, with limited yields Low reproducibility and short lifetime of the gas bubbles
 <p>Flagella streamers</p>	Microstreaming near a flexible body or a sharp edge	<ul style="list-style-type: none"> Only requires traveling waves The operating principle can also be used to manipulate microparticles 	<ul style="list-style-type: none"> Typically in the high kHz regime but difficult to predict 	<ul style="list-style-type: none"> Requires higher acoustic pressures than bubble streamers Difficult to predict the resonant frequency
 <p>Acoustic jets</p>	Droplet vaporization ignition: fast vaporization of liquid droplets trapped in a microtube via focused ultrasound	<ul style="list-style-type: none"> Powerful and easy to activate Only requires traveling waves 	<ul style="list-style-type: none"> Typically in the MHz regime 	<ul style="list-style-type: none"> Can only be activated once Poor control over speed or directionality

2.2.1 Acoustic Radiation Forces

An object in the path of a propagating sound wave generates its own scattered wave and in doing so experiences pressure because of momentum transfer. This pressure, termed acoustic radiation pressure, when integrated over the entire body of the object, leads to a net force termed acoustic radiation forces, whose presence has

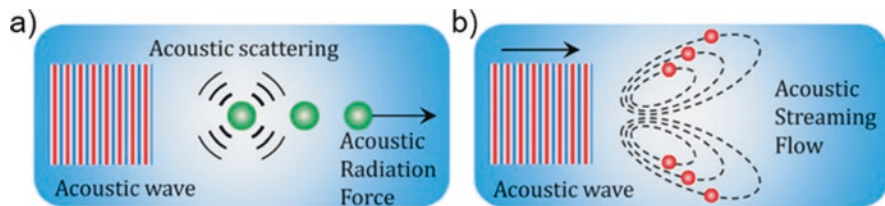


Fig. 2.2 Cartoon illustrations of acoustic radiation forces and acoustic streaming. **(a)** Acoustic wave is scattered by a large particle. The original and the scattered acoustic waves generate an acoustic radiation force on the particle. **(b)** Acoustic waves generate streaming in the fluid and small particles are convected by the streaming flow. The dynamic of a particle under ultrasound can be dominated by either the acoustic radiation force or acoustic streaming, depending on the diameter and density of the particle. Reproduced with permission [35]. **Copyright 2016, American Chemical Society**

long been known since the nineteenth century. Later, a series of seminal work from King, Yosioka and Kawasima, and Gorkov established the governing equations that describe the acoustic radiation forces acting on a small particle immersed in a viscous liquid [32]. For the special case of a standing ultrasound wave (e.g., typical for the microrod streamers discussed below), the acoustic radiation force becomes quite strong and is governed by [32]:

$$F = - \left(\frac{\pi p_0^2 V \beta_w}{2\lambda} \right) \Phi(\beta, \rho) \sin(2kd) \quad (2.1)$$

where k is the wave number, λ is the wavelength, V is the volume of the particle, and d is the distance between the particle and the node or antinode of the standing wave. The magnitude of this force is proportional to the square of the pressure amplitude (p_0) and the volume of the particle V . The term $\Phi(\beta, \rho)$ in Eq. 2.1 is the acoustic contrast factor, given by:

$$\Phi(\beta, \rho) = \frac{5\rho_c - 2\rho_w}{2\rho_c + \rho_w} - \frac{\beta_c}{\beta_w} \quad (2.2)$$

where ρ_c and ρ_w are the density of the particle and medium, respectively, and β_c and β_w are the compressibility of the particle and medium, respectively. If $\Phi(\beta, \rho) > 0$, the particle will be forced to the pressure nodes; otherwise, it will move to the antinodes. Intuitively, the larger the absolute value of $\Phi(\beta, \rho)$ of the particle, the larger the radiation force it experiences, and the stronger it responds to an incoming sound wave. This will become important in Sect. 2.3.1 for understanding why metal particles (of a larger ρ and β) are more efficient micro-/nanomotors in ultrasound than polymers.

Under the effect of an acoustic radiation force, a colloidal particle typically found in a micro-/nanomotor experiment, such as metal rods, polymer microspheres, etc., is transported to the pressure node of the standing wave, which often takes the

form of a nodal plane positioned vertical to the sound propagation direction in an acoustic chamber. The number and position of the nodal plane is governed by:

$$h = \frac{1}{2} n \lambda = \frac{1}{2} n \frac{c}{f}, n = 1, 2, 3, \dots \quad (2.3)$$

where h is the height of the acoustic chamber, λ is the wavelength of ultrasound, f is its frequency, n are integers, and c is the speed of sound in the medium ($c = 1492 \text{ m}\cdot\text{s}^{-1}$ in water). For a typical chamber of $200 \text{ }\mu\text{m}$ tall (e.g., made of two glass slides stacked on each side of a silicone spacer with a circular hole) and filled with water, the lowest resonance frequency is 3.73 MHz , corresponding to a nodal plane located at half the height of the chamber, $100 \text{ }\mu\text{m}$ from the floor or the ceiling. Doubling the frequency will generate two nodal planes that are evenly separated in the chamber by $66.7 \text{ }\mu\text{m}$ and so on. However, we note that experiments with ultrasound micro-/nanomotors have rarely explored a system with more than one nodal plane.

In a typical experiment, upon turning on an ultrasound wave of a resonance frequency, colloidal particles that have settled on the chamber bottom are quickly levitated to the nodal plane by an acoustic radiation force along the wave propagation direction. Once there, levitated particles experience an additional lateral acoustic radiation force that transports them to specific points on the nodal plane of maximum acoustic kinetic energy density, likely caused by an inhomogeneity from the energy distribution on the nodal plane for a number of possible reasons [30]. This lateral force is especially important in understanding the distribution of microrod streamers into rotating rings, and why they are only found at certain spots on the nodal plane (see Sect. 2.3.1).

What we have described above is known as the primary acoustic radiation force, levitating particles to a nodal plane and transporting them to certain “hot spots” on the plane. A secondary acoustic radiation force is also present between two colloidal particles, arising from the interaction between their scattered waves. This is also known as Bjerknes forces [36–38] and is attractive for particles on the same levitation plane but repulsive for those located along the wave propagation direction. The Bjerknes force is significant only when particles are located in close proximity, or if they are very compressible (e.g., bubbles or cells). It is partly responsible for the clumping of microrod streamers on a levitation plane (Sect. 2.3.1), and for the attraction between a bubble streamer to a nearby substrate (Sect. 2.3.2).

To summarize, ultrasound-powered micro-/nanomotors that we describe in this chapter experience a total of three types of acoustic radiation forces. An axial radiation force moves the particles strongly toward the pressure node (in the case of a standing wave), or weakly toward the pressure minimum in the case of traveling wave (often ignored in micro-/nanomotor literature). Once a particle is on a nodal plane, lateral radiation forces push it to acoustic hot spots defined by the energy landscape on that plane. Finally, secondary radiation forces (Bjerknes forces) induce the aggregation of nanomotors, or their attachment to the substrate in the case of bubble streamers. Note that none of the above forces directly propels a micro-/

nanomotor into autonomous motion. Rather, these motors are powered either by surface microstreaming (Sect. 2.3.1–2.3.3) or by jet streaming (Sect. 2.3.4), effects that we elaborate below.

2.2.2 Fundamentals of Acoustic Streaming

Acoustic streaming, also known as steady streaming, is a net fluid flow caused by the acoustic energy dissipation in a viscid fluid. When propagating in a fluid, acoustic waves force fluid elements to oscillate sinusoidally. The acoustic waves keep a constant shape during the propagation if it is an ideal fluid; therefore the time-average displacement of the fluid elements is zero. However, a viscous fluid will introduce fluctuations to the velocity and amplitude of the oscillation, resulting in a non-zero time-average displacement of the fluid elements, i.e. a net fluid flow. This nonlinear phenomenon was first theoretically studied by Rayleigh via a successive approximation technique [39], in which the acoustic streaming was given by the higher orders governing equations. The later development of the acoustic streaming theory has followed Rayleigh approach. However, it is difficult to have a unified analytical description for all the situations since acoustic streaming can vary dramatically in its speed, length scale, flow patterns, and so on. Numerical simulation has been extensively applied to study streaming that occurs in various circumstances. Here we will qualitatively introduce two common types of acoustic streaming. More detailed theoretical discussions are beyond the scope of this chapter, but interested readers may refer to the reference [33, 34, 40].

Depending on the mechanism of the acoustic energy dissipation, acoustic streaming could be classified as being driven by either bulk dissipation or boundary dissipation. The acoustic streaming driven by bulk dissipation is called as “Eckart streaming” or “quartz wind.” When an acoustic wave propagates in a bulk fluid, the viscosity of the fluid causes the amplitude of the acoustic pressure to decrease along the direction of the propagation. The dissipated energy converts to a steady momentum flux, forming a jet of fluid moving in the same direction. Since the acoustic attenuation in fluid is typically small and is proportional to the square of the acoustic frequency, significant Eckart streaming can only be observed in cases of high acoustic frequency and amplitude. It also usually requires the dimension of the fluid container in the propagating direction to be much larger than the wavelength of the acoustic wave. This type of acoustic streaming is less relevant to the propulsion of micro-/nanomotors, unless it induces bulk convection and leads to motor drifting.

The streaming driven by boundary dissipation is generally introduced at a solid/fluid interface. As the solid boundary is no-slip, the velocity of the acoustically oscillated fluid elements decreases dramatically to zero at the boundary from a non-zero velocity away from the boundary. The velocity drop is confined in a thin viscous boundary layer, the *Stokes layer*, with a thickness of $\delta = \sqrt{2\nu/\omega}$. Here ν is the kinematic viscosity of the fluid, and ω is the angular frequency of the acoustic wave, and δ is in submicron scale for megahertz acoustic waves propagating in water. The

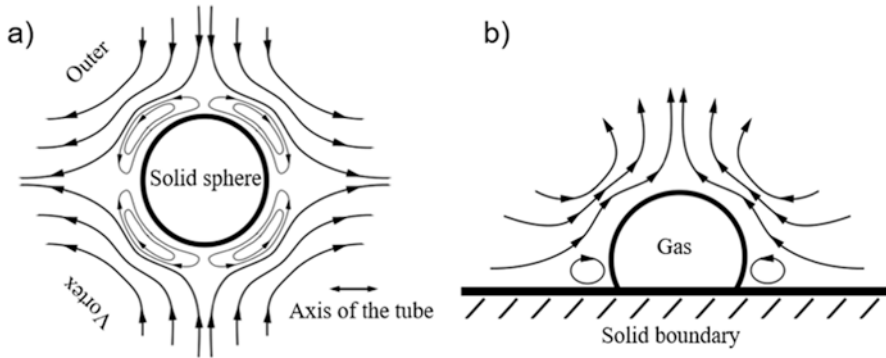


Fig. 2.3 Acoustic streaming. (a) Inner and outer layer acoustic streaming patterns around a rigid sphere in a standing acoustic field in a Kundt's tube. (b) acoustic cavitation microstreaming pattern generated by a gas bubble resting on a solid boundary. Reproduced with permission [43]. Copyright 2005, Acoustical Society of America

significant energy dissipation in such a thin layer leads to strong vortices inside this layer, named as inner boundary layer streaming or “Schlichting streaming.” Because of fluid continuity, the inner boundary layer streaming further generates counter-rotating streaming in the bulk of the fluid, called the outer boundary layer streaming or “Rayleigh streaming.” Inner and outer boundary layer streaming are typically observed in microfluidic chambers or channels with a characteristic length scale close to or smaller than the acoustic wavelength. The streaming pattern introduced by standing acoustic waves in rectangular-shaped channels or on the surface of spherical particles has been extensively analyzed and well understood both theoretically and experimentally [41, 42]. Figure 2.3a indicates a typical boundary-driven streaming pattern around a rigid sphere in a standing acoustic field. The inner and outer layer vortices are symmetrically distributed around the sphere, leading to zero net hydrodynamic force on the sphere [43].

Fluid/fluid or gas/fluid interfaces, such as those found near an oscillating bubble for certain types of motors described below, can also cause energy dissipation and acoustic streaming due to the mismatch of their viscosities. For fluids with high viscosity, the acoustic streaming pattern is similar to that on a solid/fluid interface, which includes the inner and outer boundary layer streaming. When the viscosity decreases to a certain value, the inner boundary layer disappears, leading to reversed outer boundary layer streaming. Mathematically, the streaming generated by a low viscosity fluid or gas boundary is much weaker than that generated by a solid boundary. However, gas bubbles submerged in fluid could be forced to oscillate volumetrically by acoustic waves, and the oscillation of the interface will significantly enhance the streaming. The acoustic streaming generated by oscillating gas bubbles is called *cavitation microstreaming*. At the resonant frequency, a gas bubble oscillates with the highest amplitude, leading to the strongest cavitation microstreaming that could be several orders of magnitude stronger than that induced by a solid particle of a similar size. For a bubble that is resting on a solid boundary, the

asymmetrical boundary condition leads to directional cavitation microstreaming (Fig. 2.3b) and a net hydrodynamic force on the bubble. This net force is ultimately responsible for the propulsion of a bubble streamer, discussed in Sect. 2.3.2.

Acoustic streaming of various unique properties has been implemented to different applications. For example, Rayleigh streaming was utilized to balance the gravitational force and achieve precise position control of microparticles in the vertical direction [44], while cavitation microstreaming has been widely applied for efficient fluid mixing and pumping in microfluidic devices due to its high speed [45]. In the following sections, we will see how acoustic streaming contributes to the active propulsion of micro-/nanomotors.

2.3 Designing Ultrasound Micro-/Nanomotors

In this section, we will introduce four specific types of micro-/nanomotors powered by ultrasound. The first three, microrod streamers, bubble streamers, and flagella streamers, all rely on some sort of surface microstreaming to swim. The last type, acoustic jets, is somewhat unusual and takes advantage of the sudden expansion in volume of an organic droplet trapped in a tube. In each case, we detail the notable studies reported in the literature, explain the fundamental operating mechanism, and comment on its usefulness/limitation in biomedical applications.

2.3.1 *Microrod Streamers*

This type of ultrasound micromotor refers to metallic microrods that autonomously translate, rotate, and spin in MHz ultrasonic standing waves, at a speed of ~ 100 body lengths $\cdot s^{-1}$. They are arguably the most studied type of ultrasound-powered micro-/nanomotors and have received the most attention in the form of preliminary reports of biomedical applications.

Early Discoveries

A collaborative effort between the labs of Mauricio Hoyos at ESPCI in France and that of Thomas Mallouk at Penn State in the USA discovered in 2011 that gold microrods of a few μm long and 200–300 nm in diameter [31], synthesized by electroplating in porous templates, were able to move at a dazzling speed of $\sim 200 \mu\text{m} \cdot \text{s}^{-1}$ (~ 100 body lengths $\cdot \text{s}^{-1}$) when levitated in a cylindrical half-wavelength acoustic chamber vibrating at a frequency of ~ 3.7 MHz. They did so on a levitation plane (i.e., nodal plane) halfway between the top and bottom surface of the chamber. This came as a surprise because the gold rods were orders of magnitude smaller than the sound wavelength of $\sim 400 \mu\text{m}$ irradiating on them. Beyond directional motion,

other striking observations were made, including the spontaneous assembly into a large ring of spinning rods loosely connected to each other, and gold rods that furiously and independently rotated in plane. These different modes of motion were often concurrent but sensitive to the locations on the nodal plane and the ultrasound frequency. The publication detailing these observations in 2012 [31], of which Wei Wang was an author, has been cited over 300 times and has led to many subsequent studies on mechanisms, on biomedical applications, and on basic sciences. These will be described in detail below.

Mechanisms

The discovery of surprising propulsion for micro-/nanomotors often means an initial confusion on its mechanism. This was the case during the early years following the discovery of bimetallic microrods moving by self-electrophoresis [7, 47, 48], and certainly the case for metallic microrods moving in ultrasound. In the original paper reporting this discovery [31], the authors eliminated the possibility of rods moving by ultrasonically enabled chemistry, and instead proposed that it was rather an asymmetric scattering of sound waves on a rod of asymmetric shape. In particular, the authors noted, upon close examination of the rod morphology under SEM (see Fig. 2.4b), that the electrochemically synthesized microrods were often concave on one end and convex on the other, resembling a tiny rocket ship. This non-uniformity in shape was likely due to how the plating solutions wet the alumina membrane. Following this observation, the authors argued that sound waves would be concentrated at the concave end but scattered at the convex end, creating an acoustic pressure gradient along the rod and propelling it by a mechanism termed “self-acoustophoresis.” Note that this word is derived from acoustophoresis, i.e., the transport of particles in a gradient of acoustic radiation forces [49].

However, as mentioned above, the mismatch between the dimension of microrods and that of the incoming sound waves strongly suggests that this self-acoustophoresis, if exists, would be very minor. On the other hand, the shape

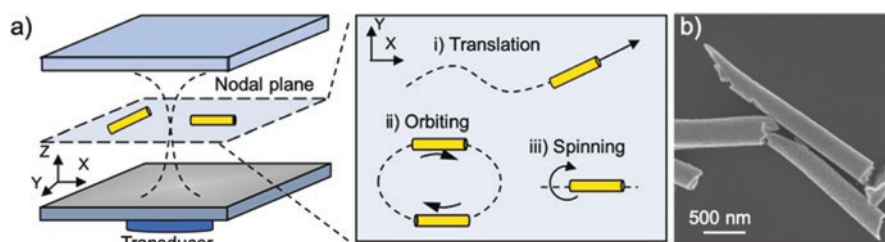


Fig. 2.4 Microrod streamers: operation. (a) Three types of behaviors (directional motion, orbiting, and spinning) observed with metallic microrods levitated by standing ultrasonic waves; (b) a scanning electron micrograph of a metallic microrod fabricated by electrodeposition, showing the sharp edges and uneven features on the rods. Reproduced with permission [46]. **Copyright 2017**, American Chemical Society

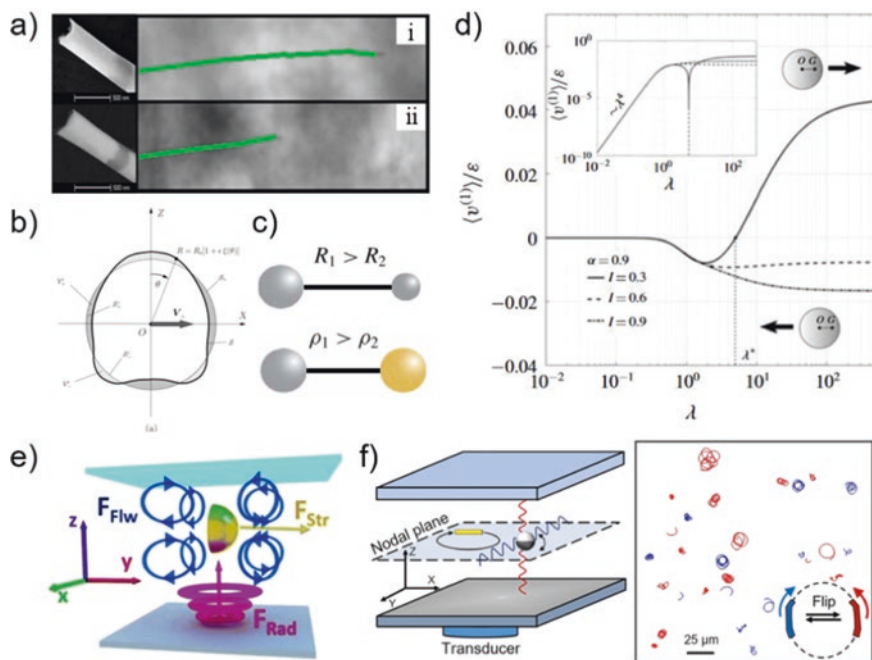


Fig. 2.5 Propulsion mechanisms of microrod streamers. (a) Metallic nanorods with a more concave end (i) swim faster than one with flat end (ii) in ultrasound. Reproduced with permission [50]. Copyright 2013, American Chemical Society. (b) Geometry of an asymmetrically shaped sphere studied for its propulsion in ultrasound. Reproduced with permission [52]. Copyright 2014, American Institute of Physics. (c) Dumbbell-shaped particles of two lobes of different sizes (top) or density (bottom) are studied for their acoustic propulsion. Reproduced with permission [53]. Copyright 2017, Cambridge University Press. (d) The direction of a bottom-heavy sphere propelled in ultrasound can be reversed when the frequency is larger than a threshold value. Reproduced with permission [54]. Copyright 2020, Cambridge University Press. (e) Acoustic propulsion of a metallic nanoshell via asymmetric surface streaming. Reproduced with permission [55]. Copyright 2016, Royal Society of Chemistry. (f) Metallic microrods and Janus microspheres twist and turn under ultrasound. Reproduced with permission [46]. Copyright 2017, American Chemical Society

asymmetry on a microrod seems to be necessary for effective propulsion, and an experiment by Garcia-Gradilla et al. showed that a microrod with a more profound concave end moved faster than one with a flat end (Fig. 2.5a) [50]. Moreover, it was noted in the original report that polymer microrods of similar shapes and sizes were not able to propel in ultrasound, but gold microspheres of a rough surface could [31]. Furthermore, a systematic study by Ahmed et al. [51] in 2016 shows that metal microrods preferred to move with the concave end forward, that a dense rod moves slower than a light rod, and that a rod made of two metals of different densities moves with the light end forward. These observations suggest a complicated interplay among ultrasound, surface morphology, and materials, which is further

connected to the acoustic properties of the particle. But how these properties give rise to propulsion remained mysterious in the early years.

An exciting breakthrough in understanding came in 2014 by Nadal and Lauga [52]. Inspired by the experimental observations of a metallic rod moving in ultrasound, but working independently from those experimental groups, Nadal and Lauga developed a model that qualitatively explained how the oscillation of an asymmetrically shaped near-spherical particle in ultrasound produces a net flow that moves it forward (Fig. 2.5b). Specifically, their mechanism centers around the concept of “asymmetric steady fluid streaming,” which essentially states that a nonzero net flow is produced by integrating the surface flow of an asymmetric particle oscillating with a finite Reynolds number. The propulsive speed of a micromotor is then directly proportional to the Reynolds number and its shape parameter, as well as the magnitude of its oscillation, which is further related to the parameters of the applied ultrasound and the acoustic properties of the particle. By inserting realistic values into this model, a speed of $\sim 20 \mu\text{m}\cdot\text{s}^{-1}$ was calculated for a microrod moving in ultrasound, one order of magnitude smaller than their actual speeds. Nevertheless, this theoretical study represents a giant leap in our understanding of how micro-/nanomotors move ultrasound.

A few years later, Collis et al. developed a modified theoretical framework (Fig. 2.5c), based on the same surface streaming effect, to explain how ultrasound powers micro-/nanomotors [53], with a focus on the previously reported dependence on the density distributions on the particle (i.e., the experimental work from Ahmed, ref. [51]). Compared with the model from Nadal and Lauga that assumed “a nearly spherical and homogeneous density particle in a low acoustic Reynolds number flow,” this new model by Collis et al. “is applicable to arbitrarily shaped axisymmetric solids with arbitrary density distributions that are being driven at arbitrary finite frequency.” To do so, this new model first studied a dumbbell made of two spheres of different sizes or densities (Fig. 2.5c), essentially working as two engines in tandem that cooperatively provide propulsion. Not only does the model agree with experiments that a rod with higher structural asymmetry moves faster, and that a rod moves with its lighter end forward, the most surprising and inspiring finding is that the directionality of a micromotor can reverse as the frequency is increased beyond a threshold, a prediction that is yet to be experimentally verified. Lauga and Michelin recently followed up on this work and provided an analytical description of the speeds of a sphere of inhomogeneous density under ultrasound [54]. Similar reversal in direction was found for varied frequencies (Fig. 2.5d).

Following the same surface microstreaming principle, a very recent theoretical paper by Voß and Wittkowski examined the propulsion of microparticles in traveling ultrasound waves instead of standing waves [56], a more realistic condition for real-life applications because standing waves are much more difficult to obtain and maintain. This theoretical work is in particular inspired by experiments by Soto et al. (Fig. 2.5e) [55], who demonstrated that metallic microcaps (“nanoshells”) move in standing wave ultrasound with the convex end leading, an observation in contrast to that reported by Ahmed et al. in which metallic microrods moved in ultrasound with their concave ends leading [51]. Specifically, Voß and Wittkowski

numerically solved the flow fields around asymmetrically shaped particles that are either half balls or cones, and either hollow inside or not. The major findings from their simulations are as follows: (1) a cup-shaped particle moves with its convex end leading, consistent with the report from Soto et al.; (2) pointed particles move faster than those with a rounded tip, and whether the particle contains a cavity is not important; and (3) the near-field flows around these particles are pusher-type. These results are inspirational for future designs of acoustic micro-/nanomotors of various shapes.

Beyond operating as micro-/nanomotors that move ballistically along a particular direction, microparticles in ultrasound are also able to rotate. They then become microrotors, a critical component in micromachinery that is potentially useful in minimally invasive surgery and micro-assembly. The rotating modes of motion were first identified in the original discovery of ultrasound micro-/nanomotors [31], where the authors noted strong in-plane rotation of metallic microrods (Fig. 2.4a ii) and spinning along their long axes (Fig. 2.4a iii). A later study by Balk et al. further quantified a surprisingly high spinning rate of 2.5 kHz [57]. As a result, tracer microspheres are seen to be advected by vortices around a spinning metallic micro-rod in ultrasound. A few years later, Sabrina et al. showed that gold microplates of twisted star shapes spontaneously rotated in ultrasound and their rotational direction was dictated by their structures [58].

Despite these experimental progress, mechanistic understanding of how microparticles rotate or spin in ultrasound has been still quite limited until recently, when Zhou et al. offered fresh insights on how ultrasound induces rotation (Fig. 2.5f) [46]. More specifically, they combined experimental results with acoustic theories to show that in-plane rotation for metallic microrods occurs predominantly at the resonance frequency and is due to the slightly bent shape of the electrochemically synthesized microrods. As the driving frequency is shifted slightly away from the resonance frequency, rotation gives way to directional motion. The axial spinning, on the other hand, is not related to shape asymmetry on the rod, but rather to the propagation of two sets of sound waves orthogonal to each other within the chamber. This theory states that a phase mismatch between these two waves creates a viscous torque that rotates a microparticle, trapped at the nodal plane where the two waves meet, at a spin rate that matches that observed in experiment.

To summarize, a collective effort from the experimentalists and theorists around the globe has put the various pieces of puzzles together and offer a consistent framework for understanding how ultrasound powers microparticles. On the experimental side, we now have a deeper appreciation of how the shape (in particular its asymmetry) and acoustic properties of a microparticle, as well as the power and frequency of the ultrasound, dictate the behavior of a micromotor in ultrasound. On the theoretical side, the local acoustic streaming around an asymmetrically shaped microparticle has been widely accepted as the dominant mechanism for its propulsion and in-plane rotation. Although some questions remain to be answered, such as the intricate coupling between the local streaming and the strong vortices around a spinning rod, the steady progress we have made over the years in understanding ultrasonic propulsion is truly remarkable and is ultimately

the key element in enabling the wide range of biomedical applications that we discuss below.

Biomedical Applications

Biocompatible, ultrasound-powered microrod streamers hold great promise for their use in practical biomedical applications. For example, micro-/nanomotors could deliver therapeutic payloads directly into a targeted region. Nevertheless, there is a need to develop novel methods to guide and steer them toward the target of interest. In this direction, ultrasound-powered microrod streamers have been coupled with magnetic segments composed of ferromagnetic materials that respond to externally induced magnetic fields for achieving directional guidance over pre-programmed paths. The external magnetic fields align a nickel magnetic segment embedded in a nanowire by applying a magnetic torque, thus redirecting the direction of locomotion in alignment with the magnetic field lines. Directional movement is possible by changing the orientation of the applied magnetic field. The nanowire can then be directed over complex trajectories and at all angles [59]. These ultrasound-powered nanorods have shown efficient locomotion control and guidance in diverse biofluids, including serum, saliva, and blood. More recently, nanorods coated with magnetite nanoparticles (Fe_3O_4) via electrostatic interactions reported long-lasting operation in high acidity environments under extended exposure, illustrating their potential use for gastrointestinal applications [60].

Ultrasound-powered nanorods have been used for triggered therapeutic release. Different pharmaceuticals have been loaded into the surface of nanorods using electrostatic interactions. Nanorods containing a negatively charged polymeric polypyrrole-polystyrene segment were loaded with positively charged brilliant green as a model drug. The polymeric segments protonate in the presence of acidic environments, causing the responsive release of the loaded drug (Fig. 2.6a) [50]. In another case, porous nanorods coated with an anionic coating were loaded with doxorubicin. The high surface area of the nanorod increased its drug loading capacity and induced a photothermal effect when exposed to NIR, resulting in the triggered release of the loaded doxorubicin [9].

Ultrasound-propelled nanorods have also been used for detoxification applications, where active biological coatings provide pathogen and toxin remediation functionalities. For example, nanorods functionalized with concanavalin A, a protein that binds with bacteria membrane polysaccharides, were used for “on-the-fly” capture and isolation of *Escherichia coli* bacteria [50]. Porous nanorods covalently functionalized with lysozyme, an enzyme capable of cleaving bacteria walls, were used for killing Gram-positive *Micrococcus lysodeikticus* and Gram-negative *Escherichia coli* bacteria [61]. The rapid motion of the nanorods induced fluid mixing and increased the interaction between the functionalized lysozyme and the pathogen, resulting in a dramatic improvement in the antibacterial efficiency over unpowered nanorods. Using a similar principle, asparaginase-functionalized nanorods were used for inhibiting cancer cell growth [62].

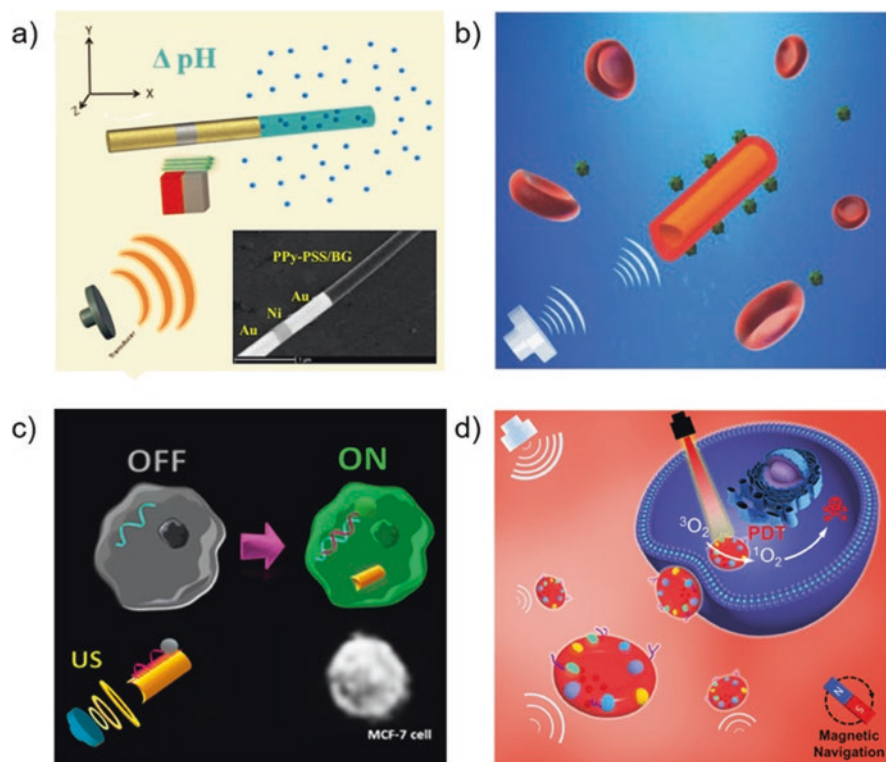


Fig. 2.6 Use of ultrasound-powered nanomotors for biomedical applications. **(a)** Use of nanorods for pH-triggered drug release. Reproduced with permission [50]. Copyright 2018, American Chemical Society. **(b)** Use of nanorods coated with red blood cell membrane for toxin absorption. Reproduced with permission [63]. Copyright 2015, Wiley-Blackwell. **(c)** Use of nanorods as intracellular mRNA fluorescent sensor. Reproduced with permission [66]. Copyright 2015, American Chemical Society. **(d)** Use of ultrasound-propelled red blood cells for photothermal therapy. Reproduced with permission [72]. Copyright 2019, American Chemical Society

Cell membrane-coated nanorods have been used for isolating pathogens and toxins. Nanorods coated with red blood cell can absorb melittin (a pore-forming toxin) using their external red blood cell coating as a sponge. This design enabled efficient locomotion in whole blood and demonstrated the reduction of hemolysis in red blood cells exposed to these toxins (Fig. 2.6b) [63]. An extension of this work combined red blood cells and platelets into a single surface coating to mimic the biological functions of these plasma cells. The platelet membrane served to capture and isolate *Staphylococcus aureus* bacteria, while the red blood cell membrane was used to absorb the secretions of α -toxin by the adhered bacteria [64].

Ultrasound-powered nanorods can also be internalized and move inside living HeLa cells after incubation with the cells for periods longer than 24 h [65]. This development has led to different intracellular applications, including cargo delivery and sensing. For example, ultrasound-powered nanorods were used to detect

miRNA from cancer cells. The nanorods were coated with graphene oxide layers that bond via electrostatic interactions with fluorescently tagged single-stranded DNA. Initially, the fluorescent tag was quenched by its interaction with the graphene oxide. Once the nanorod is internalized by a cancer cell, preferential hybridization of the probe with target miRNA dislodges it from the surface of the nanorods, resulting in the recovery of fluorescence (Fig. 2.6c) [66]. This off-on strategy was also reported for detecting RNA in human papillomavirus-positive cells [67]. The use of ultrasound-powered nanorods has also been explored for gene silencing via siRNA [68] and Cas9 [69]. In both cases, the authors reported the knockout of GFP expression by the target cells. On the other hand, ultrasound-propelled nanorods have also been used for the delivery of therapeutic cargos including oxygen [70], caspase-3 for cell apoptosis [71], and photodynamic cancer therapeutic agents (Fig. 2.6d) [72, 73].

Practical Considerations

Although diverse biomedical proof of concept applications has been proposed using ultrasound-propelled nanorods, we need to consider their clinical translation outlook.

- (a) The first challenge lies in generating acoustic standing waves inside the human body. The levitation plane where the nanorobots operate has been generated in relatively small acoustic resonators in lab-on-a-chip devices. Thus, before any acoustic nanomotor design is tested in any animal models, there is a requirement of generating controllable and tunable acoustic standing waves inside the body. Moreover, the presence of standing waves could result in an aggregation of plasma cells, forming undesired thrombolysis.
- (b) In case these limitations are resolved, we need to consider the material composition of nanorods. Most designs are composed of gold that, although is a biocompatible material, is also bio-accumulable. As a result, the use of ultrasound-propelled nanorods would require retrieval strategies. The use of metals such as zinc or iron that dissolve over time could be a solution, but metals with lower density than gold have shown less efficient locomotion [51]. Moreover, the surface coating could help avoid immune response and biofouling by the accumulation of proteins and biological agents.
- (c) Another potential use for nanorods is their usefulness in sensing on a lab-on-a-chip device. As discussed in the biomedical application section, the use of ultrasound-powered nanorods can preconcentrate biological targets on the levitation plane and enhance the contact of active materials with their target. As a result, they could be used for environmental remediation and intracellular sensing applications. Nevertheless, the reported nanorods have limited spatiotemporal motion resolution inside living cells.

- (d) Finally, current ultrasound resonators require specialized equipment and techniques, while portable models could expand the use of these microrod streamers outside of specialized places such as hospitals or research labs.

Usefulness in Basic Sciences

Beyond showing promise in various biomedical applications that we discussed above, ultrasound-powered microrod streamers are also useful in the study of basic sciences, in particular in dynamic self-assembly and in the studies of active colloids. We offer a brief introduction in this section, whereas an expanded discussion can be found in a review article published earlier [74].

On the topic of dynamic assembly, Ahmed et al. have studied how ultrasonically powered metallic microrod motors, which have a magnetic segment embedded in them, would spontaneously assemble and disassemble (Fig. 2.7c) [75]. Interestingly, dimers, trimers, and multimers formed as the ultrasound forces that drive them apart compete with the magnetic dipolar attraction. The distribution of each type of

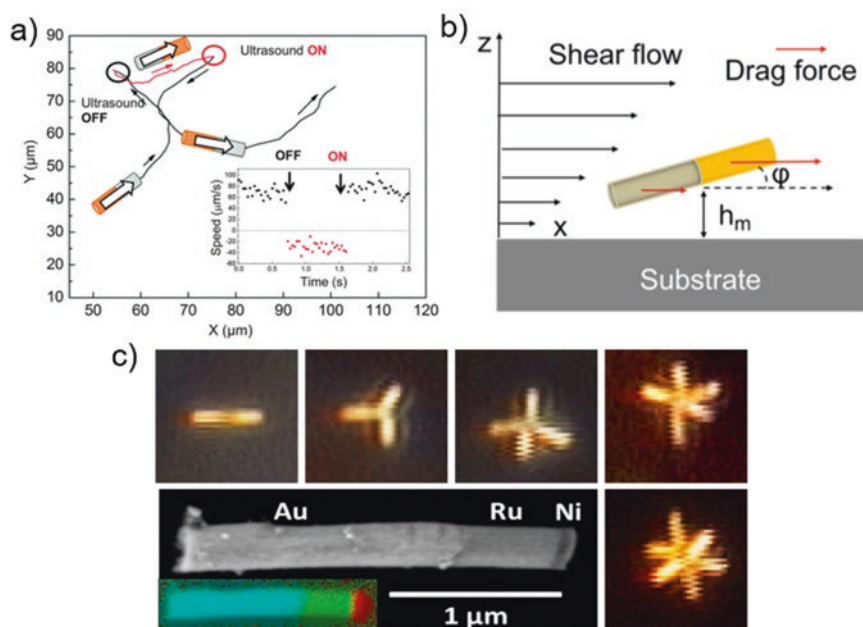


Fig. 2.7 Microrod streamers: usefulness in basic sciences. (a) Trajectory and speed changes (inset) of a levitated bimetallic micromotor as the ultrasound power is switched on and off. Reproduced with permission [76]. Copyright 2015, Royal Society of Chemistry. (b) Schematic illustration of how a metallic rod orientates in a flow. Reproduced with permission [78]. Copyright 2017, American Chemical Society. (c) Segmented bimetallic gold-ruthenium nanorods with a thin Ni segment assemble into few-particle, geometrically regular dimers, trimers, and higher multimers in ultrasound. Reproduced with permission [75]. Copyright 2014, American Chemical Society

cluster can then be controlled by varying the ultrasound power (but not the strength of the magnetic interaction that was fixed), enabling the identification of the binding energies of the individual rods within a cluster in a way inspired by chemical kinetics. A second study by Wang et al. examined how a group of nanomotors propelled by both ultrasound and chemistry assemble and disassemble in the combined forces (Fig. 2.7a) [76]. The interesting observation of active micro-/nanomotors escaping from an acoustic trap is further discussed in a separate study by Takatori et al. [77].

On the topic of active colloids, the upstream or downstream movement (i.e., positive or negative rheotaxis) of ultrasound-powered microrod streamers was studied in shear flows (Fig. 2.7b) [78]. When H_2O_2 was also present, the bimetallic microrods were dually propelled. By controlling the magnitude and directionality of the ultrasonic propulsion, both positive and negative rheotaxis can then be realized.

2.3.2 Bubble Streamers

Mechanism

Acoustic waves can generate, oscillate, and destroy gas bubbles in a fluid, and all the phenomena could be utilized to develop micro-/nanomotors [79, 80]. In this section, we will focus on the acoustic bubble streamers that are propelled by continuous cavitation microstreaming (described in Sect. 2.2.2). The common design of the bubble streamers comprises one or more microscale cavities with orifices (see examples in Fig. 2.8). The cavities are typically fabricated from or coated with hydrophobic materials, so that gas bubbles can be trapped in the cavities as they are immersed in a fluid. The gas/fluid interfaces are located at those orifices. Upon exposure to the acoustic waves, a bubble starts to oscillate and generates directional cavitation microstreaming at the orifice. Consequently, the microstreaming exerts forces on the microcavities in the opposite direction of the streaming and propels it forward. The acoustic waves are usually generated by an acoustic transducer that is attached to the fluidic container or immersed in the fluid.

The velocity of the cavitation microstreaming is determined by the amplitude of the bubble's oscillation. A bubble has a maximal amplitude of oscillation when the acoustic wave frequency matches its resonant frequency. For a spherical gas bubble that is free of any boundary restrictions, and neglecting surface tension and viscous attenuation, the acoustic resonant frequency is given by the Minnaert resonance [81]:

$$f = \frac{1}{2\pi a} \sqrt{\left(\frac{3\gamma p_A}{\rho} \right)} \quad (2.4)$$

where a is the radius of the bubble, $\gamma \sim 1.4$ is the adiabatic coefficient, p_A is the ambient pressure, and ρ is the density of the fluid. When the gas bubble is trapped in a cavity, the resonant frequency could shift, depending on the size and shape of the cavity. However, this shift is usually small, and the new resonant frequency could be

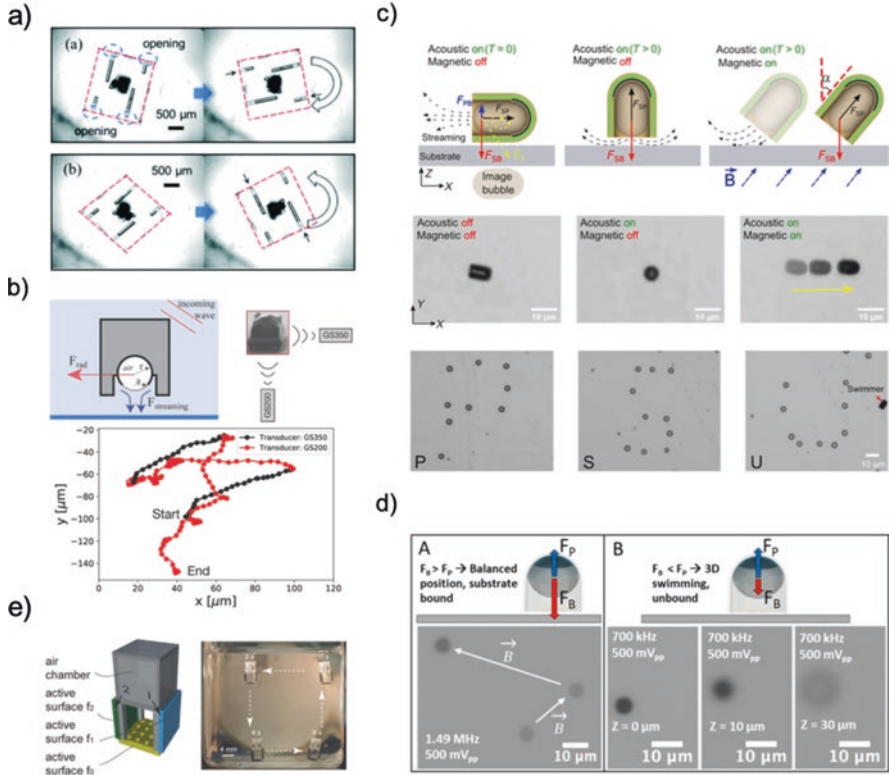


Fig. 2.8 Bubble streamers. (a) A bubble streamer that includes two different bubble sizes was rotated by selectively exciting the bubbles with different acoustic frequencies. Reproduced with permission [85]. Copyright 2016, Royal Society of Chemistry. (b) A 3D printed bubble streamer that could hover on the substrate and be guided by the direction of the traveling acoustic waves. Reproduced with permission [86]. Copyright 2018, Wiley-VCH. (c) A high bubble-to-streamer volume ratio streamer demonstrated a self-alignment behavior and required an external magnetic field to initial its translation. Multiple 4 μm silica particles were arranged into letters “PSU” on the substrate by such a swimmer. Reproduced with permission [87]. (d) A microbubble streamer switched from 2D motion to 3D motion when the acoustic wave changed from a bubble’s resonant frequency to a shape resonant frequency. Reproduced with permission [88]. Copyright 2020, American Chemical Society. (e) Schematic of a macroscale bubble streamer made from functional bubble surfaces. Each surface has its own resonant frequency. 3D motion was demonstrated by selectively activating the surfaces. Reproduced with permission [89]. Copyright 2017, Wiley-VCH

experimentally determined by scanning the driving frequency around the Minnaert resonant frequency of a spherical bubble with the equivalent volume. Theoretical prediction of the resonant frequency of the bubble streamers has also been studied by a few groups. Oguz et al. described the resonant frequency of a gas bubble that

is partially filled, i.e., an one-end-open tube, as $f = \frac{1}{2\pi} \sqrt{\left(\frac{kP_A}{\rho L_0 L_B}\right)}$, where L_B is the

length of the bubble and L_0 is the length of the liquid column between the bubble interface and the exit of the tube. k is a frequency-dependent parameter and satisfies

$1 \leq k \leq \gamma$ [82]. Ren et al. further considered the surface tension and provided a correction factor to Oguz's equation,

$f_c = f \cdot \left(1 + \frac{4\tau L_B}{kP_A a^2} \right)$, where τ is the surface tension of the liquid-gas interface [83]. However, the surface tension term is comparatively small if L_B and a are of the same order of magnitude. For a spherical

shape streamer, Bertin et al. predicted a frequency that scales as $f_{th} \sim \left(\frac{n^3 \tau}{\rho a^3 \theta_0^3} \right)^{1/2}$,

where $\theta_0 = \sin^{-1}(l/a)$ is the azimuthal angle of the orifice, l is the aperture size of the orifice, and n is the shape mode number [82]. It is worth noting that a gas bubble could have multiple resonant frequencies because of the presence of multiple oscillation modes. Finally, at the resonant frequency, the propulsion force F generated by the microstreaming is proportional to the square of the amplitude of the oscillation, which is further proportional to the input voltage from the acoustic transducers V_{pp} . Therefore, $F \sim V_{pp}^2$.

Notable Studies

The first bubble streamer was demonstrated by Dijkink et al. in 2006 [84]. This pioneering bubble streamer was made from a commercial Teflon tube that has one end sealed with glue. The 2–4-mm-long streamer has a 750 μm outer diameter and 250 μm inner diameter, and the resonant frequency was around 1.5 kHz. A maximum speed of 10 $\text{mm}\cdot\text{s}^{-1}$ (~ 3 body lengths $\cdot\text{s}^{-1}$) was observed. Despite the simple design and the preliminary results, they provided both experimental and theoretical strategies for studying the resonant frequency of a trapped bubble, the streaming pattern of such a design, and the propulsion force generated by the streaming. They also pointed out the direction to achieve diverse motions by integrating multiple bubbles oscillating at different frequencies.

From the perspective of applications in microfluidics and cell-level biomedical research, swimmers that are in the micrometer scale are preferred. Feng et al. later introduced a photolithography process for fabricating bubble streamers [90]. This method allowed them to precisely control the size and location of the gas tubes in the streamer. They were able to shrink the diameter of the gas tube into 60 μm , even though the length of the tube and the longest scale of the streamer are still a few hundreds to thousands of micrometers. In this case, the streamers were propelled by acoustic waves above 10 kHz and input voltages of over 100 V_{pp} and moved at 45 $\text{mm}\cdot\text{s}^{-1}$ (~ 50 body lengths $\cdot\text{s}^{-1}$). By combining multiple gas tubes with different lengths in one streamer and by arranging them in different orientations, they demonstrated 2D steerable and rotational motions (Fig. 2.8a) [85]. Similarly, Ahmed et al. developed a photopolymerization-based method to fabricate micro-size bubble streamers [91]. With a simple microscope, they could fabricate streamers smaller than 250 μm and place multiple gas tubes with different diameters in the streamer.

The diameters of the gas tubes are less than 100 μm , corresponding to resonant frequencies ranging from 40 kHz to 100 kHz. The streamers achieved a maximum speed of 8 $\text{mm}\cdot\text{s}^{-1}$ (50 body lengths $\cdot\text{s}^{-1}$) at an input voltage of 7 V_{pp} . Swimming in viscous fluids such as glycerol and hydrogels was also demonstrated.

In order to stabilize the gas bubbles and improve the usefulness of the bubble streamers in practical applications, Bertin et al. applied a high-resolution 3D laser printing method to reduce the size of streamer and the orifice [86]. The diameter of the spherical bubbles is 10–20 μm and the orifice of the streamers is around 5 μm . The streamers responded to ~ 320 kHz acoustic waves and moved for a few hours in salted water. Using 3D laser printing for fabrication significantly improved the versatility of the bubble streamers. Louf et al. printed swimmers (~ 20 μm) that had the bubble/water interface pointed toward the substrate (Fig. 2.8b) [86]. Such an orientation allowed the swimmers to hover above the substrate and move with low friction. A maximum speed of 350 $\text{mm}\cdot\text{s}^{-1}$ (17,500 body lengths $\cdot\text{s}^{-1}$) was demonstrated. They claimed that the bubble streamer was lifted by microstreaming and translate by acoustic radiation forces. The direction of the swimmer could be controlled by the direction of the acoustic waves.

Ren et al. further reduced the size of the streamers to less than 8 μm (2–4 μm gas bubble diameter) with the same 3D printing technique [83]. The high gas bubble to streamer volume ratio resulted in a secondary Bjerknes force that is comparable to the microstreaming propulsion force between the substrate and the streamer. Therefore, the secondary Bjerknes force aligned the streamers' bubble/water interfaces toward the substrate and confined their motion on the substrate (Fig. 2.8c). The translation of the streamers requires an external magnetic force to align the microstreaming propulsion force along the moving direction. The streamers could slide on a complicated 3D surface due to their low density and the negligible gravitational force. At a frequency of around 1 MHz, speed as fast as 2.6 $\text{mm}\cdot\text{s}^{-1}$ (~ 350 body lengths $\cdot\text{s}^{-1}$) was observed. Aghakhani et al. reported a similar capsule shape design that has a larger size (~ 25 μm) [87]. They added a fin structure to the capsule to break the symmetry of the microstreaming; therefore the streamer could translate even when vertically aligned to a surface. More recently, McNeill et al. improved on the above design by developing a wafer-scale fabrication method to overcome the limitations of resolution and throughput of the 3D printing method [88]. They were able to push the size of the streamer down to 500 nm, corresponding to resonant frequencies over 10 MHz. This improvement makes the acoustic bubble streamers available in submicron size, the same size range as chemical- or light-driven nano-/micromotors. The submicron streamers have the potential to perform many functions within limited space, such as the brain intracerebral microvascular system. In addition, the authors found that the streamers could also be powered by a so-called shape resonant frequency (~ 700 kHz) that is much lower than the bubble's resonant frequency (~ 1.5 MHz). The shape resonance could provide a microstreaming force that is strong enough for propulsion but at the same time weak secondary Bjerknes forces that minimize the streamer/substrate attraction. By switching from the bubble's resonant frequency to the shape resonant frequency, the motion of the

swimmers could be converted from a 2D mode (sliding on a surface) into a 3D mode (swimming in free space), as shown in Fig. 2.8d.

In addition to the efforts of developing bubble streamers of microscopic and nanoscopic sizes, researchers also applied microstreaming for propelling macroscopic objects. Qiu et al. designed functional surfaces ($4\text{ mm} \times 4\text{ mm}$) that contain thousands of microbubbles. The diameter of each bubble on the surface is tens micrometers and the resonant frequency is between 50 and 100 kHz. Significant propulsion force could be generated by simultaneously oscillating all the bubbles on the surface. A macroscale streamer that was assembled from the functional surfaces demonstrated a propulsion force of 0.5 mN (Fig. 2.8e) [89, 92].

The narrow bandwidth of the bubbles' resonant frequency enables users to selectively activate the bubbles in a streamer and achieve real-time manipulation. One example was recently demonstrated by Liu et al. with a structure produced by 3D laser printing [93]. The swimmer ($\sim 1\text{ mm}$) includes gas tubes of three different sizes and the tubes are oriented orthogonally. By activating the three types of bubbles independently or simultaneously, the microstreaming could lift, translate, and rotate the swimmer. A mechanism based on an uneven density distribution was also proposed to restore the swimmer's posture, so the swimmer always stands upright under the effect of gravity and buoyancy. Magnetic steering offers more precise and directional control of the bubble streamers. Ahmed et al. embedded superparamagnetic particles in the swimmer polymer matrix, so that a swimmer could be rotated or oriented into any direction by an external magnetic field [94]. Another approach to achieve magnetic steering is by coating swimmers with a thin paramagnetic film, such as nickel, during the fabrication process [88, 93].

Pickup and transport of cargos with bubble streamers have also been demonstrated [85, 88, 93]. The acoustic pressure required for bubble streamers usually has negligible effects on other objects in the same environment. It allows the streamers to move among the objects, pick up a specific target, and transport it to a new location in 2D. The target could be simply pushed by the propulsion force or dragged by the acoustic attractive force, depending on parameters such as the size of the streamers and the targets, and the acoustic pressure level. For example, Ren et al. demonstrated that microscopic bubble streamer could either push or drag microparticles/cancer cells and independently relocate multiple targets on the substrate.

Practical Considerations

Bubble streamers that operate via cavitation microstreaming offer many advantages over the other types of ultrasound-powered micro-/nanomotors. First, bubble streamers are powered by traveling acoustic waves of low pressure, which allow motors to work regardless of the shapes of fluidic containers and move independently from other objects. Second, bubble streamers of sizes ranging from a few millimeters to a few hundreds of nanometers have been developed. The wide size range enables many applications, such as the removal of tissue samples, single-cell separation, and intracellular drug delivery. Moreover, bubble streamers have demonstrated many unique functionalities by applying acoustic fields alone. By

modulating the acoustic frequency or the acoustic pressure, bubble streamers could change directions, rotate, attract microscopic objects or boundary, transition from 2D to 3D motion, and so on. Many functionalities could be developed with a simple combination of waveform generator and a piezoelectric transducer, without the need of any other equipment.

To move forward, we note that the development of bubble streamers is still at its early stage, and current research mostly focuses on design optimization and the characterization of the basic properties. One key challenge for practical applications is the low reproducibility and short lifetime of the gas bubbles in the streamers. Specifically, it has been reported that streamers from the same fabrication had slightly different resonant frequencies because of the slight but inevitable differences in the bubble size. Moreover, bubbles typically only last for a few hours because of the rectified diffusion (i.e., more gas diffusing into the bubble than out during one cycle of oscillation, leading to bubble growth). More efforts are therefore required for the large-scale production of bubble streamers with controllable bubble sizes and long lifetime. Furthermore, it usually requires sophisticated methods to fabricate 3D bubble streamers, such as nanoscopic 3D printing, which puts a practical limit on both the minimum feature size and throughput. Finally, the biocompatibility of the streamer materials also needs to be considered when it comes to biological applications.

2.3.3 *Flagellar Streamers*

Like the gas/fluid boundary generating cavitation microstreaming, a solid/fluid boundary could also introduce comparatively strong microstreaming when the solid boundary oscillates with a large amplitude. A common observation of this phenomenon is a pair of counter-rotating vortices around an acoustically activated sharp-edge tip [95, 96]. Such streaming was first utilized for fluidic mixing in microfluidics and later applied to the development of acoustic streamers. Under the excitation of acoustic waves, the tip of the sharp edge oscillates like a flagellum of microorganisms but at a much higher frequency, leading to directional microstreaming—and propulsive force in the opposite direction—around the tip. The sharp edges or such structures are often made of materials with low Young's modulus, such as polydimethylsiloxane (PDMS), so that oscillation of a large amplitude can be generated. This type of ultrasound-powered micromotors is referred here as “flagellar streamers.”

Ahmed et al. developed the first acoustic flagellar swimmer that consisted of a flexible polypyrrole flagellum and a metallic head, as shown in Fig. 2.9a, via sequentially depositing layers of materials in an alumina membrane template [97]. The rod-shaped swimmer has a diameter of 0.3 to 0.6 μm and a length of 15 to 20 μm . A traveling acoustic wave was applied to oscillate the polypyrrole flagellum and to generate microstreaming at its end. Consequently, the microstreaming pushed the swimmer to move toward its metal head. A maximum speed of $\sim 60 \mu\text{m}\cdot\text{s}^{-1}$ (3~4

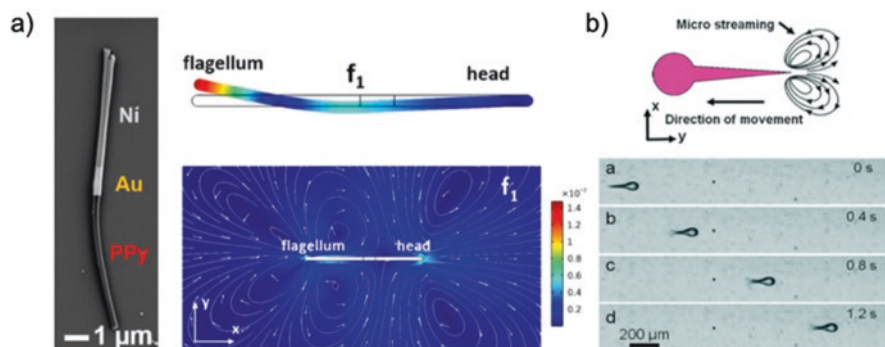


Fig. 2.9 Flagella streamers. (a) SEM image (left) of a nanowire flagellar swimmer. Numerical simulation on the right illustrates the oscillation mode of the polypyrrole tail and the microstreaming pattern associated with the oscillation. Reproduced with permission [97]. Copyright 2016, **American Chemical Society**. (b) Schematic of the sharp-edge flagellar swimmer and the microstreaming pattern near its tail, which propels the swimmer to move away from its tail. Reproduced with permission [98]. Copyright 2017, Royal Society of Chemistry

body lengths \cdot s $^{-1}$) was achieved at \sim 90 kHz and 10 Vpp input voltage. Kaynak et al. later developed a flagellar swimmer of a larger scale with photopolymerizable polymer [98]. The swimmer, around 200 μm long and 60 μm wide, has a round head and a sharp tail. In the presence of an acoustic field (\sim 4.6 kHz), the oscillation of the tail at an amplitude of 20 μm was recorded by a fast camera (Fig. 2.9b), which confirmed the propulsion mechanism of this type of swimmers. At an input voltage of 140 Vpp, a speed of 1200 μm \cdot s $^{-1}$ (6 body lengths \cdot s $^{-1}$) was achieved.

Flagellar streamers can work under traveling acoustic waves and are more stable than bubble streamers. However, the oscillation of the elastic flagella usually requires higher acoustic pressures than bubble streamers to reach the same amplitude of oscillation, because a gas/fluid interface is much easier to deform than a solid/fluid interface. However, the resonant frequency of an acoustically vibrated flagellum is commonly identified through experiments, yet results from numerical simulations did not match the experiments well. In other words, it is difficult to predict the resonant frequency of a flagella design. Deeper understanding of the flagella oscillation mode and optimization of their design are required for practical applications.

In addition to propelling the swimmers themselves, acoustic streaming generated by gas bubbles or sharp edges can also be applied to manipulate passive micro-objects in combination with the acoustic radiation force. For example, Ahmed et al. demonstrated that gas bubbles trapped in a polydimethylsiloxane wall could attract or pump microparticles, depending on the size of the particles [99]. For large objects such as *E. coli*, the strong acoustic radiation force trapped the bacteria on the surface of the bubble, while microstreaming rotated them along an axis that is perpendicular to the acoustic radiation force. Lu et al. used polymer micropillar arrays (5 μm \times 20 μm \times 20 μm) and the microstreaming around the pillars to demonstrate a similar size-dependent particle/cell manipulation [100]. In their experiments,

large cancer cells experienced a secondary acoustic radiation force that is stronger than the drag force induced by acoustic microstreaming. Therefore, the cancer cells were trapped by the pillars. However, the secondary acoustic radiation force is weaker for small-size blood cells, which are then convected by the microstreaming and were not trapped by the pillars. In this way, they could separate cancer cells from blood with high purity ($95 \pm 5\%$). By extending the micropillar design to a boundary, they discovered that the acoustic microstreaming could carry objects to move along the boundary [101]. This kind of acoustic microstreaming near a solid boundary can be exploited precisely to guide micro-objects along a predefined path, as demonstrated very recently by Ma et al. [102]

2.3.4 Acoustic Jets

The last type of ultrasound-powered micro-/nanomotor is based on the use of high-intensity ultrasound to induce acoustic jets as a propulsion mechanism. These types of micro-/nanomotors have great promise for penetrating tissue and cellular barriers due to the high mechanical forces generated under ultrasound-induced internal cavitation. Two main types of fuels have been reported to power these devices, including the use of perfluorocarbon nanoemulsions and gas nanobubbles. For example, the Wang lab pioneered a design of microbullets consisting of $5 \mu\text{m}$ hollow conical tubes loaded with perfluorocarbon emulsions (see Fig. 2.10a for its design). The application of a high-intensity focused ultrasound pulse (single 10-ms-long pulse at 2.25 MHz) vaporized the perfluorocarbon liquid nanoemulsions into gas bubbles, the rapidly expanding volume of which inside the hollow microbullet generated a strong propulsive force that moved the tube like a bullet [103]. We note that this operation mechanism carries a qualitative similarity to microjets that thrust forward by chemically producing gas bubbles from a microtube [104–106]. Based on this “droplet vaporization ignition mechanism,” a “microcannon” was designed to fire loaded nanobullets from a microtube at high speeds in the range of meters per second. The fired nanobullets reportedly penetrated $20 \mu\text{m}$ inside a hydrogel phantom tissue that simulated the mechanical and acoustic properties of human tissues [80]. Moreover, arrays of microcannons were used as a wearable transdermal patch, enabling drug payload delivery into skin that is faster and deeper than passive diffusion [107].

Unlike the above cases where liquid fuels are vaporized by ultrasound waves, there have been reports of microscopic structures that spontaneously trap nanobubbles within a cavity in a way similar to the bubble streamers described in Sect. 2.3.2. For example, polymeric, hydrophobic nano-cups can store stabilized gas nanobubbles inside their cavity as a propellant. A focused ultrasound pulse causes internal cavitation of the entrapped nanobubbles, inducing directional propulsion of the nano-cup (Fig. 2.10b) [108]. The jet-like propulsion of these nano-cups was evaluated in an animal model as a deep tissue penetration delivery platform of oncolytic virus, boasting a 1000-fold increase of gene expression for the vaccine virus over

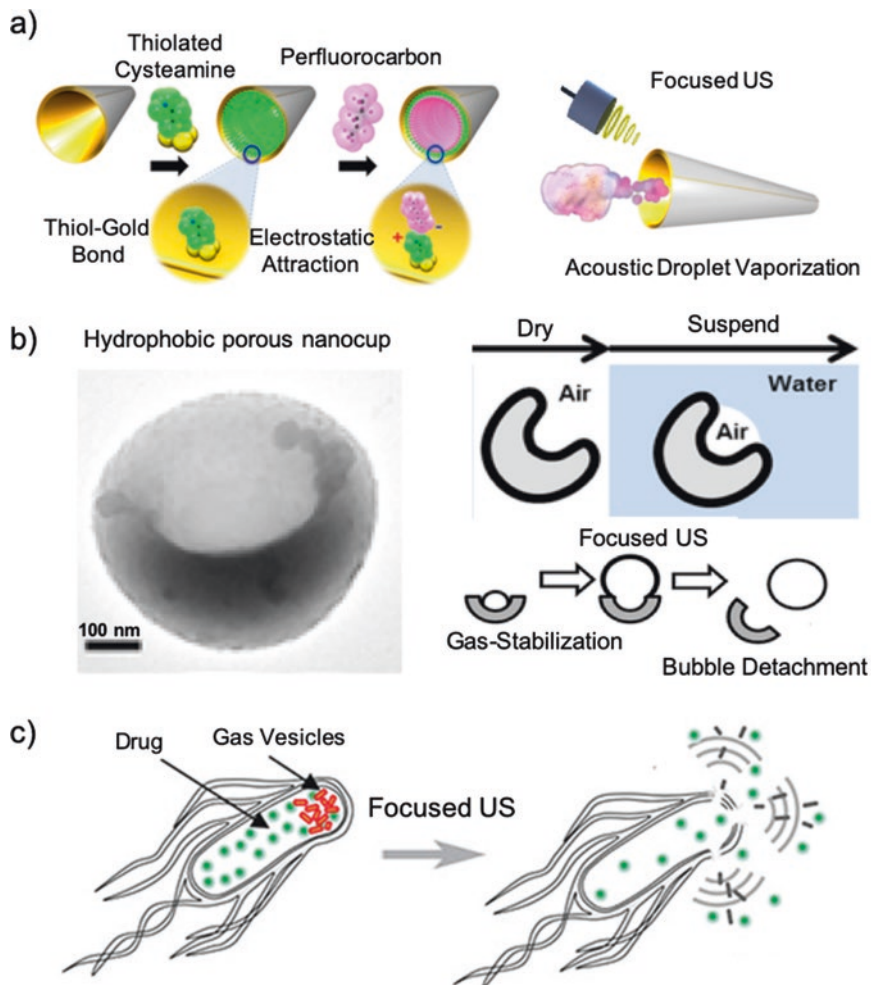


Fig. 2.10 Acoustic jets. (a) Perfluorocarbon-loaded microbullets powered by acoustic droplet vaporization. Reproduced with permission [103]. Copyright 2012, Wiley-VCH. (b) Hydrophobic porous nano-cup powered by nucleating cavitation of trapped gas nanobubbles. Reproduced with permission [108]. Copyright 2015, Wiley-VCH. (c) Genetically encoded bacteria that produce gas vesicles release payload via internal cavitation upon focused ultrasound. Reproduced with permission granted by Prof. Mikhail G. Shapiro [109]

passive diffusion [110]. More recently, genetically engineered bacterium were programmed to produce gas vesicles, which were cavitated using focused ultrasound (3 MHz, 1 MPa) to serve as remotely detonated cell-killing agents (Fig. 2.10c) [109].

The acoustic jets discussed in this section, taking advantage of a streaming/cavitation propulsion mechanism, are powerful and easy to activate. However, they can only be activated once, becoming passive after the fuel is completely vaporized, or the nanobubble detached. The fact that these jets are “single-use” puts a serious

limit on the practical usefulness of acoustic jets in scenarios where repeated activation is essential.

2.4 Conclusion and Future Prospects

In this chapter, we have reviewed the development and state of the art of nanomotors powered by ultrasound of four major types: microrod streamers that move by asymmetric surface microstreaming, bubble streamers powered by microstreaming near an oscillating microbubble, flagella streamers with a solid body that oscillates in ultrasound, and finally acoustic jets that produce jet streaming. Throughout this chapter, one focus is on introducing operating mechanisms, by first giving a general overview of acoustic radiation forces and acoustic streaming and then understanding how streaming is generated for each type of motor and how directional motion is enabled by broken symmetry. A second focus is on the various biomedical capabilities these nanomotors demonstrate. These functionalities include cargo pickup, transport and unloading (both outside a cell and across the cell membrane), cell manipulation (push, pull, rotate), exerting mechanical forces, triggered release of drugs, and magnetic steering, among others.

Beyond listing the preliminary studies and the promises they make, we also pointed out, in each section, specific hurdles that need to be overcome before each type of acoustic nanomotors can find their ways into a clinic. Without going into the detail of the various issues a nanomotor encounters during an *in vivo* operation, a topic already elaborated in a few excellent review articles [111–118], we generalize below a few key scientific and technological challenges that are particularly relevant to micro-/nanomotors powered by ultrasound:

1. Applying ultrasound. The first and foremost requirement of the successful operation of a nanomotor is a proper power source that is biocompatible and effective. Although ultrasound is considered one of the most medically safe power sources, the strategies described in this chapter that power micro-/nanomotors are not necessarily biocompatible. For example, microrod streamers typically require a standing wave to operate, yet it is practically impossible to maintain a standing wave inside human bodies of varying dimensions during the operation of a micro-/nanomotor. Bubble or flagella streamers, on the other hand, only require traveling waves and are in principle easier to implement.
2. Size vs. frequency. A persistent challenge of using nanomotors for biomedicine is a need to identify the best sizes for nanomotors, which have to balance between long retention time in circulation, better chances for cell internalization, and motor performance. This issue is further complicated for ultrasonic nanomotors that move via bubble or body microstreaming (i.e., the first three types), because their sizes determine the resonance frequency, which should ideally match the safe range of diagnostic medical imaging at 1–15 MHz [119]. In other words, a researcher interested in using these motors for biomedical applications needs to

know which sound frequency will be used and keep that number in mind when designing micro-/nanomotors with key features of matching sizes.

3. Interaction with neighbors and the environment. A micro-/nanomotor rarely moves alone in an unbounded space. Rather, it is often surrounded by peers, cells, and other microorganisms and moves in confinements such as blood vessels and extracellular matrix in tissues. The presence of neighbors and a confining environment could significantly affect the speed and directionality of a micro-/nanomotor and even fundamentally change how they behave [120–123]. For example, a microrod streamer is known to be strongly coupled to its neighbor via hydrodynamics, and they together form a spinning chain (see Sect. 2.3.1.1). Similarly, bubble streamers attract and repel with each other via streaming flows. In addition, the presence of strong Bjerknes forces between an oscillating bubble and a nearby solid boundary could make or break a motor (see Sect. 2.3.2.2). A better understanding of these interesting, significant interactions is needed before we can confidently put ultrasonic nanomotors in human bodies.

Despite the challenges and limitations described above, we are optimistic about the prospect of holding an ultrasonic imaging probe to power a micro-/nanomotor that roams blood vessels. This vision is possible, not only because MHz ultrasound is biologically safe, or because of the large number of preliminary studies demonstrating the potential of ultrasound-powered nanomotors in biomedical applications, but also because there is no fundamental reason why this cannot be done. Beyond powering micro-/nanomotors and imaging, ultrasound is also a versatile source of power that enables a range of biomedically relevant effects such as sonodynamic therapy [124], sonoporation [125], and even ultrasonic neurostimulation [126]. We then envision a medical microrobot that moves autonomously, can be imaged from a computer screen, produces therapeutic molecules on cue, breaks through cell membrane, and manipulates cells from outside or from within, all powered by medically safe ultrasound.

Acknowledgment LH and WW are grateful for the financial support by the National Natural Science Foundation of China (11774075), Natural Science Foundation of Guangdong Province (No. 2017B030306005), and the Science Technology and Innovation Program of Shenzhen (JCYJ20190806144807401), as well as past funding from Shenzhen government (KQCX20140521144102503).

References

1. Hagiya, M., Konagaya, A., Kobayashi, S., Saito, H., & Murata, S. (2014). *Accounts of Chemical Research*, 47, 1681–1690.
2. Lancia, F., Ryabchun, A., & Katsonis, N. (2019). *Nature Reviews Chemistry*, 3, 536–551.
3. Fujita, H. (1998). *Proceedings of the IEEE*, 86, 1721–1732.
4. Bryzek, J., Peterson, K., & Mcculley, W. (1994). *IEEE Spectrum*, 31, 20–31.

5. Wang, J. (2013). *Nanomachines: Fundamentals and applications*. Weinheim: Wiley-VCH Verlag GmbH & KGaA.
6. Chen, X., Zhou, C., & Wang, W. (2019). *Chemistry, an Asian Journal*, 14, 2388–2405.
7. Paxton, W. F., Kistler, K. C., Olmeda, C. C., Sen, A., Angelo, S. K. S., Cao, Y., Mallouk, T. E., Lammert, P. E., & Crespi, V. H. (2004). *Journal of the American Chemical Society*, 126, 13424–13431.
8. Fournierbidoz, S., Arsenaault, A. C., Manners, I., & Ozin, G. A. (2005). *Chemical Communications*, 441–443.
9. Garcíagràdilla, V., Sattayasamitsathit, S., Soto, F., Kuralay, F., Yardimci, C., Wiitala, D., Galarnyk, M., & Wang, J. (2014). *Small*, 10, 4154–4159.
10. Gao, W., Kagan, D., Pak, O. S., Clawson, C., Campuzano, S., Chuluunerdene, E., Shipton, E., Fullerton, E. E., Zhang, L., & Lauga, E. (2012). *Small*, 8, 460–467.
11. Balasubramanian, S., Kagan, D., Hu, C. J., Campuzano, S., Lobocastanon, M. J., Lim, N., Kang, D. Y., Zimmerman, M., Zhang, L., & Wang, J. (2011). *Angewandte Chemie*, 50, 4161–4164.
12. Zhang, X., Chen, C., Wu, J., & Ju, H. (2019). *ACS Applied Materials & Interfaces*, 11, 13581–13588.
13. Zhao, G., Seah, T. H., & Pumera, M. (2011). *Chemistry (Weinheim an der Bergstrasse, Germany)*, 17, 12020–12026.
14. Soler, L., Magdanz, V., Fomin, V. M., Sanchez, S., & Schmidt, O. G. (2013). *ACS Nano*, 7, 9611–9620.
15. Gao, W., Feng, X., Pei, A., Gu, Y., Li, J., & Wang, J. (2013). *Nanoscale*, 5, 4696–4700.
16. Yan, J., Han, M., Zhang, J., Xu, C., Luijten, E., & Granick, S. (2016). *Nature Materials*, 15, 1095–1099.
17. Gao, W., Pei, A., Feng, X., Hennessy, C., & Wang, J. (2013). *Journal of the American Chemical Society*, 135, 998–1001.
18. Maggi, C., Simmchen, J., Saglimbeni, F., Katuri, J., Dipalo, M., De Angelis, F., Sanchez, S., & Di Leonardo, R. (2016). *Small*, 12, 446–451.
19. Wang, W., Lv, X., Moran, J., Duan, S., & Zhou, C. (2020). *Soft Matter*, 16, 3846–3868.
20. Das, M., Schmidt, C. F., & Murrell, M. (2020). *Soft Matter*, 16, 7185–7190.
21. Balzani, V., Credi, A., Raymo, F. M., & Stoddart, J. F. (2000). *Angewandte Chemie*, 39, 3348–3391.
22. Purcell, E. M. (1977). *American Journal of Physics*, 45, 3–11.
23. Solovev, A. A., Mei, Y., Urena, E. B., Huang, G., & Schmidt, O. G. (2009). *Small*, 5, 1688–1692.
24. Ma, X., & Sanchez, S. (2015). *Chemical Communications*, 51, 5467–5470.
25. Moran, J. L., Wheat, P. M., & Posner, J. D. (2010). *Physical Review E*, 81, 065302.
26. Zhou, C., Zhang, H. P., Tang, J., & Wang, W. (2018). *Langmuir*, 34, 3289.
27. Ibele, M. E., Mallouk, T. E., & Sen, A. (2009). *Angewandte Chemie*, 48, 3308–3312.
28. Xu, T., Gao, W., Xu, L., Zhang, X., & Wang, S. (2017). *Advanced Materials*, 29, 1603250.
29. Chen, X., Jang, B., Ahmed, D., Hu, C., De Marco, C., Hoop, M., Mushtaq, F., Nelson, B. J., & Pane, S. (2018). *Advanced Materials*, 30, 1705061.
30. Hill, M., & Harris, N. R. (2007). Ultrasonic Particle Manipulation. In S. Hardt & F. Schönfeld (Eds.), *Microfluidic Technologies for Miniaturized Analysis Systems* (pp. 357–392). Boston, MA: Springer US.
31. Wang, W., Castro, L. A., Hoyos, M., & Mallouk, T. E. (2012). *ACS Nano*, 6, 6122–6132.
32. Bruus, H. (2012). *Lab on a Chip*, 12, 1014–1021.
33. Sadhal, S. S. (2012). *Lab on a Chip*, 12, 2292–2300.
34. Jameslighthill, S. (1978). *Journal of Sound and Vibration*, 61, 391–418.
35. Destgeer, G., Ha, B. H., Park, J., & Sung, H. J. (2016). *Analytical Chemistry*, 88, 3976–3981.
36. Moo, J. G. S., Mayorga-Martinez, C. C., Wang, H., Teo, W. Z., Tan, B. H., Luong, T. D., Gonzalez-Avila, S. R., Ohl, C.-D., & Pumera, M. (2018). *Advanced Functional Materials*, 28, 1702618.

37. Leighton, T. G., Walton, A. J., & Pickworth, M. J. W. (1990). *European Journal of Physics*, *11*, 47–50.
38. Memoli, G., Baxter, K. O., Jones, H. G., Mingard, K. P., & Zeqiri, B. (2018). *Micromachines*, *9*.
39. Strutt, J. W. (1884). *Philosophical Transactions of the Royal Society of London*, *175*, 1–21.
40. Riley, N. (2001). *Annual Review of Fluid Mechanics*, *33*, 43–65.
41. Sadhal, S. S. (2012). *Lab on a Chip*, *12*, 2600–2611.
42. Hamilton, M. F., Ilinskii, Y. A., & Zabolotskaya, E. A. (2003). *The Journal of the Acoustical Society of America*, *113*, 153–160.
43. Elder, S. A. (1959). *The Journal of the Acoustical Society of America*, *31*, 54–64.
44. Guo, F., Mao, Z., Chen, Y., Xie, Z., Lata, J. P., Li, P., Ren, L., Liu, J., Yang, J., Dao, M., Suresh, S., & Huang, T. J. (2016). *Proceedings of the National Academy of Sciences of the United States of America*, *113*, 1522–1527.
45. Ahmed, D., Mao, X., Shi, J., Juluri, B. K., & Huang, T. J. (2009). *Lab on a Chip*, *9*, 2738–2741.
46. Zhou, C., Zhao, L., Wei, M., & Wang, W. (2017). *ACS Nano*, *11*, 12668–12676.
47. Paxton, W. F., Sen, A., & Mallouk, T. E. (2005). *Chemistry – A European Journal*, *11*, 6462–6470.
48. Wang, Y., Hernandez, R. M., Bartlett, D. J., Bingham, J. M., Kline, T. R., Ayusman, S., & Mallouk, T. E. (2006). *Langmuir*, *22*, 10451–10456.
49. Lenshof, A., Magnusson, C., & Laurell, T. (2012). *Lab on a Chip*, *12*, 1210–1223.
50. Garciagradilla, V., Orozco, J., Sattayasamitsathit, S., Soto, F., Kuralay, F., Pourazary, A., Katzenberg, A., Gao, W., Shen, Y., & Wang, J. (2013). *ACS Nano*, *7*, 9232–9240.
51. Ahmed, S., Wang, W., Bai, L., Gentekos, D. T., Hoyos, M., & Mallouk, T. E. (2016). *ACS Nano*, *10*, 4763–4769.
52. Nadal, F., & Lauga, E. (2014). *Physics of Fluids*, *26*, 082001.
53. Collis, J. F., Chakraborty, D., & Sader, J. E. (2017). *Journal of Fluid Mechanics*, *825*, 29–48.
54. Nadal, F., & Michelin, S. (2020). *Journal of Fluid Mechanics*, *898*, A10.
55. Soto, F., Wagner, G. L., Garciagradilla, V., Gillespie, K. T., Lakshminpathy, D. R., Karshalev, E., Angell, C., Chen, Y., & Wang, J. (2016). *Nanoscale*, *8*, 17788–17793.
56. Voß, J., & Wittkowski, R. (2020). *Nanoscale Advances*, *2*, 3890–3899.
57. Balk, A. L., Mair, L. O., Mathai, P. P., Patrone, P. N., Wang, W., Ahmed, S., Mallouk, T. E., Liddle, J. A., & Stavis, S. M. (2014). *ACS Nano*, *8*, 8300–8309.
58. Sabrina, S., Tasinkevych, M., Ahmed, S., Brooks, A. M., La Cruz, M. O. D., Mallouk, T. E., & Bishop, K. J. M. (2018). *ACS Nano*, *12*, 2939–2947.
59. Ahmed, S., Wang, W., Mair, L. O., Fraleigh, R. D., Li, S., Castro, L. A., Hoyos, M., Huang, T. J., & Mallouk, T. E. (2013). *Langmuir*, *29*, 16113–16118.
60. Li, Z., Bai, L., Zhou, C., Yan, X., Mair, L., Zhang, A., Zhang, L., & Wang, W. (2017). *Particle & Particle Systems Characterization*, *34*, 1600277.
61. Kiristi, M., Singh, V., De Avila, B. E., Uygun, M., Soto, F., Uygun, D. A., & Wang, J. (2015). *ACS Nano*, *9*, 9252–9259.
62. Uygun, M., Juradosanchez, B., Uygun, D. A., Singh, V., Zhang, L., & Wang, J. (2017). *Nanoscale*, *9*, 18423–18429.
63. Wu, Z., Li, T., Gao, W., Xu, T., Juradosanchez, B., Li, J., Gao, W., He, Q., Zhang, L., & Wang, J. (2015). *Advanced Functional Materials*, *25*, 3881–3887.
64. Esteban-Fernández De vila, B., Angsantikul, P., Ramírez-Herrera, D. E., Soto, F., Teymourian, H., Dehaini, D., Chen, Y., Zhang, L., & Wang, J. (2018). *Science robotics*, *3*, eaat0485.
65. Wang, W., Li, S., Mair, L. O., Ahmed, S., Huang, T. J., & Mallouk, T. E. (2014). *Angewandte Chemie*, *53*, 3201–3204.
66. De Avila, B. E., Martin, A., Soto, F., Lopezramirez, M. A., Campuzano, S., Vasquezmachado, G. M., Gao, W., Zhang, L., & Wang, J. (2015). *ACS Nano*, *9*, 6756–6764.
67. Qualliotine, J. R., Bolat, G., Beltrangastelum, M., De Avila, B. E., Wang, J., & Califano, J. A. (2019). *Otolaryngology-Head and Neck Surgery*, *161*, 194599819866407.
68. De Avila, B. E., Angell, C., Soto, F., Lopezramirez, M. A., Baez, D. F., Xie, S., Wang, J., & Chen, Y. (2016). *ACS Nano*, *10*, 4997–5005.

69. Hansenbruhn, M., De Avila, B. E., Beltrangastelum, M., Zhao, J., Ramirezherrera, D. E., Angsantikul, P., Gothelf, K. V., Zhang, L., & Wang, J. (2018). *Angewandte Chemie*, *57*, 2657–2661.
70. Zhang, F., Zhuang, J., De Avila, B. E., Tang, S., Zhang, Q., Fang, R. H., Zhang, L., & Wang, J. (2019). *ACS Nano*, *13*, 11996–12005.
71. De Avila, B. E., Ramirezherrera, D. E., Campuzano, S., Angsantikul, P., Zhang, L., & Wang, J. (2017). *ACS Nano*, *11*, 5367–5374.
72. Gao, C., Lin, Z., Wang, D., Wu, Z., Xie, H., & He, Q. (2019). *ACS Applied Materials & Interfaces*, *11*, 23392–23400.
73. Wang, D., Gao, C., Wang, W., Sun, M., Guo, B., Xie, H., & He, Q. (2018). *ACS Nano*, *12*, 10212–10220.
74. Ren, L., Wang, W., & Mallouk, T. E. (2018). *Accounts of Chemical Research*, *51*, 1948–1956.
75. Ahmed, S., Gentekos, D. T., Fink, C. A., & Mallouk, T. E. (2014). *ACS Nano*, *8*, 11053–11060.
76. Wang, W., Duan, W., Zhang, Z., Sun, M., Sen, A., & Mallouk, T. E. (2015). *Chemical Communications*, *51*, 1020–1023.
77. Takatori, S. C., De Dier, R., Vermant, J., & Brady, J. F. (2016). *Nature Communications*, *7*, 10694–10694.
78. Ren, L., Zhou, D., Mao, Z., Xu, P., Huang, T. J., & Mallouk, T. E. (2017). *ACS Nano*, *11*, 10591–10598.
79. Xu, T., Soto, F., Gao, W., Garciagradilla, V., Li, J., Zhang, X., & Wang, J. (2014). *Journal of the American Chemical Society*, *136*, 8552–8555.
80. Soto, F., Martin, A., Ibsen, S., Vaidyanathan, M., Garciagradilla, V., Levin, Y., Escarpa, A., Esener, S. C., & Wang, J. (2016). *ACS Nano*, *10*, 1522–1528.
81. Minnaert, M. (1933). *Philosophical Magazine Series 1*, *16*, 235–248.
82. Bertin, N., Spelman, T. A., Stephan, O., Gredy, L., Bouriau, M., Lauga, E., & Marmottant, P. (2015). *Physical Review Applied*, *4*, 064012.
83. Ren, L., Nama, N., McNeill, J. M., Soto, F., Yan, Z., Liu, W., Wang, W., Wang, J., & Mallouk, T. E. (2019). *Science Advances*, *5*.
84. Dijkink, R., Der Dennen, J. P. V., Ohl, C., & Prosperetti, A. (2006). *Journal of Micromechanics and Microengineering*, *16*, 1653–1659.
85. Feng, J., Yuan, J., & Cho, S. K. (2016). *Lab on a Chip*, *16*, 2317–2325.
86. Louf, J., Bertin, N., Dollet, B., Stephan, O., & Marmottant, P. (2018). *Advanced Materials Interfaces*, *5*, 1800425.
87. Aghakhani, A., Yasa, O., Wrede, P., & Sitti, M. (2020). *Proceedings of the National Academy of Sciences of the United States of America*, *117*, 3469–3477.
88. McNeill, J. M., Nama, N., Braxton, J. M., & Mallouk, T. E. (2020). *ACS Nano*, *14*, 7520–7528.
89. Qiu, T., Palagi, S., Mark, A. G., Melde, K., Adams, F., & Fischer, P. (2017). *Advanced Materials Interfaces*, *4*, 1700933.
90. Feng, J., Yuan, J., & Cho, S. K. (2015). *Lab on a Chip*, *15*, 1554–1562.
91. Ahmed, D., Lu, M., Nourhani, A., Lammert, P. E., Stratton, Z., Muddana, H. S., Crespi, V. H., & Huang, T. J. (2015). *Scientific Reports*, *5*, 9744–9744.
92. Qiu, T., Palagi, S., Mark, A. G., Melde, K., Adams, F., & Fischer, P. (2016). *Applied Physics Letters*, *109*, 191602.
93. Liu, F., Cho, S. K. (2019). In *3-D Micro Swimming Drone with Maneuverability*, international conference on micro electro mechanical systems.
94. Ahmed, D., Dillinger, C., Hong, A., & Nelson, B. J. (2017). 1700050. *Advanced materials and technologies*, *2*.
95. Huang, P., Xie, Y., Ahmed, D., Rufo, J., Nama, N., Chen, Y., Chan, C. Y., & Huang, T. J. (2013). *Lab on a Chip*, *13*, 3847–3852.
96. Nama, N., Huang, P., Huang, T. J., & Costanzo, F. (2014). *Lab on a Chip*, *14*, 2824–2836.
97. Ahmed, D., Baasch, T., Jang, B., Pane, S., Dual, J., & Nelson, B. J. (2016). *Nano Letters*, *16*, 4968–4974.

98. Kaynak, M., Ozcelik, A., Nourhani, A., Lammert, P. E., Crespi, V. H., & Huang, T. J. (2017). *Lab on a Chip*, *17*, 395–400.
99. Ahmed, D., Ozcelik, A., Bojanala, N., Nama, N., Upadhyay, A., Chen, Y., Hannarose, W., & Huang, T. J. (2016). *Nature Communications*, *7*, 11085–11085.
100. Lu, X., Martin, A., Soto, F., Angsantikul, P., Li, J., Chen, C., Liang, Y., Hu, J., Zhang, L., & Wang, J. (2018). 1800374. *Advanced materials and technologies*, *4*.
101. Lu, X., Soto, F., Li, J., Li, T., Liang, Y., & Wang, J. (2017). *ACS Applied Materials & Interfaces*, *9*, 38870–38876.
102. Ma, Z., Zhou, Y., Cai, F., Meng, L., Zheng, H., & Ai, Y. (2020). *Lab on a Chip*, *20*.
103. Kagan, D., Benchimol, M. J., Claussen, J. C., Chuluunerdene, E., Esener, S. C., & Wang, J. (2012). *Angewandte Chemie*, *51*, 7519–7522.
104. Xu, B., Zhang, B., Wang, L., Huang, G., & Mei, Y. (2018). *Advanced Functional Materials*, *28*, 1705872.
105. Xu, B., & Mei, Y. (2017). *Science Bulletin*, *62*, 525–527.
106. Li, J., Rozen, I., & Wang, J. (2016). *ACS Nano*, *10*, 5619–5634.
107. Soto, F., Jeerapan, I., Silvalopez, C., Lopezramirez, M. A., Chai, I., Xiaolong, L., Lv, J., Kurniawan, J., Martin, I., & Chakravarthy, K. (2018). *Small*, *14*, 1803266.
108. Kwan, J. J., Myers, R., Coviello, C., Graham, S., Shah, A., Stride, E., Carlisle, R., & Coussios, C. (2015). *Small*, *11*, 5305–5314.
109. Barzion, A., Nourmahnad, A., Mittelstein, D. R., Yoo, S., Malounda, D., Abedi, M., Leegosselin, A., Maresca, D., & Shapiro, M. G. (2019). *bioRxiv*, 620567.
110. Myers, R., Coviello, C., Erbs, P., Foloppe, J., Rowe, C., Kwan, J. J., Crake, C., Finn, S., Jackson, E., & Balloul, J. (2016). *Molecular Therapy*, *24*, 1627–1633.
111. Ghosh, A., Xu, W., Gupta, N., & Gracias, D. H. (2020). *Nano Today*, 100836.
112. Reinisova, L., Hermanova, S., & Pumera, M. (2019). *Nanoscale*, *11*, 6519–6532.
113. Srivastava, S. K., Clergeaud, G., Andresen, T. L., & Boisen, A. (2019). *Advanced Drug Delivery Reviews*, *138*, 41–55.
114. Sitti, M. (2018). *Nature Reviews Materials*, *3*, 74–75.
115. Soto, F., & Chrostowski, R. (2018). *Frontiers in Bioengineering and Biotechnology*, *6*.
116. Sonntag, L., Simmchen, J., & Magdanz, V. (2019). *Molecules*, *24*, 3410.
117. Gao, C., Wang, Y., Ye, Z., Lin, Z., Ma, X., & He, Q. (n/a). *Advanced Materials*, 2000512.
118. Luo, M., Feng, Y., Wang, T., & Guan, J. (2018). *Advanced Functional Materials*, *28*, 1706100.
119. Nelson, T. R., Fowlkes, J. B., Abramowicz, J. S., & Church, C. C. (2009). *Journal of Ultrasound in Medicine*, *28*, 139–150.
120. Patteson, A. E., Gopinath, A., & Arratia, P. E. (2016). *Current Opinion in Colloid and Interface Science*, *21*, 86–96.
121. Bechinger, C., Leonardo, R. D., Lowen, H., Reichhardt, C., Volpe, G., & Volpe, G. (2016). *Reviews of Modern Physics*, *88*, 045006.
122. Katuri, J., Seo, K. D., Kim, D. S., & Sanchez, S. (2016). *Lab on a Chip*, *16*, 1101–1105.
123. Xiao, Z., Wei, M., & Wang, W. (2019). *ACS Applied Materials & Interfaces*, *11*, 6667–6684.
124. Rosenthal, I., Sostaric, J. Z., & Riesz, P. (2004). *Ultrasonics Sonochemistry*, *11*, 349–363.
125. Lentacker, I., De Cock, I., Deckers, R., De Smedt, S. C., & Moonen, C. T. W. (2014). *Advanced Drug Delivery Reviews*, *72*, 49–64.
126. Menz, M. D., Ye, P. P., Firouzi, K., Nikoozadeh, A., Pauly, K. B., Khuriyakub, P., & Baccus, S. A. (2019). *The Journal of Neuroscience*, *39*, 6251–6264.

Chapter 3

Manipulation and Patterning of Micro-objects Using Acoustic Waves



Citsabehsan Devendran and Adrian Neild

3.1 Introduction

Acoustics is the study of sound wave propagation within a medium (gas, liquid or solid). In fluids, sound waves are pressure waves that propagate through a medium with a certain amplitude (i.e. pressure level) and frequency (i.e. pitch). The application of acoustics is prominent in many aspects of a modern society, providing the understanding for systems addressing tasks such as noise control, musical acoustics, bioacoustics and sonar. Ultrasound or ultrasonics is a subset of acoustics that has no distinct difference in physical properties compared to that of audible sound with the exception of its frequency range. Pressure waves with frequencies in excess of 20 kHz (i.e. above the audible range of a healthy, young adult) are characterised as ultrasound. Applications of ultrasound are vast, just like its lower-frequency counterpart, being implemented in various systems such as acoustic microscopy, non-destructive testing (NDT), medical ultrasound, sonography, ultrasonic cleaning, sonochemistry, ultrasonic particle manipulation and characterisation. Ultrasonic particle manipulation and characterisation in microfluidic systems falls under the study which is generally known today as acoustofluidics.

Acoustofluidics is the term given to the study of acoustic-based manipulation or forcing of particles within microfluidic systems and will be an important part of this chapter. Since its inception, acoustophoretic devices have addressed applications including microparticle filtration [1–3], cell handling [4–6] and microdroplet handling [3, 7, 8]. The force amplitude dependence on factors such as size, shape, density and compressibility gives rise to a robust and highly practical technique for cell or particle separation.

C. Devendran · A. Neild (✉)

Laboratory for Micro Systems, Department of Mechanical and Aerospace Engineering,
Monash University, Clayton, VIC, Australia

e-mail: adrian.neild@monash.edu

© Springer Nature Switzerland AG 2022

Y. Sun et al. (eds.), *Field-Driven Micro and Nanorobots for Biology and Medicine*, https://doi.org/10.1007/978-3-030-80197-7_3

The design of acoustofluidic systems requires careful consideration of a number of key factors. Firstly the nature of the force field created needs to be chosen to suit the application in order to perform a particular task effectively (Sect. 3.2). Secondly, the excitation method must be selected such that the desired acoustic field can be generated (Sect. 3.3). Thirdly, when used in biomedical applications involving live biological cells, biocompatibility evaluation is critical. Acoustofluidics has been widely accepted as a biocompatible technique, substantiated with cell viability studies [9–13]. Indeed, typically studies are corroborated with a single viability method, most commonly live/dead staining [5, 6, 14, 15], or trypan blue exclusion [16, 17]. It should be noted, until recently, that there have been no extensive viability studies at elevated frequencies (30–600 MHz) [18]. The study shows that acoustic manipulation techniques can be biocompatible; however, this is highly dependent on the acoustic excitation parameters, namely, amplitude and frequency of operation. Furthermore, the cell type handled plays a significant role on how a cell responds to an acoustic stressor. Undesired effects have been detailed from alterations in critical biological functions such as cell attachment and spreading, as well as cell death when operating at certain frequencies and amplitudes. Furthermore, a yet to be completely understood effect of metabolic alteration in cells exposed in acoustic excitation might prove to be beneficial and harnessed for therapeutic applications in the future. Therefore, any developing or developed acoustic-based platforms that involve the manipulation of biological cells should be tested with an array of probing techniques as suggested in Fig. 3.1 to

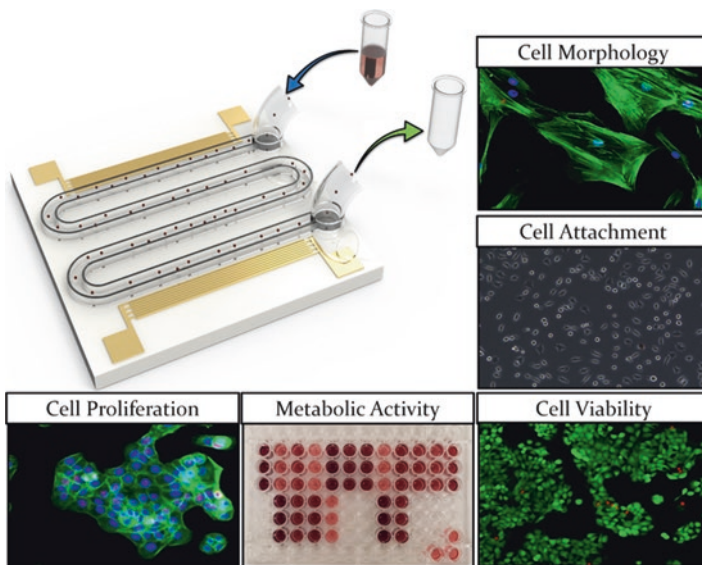


Fig. 3.1 Suggested phenotypical assessments including typical live/dead assays, cell attachment, morphology, proliferations and metabolic activity to be conducted post-acoustic exposure to ensure cell health is unaffected [Reproduced with under the terms of the Creative Commons CC BY 4.0 license from [18]

ensure no undesired phenotypical alterations are imposed, critical to adoption within clinical and life science applications.

In this chapter, the mechanisms and applications of acoustic manipulation technologies will be examined. These techniques have been widely applied to microfluidic system to enable remote manipulation of suspended material; in addition the use of acoustic forces for manipulation and visualisation in larger fluid volumes will be considered, as will the role such forces can play in micro-robotics.

3.2 Forces

When a particle or droplet is suspended within a vibrating fluid medium (liquid or gas), it experiences a force that results in a net movement of the object. This force arises from terms which when averaged over the time of a vibration cycle are non-zero; hence there is a non-linearity which causes a vibration to yield this steady-state force. This force depends on the particle's physical properties, the fluid medium and resultant pressure field. The presence of the particle within this vibrating fluid causes an exertion of three main types of forces, namely, acoustic radiation forces (ARF) [19], Bjerknes forces [20] and acoustic streaming-induced drag forces [21]. These forces along with the relevant formulae will be discussed in detail.

3.2.1 Acoustic Radiation Force

Vibration of a fluid volume will result in a pressure field. As a result of introducing a particle within this pressure field, a net force is experienced by the particle known as acoustic radiation force (ARF). There are three different scenarios that give rise to the resultant force, namely, the interaction with the incident sound wave and the particle, the scattered sound wave of the particle and finally the sound wave within the particle due to transmittance. These interrelated scenarios affect the resultant pressure field which is highly dependent on the shape, size and physical properties of the particle itself. As these vibrations are oscillating at very high frequencies (typically kHz or MHz), net motion of the particle only occurs due to time-averaged effects. Notably, due to the harmonic nature of these excited fields, the first-order pressure and velocity terms time-average to a zero value as shown in Eq. 3.2.

We let the $\langle X \rangle$ be the time average over a full harmonic oscillation,

$$X = \sin(\omega t) \quad (3.1)$$

$$\langle X \rangle = \frac{1}{T} \int_0^T \sin(\omega t) dT = 0 \quad (3.2)$$

where, the angled brackets denote the time-averaged operator, T is the period of oscillation, t is time, and ω is the angular frequency of oscillation. However, the time average of a pressure squared term is non-zero, as shown in Eq. 3.4,

$$X^2 = \sin^2(\omega t) \quad (3.3)$$

Therefore,

$$\langle X^2 \rangle = \frac{1}{T} \int_0^T \sin^2(\omega t) dT = \frac{1}{2} \quad (3.4)$$

As such, for non-zero time-averaged terms to exist, pressure and velocity squared terms must be present in the equation describing the vibration within the pressure field. For simplicity, we assume a spherical object of a particular material property when deriving the equations that dictate these forces. We employ perturbation theory to obtain the second-order governing equations in terms of the first-order (harmonic) pressure, P , and velocity fluctuations, \vec{v} [22, 23].

Now, if we consider the thermodynamic equation of state by expressing P in terms of the density, ρ (Eq. 3.5), the continuity equation for density (Eq. 3.6) and the Navier-Stokes equation for the velocity field, \vec{v} (Eq. 3.6), we have

$$P = P(\rho) \quad (3.5)$$

$$\frac{\partial \rho}{\partial t} = -\nabla \cdot (\rho \vec{v}) \quad (3.6)$$

$$\rho \frac{\partial \vec{v}}{\partial t} = -\nabla P - \rho(\vec{v} \cdot \nabla) \vec{v} + \eta \nabla^2 \vec{v} + \beta \eta \nabla (\nabla \cdot \vec{v}) \quad (3.7)$$

First-order terms in Eqs. 3.6 and 3.7 yield

$$\frac{\partial \rho_1}{\partial t} = -\rho_0 \nabla \cdot \vec{v}_1 \quad (3.8)$$

$$\rho_0 \frac{\partial \vec{v}_1}{\partial t} = -\nabla P_1 + \eta \nabla^2 \vec{v}_1 + \beta \eta \nabla (\nabla \cdot \vec{v}_1) \quad (3.9)$$

whilst second-order terms in the governing equations (Eqs. 3.6 and 3.7) yield

$$\nabla \langle \rho_1 \vec{v}_1 \rangle = -\rho_0 \nabla \cdot \langle \vec{v}_2 \rangle \quad (3.10)$$

$$\left\langle \rho_1 \frac{\partial \vec{v}_1}{\partial t} \right\rangle + \rho_0 \langle (\vec{v}_1 \cdot \nabla) \vec{v}_1 \rangle = -\nabla \langle P_2 \rangle + \eta \nabla^2 \langle \vec{v}_2 \rangle + \beta \eta \nabla (\nabla \cdot \langle \vec{v}_2 \rangle) \quad (3.11)$$

Here, the first-order harmonic terms (subscript 1) are multiplied; therefore, we have cases of squared sinusoidal terms, which will time average to non-zero steady-state values and as such are equated to second-order, nonharmonic terms (subscript 2).

If we assume an inviscid fluid, far from any walls (i.e. $>5 \delta_v$), therefore, $\eta \approx 0$ and can be neglected. The boundary layer thickness or viscous penetration depth, δ_v , is

given as, $\delta_v = \sqrt{\frac{2\eta}{\omega\rho_0}}$ where η is the shear viscosity.

Using Eqs. 3.9 and 3.11, along with $P_1 = \rho_1 c_0^2$, the following can be obtained:

$$\langle P_2 \rangle = \frac{1}{2} \kappa_0 \langle P_1^2 \rangle - \frac{1}{2} \rho_0 \langle \bar{v}_1^2 \rangle \quad (3.12)$$

where the fluid compressibility, κ_0 , is given by

$$\kappa_0 = \frac{1}{\rho_0 c_0^2} \quad (3.13)$$

Now, that we have obtained an expression of the second-order time-averaged pressure in terms of the first-order known terms (Eq. 3.12), we can formulate a numerical solution for the radiation force acting on the particle. The acoustic radiation force is given by the momentum flux equation,

$$\mathbf{F}_{\text{rad}} = \int_S \boldsymbol{\sigma} \mathbf{n} dS \quad (3.14)$$

where $\boldsymbol{\sigma}$ is the stress acting on the particle within the pressure field, \mathbf{n} is the normal vector, and \mathbf{F}_{rad} is the radiation force acting on the particle as a result of the vibrating pressure field. The integral is taken over the surface, S , of a particle moving in response to the applied force. Thus, the surface is a function of time, $S = S(t)$. To accommodate for this fluctuating surface, we add a convective momentum flux term compensating for this fluctuation, thus compensating for the error [24]. The force, in total, becomes

$$\mathbf{F}_{\text{rad}} = \int_{S_0} \boldsymbol{\sigma} \mathbf{n} dS - \int_{S_0} \rho (\bar{\mathbf{v}} \mathbf{n}) \cdot \bar{\mathbf{v}} dS \quad (3.15)$$

where $\boldsymbol{\sigma}$ is given by the second-order time-averaged pressure as shown in Eq. 3.12,

$$\boldsymbol{\sigma} = -\frac{1}{2\rho_0 c_0^2} \langle P_1^2 \rangle + \frac{1}{2} \rho_0 \langle \bar{v}_1^2 \rangle \quad (3.16)$$

Finally, we arrive at

$$\mathbf{F}_{\text{rad}} = \frac{1}{2} \rho_0 \int_{S_0} \left[\langle \bar{v}_1^2 \rangle - \frac{1}{\rho_0^2 c_0^2} \langle P_1^2 \rangle \right] \mathbf{n} dS - \rho_0 \int_{S_0} (\mathbf{n} \cdot \bar{\mathbf{v}}_1) \bar{\mathbf{v}}_1 dS \quad (3.17)$$

For cases where the compressible particle with radius, r , is much smaller than that of the acoustic wavelength, λ_{aco} (i.e. $r \ll \lambda_{aco}$), and is present within a standing wave field, an analytical solution can be found. This analytical expression is commonly known as Gor'kov's potential [25], and the equation can be used to analytically predict the motion and collection location of the suspended particles. The force, \mathbf{F}_{rad} , acting on this small, spherical particle in an unbounded domain can be calculated by

$$U_{Gor'kov} = 2\pi r^3 \rho_f \left(\frac{1}{3} \frac{\langle P_1^2 \rangle}{\rho_f^2 c_f^2} f_1 - \frac{1}{2} \langle \tilde{v}_1^2 \rangle f_2 \right)$$

$$f_1 = 1 - \frac{\kappa_p}{\kappa_f}, f_2 = \frac{2(\rho_p - \rho_f)}{2\rho_p + \rho_f} \quad (3.18)$$

where

$$\mathbf{F}_{rad} = -\nabla U_{Gor'kov} \quad (3.19)$$

where subscripts f and p denote the fluid and particle, respectively.

The direction and the force that dictate the motion of the particle depend on the material properties given by the acoustic contrast factor, Φ

$$\Phi = \frac{1}{3} f_1 + \frac{1}{2} f_2$$

$$= \frac{1}{3} \left[\frac{5\rho_p - 2\rho_f}{2\rho_p - \rho_f} - \frac{\kappa_p}{\kappa_f} \right] \quad (3.20)$$

whereby a positive Φ dictates the motion of a particle towards the local second-order time-averaged pressure node (i.e. at location where $\langle P_2 \rangle \approx 0$ or are local minima) as shown in Fig. 3.2a and the contrary is true for a negative Φ , where motion is towards the second-order time-averaged pressure antinode (i.e. location where $\langle P_2 \rangle$ is a maximum or local maxima).

3.2.2 Bjerknes Forces

Bjerknes forces were first described by Vilhelm Bjerknes in 1906 [26]; they are a type of acoustic radiation force. In this section, we will focus on the secondary Bjerknes force which arises due to a particle's interaction with a wave scattered of a nearby particle. These forces have been examined between bubble-bubble, bubble-particle (Fig. 3.2b) and particle-particle interactions via a mathematical approach [27, 28].

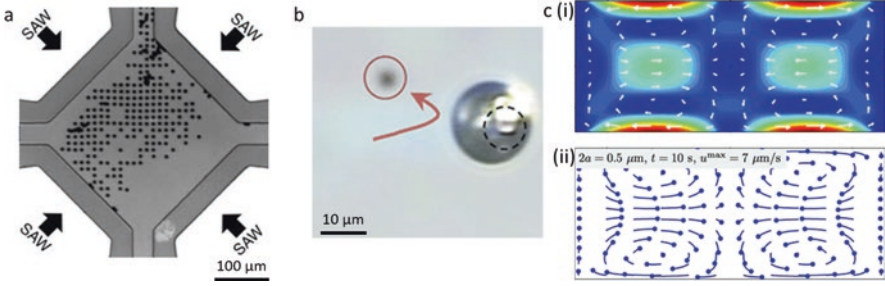


Fig. 3.2 Examples of forces as result of acoustic excitation used to pattern particles using (a) acoustic radiation forces (ARF) driven by standing surface acoustic waves in a one-cell-per-well (OCPW) system [Reproduced under the terms of the Creative Commons Attribution 4.0 International License from [5]], (b) the use of Bjerknes forces to selectively trap particles based on stiffness using an oscillating bubble, repelling a $5\mu\text{m}$ polystyrene particle whilst trapping a silica particle of the same size [Reproduced from [132] with permission from The Royal Society of Chemistry], and (c) the numerical demonstration of acoustic streaming-induced drag force on particles as a result of the steady-state streaming field developed in a bulk acoustic wave-driven system [Reproduced from [22] with permission from The Royal Society of Chemistry]

Assuming two identical spherical particles, which are much smaller than the acoustic wavelength ($r \ll \lambda_{aco}$) and are located close to each other ($d \ll \lambda_{aco}$; where d is the distance between the two particles), in a one-dimensional field, the Bjerknes force can be expressed as [29–31]

$$\mathbf{F}_{\text{Bj}} = 4\pi r^6 \left[\frac{(\rho_p - \rho_f)^2 (3 \cos^2 \theta - 1)}{6\rho_f d^4} \bar{v}_1^2 - \frac{\omega^2 \rho_f (\kappa_p - \kappa_f)^2}{9d^2} P_1^2 \right] \quad (3.21)$$

where θ is the angle between the line connecting the particles and the axis of the standing wave. Although Eq. 3.21 is not valid for larger particles and larger gaps, it does indicate how, within these limitations, these forces scale with distance and particle properties. A key feature to take away from this equation is that the Bjerknes force is highly sensitive to the gap in between the two particles, as it diminishes rapidly as d increases. This is a force which is important only when particles are in close proximity.

3.2.3 Acoustic Streaming-Induced Drag Forces

Acoustic streaming is a phenomenon of net flow within a fluid medium that is generally dominated by an oscillatory fluid particle motion [21]. There are two distinct types of streaming that arise from sound waves. Firstly, “quartz wind” or Eckart streaming is a result of a spatial attenuation of a beam of plane travelling wave. The pressure and velocity decay over a distance in the wave propagation direction results

in a net force when the time-averaged non-linear effects are considered, thus a net flow in the same direction [21]. Secondly, the effect of sound waves interacting with a fluid interface will give rise to acoustic streaming. This type of streaming is generally observed within the viscous boundary layer, δ_v , on the surface. Although the medium in the bulk fluid vibrates irrotationally, at the boundary it vibrates rotationally (i.e. with vorticity) due to the constraint of the no-slip boundary condition of the wall. This classification of streaming is known as boundary-driven streaming or ‘‘Schlichting streaming’’, and whilst generated within the boundary layer, it drives flow in the region outside δ_v known as Rayleigh streaming [22] as shown in Fig. 3.2c. Although acoustic streaming is often viewed as problematic in many scenarios where streaming generation is detrimental and disruptive to, for example, particle capture, when employed correctly, it can serve as a useful tool within microfluidic devices, offering a means to add strong local flow velocities to these systems which generally operate in low Reynolds numbers.

Streaming flows will induce a drag force on particles suspended within the fluid media; to find this, we need to express the unknown second-order streaming velocity, \bar{v}_2 , in terms of known first-order terms (calculated from a harmonic analysis of the system). Here we employ an approach introduced by Nyborg [21]. If we combine the left-hand side of Equation 6 (equated to a body force, \mathbf{F}) and Eq. 3.7, we arrive at

$$\mathbf{F} = \mathbf{F}_0 - \mathbf{F}_{\text{Reynolds}} = \frac{\partial(\rho\bar{v})}{\partial t} + \rho(\bar{v} \cdot \nabla)\bar{v} + \bar{v}\nabla \cdot \rho\bar{v} \quad (3.22)$$

where

$$\mathbf{F}_0 = \frac{\partial(\rho\bar{v})}{\partial t}; \mathbf{F}_{\text{Reynolds}} = -[\rho(\bar{v} \cdot \nabla)\bar{v} + \bar{v}\nabla \cdot \rho\bar{v}] \quad (3.23)$$

Here, once again we employ the perturbation approach with small disturbances similar to that in Eq. 3.8. We also take the time-averages terms to obtain the time-independent effect as previously demonstrated in Eqs. 3.7, 3.8 and 3.9. It should be noted that \mathbf{F}_0 time-averages to zero in steady state and therefore, $\mathbf{F} = -\mathbf{F}_{\text{Reynolds}}$. Thus, we arrive at the time-averaged time-independent second-order equations,

$$\mathbf{F} = \rho_0(\bar{v}_1 \cdot \nabla)\bar{v}_1 + \bar{v}_1\nabla \cdot \bar{v}_1 \quad (3.24)$$

$$\mathbf{F} = -\nabla P_2 + \beta\eta\nabla(\nabla \cdot \bar{v}_2) + \eta\nabla^2\bar{v}_2 \quad (3.25)$$

Based on Eqs. 3.24 and 3.25, we are able to evaluate the second-order steady-state velocity field (the acoustic streaming velocity, \bar{v}_2) based on the first-order velocity and pressure fields (subscript 1). A spherical particle that has an initial velocity, \mathbf{u} , will experience a drag force as a result of this steady-state streaming velocity field; this is given by the Stokes drag formula.

$$\mathbf{F}_{\text{drag}} = 6\pi\eta r(\vec{v}_2 - \vec{u}) \quad (3.26)$$

The drag force is proportional to the particle radius, whilst the acoustic radiation force is proportional to the radius cubed (Eq. 3.17). Hence, as the particle becomes smaller, the drag force starts to dominate, meaning the ability of the acoustic radiation force to pattern particles at force potential minima is overcome by the drag which acts to move the particle in the swirling streaming flows [22, 32].

3.3 Excitation Methods

Within acoustofluidic systems, a few major types of excitation methods have been established to excite the desired acoustic fields within the fluid medium. The major methods are known as bulk acoustic waves (BAW) (Sect. 3.3.1) and surface acoustic waves (SAW) (Sect. 3.3.2). Utilisation of particular methods is warranted by the application or task at hand as each method has their advantages and disadvantages. The major difference between the two methods is that for BAW systems the entire fluid volume is vibrated usually at a resonate frequency whilst SAW-based devices have a localised acoustic field that is dictated solely by the resonance of patterned interdigital transducers (based on the intended frequency of operation) and not the channel or chamber geometry. In this section, the theory associated with these actuation methods, fabrication and applications within microfluidic systems will be discussed.

3.3.1 Bulk Acoustic Waves

As the name indicates, bulk acoustic wave-based devices are systems in which the bulk of the piezoelectric transducer is excited, which in turn is used to excite the fluid medium. This mode of vibration is strongly dictated by the geometry of the device itself, as it is this geometry which dictates the resonant frequencies which need to be excited to establish a high amplitude sound field. Due to its geometry-dependent nature, early on, BAW devices generally operated in multi-node resonance modes and were in centimetre dimensions or larger [33, 34]. Over time, with advancements in microfabrication techniques, these dimensions were reduced to millimetre sizes and smaller, therefore, increasing the frequency of operation.

Theory

When designing a system that utilises BAW, we consider the geometry of the system. Commonly, either the width or height of the channel is considered for a continuous free flow system as shown in Fig. 3.3a. Though some systems use

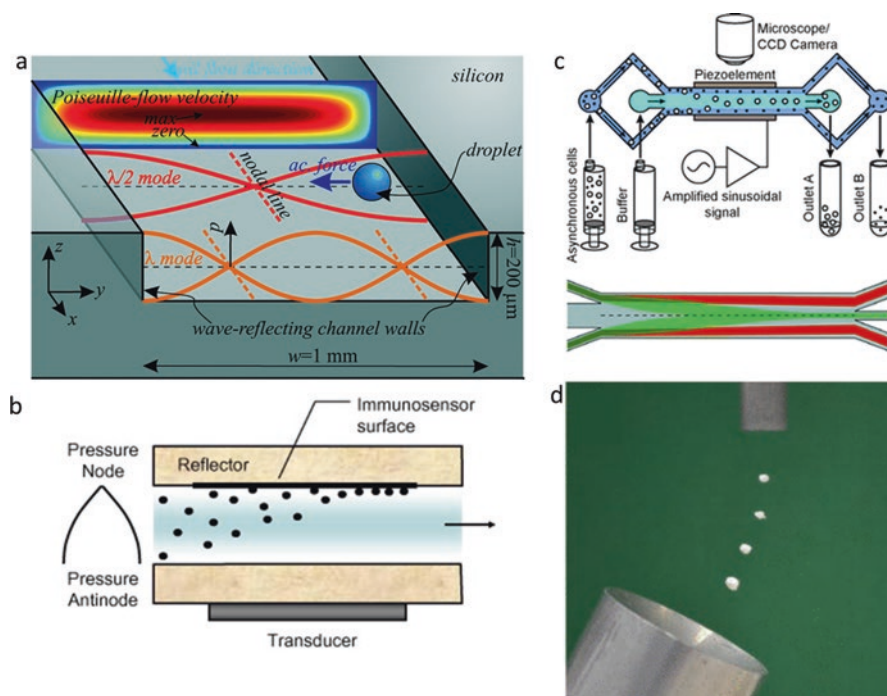


Fig. 3.3 Examples of bulk acoustic wave-driven systems to (a) handle droplets within a silicon microchip [[39] – published by The Royal Society of Chemistry under the Creative Commons Attribution 3.0 Unported Licence], (b) a quarter-wave resonator used for particle filtration [Reprinted from [36], Copyright 2008, with permission from Elsevier], (c) achieving cell cycle phase synchronisations in mammalian cells [Adapted with permission from American Chemical Society from [133]. Copyright 2010] and (d) a non-resonant acoustic levitator for particle trapping in air [Reprinted from [43], with the permission of AIP Publishing]

two-dimensional sound fields, which may dictate the need to consider both the width and length dimensions. Essentially, the dimension that is parallel to the wave propagation direction is important in the design process. In order to establish a resonant mode or resonance, the characteristic channel or chamber dimensions should be a multiple of half a wavelength. It should be noted this is only the case if the channel or chamber alone dictates the field. However, if a resonant reflector that imposes a pressure release boundary condition as discussed by Hill et al [35–37] is used, the chamber can be designed to establish a quarter-wavelength (Fig. 3.3b) acoustic field that pushes suspended particles towards the reflector surface. A great benefit of decreasing the size of the system is the increase in the frequency of operation. By increasing the frequency, the radiation forces associated increase as well; therefore, efficient particle manipulation can be achieved [38]. The primary axial force, F_{ax} , acting upon a particle in suspension, in a standing wave, is given by

$$\mathbf{F}_{ax} = 4\pi r^3 E_{ac} k_f \sin(2k_f x) \Phi \quad (3.27)$$

where r is the particle radius, E_{ac} is the acoustic energy density, x is the particle position in the wave propagation direction, Φ is the acoustic contrast factor as given in Eq. 3.20, and k_f is the wave number given by

$$k_f = \frac{\omega}{c_f} = \frac{2\pi f}{c_f} \quad (3.28)$$

where f is the frequency and c_f is the speed of sound of the fluid medium.

3.3.2 Design Considerations

The acoustic energy density, E_{ac} , is given by

$$E_{ac} = \frac{P_a^2}{4\rho_f c_f^2} = \frac{1}{4} \rho_f v_a^2 \quad (3.29)$$

where P_a and v_a are the absolute pressure and velocity fields.

The wavelength of a system is given by rearranging the velocity of an oscillating wave equation to arrive at

$$\lambda_f = \frac{c_f}{f} \quad (3.30)$$

Therefore, the channel dimensions are fabricated based on the wavelength, λ_f , or multiples thereof depending on requirements of the system.

There are two major types of transducer designs or configurations that are generally associated with bulk acoustic waves, namely, layered resonator [35] and transversal resonators [39–41]. Layered resonators typically consist of a piezoelectric element (i.e. transducer), a coupling layer, a matching layer, the fluid layer and a reflector. Each of these layers plays a major role in building an efficient resonator. Firstly, the piezoelectric layer excites (i.e. generates the sound wave) the resonator based on an input A/C signal. The coupling layer serves as an adhesive layer and also transmits the generated sound wave from the transducer to the next layer. Next follows the matching layer (also known as the carrier layer or transmission layer), which acts as a good acoustic transmission layer and also forms the bottom of the resonating chamber. The fluid layer where the suspended particle or cells are manipulated is then sandwiched between the matching layer and the reflector as shown in Fig. 3.3b. Typical dimensions (i.e. thickness of individual layers) that are used for optimum energy transmission into the fluid medium

are included. However, quarter-wavelength fluid layers can be designed albeit less efficient, by altering the design criteria of the reflector layer to ensure it acts as a pressure release boundary [35–37].

Consideration of the material selection for each individual layer, especially the matching layer, should be taken into account as well, to ensure maximum energy transfer. At an interface, part of the energy is transmitted, and another part is reflected depending on the material properties and incident angle, thus, strongly influencing the amount of damping and efficiency of the device at a particular resonance mode. If we consider a normal incidence, the reflected energy, R_E , and transmitted energy, T_E , are given by [42]

$$R_E = \frac{(Z_2 - Z_1)^2}{(Z_2 + Z_1)^2} \quad (3.31)$$

$$T_E = 1 - R_E = \frac{4Z_1Z_2}{(Z_2 + Z_1)^2} \quad (3.32)$$

where $Z_i = \rho_i c_i$ are the characteristic impedances of the two materials respectively and dictate the energy transfer characteristics of the system. Therefore, materials that are impedance matched with each other allow for efficient device operation and should be used if possible.

In contrast to layered resonators, a transversal resonator operates such that the standing wave orientation is perpendicular to the direction of the electrical field applied to the transducer. Here, the channel width corresponds to a multiple of half wavelength, when operated at resonance. A major benefit of using transversal resonators as opposed to layered resonators is that focusing of particles occurs in a vertical plane within the fluid volume allowing for ease of visual observation and also allowing for easy integration with other microfluidic components, for example, channel branches to split the flow and extract a concentrated solution of particles (Fig. 3.3c). BAW systems can also be used to achieve particle trapping in air, known as acoustic air levitation (Fig. 3.3d) with the use of Langevin transducers and reflectors [43].

3.3.3 Surface Acoustic Waves

In 1885, Lord Rayleigh first introduced the theory of surface waves [44]. In this work, he investigated the characteristics of a wave on a free surface of an infinite homogeneous isotropic elastic solid, such that the disturbances are confined to a small region comparable in depth to the size of the wavelength. He went on to draw comparisons with deep-water waves, with the exception that the restoring forces are dependent on the “elastic resilience” (i.e. elastic forces of the solid) instead of gravity and surface tension as in liquids. Due to the nature of surface wave propagation which predominantly spreads in two dimensions only, amplitude decays occur at a

slower rate with distance as compared to bulk elastic waves [42]. At its inception, surface waves were seen as most significant in understanding seismology. However, many decades later, with the application of microfabrication techniques and piezoelectrics, the scales of these systems have decreased and thus been applied to various different fields such as surface testing, electronic filters and sensors [45] as well as microfluidics.

A major difference between SAW and BAW is that the acoustic wave generation within the fluid medium is exclusively within the vicinity of the wave generation rather than the entire fluid volume being resonated. SAW-based acoustic devices also offer a major advantage of operating at much higher frequencies as compared to BAW devices, which allows for much better control of particle manipulation. Generation of SAW, utilising a single set of interdigital transducers (IDTs), allows for the formation of travelling surface acoustic waves (TSAWs) or two opposing sets of IDTs to establish standing surface acoustic waves (SSAWs) independent of channel geometry. The inherent nature of SAW means the wave propagation is restricted to the surface; hence, energy dissipation is low.

Theory

To generate a SAW, a series of IDTs are patterned on a piezoelectric substrate as shown in Fig. 3.4a–e. When an A/C signal is applied across the patterned array of IDTs, a surface displacement is observed due to the piezoelectric nature of the substrate. These IDTs are patterned with a certain design to ensure efficient generation of a SAW propagating along the surface and transmitting into the intended fluid volume. The IDTs are designed to ensure the emanating SAW is reinforced by each finger pair. Therefore, the width of each finger and the spacing between them are designed in accordance with the intended operational frequency. The frequency, f , is given by

$$f = \frac{c_{SAW}}{\lambda_{SAW}} \quad (3.33)$$

where c_{SAW} is the phase velocity of the piezoelectric substrate which differs based on the direction of propagation [46] given the anisotropic nature of the piezoelectric substrate and λ_{SAW} is the resonant SAW wavelength produced.

The most common design of IDTs for use in acoustofluidics constitutes $\frac{1}{4}\lambda_{SAW}$ wide fingers and patterned with a gap between finger pairs of the same dimensions. Predominantly, lithium niobate (LiNbO_3) is used as the piezoelectric element as it has favourable characteristics such as its high spontaneous polarisation and electro-mechanical coupling coefficients [47, 48] and low acoustic attenuation [49]. A propagating SAW along a surface will radiate energy at an angle (Fig. 3.4a) when it encounters a solid-fluid interface. This angle is known as the Rayleigh angle, θ_R ,

and is defined as the angle of propagation into the fluid from the normal to the substrate, given by the Snell's law [42],

$$\theta_R = \sin^{-1} \left(\frac{c_f}{c_{SAW}} \right) \quad (3.34)$$

This transmitted wave is known as the leaky Rayleigh wave as the Rayleigh wave leaks energy into the fluid medium as it travels along the fluid-solid interface. It should be noted that attenuation along a solid-gas interface occurs but is relatively small and therefore can be neglected. The attenuation coefficient, α_R , of the leaky Rayleigh wave due to radiation of a compression wave along a fluid-solid interface is given by [50]

$$\alpha_R = \frac{\rho_f c_f}{\rho_{substrate} c_{SAW} \lambda_{SAW}} \left[\text{in m}^{-1} \right] \quad (3.35)$$

where $\rho_{substrate}$ is the density of the piezoelectric substrate. It should be noted that there is an additional energy loss due to frictional losses [50] but is typically small and, therefore, often neglected.

In addition to consideration of attenuation within the liquid and IDT finger spacing, the number of finger pairs also plays an integral role in ensuring efficient operation. Besides reinforcing the propagating wave, the additional IDT pairs alter the electrical impedance of the system. In a similar way, whereby acoustically impedance matched systems operate optimally, an electrically impedance matched circuit ensures maximum energy transfer from the external power source (i.e. signal generator and power amplifier) to the IDTs and, therefore, maximum power transmission to the piezoelectric substrate and, thus, the fluid medium. It should be noted the number of finger pairs is not critical for operation as systems would still function, albeit not optimally. It is also worth noting that there are other designs of IDTs which are used for various different applications in acoustofluidics as shown in Fig. 3.4b and d. Each of these IDT configurations results in a different displacement field and thus a different pressure field within the fluid medium. The normal or straight IDTs are most commonly used in microfluidic devices as it is the most efficient design in terms of operation. This configuration operates at a single frequency as dictated by the uniform finger width and spacing as shown in Fig. 3.4c and e, thus making it easy to define the displacement and resultant pressure field. Focused or curved IDTs [51] consist of pairs of annular electrodes and can operate at a single frequency or multiple frequencies as well but direct the propagating wave and energy to a small focal point, where, this high acoustic intensity region is desirable in applications such as microdroplet production [52]. The slanted IDTs, on the other hand, consist of a varying finger width along its length, allowing for the generation of narrow SAW beams of varying frequencies [53]. Chirped IDTs [54] similarly allow for variation but in terms of frequency of operation, where a range of frequencies can be excited as opposed to a single frequency. This is as a direct result of the variation in finger widths throughout the IDT set. Due to the benefit of operating

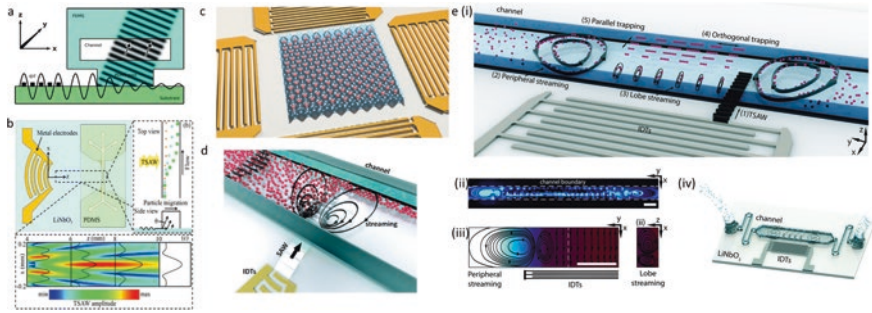


Fig. 3.4 Surface acoustic waves (SAW) employed as travelling waves (a) via the use of PDMS as a waveguide enabling acoustic fluorescence-activated cell sorting [Reproduced from [3] with permission from The Royal Society of Chemistry] and (b) for the size-based separation of particles [Reproduced from [134] with permission from The Royal Society of Chemistry]. (c) SAW used to pattern one cell per well in defined configurations using a two-dimensional wave field, enabled by two opposing pairs of IDTs [Reproduced under the terms of the Creative Commons Attribution 4.0 International License from [5]]. (d) Travelling SAW induced microvortex to continuously focus nanoparticles along a defined path [Reproduced from [135] with permission from The Royal Society of Chemistry]. (e) Depictions of broad range of phenomena inherent within surface acoustic wave platforms as a result of diffraction [Reproduced from [59] with permission from The Royal Society of Chemistry]

over a range of frequencies, chirped IDTs allow for a sweep of frequencies to be used which is highly beneficial for migrating particles beyond a wavelength [55]. It is worth noting the configuration of chirped IDTs can be integrated with that of curved IDT designs to emanate a propagating wave with a high spatial amplitude gradient (i.e. focal point) over a range of frequencies.

More recently, diffractive effects based on the Huygens-Fresnel principle have been examined to capture the “knife-edge” effect induced by the channel walls, giving a more detailed description of the more complex aspects of the established pressure fields [56–58]. In addition, due to the finite width of the IDTs (i.e. aperture), diffraction is known to affect the resultant surface displacement profiles, thus the consequent pressure field within the bulk fluid [32, 59]. These effects should be considered whilst designing and fabricating SAW-driven acoustofluidic platforms as they significantly alter the resultant pressure fields and therefore the intended particle behaviour. Clever manipulation of these effects can lead to beneficial outcomes as well, enabling relatively simple excitation methods to achieve the same or an enhanced outcome [60, 61].

3.3.4 Tweezing

Acoustic tweezing is a subset of acoustofluidics that utilises pressure fields to control and manipulate the location of individual or a group of particles, akin to that of optical tweezers developed by Arthur Ashkin [62] in 1986 who went on to win the 2018 Nobel Prize in Physics for this discovery. Acoustic tweezers have been

commonly used to describe most acoustofluidic-based manipulation techniques, including that of standing and travelling wave platforms, via BAW and SAW, as described earlier. However, in this chapter, the term acoustic tweezing is used specifically to refer to the selective manipulation of individual or a defined group of suspended matter. Such an ability is immensely useful to a wide range of applications, specifically in microbiology, microscopy and micro-robotic platforms (including therapeutics and drug delivery). Acoustic tweezers offer benefits over its optical counterpart as it is applicable within opaque objects, such as biological tissue, and is able to penetrate deeper due to its lower attenuation effects. Furthermore, acoustic manipulation is considered a safer option for *in vivo* operations as compared to optical tweezers which tend to have detrimental effects in terms of localised heating induced by the laser [63]. There are three distinct methods used to enable acoustic tweezers, namely, ultrasonic arrays, hologram planes and acoustic vortex beams.

Ultrasonic Beams

As proposed by Wu in 1991 [64], these types of acoustical tweezers were based on a stable force potential well located at a focal point enabled by the use of focused ultrasonic beams. The study went on to use two opposing collimated focused ultrasonic beams, driven by broadband lead-zirconate-titanate (PZT) focusing transducers, to trap particles and frog eggs. This concept was developed to increase its robustness and flexibility, using a single beam, driven by a single-element transducer, theoretically [65] and experimentally, to achieve transversal trapping but not axial trapping [66].

However, single-beam trapping in both the transverse and axial direction is difficult to achieve. This is due to the competing nature of the attractive gradient force enabling trapping in the transverse direction but a repulsive force induced by the backscattering in the axial direction. Baresch et al. proposed the use of acoustic vortices (Fig. 3.5a) to trap particles in three dimensions, further improving the efficacy of acoustic tweezers [67]. The concept was based on using focused axisymmetric vortex beams driven by spherical transducers that consist of a pressure minima at the central core of the beam, minimising undesired effects arising from the wave backscattering, enabling the trapping and physical translation of relatively dense and stiff particles [68].

Ultrasonic Arrays

Although simple standing wave, travelling wave and acoustic beam fields are powerful tools enabling a wider range of manipulation and dexterity, the ability to shape the phase and amplitude of a field spatio-temporally further increases the applicability and integration of these systems, enabling relatively complex particle manipulation along a defined trajectory. A single-element transducer is restricted in terms of the field it can establish and, therefore, difficult to generate complex pressure fields.

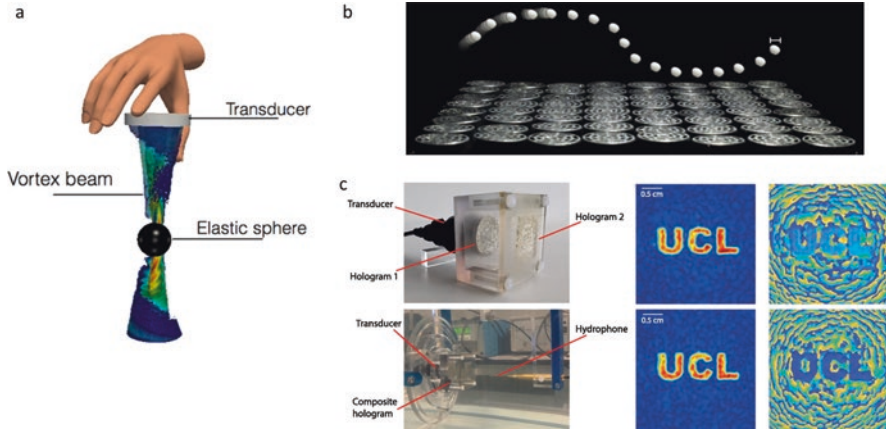


Fig. 3.5 (a) Rendered image depicting the use of acoustic vortices as tweezers to trap and manipulate elastic spheres [Reprinted from [136], Copyright 2017, with permission from Elsevier]. (b) The development of phased arrays enabling the ability to manipulate individual particles along complex defined trajectories [Reproduced under the terms of the Creative Commons Attribution 4.0 International License from [69]]. (c) The use of holographic phased delay plates to control the phase and amplitude of the acoustic field, allowing for the development of complex patterns at a defined plane [Reprinted from [137], with the permission of AIP Publishing]

Ultrasonic arrays, as implied by the name, constitute an array of transducers arranged in a specific configuration and driven with a phase-controlled output to establish complex pressure fields enabling tweezing [69]. This technology is enabled via the development of microfabrication as well as driving circuitry that allows for the independent control of frequency, phase, intensity and pulse duration of each transducer. This has enabled the ability to transport particles over relatively large distances (i.e. multiple λ_{ac}) (Fig. 3.5b) [70, 71]. The use of optimised phase delays to drive an array of transducers has been used to establish complex pressure fields as well as reproduce acoustic vortex beams without the need for physical fixed acoustic lenses. The direct consequence of this enables the ability to accurately levitate, trap, move and rotate suspended particles in an intended medium.

Acoustic Structures

There's an undeniable advantage of dynamic control enabled by the use of phased arrays to achieve accurate spatio-temporal control of complex pressure fields. However, to drive these systems, a relatively complex configuration of transducers coupled with advanced electronics to individually control each acoustic element is required, making this approach relatively complex and costly [72].

To this end, multiple studies have looked at using intermediate structures, using acoustic metamaterials and holographic planes to establish pressure fields that are beneficial for complex particle manipulation. These structures are

independent of the driving architecture (i.e. acoustic transducer and circuitry) and, thus, can be fabricated based on the intended task and made disposable at a low cost [73]. Acoustic metamaterials [74] are materials that are designed to control, direct or amplify an incident acoustic wave based on how it is engineered. Due to this unique feature, phononic crystals integrated with SAW- and BAW-based devices have been able to tune the spatial intensity of the acoustic energy based on the task at hand [75].

More recently, the use of monolithic acoustic holograms akin to optical kinoforms that enable the reconstruction of diffraction-limited pressure fields has been shown to manipulate liquids and solids in both air and liquid mediums [73]. The simple reconstruction of complex wave fields can be established by determining the phase distribution required based on an arbitrary intended field. This phase distribution information is later introduced and controlled using a printed holographic plane of varying thickness (i.e. dictated by the intended phase delay). By attaching this customised holographic plane to an acoustic transducer, the desired arbitrary pressure field can be established on the image plane at a defined distance from the transducer as per Fig. 3.5c. As the phase difference here is dictated by the holographic plane, there's no need for a transducer array, and therefore, this can be easily integrated with single transducer elements.

3.4 Applications

To dictate the location or configuration of suspended matter (i.e. particles, droplets and biological cells), a well-established pressure field with a sufficient acoustic gradient, therefore force, is required. Whilst acoustofluidics has enabled a wide range of applications, ranging from fluid mixing, drug discovery, particle concentration and sorting, for the purposes of this chapter, the developed applications discussed will be focused on the patterning, transport and selective manipulation of individual or a group of particles or droplets. A key factor influencing the migration speed and trajectory of the manipulated particle is the relative compressibility and density in relation to the medium it is suspended in.

3.4.1 *Standing Waves*

A promising candidate for suspended matter manipulation is the use of standing acoustic waves. This is due to the relative simplicity in establishing strong acoustic gradients with stable well-defined locations, known as potential wells that enable the precise transportation and pattern configuration of particles and biologicals. There are two distinct methods of producing an acoustic standing wave within microfluidic systems. Firstly, an acoustic standing wave resonator is composed of a single acoustic source and a reflective boundary located at the opposing end. The

interference between the incident wave, emanating from the acoustic transducer and the reflected wave, results in an acoustic standing wave. If designed well, these resonators can establish strong acoustic fields with a desired periodicity and pattern. However, there is a strong dependence on the channel geometry and material, as these significantly influence the resultant pressure fields. Secondly, an acoustic standing wave can be established by the interference of at least two or more acoustic transducers. This method allows for a greater flexibility in the established pressure field as the relative nodal and anti-nodal locations can be precisely controlled by altering the input frequency and phase of each transducer element.

Early on with BAW systems, these devices were relatively large (i.e. on the order of multiple wavelengths) [76] and progressively were reduced in size to half-wavelength resonators [77]. This was later simplified to a quarter-wave resonators by Townsend et al. [78] and Hill et al. [36]. Although quarter-wavelength resonators are less energy efficient than their half-wavelength counterpart, the use of these systems simplifies the detection and sensing process as particles move towards the surface, thus the need of a stream to be split into two (i.e. one stream containing the concentrate and another the clarified stream) as opposed to half-wavelength resonators where the clarified stream is on either side of the concentrate stream. Simultaneous sorting and concentration of particles have also been studied for similar applications when two or more species of particles or cells are present within the sample. Systems such as split-flow thin (SPLITT) fractionation were developed to separate two species of particles when exposed to an external force field [79]. This system is based on the principle that larger particles will be more affected by the external force field and will migrate more in comparison to the smaller particles, therefore, moving the larger particles beyond the flow splitter. Johnson and Feke [80] built the first acoustic-based SPLITT fractionator. Lenshof et al. [81] applied a similar concept to separate larger leukocyte cells from the smaller platelets. The concept of utilising the force contrast between two particles of different sizes has since been applied to other acoustophoretic-based devices to sort more than two species of particles as shown in Fig. 3.6a [82, 83]. Furthermore, the exploitation of negative contrast factor particles such as lipid has been used within acoustic-based sorting devices. BAW systems have been extensively used to perform particle positioning within lines in a chamber [84], in channels to be used with a microgripper [85], patterning of particles and cells in clusters within a two-dimensional field [40], positioning of particles within an octagonal sonotweezer (Fig. 3.6b) [86], and in a full three-dimensional sound field [11]. Furthermore, BAW platforms have shown the capability of transporting particles to arbitrary locations within a half- and quarter-wave resonator [87] and within a resonant cavity by altering the excitation frequency to a higher harmonic. Manneberg et al. demonstrated the use of linear frequency sweeping to align and subsequently transport particles which can be used to control the motion and position of cells for high-resolution optical microscopy [88].

SSAWs have been extensively developed to enable the establishment of 1D standing wave fields to focus particle to the central channel locations [89], to alter the particle trajectory to distinct outlets based on size and particle type [54, 90] and

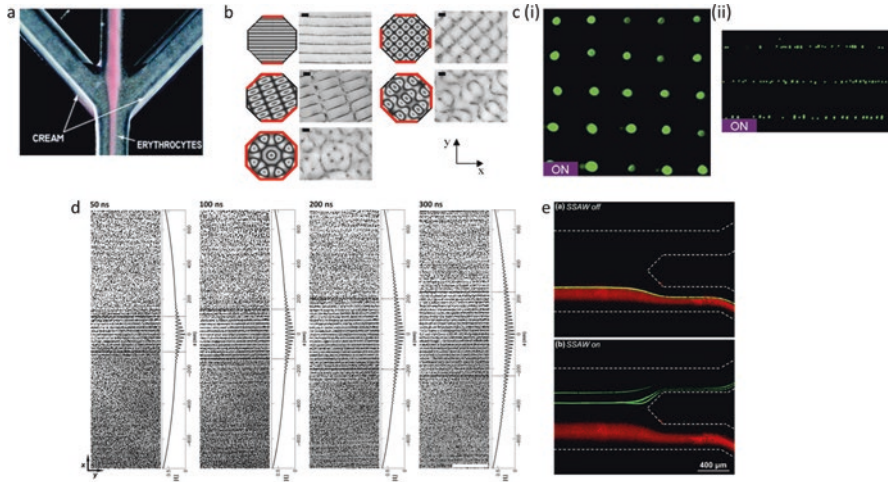


Fig. 3.6 Applications using acoustic standing waves to (a) separate lipids from blood via a bulk acoustic wave-driven system [Reproduced from [82] with permission from The Royal Society of Chemistry], (b) manipulation of particles within an octagonal sonotweezer in multiple configurations [Reprinted from [86], with the permission of AIP Publishing], (c) pattern particles within clusters in a (i) grid and (ii) lines [Reproduced from [138] with permission from The Royal Society of Chemistry], (d) to allow regional patterning of particles using pulsed surface acoustic waves [Reproduced under the terms of the Creative Commons Attribution-NonCommercial license from [139]] and (e) enable cell washing via the use of standing surface acoustic waves [Reproduced from [93] with permission from The Royal Society of Chemistry]

to selectively pattern particles in arbitrarily controlled regions using ns pulses and phase delays [58]. More complex 2D fields have also been established using multiple pairs of IDTs, enabling patterning of particles, droplets and cells in a defined array (Fig. 3.6c), similar to that of its BAW 2D counterpart. Guo et al. demonstrated the use of 2D SSAW to control intercellular distance and assemble and maintain cells in distinct geometries for purposes of understanding cell-cell interaction [91]. Meng et al. demonstrated the use of 2D configured SSAW setup, to direct the path of engineered microbubbles towards a target cells, and subsequently trigger the collapse of the bubble, enabling single-cell, localised sonoporation [92]. Furthermore, the added benefit of using higher frequencies common amongst SAW-based platforms, the ability to control individual particles and cells, known as one-cell-per-well (OCPW) is realised [5]. As the individual manipulation of cells or a microparticle is dependent on its relative size as compared to the λ_{ac} , a smaller wavelength would result in a better manipulation resolution, therefore beneficial to operate at a higher excitation frequency. Collins et al. [58] further exploited the use of short λ_{ac} , using sub-time-of-flight excitation pulses to localise particle patterning locations (Fig. 3.6d). The use of chirped IDT configurations has also been developed to trap and transport particles selectively based on their size [55]. Chirped IDTs have also been used to manipulate individual particles and cells by exploiting the wide frequency bands to control the SSAW field in real time, enabling the precise control of

a desired particle trajectory [54]. The use of SSAW integrated with a flow has been extensively used to sort particles based on their size (Fig. 3.6e) [1, 90, 93].

The ability to pattern cells in a suspended medium leads to the ability to better control processes within tissue engineering. For example, the use of standing waves in a heptagonal acoustic platform to direct and study the development of Schwann cells, in different configurations, has been shown to guide neurite outgrowth [94]. Moreover, acoustic patterning of myoblasts in gelatin methacryloyl (GelMA) has been shown to significantly enhance myofibrillogenesis and promote muscle fibre formation [95]. SSAW-based platforms have also been used to pattern cardiac cells within GelMA hydrogels, successfully, demonstrating cell beating within a 5–7-day time period [15].

3.4.2 Travelling Waves

As the name implies, travelling waves are a unidirectional propagating wave emanating from an acoustic source. TSAWs are a common method of introducing acoustic waves within a microfluidic system, typically composed of a single set of IDT and ensuring reflected waves are absorbed by the channel material or diffusers located at the far end. Similar to SSAW, TSAWs have been used to sort and direct particles based on their compressibility and size, with the added benefit of a working range larger than half the SAW or acoustic wavelength (Fig. 3.7a,b). The enhanced separation technique has been exhibited on cells at high speeds in a range of studies [6, 96]. The addition of acoustic waveguides (Fig. 3.4a), via the incorporation of PDMS posts as developed, allowing for a larger tolerance in alignment, further increases the adaptability of this technique [97]. Ng et al. [98, 99] demonstrated the use of a combination of TSAW and SSAW, exploiting the inherent decaying properties of SAW as it couples energy into the fluid (as per Eq. 3.35) to improve the efficiency and sensitivity of sorting particles. In addition to manipulating particles, suspended droplets within an aqueous medium have been demonstrated using TSAWs. The ability to merge (Fig. 3.7c), steer (Fig. 3.7d) and split droplets has been effectively demonstrated [7, 8, 100–102].

More recently, TSAW systems have been developed to trap and form stable collection locations (Fig. 3.7e), in contrast to the conventional use to move or push particles and droplet in a unidirectional method. These platforms exploit the inherent diffractive effect leading to periodic high- and low-pressure regions allowing for particle patterning [56] and have been shown to have complex repercussions on the established pressure and streaming field [23, 32, 59]. Further development integrating the use of channels (Fig. 3.7f) [57, 60] and structures [103, 104] as waveguides allows for the development and establishment of complex wave fields that enable particle patterning using TSAW, further reducing the need for a high degree of alignment. The inherent diffractive effects based upon previous studies [56, 57] enabled the development of an on-chip acoustic erythrocytometer to mechanically probe a population of red blood cells at single-cell level [61].

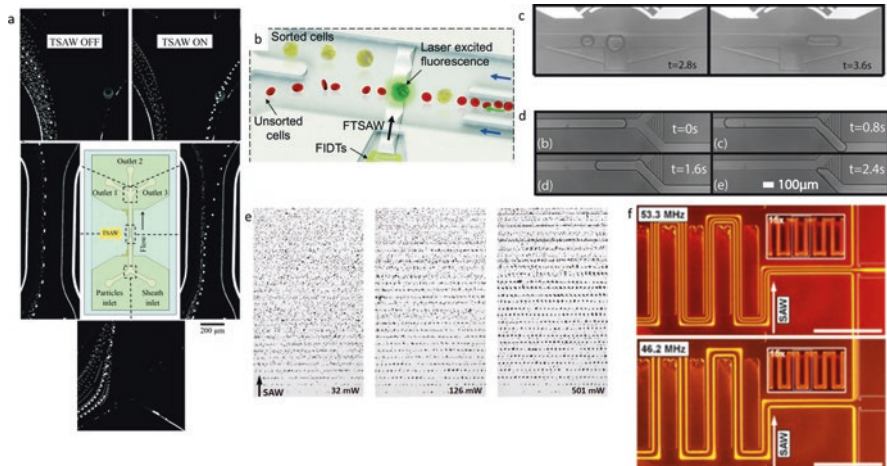


Fig. 3.7 Applications enabled by exploiting travelling waves for (a) continuous separation of particles in a PDMS microchannel using travelling surface acoustic waves (TSAWs) [Reproduced from [134] with permission from The Royal Society of Chemistry], (b) to enable fluorescence-activated cell sorting via focused TSAWs [Reproduced from [140] with permission from The Royal Society of Chemistry], (c) droplet merging [Reproduced from [100] with permission from The Royal Society of Chemistry] and (d) steering using TSAWs [Reproduced from [8] with permission from The Royal Society of Chemistry], (e) particle patterning, arising from the inherent Huygens-Fresnel diffractive effects [Reproduced [56] with permission from American Physical Society] and (f) particle focusing using PDMS microchannels as self-aligned waveguides [Reproduced [57] with permission from American Physical Society]

3.4.3 Acoustic Tweezing and Micro-robots

Acoustic tweezers have a great promise of being a viable substitute to optical tweezers. The introduction of acoustic vortices, allows for the focusing of a single beam to trap particles in 3D, which in turn enables the subsequent movement of the intended particle in any direction [68, 105]. Further simplification using a 3D-printed Fresnel lens, bonded to a two-element piezoceramic transducer disk, was developed to produce a stable acoustic trap in water capable of trapping microparticles [106]. The use of Bessel beams as developed theoretically by Marston et al. [107, 108] was later applied to develop stable acoustic tractor beams that were capable of axially pulling and transversely trapping suspended particles. Karlsen et al. theoretically proposed the use of Bessel-function acoustic vortices to spatio-temporally manipulate high-concentration regions within a lower concentration medium [109]. In 2019, Baudoin et al. developed the first flat, compact, single electrode focalised acoustic tweezer, effectively folding a spherical transducer onto a flat piezoelectric substrate (Fig. 3.8a) [110]. This platform allowed the precise ability to pick and displace a micron-sized object with a high degree of selectivity using a relatively simple approach, enabling widespread adoption in microbiology, micro-robotics

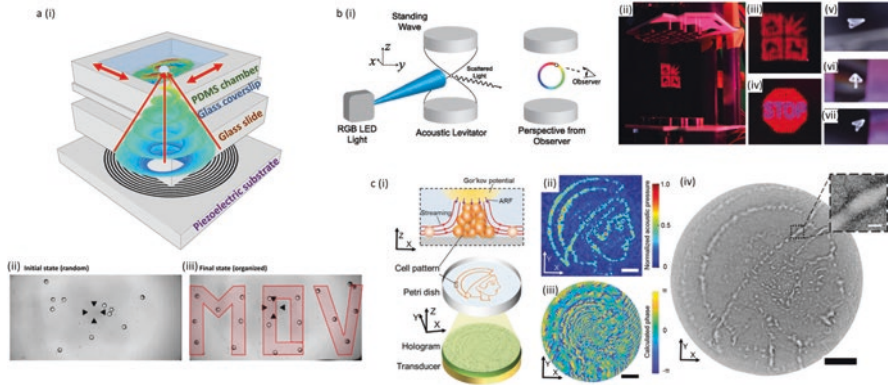


Fig. 3.8 The use of acoustic tweezers enabled by (a) acoustical vortex to selectively move particles with a high degree of accuracy [Reproduced under the terms of the Creative Commons Attribution-Non Commercial license from [110]], (b) phased arrays enabling acoustophoretic volumetric displays using fast-moving particles [Reprinted from [115] with the permission of AIP Publishing] and (c) acoustic holograms to pattern cells within biocompatible hydrogels [Reproduced under the terms of Creative Commons Attribution License from [124]]

and microscopy. Recently, the use of acoustic vortices to simultaneously trap nanoparticle laden microbubbles and subsequently trigger an activated release through centimetre-thick bio-mimicking layers has been demonstrated [111].

As described in Sect. 3.3.4.2, the ability to shape and modulate a pressure field into arbitrary shapes further improves the dexterity of the platform. Ultrasonic arrays enable the establishment of these complex fields by individually controlling the excitation parameters of each transducer in a defined manner and are capable of ad hoc alterations, effectively allowing on-demand spatio-temporal particle manipulation. A 12-element 1D array coupled to a rectangular capillary platform developed by Glynne-Jones et al. demonstrated the ability to transport particles over the entire channel length by switching active array elements [112]. A similar approach using Langevin transducers demonstrated the continuous planar transport of matter in air along a defined path, the stretching and merging of droplets in air [70] and later orbital transport and spinning [113]. In 2015, Marzo et al. demonstrated the ability to acoustically levitate, translate and manipulate particles using a single-sided emitter by optimising the phase delays between each array element [69]. This concept was further improved, exploiting the ability to move particles along a defined path in a rapid manner to realise volumetric displays (Fig. 3.8b) [114, 115]. Building upon Smalley et al. [116], the clever use of synchronised coloured light source illumination at targeted points in space to coinciding with the particle's path allows for the rendering of continuous images akin to a movie playing in 3D, viewable from all directions. Phased arrays have more recently been used to produce acoustic beams that are capable of transporting glass spheres along a programmed path in the urinary bladder of live pigs, showing great promise of a non-invasive method of in vivo drug delivery [117].

The use of structured elements is another alternative to ultrasonic arrays that allow the establishment of complex fields with a relatively simple excitation setup required. This is due to the fact that the shaping of the field is manipulated by the acoustic metamaterial or holographic plane and not the driving transducer. The Cooper lab used phononic crystals in combination with SAW to modulate the spatial intensity of the resultant pressure fields, demonstrating the ability to more precisely affect specific regions of a fluid volume for purposes of particle manipulation and droplet ejection from a substrate [75, 118–121]. The stacking and assembly of predefined metamaterial bricks to establish any diffraction-limited acoustic field enabled the experimental demonstration of an acoustic tractor beam, realising a simplified single-sided airborne spatial modulator [122].

Melde et al. went on to reconstruct complex acoustic field distributions via the integration of a printed holographic plane attached to a single transducer [73]. The holographic plane was composed of varying thicknesses to emulate the required phase lag to achieve the target image. As the amplitude and the phase distribution of the field can be controlled by the hologram, particles can be guided along an intended path at the image plane, pushed along by the phase gradients. By placing the holographic plane across from the transducer, acoustic levitation in air could be achieved as well when used in a reflection mode. This platform was further developed to enable the assembly and consequent UV-triggered cross-linking of complex, mechanically stable parts [123]. The formation of irregular, nonsymmetric assemblies of cells within hydrogels can be achieved using acoustic holograms (Fig. 3.8c) [124]. The consequent gelation of the hydrogels, immobilises the patterned cells, enabling them to thrive within the matrix. This shows great promise of integrating the use of non-contact approaches for 3D cell culture, with a wide range of applications in tissue engineering and mechanobiology.

Marmottant et al. developed a microbubble-driven transport of particles within microfluidic channels, by exploiting the inherent acoustic streaming effects [125, 126]. This was further developed to propel microswimmers carrying payloads, opening up possibilities in applications within the biosensing, drug delivery and imaging space [127]. Ahmed et al. later developed a platform that was capable of driving microswimmers consisting of trapped microbubbles in highly viscous fluids (Fig. 3.9a) [128]. These trapped oscillating microbubbles within microchannels are used to accurately rotate colloids and cells, further improving optical microscopy sample control [129]. Acousto-magnetic hybrid technology has been shown to successfully achieve bubble-driven propulsion aided by magnetic alignment by an external field, enabling precise manoeuvring capabilities [130]. Furthermore, nano-swimmers have also been shown to be effective via the introduction of travelling acoustic waves. The propulsion of artificially fabricated nanoswimmers with flexible tails (Fig. 3.9b), akin to flagellum, has been demonstrated [131].

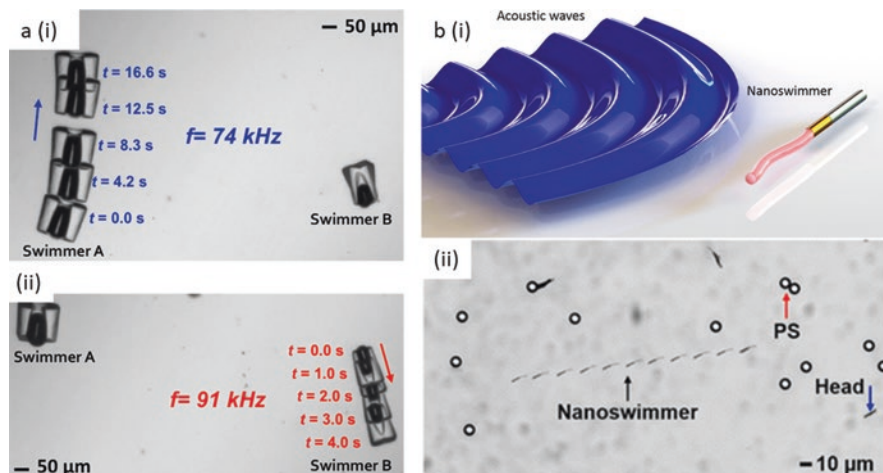


Fig. 3.9 Demonstration of (a) microswimmers driven by vibrating microbubbles [Reproduced under the terms of the Creative Commons Attribution 4.0 International License from [128]] and (b) artificial swimming nanoswimmers by an acoustically activated flagella [Reprinted (adapted) with permission from [131]. Copyright 2016 American Chemical Society]

3.5 Conclusions and Outlook

As discussed in this chapter, the use of acoustics to manipulate and control particles, droplets and cells has been extensively studied and reported. The immense potential of integrating this external field into microfluidics has gained significant traction over the last few decades. The use of this non-contact approach in the form of standing waves and travelling waves to trap, sort, steer and pattern particles and biological matter enabled predominantly by the gentle nature of bulk acoustic wave and surface acoustic wave actuated systems integrated within microfluidic platforms has been discussed throughout the chapter.

More recently, the use of acoustic manipulation and control of micro-robots have begun to develop with advent of high accuracy acoustic tweezing systems. These tweezers, either driven by acoustic vortices, phased arrays or acoustic holographic planes, have facilitated the accurate control of individual or a group of particles and cells along complex trajectories and aggregation in non-periodic patterns (beyond that of λ_{ac}). The development of these control methods and the establishment of arbitrary fields have unlocked the potential of using acoustic manipulation to drive micro-robots *in vivo* as well as enable the three-dimensional culture of heterogeneous tissue in complex patterns, more akin to tissues and organs of living organisms.

The acoustic tweezing approach has overcome many of the limitations imposed by its more conventional counterpart (BAW and SAW), such as spatial independence and individual control of microparticles and micro-robots. Furthermore,

acoustic tweezers are considered a preferred alternative to optical tweezers, especially for in vivo applications due to the inherently larger penetration depth and suppression of detrimental effects arising from localised heating. However, some limitations still exist for each of the tweezing methods discussed. For example, acoustic vortices and phased arrays still require complex fabrication and control of its transducers. On the other hand, whilst it is relatively cheap and easy to fabricate acoustic holograms via 3D-printed structures, they lack the dynamic control possessed by its optical spatial light modulator counterpart. The dynamic control of acoustic holograms would further increase to adoption of acoustic control methods in a wide range of micro-robotic and tissue engineering applications.

In its present state, these relatively recent control approaches still require better understanding of the established acoustic fields and its resultant acoustic forces at play. In regard to biocompatibility, better understanding of the biological effects as a result of acoustic exposure is warranted. This would not only lead to a safe implementation of acoustic control, especially for work with biological matter and in vivo operation, but potentially enable the use of acoustics as a therapeutic mechanism.

Received: (will be filled in by the editorial staff)

Revised: (will be filled in by the editorial staff)

Published online: (will be filled in by the editorial staff)

References

1. Fakhfour, A., Devendran, C., Collins, D. J., Ai, Y., & Neild, A. (2016). *Lab on a Chip*, 16, 3515.
2. Devendran, C., Gralinski, I., & Neild, A. (2014). *Microfluidics and Nanofluidics*, 17.
3. Schmid, L., Weitz, D. A., & Franke, T. (2014). *Lab on a Chip*, 14, 3710.
4. Ozcelik, A., Rufo, J., Guo, F., Gu, Y., Li, P., Lata, J., & Huang, T. J. (2018). Acoustic tweezers for the life sciences. *Nature Methods*.
5. Collins, D. J., Morahan, B., Garcia-Bustos, J., Doerig, C., Plebanski, M., & Neild, A. (2015). *Nature Communications*, 6, 8686.
6. Franke, T., Braunmuller, S., Schmid, L., Wixforth, A., & Weitz, D. A. (2010). *Lab on a Chip*, 10, 789.
7. Sesen, M., Devendran, C., Malikides, S., Alan, T., & Neild, A. (2017). *Lab on a Chip*, 17, 438.
8. Sesen, M., Alan, T., & Neild, A. (2015). *Lab on a Chip*, 15, 3030.
9. Augustsson, P., Karlsen, J. T., Su, H.-W., Bruus, H., & Voldman, J. (2016). *Nature Communications*, 7, 11556.
10. Hultström, J., Manneberg, O., Dopf, K., Hertz, H. M., Brismar, H., & Wiklund, M. (2007). *Ultrasound in Medicine & Biology*, 33, 145.
11. Manneberg, O., Vanherberghen, B., Svennebring, J., Hertz, H. M., Önfelt, B., & Wiklund, M. (2008). *Applied Physics Letters*, 93, 63901.
12. Li, S., Glynne-Jones, P., Andriotis, O. G., Ching, K. Y., Jonnalagadda, U. S., Oreffo, R. O. C., Hill, M., & Tare, R. S. (2014). *Lab on a Chip*, 14, 4475.
13. Burguillos, M. A., Magnusson, C., Nordin, M., Lenshof, A., Augustsson, P., Hansson, M. J., Elmér, E., Lilja, H., Brundin, P., Laurell, T., & Deierborg, T. (2013). *PLoS One*, 8, 1.
14. Ung, W. L., Mutafulos, K., Spink, P., Rambach, R. W., Franke, T., & Weitz, D. A. (2017). *Lab on a Chip*, 17, 4059.

15. Naseer, S. M., Manbachi, A., Samandari, M., Walch, P., Gao, Y., Zhang, Y. S., Davoudi, F., Wang, W., Abrinia, K., Cooper, J. M., et al. (2017). *Biofabrication*, 9, 15020.
16. Pui, P. W. S., Trampler, F., Sonderhoff, S. A., Groeschl, M., Kilburn, D. G., & Piret, J. M. (1995). *Biotechnology Progress*, 11, 146.
17. Doblhoff-Dier, O., Gaida, T., Katinger, H., Burger, W., Groschl, M., & Benes, E. (1994). *Biotechnology Progress*, 10, 428.
18. Devendran, C., Carthew, J., Frith, J. E., & Neild, A. (2019). *Advancement of Science*, 6, 1902326.
19. Settnes, M., & Bruus, H. (2012). *Phys. Rev. E - Stat. Nonlinear, Soft Matter Phys*, 85, 016327.
20. Doinikov, A. A. (1999). *The Journal of the Acoustical Society of America*, 106, 3305.
21. Nyborg, W. L. M. (1965). *Physical Acoustics* (Vol. 2, pp. 265–331). New York: Academic Press.
22. Muller, P. B., Barnkob, R., Jensen, M. J. H., & Bruus, H. (2012). *Lab on a Chip*, 12, 4617.
23. Devendran, C., Albrecht, T., Brenker, J., Alan, T., & Neild, A. (2016). *Lab on a Chip*, 16, 3756.
24. Doinikov, A. A., & Fluid, J. (1994). *Mech.*, 267, 1.
25. GOR'KOV, L. P. (1962). *Soviet Physics – Doklady*, 6, 773.
26. Bjerknes, V. F. K. (1906). *Fields of force*. New York: Columbia University Press.
27. Doinikov, A. A., & Zavtrak, S. T. (1995). *Physics of Fluids*, 7, 1923.
28. Doinikov, A. A., & Zavtrak, S. T. (1996). *Ultrasonics*, 34, 807.
29. Weiser, M. A. H., Apfel, R. E., & Neppiras, E. A. Interparticle Forces on Red Cells in a Standing Wave Field. *Acta Acust. united with Acust*, 56, 114–119.
30. Laurell, T., Petersson, F., & Nilsson, A. (2007). *Chemical Society Reviews*, 36, 492.
31. Silva, G. T., & Bruus, H. *Phys. Rev. E – Stat. Nonlinear, Soft Matter Phys*, 2014, 90, 063007.
32. Fakhfour, A., Devendran, C., Ahmed, A., Soria, J., & Neild, A. (2018). *Lab on a Chip*, 18, 3926.
33. Trampler, F., Sonderhoff, S. A., Pui, P. W. S., Kilburn, D. G., & Piret, J. M. (1994). *Bio/Technology*, 12, 281.
34. Grösch, M., Burger, W., Handl, B., Doblhoff-Dier, O., Gaida, T., & Schmatz, C. (1998). *Acta Acust. united with Acust*, 84, 815.
35. Hill, M., Shen, Y., & Hawkes, J. J. (2002). *Ultrasonics*, 40, 385.
36. Hill, M., Townsend, R. J., & Harris, N. R. (2008). *Ultrasonics*, 48, 521.
37. Hill, M., & Wood, R. J. K. (2000). *Ultrasonics*, 38, 662.
38. Yosioka, K., & Kawasima, Y. (1955). *Acta Acust. united with Acust*, 5, 167.
39. Leibacher, I., Reichert, P., & Dual, J. (2015). *Lab on a Chip*, 15, 2896.
40. Haake, A., Neild, A., Radziwill, G., & Dual, J. (2005). *Biotechnology and Bioengineering*, 92, 8.
41. Neild, A., Oberti, S., Beyeler, F., Dual, J., Nelson, B. J., & Micromechanics, J. (2006). *Microengineering*, 16, 1562.
42. Laurell, T., & Lenshof, A. (2014). *Microscale Acoustofluidics*. Royal Society of Chemistry.
43. Andrade, M. A. B., Pérez, N., & Adamowski, J. C. (2015). *Applied Physics Letters*, 106, 014101.
44. Rayleigh, L. (1885). *Proc. London Math. Soc.*, 17, 4–11.
45. Oliner, A. A. (1978). In *Berlin and New York, Springer-Verlag (Topics in Applied Physics. Volume 24)*, 1978. 342 p (For individual items see A79-16052 to A79-16055); Vol. 24.
46. Holm, A., Stürzer, Q., Xu, Y., & Weigel, R. (1996). *Microelectronic Engineering*, 31, 123.
47. Smith, R. T., & Welsh, F. S. (1971). *Journal of Applied Physics*, 42, 2219.
48. Tressler, J. F., Alkoy, S., & Newnham, R. E. (1998). *Journal of Electroceramics*, 2, 257.
49. Campbell, C. (1998). *Surface acoustic wave devices for mobile and wireless communications*. Academic Press.
50. Cheeke, J. D. N. (2010). *Fundamentals and applications of ultrasonic waves*. CRC press.
51. Wu, T.-T., Tang, H.-T., Chen, Y.-Y., & Liu, P.-L. (2005). *Ultrason. Ferroelectr. Freq. Control. IEEE Trans.*, 52, 1384.
52. Collins, D. J., Alan, T., Helmersson, K., & Neild, A. (2013). *Lab on a Chip*, 13, 3225.
53. Yatsuda, H. (1997). *Ultrason. Ferroelectr. Freq. Control. IEEE Trans.*, 44, 453.

54. Ding, X., Lin, S.-C. S., Kiraly, B., Yue, H., Li, S., Chiang, I.-K., Shi, J., Benkovic, S. J., & Huang, T. J. (2012). *PNAS*, *109*, 11105.
55. Devendran, C., Gunasekara, N. R., Collins, D. J., & Neild, A. (2016). *RSC Advances*, *6*.
56. Devendran, C., Collins, D. J., Ai, Y., & Neild, A. (2017). *Physical Review Letters*, *118*.
57. Collins, D. J., O'Rourke, R., Devendran, C., Ma, Z., Han, J., Neild, A., & Ai, Y. (2018). *Physical Review Letters*, *120*.
58. Collins, D. J., Devendran, C., Ma, Z., Ng, J. W., Neild, A., & Ai, Y. (2016). *Science Advances*, *2*.
59. Fakhfour, A., Devendran, C., Albrecht, T., Collins, D. J., Winkler, A., Schmidt, H., & Neild, A. (2018). *Lab on a Chip*, *18*, 2214.
60. Devendran, C., Choi, K., Han, J., Ai, Y., Neild, A., & Collins, D. (2020). *Lab on a Chip*, *20*, 2674.
61. Link, A., & Franke, T. (2020). *Lab on a Chip*, *20*, 1991.
62. Ashkin, A., Dziedzic, J. M., Bjorkholm, J. E., & Chu, S. (2016). *Optical Angular Momentum* (Vol. 11, pp. 196–198). CRC Press.
63. Liu, Y., Cheng, D. K., Sonek, G. J., Berns, M. W., Chapman, C. F., & Tromberg, B. J. (1995). *Evidence for Localized Cell Heating Induced by Infrared Optical Tweezers*, *68*.
64. Wu, J. (1991). *The Journal of the Acoustical Society of America*, *89*, 2140.
65. Lee, J., Ha, K., & Shung, K. K. (2005). *The Journal of the Acoustical Society of America*, *117*, 3273.
66. Lee, J., Teh, S. Y., Lee, A., Kim, H. H., Lee, C., & Shung, K. K. (2009). *Applied Physics Letters*, *95*, 073701.
67. Baresch, D., Thomas, J.-L., & Marchiano, R. (2013). *The Journal of the Acoustical Society of America*, *133*, 25.
68. Baresch, D., Thomas, J. L., & Marchiano, R. (2016). *Physical Review Letters*, *116*, 024301.
69. Marzo, A., Seah, S. A., Drinkwater, B. W., Sahoo, D. R., Long, B., & Subramanian, S. (2015). *Nat. Commun.*
70. Foresti, D., Nabavi, M., Klingauf, M., Ferrari, A., & Poulidakos, D. (2013). *Proceedings of the National Academy of Sciences*, *110*, 12549.
71. Foresti, D., Bjelobrk, N., Nabavi, M., & Poulidakos, D. (2011). *Journal of Applied Physics*, *109*, 93503.
72. Neild, A. (2016). Acoustics: Motion controlled by sound. *Nature*, *537*, 493–494.
73. K. Melde, A. G. Mark, T. Qiu, P. Fischer, *Nature* 2016.
74. Ma, G., & Sheng, P. (2016). Acoustic metamaterials: From local resonances to broad horizons. *Science Advances*, *2*, e1501595.
75. Bourquin, Y., Wilson, R., Zhang, Y., Reboud, J., & Cooper, J. M. (2011). *Advanced Materials*, *23*, 1458.
76. Gupta, S., & Feke, D. L. (1998). *AIChE Journal*, *44*, 1005.
77. Hawkes, J. J., & Coakley, W. T. (2001). *Sensors and Actuators B: Chemical*, *75*, 213.
78. Townsend, R. J., Hill, M., Harris, N. R., & McDonnell, M. B. (2008). *Ultrasonics*, *48*, 515.
79. Lenshof, A., & Laurell, T. (2010). *Chemical Society Reviews*, *39*, 1203.
80. Johnson, D. A., & Feke, D. L. (1995). *Separations Technology*, *5*, 251.
81. Lenshof, A., Magnusson, C., & Laurell, T. (2012). *Lab on a Chip*, *12*, 1210.
82. Petersson, F., Nilsson, A., Holm, C., Jönsson, H., & Laurell, T. (2004). *Analyst*, *129*, 938.
83. Petersson, F., Åberg, L., Swärd-Nilsson, A.-M., & Laurell, T. (2007). *Analytical Chemistry*, *79*, 5117.
84. Neild, A., Oberti, S., & Dual, J. (2007). *Sensors and Actuators B: Chemical*, *121*, 452.
85. Beyeler, F., Neild, A., Oberti, S., Bell, D. J., Sun, Y., Dual, J., & Nelson, B. J. (2007). *Journal Microelectromechanical Syst*, *16*, 7.
86. Bernassau, A. L., Courtney, C. R. P., Beeley, J., Drinkwater, B. W., & Cumming, D. R. S. (2013). *Applied Physics Letters*, *102*, 164101.
87. Glynne-Jones, P., Boltryk, R. J., Harris, N. R., Cranny, A. W. J., & Hill, M. (2010). *Ultrasonics*, *50*, 68.

88. Manneberg, O., Vanherberghen, B., Önfelt, B., & Wiklund, M. (2009). *Lab on a Chip*, 9, 833.
89. Shi, J., Mao, X., Ahmed, D., Colletti, A., & Huang, T. J. (2008). *Lab on a Chip*, 8, 221.
90. Collins, D. J., Alan, T., & Neild, A. (2014). *Lab on a Chip*, 14, 1595.
91. Guo, F., Li, P., French, J. B., Mao, Z., Zhao, H., Li, S., Nama, N., Fick, J. R., Benkovic, S. J., & Huang, T. J. (2015). *Proceedings of the National Academy of Sciences of the United States of America*, 112, 43.
92. Meng, L., Cai, F., Jiang, P., Deng, Z., Li, F., Niu, L., Chen, Y., Wu, J., & Zheng, H. (2014). *Applied Physics Letters*, 104, 073701.
93. Li, S., Ding, X., Mao, Z., Chen, Y., Nama, N., Guo, F., Li, P., Wang, L., Cameron, C. E., & Huang, T. J. (2015). *Lab on a Chip*, 15, 331.
94. Gesellchen, F., Bernassau, A. L., Déjardin, T., Cumming, D. R. S., & Riehle, M. O. (2014). *Lab on a Chip*, 14, 2266.
95. Armstrong, J. P. K., Puetzer, J. L., Serio, A., Guex, A. G., Kapnisi, M., Breant, A., Zong, Y., Assal, V., Skaalure, S. C., King, O., Murty, T., Meinert, C., Franklin, A. C., Bassindale, P. G., Nichols, M. K., Terracciano, C. M., Hutmacher, D. W., Drinkwater, B. W., Klein, T. J., Perriman, A. W., & Stevens, M. M. (2018). *Advanced Materials*, 30, 1802649.
96. Ma, Z., Zhou, Y., Collins, D. J., & Ai, Y. (2017). *Lab on a Chip*, 17, 3176.
97. Ma, Z., Collins, D. J., & Ai, Y. (2016). *Analytical Chemistry*, 88, 5316.
98. Ng, J. W., Devendran, C., & Neild, A. (2017). *Lab on a Chip*, 17, 3489.
99. Ng, J. W., Collins, D. J., Devendran, C., Ai, Y., & Neild, A. (2016). *Microfluidics and Nanofluidics*, 20.
100. Sesen, M., Alan, T., & Neild, A. (2014). *Lab on a Chip*, 14, 3325.
101. Wixforth, A., Strobl, C., Gauer, C., Toegl, A., Scriba, J., & Guttenberg, Z. V. (2004). *Analytical and Bioanalytical Chemistry*, 379, 982.
102. Zhang, S. P., Lata, J., Chen, C., Mai, J., Guo, F., Tian, Z., Ren, L., Mao, Z., Huang, P. H., Li, P., Yang, S., & Huang, T. J. (2018). *Nature Communications*, 9, 1.
103. Collins, D. J., O'Rorke, R., Neild, A., Han, J., & Ai, Y. (2019). *Soft Matter*, 15, 8691.
104. Raymond, S. J., Collins, D. J., O'Rorke, R., Tayebi, M., Ai, Y., & Williams, J. (2020). *Scientific Reports*, 10, 1.
105. Baresch, D., Thomas, J. L., & Marchiano, R. (2013). *Journal of Applied Physics*, 113, 184901.
106. Franklin, A., Marzo, A., Malkin, R., & Drinkwater, B. W. (2017). *Applied Physics Letters*, 111, 094101.
107. Marston, P. L. (2006). *The Journal of the Acoustical Society of America*, 120, 3518.
108. Zhang, L., & Marston, P. L. (2011). *Phys. Rev. E – Stat. Nonlinear, Soft Matter Phys*, 84, 035601.
109. Karlsen, J. T., & Bruus, H. (2017). *Physical Review Applied*, 7, 034017.
110. Baudoin, M., Gerbedoen, J. C., Riaud, A., Matar, O. B., Smagin, N., & Thomas, J. L. (2019). *Sci. Adv*, 5, eaav1967.
111. Baresch, D., & Garbin, V. (2020). *Proceedings of the National Academy of Sciences of the United States of America*, 117, 15490.
112. Glynne-Jones, P., Démoré, C. E. M., Ye, C., Qiu, Y., Cochran, S., & Hill, M. (2012). *IEEE Transactions on Ultrasonics, Ferroelectrics, and Frequency Control*, 59, 1258.
113. Foresti, D., & Poulidakos, D. (2014). *Physical Review Letters*, 112, 024301.
114. Hirayama, R., Martinez Plasencia, D., Masuda, N., & Subramanian, S. (2019). *Nature*, 575, 320.
115. Fushimi, T., Marzo, A., Drinkwater, B. W., & Hill, T. L. (2019). *Applied Physics Letters*, 115, 064101.
116. Smalley, D. E., Nygaard, E., Squire, K., Van Wagoner, J., Rasmussen, J., Gneiting, S., Qaderi, K., Goodsell, J., Rogers, W., Lindsey, M., Costner, K., Monk, A., Pearson, M., Haymore, B., & Peatross, J. (2018). *Nature*, 553, 486.
117. Ghanem, M., Maxwell, A., Wang, Y.-N., Cunitz, B., Khokhlova, V., Sapozhnikov, O., & Bailey, M. (2020). *Proceedings of the National Academy of Sciences*, 117, 202001779.
118. Bourquin, Y., Reboud, J., Wilson, R., & Cooper, J. M. (2010). *Lab on a Chip*, 10, 1898.

119. Wilson, R., Reboud, J., Bourquin, Y., Neale, S. L., Zhang, Y., & Cooper, J. M. (2011). *Lab on a Chip*, *11*, 323.
120. Reboud, J., Wilson, R., Zhang, Y., Ismail, M. H., Bourquin, Y., & Cooper, J. M. (2012). *Lab on a Chip*, *12*, 1268.
121. Reboud, J., Bourquin, Y., Wilson, R., Pall, G. S., Jiwaji, M., Pitt, A. R., Graham, A., Waters, A. P., & Cooper, J. M. (2012). *Proceedings of the National Academy of Sciences of the United States of America*, *109*, 15162.
122. Memoli, G., Caleap, M., Asakawa, M., Sahoo, D. R., Drinkwater, B. W., & Subramanian, S. (2017). *Nature Communications*, *8*, 1.
123. Melde, K., Choi, E., Wu, Z., Palagi, S., Qiu, T., & Fischer, P. (2018). *Advanced Materials*, *30*, 1704507.
124. Ma, Z., Holle, A. W., Melde, K., Qiu, T., Poeppe, K., Kadiri, V. M., & Fischer, P. (2020). *Advanced Materials*, *32*, 1904181.
125. Marmottant, P., & Hilgenfeldt, S. (2004). *Proceedings of the National Academy of Sciences of the United States of America*, *101*, 9523.
126. Marmottant, P., Raven, J. P., Gardeniers, H., Bomer, J. G., & Hilgenfeldt, S. (2006). *Journal of Fluid Mechanics*, *568*, 109.
127. Feng, J., Yuan, J., & Cho, S. K. (2015). *Lab on a Chip*, *15*, 1554.
128. Ahmed, D., Lu, M., Nourhani, A., Lammert, P. E., Stratton, Z., Muddana, H. S., Crespi, V. H., & Huang, T. J. (2015). *Scientific Reports*, *5*, 1.
129. Ahmed, D., Ozcelik, A., Bojanala, N., Nama, N., Upadhyay, A., Chen, Y., Hanna-Rose, W., & Huang, T. J. (2016). *Nat. Commun.*
130. Ahmed, D., Dillinger, C., Hong, A., & Nelson, B. J. (2017). *Adv. Mater. Technol.*, *2*, 1700050.
131. Ahmed, D., Baasch, T., Jang, B., Pane, S., Dual, J., & Nelson, B. J. (2016). *Nano Letters*, *16*, 4968.
132. Rogers, P., & Neild, A. (2011). *Lab on a Chip*, *11*, 3710.
133. Thévoz, P., Adams, J. D., Shea, H., Bruus, H., & Soh, H. T. (2010). *Analytical Chemistry*, *82*, 3094.
134. Destgeer, G., Lee, K. H., Jung, J. H., Alazzam, A., & Sung, H. J. (2013). *Lab on a Chip*, *13*, 4210.
135. Collins, D. J., Ma, Z., Han, J., & Ai, Y. (2017). *Lab on a Chip*, *17*, 91.
136. Thomas, J. L., Marchiano, R., & Baresch, D. (2017). Acoustical and optical radiation pressure and the development of single beam acoustical tweezers. *Journal of Quantitative Spectroscopy and Radiation Transfer*, *195*, 55–65.
137. Brown, M. D. (2019). *Applied Physics Letters*, *115*, 053701.
138. Shi, J., Ahmed, D., Mao, X., Lin, S.-C. S., Lawit, A., & Huang, T. J. (2009). Acoustic tweezers: Patterning cells and microparticles using standing surface acoustic waves (SSAW). *Lab on a Chip*, *9*, 2890–2895.
139. Collins, D. J., Devendran, C., Ma, Z., Ng, J. W., Neild, A., & Ai, Y. (2016). *Science Advances*, *2*, e1600089.
140. Ma, Z., Zhou, Y., Collins, D. J., & Ai, Y. (2017). *Lab on a Chip*, *17*, 3176.

Chapter 4

Light-Driven Microrobots: Mechanisms and Applications



Shuailong Zhang, Fan Nan, and Steven L. Neale

4.1 Introduction

Microrobots are typically submillimeter particles that can be made to do mechanical work and can be classified on the basis of their driving forces, including magnetic [1–4], electric [5, 6], acoustic [7–9], and optical forces [10–14]. Microrobots that are powered by light are particularly appealing, given the maturity and diversity of beam-modulation and optical microscopy techniques that can be used [11–14], and light-driven microrobots can be subclassified into three categories based on their operating principles. The first category, known as optical microrobots, relies on direct manipulation of microscale objects by illumination with light – the most prevalent example being optical tweezers (OTs) [10–14]. OTs leverage the forces that arise from focusing light with strong intensity gradients, which permits fine and noninvasive control and actuation of microscale objects suspended in air or liquid. To date, there have been various demonstrations of OTs-actuated microrobots that

S. Zhang (✉)

School of Mechatronic Engineering, Beijing Institute of Technology,
Beijing, People's Republic of China

Beijing Advanced Innovation Center for Intelligent Robots and Systems, Beijing Institute
of Technology, Beijing, People's Republic of China

Key Laboratory of Biomimetic Robots and Systems, Beijing Institute of Technology, Ministry
of Education, Beijing, People's Republic of China

e-mail: shuailong.zhang@bit.edu.cn

F. Nan

Institute of Nanophotonics, Jinan University, Guangzhou, People's Republic of China

Department of Applied Physical Sciences, University of North Carolina at Chapel Hill,
Chapel Hill, North Carolina, USA

S. L. Neale

James Watt School of Engineering, University of Glasgow, Glasgow, UK

can carry out complex mechanical operations for physical and biomedical applications [15–17]. The second category, opto-mechanical soft microrobots, relies on the interaction between light and photosensitive, mechanically responsive materials such as liquid crystal polymers (LCPs) [18–25]. This form of microrobot is an interesting and fast-growing research topic, with demonstrations of “pick and place” gripper [20], artificial flytrap [21], and other biomimetic structures [22–24]. The third category, opto-chemical microrobots, relies on photochemical reactions such as photochromic and photocatalytic effects to generate propulsion forces [26–29], thus converting chemical energy into mechanical movement. Opto-chemical microrobots normally require highly specific operating conditions, including microrobots formed from photoactive materials and an environment that contains photochemically active reagents. These opto-chemical microrobots have been mainly used for biomedicine and sensing applications.

In this chapter, we will first introduce the working mechanisms and principles for the three categories of microrobots and their relative advantages and limitations. Then representative works and applications of each category of microrobot are introduced and discussed, and the chapter finally ends with conclusion and future prospects on the light-driven microrobots.

4.2 Optical Microrobot

Optical microrobot is a type of microrobot based on optical micromanipulation technologies – with the most prevalent example being optical tweezers (OTs), which were invented by Nobel laureate Arthur Ashkin who had been working on the manipulation of particles with laser light since the 1960s and invented the first single-beam OTs in 1986 [30]. OTs were mainly used to control and manipulate biological samples such as biomolecules, cells and bacteria [31]. In recent years, several groups have started to investigate the use of OTs to control specifically designed artificial microstructures for different applications [16, 32–34], leading to the invention and fast development of optical microrobots.

OTs rely on the transfer of momentum from the photon to the particle when light interacts with the object, as shown in Fig. 4.1a [35]. By employing a tightly focused laser beam, objects with high refractive index can be trapped near the beam focus due to the intensity gradient force. The optical gradient forces exerted on objects can be described and calculated using a ray optics model. Apart from the optical gradient force, optical radiation pressure force, resulting from the absorption or the scattering of light by the sample, also plays an important role in OTs. By carefully balancing the optical gradient force and optical radiation pressure force, the position of the sample can be controlled in three-dimensional space. Light also carries angular momentum. For example, in a circularly polarized optical field, the electric field vector is rotating in a plane perpendicular to the direction of the wave. Spinning angular momentum can interact with a birefringent object, which alters the polarization state of the light (can change circularly polarized state to linearly or elliptically

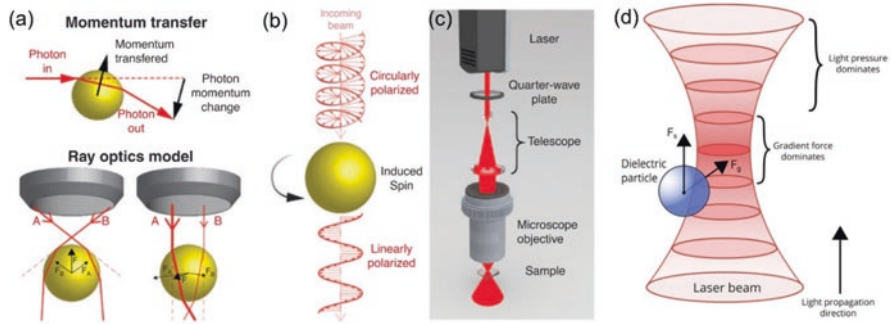


Fig. 4.1 Working mechanisms of OTs. (a) Schematics illustrating the interaction of photons with objects and the linear momentum transfer process that lead to the generation of optical gradient force. (b) Transfer of optical angular momentum to an object, leading it to spin. (c) Schematic experimental setup for OTs. (a)–(c) Reproduced with permission from reference 35. (d) Schematics showing OTs based on a focused Gaussian beam, in which a dielectric particle experiences radiation pressure force and optical intensity gradient force. (d) Reproduced with permission from reference 15

polarized state), as shown in Fig. 4.1b. During this process, a torque will be exerted to the birefringent object and cause it to rotate due to the conservation of momentum [36]. More complex beam profiles are also capable of having orbital angular momentum which can be assted to absorbing particles. Shown in Fig. 4.1c is a standard OTs system, comprising a laser, a couple of optics, and a microscope objective lens. These opto-mechanics hardware are mainly used to collimate the laser light into a tightly focused beam for optical manipulation. The lasers are normally linearly polarized that carries linear optical momentum. By adding a quarter-wave plate in the laser path, the linearly polarized light can be converted into circularly polarized light and therefore carrying an angular momentum, which can be used to rotate a target object. For the control and manipulation of microrobots using OTs, focused Gaussian light beams are widely used to generate optical manipulation forces [15], as shown in Fig. 4.1d.

Presented in Fig. 4.2 are examples of OTs-actuated microrobots with different functions. These microrobots have small feature sizes (a few microns to a few tens of microns) and well-designed mechanical structures and were mostly fabricated using photo-curable polymer materials and two-photon polymerization techniques. Shown in Fig. 4.2a is a schematic of an OT-actuated surface scanning probe [37]. Its detailed mechanical structure is illustrated in Fig. 4.2b. By using two laser beams to control and manipulate the probe, it can be applied for surface topography reconstruction with submicron resolution. Another probe capable of manipulating a light field was also developed [38], as shown in Fig. 4.2c. This probe consists of a bent waveguide sitting atop a supporting structure with spheroidal handles for OTs actuation. Different tip structures of the probe can be fabricated to confine the light and generate light beams with different profiles, helping breakthrough the optical diffraction limit. Another demonstrated application of OTs-actuated microrobots is for

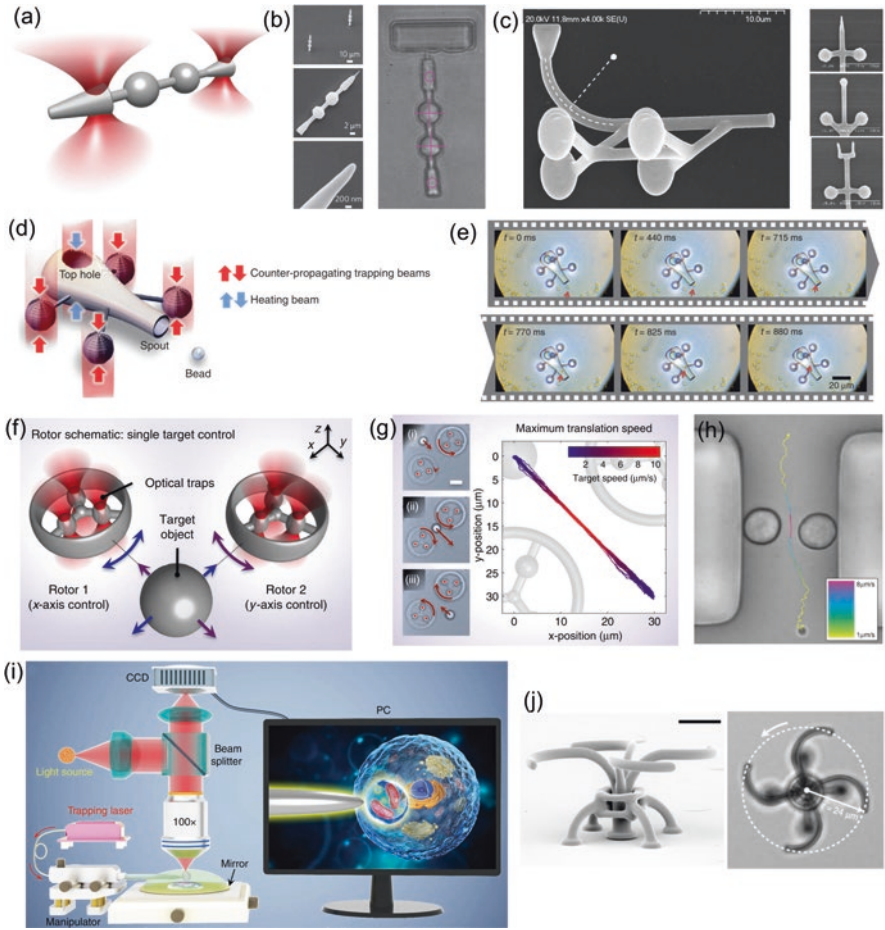


Fig. 4.2 OTs-actuated microrobots. **(a)** Schematic model of a surface scanning probe controlled by OTs. **(b)** Scanning electron microscope (SEM) images of the fabricated surface scanning probe and optical image of the probe as it is scanned along the surface of a sample. **(a)–(b)** Reproduced with permission from reference 37. **(c)** SEM images of a probe consisting of a bent waveguide and spheroidal handles. Different tip structures of the probe can be fabricated. **(c)** Reproduced with permission from reference 38. **(d)** Schematic of the microrobot with cargo loading/unloading function. The use of multiple optical trapping beams allows the actuation of the microrobot. Additional laser beam aimed at the microrobot’s top hole is used for creating thermal convection flow. **(e)** Microscope images showing the process of loading cargo into the microrobot. **(d)–(e)** Reproduced with permission from reference 39. **(f)** Schematic of using a pair of rotating microrobots to control a single target. **(g)** Trajectory of a target as it is propelled back and forth between two rotating microrobots. Line color shows target speed. Insets (i)–(iii) are microscope images showing the movement of the target. **(f)–(g)** Reproduced with permission from reference 40. **(h)** Trajectory of a 1µm silica particle pumped by a pair of rotating microrobots and going through a 15-µm-wide microfluidic channel. **(h)** Reproduced with permission from reference 41. **(i)** Schematic illustration of the experimental setup for the cell-based OTs-actuated bio-magnifier. **(i)** Reproduced with permission from reference 45. **(j)** SEM image of a microrobot and an optical image showing the microrobot can convert optical energy into mechanical rotation. **(j)** Reproduced with permission from reference 46

cargo transport and delivery. Figure 4.2d and c demonstrates a microrobot equipped with a syringe function [39]. This microrobot has a hollow body connected with four spheroidal handles for OTs actuation. The body of the microrobot has two openings: one serves as the spout where cargo can be loaded and ejected, and the other one is located on top of the microrobot, allowing for the generation of photo-thermally induced convection currents within the body of the microrobot. This OTs-actuated microrobot is capable of loading, transporting and unloading cargo such as silica and polystyrene microbeads. For this microrobot, laser beams were not only used to provide optical actuation force but to create photothermally induced convection currents for unloading cargo. Shown in Fig. 4.2f is another kind of OTs-actuated microrobot, which can be made to rotate to induce localized fluidic flow to exert hydrodynamic forces on “secondary” objects such as microparticles and biological cells [40]. By precisely piloting the motion of the microrobots using a closed-loop feedback system, highly localized flow fields can be sculpted to move and accelerate/decelerate target objects, as shown in Fig. 4.2g. Additionally, multiple microrobots can be controlled independently/simultaneously to trap, stabilize and move micro-objects with nanoscale positioning precision. This indirect optical micromanipulation through microrobots expands the capabilities of OTs to control and manipulate objects that cannot be directly optically trapped, e.g., sensitive biological samples which are easily photodamaged. Similar results were also demonstrated for two counter rotating birefringent particles trapped within a microfluidic channel and driven using OTs based on the transfer of optical angular momentum from a circularly polarized laser beam [41]. The rotating birefringent particles are able to displace fluid in microchannels and work as a microfluidic pump to accelerate/decelerate silica microparticles, as shown in Fig. 4.2h. Apart from using birefringent particles, biological cells/particles with full biocompatibility were also rotated by OTs to create micro-vortex and exert hydrodynamic forces on surrounding cells, with demonstrations on indirect cell manipulation [42], guided tissue growth [43], and disruption of biological aggregates such as blood clots [44]. The use of OTs-actuated microrobots to induce hydrodynamic forces for indirect optical manipulation is an interesting topic that has attracted much research interest in recent years. This expands the capabilities of OTs technology for the manipulation of fragile and light-sensitive biological samples that are difficult to be manipulated with OTs directly. Figure 4.2i shows another application of OTs-actuated cell [45]. The cell was trapped on a fiber tip. Due to the spherical structure, the cell can act as a biomagnifier to overcome the optical diffraction limit and probe nanostructures with a resolution of 100 nm under a white-light microscope. Besides, the focus of the biomagnifier formed a nano-optical trap that allows precise manipulation of individual nanoparticles with a radius of 50 nm. Therefore, this cell-based OTs-actuated biomagnifier is a useful tool for simultaneous optical imaging and assembly of nanomaterials. Shown in Fig. 4.2j is another kind of microrobot which is actuated based on conversion of the optical energy into mechanical energy via transfer of optical momentum [46]. This microrobot, with a mechanical structure similar to a micro-turbine, can effectively harvest optical energy and convert it into mechanical rotation once light is input into its cured waveguide arms, as shown in Fig. 4.2j. Similar

strategy to convert optical energy into mechanical energy can be found in other optical microrobot works as well [36, 47, 48], and the energy conversion efficiency highly depends on the capability of the microrobot's mechanical structure to reroute the light beam and exchange optical momentum. Apart from 2D manipulation, OTs can also manipulate and assemble microrobots in 3D [49–51].

Although microrobots based on OTs have been demonstrated for many impressive applications as introduced above, there are some limitations for this type of system. First, OTs are only capable of actuating small objects (although some studies have shown the manipulation of particles of tens of microns in size [52]) as the optical force is typically on the order of piconewtons (10^{-12} N). This restricts the design, structure, materials, and tools used to form/fabricate the microrobots and sets limits on their applications, particularly for those involving larger structures. Second, while it is possible to manipulate multiple microrobots in parallel with OTs, this functionality requires dramatic increases in complexity, as it necessitates specialized and expensive beam-modulation hardware and control software. To overcome these limitations, substantial efforts have been devoted to the development of other optical micromanipulation technologies such as optothermal tweezers [53–56], optoacoustic tweezers [57, 58], and optoelectronic tweezers (OETs) [59–61]. Among these technologies, OETs are a promising strategy that has attracted much attention since their invention by Ming C. Wu and co-workers in 2005 [59]. OETs rely on light-induced dielectrophoresis (DEP) force for the actuation of nano-/micro-objects, which combines the merits of optics and electronics and offers a user-friendly approach that enables programmable, touch-free, and reliable micromanipulation. Different from OTs which require very high optical intensities, the optical source in an OET system can be a digital micromirror device (DMD) with an LED source, which is used to project programmable/animated light patterns through an optical microscope onto a photoconductive substrate [in most cases – hydrogenated amorphous silicon (a-Si:H)]. OET relies on the unique features of the photoconductive substrate: in the dark, the impedance of the photoconductive substrate is high, and it behaves like a resistor; when the photoconductive substrate is illuminated with light, its impedance reduced significantly, and the photoconductive substrate behaves like a conductor. Therefore, by creating bright and dark regions on the photoconductive substrate, “light-activated virtual electrodes” are formed, which can induce nonuniform electric field in the liquid medium above the photoconductive substrate, as shown in Fig. 4.3a. This nonuniform electric field interacts with the samples in the liquid medium, producing DEP force that can control their positions [62]. OETs are capable of exerting stronger manipulation force (nanonewtons, 10^{-9} N) and actuating larger objects (sizes over 100 microns) compared with OTs [63–65], and in addition, by projecting independently varying illumination patterns, it is particularly straightforward to use OET for parallel manipulation (e.g., creating 10,000 traps at the same time) [59]. These features make OETs an ideal optical tool to control microrobots.

Presented in Fig. 4.3b–d is an example of an OETs-actuated “cogwheel”-shaped microrobot, which has eight cogs arranged symmetrically around a central chamber [65]. The microrobot is more than $200\mu\text{m}$ across, much larger than objects that can

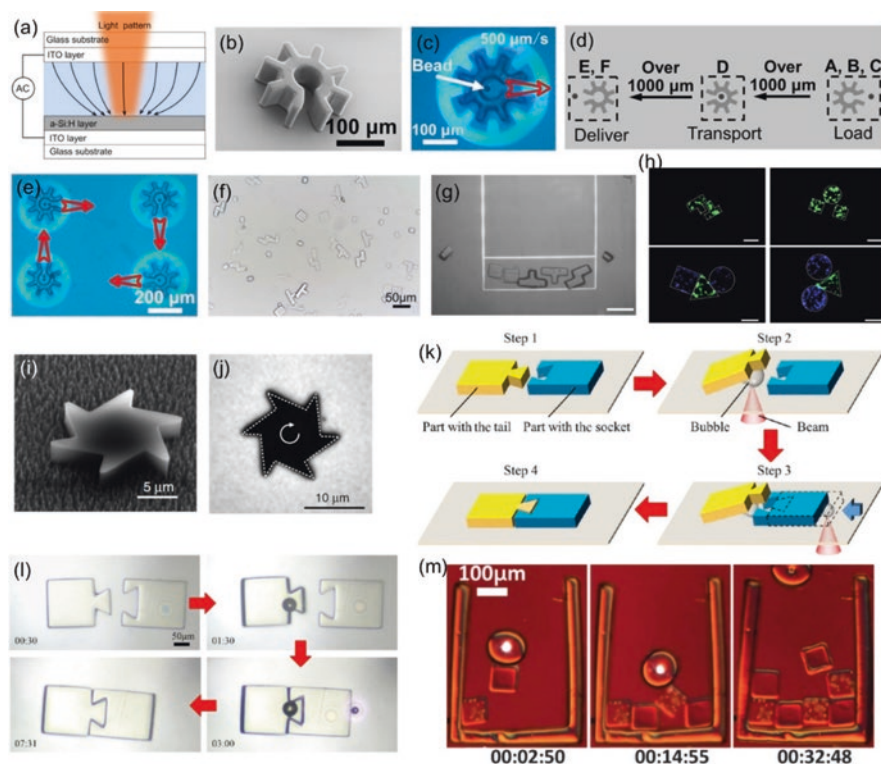


Fig. 4.3 Microrobots based on OETs and optothermal effect. (a) Schematic of OETs. (b) SEM image of a “cogwheel”-shaped microrobot. (c) Microscope image showing the use of light pattern to control a “cogwheel”-shaped microrobot, which carries a microparticle. (d) Schematic process of loading, transporting, and delivery of payloads using microrobot. (e) Microscope image showing the simultaneous translation of four “cogwheel”-shaped microrobots bearing payloads (one or two microparticles) and moving in different directions. (b)–(e) Reproduced with permission from reference 39. (f) Hydrogel microrobots with Tetris structures. (g) Assembly of Tetris hydrogel microrobots with OETs. (h) Fluorescent microscope image showing the assembly of cell-encapsulating Tetris hydrogel microrobots. L929 fibroblast cells were stained green and HEK-293 cells were stained blue. (f)–(h) Reproduced with permission from reference 39. (i) SEM image of a light-absorbing microrobot with asymmetric structure. (j) Microscope image of a spinning light-absorbing microrobot. (i)–(j) Reproduced with permission from reference 67. (k) Schematic and (l) microscope images showing the use of bubble microrobot to assemble micro-parts into a tightly connected entity. (k)–(l) Reproduced with permission from reference 68. (m) Manipulation of agarose microgel blocks using light-driven bubble microrobot. Half of the microgel blocks contain yeast cells. (m) Reproduced with permission from reference 69

be manipulated by OTs. Because of the large feature size, the microrobots can be massively fabricated using UV-curable polymer materials and standard photolithography technique and can take nearly any desirable shape (not limited to the “cogwheel” shape). By using a light pattern that forms a negative relief of the perimeter of the microrobot (Fig. 4.3c), negative DEP force is produced, causing the microrobot to be trapped into the “dark” center of the projected light pattern. By moving the

light pattern, the “cogwheel”-shaped microrobot can be programmed to move, rotate, and carry out sophisticated, multi-axis operations. One particularly useful program demonstrated here (Fig. 4.3d) is a serial combination of “load,” “transport,” and “deliver,” which can be applied to manipulate micron-dimension payloads. It has been demonstrated that the microrobot programmed in this manner can cause less stress on fragile mammalian cells than conventional OETs technique. Besides, a key feature for this OET-actuated microrobotic system is the capability to manipulate multiple microrobots simultaneously, allowing for independent and parallel control, as shown in Fig. 4.3e. More importantly, this OETs-actuated microrobot is multifunctional, with applications successfully demonstrated for single-cell isolation, clonal expansion, RNA sequencing, controlling cell-cell interactions, and isolating precious micro-tissues from heterogeneous mixtures [65]. In addition to polymer-based microrobots, shown in Fig. 4.3f–h are examples of hydrogel microrobots with Tetris structures, which were manipulated and assembled by OETs [66]. The hydrogel microrobots have high biocompatibility and can encapsulate cells with different species. Therefore, hydrogel microrobots containing different cells can be assembled to form desired geometry with specific shape and size (Fig. 4.3h), useful for microscale tissue engineering.

Apart from OTs and OETs, optical micromanipulation techniques based on optothermal effect can also be used to control and manipulate microrobots, as shown in Fig. 4.3i and j [67]. This asymmetric microrobot structure was uniformly coated with a layer of light-absorbing material and sitting on a liquid-air interface. By illuminating the microrobot with incoherent light, it can efficiently convert absorbed light into rotational motion through thermocapillary effect. Other microrobot examples based on an optothermal actuation mechanism are shown in Fig. 4.3k and l [68]. In this work, a laser is focusing on a photothermal substrate to create a surface bubble, which can be used as a microrobot to move, fix, lift, and drop micro-parts and assemble them into a tightly connected entity. The generation, rate of growth, and motion of the bubble-based microrobot can be well controlled by modulating the power of the used laser. Shown in Fig. 4.3m is a demonstration of the use of a bubble-based microrobot to move and assemble agarose microgel blocks, with half of them containing yeast cells [69]. After the assembly, the patterned cell-laden microgels were cultured and the yeast cells successfully multiplied [69]. It should be noted that there are many other reports of using optothermal effect to actuate microrobots or microswimmers in fluidic environments [70–72]. We believe that with the development and further improvement of different optical micromanipulation technologies, more types of microrobot will be invented, and various applications will be explored. It is expected that optical microrobots based on optical micromanipulation technologies will continue to thrive and play important roles in a wide range of applications in physics, engineering, biomedical science, and beyond.

4.3 Opto-mechanical Soft Microrobots

An opto-mechanical soft microrobot is a type of microrobot that relies on the interactions between light and photosensitive, mechanically responsive materials – with the most prevalent example being liquid crystal polymers (LCPs), which are soft, polymeric systems with ordered molecular alignment/arrangement. Under external stimuli, LCPs can undergo a transition from anisotropic molecular phase (in most cases the nematic phase) into isotropic molecular phase, turning an ordered polymeric system into a disordered one. For light-responsive LCPs, this order-to-disorder transition is induced by light as the source of stimuli. Since the LCP molecules (most often with rod-like structures) are confined within ordered polymer networks, the order-to-disorder transition reduces the spacing between molecules along the alignment direction (the director) and increases the spacing in the perpendicular direction. Therefore, the LCP material undergoes a shape change, with contraction happening in the director direction and expansion happening in the direction perpendicular to the director, as illustrated in Fig. 4.4a [19]. This characteristic of light-induced shape deformation allows the use of LCPs as “artificial muscles” to provide an actuation force for opto-mechanical soft microrobots.

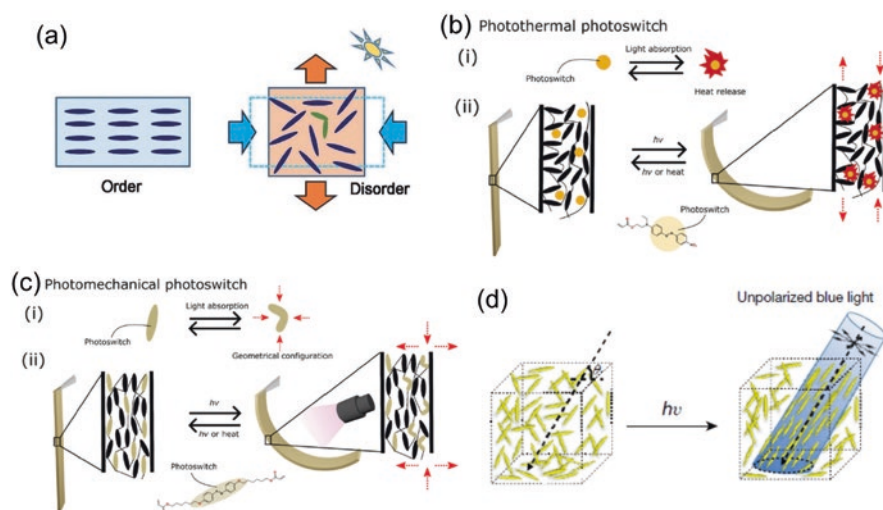


Fig. 4.4 Basic mechanisms of light-responsive LCPs. (a) Schematic of the light-induced shape deformation of LCPs, resulting from the order-to-disorder molecular phase transition. (a) Reproduced with permission from reference 19. (b) Schematic of doping photothermal dye into LCP network to induce its shape change upon light illumination. (c) Schematic of doping photomechanical into LCP network to induce its shape change upon light illumination. (b)–(c) Reproduced with permission from reference 73. (d) Schematic showing the orientation of LCP molecules upon illumination with non-polarized blue light. (d) Reproduced with permission from reference 25

Based on different actuation mechanisms, there are three approaches to design and make light-responsive LCP materials for opto-mechanical soft microrobots. The first approach relies on the photothermal effect [73], in which LCP materials are doped with photothermal dyes (such as graphene, gold nanoparticles, carbon nanotubes, etc.) that can absorb light and convert it to heat, as shown in Fig. 4.4b. The generated heat can be dissipated to the LCP network, inducing order-to-disorder molecular phase transition and macroscopic shape deformation. The second approach relies on the photomechanical effect [73], in which LCP materials are doped with photomechanical dyes that can absorb light and convert it to geometrical changes (based on isomerization), as shown in Fig. 4.4c. Upon illumination, these photomechanical dyes can exert a stress force on the surrounding LCP molecular network, causing the disruption of the molecular alignment and inducing macroscopic volumetric change. In some cases, photomechanical dyes can also release heat, resulting in a combination of thermal and mechanical contributions to the shape deformation of LCPs. The third approach relies on the photo-orientation effect, in which LCPs with photo-orientation dyes can orientate the alignment direction of molecules upon exposure to non-polarized UV/blue light or polarized blue-green-red light (Fig. 4.4d). This photo-orientation effect, also known as trans-cis-trans reorientation or Weigert effect [25], can induce reversible shape change of LCP materials, which can be utilized for microrobot actuation.

Different methods were used to fabricate opto-mechanical soft microrobots, such as photolithography, soft lithography, 3D printing, direct laser writing, and laser scribing. LCP materials were normally processed in liquid phase and later cured to form the solid mechanical structures of the opto-mechanical soft microrobots. Shown in Fig. 4.5 are examples of versatile opto-mechanical soft microrobots with different designs and functions. Illustrated in Fig. 4.5a is a SEM image of a light-driven microscopic walker on a human hair [19, 74]. The microscopic walker has four legs, which were attached to the body at an angle of about 45° to create an asymmetry in the friction with the surface. When illuminated with periodic laser light, the body of the microscopic walker performs contraction-expansion cycles, allowing the robot to demonstrate different locomotion behaviors, such as random/directional walking, rotation, and jumping. Moving from walking to swimming and from air to liquid environments, microswimmers based on light-responsive LCPs were developed, which were driven by a dynamic light pattern from a DMD projector [22], as shown in Fig. 4.5b. The DMD projector can generate dynamic light patterns to illuminate parts of the microswimmer, and only the body sections of microswimmer that are illuminated deform, while the remainder remains relaxed. Therefore, dynamic light patterns can induce travelling-wave body deformations of the microswimmer, making itself propelled through the liquid environment (Fig. 4.5c). Inspired by caterpillar crawling, an inch-long biomimetic opto-mechanical soft microrobot was developed [24], as illustrated in Fig. 4.5d and e. Using a scanning laser to create travelling-wave body deformation, the microrobot can move forward in the laser scanning direction based on curling-type locomotion. This “caterpillar”-like microrobot is capable of climbing a slope, squeezing through a narrow slit, and moving payloads. Figure 4.5f and g show the images of an

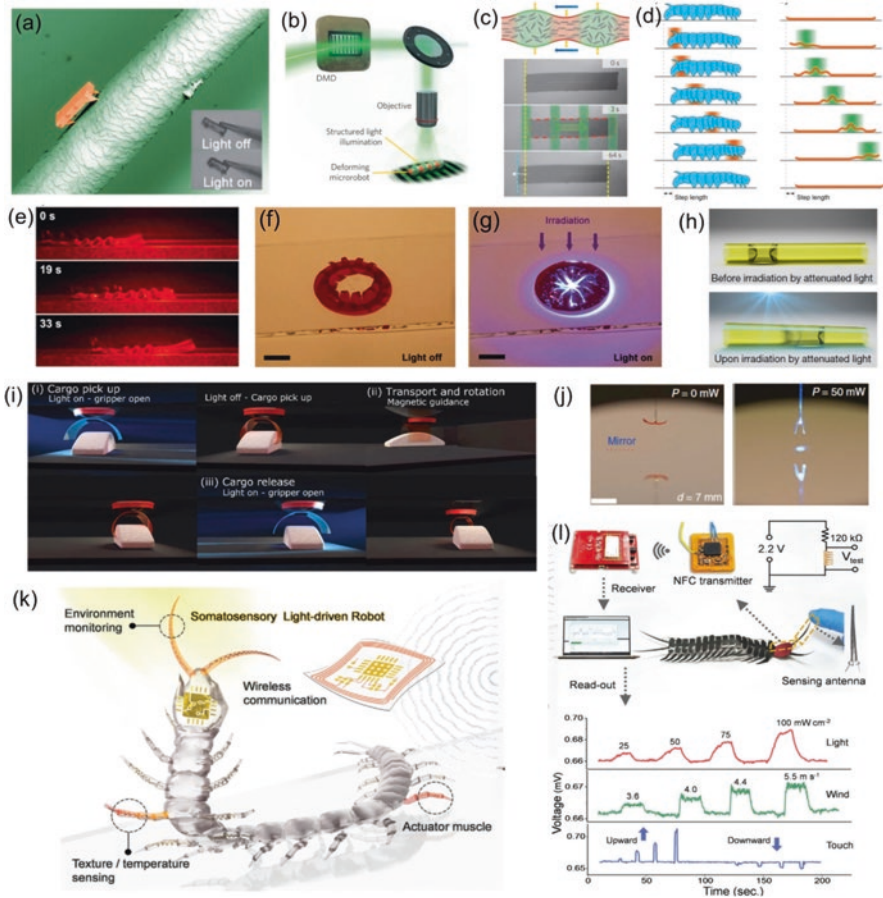


Fig. 4.5 Opto-mechanical soft microrobots and their applications. (a) SEM image of a microscopic walker on a human hair. The insets show the actuation method: light on, body contracts; light off, body extends. (a) Reproduced with permission from reference 19. (b) Schematic setup of using a DMD projector to image a dynamic light pattern onto a microrobot. (c) Upon light pattern illumination, the microrobot propels itself based on a travelling-wave shape deformation. (b)–(c) Reproduced with permission from reference 22. (d) Schematic of using a scanning laser beam to trigger curling deformation of a microrobot, making it move like a caterpillar. (d)–(e) Reproduced with permission from reference 24. (e) Series of images for the light-driven “caterpillar”-style locomotion of the microrobot. A laser beam is scanned along the robot body to trigger curling deformation. (d)–(e) Reproduced with permission from reference 24. (f) and (g) A light-responsive artificial iris autonomously opens/closes upon weak/strong light irradiation. (f)–(g) Reproduced with permission from reference 75. (h) Schematics showing the motion of a droplet confined in a tubular microactuator driven by asymmetric photodeformation. With the light intensity decreasing from left to right, shape transformation of the tubular microactuator from cylindrical to conical is induced, causing the movement of the droplet to the narrower end of the tubular microactuator. (h) Reproduced with permission from reference 25. (i) Schematic illustration of the cargo pickup, transport, rotation, and release using a robotic micro-gripper. (i) Reproduced with permission from reference 20. (j) A light-driven artificial “flytrap” closes upon light irradiation. (j) Reproduced with permission from reference 21. (k) Schematic illustration of the functionalities of a light-driven robotic centipede. (l) Use of robotic centipede’s antenna to sense light intensity, wind speed, and human touch. The measured voltage signal can transmit wirelessly to a receiver via near-field communication. (k) and (l) Reproduced with permission from reference 23

artificial iris that can perform automatic shape adjustment by reacting to the power density of incident light [75]. This self-regulating light-responsive artificial iris can close under increasing light intensity and reduce the light transmission power by a factor of seven. This method provides a new solution for automatic/adaptive optical systems. Shown in Fig. 4.5h is a LCP-based tubular microactuator capable of manipulating fluid droplets based on light-induced asymmetric deformation, which can generate capillary force for liquid propulsion [25]. This photodeformable tubular microactuator can be fabricated into different structures, such as straight, “Y”-shaped, serpentine, and helical. It was also demonstrated that the microactuator could exert photocontrol of a wide diversity of liquids over a long distance with controllable velocity and direction, and hence to mix multiphase liquids, to merge liquids, and even to make liquids run uphill. These liquid handling capabilities are useful for applications in micro-reactors, lab-on-a-chip settings, and micro-mechanical systems. The “pick and place” micro-gripper is another interesting demonstration of opto-mechanical soft microrobots. Shown in Fig. 4.5i is a dual magneto- and photo-responsive soft robotic micro-gripper, capable of loading, transport, rotation, and release of cargo [20]. This micro-gripper mainly consists of a light-responsive LCP thin film coated with a magnetically responsive layer. Light is used to trigger the micro-gripper to grab, pick up, and release cargo with a high degree of control. Magnetic control is employed to conduct the translation and rotation of the micro-gripper. A similar strategy was employed for a light-responsive “flytrap” [21], which can open and close in response to different optical powers, as shown in Fig. 4.5j. This “flytrap” is mounted on a fiber tip, which functions not only as a power source but also as a probe to sense the environment. Based on optical feedback (the target’s ability to absorb and reflect light), the “flytrap” is capable of autonomous closing/opening and object recognition. Another interesting opto-mechanical soft microrobot is shown in Fig. 4.5k, in which a light-driven robotic centipede was built based on smart thin-film composite tightly integrating actuation and multisensing [23]. Based on the piezoelectric and piezoresistive responses of the materials, this light-driven robotic centipede is capable of multitask functions and information feedback, such as sensing locomotive gaits, body temperatures, surface hardness/softness, and surface hotness/coldness. More importantly, with a sensing antenna and a wireless communication unit, this light-driven robotic centipede can sense light intensity, wind speed, and human touch and transmit the measured piezoelectric signals wirelessly to a receiver for analysis, as shown in Fig. 4.5l. It is expected that this light-driven robotic centipede will find important applications in human-robot interaction and environmental data collection.

Apart from the opto-mechanical soft microrobots introduced above, there are many other types of opto-mechanical soft microrobots developed by different research groups worldwide [19, 73, 76–83]. With the development and further improvement of the light-responsive materials, it is expected that the field of opto-mechanical soft microrobots will continue to develop and thrive. Future work in this field will not only be limited to the demonstration of complex locomotion behaviors of the microrobots, but will expand to integrate different sensing, control, and feedback functions to the microrobots, making it a powerful robotic platform that can

have anthropomorphic receptions and do sophisticated mechanical work. It is believed that opto-mechanical soft microrobots, with unique material characteristics, will continue to play important roles in future robotic studies.

4.4 Opto-chemical Microrobots

Opto-chemical microrobot is a type of microrobot that relies on photochemical reactions to generate propulsion forces. This type of microrobot requires specific working conditions, including microrobots formed from photoactive materials, an environment that contains photochemically active reagents, and light source with specific wavelength and intensity that can trigger the photochemical reactions. The idea/concept of an opto-chemical microrobot is inspired by living microorganisms in nature (Fig. 4.6a) [27, 84], such as algae and cyanobacteria, which can survive by converting solar energy into biochemical energy through the photosynthetic process. In a similar way, opto-chemical microrobots made of photoactive materials can harvest light energy and convert it into kinetic energy, generating propulsion forces that can make them move accordingly. Figure 4.6b and c show the two main morphological structures of opto-chemical microrobots [27]. The first one is spherical Janus particle (Fig. 4.6b), whose surfaces are made of two different materials or bearing two different functional groups. The two different surfaces of a Janus particle allow two different types of physics/chemistry to occur on the same particle, giving it unique properties. The second main morphological structure used for opto-chemical microrobots is a tubular or rod-like structure (Fig. 4.6c), which can show “rocket”-like locomotion behaviors based on asymmetric chemical reactions at different parts of the microrobot (such as in the inner cavity and outer surface). The most common photoactive materials used for making opto-chemical microrobots are semiconductors with definite bandgaps, which can generate electron and hole pairs upon irradiation with light bearing energy larger than the bandgap of the semiconductor. The photoexcited charge carriers can move to the surface and participate in redox chemical reactions. This process is shown by the schematic in Fig. 4.6d [26].

Figure 4.6e–f illustrates the three motion mechanisms of opto-chemical microrobots, including self-diffusiophoresis, self-electrophoresis, and bubble ejection. Upon light irradiation, the opto-chemical microrobots can produce a disproportional distribution of chemical products, electric charges, and gas bubbles, respectively, which triggers their motion. Figure 4.6e shows the self-diffusiophoretic motion of an opto-chemical microrobot, induced by self-generated chemical gradients [85]. Like most chemical reactions, the photochemical reaction for opto-chemical microrobots occurs with the depletion of reactants and the generation of reaction products. Owing to asymmetric chemical reactivity, there exists a concentration gradient of reaction products across the microrobot, resulting in the diffusion of chemical substances that can lead to the phoretic movement of microrobots known as self-diffusiophoresis. For instance, Au-WO₃@C microrobot has WO₃ nanoparticles attached to its carbon surface, and these WO₃ nanoparticles can block

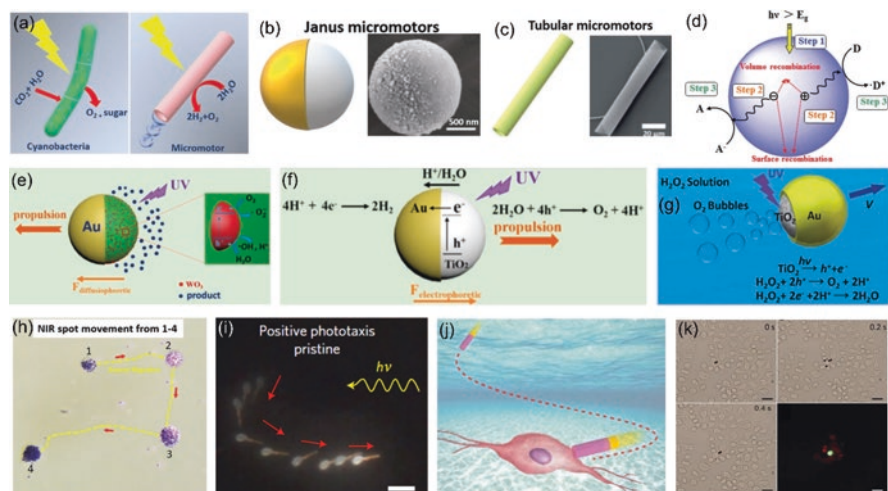


Fig. 4.6 Opto-chemical microrobots: mechanisms and applications. **(a)** Schematic illustration of light energy transformation performed by microorganisms and artificial opto-chemical microrobots. **(b)** Schematic and SEM image of a spherical Janus microrobot. **(c)** Schematic and SEM image of a tubular microrobot. **(a)–(c)** Reproduced with permission from reference 27. **(d)** Process of a photochemical reaction of a semiconductor particle upon light irradiation. “A” is electron acceptor; “D” is electron donor. **(d)** Reproduced with permission from reference 26. **(e)** Schematic illustration of self-diffusiophoresis motion of Au-WO₃@C spherical Janus microrobot. **(f)** Schematic illustration of self-electrophoresis motion of TiO₂/Au spherical Janus microrobot. **(e)–(f)** Reproduced with permission from reference 85. **(g)** Schematic illustration of bubble-ejection motion of TiO₂/Au spherical Janus microrobot in H₂O₂ solution. **(g)** Reproduced with permission from reference 86. **(h)** Collective migration of a swarm of microrobots under NIR navigation. The microrobot swarm forms at location 1 and migrates to location 2, 3, and 4, following the NIR laser beam. **(h)** Reproduced with permission from reference 90. **(i)** Positive phototaxis of a tree-shaped microrobot. The microrobot can align to the direction of incoming light due to asymmetric chemical reaction speeds. **(i)** Reproduced with permission from reference 91. **(j)** Schematic illustration of a light-guided microrobot to target and activate a neuronal retinal ganglion cell. **(j)** Reproduced with permission from reference 92. **(k)** Bright-field and fluorescent microscope images showing the movement of a microrobot to target HeLa cells under low-power NIR light and the apoptosis of HeLa cells by irradiating the microrobot with high-power NIR light. **(k)** Reproduced with permission from reference 93

the electron transfer from the carbon core to the Au surface, leading to a higher concentration of the reaction products on the side with WO₃ nanoparticles. As a result, an osmotic flow appears from low to high chemical concentration regions, which propels the microrobot pointing to the Au side. Electrokinetic effect can also induce the propulsion of opto-chemical microrobots owing to uneven distribution of electric charges and ions across the opto-chemical microrobots [84]. As shown in Fig. 4.6f [85], upon UV light irradiation, a TiO₂/Au Janus microrobot cannot symmetrically consume or generate H⁺ ions, as the reduction process of H⁺ to H₂ at the Au side is slower than the oxidation process at the TiO₂ side. This results in an accumulation of H⁺ on the TiO₂ side. The H⁺ ion gradient induces a local electric field, which can propel the microrobot with the TiO₂ side facing forward. This effect

is known as self-electrophoresis motion of an opto-chemical microrobot. Another motion mechanism for an opto-chemical microrobot relies on the asymmetric generation and ejection of gas bubbles. As shown in Fig. 4.6g [86], the opto-chemical microrobot decomposes H_2O_2 and generates gaseous oxygen at the TiO_2 side, which can propel the microrobot forward with the Au side facing forward. This bubble-ejection motion mechanism is mainly adopted by tubular-shaped microrobots because the generated gas can accumulate more effectively inside a microtube structure to generate bubbles [84, 87–89].

Opto-chemical microrobots can interact with each other and exhibit collective behaviors, which are influenced by external fields, surface electric charges, surface chemistry groups, and fluidic flows. Besides, opto-chemical microrobots can sense the light direction and align accordingly, an important behavior known as phototaxis. The phototaxis movement can be toward the light source (positive phototaxis) or away from it (negative phototaxis), depending on the surface chemistry groups of the microrobot. Figure 4.6h shows the controlled manipulation of a swarm of microrobots under NIR light navigation [90]. These microrobots can move individually upon UV light irradiation, without showing any collective behavior. However, by turning off the UV light and turning on a NIR laser, the microrobots show accumulation behaviors and migrate toward the center of the NIR laser beam. By changing the position of the NIR laser beam, the microrobot swarm can be moved to different places (Fig. 4.6h). This light-induced positive phototaxis behavior of the microrobots is caused by convection and Marangoni flows generated by photothermal heating of the liquid medium. Figure 4.6i shows a tree-shaped opto-chemical microrobot, whose orientation is along the direction of incoming light [91]. This self-aligning behavior is caused by the anisotropic absorption of light. If the absorption mainly happens perpendicular to the microrobot's main axis, asymmetric generation of reaction products will lead to a torque imposed on the tree-shaped microrobot, making it align to the direction of the incoming light.

Owing to unique light-responsive behaviors, opto-chemical microrobots were demonstrated for many impressive applications [26–29, 84], such as cargo transport, micro/nano-assembly, environmental remediation, drug delivery, and photothermal therapy. Figure 4.6j shows the use of a wire-shaped opto-chemical microrobot to activate a neuronal retinal ganglion cell (RGC) [92]. This microrobot can self-propel in pure water under low levels of UV irradiation and is capable of targeting neuronal RGC with high precision. After reaching the targeted cell, a locally generated electric field from the microrobot can be utilized as a stimulus to activate the cell through its calcium ion channel. Therefore, the microrobot can be used for monitoring and controlling cellular behavior. Another important application of opto-chemical microrobots is shown in Fig. 4.6k [93], in which the microrobot is used to target cancer cells and trigger photothermal effect to kill the cancer cells. In this work, the microrobot is actuated by a NIR laser beam. Once the microrobot reaches the target HeLa cells, the power of the NIR laser is increased, and the microrobot can absorb the laser light and convert it to heat. This induces the temperature rise around the microrobot, leading to the apoptosis of HeLa cells surrounding the microrobot. Biomedicine and drug delivery are regarded as the main

applications of opto-chemical microrobots, and many research groups are working in this field [26–29, 84]. To make opto-chemical microrobots work *in vivo*, the microrobots need to have high moving speeds to overcome blood flow. Besides, UV/visible light cannot penetrate human body and thus cannot provide the actuation force for the microrobot work *in vivo*. These challenges need to be overcome to make opto-chemical microrobotic technology a useful biomedical tool for real-world problems.

4.5 Conclusion and Outlook

Light-driven microrobots have attracted significant research interest and have been explored for different uses in various research fields. In this chapter, we comprehensively reviewed the working principles of three categories of light-driven microrobots and demonstrated their versatile applications in engineering and biomedical research. This inspires us to further explore the potentials of light-driven microrobots in multidisciplinary fields. However, there still exist several key challenges that hinder the development of light-driven microrobots and limit their applications.

For optical microrobots that rely on optical micromanipulation technologies, the actuation force is in the range of nanonewton (10^{-9} N) to pico-Newton regime (10^{-12} N), not enough to actuate microrobots with large sizes and weight. This limits the designs, materials, and tools used to form/fabricate the microrobots and sets limits on their applications. Besides, most optical micromanipulation technologies require the use of complex, bulky, and expensive setups, which relegate the optical microrobots to niche applications mainly used in research labs. Opto-mechanical soft microrobots rely on light-responsive materials; the physical, chemical, and mechanical properties of these materials are important factors that influence the performance of microrobots. There still exist key challenges including biocompatibility, water/temperature resilience, and structure stability that limit the use of opto-mechanical soft microrobots for applications in complex environments. Opto-chemical microrobots rely on photochemical reactions, and specific working conditions are required, including microrobots formed from photoactive materials, a liquid environment that contains chemical reagents, and light source with specific wavelength that can trigger the chemical reactions. These conditions set firm limitations on the working scenarios of opto-chemical microrobots.

To overcome these challenges, there is no single solution, and efforts should be made comprehensively to improve the light-driven microrobotic technologies. For example, advanced beam shaping and modulation techniques are desirable for microrobot control for complex tasks and operations; high-throughput and high-resolution fabrication techniques are important for microrobot prototyping and manufacturing; innovative light-responsive materials with excellent mechanical/chemical properties can significantly improve the performance of microrobots in complex environments. Other aspects such as the improvement of control software and automation algorithms can also have positive impacts on the development of

light-driven microrobotic technologies. Thanks to the joint efforts made by worldwide researchers with diverse and complementary research backgrounds, it is expected that light-driven microrobotic technologies will continue to thrive and play an increasingly important role in a variety of scientific applications in future.

References

1. Tottori, S., Zhang, L., Qiu, F., Krawczyk, K. K., Franco-Obregón, A., & Nelson, B. J. (2012). Magnetic helical micromachines: Fabrication, controlled swimming, and cargo transport. *Advanced Materials*, *24*, 811–816.
2. Alapan, Y., Yigit, B., Beker, O., Demirörs, A. F., & Sitti, M. (2019). Shape-encoded dynamic assembly of mobile micromachines. *Nature Materials*, *18*, 1244–1251.
3. Hu, W., Lum, G. Z., Mastrangeli, M., & Sitti, M. (2018). Small-scale soft-bodied robot with multimodal locomotion. *Nature*, *554*, 81–85.
4. Li, A., Li, H., Li, Z., Zhao, Z., Li, K., Li, M., & Song, Y. (2020). Programmable droplet manipulation by a magnetic-actuated robot. *Science Advances*, *6*, eaay5808.
5. Shields, C. W., IV, Han, K., Ma, F., Miloh, T., Yossifon, G., & Velev, O. D. (2018). Supercolloidal spinners: Complex active particles for electrically powered and switchable rotation. *Advanced Functional Materials*, *28*, 1803465.
6. Xu, X., Liu, C., Kim, K., & Fan, D. L. (2014). Electric-driven rotation of silicon nanowires and silicon nanowire motors. *Advanced Functional Materials*, *24*, 4843–4850.
7. Kaynak, M., Ozcelik, A., Nourhani, A., Lammert, P. E., Crespi, V. H., & Huang, T. J. (2017). Acoustic actuation of bioinspired microswimmers. *Lab on a Chip*, *17*, 395–400.
8. Kaynak, M., Ozcelik, A., Nama, N., Nourhani, A., Lammert, P. E., Crespi, V. H., & Huang, T. J. (2016). Acoustofluidic actuation of in situ fabricated microrotors. *Lab on a Chip*, *16*, 3532–3537.
9. Wang, W., Li, S., Mair, L., Ahmed, S., Huang, T. J., & Mallouk, T. E. (2014). Acoustic propulsion of nanorod motors inside living cells. *Angewandte Chemie, International Edition*, *53*, 3201–3204.
10. Ashkin, A., Dziedzic, J. M., & Yamane, T. (1987). Optical trapping and manipulation of single cells using infrared laser beams. *Nature*, *330*, 769–771.
11. Grier, D. G. (2003). A revolution in optical manipulation. *Nature*, *424*, 810–816.
12. Dholakia, K., & Čížmár, T. (2011). Shaping the future of manipulation. *Nature Photonics*, *5*, 335–342.
13. Padgett, M., & Bowman, R. (2011). Tweezers with a twist. *Nature Photonics*, *5*, 343–348.
14. Woerdemann, M., Alpmann, C., Esseling, M., & Denz, C. (2013). Advanced optical trapping by complex beam shaping. *Laser & Photonics Reviews*, *7*, 839–854.
15. Daly, M., Sergides, M., & Chormaic, S. N. (2015). Optical trapping and manipulation of micrometer and submicrometer particles. *Laser & Photonics Reviews*, *9*, 309–329.
16. Palima, D., & Glückstad, J. (2013). Gearing up for optical microrobotics: Micromanipulation and actuation of synthetic microstructures by optical forces. *Laser & Photonics Reviews*, *7*, 478–494.
17. Bunea, A. I., & Glückstad, J. (2019). Strategies for optical trapping in biological samples: Aiming at microrobotic surgeons. *Laser & Photonics Reviews*, *13*, 1800227.
18. Zeng, H., Martella, D., Wasylczyk, P., Cerretti, G., Lavocat, J. C., Ho, C. H., Parmeggiani, C., & Wiersma, D. S. (2014). High-resolution 3D direct laser writing for liquid-crystalline elastomer microstructures. *Advanced Materials*, *26*, 2319–2322.
19. Zeng, H., Wasylczyk, P., Wiersma, D. S., & Priimagi, A. (2018). Light robots: Bridging the gap between microrobotics and photomechanics in soft materials. *Advanced Materials*, *30*, 1703554.

20. Pilz da Cunha, M., Foelen, Y., van Raak, R. J., Murphy, J. N., Engels, T. A., Debije, M. G., & Schenning, A. P. (2019). An untethered magnetic-and light-responsive rotary gripper: Shedding light on Photoresponsive liquid crystal actuators. *Advanced Optical Materials*, 7, 1801643.
21. Wani, O. M., Zeng, H., & Priimagi, A. (2017). A light-driven artificial flytrap. *Nature Communications*, 8, 15546.
22. Palagi, S., Mark, A. G., Reigh, S. Y., Melde, K., Qiu, T., Zeng, H., Parmeggiani, C., Martella, D., Sanchez-Castillo, A., Kapernaum, N., Giesselmann, F., Wiersma, D. S., Lauga, E., & Fischer, P. (2016). Structured light enables biomimetic swimming and versatile locomotion of photoresponsive soft microrobots. *Nature Materials*, 15, 647–653.
23. Wang, X. Q., Chan, K. H., Cheng, Y., Ding, T., Li, T., Achavananthadith, S., Ahmet, S., Ho, J. S., & Ho, G. W. (2020). Somatosensory, light-driven, thin-film robots capable of integrated perception and motility. *Advanced Materials*. 2000351.
24. Rogóż, M., Zeng, H., Xuan, C., Wiersma, D. S., & Wasylczyk, P. (2016). Light-driven soft robot mimics caterpillar locomotion in natural scale. *Advanced Optical Materials*, 4, 1689–1694.
25. Lv, J., Liu, Y., Wei, J., Chen, E., Qin, L., & Yu, Y. (2016). Photocontrol of fluid slugs in liquid crystal polymer microactuators. *Nature*, 537, 179–184.
26. Xu, L., Mou, F., Gong, H., Luo, M., & Guan, J. (2017). Light-driven micro/nanomotors: From fundamentals to applications. *Chemical Society Reviews*, 46, 6905–6926.
27. Villa, K., & Pumera, M. (2019). Fuel-free light-driven micro/nanomachines: Artificial active matter mimicking nature. *Chemical Society Reviews*, 48, 4966–4978.
28. Sridhar, V., Park, B. W., & Sitti, M. (2018). Light-driven Janus hollow mesoporous TiO₂-Au microswimmers. *Advanced Functional Materials*, 28, 1704902.
29. Palagi, S., Singh, D. P., & Fischer, P. (2019). Light-controlled micromotors and soft microrobots. *Advanced Optical Materials*, 7, 1900370.
30. Ashkin, A., Dziedzic, J. M., Bjorkholm, J. E., & Chu, S. (1986). Observation of a single-beam gradient force optical trap for dielectric particles. *Optics Letters*, 11, 288–290.
31. Jones, P. H., Maragò, O. M., & Volpe, G. (2015). *Optical tweezers: Principles and applications*. Cambridge University Press.
32. Phillips, D. B., Gibson, G. M., Bowman, R., Padgett, M. J., Hanna, S., Carberry, D. M., Miles, M. J., & Simpson, S. H. (2012). An optically actuated surface scanning probe. *Optics Express*, 20, 29679–29693.
33. Asavei, T., Nieminen, T. A., Loke, V. L., Stilgoe, A. B., Bowman, R., Preece, D., Padgett, M. J., Heckenberg, N. R., & Rubinsztein-Dunlop, H. (2013). Optically trapped and driven paddle-wheel. *New Journal of Physics*, 15, 063016.
34. Di Leonardo, R., Búzás, A., Kelemen, L., Vizsnyiczai, G., Oroszi, L., & Ormos, P. (2012). Hydrodynamic synchronization of light driven microrotors. *Physical Review Letters*, 109, 034104.
35. Favre-Bulle, I. A., Stilgoe, A. B., Scott, E. K., & Rubinsztein-Dunlop, H. (2019). Optical trapping in vivo: Theory, practice, and applications. *Nano*, 8, 1023–1040.
36. Neale, S. L., MacDonald, M. P., Dholakia, K., & Krauss, T. F. (2005). All-optical control of microfluidic components using form birefringence. *Nature Materials*, 4, 530–533.
37. Phillips, D. B., Padgett, M. J., Hanna, S., Ho, Y. L., Carberry, D. M., Miles, M. J., & Simpson, S. H. (2014). Shape-induced force fields in optical trapping. *Nature Photonics*, 8, 400–405.
38. Palima, D., Bañas, A. R., Vizsnyiczai, G., Kelemen, L., Ormos, P., & Glückstad, J. (2012). Wave-guided optical waveguides. *Optics Express*, 20, 2004–2014.
39. Villangca, M. J., Palima, D., Banas, A. R., & Glückstad, J. (2016). Light-driven micro-tool equipped with a syringe function. *Light: Science and Applications*, 5, e16148.
40. Bütaitė, U. G., Gibson, G. M., Ho, Y. L., Taverne, M., Taylor, J. M., & Phillips, D. B. (2019). Indirect optical trapping using light driven micro-rotors for reconfigurable hydrodynamic manipulation. *Nature Communications*, 10, 1215.
41. Leach, J., Mushfique, H., di Leonardo, R., Padgett, M., & Cooper, J. (2006). An optically driven pump for microfluidics. *Lab on a Chip*, 6, 735–739.

42. Zou, X., Zheng, Q., Wu, D., & Lei, H. (2020). Controllable cellular micromotors based on optical tweezers. *Advanced Functional Materials*, *30*, 2002081.
43. Wu, T., Nieminen, T. A., Mohanty, S., Miotke, J., Meyer, R. L., Rubinsztein-Dunlop, H., & Berns, M. W. (2012). A photon-driven micromotor can direct nerve fibre growth. *Nature Photonics*, *6*, 62–67.
44. Xin, H., Zhao, N., Wang, Y., Zhao, X., Pan, T., Shi, Y., & Li, B. (2020). Optically controlled living micromotors for the manipulation and disruption of biological targets. *Nano Letters*, *20*, 7177–7185.
45. Li, Y., Liu, X., & Li, B. (2019). Single-cell biomagnifier for optical nanoscopes and nanotweezers. *Light: Science and Applications*, *8*, 61.
46. Bianchi, S., Vizsnyiczai, G., Ferretti, S., Maggi, C., & Di Leonardo, R. (2018). An optical reaction micro-turbine. *Nature Communications*, *9*, 4476.
47. Galajda, P., & Ormos, P. (2001). Complex micromachines produced and driven by light. *Applied Physics Letters*, *78*, 249–251.
48. Lin, X. F., Hu, G. Q., Chen, Q. D., Niu, L. G., Li, Q. S., Ostendorf, A., & Sun, H. B. (2012). A light-driven turbine-like micro-rotor and study on its light-to-mechanical power conversion efficiency. *Applied Physics Letters*, *101*, 113901.
49. Zhang, D., Barbot, A., Lo, B., & Yang, G. Z. (2020). Distributed force control for microrobot manipulation via planar multi-spot optical tweezer. *Advanced Optical Materials*, *8*, 2000543.
50. Köhler, J., Ksouri, S. I., Esen, C., & Ostendorf, A. (2017). Optical screw-wrench for microassembly. *Microsystems & Nanoengineering*, *3*, 16083.
51. Avcı, E., Grammatikopoulou, M., & Yang, G. Z. (2017). Laser-printing and 3D optical-control of untethered microrobots. *Advanced Optical Materials*, *5*, 1700031.
52. Thalhammer, G., Steiger, R., Bernet, S., & Ritsch-Marte, M. (2011). Optical macro-tweezers: Trapping of highly motile micro-organisms. *Journal of Optics*, *13*, 044024.
53. Lin, L., Wang, M., Peng, X., Lissek, E. N., Mao, Z., Scarabelli, L., Adkins, E., Coskun, S., Sahin, U., Unalan, H. E., Korgel, B. A., Liz-Marzán, L. M., Florin, E. L., & Zheng, Y. (2018). Opto-thermoelectric nanotweezers. *Nature Photonics*, *12*, 195–201.
54. Lin, L., Zhang, J., Peng, X., Wu, Z., Coughlan, A. C. H., Mao, Z., Bevan, M. A., & Zheng, Y. (2017). Opto-Thermophoretic assembly of colloidal matter. *Science Advances*, *3*, e1700458.
55. Liu, F., Zhang, Z., Wei, Y., Zhang, Q., Cheng, T., & Wu, X. (2014). Photophoretic trapping of multiple particles in tapered-ring optical field. *Optic Express*, *22*, 23716–23723.
56. Esseling, M., Rose, P., Alpmann, C., & Denz, C. (2012). Photophoretic trampoline—Interaction of single airborne absorbing droplets with light. *Applied Physics Letters*, *101*, 131115.
57. Xie, Y., Zhao, C., Zhao, Y., Li, S., Rufo, J., Yang, S., Guo, F., & Huang, T. J. (2013). Optoacoustic tweezers: A programmable, localized cell concentrator based on opto-thermally generated, acoustically activated, surface bubbles. *Lab on a Chip*, *13*, 1772–1779.
58. Zharov, V. P., Malinsky, T. V., & Kurten, R. C. (2005). Photoacoustic tweezers with a pulsed laser: Theory and experiments. *Journal of Physics D: Applied Physics*, *38*, 2662–2674.
59. Chiou, P. Y., Ohta, A. T., & Wu, M. C. (2005). Massively parallel manipulation of single cells and microparticles using optical images. *Nature*, *436*, 370–372.
60. Wu, M. C. (2011). Optoelectronic tweezers. *Nature Photonics*, *5*, 322–324.
61. Hwang, H., & Park, J. K. (2011). Optoelectrofluidic platforms for chemistry and biology. *Lab on a Chip*, *11*, 33–47.
62. Pethig, R. (2010). Review article-Dielectrophoresis: Status of the theory, technology, and applications. *Biomicrofluidics*, *4*, 022811.
63. Zhang, S., Juvert, J., Cooper, J. M., & Neale, S. L. (2016). Manipulating and assembling metallic beads with optoelectronic tweezers. *Scientific Reports*, *6*, 32840.
64. Juvert, J., Zhang, S., Eddie, I., Mitchell, C. J., Reed, G. T., Wilkinson, J. S., Kelly, A., & Neale, S. L. (2016). Micromanipulation of InP lasers with optoelectronic tweezers for integration on a photonic platform. *Optic Express*, *24*, 18163–18175.
65. Zhang, S., Scott, E. Y., Singh, J., Chen, Y., Zhang, Y., Elsayed, M., Chamberlain, M. D., Shakiba, N., Adams, K., Yu, S., Morshead, C. M., Zandstra, P. W., & Wheeler, A. R. (2019).

- The optoelectronic microrobot: A versatile toolbox for micromanipulation. *PNAS*, *116*, 14823–14828.
66. Yang, W., Yu, H., Li, G., Wang, Y., & Liu, L. (2017). High-throughput fabrication and modular assembly of 3D heterogeneous microscale tissues. *Small*, *13*, 1602769.
 67. Maggi, C., Saglimbeni, F., Dipalo, M., De Angelis, F., & Di Leonardo, R. (2015). Micromotors with asymmetric shape that efficiently convert light into work by thermocapillary effects. *Nature Communications*, *6*, 7855.
 68. Dai, L., Lin, D., Wang, X., Jiao, N., & Liu, L. (2020). Integrated assembly and flexible movement of microparts using multifunctional bubble microrobots. *ACS Applied Materials & Interfaces*, *12*, 57587–57597.
 69. Hu, W., Ishii, K. S., Fan, Q., & Ohta, A. T. (2012). Hydrogel microrobots actuated by optically generated vapour bubbles. *Lab on a Chip*, *12*, 3821–3826.
 70. Kim, Y., Ding, H., & Zheng, Y. (2020). Enhancing surface capture and sensing of proteins with low-power optothermal bubbles in a biphasic liquid. *Nano Letters*, *20*, 7020–7027.
 71. Peng, X., Chen, Z., Kollipara, P. S., Liu, Y., Fang, J., Lin, L., & Zheng, Y. (2020). Opto-thermoelectric microswimmers. *Light: Science and Applications*, *9*, 141.
 72. Dai, L., Ge, Z., Jiao, N., & Liu, L. (2019). 2D to 3D manipulation and assembly of microstructures using Optothermally generated surface bubble microrobots. *Small*, *45*, 1902815.
 73. da Cunha, M. P., Debije, M. G., & Schenning, A. P. (2020). Bioinspired light-driven soft robots based on liquid crystal polymers. *Chemical Society Reviews*, *49*, 6568–6578.
 74. Zeng, H., Wasylczyk, P., Parmeggiani, C., Martella, D., Burresti, M., & Wiersma, D. S. (2015). Light-fueled microscopic walkers. *Advanced Materials*, *27*, 3883–3887.
 75. Zeng, H., Wani, O. M., Wasylczyk, P., Kaczmarek, R., & Priimagi, A. (2017). Self-regulating iris based on light-actuated liquid crystal elastomer. *Advanced Materials*, *29*, 1701814.
 76. Nocentini, S., Parmeggiani, C., Martella, D., & Wiersma, D. S. (2018). Optically driven soft micro robotics. *Advanced Optical Materials*, *6*, 1800207.
 77. Lu, X., Zhang, H., Fei, G., Yu, B., Tong, X., Xia, H., & Zhao, Y. (2018). Liquid-crystalline dynamic networks doped with gold nanorods showing enhanced photocontrol of actuation. *Advanced Materials*, *30*, 1706597.
 78. Li, Y., Liu, Y., & Luo, D. (2020). Polarization dependent light-driven liquid crystal elastomer actuators based on Photothermal effect. *Advanced Optical Materials*, 2001861.
 79. Pilz da Cunha, M., Ambergen, S., Debije, M. G., Homburg, E. F., den Toonder, J. M., & Schenning, A. P. (2020). A soft transporter robot fueled by light. *Advancement of Science*, *7*, 1902842.
 80. Han, B., Zhang, Y. L., Zhu, L., Li, Y., Ma, Z. C., Liu, Y. Q., Zhang, X. L., Cao, X. W., Chen, Q. D., Qiu, C. W., & Sun, H. B. (2019). Plasmonic-assisted graphene oxide artificial muscles. *Advanced Materials*, *31*, 1806386.
 81. Hu, Y., Li, Z., Lan, T., & Chen, W. (2016). Photoactuators for direct optical-to-mechanical energy conversion: From nanocomponent assembly to macroscopic deformation. *Advanced Materials*, *28*, 10548–10556.
 82. Lahikainen, M., Zeng, H., & Priimagi, A. (2018). Reconfigurable photoactuator through synergistic use of photochemical and photothermal effects. *Nature Communications*, *9*, 4148.
 83. Huang, C., Lv, J. A., Tian, X., Wang, Y., Yu, Y., & Liu, J. (2015). Miniaturized swimming soft robot with complex movement actuated and controlled by remote light signals. *Scientific Reports*, *5*, 17414.
 84. Palagi, S., & Fischer, P. (2018). Bioinspired microrobots. *Nature Reviews Materials*, *3*, 113–124.
 85. Zhang, Q., Dong, R., Wu, Y., Gao, W., He, Z., & Ren, B. (2017). Light-driven Au-WO₃@ C Janus micromotors for rapid photodegradation of dye pollutants. *ACS Applied Materials & Interfaces*, *9*, 4674–4683.
 86. Li, Y., Mou, F., Chen, C., You, M., Yin, Y., Xu, L., & Guan, J. (2016). Light-controlled bubble propulsion of amorphous TiO₂/Au Janus micromotors. *RSC Advances*, *6*, 10697–10703.

87. Solovev, A. A., Mei, Y., Bermúdez Ureña, E., Huang, G., & Schmidt, O. G. (2009). Catalytic microtubular jet engines self-propelled by accumulated gas bubbles. *Small*, *5*, 1688–1692.
88. Fomin, V. M., Hippler, M., Magdanz, V., Soler, L., Sanchez, S., & Schmidt, O. G. (2013). Propulsion mechanism of catalytic microjet engines. *IEEE Transactions on Robotics*, *30*, 40–48.
89. Mou, F., Li, Y., Chen, C., Li, W., Yin, Y., Ma, H., & Guan, J. (2015). Single-component TiO₂ tubular microengines with motion controlled by light-induced bubbles. *Small*, *21*, 2564–2570.
90. Deng, Z., Mou, F., Tang, S., Xu, L., Luo, M., & Guan, J. (2018). Swarming and collective migration of micromotors under near infrared light. *Applied Materials Today*, *13*, 45–53.
91. Dai, B., Wang, J., Xiong, Z., Zhan, X., Dai, W., Li, C. C., Feng, S. P., & Tang, J. (2016). Programmable artificial phototactic microswimmer. *Nature Nanotechnology*, *11*, 1087–1092.
92. Chen, B., Liu, L., Liu, K., Tong, F., Wang, S., Fu, D., Gao, J., Jiang, J., Ou, J., Ye, Y., & Wilson, D. A. (2020). Photoelectrochemical TiO₂-Au-Nanowire-based Motor for Precise Modulation of single-neuron activities. *Advanced Functional Materials*, 2008667.
93. Wu, Z., Lin, X., Wu, Y., Si, T., Sun, J., & He, Q. (2014). Near-infrared light-triggered “on/off” motion of polymer multilayer rockets. *ACS Nano*, *8*, 6097–7105.

Chapter 5

Electric-Field-Driven Micro/Nanomachines for Biological Applications



Hyungmok Joh and Donglei (Emma) Fan

5.1 Introduction

The exploitation of nanostructured materials for biomedical applications has seen heightened demand due to many benefits they bring, including unique optical, magnetic, and electric properties and large specific surface areas that enable their sensitive physical and chemical interactions with molecules for molecular capture, storage, sensing, and release. Owing to the tunable size from the molecular to cellular levels, nanostructures also are excellent candidates for cellular drug delivery and surgery. However, precision control and versatile manipulation of nanomaterials at such a small scale have been a major obstacle that hinders practical bio-applications. Substantial efforts have been devoted on finding innovative working mechanisms to guide and propel individual nanoparticles as miniaturized machines or motors and control their swarming behaviors by exploiting optical [1, 2], magnetic [3–5], and acoustic fields [6–9], as well as chemical reactions [10].

Yet, these innovative techniques are not without their respective limitations when applied for bio-applications. The high energy from the source of optical tweezers may induce damage to biological cells by Joule heating, and the highly localized nature of the system makes the control of only select molecules possible in multi-particle systems. Magnetic and acoustic manipulations are important and useful due to their biocompatibility and large operation range. However, magnetic tweezers are limited by the selection of materials. When dealing with nonmagnetic materials, magnetic materials such as Ni or hematite need to be incorporated into a material system, complicating the fabrication processes. Acoustic fields are highly powerful

H. Joh

Materials Science and Engineering Program, Texas Materials Institute, The University of Texas at Austin, Austin, TX, USA

D. (Emma) Fan (✉)

Department of Mechanical Engineering, The University of Texas at Austin, Austin, TX, USA
e-mail: dfan@austin.utexas.edu

and have already been used in medical practice, such as acoustic imaging; however, their spatial resolution largely depends on the frequency of acoustic waves, which is often restricted in the micrometer to millimeter region.

The electric tweezers based on combined AC and DC electric (E-)fields provide a powerful means to control entities with precise position, velocity, and orientation [11, 12]. Herein, we discuss the fundamentals behind the manipulation mechanism and how they have been utilized for bio-applications.

5.2 Fundamentals

We begin by briefly covering the fundamentals of the locomotion of micro-/nanomotors under E-fields. One must understand the fluid dynamics for low Reynolds number regime micro-/nanoscale motors and consider physics that governs motions of micro-/nanomotors when an E-field is applied: under an E-field, electrophoresis, dielectrophoresis, and electroosmosis often play major roles in the propulsion of the motors.

5.2.1 Low Reynolds Number Physics and Laminar Flow

The Reynolds number (Re) is a dimensionless quantity defined as the ratio of inertial force to viscous force within a fluid. It serves to determine the degree of laminar or turbulent flow and can be expressed as in the following equation [13]:

$$\text{Re} = \frac{au\rho}{\eta} = \frac{au}{\nu}$$

where a and u are the dimension and velocity of the object flowing through a fluid, respectively, and ρ and η are the density and viscosity of the fluid, respectively. The ratio between the latter two is also defined as the kinematic viscosity and is shown as ν . As can be seen from the equation, the Re value is directly proportional to the dimension of the object inside the fluid and becomes smaller and smaller as the size of the object decreases.

In the case of a micro-/nanomotor system, it is apparent that the size scales in the micro-/nanometer regime lead to a very low Re value, e.g., in the range of 10^{-4} to 10^{-6} . This indicates that the viscous force dominates over the inertial force and laminar flow occurs. At low Re values, the inertial terms in the Navier-Stokes equation become negligible (*right part of the equation*):

$$-\nabla P + \eta \nabla^2 \mathbf{u} = \rho \left(\frac{\partial \mathbf{u}}{\partial t} + (\mathbf{u} \cdot \nabla) \mathbf{u} \right) = 0$$

where P is the fluid pressure and ∇^2 is the Laplacian operator. According to the scallop theorem, the absence of inertial terms at low Re results in kinematic reversibility, meaning forward propulsion cannot be achieved through reciprocal motion. As a result, for E-field-driven micro-/nanomotors, an instantaneous cease of movement when the E-field is removed can be observed.

When a low Re object moves through a fluid in an E-field, the laminar flow that usually forms moves the surrounding solution along with it. The flow of the fluid can be seen as layers of fluids moving at linearly decreasing speeds, with the fluids closer to the moving body having a higher speed than the fluids further away. In other words, the velocity profile is linear with the fluid moving at the same speed at the immediate vicinity of the moving object and not moving at all when in a position far away.

5.2.2 Electrophoresis and the Electric Double Layer

When a direct current (DC) E-field is applied to a charged particle in suspension as shown in Fig. 5.1, the particle theoretically experiences an electric force proportional to its total charge, which can be simply calculated with the following equation:

$$F = qE$$

where q is the amount of the charge and E is the E-field. As q and E are scalar and vector quantities, respectively, the force F is also a vector quantity. However, the process of calculating the actual applied force on a charged particle under an E-field is not as simple as just plugging numbers into the equation; one important factor to consider is the formation of the electric double layer (EDL) on the charged surface.

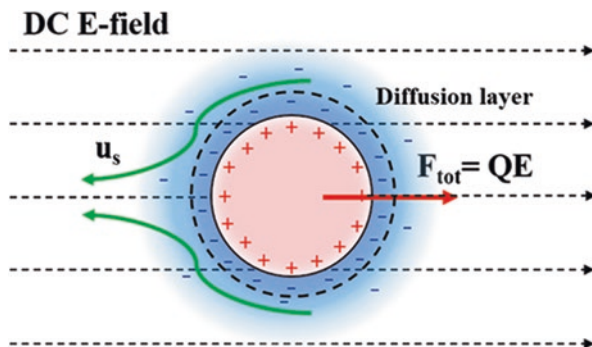


Fig. 5.1 Forces applied on a spherical conductive particle under a DC E-field. Due to the electric double layer effect, an electroosmotic flow with slip velocity u_s is formed in the opposite direction of the force applied to the particle. Green arrows indicate slip flow direction and red arrow indicates applied force on the particle

The EDL is formed due to the attraction between the charges on the surface of the particle and from the counterions that exist in the solution, which have a screening effect on the original charge and lower the effective charge of the particle. The EDL thickness κ^{-1} (defined as the Debye screening length) can be expressed as the following [14]:

$$\kappa^{-1} = \sqrt{\frac{\epsilon_0 \epsilon_m k_B T}{q^2 \sum_i z_i^2 c_{i\infty}}}$$

where ϵ_0 , ϵ_m , k_B , T , q , z_i , and $c_{i\infty}$ are the dielectric constant of vacuum, relative dielectric constant of the medium, Boltzmann constant, temperature, charge of an electron, valence, and bulk concentration of a collection of ions i , respectively. Intuitively, one can consider that the EDL thickness is decided by the competition between thermal agitation and electrical attraction: with higher ionic strength of the bulk solution (higher q , z , and c values) and lower agitation due to heat (lower T values), the counterions are more densely packed at the surface of the charged particle and result in a thinner EDL.

The steady-state velocity is the result of electroosmotic flow around the moving object and is established when the electric force equals the viscous drag force. The E-field also interacts with the charged ions in the EDL which subsequently drags the surrounding fluid. When the EDL thickness is much smaller than the particle radius, the electrophoretic steady-state velocity (v) and the slip velocity of the osmotic flow (μ_s) are given by the Helmholtz-Smoluchowski equation:

$$\mu_s = \frac{v}{E} = \frac{\epsilon_0 \epsilon_m \zeta}{\eta}$$

ζ , the zeta potential, is the electrical potential difference between the fluid and the stationary fluid at the moving body surface. As such, the zeta potential is located at the shear plane of the EDL where the velocity is 0 at the surface of the body. The zeta potential can be expressed as the following [15]:

$$\zeta = \frac{q}{\epsilon_0 \epsilon_m} \kappa^{-1}.$$

5.2.3 Dielectrophoresis and the Clausius-Mossotti Factor

When a dielectric particle in a solution is subject to a nonuniform E-field, positive or negative dielectrophoretic (DEP) force is exerted depending on the electronic properties of the particle and suspension medium as well as the gradient of the electric field. For a spherical particle with radius R , the DEP force can be approximated as the following:

$$F_{DEP} = (p \bullet \nabla) E = 4\pi R^3 \epsilon_0 \epsilon_m \operatorname{Re}[CM](E \bullet \nabla) E,$$

where $\operatorname{Re}[CM]$ is the real part of the Clausius-Mossotti factor and p is the induced dipole moment which can be expressed as:

$$p = \alpha V E,$$

α is the polarizability and V and E are the volume and E-field, respectively. Furthermore, $[CM]$ can be expressed as:

$$[CM] = \frac{\epsilon_p^* - \epsilon_m^*}{\epsilon_p^* + 2\epsilon_m^*}.$$

The $[CM]$ value indicates the relative polarizability between the particle and the fluid: A negative value indicates that the medium solution is more polarizable than the particle and vice versa. ϵ_p^* and ϵ_m^* are the complex permittivities of the particle and medium which can be further expressed as:

$$\epsilon_p^* = \epsilon_p - j \frac{\sigma_p}{\omega} \text{ and } \epsilon_m^* = \epsilon_m - j \frac{\sigma_m}{\omega},$$

where ϵ_p , σ_p , ϵ_m , and σ_m and ω are the permittivities and conductivities of the particle and medium and the angular frequency of the applied field, respectively. As can be seen by the equations above, the sign of the DEP force is dependent on $\operatorname{Re}[CM]$, which can have a value between -0.5 and 1 depending on the angular frequency. It is apparent from the equation for DEP force that depending on the $\operatorname{Re}[CM]$ value, the particle will move either toward or away from the electrode.

The nature of the DEP force allows unique assemblies of particles through designed electrodes, which is often useful for bio-related applications. For example, *S. cerevisiae* and *M. lysodeikticus* cells, having different DEP signs, behave differently under an E-field. The different signs of the DEP force were used to separate cells [16]: Here, *M. lysodeikticus* exhibited positive DEP force and were attracted to the electrodes (Fig. 5.2a, red circle), while *S. cerevisiae* exhibited negative DEP force and were repelled from the electrodes (Fig. 5.2a, blue circle). Another example is illustrated in Fig. 5.2b, where quadruple electrodes were efficiently used for the separation of *M. lysodeikticus* (**red**) and *E. coli* (**blue**). It should be noted that there is also a frequency where the $\operatorname{Re}[CM]$ value is equal to zero; this is called the crossover frequency, and at this frequency the DEP force is zero.

When the AC E-field is uniform, the forces on the induced dipoles cancel each other out, and the resulting net DEP force applied on an object is zero, as can be seen in Fig. 5.3a. (This is also apparent from the DEP force equation; in a uniform E-field, the divergence of the E-field equals to zero, and $F_{DEP} = 0$.) However, depending on the orientation of the dipole relative to the E-field direction, other interactions such as electroorientation may occur. Consider a dipole in an E-field E with a dipole moment p that is not aligned with the E-field direction (Fig. 5.3b). Here, the

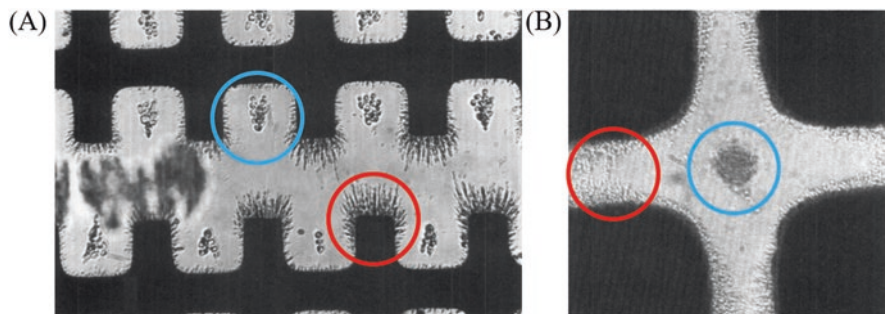


Fig. 5.2 Separation of biological cells using positive (red) and negative (blue) DEP forces, based on (a) castellated interdigitated electrodes and (b) quadruple electrodes. Reproduced with permission [16]. Copyright 1994, Microbiology Society

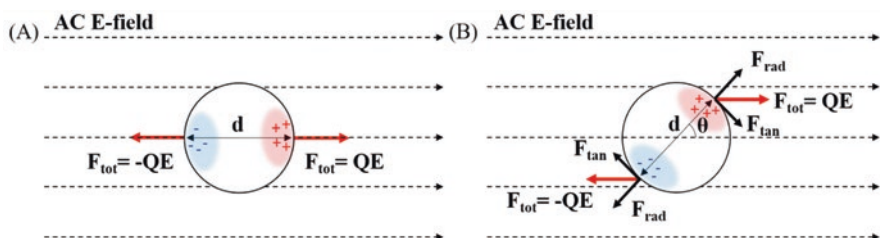


Fig. 5.3 Forces applied on a spherical dielectric particle with a diameter of d , when the electric dipole is (a) aligned and (b) not aligned with the AC E-field direction

charge at the end of the dipole experiences coulombic force given by $F = QE$. While the amount of force applied to each dipole end is equal in magnitude, a torque arises from the tangential forces as the forces are not applied on the same line. At each end, there is a torque that equals $T = Q(d/2)E\sin\theta = F_{\tan}(d/2)$. Therefore, the total torque applied to the body in this scenario is $T = QdE\sin\theta = pE\sin\theta$. Using electro-orientation, it is also possible to achieve continuous rotation of entities by constantly changing the E-field direction.

5.2.4 DC and AC Electroosmosis

Electroosmosis, the movement of fluids under an E-field, can be induced by both DC E-fields and AC E-fields. While the underlying fundamentals regarding the phenomenon are the same, the resulting E-field or particle movement is different. The main difference between these two electroosmotic flows comes from how the DC or AC E-field is applied to the suspension and how the electrodes are positioned relative to the surface. In the case of the former, a DC E-field is applied parallel to the

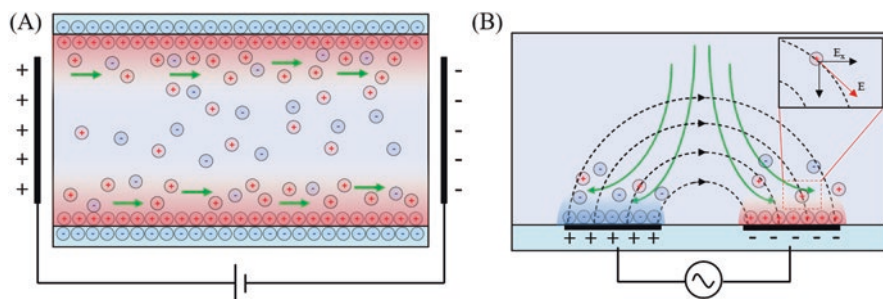


Fig. 5.4 Schematic of (a) a DC electroosmosis and (b) an AC electroosmosis setup. Green arrows indicate the fluid flow direction

substrate surface (Fig. 5.4a), while in the latter an AC E-field is applied on planar microelectrodes directly on top of the substrate surface (Fig. 5.4b).

DC Electroosmosis

As mentioned above, a DC electroosmosis setup includes a pair of electrodes applied parallel to the substrate surface. Figure 5.4a depicts a case where the surface is negatively charged, which would be the case for a glass substrate; here positive counterions in the solution are attracted to the surface and contribute to the (i) tightly bound cations creating an electric double layer in close proximity of the surface and (ii) cation-rich slipping part of the electric double layers. When an E-field is applied to this system, these cations in the slipping part of the electric double layer are attracted to the cathode, creating a drag flow around the surface of the substrate. This directional flow is the DC electroosmosis phenomena and is used in various applications such as the separation of charged species, which utilizes the different speeds of cations depending on their charges and sizes.

AC Electroosmosis

The fundamentals of AC electroosmosis is similar to that of DC electroosmosis. However, in the AC electroosmosis setup [Fig. 5.4b], the electrodes are positioned in a way that the electrodes create an E-field resulting in a net force toward the outside of the electrode and fluid movement (Fig. 5.4b, green lines). The force that a charged particle experiences is depicted in the inset of Fig. 5.4b: As the electrodes are placed next to each other, the corresponding E-field is formed in a nonlinear nature. Correspondingly, an electric force in the direction of the tangential direction of the E-field is applied to the charged particle which can be divided into vertical and horizontal components. The horizontal component of the E-field (E_x) induces sideways movement of the charged particle, dragging the nearby fluid with it as was the case for DC electroosmosis. The alternating polarity of the AC field does not

change the direction of the flow, since the type of charges of the ions that drag the flow is also altered correspondingly.

5.2.5 Combined AC and DC E-Fields for E-Field-Assisted Nano-manipulation

By combining the effects of electrophoresis/electroosmosis and dielectrophoresis covered in Sects. 2.2. and 2.3., as well as the low Reynolds number conditions of nanomotors, it is possible to achieve simultaneous and precise control over the position and orientation of a longitudinal object in a suspension. This technique, also known as electric tweezers, is a powerful tool that can be used in many applications from micro/nanopropellers to complex biochemical sensing applications, as will be introduced in Sect. 3. To realize a full 2D translational and rotational control, a quadruple microelectrode setup is generally used to change the direction and intensity of the applied DC and AC E-fields (Fig. 5.5). The applied AC E-field is uniform in this case, meaning that it does not induce movement from DEP force and can be used to align and rotate the subject object toward a specific direction.

5.2.6 Other Factors to Consider

Brownian Motion and Joule Heating

Brownian motion, named after Robert Brown who first described the phenomenon, refers to the random movement of particles in a medium without the presence of an external force. Often visualized as the position change of particles due to random bombardments from water molecules, Brownian motion was first theoretically explained by Albert Einstein using diffusion theory to derive the mean-squared displacement (MSD) [17]. The MSD ($\langle \Delta x^2(t) \rangle$) is a function of time and can be expressed as the following:

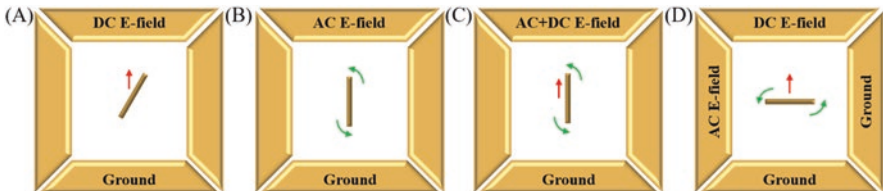


Fig. 5.5 Effects of (a) a single DC E-field, (b) a single AC E-field, (c) combined AC/DC E-fields applied on an object, and (d) combined AC/DC E-fields with controlled relative alignment, when the real part of the Clausius-Mossotti factor is positive. The red arrow indicates translational motion, while the green arrow indicates rotation

$$\langle \Delta x^2(t) \rangle = \frac{k_B T}{m} t^2,$$

where k_B , T , m , and t are the Boltzmann constant, temperature, mass, and time, respectively. Many other theories have been reported since then, considering additional factors such as inertia of the particle as well as the fluid [18]. As shown by the equation above, the Brownian motion of particles is largely determined by the mass of the particle; due to the low mass of micro-/nanomotors, the amount of fluctuation of the orientation and position is more apparent compared to those with larger bodies. The equation also highlights the importance of the solution temperature that houses the micro-/nanomotors, as it also is directly proportional to the MSD.

One major heating source to consider is Joule heating: When an E-field is applied to the system, Joule heating naturally occurs in the solution as particle systems themselves are conductive, regardless how small they may be. The temperature change can be expressed as the following under steady-state conditions [19]:

$$\Delta T \approx \frac{\sigma V^2}{k},$$

where k and σ are the thermal and electrical conductivities of the fluid. Joule heating should be considered and controlled as it could dramatically change the system dynamics. For example, in the case of DI water, which is commonly used in the application of the electric tweezers, the permittivity and electric conductivity change by about -0.4% and 2% , respectively, when the temperature is increased by 1K around room temperature [19]. This may lead to additional flows inside the solution from AC electrothermal effects. A comprehensive review on AC electrothermal effects is presented elsewhere [19, 20].

Properties of the Suspension Medium

While the properties of the particles play an essential role in determining how they respond to an E-field, the effects that the medium have on the electrophoretic and dielectrophoretic forces are of paramount importance as well. Many factors, such as the medium conductivity, permittivity, and the ions in the medium, may affect the electrokinetics of the particle system: first, as stated in Sect. 2.6.1., an increase in medium conductivity may induce unwanted thermal effects, leading to electrothermal flows within the system. Second, the medium permittivity is directly related to the Clausius-Mossotti factor covered in Sect. 2.3. Depending on the permittivity value, the signs as well as the intensity of the DEP forces applied on the particle may change. Last, depending on the types of ions in a solution, the screening effect the ions have on a particle and how it affects the EDL thickness can differ as is covered in Sect. 2.2. In most cases, the effective charge of a particle inside of a solution can be controlled by changing the pH value of the medium. The introduction of

mobile protons or hydroxides changes the surface state of the particle, dictated by the Henderson-Hasselbalch equation. When the effective charge of the particle equals 0 due to this introduction of ions from the medium, an isoelectric point is reached, and the particle will not be propelled by an electrophoretic force.

5.3 Applications of the Electric-Tweezer Manipulation in Biological Research

Recently, the employment of the electric tweezers has demonstrated various applications in biological research, including the delivery of cytokine molecules to a single live cell [21], release of biochemicals at tunable rate with controlled rotation of a nanomotors [22], precision assembly of quantum-dot-nanorod arrays for bio-sensing [23], and enhancement of the capture and detection speed of low-concentration DNA with retained high sensitivity [24].

5.3.1 Cytokine Molecule Delivery

Through surface modification, it has been shown that cytokine molecules such as tumor necrosis factor (TNF- α) can be loaded directly onto a nanomotor's surface for subsequent delivery onto individual cells (Fig. 5.6a) [21]. This is the first demonstration of the concept of using motorized nanoparticles for the delivery of biochemical stimuli to a single cell amidst many. The precision offered by the electric-field-driven nanomotors is particularly important for these cytokines as they can potentially induce lethal results such as septic shock.

For single-cell drug delivery, gold nanowires are first fabricated using electrodeposition through nanoporous templates and are subsequently treated with 1-dodecanethiol to increase the surface hydrophobicity for the adsorption of TNF- α . Due to the surface adsorption of TNF- α , the gold nanowires are charged and can be manipulated via E-fields. Here, the uniform AC E-field does not generate any DEP force, but is used to align the nanowire along the E-field direction. By combining a uniform AC E-field with a DC E-field, the transportation of nanowires to a single cell (Fig. 5.6b), as well as its control of the position and orientation on a cell (Fig. 5.6c), is demonstrated.

The delivery of TNF- α is confirmed through nuclear factor-kappaB (NF- κ B) activation, which is released from the cytosol into the nucleus once activated by TNF- α . The effectiveness of the delivery and its effect on the cells are shown in Fig. 5.6D: a comparable increase of the NF- κ B response can be found when the TNF- α is delivered by a nanowire at a concentration where each cell is exposed to ~1–2 nanowires (Fig. 5.6e). The profile of the TNF- α delivery exhibited a good

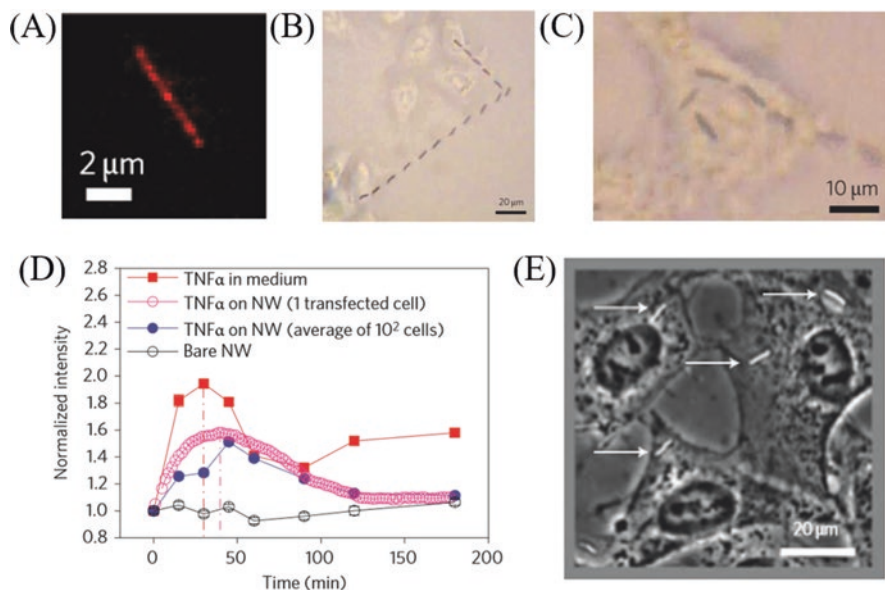


Fig. 5.6 (a) TNF- α molecules highlighted in red, conjugated on a Au nanowire surface. Delivery of a single nanowire to (b) a single cell and (c) its manipulation over a cell with the electric tweezers. (d) TNF- α response comparison with TNF- α in medium (red), on nanowires (pink and blue) and bare nanowires (black). (e) Successful delivery of ~ 1 TNF- α -loaded nanowire per cell through concentration control. Reproduced with permission [21]. Copyright 2010, Springer Nature Limited

match with computational analysis, indicating an exponential, local release of TNF- α from the nanowires into the cell.

5.3.2 Cargo Delivery

For the delivery of larger cargos than molecules such as TNF- α , different strategies have to be employed as it is more difficult to directly attach larger cargos to the surface as that for the work described above. One example of such strategy can be seen in Fig. 5.7a, where the direct capture, transport, and release of large cargo have been demonstrated by the use of catalytic Au-Pt nanomotors paired with the combined AC and DC E-fields [25]. Here, the catalytic reactions from the nanomotors are the main source of thrust; the AC E-field is used to guide the motions by electro-orientation, and the DC E-field is used to control the speed or even reverse the moving direction of the nanomotor.

The capture, transport, and release of cargo are demonstrated in Fig. 5.7b: First, the nanomotor and cargo are aligned by applying a uniform AC E-field. Here, the location of the cargo does not change while the nanomotor approaches it as it does not have a means of propulsion. On the contrary, the nanomotor can move to the

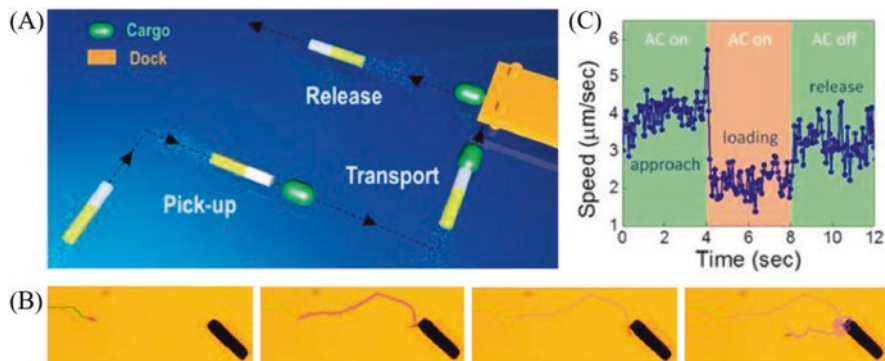


Fig. 5.7 (a) Scheme of targeted cargo delivery using Pt-Au catalytic nanomotors. (b) Images of a nanomotor applied for loading, transporting, and releasing a cargo onto a designated microdock. (c) Changes in speed during different delivery phases. Reproduced with permission [25]. Copyright 2018, American Chemical Society

cargo via catalytic decomposition of the H_2O_2 fuel. Second, when the nanomotor and cargo are in close proximity to each other, the tips are attached to each other due to the interactions between the induced E-fields from the dipoles of the nanomotor and cargo. Third, the cargo-attached nanomotor is then transported under an AC E-field for direction control to a metallic microdock, where the cargo is anchored due to a similar interaction between induced electric dipoles. The cargo is detached from the nanomotor and attached to the microdock by momentarily turning off and on the AC E-field and removing the induced dipole E-fields. The process of cargo attachment and detachment can be determined quantitatively by comparing the movement speed before, during, and after transport (Fig. 5.7c). It is apparent by the decrease in speed during transport that there is an extra load on the nanomotor.

This work utilizes the combined effect of catalytic reduction and oxidation reaction, as well as electrophoresis, electroosmosis, and dielectrophoresis. Similar to the work above, the AC E-field changes the alignment, while the DC E-field changes the transport speed of the nanomotors. Interestingly, a 3D orthogonal microelectrode setup which enables 3D control over the nanomotor was also used, further increasing the functionality.

5.3.3 Tunable Release of Biochemicals for Ultrasensitive SERS Detection

Tunable release of biochemicals with nanomotors is highly desirable for their potential applications in drug/cargo delivery, single cell stimulation, and the study of cell-cell communications [26]. With carefully designed plasmonic nanoparticles and nanomagnets that are controlled by electric tweezers, nanomotors that can tunably release biochemicals and detect their release dynamics with SERS have been

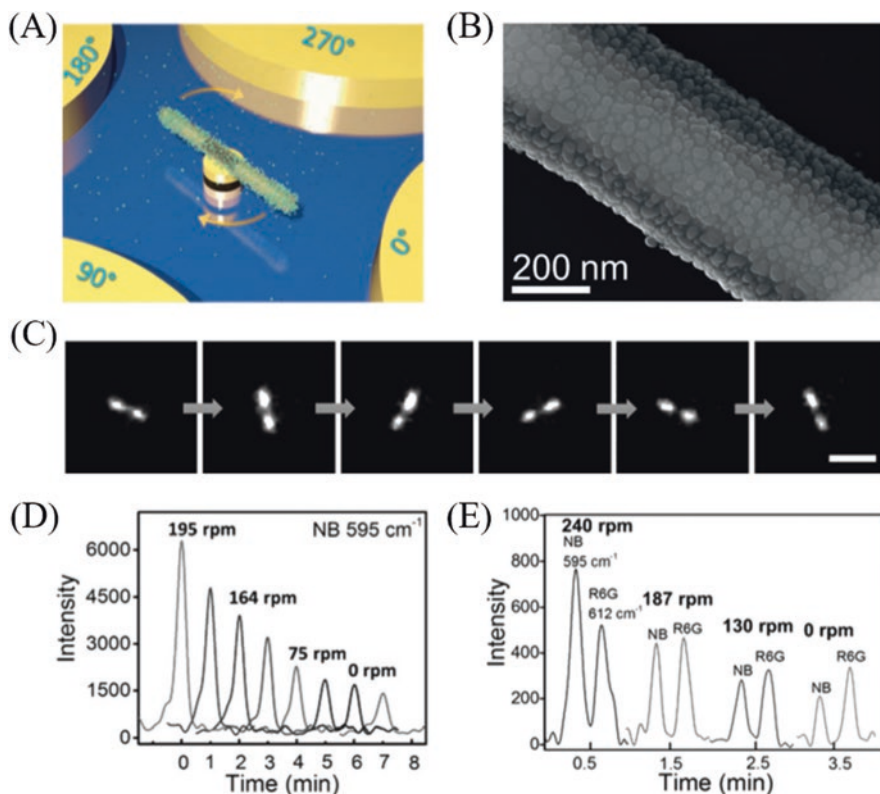


Fig. 5.8 (a) Schematic of a nanomotor sensor attached to a nanomagnet, rotating in an AC E-field provided by a quadruple microelectrode. (b) SEM images of the silica-coated Au-Ni-Au nanowires with dense surface-distributed Ag nanoparticles. (c) Raman images of a rotating nanomotor functionalized with NB. Snapshots taken every sixth of a second. (d) Respective Raman spectra of NB at different time stamps with differing rotation speeds, showing the release rate. (e) Respective Raman spectra of a mixture of NB and R6G, at different time stamps with differing rotation speeds. Reproduced with permission [22]. Copyright 2018, John Wiley & Sons, Inc.

realized [22]. The nanomotors consist of Au-Ni-Au segments that rotate with an external AC E-field, where the Ni segment can readily attach to prefabricated nanomagnets on the substrate (Fig. 5.8a). The nanomotors are coated with thin silica that supports the growth of dense silver nanoparticles (Fig. 5.8b). The distance between the silver nanoparticles is carefully optimized to generate narrow junctions as hotspots for ultrasensitive SERS detection.

The nanomotors are rotated from 195 rpm to 0 rpm, and the release dynamics of Nile blue (NB) molecules adsorbed on their surface are detected in quasi-real time simultaneously. At a given rotation speed, the concentration of the NB molecules monotonically decreases with time, obtained from a customized Raman spectroscopy equipped with an ultrasensitive high-speed CCD camera (Fig. 5.8c). The higher the rotation speed, the higher the release rate of the molecules (Fig. 5.8d).

This phenomenon was explained based on the understanding of the Nernst diffusion layer theory: the increase of release rate at a higher rotation speed is due to the thinning of the stationary layer next to the solid surface. The experimental results demonstrate a power-law dependence between the release rate k and rotation speed ω , confirming the success of the tunable release of biochemicals.

The mechanism was also found to be applicable to the release of multiplex biochemical mixtures consisting of a NB and R6G. The simultaneous detection of each biochemical can be possible due to the difference in their Raman spectra (Fig. 5.8e), and it was shown that the release rate of each biochemical has a similar power-law dependence with the rotation speed.

5.3.4 Electrical Capture of Biochemical Molecules

Design, fabrication, and manipulation of a superstructural Raman nanosensor with the capability to control the molecule release rate have also been reported but based on a distinct mechanism from the above [27, 28]. The unique superstructural nanomotor consists of a gold nanorod covered by a silica shell with arrays of embedded nanocavities with a high density of silver nanoparticles grown in them (Fig. 5.9a) [27]. The nanocavities in the silica shell are fabricated by repeated coatings of PS nanospheres and silica layers on the surface of the gold nanowire. At 550 °C in air,

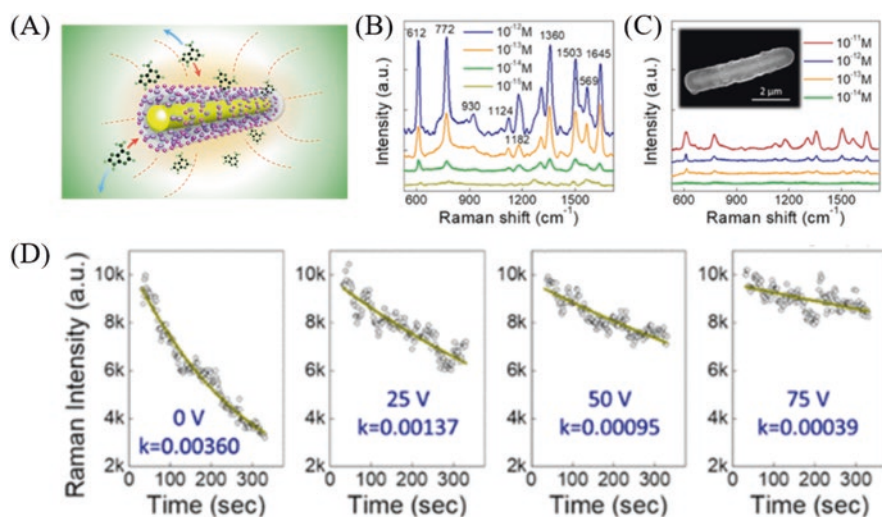


Fig. 5.9 (a) Schematic of nanoporous superstructural Raman sensors. Raman spectra of R6G molecules detected from nanosensors (b) with and (c) without the embedded hierarchical nanocavities with surface-grown Ag nanoparticles. (d) Change of release rate of NB molecules with differing AC field intensities

only the PS nanospheres are removed and an empty space is left. Silver nanoparticles are then grown both inside these nanocavities and the outer silica surface.

The nanocavities in the silica shells serve a dual purpose: First, it provides increased space for sustaining biomolecules, as much up to three times when compared to a solid control sample. Second, it increases the number of silver nanoparticles a nanomotor can accommodate, which in turn increases the number of hotspots for enhanced SERS detection.

As can be seen in Fig. 5.9b, c, the presence or absence of the nanoporous structures has a marked influence on the biochemical detection of probe molecules R6G. With the structures, an improvement of at least 1 order of magnitude with a sensing limit as low as 10^{-15} M is realized.

The main takeaway from this work is that the release rate of the molecules in an AC E-field can be directly tuned by changing the E-field strength and density, which induces DEP forces in the vicinity of the junction of the silver nanoparticles. Owing to the induced DEP force, the release rate of various biomolecules such as NB molecules can be successfully controlled, as is apparent in Fig. 5.9d.

5.3.5 *Assembly of Quantum Dot Nanowires for Location Deterministic Biomolecule Sensing*

Location deterministic biochemical detection was demonstrated using unique QD-nanowire hybrid nanostructures by the control of particle movement and interactions in E-fields [23]. These hybrid nanostructures are a formation of nanowires on patterned microelectrodes with semiconductor QDs on the tip of the wires, where the synergetic effect of dielectrophoresis and AC electroosmosis is used for assembly: Au nanowires are found to align and assemble on patterned microelectrodes upon applying an AC E-field, with differing chain lengths under different AC E-field frequencies due to the frequency-dependent nature of the electric dipole moment. For example, a length of 5.47 μm and 12.33 μm was observed at 70 kHz and 800 kHz, respectively.

For the purpose of biomolecule sensing, it was found that an optimized condition of 20 V at 70 kHz can be used to assemble a layer of single nanowires on the edges while subsequently using 20 V at 50 kHz to position semiconductor QD nanosensors at the tip of the nanowires (Fig. 5.10a). The hybrid QD-nanowire assemblies can be used for position deterministic biochemical sensing as the position of the nanowire tips can be used to determine the position of the QDs. Furthermore, by applying a thin PMMA layer and silica layer on the microelectrodes and nanowires, respectively, the authors are able to block any quenching effects that the QDs and organic dyes can have when in touch with the metal surfaces, as well as assemble an equally spaced sensor array.

For biomolecule detection, the QDs are conjugated with streptavidin, which bond strongly with biotin molecules. As a result, characteristic fluorescent signals

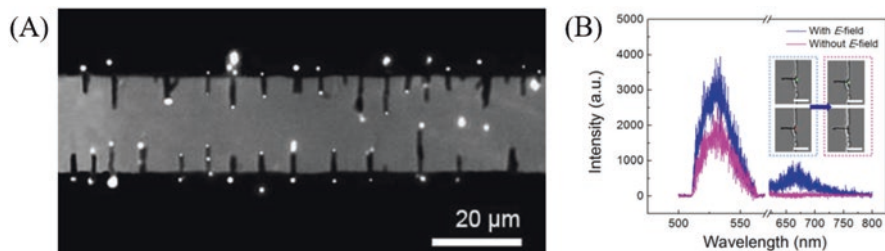


Fig. 5.10 (a) Quantum dots positioned on the tips of nanowire arrays under an AC E-field. (b) Fluorescent spectrum of QDs and Cy6-biotin molecules with (blue) and without (magenta) AC E-fields. Reproduced with permission [23]. Copyright 2014, AIP Publishing LLC

could be observed when Cy5-labeled biotin molecules are introduced into the system. It has been also demonstrated that the presence of an AC E-field, which assembles QDs onto the tips of the nanowires, also attracts and focuses biomolecules onto the tips as well, enhancing the detection efficiency at 20 nM. A marked difference of the fluorescent intensity between when an E-field is present and is absent can be observed after the AC E-field was removed (Fig. 5.10b). Due to these effects, only a few minutes were needed for the fluorescent signals to show, while at least 30 min were required for other works.

Related to the above exploitation of electric fields to attract molecules directly to the quantum-dot-nanowire assemblies for enhanced detection efficiency, it is worth to mention that recently, diatom-frustule-based SERS microsensors are synthesized that can rotate with controlled speed up to 1200 rpm in an external magnetic field created by a magnetic stirrer [24]. The diatom-frustule microsensors with optoplasmonic enhancement for SERS detection offer ultrahigh SERS sensitivity with an enhancement factor on the level of at least 10^9 to 10^{10} . The microsensors are assembled one on one into individual microwells and continuously rotate up to an hour, which provides robust operation for the durable detection of molecule capture dynamics. DNA molecules of the salmon sperms have been tested in the detection. It clearly shows that the higher the rotation speed, the sooner the DNA molecules reach the adsorption saturation on the surface of the sensor. The characteristic time can readily change for four- to sixfold by tuning the speed of rotation (Fig. 5.11). This effect has been theoretically modelled, calculated, and simulated, which for the first time unveils the impact of liquid flows generated by the locomotion of micro-/nanomotors or machines in the narrowing of the thickness of diffusion layer and thus the enhancement of the transport of biomolecules toward their surfaces. The understanding guides the application of the micromotor sensors in overcoming a dilemmatic problem in nano-biosensing, i.e., the difficulties in obtaining both high detection speed and sensitivity. It is found that with simple continuous mechanical rotation of the sensor, the time required to detect DNA molecules of 80 nM can be readily reduced from ~ 10 min to ~ 3 min with retained high sensitivity.

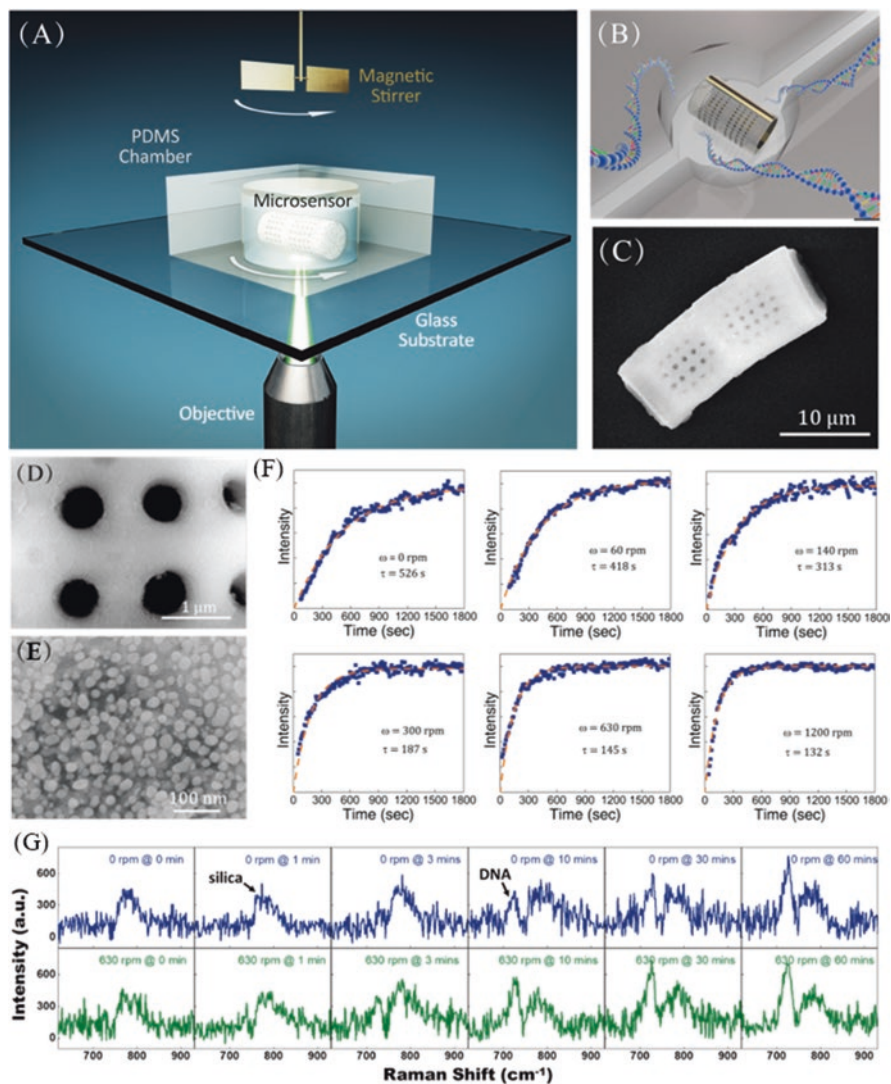


Fig. 5.11 (a–b) Schematic of a biosilica opto-plasmonic microsensor rotating in a microwell. (c–d) Diatom frustules with periodic nanopores and (e) high-density surface growth of Ag nanoparticles. (f) Dynamic capture of the DNA molecules on the surface of a microsensor at different rotation speeds. (g) Raman signals detected from dilute DNA molecules (80 nM) for an hour from a stationary (in blue) and a rotating microsensor at 630 rpm (in green). Reproduced with permission [24]. Copyright 2014, American Chemical Society

5.4 Conclusion

By combining the effects of AC and DC E-fields, electric tweezers provide a versatile, precise, and efficient means to transport and control the rotary alignment of micro/nanoobjects. Recently, many efforts have been made to explore the controlled positioning and orientation of micro-/nanomotors for applications in the bio-sector. Thanks to these efforts, applications, including drug delivery, cargo transport, tunable biomolecule release, enhanced capturing, and sensing have been realized. With in-depth investigating and understanding the fundamentals behind electric field, flow, and micro/nanoobjects, we expect a new level of manipulation control, automation, and applications of micro-/nanomotors in the future.

Acknowledgments The authors are grateful for the support of the National Science Foundation (grant no. 1710922 and 1930649) and The Welch Foundation (grant no. F-1734).

Revised: ((will be filled in by the editorial staff)).

Published online: ((will be filled in by the editorial staff)).

References

1. Ashkin, A., Dziedzic, J. M., Bjorkholm, J. E., & Chu, S. (1986). Observation of a single-beam gradient force optical trap for dielectric particles. *Optics Letters*, *11*(5), 288–290.
2. Wang, J., Xiong, Z., Zhan, X., Dai, B., Zheng, J., Liu, J., & Tang, J. (2017). A Silicon Nanowire as a Spectrally Tunable Light-Driven Nanomotor. *Advanced Materials*, *29*(30), 1701451.
3. Pal, M., Somalwar, N., Singh, A., Bhat, R., Eswarappa, S. M., Saini, D. K., & Ghosh, A. (2018). Maneuverability of magnetic nanomotors inside living cells. *Advanced Materials*, *30*(22), 1800429.
4. Venugopalan, P. L., Jain, S., Shivashankar, S., & Ghosh, A. (2018). Single coating of zinc ferrite renders magnetic nanomotors therapeutic and stable against agglomeration. *Nanoscale*, *10*(5), 2327–2332.
5. Liu, M., Wu, F., Piao, H., Huang, X., Cong, J., Luo, Z., Pan, L., & Liu, Y. (2017). Rod-shaped nanomotor powered by magnetic field gradients and its application to surface-enhanced Raman-scattering-based detection. *Applied Physics Express*, *10*(4), 045202.
6. Esteban-Fernández De Ávila, B., Angell, C., Soto, F., Lopez-Ramirez, M. A., Báez, D. F., Xie, S., Wang, J., & Chen, Y. (2016). Acoustically propelled nanomotors for intracellular siRNA delivery. *ACS Nano*, *10*(5), 4997–5005.
7. Soto, F., Wagner, G. L., Garcia-Gradilla, V., Gillespie, K. T., Lakshminpathy, D. R., Karshalev, E., Angell, C., Chen, Y., & Wang, J. (2016). Acoustically propelled nanoshells. *Nanoscale*, *8*(41), 17788–17793.
8. Ding, X., Lin, S. C. S., Kiraly, B., Yue, H., Li, S., Chiang, I. K., Shi, J., Benkovic, S. J., & Huang, T. J. (2012). On-chip manipulation of single microparticles, cells, and organisms using surface acoustic waves. *Proceedings of the National Academy of Sciences*, *109*(28), 11105–11109.
9. Melde, K., Mark, A. G., Qiu, T., & Fischer, P. (2016). Holograms for acoustics. *Nature*, *537*(7621), 518–522.

10. Paxton, W. F., Kistler, K. C., Olmeda, C. C., Sen, A., Angelo, S. K. S., Cao, Y., Mallouk, T. E., Lammert, P. E., & Crespi, V. H. (2004). Catalytic nanomotors: autonomous movement of striped nanorods. *Journal of the American Chemical Society*, *126*(41), 13424–13431.
11. Fan, D. L., Zhu, F. Q., Cammarata, R. C., & Chien, C. L. (2011). Electric tweezers. *Nano Today*, *6*(4), 339–354.
12. Fan, D. L., Cammarata, R. C., & Chien, C. L. (2008). Precision transport and assembling of nanowires in suspension by electric fields. *Applied Physics Letters*, *92*(9), 093115.
13. Purcell, E. M. (1977). Life at low Reynolds number. *American Journal of Physics*, *45*(1), 3–11.
14. Pethig, R. R. (2017). *Dielectrophoresis: Theory, methodology and biological applications*. Hoboken: Wiley.
15. Liang, Z., Guo, J., & Fan, D. L. (2019). *Manipulation, assembling, and actuation of nanomotors by electric tweezers*. Sawston/Cambridge: Woodhead Publishing.
16. Markx, G. H., Huang, Y., Zhou, X., & Pethig, R. (1994). Dielectrophoretic characterization and separation of micro-organisms. *Microbiology*, *140*(3), 585–591.
17. Einstein, A. (1905). On the motion of small particles suspended in liquids at rest required by the molecular-kinetic theory of heat. *Annals of Physics*, *322*, 549.
18. Bian, X., Kim, C., & Karniadakis, G. E. (2016). 111 years of Brownian motion. *Soft Matter*, *12*(30), 6331–6346.
19. Ramos, A., Morgan, H., Green, N. G., & Castellanos, A. (1998). Ac electrokinetics: a review of forces in microelectrode structures. *Journal of Physics D: Applied Physics*, *31*(18), 2338.
20. Salari, A., Navi, M., Lijnse, T., & Dalton, C. (2019). AC electrothermal effect in microfluidics: A review. *Micromachines*, *10*(11), 762.
21. Fan, D., Yin, Z., Cheong, R., Zhu, F. Q., Cammarata, R. C., Chien, C. L., & Levchenko, A. (2010). Subcellular-resolution delivery of a cytokine through precisely manipulated nanowires. *Nature Nanotechnology*, *5*(7), 545–551.
22. Xu, X., Kim, K., & Fan, D. (2015). Tunable release of multiplex biochemicals by plasmonically active rotary nanomotors. *Angewandte Chemie*, *127*(8), 2555–2559.
23. Liu, C., Kim, K., & Fan, D. L. (2014). Location deterministic biosensing from quantum-dot-nanowire assemblies. *Applied Physics Letters*, *105*(8), 083123.
24. Guo, J., Liang, Z., Huang, Y., Kim, K., Vandeventer, P., & Fan, D. E. (2020). Acceleration of Biomolecule Enrichment and Detection with Rotationally Motorized Opto-Plasmonic Microsensors and the Working Mechanism. *ACS Nano*, *14*(11), 15204–15215.
25. Guo, J., Gallegos, J. J., Tom, A. R., & Fan, D. (2018). Electric-field-guided precision manipulation of catalytic nanomotors for cargo delivery and powering nanoelectromechanical devices. *ACS Nano*, *12*(2), 1179–1187.
26. Kim, K., Xu, X., Guo, J., & Fan, D. L. (2014). Ultrahigh-speed rotating nanoelectromechanical system devices assembled from nanoscale building blocks. *Nature Communications*, *5*(1), 1–9.
27. Liu, J., Guo, J., Meng, G., & Fan, D. (2018). Superstructural raman nanosensors with integrated dual functions for ultrasensitive detection and tunable release of molecules. *Chemistry of Materials*, *30*(15), 5256–5263.
28. Liu, C., Wang, Z., Li, E., Liang, Z., Chakravarty, S., Xu, X., Wang, A. X., Chen, R. T., & Fan, D. (2017). Electrokinetic manipulation integrated plasmonic–photonic hybrid raman nanosensors with dually enhanced sensitivity. *ACS Sensors*, *2*(3), 346–353.

Chapter 6

Electrophoresis-Based Manipulation of Micro- and Nanoparticles in Fluid Suspensions



Kaiyan Yu

Micro- and nanoagents with functional components can be used in an extensive variety of applications, ranging from biomanipulation to targeted drug delivery. The automated, very precise manipulation of nano- and microscale objects has shown great promise in delivering therapeutic agents to specific sites, which paves the way toward targeted drug delivery. The robust, efficient, and independent manipulation of multiple agents or particles is limited by the global and coupled influence of wireless, external fields. This article presents motion control and planning schemes to manipulate multiple micro- and nanoparticles that share global external electric fields. Although we focus on the electrophoresis (EP)-based actuation, the proposed strategies will work with other wireless field-based applications to control multiple agents and particles for bio-assembly and manipulation when they are coupled or intertwined.

6.1 Introduction

Nanotechnology is rapidly revolutionizing traditional therapeutic and diagnostic approaches in biomedical studies because of the distinct chemical, mechanical, electrical, and biological properties of nanomaterials [1, 2]. Nanomedicine and nano-based delivery systems have shown great promise in delivering therapeutic agents to specific sites in a controlled manner, which paves the way toward target-oriented drug delivery and precision medicine [3, 4]. Iron oxide nanoparticles have been used for tumor therapy and stem cell tracking using magnetic resonance imaging [5], and a multicenter preclinical study has evaluated the efficacy and safety of nanoscale albumin-bound paclitaxel for metastatic breast cancer, to name a few [6].

K. Yu (✉)

Department of Mechanical Engineering, Binghamton University, Binghamton, NY, USA
e-mail: kyu@binghamton.edu

A system to deliver molecular doses of drugs or biologically active chemicals to one specified cell or a precise subcellular location must function reliably before we can understand the interaction of the functionalized micro- and nanoparticles with the target cells [7]. Automated, precise manipulation of functionalized micro- and nanoagents that carry specific charges, chemicals, and drugs by using external fields would dramatically improve our ability to transport the drug delivery vehicles along any prescribed trajectory or orientation to a specific location with subcellular resolution. The ability to precisely and efficiently control the multiple microscopic objects independently is of major interest for various research applications [8]. A fully autonomous fleet of micro- and nanorobots and agents could revolutionize the manufacture of scalable functional nanodevices and interconnects, precisely deliver drugs to target cells, better identify biopsy locations, and transform cell manipulation and biosensing techniques, to name a few potential applications [9–12].

Miniaturizing robots through modern fabrication techniques comes with the challenge of accommodating onboard power, actuation, sensing, communication, and control. Often, a robot's size needs to be scaled up to accommodate those accessories [11]. Facing the fact that the next-generation micro- and nanorobotic systems are likely to have very minimal onboard actuation or communication abilities [13], the challenge becomes how to have autonomous robots or agents be small enough but still be able to perform the aforementioned tasks. Therefore, it is straightforward to outsource the power, actuator, sensor, communication, and control components to an off-board system to simultaneously direct the independent motion of the micro- and nanoagents.

Wireless actuation is a promising way to position micro- and nanoscale objects. Commonly used noncontact actuation techniques include magnetic actuation [12, 14–17], electric field actuation [18–21], and optical tweezers [22, 23]. Manipulation via actuated flows is an alternative approach, using electroosmosis, micromechanics, electrohydrodynamics, thermocapillary pumping, or other methods [24–27]. Among those approaches, using a magnetic, electric, fluid, or another field has shown great capability for remote control in medical procedures, microfluidic tools, and micro- and nano-factories [21, 28, 29]. Field-based nanomanipulation is less costly, superior in scalability, and easier to implement for parallel motion control of micro- and nanoparticles than optical and tip-based methods [30].

Field-based manipulation methods are severely hampered by the global and coupled influence of the wireless external actuation in the workspace, which limits the robust, independent, and simultaneous control of multiple micro- and nanoparticles [11]. The motion of the agents or particles in the existing work is always coupled, and automation has been mostly restricted to moving a limited number of components in small workspaces [23]. Therefore, we will discuss our efforts in light of the challenges mentioned above to manipulate independently and simultaneously multiple micro- and nanoparticles with the coupled actuation from the global electric field.

6.2 Electric Field-Based Particle Manipulation

Electric field-based methods are widely discussed as a way to manipulate entities suspended in a liquid because they are efficient, easy to implement, and low-cost [10, 31]. Without moving mechanical parts, electric fields can apply a force to precisely manipulate particles that are suspended in a fluid. With precisely controlled electric fields, electrophoresis (EP) [32], electroosmosis (EO) [24], and dielectrophoresis (DEP) [7] could be used as driving forces to steer small-scale particles.

Under DC electric fields, particles in fluid suspensions experience an electrophoretic force, while the fluid experiences EO forces [33]. The EP force magnitude is proportional to the effective electrokinetic potential (also known as the zeta potential) and the electric-field strength. Besides EP and EO, the induced dipole moment of the particle interacts with a nonuniform field to give rise to a frequency-dependent dielectrophoretic force.

The DEP force is proportional to the polarizability of the particle and the spatial gradient of the square of the electric field. A particle can be attracted or repelled by field concentrations depending on the sign of the polarizability. By controlling the field gradient and the frequency of the applied electric field, the DEP-based actuation can be used to manipulate particles in fluid suspensions [19–21]. Most existing works on DEP-based manipulation focus on positioning and sorting spherical microparticles such as beads and biological cells [18, 34–45]. The manipulation of high-aspect-ratio nanowires and nanotubes using DEP, although less common, is reported in the literature [7, 46–53]. However, most of the research uses the open-loop control of electrodes and does not consider the distributed feedback control with programmable electrode arrays [32].

Indeed, the DEP force depends on the spatial gradient of the square of the electric field, while the EP force is proportional to the electric-field strength. The use of EP force as an actuation source is convenient in that even nominally electrically neutral particles typically have a nonzero effective electrokinetic potential at the slip plane in the interfacial double layer in some solvents or at some pH values [54]. In systems with micro- or nanoparticles, the EP force generated by a designed electrode pattern could be a dominant actuation source for controlling agents or particles with relatively large effective electrokinetic potentials. Therefore, EP-based manipulation is simple, requires less electric-field strength, and is easier to implement for long-range motions for the application of the small-scale particle manipulation [32, 55].

The EO-based flow actuation is another way to steer small-scale particles. In EO-based systems, multiple electrodes in the microfluidic channel generate an EO flow that steers multiple nanoparticles [24–26]. EO modeling and optimization algorithms are used to steer and manipulate particles. However, the control regions of those designs are always limited, and the number of particles that can be independently controlled is constrained by the actuating electrodes. Therefore, those approaches are difficult to scale up for large numbers of particles.

Without loss of generality, in this article, we focus on manipulating small-scale particles with global DC electric fields. In such an electric-field-based system, the EP force and the EO flow are significant to the particle motion. However, because of the lack of precise knowledge of the boundary conditions, especially for the unknown zeta potentials of the particles and device boundaries, exact modeling of EP and EO actuation is difficult [32]. As shown in the experiments in [56], the EO-induced disturbances are not always aligned with the electric-field direction due to the complicated boundary conditions, and the existing models of the EO flow cannot be directly applied to our application. Considering the modeling uncertainties of the EO flow and the unknown zeta potentials, we design adaptive and robust motion control and planning algorithms that model the EP driving force and simultaneously compensate for the EO-induced motion disturbance.

In our works, EP-based manipulation strategies have been developed to precisely drive single [32] and simultaneous multiple [55, 57, 58] micro- and nanoparticles in a fluid suspension to their desired locations using a generic array of microfabricated electrodes. In [32, 56, 59], we steer and drive a single particle using EP-based motion planning and manipulation algorithms. This is extended to manipulate multiple particles in [31, 57, 60, 61]. In those works, a robust motion control strategy guarantees the convergence of the path-following error to zero for individual particles. The parametric uncertainty in the system model, i.e., the mobilities of the particles, is estimated offline before each manipulation. Our EP-based motion controllers can compensate for the unmodeled EO flow induced by the electric fields acting on the fluid.

Because of the particles' differences in various properties (geometric shapes, materials, charges, dimensions, etc.), each particle in the fluid suspension could have a different range of the zeta potentials. We design an adaptive control scheme to estimate the unknown zeta potentials online, which enables more efficient and accurate manipulation [55, 62]. To provide robust stability guarantees under the unmodeled dynamics, we have developed an adaptive tube model predictive control scheme for the simultaneous manipulation of multiple particles under coupled electric fields in fluid suspensions [63, 64].

To generate the desired trajectories for all the particles, heuristic [32], network flow [57], sampling [9, 55, 61], and supervised learning [58]-based motion planning algorithms have been used to steer micro- and nanoparticles in fluid suspensions and achieve the shortest-distance and minimum-time objectives. The motion planning strategies coordinate the actuation of electrodes in a combinatorial way to find optimal trajectories for the particles.

Recently, we constructed a novel integrated online adaptive manipulation scheme that includes an adaptive robust motion controller, a computationally efficient anytime motion planner, and a motion estimator [55]. The motion controller estimates the unknown zeta potentials in the system's dynamic model, the motion estimator predicts the positions of the particles for a given prediction horizon, and the motion planner replans the near-optimal trajectories online based on the estimated zeta potentials and the predicted positions of the manipulated particles. In the integrated online adaptive manipulation scheme, we coordinate the motion planner and the motion controller with the prediction process from the motion estimation to update the desired trajectory online with estimated zeta potentials.

Although we use the EP force to actuate the micro- and nanoparticles in our current experimental setup, the proposed integrated manipulation strategies and the motion planners are not limited to the EP actuation and can be generalized to other field-based applications, in which the actuation among a group of multiple agents is coupled or intertwined.

In this article, we will summarize the EP-based manipulation strategies to precisely and independently control the motion of micro- and nanoparticles, estimate their unknown mobilities, and plan their desired trajectories. The rest of the discussion is organized as follows: In Sect. 6.3, we present the EP-based motion model and problem formulation with a simple, generic set of controllable electrodes to drive, orient, and deposit particles in fluid suspensions. The motion control strategies are described in Sect. 6.4, which includes the nonlinear feedback controller, the adaptive controller, and the adaptive tube model predictive control design. The motion planning algorithms are described in Sect. 6.5. We then present the integrated online adaptive manipulation scheme in Sect. 6.6, and conclude the article in Sect. 6.7.

6.3 EP-Based Motion Model and Problem Formulation

In this section, we briefly introduce the EP-based motion model of particles immersed in a viscous fluid under an external DC electric field, which has been developed in [32, 55, 57].

6.3.1 System Configuration

To scalably manipulate micro- and nanostructures, a simple and generic set of $N \times N$ lattice-shaped distributed electrodes is designed to actuate particles in fluid suspensions. Figure 6.1 shows the schematic of the microfluidic device with $N \times N$ electrodes on the bottom. The circular electrodes with diameter $L/2$ are fabricated on a glass substrate with equal distances L between the electrode centers as measured along the x and y axes. Each electrode is independently actuated with a DC voltage. The electrode array is covered by a fluid that contains a dilute concentration of particles. The use of the electrodes on the nonconducting substrate creates an electric field inside the fluid reservoir that is primarily parallel to the substrate surface. Therefore, the precisely controlled electric fields generated by the electrode array can be used to control the horizontal motion of the suspended particles. An indium tin oxide (ITO)-coated coverslip is used as an additional electrode to control the vertical position of the particles. Once the particles reach their targets in the horizontal plane, the bottom electrodes in the array are turned off, and the top ITO electrode is turned on to vertically align and drive the particles to the desired

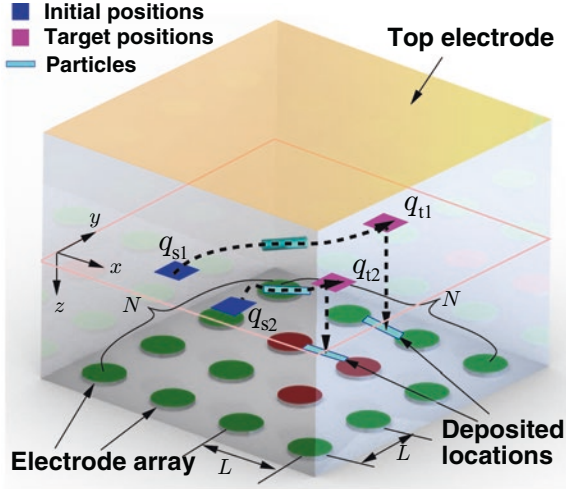


Fig. 6.1 Schematic of the microfluidic device with $N \times N$ independently actuated electrodes on the bottom substrate and a common top electrode. The array of circular electrodes with diameter $L/2$ is fabricated with equal distances L between the electrode centers as measured along the x and y axes. Each electrode is independently actuated with a DC voltage. Two particles are actuated by the electric field generated by the electrodes. (Reproduced with permission [55], 2020, IEEE)

locations on the substrate. Finally, the electrode array is turned on again to lay down and deposit the particles onto the device surface with the desired orientations.

Figure 6.2 illustrates the general schematic of the electric-field-based particle manipulation scheme. The motion control is based on a model of particle dynamics under EP actuation, with the vision-based feedback of the particles' positions. The control system needs to compensate for the complex 3D EO flow that is unmodeled. The motion planner determines the optimized motion trajectories for given target points and particles' current positions.

6.3.2 EP-Based Motion Model

At a low Reynolds number, the viscous forces are dominant. Therefore, the inertial effects are negligible for the particle motion. Brownian motion is neglected because of large magnitudes of the viscous-flow and electric-field-induced forces relative to thermal fluctuations [65, 66]. Because the EP force is balanced by the hydrodynamic viscous drag force, the equation of motion for a particle is given as follows: [67].

$$\dot{\mathbf{r}}_i = \begin{bmatrix} v_{ix} \\ v_{iy} \end{bmatrix} = \begin{bmatrix} \zeta_{ix} \\ \zeta_{iy} \end{bmatrix} \frac{\epsilon_m \mathbf{E}(\mathbf{r}_i)}{\mu_m} + \begin{bmatrix} w_{ix} \\ w_{iy} \end{bmatrix} = \begin{bmatrix} \zeta_{ix} \\ \zeta_{iy} \end{bmatrix} C \begin{bmatrix} E_x(\mathbf{r}_i) \\ E_y(\mathbf{r}_i) \end{bmatrix} + \mathbf{w}_i, \quad (6.1)$$

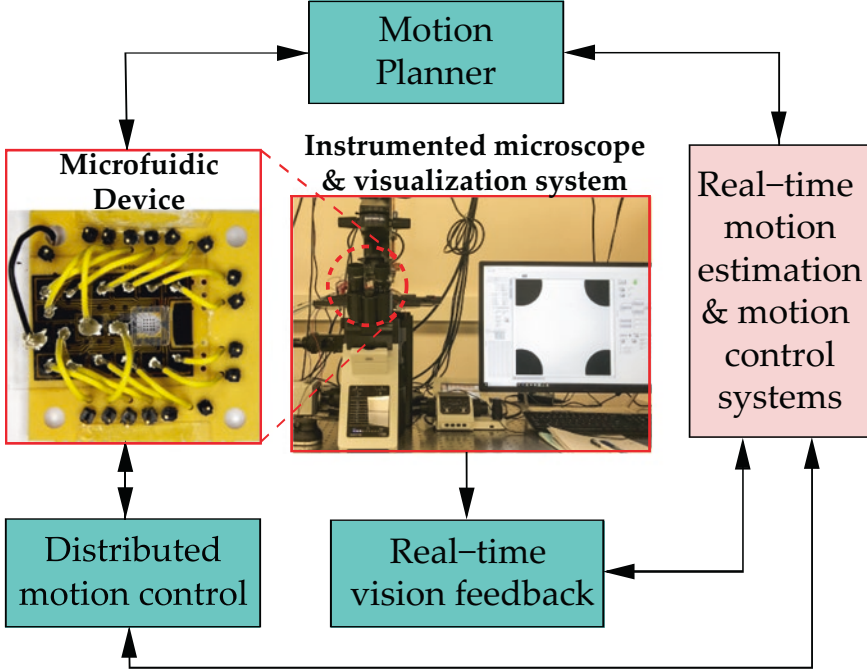


Fig. 6.2 A general schematic of the electric-field-based particle manipulation scheme. (Reproduced with permission [32]. 2020, IEEE)

where the position of the i th particle is denoted as $\mathbf{r}_i(t) = [x_i(t) \ y_i(t)]^T$, $i = 1, \dots, n$. $\mathbf{E}(\mathbf{r}_i) = [E_x(\mathbf{r}_i(t)) \ E_y(\mathbf{r}_i(t))]^T$ is the DC electric-field vector at \mathbf{r}_i . $C = \varepsilon_m/\mu_m$, μ_m is the dynamic viscosity, and ε_m is the electric permittivity. ζ_{ix} and ζ_{iy} are the zeta potentials of the i th suspended particle in the x - and y -axis directions, respectively. We model the zeta potential differently in x and y directions because of the mobility anisotropy of nonspherical particles [68]. We transform the ζ_{ix} and ζ_{iy} to the longitudinal and lateral directions according to the orientation of the i th particle. The zeta potentials will be estimated for each particle. $\mathbf{w}_i = [w_{ix}(t) \ w_{iy}(t)]^T$ is the bounded external disturbance.

To formulate the motion equations for all n particles, we first re-index the electrodes into a one-dimensional N^2 -element array with a column-wise order. We denote the electric field under unit voltage at $\mathbf{r}_i(t)$ by the j th electrode as $\mathbf{E}_j(\mathbf{r}_i(t)) = [E_{jx}(\mathbf{r}_i(t)) \ E_{jy}(\mathbf{r}_i(t))]^T$, $i = 1, \dots, n$, $j = 1, \dots, N^2$ and the corresponding controlled electrode voltage as $\mathbf{u} = \{u_j\} \in \mathbb{R}^{N^2}$, $u_{\min} \leq u_j \leq u_{\max}$, where u_{\min} and u_{\max} are, respectively, the lower and upper bounds of the applied voltages. The \mathbf{E}_j can be calculated by superposition of the effective electrodes with unit voltage, and u_j , $j = 1, \dots, N^2$ is the corresponding voltage that is applied to the $N \times N$ electrode array. Readers can refer to [32] for detailed electric-field computation.

Next, we concatenate the position vectors of all particles as $\mathbf{q}(t) = [\mathbf{r}_1^T(t) \cdots \mathbf{r}_n^T(t)]^T \in \mathbb{R}^{2n}$. By defining a *motion gain matrix*

$$\mathbf{B} = \mathbf{C} \begin{bmatrix} \mathbf{E}_1(\mathbf{r}_1(t)) & \cdots & \mathbf{E}_{N^2}(\mathbf{r}_1(t)) \\ \vdots & \ddots & \vdots \\ \mathbf{E}_1(\mathbf{r}_n(t)) & \cdots & \mathbf{E}_{N^2}(\mathbf{r}_n(t)) \end{bmatrix}, \quad (6.2)$$

we rewrite Eq. (6.1) for all particles as

$$\dot{\mathbf{q}} = \boldsymbol{\Theta} \mathbf{B} \mathbf{u} + \mathbf{w}, \quad (6.3)$$

where $\mathbf{B} \in \mathbb{R}^{2n \times N^2}$, $\boldsymbol{\Theta} = \text{diag} [\zeta_{1x}, \zeta_{1y}, \dots, \zeta_{nx}, \zeta_{ny}] \in \mathbb{R}^{2n \times 2n}$, and $\mathbf{w} \in \mathbb{R}^{2n}$ is the bounded external disturbance. The motion gain matrix \mathbf{B} depends on the positions of the particles at time t . Every two rows in Eq. (6.3) represent one particle's equation of motion.

6.3.3 Problem Formulation

From the motion model of suspended particles under EP in Eq. (6.3), the motion of the particles under EP-based actuation is independent of the particle's geometry (e.g., shape and size), provided we assume a thin double layer and uniform zeta potentials [69]. Therefore, we focus on the following motion planning and motion control problems to precisely manipulate multiple micro- and nanoparticles with different shapes and sizes.

Motion planning problem: For all particles, given the initial positions \mathbf{q}_s , target locations \mathbf{q}_t , and the estimated motion parameters $\hat{\boldsymbol{\Theta}}$, find the optimal collision-free trajectory $\sigma^*(t; \mathbf{q}_s, \mathbf{q}_t, \hat{\boldsymbol{\Theta}})$ that achieves the minimum total traveling time or the minimum total distance of all particles, depending on the goals set.

Motion control problem: Compute electrode control $\mathbf{u}(t)$ at time t to steer all particles to follow a given $\sigma^*(t; \mathbf{q}_s, \mathbf{q}_t, \hat{\boldsymbol{\Theta}})$ and estimate the unknown motion parameter $\hat{\boldsymbol{\Theta}}$.

6.4 EP-Based Particle Motion Control

From Eq. (6.3), it is important to obtain a proper bound of the zeta potentials to precisely control the particles' motions. However, micro- and nanoparticles exhibit uncontrolled variations in structures or compositions that result in different dynamic behaviors. The properties of particles with the same composition, fabricated within the same batch, or even from the same sample, may vary by orders of magnitude [70]. The work in [68] shows that the zeta potential of cylindrical-shaped particles is anisotropic.

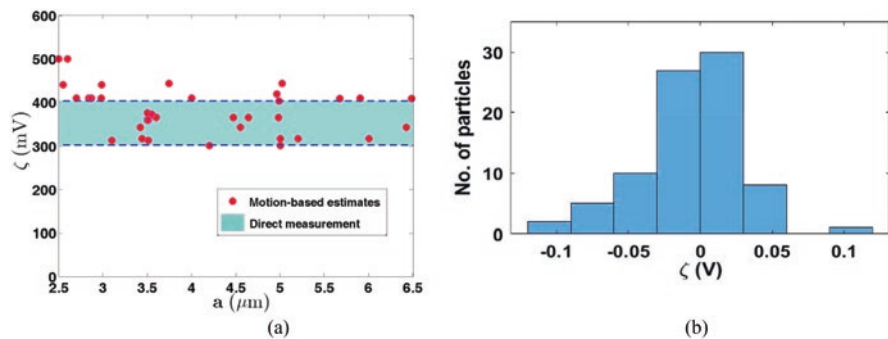


Fig. 6.3 (a) Comparison of the motion-based estimation and the independent measurement of zeta potentials (ζ) among 35 silicon nanowires for a silicon nanowire-and-oil suspension. The label “a” of the x axis is the half-length of the nanowires. Reproduced with permission [32]. 2020, IEEE. (b) Motion-based zeta potential calibration results for 80 polystyrene microbeads in the polystyrene-and-oil suspension

Therefore, we first conduct offline calibration to measure the mobilities of micro- and nanoparticles with different shapes. The offline motion-based estimation is done by applying a uniform electric field for several seconds. The particle moves along the uniform field and the position data of the particle is recorded. We then calculate the electric field acting on the particle and use least-square fitting to estimate the zeta potentials of each particle offline based on the measured velocity and the given electric field.

Figure 6.3a shows the motion-based estimation of 35 silicon nanowires’ zeta potentials, which are fabricated from the same sample and suspended in a heavy viscosity mineral oil, Drakeol 34 mineral oil, Calumet Specialty Products Partners, L.P. The electric permittivity of the fluid ϵ_m is 1.92×10^{-11} F·m⁻¹, and the dynamic viscosity μ_m is 217×10^{-3} Pa·s. All the particles in the experiments are suspended in this media. The shaded area shows the range of the zeta potentials independently measured for an identical silicon nanowire-and-oil suspension using a ZetaPALS instrument. This consistency of the motion-based estimation and the independently measured zeta potentials indirectly confirms the basic model of the EP-based particle dynamics in Sect. 6.3.2.

As the zeta potential varies for the particles in different solvents or at different pH values, we calibrate 80 polystyrene microbeads suspended in the same heavy viscosity mineral oil using the motion-based estimation. As shown in Fig. 6.3b, the zeta potentials of the polystyrene microbeads have a range of -0.12 to 0.12 V with a mean value -0.0063 V and 0.0367 V one standard deviation. From the calibration results, the particles may experience a large range of positive- and negative-induced charges.

Next, we discuss the motion control method to steer micro- or nanoparticles with an offline calibration of the induced charges. The controller works for driving multiple particles independently and simultaneously with the knowledge of the zeta potentials gained during the calibration. Then, we present the adaptive robust

control strategists to control particles, whose zeta potentials are unknown and may have various signs and magnitudes. Those uncertainties and variations in the zeta potential of micro- and nanoparticles make the online estimation of the unknown zeta potentials important to manipulate precisely and efficiently multiple individual particles simultaneously.

6.4.1 *Nonlinear Feedback Control*

To compensate for unmodeled disturbances such as EO-induced flow motions, a robust nonlinear feedback motion control strategy is developed to guarantee the path-following errors convergence to zero for individual particles [32, 57]. The nonlinear feedback controller is designed to manipulate particles with knowledge of the zeta potential values for each particle through the calibration process at the start of the experiments. Given the desired trajectories, an exponential convergence profile for the error dynamics is designed to obtain the control input. Considering the physical limit of the input electric-field amplitude, we solve the control problem using a nonlinear least-square method for the setpoint motion control and the path tracing [57].

From Fig. 6.3a, the zeta potentials of the silicon nanowires from the same sample show large differences. The difference in the zeta potentials greatly affects the precise manipulation of multiple individual particles. Therefore, we adopt a path-tracking control strategy [71] to adjust the desired velocity profile according to the tracking errors in real time. A potential function is used to generate the desired velocity that is parameterized by an auxiliary time variable. A self-placing time suspension technique is used to adjust the desired rate of the progression and then the velocity profile online at each time step. To get the desired velocity along the preplanned path, the path-tracing control strategy considers the tangential direction of the desired path, penalizes the tracking direction, and compensates for the predicted error. With the above design, we can prove that the path-following errors converge to zero [32].

Next, we show the experimental results of steering, orienting, and depositing micro- and nanowires on the device substrate to form desired patterns or assemblies using the controller design.

Sequential Particle Control and Assembly

Figure 6.4 illustrates a sequence of snapshots of steering, orienting, and manipulating a single nanowire from location *A* in a fluid suspension to location *B* and, then, depositing it on the device substrate surface. First, the nanowire is steered from *A* to *B* by the nonlinear feedback motion control algorithm (Fig. 6.4a, b). Then, by turning on the ITO electrode on the top plate, an electric field along the vertical direction is generated such that the nanowire is aligned vertically and moving toward the

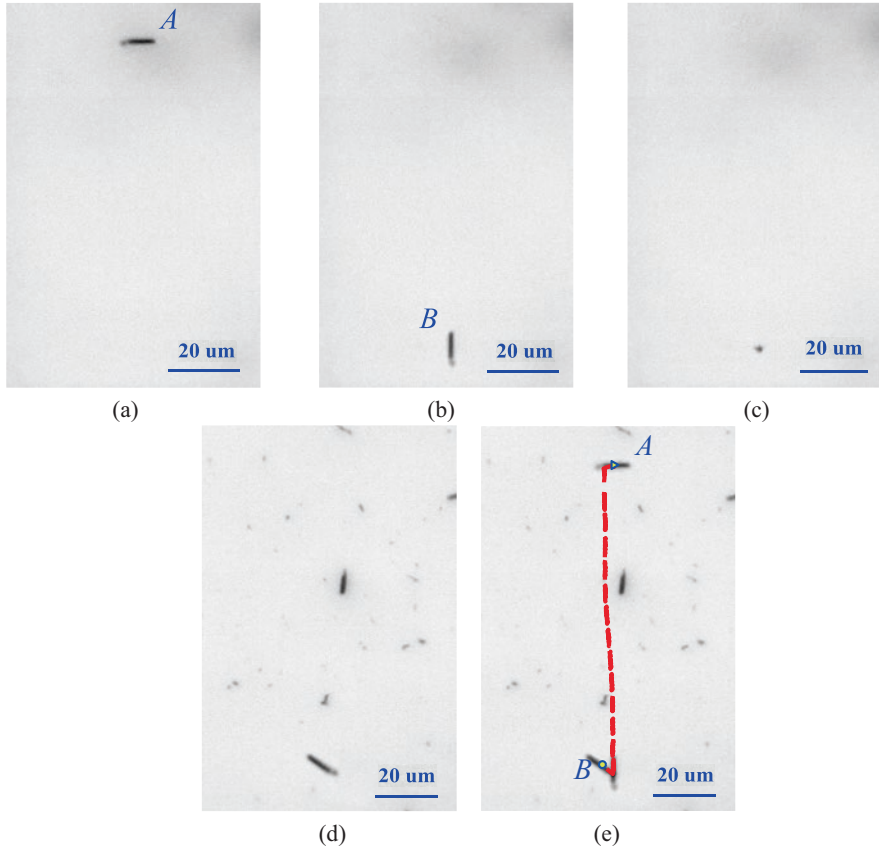


Fig. 6.4 Vertical positioning and deposition of a single nanowire on the device substrate. (a) The nanowire is at location A. (b) The nanowire is steered to location B. (c) Using the top ITO electrode, the nanowire is aligned along the vertical direction and steered to touch the bottom surface. (d) By turning on the bottom electrodes again, the nanowire is reoriented and deposited on the substrate surface with the desired orientation. Because of the change in the focal plane of the microscope for the images, several other nanowires and objects on the bottom surface that are seen clearly in (d) are not seen in the other images. (e) Overlay trajectory of the entire nanowire motion. The triangular and empty circular marks indicate the starting and ending points of the nanowire. (Reproduced with permission [32]. 2020, IEEE)

bottom surface (Fig. 6.4c). Finally, once the nanowire reaches the surface, the ITO electrode is turned off, and the electrodes on the bottom surface are turned on again to reorient and deposit the nanowire on the substrate in the desired direction, as shown in Fig. 6.4d. Figure 6.4e shows the overall trajectory of the nanowire by overlaying the image sequence that is shown in Fig. 6.4a–d [32].

Figure 6.5 demonstrates the use of the EP-based motion control and manipulation to sequentially steer and deposit individual nanowires to form various geometric patterns on the device substrate surface. In Fig. 6.5a, three nanowires are

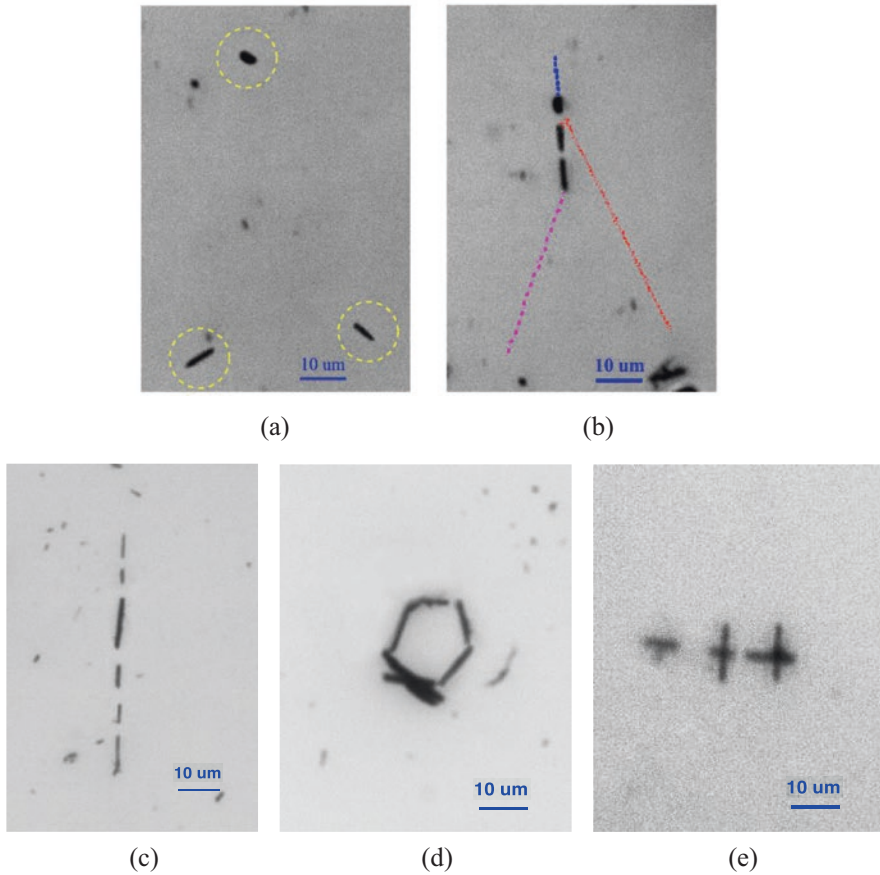


Fig. 6.5 Electric-field-based steering and manipulation of multiple nanowires to form different geometric patterns on the device substrate. (a) Initial positions of the three nanowires to form a straight line. (b) Final positions of these three nanowires after repositioning and depositing to align into a straight-line pattern. (c) A straight-line pattern using five nanowires. (d) A hexagonal pattern. (e) Three cross-shape patterns. (Reproduced with permission [32]. 2020, IEEE)

suspended in the fluid. Then, each of these three nanowires is sequentially steered and transferred to the substrate as shown in Fig. 6.5b using the procedure discussed above. Once the nanowire is settled down on the bottom substrate, it sticks to the surface because of the van der Waals interactions. The nanowire position and orientation is no longer changed by the electric field when moving and reorienting the other nanowires. Thus, we can sequentially deposit nanowires to form a larger or more complicated pattern on the substrate surface [32].

Figure 6.5c–e demonstrates a few more examples of the use of electric-field-based forces to drive and steer multiple nanowires to form more complicated geometric shapes. Figure 6.5c shows the result of moving six nanowires and depositing them in a straight line, and Fig. 6.5d shows the formation of a hexagonal pattern

with multiple nanowires, while Fig. 6.5e demonstrates cross patterns formed by depositing three nanowires perpendicularly on top of three other aligned particles [32].

Simultaneous Particle Control

Figure 6.6 shows a series of experimental results of steering multiple nanowires from different starting positions to target locations to form specific geometric shapes: a straight line with three nanowires (Fig. 6.6a); a square with four nanowires forming the corners (Fig. 6.6b); a circle with four nanowires at the 12, 3, 6, and 9 o'clock positions with an additional nanowire at the center (Fig. 6.6c); and an equilateral triangle with three nanowires at the vertices (Fig. 6.6d). Figure 6.6e further demonstrates that the motion planning and control methods can be used for continuous tracking control of three nanowires along a circular trajectory. In these figures, we show the initial and final positions of these nanowires as well as overlaid transient positions. It is interesting to observe that under the proposed motion planning and control algorithms, the individual nanowires can be steered in different and sometimes even opposite motion directions simultaneously (e.g., nanowires #1 and #2 in Fig. 6.6a) [57].

These experiments demonstrate the feasibility and performance of EP-based motion control for multiple simultaneous and individual particles. Experimental results show that the particles can be positioned with a spatial accuracy of $2\ \mu\text{m}$ [32].

6.4.2 Adaptive Control

As discussed above, because the particles may exhibit a large range of zeta potentials in the fluid suspension, it could lead to various dynamic behaviors for different particles. From Fig. 6.3, the particles may experience positive- and negative-induced charge in the media. The possibility of different charges means the proposed control scheme must control multiple particles simultaneously and precisely even with an opposite initial guess of the zeta potential from the true value.

The feedback controller design in the previous section does not include parametric uncertainties of multiple particles and relies on the offline calibration process to estimate the zeta potentials for each particle at the start of the manipulations. The online estimation of the particles' zeta potentials enables more efficient and accurate manipulation and eliminates the time-consuming calibration process before the manipulation.

A proper estimation of the zeta potentials is essential to design desired trajectories for the particles. The zeta potentials are important dynamic-model parameters for the motion planner. If the zeta potentials used to design the desired trajectories are much larger than the true values, then the desired movement could be too fast for the particles to track. If the zeta potentials are much smaller than the true values,

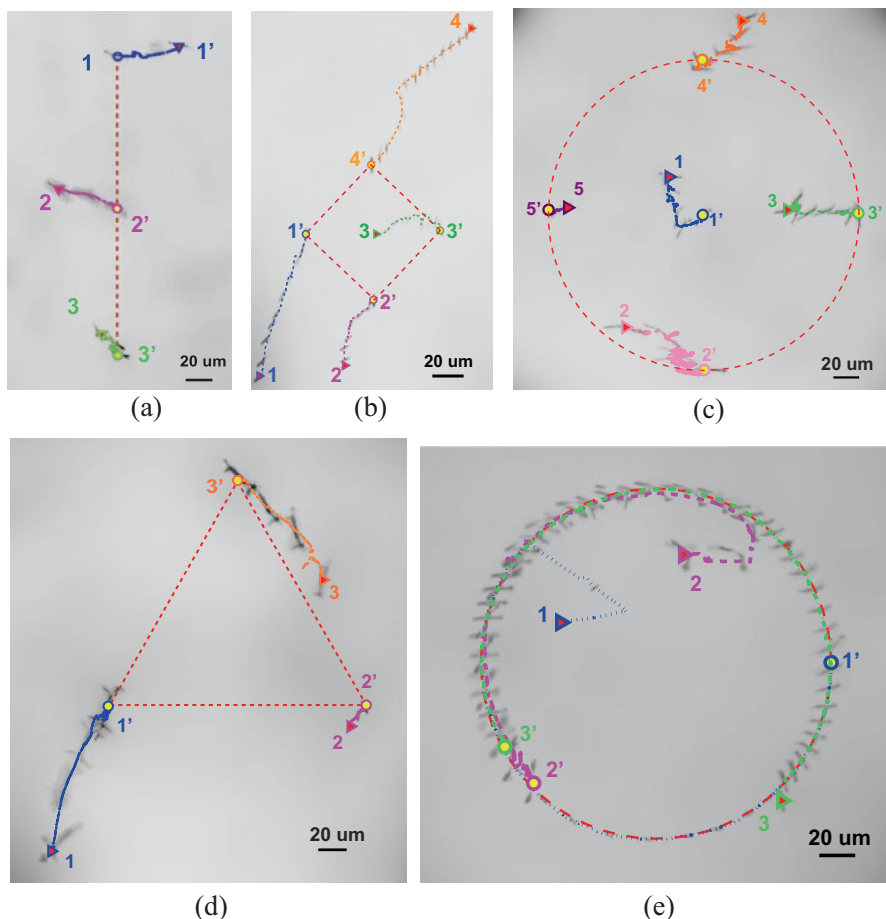


Fig. 6.6 Overlaid nanowire trajectories to form different geometric patterns. All pictures are obtained by taking and overlaying the nanowire images at a series of time snapshots. All background images are removed to clearly present the nanowire trajectories. The “▷” and “◦” marks indicate the nanowires’ initial and final positions, respectively. (a) A straight line. (b) A square. (c) A circle with one nanowire at the center. (d) An equilateral triangle. (e) Simultaneous tracking control of three nanowires to form a circle. (Reproduced with permission [57]. 2020, IEEE)

then the particles could oscillate around the desired trajectories. If some of the zeta potentials are larger and some are smaller, then the particles could easily fail to track the designed trajectories. Without the proper zeta potential estimation, designing appropriate trajectories for multiple individual but simultaneously controlled particles becomes difficult.

Instead of independent measurements of the mobilities using time-consuming instruments or complex calibration processes, it is possible to estimate unknown parameters online with adaptive control laws, making the control more precise and efficient. Unlike the previous feedback control schemes, which need prior

knowledge of each particle's zeta potentials in the suspension to precisely control the motion of the particles, we report an adaptive controller to estimate accurately the zeta potentials of the particles online [55, 62].

We apply model reference adaptive control [72] to identify the unknown mobilities of the particles in the model and control their motion to follow the desired trajectories. The adaptive controller estimates the unknown zeta potential of every particle online during the control process with the adaptive control strategy. The asymptotic stability and convergence of the adaptive controller are proved in the presence of parametric uncertainties by using a Lyapunov-based method. To stay within the physical capacity of the electric-field actuation, we adopt an intermediate variable and hyperbolic tangent function to design amplitude-limited input dynamics in the adaptive control law.

Next, we demonstrate the manipulation of nanowires and microbeads through experiments. Even with input saturation, particles follow the desired trajectories simultaneously and precisely using the adaptive control scheme.

Figure 6.7a, b presents the experimental results of controlling a silicon nanowire and a silica microsphere. Figure 6.7c shows the overlaid trajectory of one silicon nanowire that tracks the desired trajectory in a straight-line pattern. Figure 6.7d shows the overlaid trajectories of two silicon nanowires to track two horizontal desired trajectories. Figure 6.7e presents the overlaid trajectories of two nanowires that travel along two vertical straight lines moving toward each other in opposite directions [55, 62].

To verify the accuracy of the online zeta potential estimate, offline calibration experiments are done to provide the ground truth value of the zeta potentials. From the experiments, the tracking errors of controlling particles are small when compared to the motions of the particles. The online zeta potential estimation gradually converges to the calibration result. The experiment shows that the anisotropic mobility of the prolate spherical nanowire in its lateral direction is around 0.75 of that along its axial direction, which is close to the result of 0.83 stated in [68].

The experimental results confirm the adaptive controller's performance to independently manipulate single and multiple simultaneous particles with the input constraints. This similarity of the offline calibrated and online estimated zeta potentials confirms the effectiveness of the online estimation design.

6.4.3 Adaptive Tube Model Predictive Control

Considering the physical capacity of the electric-field actuation, model predictive control (MPC) can be used to address the constrained nonlinear problem of multiple particles' manipulation because MPC can incorporate the input constraints [73]. However, the quality of the MPC depends substantially on the system model. The motion model of the particle discussed in Sect. 6.3 does not consider the effects in the complex fluid suspension system, e.g., boundary conditions, fluid motion, and

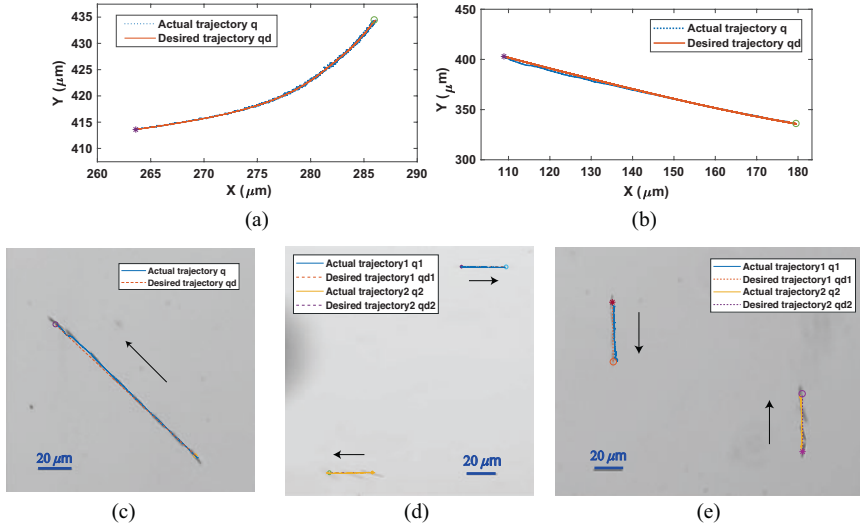


Fig. 6.7 (a) Trajectories comparison for one nanowire in the experiment. The tracking errors of controlling the nanowire remain in the range of $[-0.5, 0.5]$ μm . (b) Trajectories comparison for one silica microparticle with a diameter of $5 \mu\text{m}$ in the experiment. The tracking errors remain in the range of $[-2, 2]$ μm . (c) Overlaid trajectories of one silicon nanowire to track a straight-line trajectory in the experiment. The tracking errors of the nanowire remain in the range of $[-2, 4]$ μm . (d) Overlaid trajectories of two simultaneous nanowires to track two straight-line trajectories traveling in opposite directions in the experiment. The tracking errors of the two simultaneous nanowires remain in the range of $[-5, 5]$ μm . (e) Overlaid trajectories of two nanowires that travel along two vertical straight lines in opposite directions in the experiment. The tracking errors stay in the range of $[-2, 5]$ μm . The arrows indicate the moving directions of the two nanowires. The “*” and “o” markers indicate the nanowires’ initial and target positions, respectively. (Reproduced with permission [55]. 2020, IEEE)

particle interactions. As a result, the observed experimental trajectory often drifts away from the simulated trajectory [56].

Tube MPC is an approximate strategy to address those limitations. A virtual tube is constructed offline, together with a robust control law, which can keep the particles in the tube. The fix-shaped tube moves along a desired nominal trajectory that is generated online [74]. However, the preconstructed tube needs prior knowledge of each particle’s zeta potential in the suspension, and the tube geometry is restricted for all operating conditions, which can lead to suboptimal performance [75].

The adaptive control law [55, 62] in Sect. 6.4.2 could steer multiple particles to move along the desired trajectories to the targets and estimate the unknown mobilities online. However, the robustness of the system cannot be guaranteed because the disturbance is not considered during the controller design process. To incorporate those system uncertainties, the adaptive control law can be combined with the tube MPC approach to capture the uncertainties and potentially reduce the conservativeness of robust MPCs while providing robust stability guarantees [76].

Adaptive Tube MPC Design

In [63, 64], an adaptive tube MPC is designed to estimate the unknown mobilities of the individual particles, construct dynamic tubes online, and address the coupled actuation from the global electric field with dynamic separated tubes constructed for each particle.

The adaptive tube MPC estimates the unknown mobilities of the particles online using the set membership identification method. The parameter estimation scheme is inspired by the work in [76]. Based on the estimate, the dynamic tubes of individual particles are constructed and updated based on the bound of the external disturbance and the nonlinear dynamics. Because of the coupled actuation from the global electric fields, we construct the tubes for multiple particles under the coupled, limited input. Instead of constructing a high-dimension tube for the coupled problem, we separate the tube formulation and construct different lower-dimension tubes for multiple particles while satisfying the coupled actuation for different particles. As a result, the computational cost decreases significantly, especially for a large number of particles. The tube geometry is updated based on the online estimated unknown parameter set and nonlinear dynamics; therefore, less conservative tubes can be constructed to guarantee the robustness of the system. During the tube construction of the multiple particles, the open-loop reference trajectories are designed online by the nominal system. The input limitation is considered during the control process, and the tube MPC formulation guarantees robust constraint satisfaction for the closed-loop system. Finally, the tube MPC is proven to guarantee recursive feasibility, and the estimated parameter set shows rapid convergence; therefore, the robustness of the system can be guaranteed [63, 64].

Manipulation Capability

According to Eq. (6.1), the EP force at every particle varies with different zeta potentials and positions of the particles. We can expect that the places close to the edges of the electrodes have large velocity magnitudes but offer a narrow range of possibilities for manipulation. Because of the symmetrical layout of the $N \times N$ electrode array, the manipulation capabilities of one cell with 2×2 electrodes with $L = 600 \mu\text{m}$ are investigated using numerical simulations.

As proposed in [63], the maximum disturbance $d(q)$ under constraint satisfaction is evaluated using the shooting method. From the maximum disturbance magnitude for one particle in a 2×2 electrode cell, the motion of one particle in the center area is slower, but the particle can reject a larger magnitude of disturbance.

Similar to the Yoshikawa's manipulability index [77], we introduce a quality measure for the manipulability of particles in a cell. The approach is based on analyzing the manipulability ellipsoid that is spanned by the singular vectors of the motion gain matrix. The manipulability measure is formulated as

$\mu(q) = d(q) \sqrt{\det(\mathbf{B}(q)\mathbf{B}(q)^T)}$. If we consider the average velocities of the particles

suspended in the oil, the agile and precise manipulation of one particle in a cell can be achieved even with up to 63% velocity disturbance in one control step.

Following the same method, we evaluate the maximum disturbance and the manipulability with different numbers of particles suspended in the mineral oil. The manipulability and the maximum bounds of external disturbance under constraint satisfaction are greatly affected by the number of particles. When the number of controlled particles increases, the maximum disturbance that the system can withstand decreases significantly. The manipulability decreases exponentially with an increase in the number of particles, which means that when the number of particles increases, the ability of the global field for arbitrary manipulation of the particles decreases dramatically.

In our previous work [32], we found that the maximum number of particles that can be simultaneously and independently controlled is limited by an upper bound that depends on the number of neighboring electrodes. For an $N \times N$ electrode array, the maximum number of the particles that can be simultaneously and independently steered at each time step is $N^2/2$ without considering the uncertainties and physical limits of the electric fields. From the discussion above, after taking disturbance, input constraints, and uncertainties into consideration, the number of particles in each cell needs to be kept to two to achieve the agile simultaneous manipulation using EP forces generated by the $N \times N$ generic electrode array. If more particles need to be controlled in one cell, the trajectories of the particles need to be planned in the areas that achieve large manipulability. Those findings complement the existing work [63].

For multiple particles, the maximum disturbance and the manipulability are related to the relative position of the particles. The closer the particles are, the smaller the external disturbance the system can reject and, hence, the smaller manipulability the coupled field actuation can provide. From the numerical simulation, the minimum distance between two particles needs to be kept at $120 \mu\text{m}$ to maintain 10% manipulability and up to 15% disturbance on the velocity of two simultaneous particles in the cell. When there are more than two particles, arbitrary manipulation of all particles becomes difficult when the system experiences disturbances that are larger than 10% and the maximum manipulability drops below 3%. These relations can be used to test the designed control and online motion planning algorithm in the sense of the software-in-the-loop simulations for precise, arbitrary, and independent manipulation of multiple particles.

Experimental Result

In the experiments, we apply the adaptive tube MPC to drive the polystyrene microbeads and the silicon nanowires. We assume the target has been hit if the particle lands within $5 \mu\text{m}$ of the precise spot.

Figure 6.8a shows the experimental result of controlling one nanowire to reach the target region. Figure 6.8b shows the updated set for the unknown zeta potentials at different time steps. To validate the unknown parameter estimate, we calibrate the

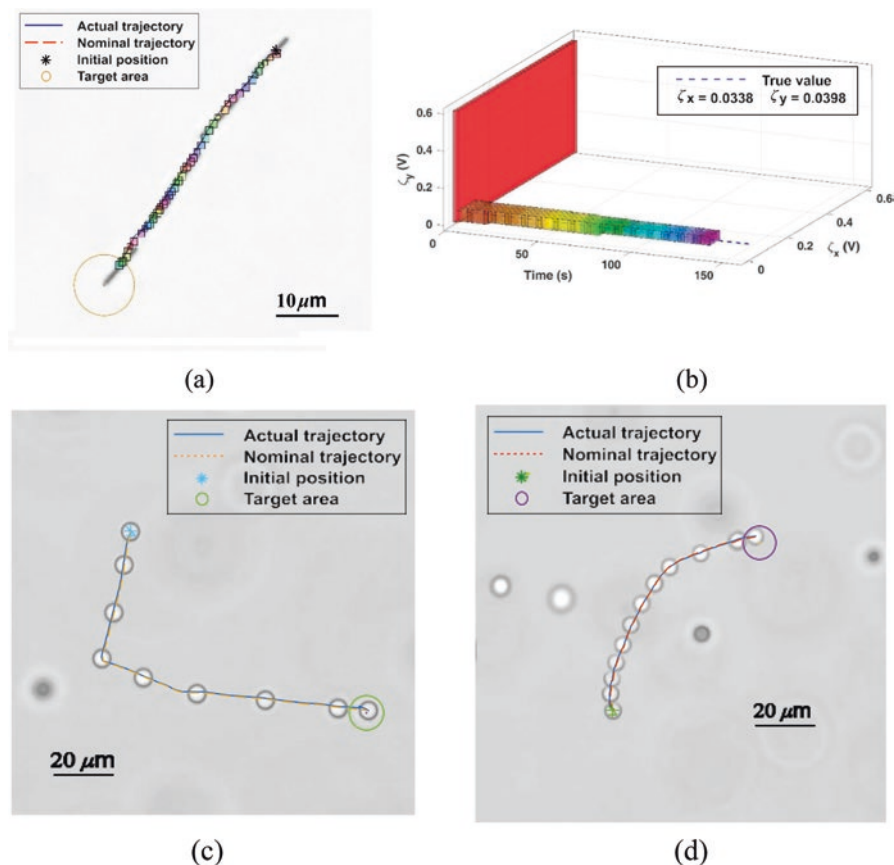
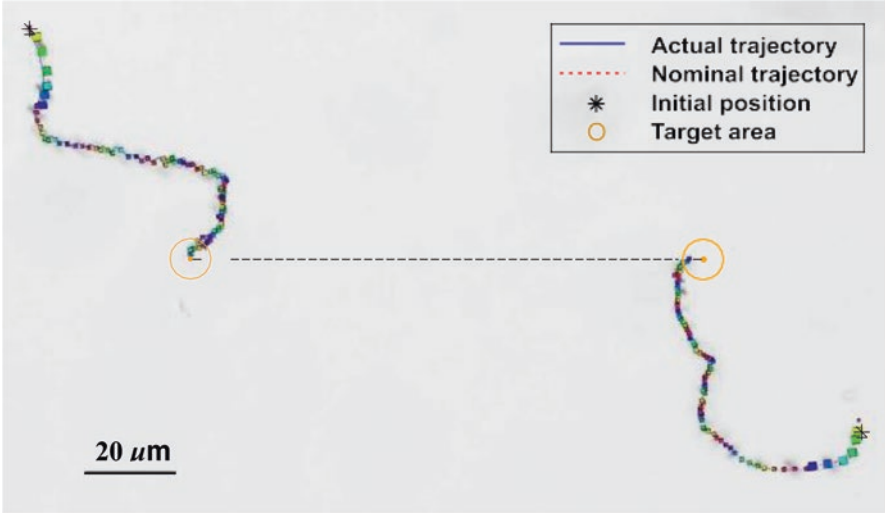
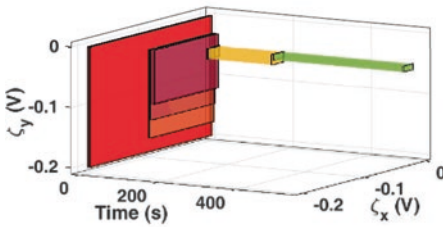


Fig. 6.8 (a) Overlaid trajectories of one nanowire as manipulated in the experiments. The color-shaded areas are the dynamic tubes. (b) The zeta potential set estimation for the nanowire in (a). (c–d) Overlaid trajectories of manipulating one polystyrene bead in the experiment. (e) Overlaid trajectories for manipulating two nanowires simultaneously to form a horizontal line in the experiments. The color-shaded areas are the dynamic tubes. (f) Zeta potential set estimations for the two simultaneous nanowires in the experiment as shown in (e), respectively. The “*” marker indicates the nanowires’ initial positions, and the “o” marker indicates the target areas. (Reproduced with permission [63]. 2020, IEEE)

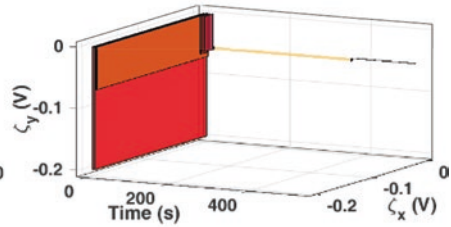
zeta potentials offline after the experiment to get their true values. The true zeta potential values from the calibration are plotted in Fig. 6.8b. From the result, the zeta potential set converges to a small set around the true value in 3 s with the large disturbance bound, while the total manipulation time is 138 s. Furthermore, Fig. 6.8c, d shows the manipulation results for steering each polystyrene microbead to its target area. The experimental results confirm that the proposed controller satisfies the constraints robustly and steers the microbeads and the nanowires to their targets precisely with accurate zeta potential estimation.



(e)



(f)



(g)

Fig. 6.8 (continued)

Next, we conduct experiments for controlling multiple particles in one cell using the proposed adaptive tube MPC. From the manipulability discussion, two particles need to be kept $120 \mu\text{m}$ distance away to maintain 10% manipulability and up to 15% disturbance on the velocity of two simultaneous particles in the cell. Therefore, we control two nanowires to form a horizontal line and their target positions are

$$120 \mu\text{m} \text{ apart. The disturbance bound is } w \in \mathbb{W} \triangleq \{w \in \mathbb{R}^2 \mid |w|_\infty \leq 0.2 \mu\text{m}\}.$$

Compared to the motion of the particles, the disturbance bound is 13% of the maximum state difference in one step. Figure 6.8e shows the overlaid trajectories of two nanowires to form a horizontal line in the experiments within the same cell controlled by the coupled electric field. Figure 6.8f, g shows the online updated sets for the unknown zeta potentials at different time steps for the two simultaneously

manipulated nanowires in the experiment, respectively. The estimated zeta potentials converge in 24 s, while the total manipulation time of the two simultaneous nanowires goes up to 524 s. The experimental results confirm the effectiveness of the proposed controller to manipulate multiple particles simultaneously under the effect of disturbance and unknown system parameters using coupled external fields [63].

In summary, the adaptive tube MPC is validated through experiments to manipulate multiple particles with uncertainties using coupled actuation. The recursive feasibility of the scheme has been proven in [63]. The manipulability and performance of the proposed controller are analyzed. We analyze the manipulation capability and maximum disturbance that the system can reject for the different numbers of particles in one cell. We quantify the relative position between two particles to achieve certain manipulability. We evaluate the maximum number of particles that can be arbitrarily, independently, and simultaneously controlled for given disturbance bounds and system constraints. Experimental results of manipulating micro- and nanoparticles with different kinds and sizes validate the proposed algorithm that satisfies the constraints robustly and steers multiple particles to their targets precisely and simultaneously with accurate zeta potential estimation. Those findings complement the existing work and provide an approach to test the designed control and online motion planning algorithm for precise, arbitrary, and independent manipulation of multiple particles [63].

6.5 EP-Based Particle Motion Planning

Motion planning of particles with a set of independently addressable electrodes is challenging because of its combinatorial optimization nature [78]. To generate optimal and efficient trajectories for multiple particles under the coupled actuation, we propose heuristic [32], network flow [57], sampling [9, 55, 61], and supervised learning [58]-based motion planning algorithms to achieve the shortest-distance and minimum-time objectives.

6.5.1 Heuristic-Based Minimum-Time Motion Planning

In [32, 56, 59], we developed EP-based minimum-time motion planning algorithms to steer and drive a single nanowire suspended in a fluid. The motion planning problem is NP-hard. To reduce the computational complexity, we take advantage of the spatial symmetry properties of the electric field generated by the electrode array and design two heuristic algorithms based on the reduced search space and the reduced number of input actuations. The heuristic motion planning strategies coordinate electrodes in a combinatorial way to find time-optimal trajectories for the particles. We compare the heuristic algorithms with other well-known benchmark motion

planning approaches. The comparisons show that the heuristic algorithms significantly reduce the computational complexity while obtaining suboptimal minimum-time trajectories.

6.5.2 Network Flow-Based Minimum-Distance Motion Planning

The heuristic search in Sect. 6.5.1 only works for planning one particle and cannot be applied to multiple particles due to the combinatorial complexity of the coupled electric-field actuation and potential collision of the multiple-particle problem. A network flow-based two-stage motion planning algorithm [57, 60] is then presented to generate the desired trajectories for multiple particles with minimum total traveling distances. In [57, 60], we further provide the control-system properties that capture the relationship between the maximum number of the simultaneously and independently controllable particles and the given number of neighboring electrodes and the physical input limitation.

The global-routing stage of the two-stage motion planning algorithm is built on the min-cost-max-flow (MCMF) problem [79, 80] to generate feasible 2×2 cells while allowing the simultaneous and independent motion control. The MCMF-based global-routing algorithm finds the minimum number of non-detour and non-overload cells for each particle and updates the global routes online using an A* [78]-like replanning structure.

After obtaining the sequenced cells for each particle, the second stage of the algorithm constructs the road map in the reduced search area to obtain the obstacle-avoiding optimal trajectory. A collision-free trajectory is generated among the selected cells using the visibility graph-based shortest path planning method and a rapidly exploring random tree (RRT) [78]-based collision-avoidance strategy along the shortest path. Results in [57, 60] demonstrate that the two-stage algorithm minimizes the total travel distances for all the particles and reduces the computational complexity significantly when compared with the benchmark algorithms.

6.5.3 Sampling-Based Motion Planning

The two-stage planning approach discussed above takes advantage of the straight-line constraint to quickly generate the shortest-distance trajectories for multiple particles, but the total traveling time cannot be optimized. The performance of the two-stage algorithm can be further improved in the following aspect: First, as demonstrated in [60], the shortest-distance trajectory does not demonstrate the shortest time. Indeed, the shortest traveling-time trajectory is not the straight line connecting the starting to target points because of the electric-field distribution. Therefore, it is

desirable to obtain the minimum-time trajectory for more efficient manipulation. Second, because of the straight-line constraint, the maximum number of particles that can be simultaneously steered in the two-stage algorithm is limited to an upper bound. It is desirable to find an alternative motion planner to relax such constraints.

To improve manipulation efficiency, sampling-based planners are discussed in [9, 55, 61] to minimize the total traveling time for multiple particles. The work in [61] considers a time-optimal motion planning strategy for multiple particles in fluid suspensions. Inspired by the sparse RRT [81] and RRT* [82] approaches, an improved sparse RRT*-based motion planning algorithm, SRRT*, is discussed to generate the asymptotically near-optimal minimum-time trajectories of multiple particles. The algorithm is not restricted to the time-optimal cost function, and any other additive cost (i.e., time, energy, distance, etc.) can be incorporated into the algorithm. Moreover, unlike the two-stage planning approach, the maximum number of particles that can be steered at one time is not limited by the upper bound that depends on the number of neighboring electrodes and the input constraints. The SRRT* algorithm takes the advantages of the rewiring strategy of the RRT* and the stable sparse structure of the sparse RRT to efficiently achieve the near-optimal trajectories with several heuristic techniques. From the performance evaluation, the SRRT* algorithm reduces the computational complexity significantly when compared with the benchmark algorithm and guarantees the asymptotically near-time-optimal performance for multiple particles. Therefore, the SRRT* algorithm is capable of generating high-quality trajectories.

Because the SRRT* samples in the state space, a two-point boundary value problem (BVP) has to be solved in the state space of the underlying dynamical system, which limits the performance of the planners based on the RRT framework. To efficiently steer large numbers of particles online, the supervised learning-based algorithm in [58] shifts the intensive optimal-cost metric computation of the BVPs of the system dynamics to offline training using supervised learning to enable online-planning performance. The learning-based algorithm achieves superior computational performance for up to seven nanowires in real time with one order quicker computational cost per iteration than the SRRT* algorithm.

However, the performance of the supervised learning algorithm greatly depends on the quality and quantity of the input dataset. The scheme takes advantage of the symmetry of the electric-field distribution to reduce the sample areas for data generation. For a large dimensional state space, it is computationally intractable to densely sample all the state space and solve for the corresponding optimal trajectories due to the curse of dimensionality. The algorithm is based on the assumption that the particles' mobility properties are known. As a result, it is time-consuming to regenerate the dataset and retrain the network before the manipulation process because of different particles' mobility properties. Therefore, an efficient, online replanning strategy with updating parametric uncertainties for manipulating multiple simultaneous particles without preprocessing is needed.

We consider motion planners that have good anytime performance and convergence ability toward an optimal solution. Anytime performance represents the

ability to find an initial trajectory, and it can be quantified by the computational time needed to find the first trajectory or a trajectory with quality approaching optimality. Without solving BVPs, the stable sparse RRT (SST) kinodynamic motion planning approaches sample from the input space and take advantage of the sparse structure to return a solution quickly and converge to a suboptimal solution. The SSTs, i.e., SST [81] and iSST [83], have achieved asymptotic optimality for kinodynamic planning using incremental sampling-based planners. However, the performance of these algorithms degrades as the dimension of the system increases.

Inspired by the SST and bidirectional RRT approaches, we further develop informed bidirectional SST-based anytime motion planning algorithms, Bi-iSST, Ref-iSST, and their variants in [9, 55]. The planners maintain two sparse trees to increase the probability of finding a solution and generate the asymptotically near-optimal trajectories for multiple agents sharing global fields. The algorithms guarantee anytime planning performance, which quickly generates feasible trajectories, to efficiently schedule large numbers of particles online according to the updating particle mobilities.

The Bi-iSST algorithms [55] take the bidirectional approach to speed up the searching process. The Bi-iSST and its variants, the opt-Bi-iSST and the exp-Bi-iSST, use the workspace information, heuristics, and optimization to effectively guide the search process. A novel connection process is proposed to connect two trees efficiently by applying an optimization procedure in the opt-Bi-iSST algorithm. The exp-Bi-iSST algorithm employs another connection method that iterates and explores all the bang-bang control input space with the finite number of electrodes to search for the minimum-time solution.

To evaluate the motion planners, we compare the anytime computational performance in Fig. 6.9 and the average solution cost through time in Fig. 6.10 for two to six simultaneous particles among the iSST (benchmark), the Bi-iSST (without the connection process), the exp-Bi-iSST, and the opt-Bi-iSST algorithms.

Figure 6.9 illustrates the anytime computational performance of the algorithms, which shows the averaged success ratio of returning a feasible trajectory against time. The computational cost increases as the number of particles increases, but the opt-Bi-iSST algorithm still achieves 100% success given the same computational budget. In contrast, the state-of-the-art benchmark algorithm iSST is not suitable for online problem-solving in the application with more than two simultaneous particles. From the anytime performance comparison, the proposed opt-Bi-iSST algorithm can perform online replanning to return a feasible solution within a properly selected period. This period is used as the prediction horizon in the integrated online manipulation scheme. The prediction horizon should be selected to be longer than the time of the planner to achieve a 100% successful ratio given the number of the particles.

To evaluate optimality, Fig. 6.10 compares solution costs through time among the optimal-time trajectories generated by the planners. From Fig. 6.10a, all three Bi-iSST-based algorithms converge to the near-optimal solution as the iSST benchmark is asymptotically near-optimal. Particularly, the opt-Bi-iSST algorithm outperforms other algorithms in that (1) it converges to much more efficient trajectories

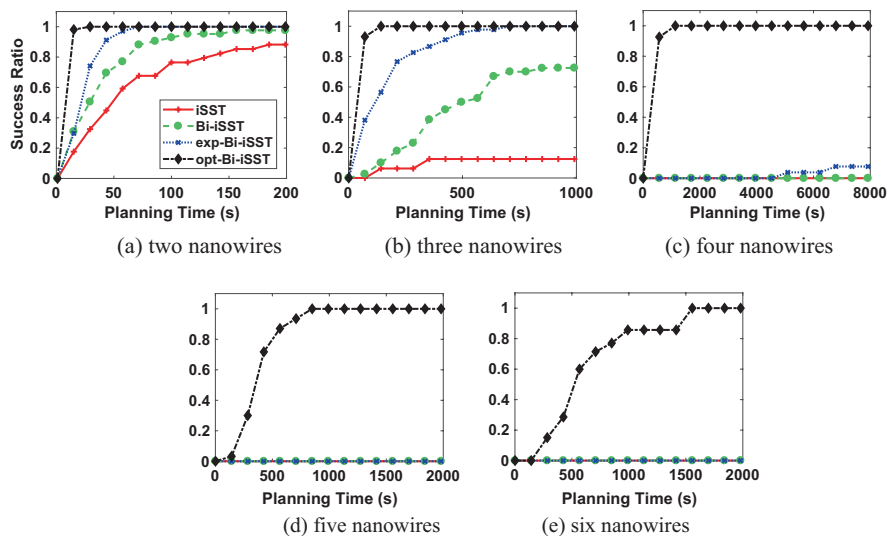


Fig. 6.9 The success ratio of found solutions to planner attempts through time for two to six simultaneously moving nanowires. The nanowires' initial and target positions are randomly chosen but kept the same among all the compared algorithms. Every planner was given 30 opportunities to return a result within its computational budget. The lines show the mean value at each time instance for an overall evaluation. Ratios closer to one are better. The computational budgets for planning different numbers of nanowires are (a) 400, (b) 600, (c) 1000, (d) 5000, (e) 8000 iterations, respectively. (Reproduced with permission [55]. 2020, IEEE)

than the benchmark, (2) it generates near-time-optimal trajectories for more particles (up to six) while others fail when the particle number is four or more, and (3) its convergence speed is quicker than the other algorithms.

From Figs. 6.9 and 6.10, when compared with the state-of-the-art algorithms, the opt-Bi-iSST algorithm achieves the best anytime computational performance, quickly updates feasible solutions with the online estimated mobilities of multiple particles, and converges to a near-optimal, minimum-time solution to increase the efficiency of simultaneous manipulation of the particles.

To further improve the anytime performance of the opt-Bi-iSST, the Ref-iSST approach [9] uses the workspace information to quickly generate global-routing trajectories as references and then guides the search process more effectively by getting more accurate heuristics according to the global-routing reference trajectory. Compared to the state-of-the-art algorithms, the Ref-iSST quickly updates feasible solutions and converges to a near-optimal, minimum-time solution to increase the efficiency of the simultaneous manipulation of multiple micro- or nanoagents using global external fields.

In summary, without complex characterization of each particle's mobility, the particles can be steered simultaneously and efficiently to achieve precisely controlled positions without collisions. Compared with other RRT variants, the bidirectional, informed kinodynamic planning algorithms: (1) sample from the finite input

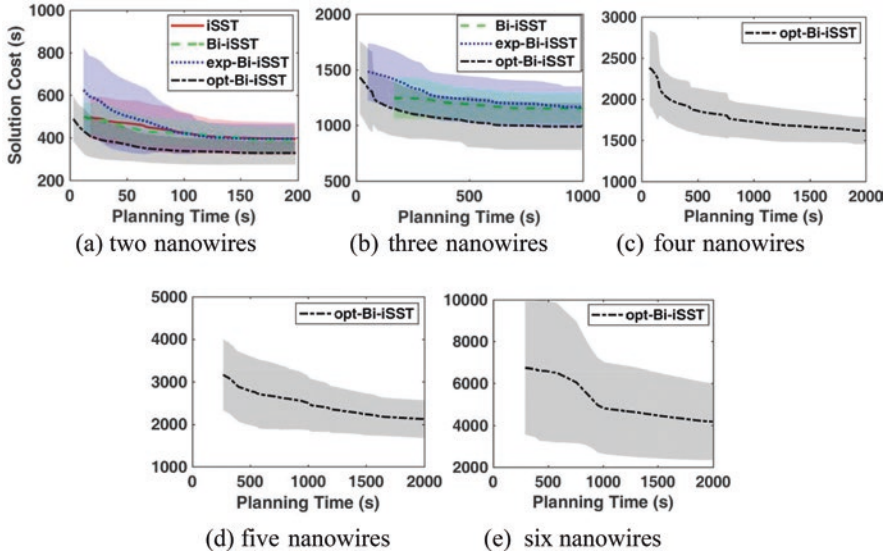


Fig. 6.10 Average solution cost through time for two to six simultaneous nanowires. The plots show the statistical result from 30 runs per planner to update its best result within the computational budget. The lines show the mean value of all solutions at each time instance for an overall evaluation. Shaded areas are the one standard deviations among the 30 runs. Lower solution costs are better. We omit the data if the success ratio is lower than 0.2. (Reproduced with permission [55]. 2020, IEEE)

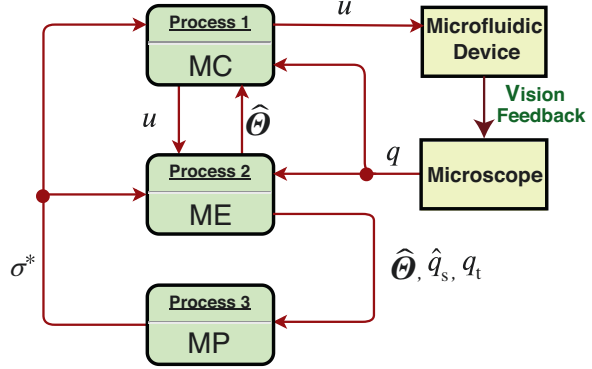
space to avoid solving the BVPs at each propagation step and to increase computational efficiency, (2) maintain two sparse trees with a linearized optimization-based connection process to increase the probability of finding a solution, and (3) use appropriate heuristics and workspace information to guide the exploration to focus on the useful subset of the state space.

Although we focus on the DC electric-field actuated multiple-micro-agent system, the proposed informed kinodynamic planning strategies can be used in other robotics applications.

6.6 EP-Based Adaptive Manipulation Scheme of Micro- and Nanoparticles

In the end, we discuss the adaptive online manipulation scheme to estimate unknown parameters of the system and precisely manipulate multiple micro- and nanoparticles simultaneously and independently under the coupled electric field with limited input voltages [55]. The adaptive manipulation scheme is built on and extended by the general manipulation scheme as shown in Fig. 6.2. The adaptive online manipulation scheme consists not only of the motion planner (MP) and the adaptive motion

Fig. 6.11 A diagram of the EP-based adaptive manipulation structure. (Reproduced with permission [55]. 2020, IEEE)



controller (MC), but also the coordination between the MP and MC through a motion estimator (ME). Figure 6.11 illustrates the schematic of the integrated adaptive online manipulation system. The MC (i.e., the adaptive controllers in Sects. 6.4.2 and 6.4.3) estimates the unknown zeta potentials in the system's dynamic model, the ME predicts the positions of the particles for a given prediction horizon, and the MP (i.e., the bidirectional, informed kinodynamic planning algorithms discussed in Sect. 6.5.3) replans the near-optimal trajectories online based on the estimated zeta potentials and predicted positions of particles.

The MP searches for the desired trajectory $\sigma^*(t; q_s, q_t, \hat{\Theta})$ according to the estimated zeta potentials $\hat{\Theta}$ and the predicted replanned positions \hat{q}_s . The MC tracks $\sigma^*(t; q_s, q_t, \hat{\Theta})$ and updates the zeta potentials $\hat{\Theta}$ online. The ME estimates the zeta potentials using a motion-based data-driven approximation to guide the convergence of $\hat{\Theta}$ to the true values. The ME predicts \hat{q}_s , the start positions of the particles when the desired trajectory is replanned. The replan positions, \hat{q}_s , are predicted positions at the end of the prediction horizon according to the estimated zeta potentials $\hat{\Theta}$ and the predicted tracking error. The prediction horizon is a constant that is selected according to the statistical elevation of the MP's anytime performance, as discussed in Sect. 6.5.3.

When any tracking error exceeds the predefined threshold or the estimated zeta potentials tend to converge, the ME predicts \hat{q}_s at the prediction horizon, the MC steers the particles to the predicted \hat{q}_s , and the MP replans a new desired trajectory starting at \hat{q}_s with the updated zeta potentials. The MP keeps sending the best-replanned trajectory back to the MC while refining the current one until the next replanning. The coordination of MP and MC through ME improves the real-time performance of the control system and allows the planner to converge to a better solution. MP is guaranteed to generate a feasible solution within the selected prediction horizon using the updated \hat{q}_s and $\hat{\Theta}$. During tracking, the solution trajectory can be refined or updated by a less costly one.

Figure 6.12 shows the experimental result of the integrated adaptive online manipulation scheme. The prediction horizon is selected to be 20 s and the error threshold is $\pm 5 \mu\text{m}$. Figure 6.12a shows the overlaid trajectories of one nanowire tracking the minimum-time trajectory planned by the motion planner opt-Bi-iSST in the experiment. The initial desired trajectory is faster than the actual mobilities of

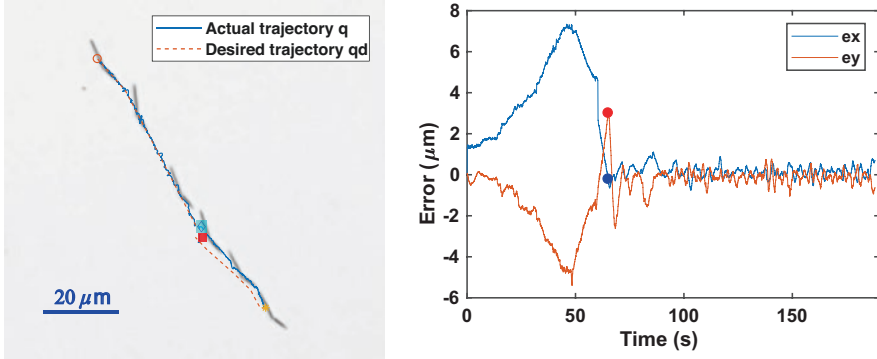


Fig. 6.12 Overlaid trajectories of nanowires that track the minimum-time trajectory planning by the motion planner opt-Bi-iSST in the experiment. (a) One silicon nanowire tracks the online planned trajectories. The pink square indicates the predicted replan position. The blue diamond marks the nanowire position when the replanned trajectory is received. The tracking errors are shown in Fig. 6.12b. (b) The tracking errors of the nanowire in Fig. 6.12a. The marked points indicate the time (at 60 s) when the replanned trajectory is received by the motion controller. (Reproduced with permission [55]. 2020, IEEE)

the nanowire; it is difficult for the nanowire to track the desired trajectory. The tracking errors keep increasing until they reach the error threshold at about 40 s. Once the tracking errors reach the error threshold, the motion planner receives the replanning request. The replan position \hat{q}_s is predicted for the prediction horizon 20 s by the motion estimator. The replan position is marked by a pink square in Fig. 6.12a. The current estimated zeta potentials are sent to the motion planner. The motion controller then starts to steer the nanowire to the replanned position. The actual position of the nanowire at 60 s is marked by a blue diamond in Fig. 6.12a. The tracking errors are presented in Fig. 6.12b, which remain in the range of $[-1, 1]$ μm after the online replanning [55].

The experiment shows the feasibility and performance of the online adaptive manipulation scheme for precisely steering particles, tracking the desired trajectories under disturbances, estimating unknown parameters of the system, and updating the desired trajectories accordingly. The adaptive manipulation scheme enables more efficient and accurate manipulation of micro- and nanoparticles.

6.7 Conclusion

Micro- and nanoagents with functional components can be used in an extensive variety of applications, ranging from biomanipulation to targeted drug delivery. The automated, efficient, highly precise manipulation of nano- and microscale objects paves the way toward target-oriented drug delivery. Actuating these agents with a global electric or magnetic field is a great way of achieving wireless control.

However, the field-based manipulation methods are severely hampered by the global and coupled influence of the global external actuation in the workspace, which limits the capability to robustly control multiple micro- and nanoagents independently and simultaneously. To enable this capability, we have developed and demonstrated the EP-based manipulation strategies to simultaneously, independently, and precisely manipulate the motion of micro- and nanoparticles, estimate their unknown mobilities, and plan their desired trajectories online. The manipulation schemes address the coupled influence from the global electric field in the workspace and can be applied to the motion planning and control of an autonomous fleet of micro- and nanorobots, which have tremendous potentials in many fields, such as in biology, medicine, and advanced manufacturing.

While many solutions have been discussed, most of these potential applications call for high-throughput parallel manipulation in three dimensions. Such parallel manipulation is capable of precisely and reliably manipulating a huge number of small-scale agents and components of varying shapes and materials. The high-throughput parallel manipulation could facilitate better diagnoses or treatment, revolutionize the manufacture of scalable functional devices, transform cell manipulation techniques, and improve on-target drug delivery, biopsy operations, and biological structures construction. Facing this largely unmet challenge, we have provided the first foundational step by developing effective motion control strategies and efficient motion planning algorithms to simultaneously and independently manipulate multiple micro- and nanoparticles with different shapes and materials using a simple, scalable, and generic set of electrodes. We analyze the manipulation capability for the different numbers of particles in one atomic cell and evaluate the maximum number of particles that can be arbitrarily, independently, and simultaneously manipulated for given disturbance bounds and system constraints. Those findings complement the existing work and provide an approach for scalable manipulation of multiple particles to perform parallel complex tasks with higher efficiency.

References

1. Bai, X., Liu, F., Liu, Y., Li, C., Wang, S., Zhou, H., Wang, W., Zhu, H., Winkler, D. A., & Yan, B. (2017). *Toxicology and Applied Pharmacology*, 323, 66–73.
2. Hilmer, A. J., & Strano, M. S. (2010). *Nature Nanotechnology*, 5, 481.
3. Patra, J. K., Das, G., Fraceto, L. F., Campos, E. V. R., del Pilar Rodriguez-Torres, M., Acosta-Torres, L. S., Diaz-Torres, L. A., Grillo, R., Swamy, M. K., Sharma, S., Habtemariam, S., & Shin, H.-S. (2018). *Journal of Nanobiotechnology*, 16, 71.
4. Jahangirian, H., Lemraski, E. G., Webster, T. J., Rafiee-Moghaddam, R., & Abdollahi, Y. (2017). *International Journal of Nanomedicine*, 12, 2957.
5. Houpeau, J.-L., Chauvet, M.-P., Guillemin, F., Bendavid-Athias, C., Charitansky, H., Kramar, A., & Giard, S. (2016). *Journal of Surgical Oncology*, 113, 501–507.
6. Lee, K. S., Chung, H. C., Im, S. A., Park, Y. H., Kim, C. S., Kim, S.-B., Rha, S. Y., Lee, M. Y., & Ro, J. (2008). Multicenter phase II trial of Genexol-PM, a Cremophor-free, polymeric

- micelle formulation of paclitaxel, in patients with metastatic breast cancer. *Breast Cancer Research and Treatment*, 108, 241–250.
7. Fan, D., Yin, Z., Cheong, R., Zhu, F. Q., Cammarata, R. C., Chien, C. L., & Levchenko, A. (2010). *Nature Nanotechnology*, 5, 545–551.
 8. Yu, K., Yi, J., & Shan, J. W. (2018). *Lab on a Chip*, 18, 1494–1503.
 9. Li, X., & Yu, K. (2020). *Proceedings of IEEE international conference on automation science and engineering*, Hong Kong, China.
 10. Fan, D. L., Zhu, F. Q., Cammarata, R. C., & Chien, C. L. (2011). *Nano Today*, 6, 339–354.
 11. Adam, G., Chowdhury, S., Guix, M., Johnson, B. V., Bi, C., & Cappelleri, D. (2019). *Robotics*, 8, 69.
 12. Chowdhury, S., Jing, W., & Cappelleri, D. (2016). *Micromachines*, 7, 3.
 13. Becker, A., Onyuksel, C., Bretl, T., & McLurkin, J. (2014). *International Journal of Robotics Research*, 33, 1626–1644.
 14. S. Salmanipour, E. Diller, (2018). *Proceedings IEEE international conference on robotics and automation*, Brisbane, Australia.
 15. Arcese, L., Fruchard, M., & Ferreira, A. (2013). *IEEE Transactions on Robotics*, 29, 1060–1067.
 16. Peyer, K. E., Zhang, L., & Nelson, B. J. (2013). *Nanoscale*, 5, 1259–1272.
 17. Gosse, C., & Croquette, V. (2002). *Biophysical Journal*, 82, 3314–3329.
 18. Zemanek, J., Michalek, T., & Hurak, Z. (2018). *Lab on a Chip*, 18, 1793–1801.
 19. Pethig, R. (2010). *Biomicrofluidics*, 4, Paper #022811.
 20. Gascoyne, P. R. C., & Vykoukal, J. V. (2004). *Proceedings of the IEEE*, 92, 22–42.
 21. Voldman, J. (2006). *BioMEMS and biomedical nanotechnology, Vol IV: Biomolecular sensing, processing and analysis*. New York: Springer.
 22. Grier, D. G. (2003). *Nature*, 424, 810–816.
 23. Banerjee, A. G., Rajasekaran, K., & Parsa, B. (2018). *Proceedings of the IEEE international conference on automation science and engineering*. Munich, Germany.
 24. Probst, R., Cummins, Z., Ropp, C., Eaks, E., & Shapiro, B. (2012). *IEEE Control Systems Magazine*, 32, 26–53.
 25. Mathai, P. D., Carmichael, P. T., Shapiro, B. A., & Liddle, J. A. (2013). *RSC Advances*, 3, 2677–2682.
 26. Chaudhary, S., & Shapiro, B. (2006). *IEEE Transactions on Control Systems Technology*, 14, 669–680.
 27. Mallea, R. T., Bolopion, A., Beugnot, J., Lambert, P., & Gauthier, M. (2018). *IEEE/ASME Transactions on Mechatronics*, 23, 1543–1554.
 28. Morgan, H., & Green, N. G. (1997). *Journal of Electrostatics*, 42, 279–293.
 29. Raychaudhuri, S., Dayeh, S. A., Wang, D., & Yu, E. T. (2009). *Nano Letters*, 9, 2260–2266.
 30. Zhang, Y. L., Li, J., S. To, Zhang, Y., Ye, X., You, L., & Sun, Y. (2012). *Nanotechnology*, 23, 065304.
 31. Yu, K., Yi, J., & Shan, J. (2018). *Proceedings of the IEEE international conference on automation science and engineering*. Munich, Germany.
 32. Yu, K., Yi, J., & Shan, J. (2015). *IEEE Transactions on Automation Science and Engineering*, 12, 37–49.
 33. Hunter, R. (1989). *Foundations of colloid science*. Oxford: Oxford University Press.
 34. Yu, C., Vykoukal, J., Vykoukal, D. M., Schwartz, J. A., Shi, L., & Gascoyne, P. R. C. (2005). *Journal of Microelectromechanical Systems*, 14, 480–487.
 35. Taff, B. M., & Voldman, J. (2005). *Analytical Chemistry*, 77, 7976–7983.
 36. Cohen, A. E., & Moerner, W. E. (2005). *Applied Physics Letters*, 86, Paper 093109.
 37. Cohen, A. E. (2005). *Physical Review Letters*, 94, Paper 118102.
 38. Hunt, T. P., & Westervelt, R. M. (2006). *Biomedical Microdevices*, 8, 227–230.
 39. Kralj, J. G., Lis, M. T. W., Schmidt, M. A., & Jensen, K. F. (2006). *Analytical Chemistry*, 78, 5019–5025.

40. Wang, L., Flanagan, L., & Lee, A. P. (2007). *Journal of Microelectromechanical Systems*, 16, 454–461.
41. Lee, S.-W., Li, H., & Bashir, R. (2007). *Applied Physics Letters*, 90, Paper 223902.
42. Kua, C. H., Lam, Y. C., Rodriguez, I., & Yang, C. (2008). *Analytical Chemistry*, 80, 5454–5461.
43. Wang, L., Lu, J., Monuki, S. A., Flanagan, L., & Lee, A. P. (2009). *Ecological Psychology*, 30, 782–791.
44. Cui, H., Voldman, J., He, X., & Lim, K. (2009). *Lab on a Chip*, 9, 2306–2312.
45. Desai, S. P., Vahey, M. D., & Voldman, J. (2009). *Langmuir*, 25, 3867–3875.
46. Fan, D. L., Zhu, F. Q., Cammarata, R. C., & Chien, C. L. (2004). *Applied Physics Letters*, 85, 4175–4177.
47. Fan, D. L., Zhu, F. Q., Cammarata, R. C., & Chien, C. L. (2005). *Physical Review Letters*, 94, Paper 247208.
48. Edwards, B., Engheta, N., & Evoy, S. (2007). *Journal of Applied Physics*, 98, Paper 124314.
49. Fan, D. L., Zhu, F. Q., Cammarata, R. C., & Chien, C. L. (2006). *Applied Physics Letters*, 89, Paper 223115.
50. Edwards, B., Mayer, T. S., & Bhiladvala, R. B. (2006). *Nano Letters*, 6, 626–632.
51. Edwards, B., Engheta, N., & Evoy, S. (2007). *Journal of Applied Physics*, 102, Paper 024913.
52. Fan, D. L., Cammarata, R. C., & Chien, C. L. (2008). *Applied Physics Letters*, 92, Paper 093115.
53. Kumar, S., Peng, Z., Shin, H., Wang, Z. L., & Hesketh, P. J. (2010). *Analytical Chemistry*, 82, 2204–2212.
54. Hunter, R. J. (2013). *Zeta potential in colloid science: Principles and applications*. London: Academic.
55. Wu, J., Li, X., & Yu, K. (2020). *IEEE/ASME Transactions on Mechatronics*, 25, 638–649.
56. Yu, K., Lu, X., Yi, J., & Shan, J. (2013). *Proceedings of the IEEE international conference on automation science and engineering*. Madison, WI.
57. Yu, K., Yi, J., & Shan, J. (2018). *IEEE Transactions on Automation Science and Engineering*, 15, 80–91.
58. Yu, K., Yi, J., & Shan, J. W. (2018). *The International Journal of Intelligent Robotics and Applications*, 2, 383–399.
59. Yu, K., Yi, J., & Shan, J. (2014). *Proceedings of the IEEE/ASME international conference on advanced intelligent mechatronics*. Besancon, France.
60. Yu, K., Yi, J., & Shan, J. (2015). *Proceedings of the IEEE international conference on automation science and engineering*. Gothenburg, Sweden.
61. Yu, K., Yi, J., & Shan, J. (2016). *Proceedings of the IEEE international conference on automation science and engineering*. Dallas, TX.
62. Wu, J., & Yu, K. (2019). *Proceedings of the ASME dynamic systems and control conference*. Park City, UT. Paper # DSCC2019–9051.
63. Wu, J., & Yu, K. (2020). *Proceedings of the IEEE/ASME international conference on advanced intelligent mechatronics*. Boston, MA.
64. Wu, J., & Yu, K. (2020). *Proceedings of the IFAC World Congress*. Berlin, Germany.
65. Larson, R. G. (1999). *The structure and rheology of complex fluids*. Oxford: Oxford University Press.
66. Castellano, R. J., Akin, C., Giraldo, G., Kim, S., Fornasiero, F., & Shan, J. W. (2015). *Journal of Applied Physics*, 117, 214306.
67. Jones, T. B. (2005). *Electromechanics of particles*. Cambridge: Cambridge University Press.
68. Van den Heuvel, M., De Graaff, M., Lemay, S., & Dekker, C. (2007). *Proceedings of the National Academy of Sciences of the United States of America*, 104, 7770–7775.
69. Solomentsev, Y., & Anderson, J. L. (1995). *Industrial and Engineering Chemistry Research*, 34, 3231–3238.
70. Akin, C., Yi, J., Feldman, L. C., Durand, C., Li, A.-P., Filler, M. A., & Shan, J. W. (2015). *ACS Nano*, 9, 5405–5412.
71. Tanelli, M., Corno, M., & Saveresi, S. (2014). *Modelling, simulation and control of two-wheeled vehicles*. New York: Wiley.

72. Landau, Y. (1979). *Adaptive control: The model reference approach*. New York: Marcel Dekker.
73. Garcia, C. E., Prett, D. M., & Morari, M. (1989). *Automatica*, 25, 335–348.
74. Mayne, D. Q., Raković, S., Findeisen, R., & Allgöwer, F. (2006). *Automatica*, 42, 1217–1222.
75. Lopez, B. T., Howl, J. P., & Slotine, J.-J. E. (2019). *Proceedings of the American control conference*. Philadelphia, PA.
76. Lu, X., & Cannon, M. (2019). *Proceedings of the American control conference*. Philadelphia, PA.
77. Yoshikawa, T. (1985). *International Journal of Robotics Research*, 4, 3–9.
78. LaValle, S. (2006). *Planning algorithms*. New York: Cambridge University Press.
79. Ford, L. R., Jr., & Fulkerson, D. R. (2015). *Flows in networks*. Princeton: Princeton University Press.
80. Busacker, R. G., & Gowen, P. J. (1960). *Technical report, technical paper ORO-TP-15*. Maryland: Operations Research Office, The Johns Hopkins University, Bethesda.
81. Li, Y., Littlefield, Z., & Bekris, K. E. (2016). *International Journal of Robotics Research*, 35, 528–564.
82. Karaman, S., & Frazzoli, E. (2011). *International Journal of Robotics Research*, 30, 846–894.
83. Littlefield, Z., & Bekris, K. E. (2018). *Proceedings of the field and service robotics*. Zurich, Switzerland.

Chapter 7

Magneto-Acoustic Hybrid Micro-/Nanorobot



Simon W. Sanchez and Jinxing Li

Future medical micro-/nanorobotics should be able to achieve efficient propulsion in harsh and complicated environments [1–12]. To do so, the micro-/nanorobotics need to harvest propelling forces with extremely high temporospatial resolution. Particularly, it is highly desired that micro-/nanorobotics are powered using biocompatible energy sources. Recently, the chemically powered micromotors have achieved a great success by showing the capacity to enable active and prolonged medicine delivery in living animals toward enhanced therapeutic efficacy [13–15]. Since these micromotors are mostly using onboard energy sources (Mg or Zn which can react with gastric or intestinal fluids), their lifetime is relatively short while the control and navigation have still not been explored in vivo. Alternatively, extensive efforts have been directed to the development of biocompatible fuel-free propulsion mechanisms [16–31]. Externally physical fields using optical, acoustic, or magnetic stimuli lead powerful navigation and actuation of micro-/nanorobotics. Expanding the capabilities and sophistication of such fuel-free nanomotors is imperative to design advanced micro-/nanorobotics for diverse biomedical applications (Fig. 7.1).

Among the various external fields, magnetic and acoustic fields play important roles in modern medicine. Magnetics are used in instruments such as the magnetic resonance imaging (MRI) machine, while transcranial magnetic stimulation (TMS) has shown diagnostic and therapeutic potential in the central nervous system with a wide variety of disease states in neurology and mental health. Acoustic fields with low amplitudes have been used for diagnostics and imaging. Meanwhile, many therapies use high-energy ultrasound for heating, activating, and fracturing tissues and structures within the body. Owing to their biocompatible energy transduction mechanism, magnetic and ultrasound propulsions have also led the operation of fuel-free nanomotors and hold considerable promise for biomedical applications, particularly in vivo ones.

Note: Results of this chapter are mainly based on the work published in: Li et al. *Nano Lett.* 2015, 15, 7, 4814–4821; and Ahmed et al. *Nature Commun.* 2017, 8, 770.

S. W. Sanchez · J. Li (✉)

Department of Biomedical Engineering & Institute for Quantitative Health
Science & Engineering, Michigan State University, East Lansing, MI, USA
e-mail: jl@msu.edu

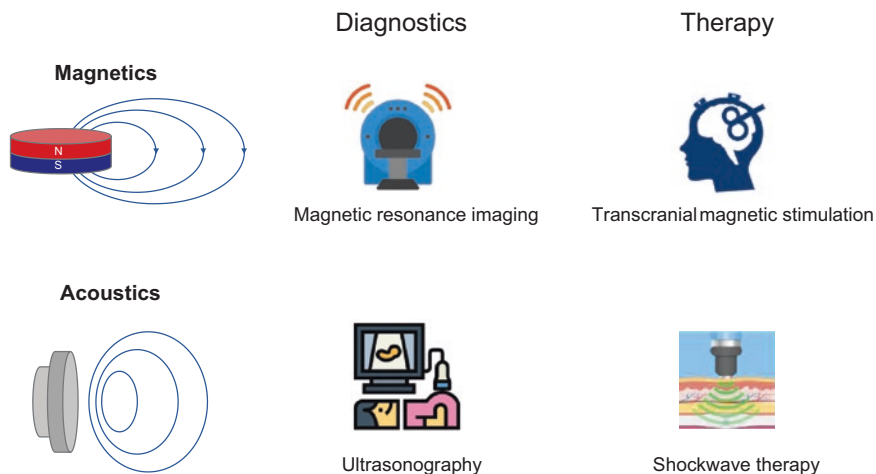


Fig. 7.1 Examples of magnetics and acoustics in modern medicine

Hybrid micro-/nanorobots, which use multiple distinct power sources for nanoscale propulsion, could lead to complex regulation of individual and collective behavior for operation in complicated environments. Hybrid nanomotors pairing fuel-powered and fuel-free propulsions in a single nanovehicle have been described recently by Wang's and Mallouk's groups [32–34]. Meanwhile, because of the high versatility and maneuverability of magnetic and acoustic fields for fuel-free operation, magneto-acoustic hybrid micro-/nanorobotics recently emerged as a valuable option for the digitalized speed regulation and reversible control of micro-/nanorobots.

The individual operation mode of magnetic and acoustic propulsion is briefly summarized in Fig. 7.2. Magnetic microrobot can mimic the helical or flexible flagellum of bacteria propulsion using either a rotational or an oscillating magnetic field. The motion of helical microswimmers is explained by slender body theory [16, 35–37], which approximates the helical structure as a slender filament by a line distribution of singularity solutions [38, 39]. For steady-state motion, the externally applied forces and torques have to equal the drag on the swimmer. This is like how a corkscrew being driven through wood rotationally with a screwdriver when the resistance is too large. Quite a few designs have been explored for undulatory magnetic propulsion using oscillating magnetic fields, including multi-linked nanoswimmers [40] and two-arm freestyle nanoswimmers [41]. Soft magnetic materials or ferrofluid droplets have recently been used to build shape-programmable magnetic miniature soft robots with attractive performance and reconfigurable actuation [42–44]. The acoustic propulsion is even more complicated and versatile. Standing waves, generated in resonant cavities, allow manipulation of objects by trapping them in the acoustic nodes [45]. Recently, such acoustic manipulation has been applied to precisely control a single microparticle/cell/organism along an arbitrary path within a single-layer microfluidic channel in two dimensions [46]. Steady

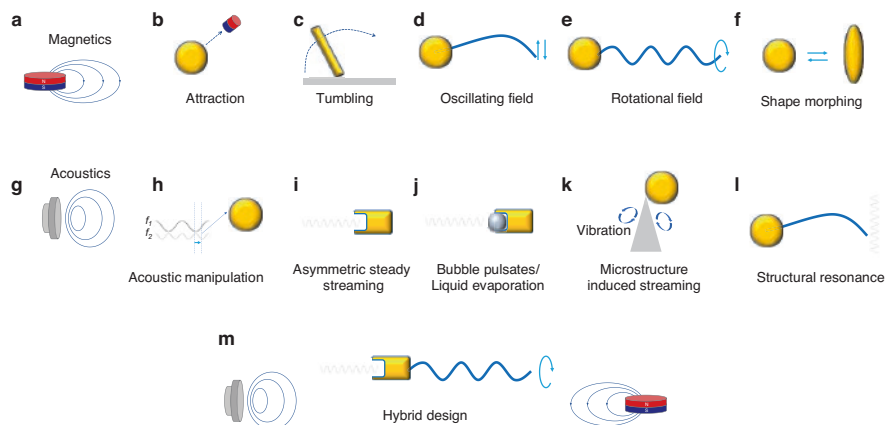


Fig. 7.2 Magnetic and acoustic actuation modes for hybrid design. **(a)** Magnetic actuation modes including **(b)** direct magnetic attraction of magnetic structures; **(c)** magnetic structure tumbling on a surface; **(d)** undulatory magnetic actuation using oscillating magnetic field; **(e)** helical magnetic actuation under a rotational magnetic field; **(f)** shape-morphing microrobot induced by magnetic field. **(g)** Acoustic actuation modes including **(h)** acoustic manipulation by switching operation frequency; **(i)** “self-propelled” motion induced by asymmetry steady streaming; **(j)** acoustic field induced bubble pulsation or liquid evaporation in a microcavity; **(k)** nanomanipulation by streaming induced by local microstructures; **(l)** structure resonance of a soft nanostructure; **(m)** an example of magneto-acoustic hybrid nanorobot combing the asymmetric steady streaming and the helical actuation

streaming around obstacles in an acoustically induced flow, either standing wave or traveling wave, can also be used to trap and precisely manipulate micro-/nanoscale objects [47, 48]. Recently, Fischer et al. demonstrated that 3D-printed surface profile encoding the phase of the desired wave front can shape acoustic fields to be used as reflection elements in air to levitate dense solids and liquids within complex traps [49]. Recent experiments from the Mallouk and Wang groups also showed that standing acoustic waves are highly promising to induce the self-proulsion of rigid metallic structures in the direction perpendicular to the acoustic wave [20, 21]. The physical mechanism for such new actuation modes is assumed to be based on the interplay between inertial forces in the fluid and the geometrical asymmetry of the particle shape [50]. Steady streaming in the fluid, the inertial rectification of the time-periodic oscillating flow, generates steady stresses on the particle which, in general, do not average to zero, resulting in a finite propulsion speed along the axis of the symmetry of the particle and perpendicular to the oscillation direction [50]. Microstructure trapping air bubble can harness acoustic waves for propulsion at incredibly high speeds [51], while microstructure loaded with liquid that evaporates under focused ultrasound can lead a one-time high-speed shot to penetrate the biological tissue [52]. Recently, Nelson et al. described a new class of nanoswimmer propelled by the small-amplitude oscillation of a flagellum-like flexible tail in both standing and traveling acoustic waves [53]. Different from the rigid asymmetric microstructures, the artificial nanoswimmers are fabricated by multistep

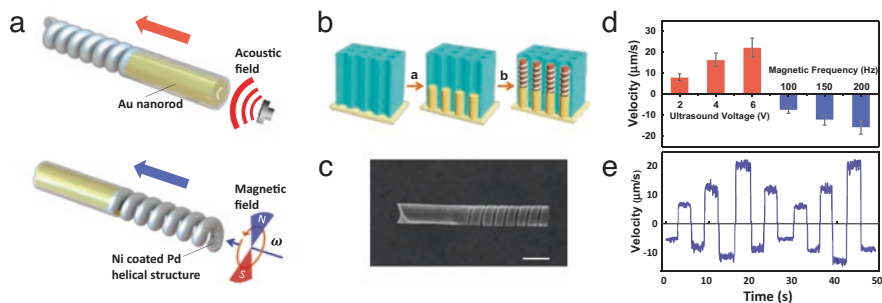


Fig. 7.3 (a) Scheme of the design of the magneto-acoustic hybrid nanomotor and its dual propulsion modes under the acoustic and magnetic fields. (b) Schematic illustration of the template-assisted fabrication of the bi-segment magneto-acoustic hybrid nanomotors. (c) SEM image of a magneto-acoustic hybrid nanomotor. Scale bar: 500 nm. (d) Quantitative velocity of the hybrid motor using magnetic frequencies of 100 Hz, 150 Hz, and 200 Hz and ultrasound voltage amplitudes of 2 V, 4 V, and 6 V (number of tracked nanomotors; $N = 20$). All the speed data are averaged by 20 nanomotors under the same propulsion conditions. (e) Digital control of the hybrid motor speed by changing the actuation mode and the corresponding ultrasound voltage and rotational magnetic frequency alternately every 3 seconds using the following sequence: Mag 100 Hz, US 2 V, Mag 150 Hz, US 4 V, Mag 200 Hz, US 6 V, Mag 150 Hz, US 4 V, Mag 100 Hz, US 2 V, Mag 150 Hz, US 4 V, Mag 200 Hz, US 6 V, Mag 150 Hz

electrodeposition techniques, comprising a rigid bimetallic head and a flexible tail. The flexibility of the tail structures allows high-frequency oscillation during the acoustic excitation, which produce high propulsive forces.

As one can see from the above summary, the many modalities to use magnetic and acoustic fields for micro-/nanorobotic propulsion open the many opportunities to develop magneto-acoustic hybrid micro-/nanorobotics. Li et al. describe the magneto-acoustic hybrid fuel-free nanomotor which can be powered by either a magnetic or ultrasound field [54]. To address the challenge of using the propulsion force from both magnetic and acoustic fields, the hybrid nanomotor is constructed from bi-segment nanomechanical elements, where a concave nanorod segment is essential to produce the asymmetric interplay between the nanostructure and the acoustic wave. Such concave end is connected to a nanohelical magnetic segment which was realized through a versatile template-assisted electrochemical deposition method followed by segment-selective chemical etching (Fig. 7.3b). The resulting nanostructures offer an impressive fuel-free magneto-acoustic hybrid nanomotor operation with the magnetic helical end serving for the magnetic propulsion and the concave nanorod for acoustic propulsion (Fig. 7.3a, bottom and top, respectively). The magneto-acoustic hybrid nanomotors can thus be powered by either the magnetic or ultrasound field and change their direction instantaneously upon alternating the applied fields. Changing the amplitude of the acoustic field or the frequency of the magnetic field leads to rapid speed regulation of such hybrid nanomotors.

Precise speed control of the hybrid nanomotor was achieved using an ultrasonic transducer at a resonant frequency of 2.66 MHz and two orthogonal Helmholtz coil pairs creating a rotational magnetic field frequency of 150 Hz. The hybrid

nanomotor was proven to move in opposite directions along the nanowire axis under the dual modes using an external magnet for alignment. Under the magnetic mode, the hybrid nanomotor moves “forward” toward its Au end. Similarly, under the acoustic mode, the hybrid nanomotor moves “backward” toward its helical end. Brownian motion is observed in the absence of both acoustic and magnetic fields. Dynamic speed changes as well as the ability to repeatedly move in opposite directions illustrate the rapid response of the hybrid nanomotor to different external stimuli. Overall, the hybrid nanomotor offers an on-demand operation and direction switching with steady-state speeds.

The speed of chemically powered nanomotors can be controlled by parameters of the chemical environment, such as fuel concentration and temperature [55]. However, real-time and rapid speed regulation is still challenging for chemical-powered nanomotors. Since the hybrid nanomotor is completely fuel-free and powered by external fields, its speed could be controlled by changing the input parameters of the corresponding field. Under acoustic mode, a nanoparticle can be viewed as a body oscillating in a uniform oscillating velocity field [50]. Based on the physical mechanism of asymmetric steady fluid streaming, the inertial rectification of the time-periodic oscillating flow generates steady stresses on the nanomotor which, in general, do not average to zero, resulting in a finite propulsion speed along the axis of the symmetry of the particle and perpendicular to the oscillation direction. The dimensional propulsion speed of the nanomotor can be expressed as [50]:

$$v_u = \varepsilon R_e V^\perp v^{(1,1)} \quad (7.1)$$

where ε is the dimensionless small shape parameter, R_e is the Reynolds number, $v^{(1,1)}$ is the leading-order dimensionless propulsion speed, and V^\perp is the relative amplitude of the particle oscillations which scales with the amplitude of the ultrasound field. Therefore, the speed of the hybrid nanomotors levitated in solution under a fixed ultrasound wave frequency can be readily controlled by changing the amplitude of the driving voltage.

The speed of helical magnetic swimmers depends upon various geometric parameters (including the diameter) and the rotation frequency, in a complex manner described in Eq. 7.2 [56, 57]:

$$v_u = \frac{(\xi_\perp - \xi_\parallel) \sin \theta \cos \theta}{2(\xi_\perp \sin^2 \theta + \xi_\parallel \cos^2 \theta)} d \omega \quad (7.2)$$

where ξ_\perp and ξ_\parallel are the drag coefficients perpendicular and parallel to the helical axis, θ is the helix angle, d is diameter of the helix, and ω is the rotational frequency. Therefore, the speed of the hybrid nanomotor in a certain fluid, operated in the magnetic mode, can be regulated by controlling the rotational frequency of the magnetic field. Overall, the speed of the new hybrid motor under the magnetic and ultrasound actuations could be controlled by controlling the rotation frequency of the magnetic field and the voltage amplitude applied on the piezoelectric transducer, respectively.

The propulsion performance was tested using different input parameters of the individual modes. In the acoustic mode, the applied voltage was increased from 2 to 4 to 6 with an observed speed increase from 8.1 to 16.4 to 22.3 $\mu\text{m/s}$, respectively, over 4 s periods in agreement with Eq. 7.1. Similarly, in the magnetic mode, the rotational frequency was increased from 100 to 150 to 200 Hz with an observed speed increase from 7.6 to 12.3 to 15.9 $\mu\text{m/s}$, respectively (Fig. 7.3d). A net speed of zero and an equilibrium state could be achieved by adjusting the ultrasound and magnetic propelling forces to be balanced. Overall, the data follows the theoretical predictions of Eqs. 7.1 and 7.2. The hybrid motor displayed rapid switching of its propulsion modes upon applying the corresponding actuation, a characteristic of an ideal hybrid motor. This capability was achieved by alternating the magnetic and acoustic fields (every 3 s) while also changing the corresponding ultrasound voltage and rotational magnetic frequency. The hybrid motor displayed an instantaneous switching between its dual modes with steady-state speeds increasing rapidly upon changing the input parameters. Careful analysis indicates that the hybrid motor can reverse its moving direction within less than 50 ms (Fig. 7.3e). In conclusion, rapid, on-demand, and programmable speed and direction control are achievable with the combination of acoustic and magnetic fields.

In order to test the critical role of the bi-segment configuration for optimal hybrid propulsion in both modes, the hybrid motor with that of its individual segments, an Au nanorod or a Pd nanospring (both coated with 10-nm Ni thin layer), was also tested. The results demonstrate that the magnetic nanospring structure can still lead to a useful hybrid operation. However, the hybrid spring-rod nanomotors can harvest and translate the propelled forces more efficiently. Overall, the bi-segment nanowire design of the hybrid nanomotor does not compromise the performance of the individual propulsion modes.

For practical biomedical applications of the new hybrid nanomotors, it is important to test their propulsion behavior in different complex environments. It was observed that magneto-acoustic hybrid nanomotors exhibit slower speed in biological medium such as serum and blood. These changes reflect the increased environmental viscosity of these biofluids. Chemically powered nanomotors cannot operate in high ionic strength environments (such as seawater and blood) because these media interfere with their self-electrophoresis propulsion mechanism. While these environments affect the speed of the hybrid nanomotors, these motors still move efficiently in both modes in the different viscous fluids.

Collective behavior, a very common phenomenon in the biological world [58], inspired us to investigate how groups of the hybrid motors behave under the external field inputs. The acoustic field (frequency 618 kHz) is capable to trigger the standing wave formation which leads to the rapid assembly and aggregation of the hybrid nanomotors toward the acoustic field node. In contrast, the magnetic actuation induces disassembly of the aggregate hybrid motors and directs the directional motion of the nanomotor swarm. Such reversible assembly and directional swarm movement is achieved by alternating the acoustic and magnetic fields. This switchable collective behavior can be repeated with multiple cycles. Thus, with proper application of the acoustic and magnetic fields, a fully reversible swarm with

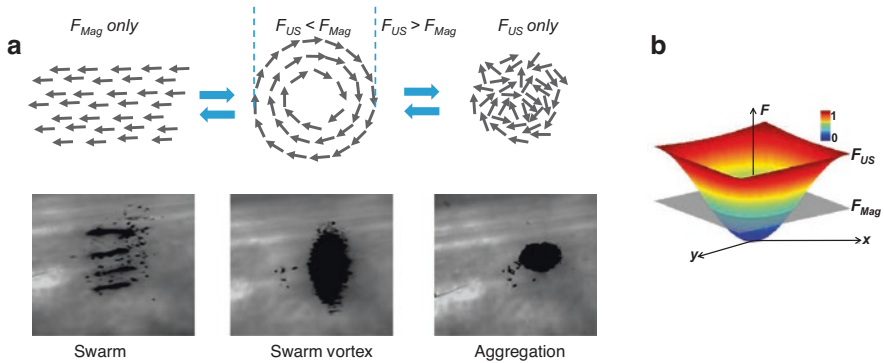


Fig. 7.4 (a) Illustration of swarm vortex formation in a round boundary system: The hybrid nanomotors display directional swarm motion when only the magnetic field is “on”; rapid re-formation of the swarm vortex upon turning the ultrasound field “on” again; a stable aggregation is formed when only the ultrasound field is turned “on.” (b) Normalized distribution of the acoustic force gradient F_{us} and magnetic force F_{mag} near the ultrasound pressure node in the acoustic cell. The magnetic force is considered to have a uniform distribution, shown by the gray plane

aggregation and dispersion of the nanomotors can be obtained. It is anticipated that the nanomotor swarm can be moved in a controlled way by varying the applied acoustic frequency which changes the location of the pressure nodes and leads to migration of the swarm to a new location.

The collective behavior of hybrid nanomotors in the presence of both the acoustic and magnetic fields (i.e., a “dual operation mode”) is particularly intriguing as three distinct states are observed (Fig. 7.4). Interestingly, unlike the directional swarm motion observed under the magnetic field alone or the stable aggregation under the acoustic field, a swarm vortex is formed when both of the fields are turned “on.” Turning the acoustic field “off” in such a state leads to directional moving swarm of the nanomotors under the rotational magnetic field. Applying the acoustic field again leads to rapid migration of the hybrid motors toward the original node position and re-formation of a swarm vortex, although the magnetic field is still “on.” Upon removal of the magnetic field, the acoustic field prevails, and a stable assembly is formed again. The three different states of the swarm vortex (when both fields “on”), directional swarm motion (only the Mag is “on”), and the stable assembly (only the US “on”) are highly switchable and reversible (Fig. 7.4a).

Such flexible switching of the collective behavior results from the competition between the magnetic and acoustic forces. At steady state, the imposed propelling force is always counterbalanced by the Stokes drag force. From Eq. 7.2, one can note that the magnetic propelling force imposed on a hybrid nanomotor is always consistent at a fixed frequency. Under the acoustic actuation with a frequency of 618 kHz, a plane standing wave field arises from the superposition of two waves (one is generated by the transducer, while the other is reflected by the cover slide) of equal wavelength and amplitude traveling in opposite directions. The interference between the waves results in the formation of antinodes and nodes, with zero

levitation force at the pressure nodes. The acoustic force can be divided into the primary radiation force (PRF) and the secondary radiation force (SRF). The PRF, which is the main force in the field of acoustic waves, can be subdivided into an axial component F_z and a transverse component F_{xy} [59, 60]. The F_z component of the PRF is the force that drives the migration of microparticles to the nearest pressure node or antinode plane, while the F_{xy} component leads to their aggregation within the nodal plane. The experiment depends on the theoretical understanding of the F_z component of the PRF which drives the nanomotor in a standing ultrasound wave field [59, 60].

$$F_z = VE_{ac} \frac{2\pi}{\lambda} Q \sin\left(\frac{4\pi}{\lambda} z\right) \quad (7.3)$$

Here V is the nanomotor volume, z is the axial distance from the transducer to the node or antinode plane, λ is the wavelength, and Q is the acoustic contrast factor which is related to the particle fluid interactions. The acoustic energy density E_{ac} is equal to the sum of the average potential and kinetic energy densities. As indicated from Eq. 7.3, the acoustic force exhibits a sinusoidal dependence of the axial distance from the transducer to the node or antinode plane. Therefore, the acoustic force drops rapidly near the node and becomes zero at the node (Fig. 7.4b). In this case, within a certain distance from the node position, the magnetic propelling force is larger than the acoustic radiation force. Once the nanomotor approaches the equilibrium round boundary where the magnetic and acoustic forces become equal, the nanomotors can no longer achieve directional motion, and instead aggregate rapidly into a swarm vortex configuration with zero density in the center. Since the ultrasound radiation force boundaries are reflecting, the velocity perpendicular to the boundary is suppressed in the course of collisions with other nanomotors on the way back from the boundary [61]. As a consequence, the velocity parallel to the wall survives and becomes a natural attractor for the dynamics. The circular system boundaries conform perfectly to parallel velocity, resulting in a tight vortex formation. At the position beyond the equilibrium boundary, the increased acoustic force will dominate the motion of the nanomotor and tow the nanomotor again toward the node position. Further aggregation with magnetic field off is facilitated by the SRF, which is associated with the sound waves that are scattered by individual nanomotors. The SRF is responsible for particle-particle interactions, making them either to attract or repel each other, as well as forming stable multiparticle spherical structures [59, 60]. Such diverse and unique collective behaviors, e.g., vortex formation and swarm motion, of the hybrid nanomotor system, can serve as a good model for complex open systems such as bacterial chemotaxis or cell migrations [61, 62].

The biocompatible and versatile propulsion enabled by the hybridization of magnetic and acoustic fields leads to great potential for actuation in complex biological structures and environments. Specifically, controlled propulsion within vascular environments offers exciting possibilities to access the whole body and to provide localized treatments for cardiovascular diseases. Precise control and motion of

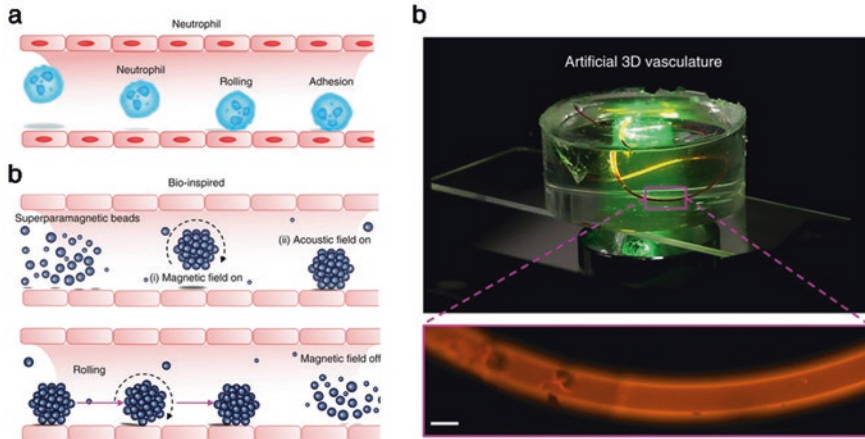


Fig. 7.5 Magneto-acoustic neutrophil-inspired microrobots [63]. (a) Neutrophil rolls on vasculature before transmigrating into tissue. (b) Hybridization of magnetic and acoustic propulsion leads to three-dimensional control motion of reconfigurable particle assemblies moving a vessel wall mimicking a neutrophil rolling on a wall. (c) A three-dimensional PDMS-based artificial vasculature which can be navigated through by the magneto-acoustic neutrophil-inspired microrobots

micro- or nanoswimmers provide a pathway for targeted therapeutics and noninvasive surgery. Moving and navigation in such complicated environment requires propulsion mechanisms beyond two-dimensional settings with limited control at the boundaries. Ahmed et al. show a mechanism in which to use micro-sized particles in a microvascular environment that are capable to be propelled by the combination of magnetic and acoustic fields [63]. Such hybridization of magnetic and acoustic propulsion leads to three-dimensional control motion of reconfigurable particle assemblies moving along vessel wall mimicking a neutrophil rolling on a wall (Fig. 7.5a). A rolling motion is achieved by using micro-sized superparamagnetic particles in a channel after a rotational magnetic field is applied (Fig. 7.5b). The aggregations are formed due to the dipole-dipole interactions. When an acoustic field with an appropriate frequency is applied, the assembled particles migrate to the boundary in an acoustic field which resulted in a rolling motion along vessel wall. The assembled particles become dispersed again when the magnetic field is off.

Using a polydimethylsiloxane (PDMS)-based microchannel as the artificial vasculature system (Fig. 7.5c), the authors investigated the migration of the particles toward the sidewall of the channel by using various sized particles of different material properties. There are several acoustic forces that can contribute to particle motion including acoustic radiation force and the streaming-induced drag. Of the acoustic radiation force, there are the primary and secondary radiation forces. The primary radiation force was observed to mainly contribute to migration. For small particles, the sidewall-induced streaming drag force dominates particle motion until a certain size is met then which the radiation force becomes dominant. This work illustrates a mechanism in which superparamagnetic particles self-aggregate and

move along a boundary of a microchannel with a combined acoustic and magnetic actuation technique. This mechanism provides a foundation site-specific drug delivery and various other biomedical applications. The combined propulsion mechanism with a high-resolution imaging technique for *in vivo* treatment could provide a way to treat various diseases in hard-to-reach locations. The biocompatible magnetic particles are advantageous over already established microswimmers with costly fabrication procedures and limited biocompatibility.

The use of the combination of magnetic and acoustic fields to power a hybrid device offers a wider scope of operation and holds substantial promise for designing smart nanovehicles that autonomously adapt and reconfigure their operation in response to changes in their surrounding environment. Addressing the distinct requirements of the magnetic and acoustic propulsions within a single nanoscale device requires high-precision fabrication techniques to make structures that can harvest both the magnetic and acoustic forces. The resulting hybrid nanomotor can take advantage of the propelling forces from both magnetic and acoustic fields for efficient fuel-free dual-mode hybrid motor operation. The speed and directionality of the hybrid nanomotors can be swiftly controlled by changing the parameters of the field inputs. The hybrid nanomotors can also achieve efficient propulsion in biological media and demonstrate impressive switchable collective behaviors. Dynamic and reversible change between a tight assembly, swarm motion, and swarm vortex state can be achieved in response to a change of the acoustic and/or magnetic actuations. Such multimode fuel-free propulsion capability offers a wider scope of operation and substantial promise for adaptive performance under various scenarios in dynamically changing environments. Such adaptive and hybrid operation provide a versatile route to precisely control a single or a large number of nanomotors which could not be achieved by using only one propulsion mode.

Overall, the magneto-acoustic hybrid nanomotors can function individually and collectively, with rapid switching between the magnetic and acoustic modes and precise temporal-spatial control and regulation. Future efforts will lead to intelligent hybrid vehicles to be coupled with conventional magnetic and ultrasound diagnostic devices with real-time autonomous mode switching in response to changing conditions. Meanwhile, various medical functions, such as imaging and drug delivery, could be integrated on the nanomotors for multitask response and operation. Owing to their impressive performance, the new hybrid magneto-acoustic nanomotors are expected to advance the field of artificial nanomachines and to offer considerable promise for a broad range of practical applications ranging from nanoscale manipulation to nanomedicine. Beyond hybrid actuation, researchers should also take advantage of the imaging functions of magnetics and acoustics to eventually achieve four-dimensional control and navigation of individual microrobot or a swarm of micro-/nanorobots in body, so that the “fantastic voyage” can be realized.

References

1. Purcell, E. M. (1977). Life at low Reynolds number. *American Journal of Physics*, 45, 3–11.
2. Schliwa, M., & Woehlke, G. (2003). Molecular motors. *Nature*, 422, 759–765.
3. van den Heuvel, M. G. L., & Dekker, C. (2007). Motor proteins at work for nanotechnology. *Science*, 317, 333–336.
4. Guix, M., Mayorga-Martinez, C. C., & Merkoçi, A. (2014). Nano/micromotors in (bio)chemical science applications. *Chemical Reviews*, 114, 6285–6322.
5. Ozin, G. A., Manners, I., Fournier-Bidoz, S., & Arsenault, A. (2005). Dream nanomachines. *Advanced Materials*, 17, 3011–3018.
6. Wang, J. (2013). *Nanomachines: Fundamentals and applications*. Wiley-VCH.
7. Mei, Y., Solovev, A. A., Sanchez, S., & Schmidt, O. G. (2011). Rolled-up nanotech on polymers: From basic perception to self-propelled catalytic microengines. *Chemical Society Reviews*, 40, 2109–2119.
8. Mallouk, T. E., & Sen, A. (2009). Powering nanorobots. *Scientific American*, 300, 72–77.
9. Nelson, B. J., Kaliakatsos, I. K., & Abbott, J. J. (2010). Microrobots for minimally invasive medicine. *Annual Review of Biomedical Engineering*, 12, 55–85.
10. Moo, J. G. S., & Pumera, M. (2015). Chemical energy powered nano/micro/macromotors and the environment. *Chemistry – A European Journal*, 21, 58–72.
11. Li, J., de Ávila, B. E.-F., Gao, W., Zhang, L., & Wang, J. (2017). Micro/nanorobots for biomedicine: Delivery, surgery, sensing, and detoxification. *Science Robotics*, 2.
12. Alapan, Y., et al. (2019). Microrobotics and microorganisms: Biohybrid autonomous cellular robots. *Annual Review of Control, Robotics, and Autonomous Systems*, 2, 205–230.
13. Gao, W., et al. (2015). Artificial micromotors in the mouse’s stomach: A step toward in vivo use of synthetic motors. *ACS Nano*, 9, 117–123.
14. Li, J., et al. (2016). Enteric micromotor can selectively position and spontaneously propel in the gastrointestinal tract. *ACS Nano*, 10, 9536–9542.
15. de Ávila, B. E.-F., et al. (2017). Micromotor-enabled active drug delivery for in vivo treatment of stomach infection. *Nature Communications*, 8, 272.
16. Dreyfus, R., et al. (2005). Microscopic artificial swimmers. *Nature*, 437, 862–865.
17. Liu, M., Zentgraf, T., Liu, Y., Bartal, G., & Zhang, X. (2010). Light-driven nanoscale plasmonic motors. *Nature Nanotechnology*, 5, 570–573.
18. Loget, G., & Kuhn, A. (2010). Propulsion of microobjects by dynamic bipolar self-regeneration. *Journal of the American Chemical Society*, 132, 15918–15919.
19. Chang, S. T., Paunov, V. N., Petsev, D. N., & Velev, O. D. (2007). Remotely powered self-propelling particles and micropumps based on miniature diodes. *Nature Materials*, 6, 235–240.
20. Wang, W., Castro, L. A., Hoyos, M., & Mallouk, T. E. (2012). Autonomous motion of metallic microrods propelled by ultrasound. *ACS Nano*, 6, 6122–6132.
21. Garcia-Gradilla, V., et al. (2013). Functionalized ultrasound-propelled magnetically guided nanomotors: Toward practical biomedical applications. *ACS Nano*, 7, 9232–9240.
22. Schamel, D., et al. (2014). Nanopropellers and their actuation in complex viscoelastic media. *ACS Nano*, 8, 8794–8801.
23. Qiu, T., et al. (2014). Swimming by reciprocal motion at low Reynolds number. *Nature Communications*, 5, 5119.
24. Venugopalan, P. L., et al. (2014). Conformal cytocompatible ferrite coatings facilitate the realization of a nanovoyager in human blood. *Nano Letters*, 14, 1968–1975.
25. Ghosh, A., & Fischer, P. (2009). Controlled propulsion of artificial magnetic nanostructured propellers. *Nano Letters*, 9, 2243–2245.
26. Wu, Z., et al. (2014). Turning erythrocytes into functional micromotors. *ACS Nano*, 8, 12041–12048.
27. Loget, G., & Kuhn, A. (2011). Electric field-induced chemical locomotion of conducting objects. *Nature Communications*, 2, 535.

28. Wu, Z., et al. (2014). Near-infrared light-triggered “on/off” motion of polymer multilayer rockets. *ACS Nano*, 8, 6097–6105.
29. Sridhar, V., et al. (2020). Carbon nitride-based light-driven microswimmers with intrinsic photocharging ability. *Proceedings of the National Academy of Sciences*, 117, 24748–24756.
30. Dong, X., et al. (2020). Bioinspired cilia arrays with programmable nonreciprocal motion and metachronal coordination. *Science Advances*, 6, eabc9323.
31. Palagi, S., et al. (2016). Structured light enables biomimetic swimming and versatile locomotion of photoresponsive soft microrobots. *Nature Materials*, 15, 647–653.
32. Gao, W., Manesh, K. M., Hua, J., Sattayasamitsathit, S., & Wang, J. (2011). Hybrid nanomotor: A catalytically/magnetically powered adaptive nanowire swimmer. *Small*, 7, 2047–2051.
33. Gao, W., D’Agostino, M., Garcia-Gradilla, V., Orozco, J., & Wang, J. (2013). Multi-fuel driven Janus micromotors. *Small*, 9, 467–471.
34. Wang, W., et al. (2014). A tale of two forces: Simultaneous chemical and acoustic propulsion of bimetallic micromotors. *Chemical Communications*, 51, 1020–1023.
35. Bell, D. J., Leutenegger, S., Hammar, K. M., Dong, L. X., & Nelson, B. J. (2007). Flagella-like propulsion for microrobots using a nanocoil and a rotating electromagnetic field. In *Proceedings 2007 IEEE international conference on robotics and automation* (pp. 1128–1133). <https://doi.org/10.1109/ROBOT.2007.363136>
36. Zhang, L., et al. (2009). Artificial bacterial flagella: Fabrication and magnetic control. *Applied Physics Letters*, 94, 064107.
37. Zhang, L., et al. (2009). Characterizing the swimming properties of artificial bacterial flagella. *Nano Letters*, 9, 3663–3667.
38. Lighthill, J. (1976). Flagellar hydrodynamics. *SIAM Review*, 18, 161–230.
39. Brennen, C., & Winet, H. (1977). Fluid mechanics of propulsion by cilia and flagella. *Annual Review of Fluid Mechanics*, 9, 339–398.
40. Jang, B., et al. (2015). Undulatory locomotion of magnetic multilink nanoswimmers. *Nano Letters*, 15, 4829–4833.
41. Li, T., et al. (2017). Highly efficient freestyle magnetic nanoswimmer. *Nano Letters*, 17, 5092–5098.
42. Fan, X., Dong, X., Karacakol, A. C., Xie, H., & Sitti, M. (2020). Reconfigurable multifunctional ferrofluid droplet robots. *Proceedings of the National Academy of Sciences*, 117, 27916–27926.
43. Kim, Y., Yuk, H., Zhao, R., Chester, S. A., & Zhao, X. (2018). Printing ferromagnetic domains for untethered fast-transforming soft materials. *Nature*, 558, 274–279.
44. Huang, H.-W., Sakar, M. S., Petruska, A. J., Pané, S., & Nelson, B. J. (2016). Soft micromachines with programmable motility and morphology. *Nature Communications*, 7, 12263.
45. Wixforth, A., et al. (2004). Acoustic manipulation of small droplets. *Analytical and Bioanalytical Chemistry*, 379, 982–991.
46. Ding, X., et al. (2012). On-chip manipulation of single microparticles, cells, and organisms using surface acoustic waves. *Proceedings of the National Academy of Sciences*, 109, 11105–11109.
47. Lu, X., et al. (2019). A human microrobot interface based on acoustic manipulation. *ACS Nano*, 13, 11443–11452.
48. Nama, N., Huang, P.-H., Huang, T. J., & Costanzo, F. (2014). Investigation of acoustic streaming patterns around oscillating sharp edges. *Lab on a Chip*, 14, 2824–2836.
49. Melde, K., Mark, A. G., Qiu, T., & Fischer, P. (2016). Holograms for acoustics. *Nature*, 537, 518–522.
50. Nadal, F., & Lauga, E. (2014). Asymmetric steady streaming as a mechanism for acoustic propulsion of rigid bodies. *Physics of Fluids*, 26, 082001.
51. Aghakhani, A., Yasa, O., Wrede, P., & Sitti, M. (2020). Acoustically powered surface-slipping mobile microrobots. *Proceedings of the National Academy of Sciences*, 117, 3469–3477.

52. Kagan, D., et al. (2012). Acoustic droplet vaporization and propulsion of perfluorocarbon-loaded microbullets for targeted tissue penetration and deformation. *Angewandte Chemie, International Edition*, 51, 7519–7522.
53. Ahmed, D., et al. (2016). Artificial swimmers propelled by acoustically activated flagella. *Nano Letters*, 16, 4968–4974.
54. Li, J., et al. (2015). Magneto-acoustic hybrid nanomotor. *Nano Letters*, 15, 4814–4821.
55. Wang, J., & Manesh, K. M. (2010). Motion control at the nanoscale. *Small*, 6, 338–345.
56. Tottori, S., et al. (2012). Magnetic helical micromachines: Fabrication, controlled swimming, and cargo transport. *Advanced Materials*, 24, 811–816.
57. Lauga, E., & Powers, T. R. (2009). The hydrodynamics of swimming microorganisms. *Reports on Progress in Physics*, 72, 096601.
58. Vicsek, T., & Zafeiris, A. (2012). Collective motion. *Physics Reports*, 517, 71–140.
59. Laurell, T., Petersson, F., & Nilsson, A. (2007). Chip integrated strategies for acoustic separation and manipulation of cells and particles. *Chemical Society Reviews*, 36, 492–506.
60. Xu, T., et al. (2015). Reversible swarming and separation of self-propelled chemically powered nanomotors under acoustic fields. *Journal of the American Chemical Society*, 137, 2163–2166.
61. Grossman, D., Aranson, I. S., & Jacob, E. B. (2008). Emergence of agent swarm migration and vortex formation through inelastic collisions. *New Journal of Physics*, 10, 023036.
62. Ingham, C. J., & Jacob, E. B. (2008). Swarming and complex pattern formation in *Paenibacillus* vortex studied by imaging and tracking cells. *BMC Microbiology*, 8, 36.
63. Ahmed, D., et al. (2017). Neutrophil-inspired propulsion in a combined acoustic and magnetic field. *Nature Communications*, 8, 770.

Chapter 8

Colloidal Microrobotic Swarms



Qian Zou, Yibin Wang and Jiangfan Yu

8.1 Introduction

Swarms consisting of living animals widely exist throughout nature. Various types of patterns and structures are formed by thousands or even millions of individual creatures, purely through local communications, such as bacteria colonies, bird flocks and insect swarms. These animals can change their swarm patterns through communication, in order to adapt to the ambient environments they interact with. In the past two decades, researchers are dedicated in developing robotic swarms by learning from natural swarm intelligence, aiming to realize complex tasks that are overwhelming for a single robot. It is well known that macroscale robotic swarms have been applied in many areas, including cargo allocation, terrain mapping and entertainment industry, and the small-scale swarms consisting of a large number of microrobotic agents can also play important roles in critical areas, such as biomedicine.

The actuation and control strategies for individual untethered microrobots were developed two decades ago. Driven by external physical fields, microrobots are capable of performing complex tasks at the microscale, such as micromanipulation, targeted drug delivery and even biopsy [1–3]. Drugs or cells (e.g. stem cells) can be loaded onto microrobots, and using external fields, they are navigated to pass through constrained environments towards targeted locations for in vivo localized

Q. Zou · Y. Wang

School of Science and Engineering, The Chinese University of Hong Kong, Shenzhen, Shenzhen, China

J. Yu (✉)

School of Science and Engineering, The Chinese University of Hong Kong, Shenzhen, Shenzhen, China

Shenzhen Institute of Artificial Intelligence and Robotics for Society, Shenzhen, China
e-mail: yujiangfan@cuhk.edu.cn

therapies [4–8]. However, the capacity of loading drugs, in vivo imaging feedback signal strength, the capability of resisting flow and motion dexterity of an individual microrobot may meet critical limitations, owing to the constraints of their small sizes and volumes. Therefore, microrobotic swarms begin to attract worldwide extensive attention recently. By applying swarm control, drug dose that can be delivered at one time increases significantly [9, 10], and feedback signal of medical imaging systems [11], motion dexterity and robustness against external disturbances can be enhanced.

To date, to realize pattern control and motion control of a microrobotic swarm is still challenging [12–15], due to the inaccessibility of integrating onboard processors, sensors and actuators onto each of microrobotic agents. Therefore, the physical and/or chemical among the agents needs to serve the role of “wireless communication” [16], which still requires further investigation. Colloidal systems are ideal simplified models to study swarm behaviours, because the systems are homogeneous, the agents are isotropic, and the agent-agent interactions can be modelled. To date, progresses have been made. Generating a stable pattern is the first step in swarm pattern control. Previously, it has been reported that functionalized Janus particles could self-assemble into complex predefined lattices or synchronization-selected microtubes [17–19]. Controllable and reversible process of forming ribbon-like and ring-like structures, using colloidal silica rods coated with hemicylindrical magnetic layers, have been reported [20]. In addition, optical fields [21, 22], ultrasound [23], magnetic fields [24, 25] and chemical signaling [26] are capable of triggering formation of microrobotic swarm behaviours.

After forming a stable swarm pattern, how to control its motion is another critical issue. Magnetic fields are widely used for the motion control of microrobotic swarms, due to its high precision, high response frequency and good penetration to biological tissues. By forming a dynamically stable swarm and realizing its translational locomotion as an entity, the targeting rate of delivery, motion flexibility and controllability can be enhanced. It has been reported that magnetic microparticles exhibited spontaneous formation of dynamic localized snake-like patterns in an alternating magnetic field [27]. The pattern was formed on a liquid-air interface, and its motion is controllable. After 2017, the controllability of microrobotic swarm features, e.g. generation, pattern reconfiguration and motion control, has been significantly improved [28–30]. Two major research purposes are focused with the development of microrobotic swarms, i.e. fundamental investigation for guiding principles and rules that govern the swarm behaviours [31], and developing promising swarms that are practical for different applications, especially biomedical applications, such as minimally invasive surgeries [32, 33].

In this chapter, we will firstly summarize swarm behaviours driven by different external physical fields, including magnetic, electric, optical and acoustic fields. In addition, swarms triggered by chemical signaling will also be reviewed. Then, we will focus on two types of magnetic field-driven swarms, i.e. vortex-like swarms and ribbon-like swarms. The governing principles, control strategies and potential biomedical applications will also be reviewed.

8.2 Field-Driven Microrobotic Swarms

Swarm behaviours of micro-/nanorobots driven by magnetic fields have been intensively investigated. Tiny structures, such as magnetic particles, nanorods, helices and magnetotactic bacteria, have been used as microrobotic agents for swarms. Magnetic fields have fast response to input current, are easy to be tuned on-demand and have good penetration to biological tissues. Magnetotactic bacteria (MTB) with flagella can perform locomotion at low Reynolds number fluids, and due to the magnetosome chains inside their bodies, their moving direction can be controlled by tuning external magnetic fields. A swarm of MC-1 bacteria gathered using magnetic field gradients could perform micromanipulation and assembly of complex planar structures in fluids (Fig. 8.1A1), indicating the high precision of magnetic field-driven swarms [15]. The colloidal asters from suspended magnetic microparticles could be formed at liquid-liquid interfaces (Fig. 8.1A2), under a high-frequency oscillating magnetic field. The aster-like swarms could perform reversible pattern opening/closing and targeted locomotion. Similarly, the field can also trigger the formation of snake-like swarms. They spontaneously broke the symmetry of surface flow and generated asymmetric vortices at their tips, and thus, they were capable of propelling themselves (Fig. 8.1A3). Recently, the patterns of particle swarms floating at an air-liquid interface could be controlled in a time-varying manner, using arrays of permanent magnets [34]. The equilibrium of magnetic interactions and surface tension was reached, which resulted in the swarm pattern generation (Fig. 8.1A4). The swarms were capable of passing through complex and confined environments and were highly reconfigurable for cooperative manipulation tasks.

Electric fields can trigger swarm behaviours of polarized agents. The generation of electric field-driven swarms is significantly influenced by the electrical properties of the agents and their surround media. In general, the mechanisms of the swarm behaviours can be categorized into two types, i.e. electrostatic interactions and electrohydrodynamics. Yan et al. reported various collective states of metal-dielectric Janus colloids were reconfigured by introducing electrostatic imbalance (Fig. 8.1B1) [35]. The phenomenon was caused due to the different polarization of metal and dielectric hemispheres colloids in AC electric fields. Dipolar interactions between particles were negligibly weak at low frequencies (\sim kHz), due to strong ionic screening effects. In this state, the particles were in a gas-like state. At moderate frequencies (20–50 kHz), ionic screening effects were reduced, and the dipolar repulsion between metallic hemispheres led to the formation of coherent swarms. At MHz-level frequencies, ions barely responded to high-frequency oscillating field, and thus the particles formed chains through head-to-tail dipolar interactions. In a sufficiently high-strength DC electric field, a kind of electrohydrodynamics phenomenon, i.e. Quincke rotation, will be induced when particles are less conductive compared with their surrounding liquid. The curved trajectories of the rolling particles resulted from their asymmetric shape, and the trajectory curvature was related with the applied electric field strength (Fig. 8.1B6). At a low particle

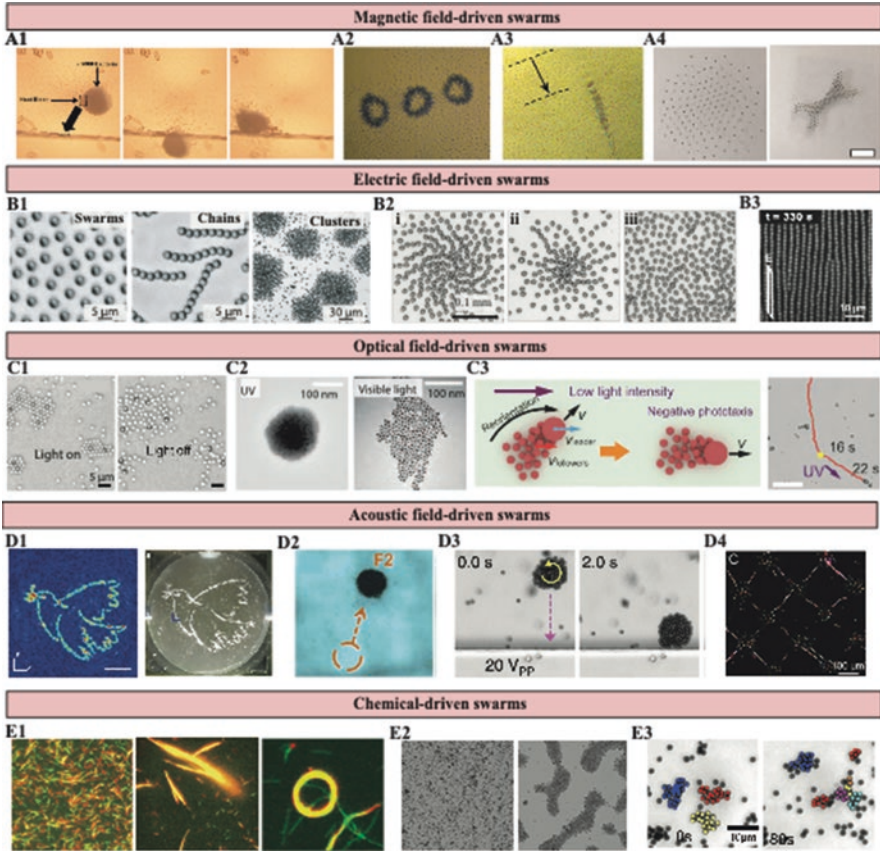


Fig. 8.1 (A) Magnetic field-driven swarms. (A1) Micromanipulation using a swarm of magnetotactic bacteria [15]. (A2) Self-assembled magnetic asters formed at a liquid-liquid interface [10]. (A3) Self-propulsion of a snake-like swarm [27]. (A4) Pattern formation of microrobots on a liquid-air interface driven by permanent magnets [34]. (B) Electric field-driven swarms. (B1) Swarms, chains and clusters formed by Janus particles [35]. (B2) Local ordering of pear-shaped particles in (i) “heads-out” vortex, with the particles oriented away from the vortex centre; (ii) “heads-in” vortex, with the particles oriented towards the vortex centre; and (iii) rotating flocks, with the particles synchronously pointing in one direction while the flock itself rotates [36]. (B3) Formation of sheet-like and chain-like patterns of polymer particles in electric fields [37]. (C) Optical field-driven swarms. (C1) Active $\text{TiO}_2/\text{SiO}_2$ Janus particles and passive silica particles form reversible crystal patterns due to the catalytic decomposition of hydrogen peroxide under UV light [38]. (C2) Reversible aggregation of functionalized gold nanoparticles induced by UV light, due to photoisomerization, which disassembles by applying visible light [39]. (C3) Negative and positive phototaxis of a hierarchical swarm at low and high UV light intensity, respectively [40]. (D) Acoustic-driven swarms. (D1) By applying a 3D-printed transmission hologram, desired phase information is encoded onto the hologram surface, and precise micromanipulation can be realized [41]. (D2) Controlled movement of a nanomotor swarm [23]. (D3) A particle swarm formed by a rotating magnetic field can move towards a wall in an acoustic field [42]. (D4) Experimental results of SSAW-assisted nanowire patterning technique [43]. (E) Swarms triggered by chemical signaling. (E1) Linear and circular swarms can be formed using rigid and soft DNA-functionalized microtubules, respectively, with the presence of linker DNA [44]. (E2) Reversible generation of gold microparticle swarms induced by adding or removing hydrazine [26]. (E3) Dynamic swarming of self-propelled gold colloids with half-spherical platinum covers. The coloured particles indicate the exchanges between different clusters [45]

concentration, the particles formed a vortex swarm. They aligned their directions away from the vortex centre when electric field strength was lower while pointing towards the centre when the strength was higher. With a high particle concentration and a strong field strength, the particles formed rotating flocks. Charged polymer spheres exhibited different crystalline phases, due to the counterbalance between charge repulsion and dipolar attractions (89). Applying a uniaxial and a biaxial electric field, the particles were further self-assembled into strings (1D) and sheets (2D), respectively (Fig. 8.1B3) [37].

Microrobotic agents with light-sensitive properties can form swarms under specific optical stimuli. Local ionic concentration gradient induces diffusiophoretic attraction to trigger swarm behaviours, e.g. the assembly of passive silica particles onto active $\text{TiO}_2/\text{SiO}_2$ Janus particles to form dynamic crystals (Fig. 8.1C1) [38]. One of the key principles for assembling functionalized gold nanoparticles is photoisomerization of azobenzene. Few azobenzene ligands can be decorated onto nanoparticles to enable their reversible formation of metastable crystals with the illumination of UV and visible light (Fig. 8.1C2). In addition, a high concentration of azobenzene ligands resulted in irreversible and permanently cross-linked structures [39]. Phototaxis is an intelligence existing in many natural creatures. Light-driven swarms mimicking phototactic behaviours have been reported recently. A hierarchical swarm consisting of a large TiO_2 particle and several small SiO_2 particles exhibiting positive or negative phototaxis was demonstrated, which depended on the direction and intensity of the applied UV light (Fig. 8.1C3) [40]. The particle swarm stopped moving or exhibited phototactic characteristics when UV light was vertical to the experimental plane or applied sideways, respectively.

Acoustic fields can also trigger swarm behaviours of microrobotic swarms. Through modifying acoustic waves, holographic techniques were applied for complex patterning of microrobotic agents (Fig. 8.1D1) [41]. A 3D-printed transmission element whose material had a sound transmission speed different from the surrounding medium was made for the hologram. The special structure reconstructed diffraction-limited acoustic pressure fields and changed the ultrasound waves. Manipulation with a precision at the microscale and assembly of particles into arbitrary static patterns were realized assisted by acoustic holograms. Reversible assembly and controlled movement of chemically powered nanomotor swarms were demonstrated (Fig. 8.1D2) [23], as well as the separation of spherical Janus motors and Au-Pt nanowires. The applied acoustic pressure exerted by the acoustic fields is the main reason for the migration of the nanomotor swarms. By tuning the acoustic frequency, the moving direction can be controlled as well. Ahmed et al. reported the neutrophil-inspired propulsion of superparamagnetic microparticle swarms in a channel (Fig. 8.1D3) [42]. Superparamagnetic microparticles experienced dipole-dipole interactions and aggregated into spinning swarms in a rotating magnetic field. Acoustic fields were applied in order to provide forces to pull the swarms to a solid boundary. Due to the wall effect, i.e., the viscosity near a solid boundary is larger than that far from it, the swarm was moved along the wall. Besides acoustic field gradient, standing surface acoustic wave (SSAW) was also used for nanopatterning tasks. Dispersed nanowires in suspension and on solid substrate can be

tuned to form patterns using SSAW [43]. The vibrations caused by SSAW induced a nonuniform charge distribution on the substrate, which generated electric fields from positive charges to negative charges. Because of dielectrophoresis effect, the metallic nanowires were aligned and patterned, e.g. parallel and perpendicular arrays (Fig. 8.1D4).

Besides the aforementioned physical interactions, chemical signaling is also an important method for regulating interactions among agents for swarm formation. Chemical-based or molecular-based binding, such as antibody-antigen and DNA-based binding, is highly selective. DNA-functionalized microtubes can move on a kinesin-coated substrate with the presence of adenosine triphosphate (ATP) [44]. When linker DNA was added, the microtubes moved towards each other and formed swarms with increasing sizes (Fig. 8.1E1). The larger swarms maintained their translational motion with a velocity close to that of individual microtubes. When flexible microtubes were applied, the swarms will perform circular motion, which has no crosstalk with mixed rigid microtubes, indicating the high selectivity of DNA-based linking. The concentration gradient of electrolytes enables ion exchanges, and in some cases, the diffusion coefficients (i.e. diffusing speed and diffusivity) of cations and anions are different. Therefore, a local electric field is generated, resulting in electrophoretic motion of the particles and electroosmotic motion of the fluid. Hydrazine can trigger reversible swarm behaviours of gold microparticles in hydrogen peroxide solution (Fig. 8.1E2) [26]. The reaction between hydrogen peroxide and hydrazine was catalysed by gold surface, and H^+ , N_2H_5^+ and OH^- were generated. The induced local electric field acted phoretically on the nearby gold particles (i.e. electrophoretic motion), pulling them towards the highest electrolyte concentration (centre of the swarm). Meanwhile, electroosmotic effect also pumped the fluid towards the particles. The combination of these two effects resulted in the formation of particle swarms. Gold microparticles half-coated with platinum layers will dynamically cluster with the presence of hydrogen peroxide (Fig. 8.1E3) [45]. Upon the addition of H_2O_2 , particle clusters coexisting with spread particles (gas phase) appeared. The clusters dynamically merged and disassembled with particles moving in and out.

8.3 Vortex-Like Swarms

In order to realize the formation of colloidal swarms, two critical types of interactions can be utilized, i.e. medium-based interactions and field-induced agent-agent interactions. Medium-based interactions indicate the interactions exerted via fluid, interface and boundaries, while agent-agent interactions indicate the interactions exerted among different agents.

As our previously published results [30], theoretically, paramagnetic nanoparticles are likely to perform a chain structure by attracting the adjacent particles. Thus, the nanoparticle chain is considered as the minimum block in the following analysis. This minimum unit will generate a local fluidic vortex. Figure 8.2 shows

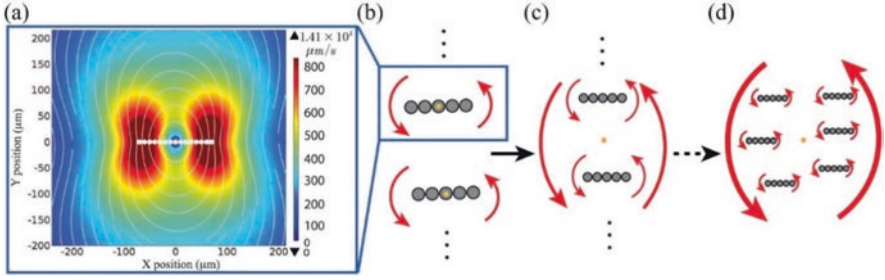


Fig. 8.2 Merging process of the vortices. (a) Local flow induced by a rotating particle chain with a frequency of 5 Hz, while the magnitudes of velocity field are illustrated by colour profile. (b)–(d) Paramagnetic nanoparticles are indicated by the grey circles, the red arrows represent induced velocity flows, the thicker red arrows denote vortex flows with higher velocity magnitude, and the yellow spots are the co-rotating centres of these chains

simulation results of this process. As shown in Fig. 8.2a, the flow velocity near two edges is higher than those near the centre where the velocity magnitude of flow is zero. The velocity field induced by individual rotating chains is shown by white lines. The following formula presents the vorticity ξ of a flow field:

$$\vec{\xi} = \nabla \times \vec{\mu} = \left(\frac{\partial u_z}{\partial y} - \frac{\partial u_y}{\partial z}, \frac{\partial u_x}{\partial z} - \frac{\partial u_z}{\partial x}, \frac{\partial u_y}{\partial x} - \frac{\partial u_x}{\partial y} \right) \quad (8.1)$$

where $\vec{\mu}$ denotes velocity distribution and u_x , u_y and u_z are the three components of $\vec{\mu}$ along the three axes of Cartesian coordinates. If the flow is confined in a two-dimensional vortex, Eq. (8.1) can be simplified as follows:

$$\vec{\xi} = \left(\frac{\partial v_y}{\partial x} - \frac{\partial v_x}{\partial y} \right) \vec{z} \quad (8.2)$$

According to its definition, circulation Γ is the line integral around a closed curve of the velocity field. Thus, it can be presented as:

$$\Gamma = \oint_C \vec{u} \cdot d\vec{l} = \int_A \vec{\xi} \cdot \vec{n} \, ds \quad (8.3)$$

where A represents a reducible closed surface and C is the surface contour. The relationship between vorticity and the angular velocity of the vortex ω can be mathematically shown as $\xi = 2\omega$. VPNS is regarded as the core region of the vortex with a rigid rotation. Thereby, we can estimate the vorticity of VPNS.

8.3.1 Vortices Merging

The merging process of vortices which is induced by the rotating particle chains strictly determines the generation of a VPNS, as depicted in Fig. 8.2b–d. Firstly, the particle chains are dispersed in the fluid. They rotate around their chain centre when they are subjected to a rotating magnetic field, which leads to a vortex. This vortex generates long-range attracting forces which attract the adjacent chains. Therefore, the distances between each chain are reduced compared with original distance. Once the distance between two rotating chains is lower than a predefined threshold, they rotate around the same axis, and they begin to merge. Figure 8.2b, c shows the schematic illustration of the merging process. The pair of chains rotates around their centre. The thicker red arrows in Fig. 8.2c represent a stronger flow field after the merging of two vortices. Moreover, the vortex generated by the pair chains can also merge with other vortices, which leads to a huge system with dynamic equilibrium. This means more larger vortices will be generated after merging. In the internal part of a stable VPNS, the schematic depiction of forces exerted on i th chain is displayed in Fig. 8.3. These forces include a repulsive fluidic forces F_{i+1}^v induced by short-range interaction within two vortices, a magnetic repulsive force F_{i+1}^r induced by $i + 1$ th chain and an internal force F_i^a inwardly generated by the vortex flow. The resultant force of the three dynamical-equilibrium forces is a centrifugal force which enables the rotation of the i th chain around the swarm centre.

If the separation distance d between two vortices is larger than the vortex core radius a , a slow viscous revolution is performed. Specifically, if the ratio of vortex core radius and distance is equal to a critical value $(a/d)_c = 0.3$, the merging process of vortices starts. The value of proposed ratio a/d will determine this merging process. Figure 8.4 shows a simulated merging phenomenon of two vortices and the distribution of two identical vortices. The advection of vorticity which is also known as the long-range attractive interaction propels the motion of vortices at the beginning. They move towards each other and instantly deformed into prolate shapes when two vortices begin to contact. Simultaneously, a diffusion phenomenon drives the vorticity field into one distribution, which is depicted in Fig. 8.4b. Figure 8.4c illustrates a third stage where the vortices coalesce into an elliptical shape and two strong filaments of vorticity eject. As shown in Fig. 8.4d, a circular axisymmetric vortex is produced in the final stage. Meanwhile, the filaments steadily roll up around the vortex core and dissipate. The simulation results can strongly support the hypothesis of merging phenomenon and VPNS generation.

8.3.2 Minimum Particle Concentration of Generating a VPNS

The minimum particle concentration to generate a VPNS is easily estimated with a known critical value $(a/d)_c$. The total mass M is computed as $M = C_0 V_0$, where C_0 is original suspension and V_0 indicates the volume. Thus, the total volume of

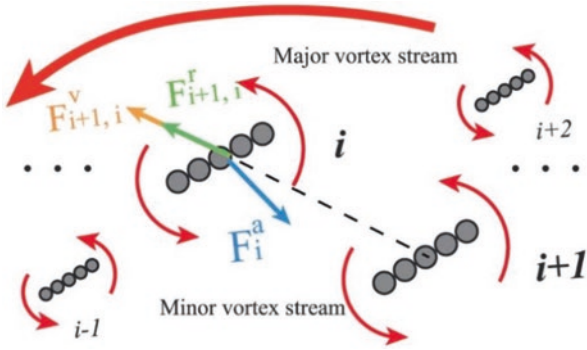


Fig. 8.3 Interaction forces exerted on the i th chain by the $i + 1$ th chain. The blue arrows are the inward fluidic force exerted by the major vortex stream, the yellow arrows denote a repulsive force by the short-range vortex-vortex interaction, and the green arrows represent a repulsive magnetic force

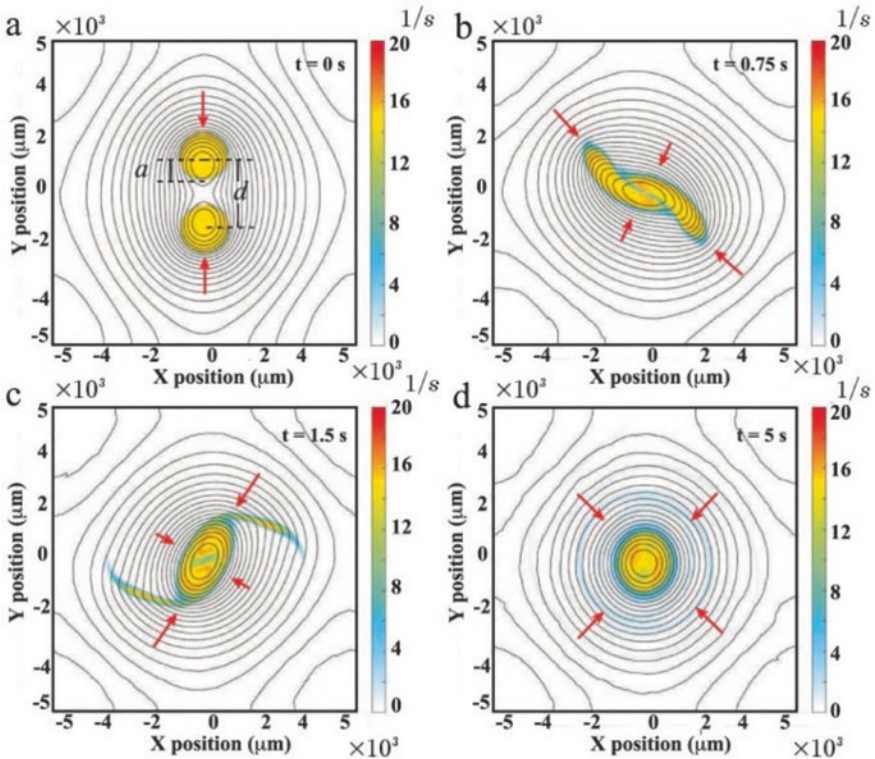


Fig. 8.4 Simulation results of the merging process of two identical vortices. The vorticity field is shown using the colourmap. Initially, $a/d = 0.3$, vortices radius is $800 \mu\text{m}$, and vorticities distribution is uniform. a denotes the core radius of each vortex, while d indicates the relative distance between two vortices. The direction of fluidic pressure at the points is illustrated by red arrows

Table 8.1 Key parameters used in the calculation of the minimum nanoparticle concentration for generating a VPNS

Parameter	Value
C_o	4.5 $\mu\text{g}/\mu\text{l}$
V_o	12 μl
ρ	5180 kg/m^3
r_c	5 μm
h	50 μm
$(ald)_c$	0.3

nanoparticles is $V_p = M/\rho$, with the density of magnetite ρ . Then, the average volume of each nanoparticle chain is estimated using $V_c = \pi r_c^2 h$; here, r_c is cross-section radius, and h implies an estimated height with a Mason number model at 10 Hz [46]. Therefore, the total number of nanoparticle chains is computed as $N_c = V_o/V_c$ under an assumption that the chains are uniformly and densely distributed. Finally, the minimum nanoparticle concentration is calculated to be 3.2 $\mu\text{g}/\text{mm}^2$ using these parameters in Table 8.1.

8.4 Characteristics of a VPNS

It is significantly important to investigate the characteristics of a VPNS for tough robotics tasks. Those characteristics include the motion equation and the fluidic interactions inside or outside the vortex core. Before introducing the equation of motion, the momentum equation in an internal frame of reference is expressed as follows:

$$\frac{D\bar{u}}{Dt} = \frac{\partial\bar{u}}{\partial t} + (\bar{u} \cdot \nabla)\bar{u} = \frac{-\nabla P}{\rho} + \frac{\nabla \cdot \tau}{\rho} + \bar{g} \quad (8.4)$$

where \bar{u} is flow velocity distribution, P denotes a local pressure, ρ is a local fluid density, τ is stress tensor, D/Dt represents Lagrangian derivative, and the body forces per unit mass are indicated as \bar{g} . Equation (8.4) can be rewritten as:

$$\frac{\partial\bar{u}}{\partial t} + \nabla \left(\frac{\bar{u} \cdot \bar{u}}{2} \right) - \bar{u} \times \bar{\xi} = \frac{-\nabla P}{\rho} + \frac{\nabla \cdot \tau}{\rho} + \bar{g} \quad (8.5)$$

by utilizing $(\bar{u} \cdot \nabla)\bar{u} = \nabla \left(\frac{1}{2} \bar{u} \cdot \bar{u} \right) - \bar{u} \times \bar{\xi}$. By taking the curl, Eq. (8.5) can be expressed as:

$$\begin{aligned} \frac{D\bar{\xi}}{Dt} &= -\bar{\xi} (\nabla \cdot \bar{u}) + (\bar{\xi} \cdot \nabla)\bar{u} + \frac{1}{\rho^2} \nabla_\rho \times \nabla P \\ &\quad - \frac{1}{\rho^2} \nabla_\rho \times (\nabla \cdot \tau) + \frac{1}{\rho} \nabla \times (\nabla \cdot \tau) + \nabla \times \bar{g} \end{aligned} \quad (8.6)$$

In this case, the flow is regarded as a Newtonian fluid with consistent density and viscosity. Thus, the second, fourth, fifth and seventh parts of Eq. (8.6) can be neglected. By using $\nabla \cdot \tau = \mu \nabla^2 \bar{u}$, a simplified equation is given as:

$$\frac{D\bar{\xi}}{Dt} = (\bar{\xi} \cdot \nabla) \bar{u} + \nu \nabla^2 \bar{\xi} \quad (8.7)$$

where ν denotes fluidic kinetic viscosity. Despite of the mathematical expression of Equation [7], there is physical diffusion phenomenon. The Lamb-Oseen vortex is a typical example. During this diffusion process, a two-dimensional axisymmetric vortex is placed in an initially inviscid and infinite fluid. Based on Eq. (8.7), a clarified equation is written in a following form:

$$\frac{\partial \bar{\xi}}{\partial t} + (\bar{u} \cdot \nabla) \bar{\xi} = (\bar{\xi} \cdot \nabla) \bar{u} + \nu \nabla^2 \bar{\xi} \quad (8.8)$$

The Oseen vortex is two-dimensional, which means that $\nabla \bar{u}$ is confined into a two-dimensional plane. Since $\bar{\xi}$ is perpendicular to this plane, the third term of Eq. (8.8) is considered as zero. Additionally, a radially directed $\nabla \bar{\xi}$ is orthogonal to purely tangential \bar{u} , which leads to a vanished second term. Therefore, Eq. (8.8) can be simplified as:

$$\frac{\partial \xi_z}{\partial t}(r, t) = \nu \nabla^2 \xi_z(r, t) \quad (8.9)$$

The Poisson equation can be solved with a similarity variable solution $\xi_z = f(\eta)/t$, here, $\eta = r / \sqrt{\nu t}$, and r denotes the separation distance from the vortex core. The approximate solution is shown as following:

$$\xi_z(r, t) = \frac{\Gamma_0}{4\pi\nu t} \exp\left(-\frac{r^2}{4\nu t}\right) (r > R) \quad (8.10)$$

$$u_\theta = \left(\frac{\Gamma_0}{2\pi r}\right) \left[1 - \exp\left(-\frac{r^2}{4\nu t}\right)\right] (r > R) \quad (8.11)$$

where u_θ denotes the tangential velocity distribution, R is the radius of the vortex core, and Γ_0 represents the original circulation of the vortex. The proposed model clearly illustrates the ambient flow generated by a VPNS for the following reasons: [1] because of fluid vorticity, the vorticity decays with the decreased distance to the VPNS core; [2] the inertia forces could be neglected, and the laminar Navier-Stokes equation can be applied in this model; [3] there are no axial or radial velocities generated in this model, and the rotating frequency is fixed.

Since the core of VPNS is propelled by the external magnetic field, the vorticity of the core part will not decay. Thus, hypotheses that the VPNS core performs rigid rotation, vorticity maintains an identical value in the core part, and the velocity distribution and the distance to the core part have a linear relationship are pre-defined. Thereby, the mathematical formula of vorticity and velocity distribution can be calculated as:

$$\xi_z = \frac{\Gamma_0}{\pi R^2}(r < R) \tag{8.12}$$

$$u_\theta = \frac{\Gamma_0 r}{2\pi R^2}(r < R) \tag{8.13}$$

The vortex can be demonstrated with the proposed model of tangential velocity and vorticity, as depicted in Fig. 8.5a, b, respectively. This model is used to analyse a VPNS with a radius of 8×10^{-4} m. The flow tangential velocity presents a linear increase and vorticity maintains constant in VPNS core ($r < 8 \times 10^{-4}$ m). However, the flow tangential velocity performs a gradual decrease, and the vorticity presents a rapid decline (approximately decrease to 1/s at 1.5 mm apart from the core centre). To straightforwardly illustrate the velocity distribution of the whole system, a schematic diagram is depicted in Fig. 8.5c. The magnitude of the flow velocity is represented by the size of the arrows. The red arrows denote the velocity distribution in the vortex core, while the blue ones represent the same parameter in the ambient

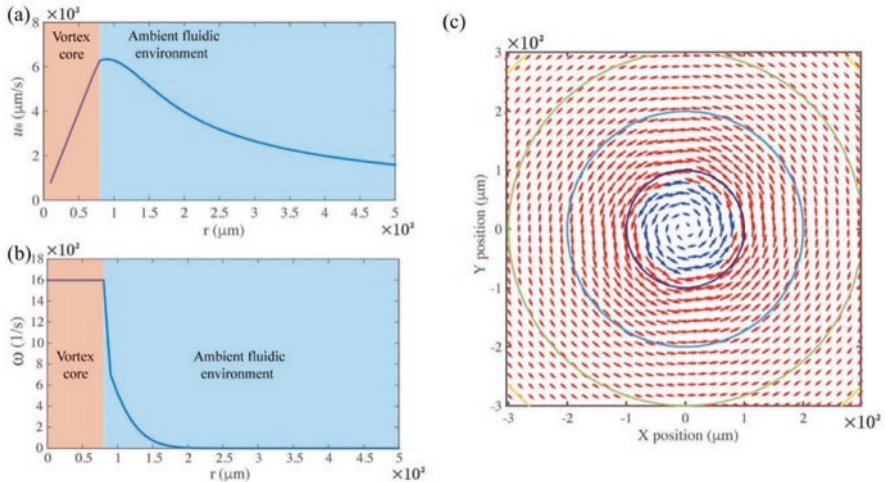


Fig. 8.5 Tangential velocity distribution (a) and vorticity distribution (b). (c) depicts the tangential velocity of vortex. The blue arrows denote the flow inside vortex core, while the red arrows represent that outside the core. The magnitude of flow velocity is denoted by the arrow size and the gradient of vortex vorticity is represented by coloured circles

flow. As shown in Fig. 8.5a, c, we conclude that the tangential velocity of the flow reaches the maximum value approximately at the edge of VPNS core.

8.5 Pattern Transformation of VPNS

8.5.1 Core Size Modification

It is necessary to alter the core size of VPNS if it encounters a complex fluidic environment such as there are some microchannels with various diameters. Theoretically, we know the circulation is an integration given by $\Gamma = \oint_c \vec{u} dl$. Thus, if we take the derivative:

$$\frac{d}{dt} = \frac{d}{dt} \oint_c \vec{u} dl \quad (8.14)$$

Based on Kelvin's theorem:

$$\Gamma_a = \Gamma + f_c A_n \quad (8.15)$$

where f_c is the Coriolis parameter and A_n denotes the area of the vortex. By taking the derivative of Eq. (8.15), we can get $\frac{d\Gamma}{dt} = -f_c \frac{dA_n}{dt}$. Combining previously mentioned equations, we can further obtain:

$$\frac{d}{dt} 2\pi r u = -f_c \frac{d}{dt} \pi r^2 \quad (8.16)$$

According to the circulation conservation, the circulation of VPNS maintains the same value although the size is changing:

$$2\pi r u + \pi f_c r^2 = 2\pi r_0 u_0 + \pi f_c r_0^2 \quad (8.17)$$

where u_0 and r_0 , respectively, represent the initial tangential flow velocity and the initial radius of the vortex core. Thus, the mathematical relationship between the coverage area of the pattern and the rotating frequency can be expressed by:

$$w = \frac{f_c (r_0^2 - r^2) + 2v_0 r_0}{2r^2} \quad (8.18)$$

Notably, the experimental section will discuss the comparison and analysis between the theoretical model and experimental results.

8.5.2 Spread State

Since a VPNS is able of performing pattern swelling, they can be utilized as reconfigurable robotic end effector. As previously illustrated in Fig. 8.2, these chains perform a dynamic balance inside a stable VPNS. This is because the three major forces, namely, the magnetic repulsive forces, vortex short-range interactions which are activated by single-chain rotation and inward vortex forces induced by the major vortex, are dynamically balanced. The swarm swelling is merely confined by inward vortex forces which maintain the vortex-like pattern of the swarm. The vorticity and inward forces have an approximately linear relationship. This means that reducing vorticity will cause a decrease of inward forces, which will further cause a decrease of rotating frequency. The magnetic forces dominate the behaviour of this particle swarm when the inward forces decline, which means that the VPNS pattern is capable of swelling with high flexibility.

However, long chains will develop if we only reduce the rotating frequency of the input magnetic field f_i . This is due to the attractive interactions between head-to-tail chains. These long chains will cause predominantly modified vortices and a vanishment of vortex-like swarm. Increasing the input magnetic field f_i is one of those approaches to avoid this situation. Their rotating frequency f_{cr} declines due to the step-out behaviour of rotating chains, which will cause the change of inward vortex forces. Thereby, it is required to investigate the relationship between the input magnetic field f_i and the rotating frequency f_{cr} . This enables the estimation of swelling area of a VPNS in the spread state.

To estimate the rotating frequency of a step-out paramagnetic particle chain, a schematic demonstration is shown in Fig. 8.6. At the initial stage, the long axis of the chain coincides with the direction of the external magnetic field at position 1 (P1) depicted in Fig. 8.6a. The field and chain rotate with angular velocity ω_f and ω_c , respectively. When magnetic field rotates θ_f and reaches position 2 (P2), the direction of the chain is coincidentally perpendicular to the direction of magnetic field. This leads to a 90° phase lag. When θ_1 exceeds 90° , the chain performs a counter-wise rotation due to the paramagnetic nature of the particles, which means that the chain rotates in a reverse direction compared with its original direction. Meanwhile, the magnetic field maintains the same direction which is clockwise (shown in Fig. 8.6b). Eventually, the chain and the magnetic field obtain coincidence again. The reverse angle of the chain is θ_b , which is depicted in Fig. 8.6c. A whole step-out cycle is demonstrated using Fig. 8.6. We predefine t_1 , t_2 as the time where the phase lag changes from position 1 to position 2 and from position 2 to position 4 and θ_p as the rotating angle of the chains. Thus, they can be expanded as the following equations:

$$t_1 = \frac{\pi / 2}{2\pi(f_i - f_{cr})} \quad (8.19)$$

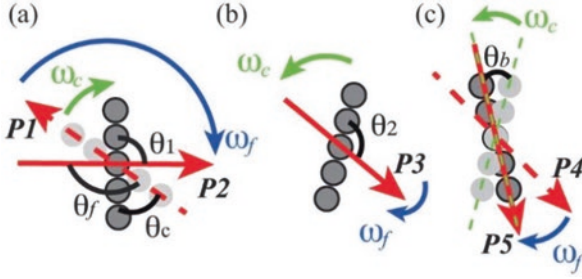


Fig. 8.6 Step-out rotating process of a paramagnetic nanoparticle chain. The green arrows indicate the angular velocity of particle chain ω_c , while the blue ones denote the rotating magnetic field ω_f . The direction of magnetic field is denoted by red dotted arrows, and the particle chain at the last moment is represented by the lighter grey particles. The chain rotates θ_c , whereas the field rotates θ_f in (a). In (a)–(b), θ_1 and θ_2 denote the phase lag at different moments. The chain rotates reversely with an angle θ_b , shown in (c)

$$t_2 = \frac{\pi / 2}{2\pi(f_f + f_{cr})} \quad (8.20)$$

$$\theta_p = \theta_c - \theta_b = \frac{\pi f_{cr}^2}{f_f^2 - f_{cr}^2} \quad (8.21)$$

$$T_0 = t_1 + t_2 = \frac{f_f}{2(f_f^2 - f_{cr}^2)} \quad (8.22)$$

where $\theta_c = \omega_c t_1 = \frac{\pi f_{cr}}{2(f_f - f_{cr})}$, $\theta_b = \omega_c t_2 = \frac{\pi f_{cr}}{2(f_f + f_{cr})}$, $f_{cr} = \frac{\omega_c}{2\pi}$ represents the rotating frequency of chain, and $f_f = \frac{\omega_f}{2\pi}$ denotes the rotating frequency of the

field. Since there are $N = \frac{2\pi}{\theta_p}$ cycles in a round (2π). Therefore, the average frequency of a step-out chain is shown as follows:

$$f_r = \frac{1}{NT_0} = \frac{f_{cr}^2}{f_f} \quad (8.23)$$

To obtain the relationship between input rotating frequency and the inward vortex forces, it is necessary to make the following assumptions: [1] the inward vortex forces are proportional to the rotating frequency of the vortex f_v ; [2] the vortex and the input rotating frequency have a linear relationship.

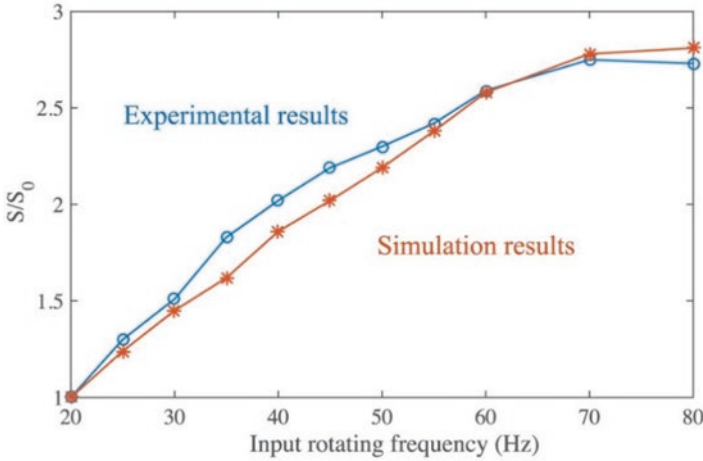


Fig. 8.7 Experimental and simulation results of changing ratio of pattern area in spread state. The area when input rotating frequency is 20 Hz is represented by S_0

We use COMSOL to conduct the simulation during which the short chains are considered as single particles. At the beginning, magnetic repulsive forces will be exerted between the particles. Meanwhile, the pattern will swell because the high input rotating frequencies cause the decline of inward vortex forces. Therefore, we can estimate the change of inward vortex force by combining Eq. (8.23) and the proposed hypotheses. When the chain rotates at their step-out frequencies (20 Hz), it reaches the maximum inward vortex force. During the simulation, we apply an inward vortex force to balance the magnetic repulsive forces when the input rotating frequency is 20 Hz. The reason on applying this inward force is to maintain the particles confined in the original regions. Consequently, we can estimate the maximum inward vortex forces. Additionally, they can also be estimated utilizing the changing ratio of the applied rotating frequencies since they are proportional to the rotating frequency of VPNS. Figure 8.7 shows the results of changing regions with different inward forces applied. These forces can be regarded as the inward vortex forces. Practically, the input rotating frequency f_i is not identical to the rotating frequency f_v of a VPNS and, mostly, $f_i > f_v$. Therefore, these two values should be calibrated rather than directly applying the input rotating frequency f_i . Section 5.3 will introduce the calibration approaches. Both curves of simulation and experimental results climb with the increase of input rotating frequency after this calibration. Before the input frequency reaches 70 Hz, the curve of simulation presents a linear increase. It levels out after the frequency reaches 70 Hz. Similarly, the curve of experimental results performs a climb when the frequency is low (20–45 Hz), and it gradually maintains the approximately same value when the frequency presents a continuous increase. Both simulation results and experimental results reach a value of 2.7 when the frequency reaches 80 Hz. Table 8.2 shows the core parameter which is applied in the simulation process, such as magnetic susceptibility χ_p , permeability μ_0 , the volume of the particles V_p and the magnetic field strength B .

Table 8.2 Key parameters used in the simulation to estimate the swelling pattern areas in spread state

Parameter	Value
λ_p	0.8
Original area of VPNS	$3.6 \times 10^{-7} \text{ mm}^2$
μ_0	$1.257 \times 10^{-6} \text{ V}\cdot\text{s}/(\text{A}\cdot\text{m})$
B	10^{-3} T
V_p	$2.12 \times 10^{-14} \text{ m}^3$

8.6 Experimental Results and Discussion

8.6.1 *Generating a Vortex-Like Swarm*

Figure 8.8 illustrates a generation process of a VPNS, where the nanoparticles are initially dispersed in the empty workspace. Then, we apply a rotating magnetic field. Firstly, it can be observed that the particle chain performs a self-rotation and next a highly concentrated region of particles is generated. Finally, a VPNS with dynamic equilibrium forms. We can also observe a self-rotation of particle chain in the peripheral area of the particle swarm. Meanwhile, they rotate around the vortex centre with the approximately equal radius. This is because the radial components of the interaction forces are dynamically balanced. When time t reaches 80s, the majority of particle chains aggregate into the vortex core, as shown in Fig. 8.8. However, some chains fail to be attracted due to the fluidic influence. Moreover, these particle chains are not attracted as a solid entity inside the cortex core. During the centripetal attraction process, some can be successfully attracted into the core, while the others are ejected because of centrifugal forces. To conclude, the vortex is a dynamically balanced system, which closely matches the theories discussed in Sect. 2.

Region I of Fig. 8.8 shows that the nanoparticles induce vortices using weak fluidic interactions at low rotating frequency (e.g. 2 Hz). This means that the nanoparticle can only perform chain-like structure. However, the coverage area does not shrink which is shown in the inset (6 mT, 2 Hz). The fluidic inward forces steadily increase when the frequencies reach 3 Hz. Region II (blue square) in Fig. 8.8 well illustrates this stage. The particle chains tend to aggregate into a smaller area with approximately 40% of them ejected. Simultaneously, the swarm is unstable due to their loose aggregation inside the VPNS, which is discussed previously. The VPNS forms in the region III, in which most particle chains are successfully aggregated. Lower strengths (4 mT) of magnetic field lead to a narrow range (3.5–5 Hz) of rotating frequency, while larger strengths (10 mT) can enlarge the range (4–10 Hz) of rotating frequency. When the strengths are higher than the upper red dotted line (region IV), the VPNS forms with much more loss again. This is because the fluidic forces are not capable of aggregating the majority of nanoparticle chains, which cause a smaller core. In region V, the nanoparticles tend to form multiple vortex-like swarms with a continuous increase of rotating frequency. This is because there is no dominating vortex that forms with the fluidic forces and chain lengths decrease. Consequently, some multiple vortices with much smaller size form.

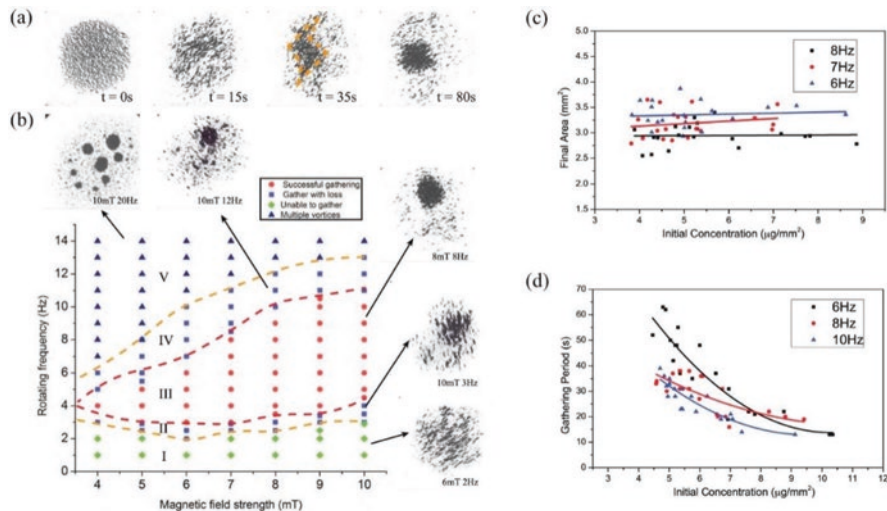


Fig. 8.8 (a) The generation process of a VPNS. (b) A successful formation of a dynamically balanced VPNS. It presents four different states of swarm, namely, successful aggregation, aggregation with loss, failure to aggregate and multiple vortices formation, shown in different icons. The red and yellow dotted curves are highlighted as boundaries of these four states. The figure insets show the experimental results. (c) The relationship between the initial concentrations and the final areas under the rotating fields with frequencies of 6, 7 and 8 Hz. The strength of magnetic field is valued as 8 mT and the data points fit the lines. (d) The aggregation periods with different initial concentrations and input rotating frequencies

8.6.2 Characterization of a VPNS

We conduct the aggregation process in region III in which the nanoparticles are successfully aggregated with different initial concentrations of particles and rotating frequencies to evaluate the effectiveness of this proposed approach. In fact, the same amount of particles and the same fixed initial conditions such as rotating frequencies, field strength and total amount of particles will lead to the same final areas of the patterns. Thus, different initial concentrations of nanoparticles cause different final areas of pattern, as illustrated in Fig. 8.8c. However, the curves maintain constant with the increase of initial particle concentration. The increasing rate of these curves is lower than 10%. The small increasing rate demonstrates that the final areas are weakly coupled with the initial concentrations, which shows the high efficiency of this method in aggregating dispersed paramagnetic nanoparticles. A lower initial concentration of particles leads to a larger initial coverage area if the amount of particles is equal. Since the fluidic forces are too low to successfully aggregate the particles in the peripheral region, the curves increase slightly.

As shown in Fig. 8.8c, the maximum rotating frequency 8 Hz leads to the minimum pattern, while the minimum rotating frequency 6 Hz leads to maximum final area. Circulation conservation which is expressed in Eq. (8.15) is a good

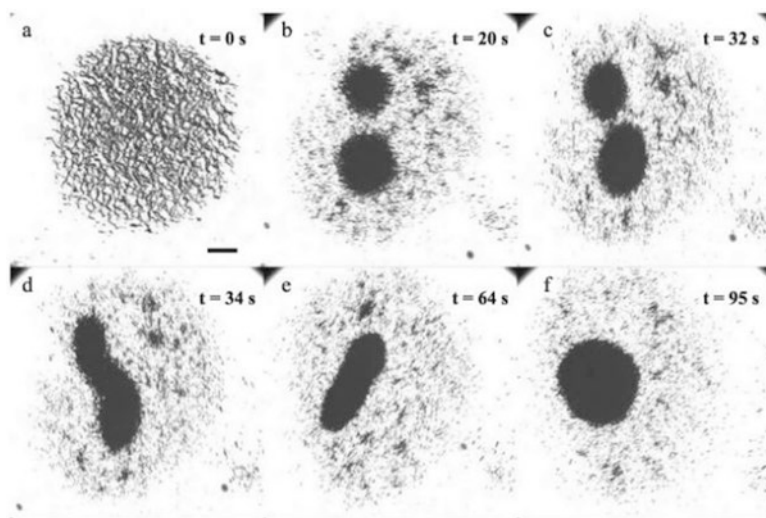


Fig. 8.9 Self-merging process of two individual VPNSs. The magnetic field strength is 7.5 mT, the rotating frequency is 8 Hz, and the scale bar is 500 μm

explanation of these results. Figure 8.8d shows the aggregation periods of the vortex-like swarm with different initial nanoparticle concentration. A higher initial particle concentration causes shorter average distance between particle chains. This also leads to the decrease of aggregation periods with initial particle concentration among the whole particle concentration range. Thus, it takes less time to attract particle chains towards each other before the merging process. The curves will gradually keep the equal value with initial concentration increases. Unfortunately, the results present some uncertainties due to the random assembly process. The uncertainties include different amounts of particle loss and measurement error of coverage areas. To statistically depict the principles of particle aggregation process, we use scatter diagrams and linear fitting. The self-merging process of two independent VPNSs is conducted to validate the simulation results. Figure 8.9 shows the experimental results. In the initial stage, a magnetic field which is located in region V (Fig. 8.8a) is applied and particles have a low suspended concentration ($5 \mu\text{g}/\text{mm}^2$). Two self-governed VPNSs have been generated during the experiments. The relative distance between the two VPNSs can reach the critical value $(a/d)_c$, illustrated in Fig. 8.8b. The distance of them will decrease gradually. The attractive fluidic interactions cause the deformation of them before they start to contact with each other. This is demonstrated in Fig. 8.8c. Figure 8.8d, e illustrates the merging process of the two swarms when they begin to contact. The merged swarm presents a prolate shape. The difference between long axis and short axis of the swarm performs a gradual decrease. An axisymmetric circular VPNS is finally generated. This means the simulation results closely match the experimental results.

8.6.3 Pattern Transformation of a VPNS

Change of Core Size

Using the blue curve in Fig. 8.10, the change of pattern area has been demonstrated. The final pattern area of swarm decreases with the rotating frequency increasing from 5 to 10 Hz. We use red circles to label the experimental results. The differences between the experimental data and the model are slightly low (approximately 5%) at lower rotating frequency (< 6 Hz). However, they reach more than 20% if the input rotating frequency is larger than 7 Hz. The inconsistency of rotating frequency causes this phenomenon. We assume that the frequency of rotating vortex f_v and the input frequency f_i are identically valued with a constant f_a in the mathematical model. To induce a vortex with a frequency of $f_v = f_a$, the input frequency of magnetic field should be larger than the threshold f_a . Thus, the experimental rotating frequency should be higher than those of the model for any changing ratio of pattern area.

The original mathematical equation is required to be modified if we demand a better estimation for changing ratio. It is difficult to attain the analytical model since the difference between the frequency of rotating vortex f_v and the input frequency f_i is the main error. Thus, it is calibrated using experimental data shown in Fig. 8.11. The reflection between two frequencies is given by the linear fitting lines. The model is modified by unifying two frequencies (f_v and f_i) based on the previous relationship. It is also illustrated using yellow curves in Fig. 8.11. The changing ratio can be estimated using this modified model with a higher performance among all frequency ranges.

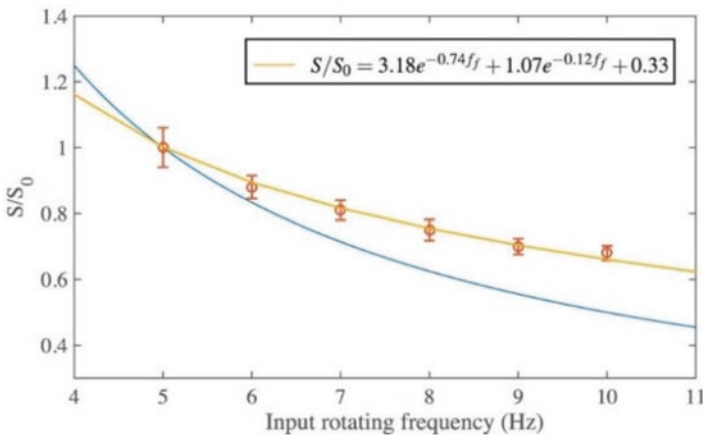


Fig. 8.10 The relationship between the pattern area and the input rotating frequency. The blue curve indicates the original model, and the yellow curve denotes the modified model. The red circles represent the experimental data. S_0 denotes the coverage area at rotating frequency of 5 Hz

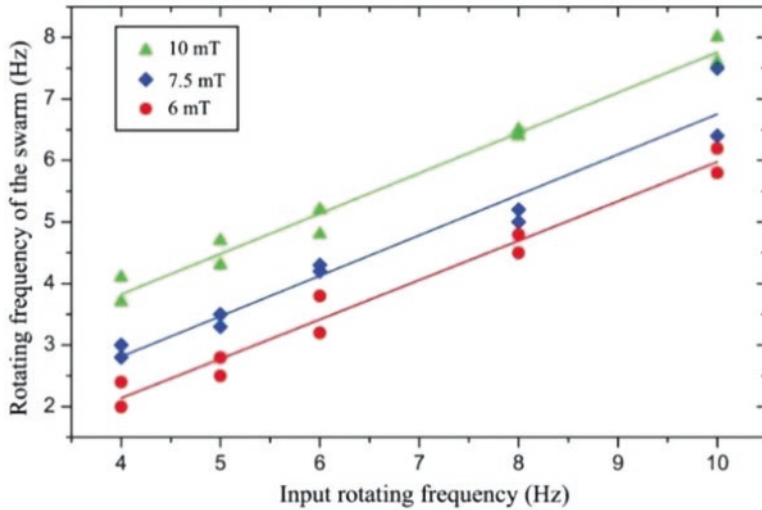


Fig. 8.11 Calibrated results between the input frequency and the rotating frequency of a VPNS. The relationship of them under field strength of 10 mT, 7.5 mT and 6 mT is denoted by green, blue and red lines

Spread State of VPNS

The pattern area is strongly relevant to the input frequency of magnetic field if a stable VPNS is generated. Figure 8.12 depicts the results in the frequency range of 0–90 Hz. Initially, the paramagnetic particles are dispersed and a VPNS is generated gradually. We predefine the original coverage area as S_0 and we choose 5 Hz as the original rotating frequency. With the increase of rotating frequency, the pattern area shrinks to $0.65S_0$. Then, the VPNS encounter a stable period with the rotating frequency ranging from 10 to 20 Hz. During this period, the pattern area keeps approximately same size. A VPNS with a high particle concentration forms within this frequency range, which is illustrated in the corresponding inset in Fig. 8.12. Interestingly, the VPNS performs a spread state when the rotating frequency exceeds 20 Hz (from 20 to 70 Hz). It swells three times larger than its initial area (from $0.65S_0$ to $1.85S_0$). A spindle-like pattern forms which is shown in the Fig. 8.12 inset. The frequency range where an effective VPNS can be generated with a stable contour and dynamically balanced characteristics is shown in Fig. 8.13 using red region. The step-out behaviour of particle chain causes a significant decrease of inward vortex forces during this spread state. Thus, we can observe some vital features of a dynamically balanced VPNS in this state. For example, few nanoparticle chains rotate around the vortex centre, the swarm contour is unstable, and it is difficult to remain the vortex-like structure during locomotion.

In fact, during the spread state, a high input frequency can propel a VPNS to enter the spread state, and reversely, the particle swarm can reform an effective VPNS once the input frequency is lower than 20 Hz. This reversed state is shown in

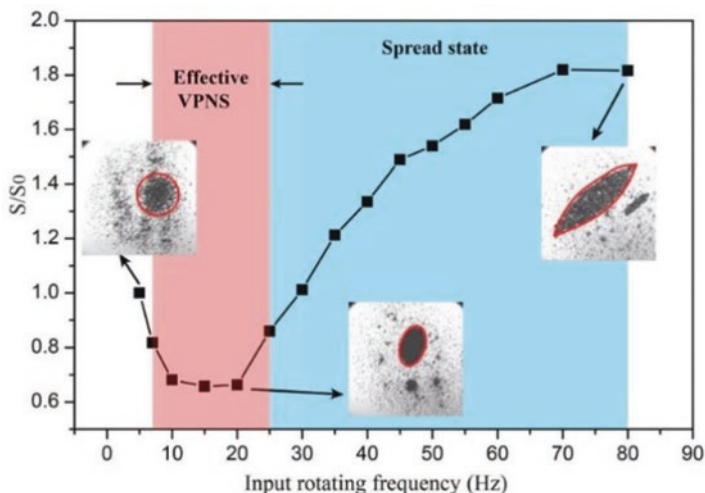


Fig. 8.12 The relationship between the pattern area and the input frequency. The red region represents a dynamically balanced VPNS which is assembled by paramagnetic nanoparticles with a stable contour. The spread state is denoted by the blue region. Three insets show the pattern area when the input rotating frequency is 5, 20 and 80 Hz with a field strength of 7.5 mT

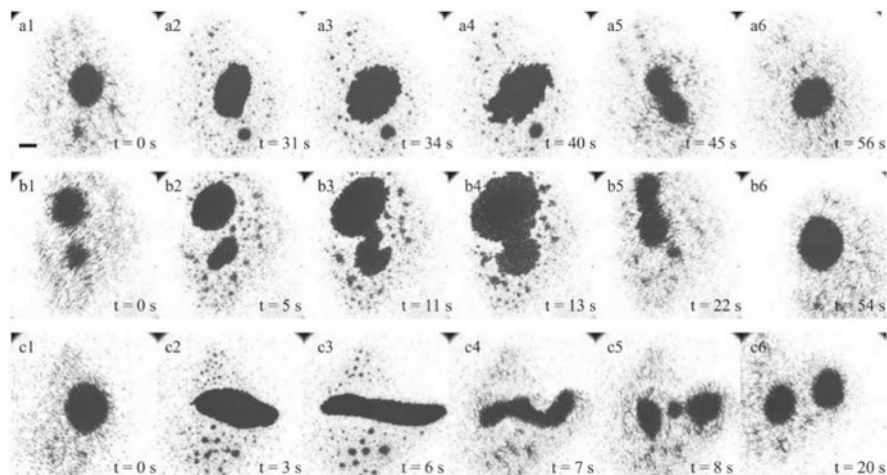


Fig. 8.13 Experimental results. (a1)–(a6) show the reversible state, (b1)–(b6) denote the merging process of two VPNSs, and (c1)–(c6) represent the splitting process of a merged VPNS. The field strength is 7.5 mT and the scale bar is 600 μm

Fig. 8.13a1–a6. We apply a rotating magnetic field with 8 Hz frequency to generate a VPNS, which is demonstrated in Fig. 8.13a1. The rotating frequency increases to 25 Hz at $t = 30$ s, which can trigger the spread state. Figure 8.13a2 shows that the VPNS pattern presents an immediate swelling after triggering. The swarm contour

becomes extremely unstable and shows a gear-like pattern when the input frequency continuously increases to 40 Hz at $t = 32$ s. This phenomenon is shown in Fig. 8.13a3, a4. At the final stage, the VPNS recovers the original state and presents a stable circular structure.

The parameter of the actuating rotating magnetic field locates in region V in Fig. 8.8 in the aggregation process, which leads to the generation of multiple vortex-like swarms. Motion control and path planning can be easily implemented if those vortex-like swarms can be merged into one dominating swarm. Figure 8.13b1–b6 shows this merging process. We apply a 12 Hz input rotating frequency, and the originally dispersed particles are transferred to two VPNSs. The condition of critical value $(a/d)_c$ is not reached since the self-merging phenomenon cannot remain more than 60 s. Therefore, we require a new strategy to merge the multiple vortices during the simulation. The input frequency reaches 40 Hz, and the pattern swells significantly at $t = 2$ s. Afterwards, the critical situation of the merging process during which two swarms start to contact with each other appears, which is demonstrated in Fig. 8.13b3, b4. The merging process completes after the input frequency declines to 6 Hz, illustrated in Fig. 8.13b5, b6.

As stated previously, the merging process is reversible. Figure 8.13c1–c6 demonstrates the reversely splitting process of merging. During this process, a dominating VPNS is split into two individual nanoparticle swarms with smaller size. To trigger the spread state, we apply an elliptically rotating magnetic field with an 80 Hz frequency. The strength along the short axis is three times higher than the strength along the long axis. This field can also enlarge the pattern area. Figure 8.13c2, c3 depicts the generation of a strip-shaped pattern. With the field frequency decreasing to 12 Hz, a circular rotating field forms again after $t = 6$ s. Figure 8.13c4 shows the distortion of the pattern. In fact, the spread state presents a shorter period if the recover frequency is low (8 Hz). This causes that the pattern will not be distorted and start to rotate around its centre. By applying a larger recover frequency, we can observe the splitting process. During this process, the particle chains shorten, and the influence range of vortex force is smaller. As illustrated in Fig. 8.13c5, c6, the swarm in different regions tends to aggregate locally. Finally, two VPNSs form.

8.6.4 Morphology of Swarm Pattern During Locomotion

Motion in a Synchronized Fashion

When an object starts to contact a wall, the drag coefficient increases. This causes unbalanced fluidic interaction forces which are exerted on different regions of this object. Therefore, the motion velocity of the main part of the object is larger than those of the other parts. By increasing the pitch angle of the input rotating frequency, the two-dimensional locomotion can be realized. Notably, the velocity of a moving VPNS and its morphology are significantly determined by the pitch angle,

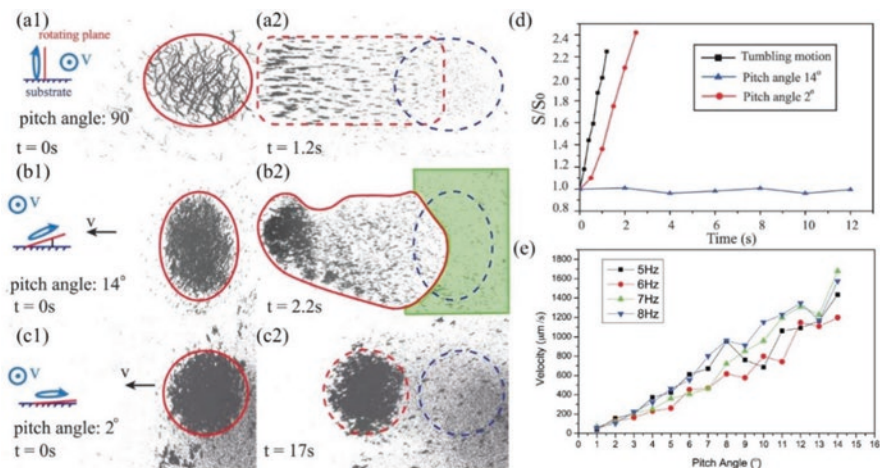


Fig. 8.14 Changes of swarm pattern morphology during the locomotion. The red circles in (a1), (b1) and (c1) show the original swarm shape, while the red dotted circles in (a2), (b2) and (c2) denote the final areas. The blue dotted circles in (a2), (b2) and (c2) show the original locations of the swarm. Spread particles in the green region are not initially located in the swarm; thus the region is not included into the area of the swarm. Schematic illustrations in (a1), (b1) and (c1) demonstrate the relationship between the applied magnetic field and the direction of the translational locomotion of the swarm. The VPNS moves perpendicular to the inclination direction of the magnetic field. The areal change in different motion modes with time is shown in (d), and the moving velocity of a VPNS with different pitch angles is shown in (e)

which is depicted in Fig. 8.14. The nanoparticle chains fail to form in an in-plane fluidic vortex if the value of pitch angle is 90° . The paramagnetic nanoparticle chain will attract each other head-to-tail in the tumbling motion. Thereby, there are many chains with different lengths. This causes different moving velocities of chains. Figure 8.14a1, a2 demonstrates an enlarged swarm pattern. The VPNS pattern cannot be remained and the vortex steadily decays if the value of pitch angle decreased to 14° . This is shown in Fig. 8.14b1, b2. If the pitch angle further decreases to 10° , the VPNS recovers its original morphology and a dynamic equilibrium can be remained in motion. As demonstrated in Fig. 8.14c1, c2, the majority of particle chains are confined inside the vortex core and move with a synchronized fashion when the value of pitch angle is lower than 2° . Figure 8.14b shows the changing ratios of the coverage area of swarm pattern. These ratios are propelled by rotating frequency with different values of pitch angle: 90° , 14° and 2° . The coverage area which can make tumbling motion presents a significant swelling over 90% in 1 s with a constant increasing rate. The coverage area performs a slow increase in 0.5 s and presents an equal increasing rate which is discussed before when the pitch angle is 14° . The dynamically balanced state cannot be remained since the vortical shape is unstable. Thus, this causes irregular fluidic interaction forces and a large loss of nanoparticles which is simultaneously out of control. The changing range of coverage area is less than 5% which explains a stable VPNS during the motion.

By controlling the morphology of VPNS, the delivery of nanoparticles can be realized synchronously. Next section will well demonstrate the critical input parameters. Using a larger pitch angle to actuate a swarm can lead to an elongated pattern and a higher translational velocity. However, this enlarged pattern will cause a low access rate and precision. Thus, it is necessary to actuate a particle swarm as a VPNS because the pattern is under control in the motion. Additionally, it can generate a higher access rate for a targeted delivery.

Figure 8.14e shows the velocities of a mobile VPNS. We have applied a rotating field with different frequencies and pitch angles to propel the VPNS. The translational velocities perform a linearly increasing relationship with its pitch angle. As shown in Fig. 8.14e, we can conclude that the translational velocity and the rotating frequency are loosely coupled. This is because a higher frequency splits chains into shorter chains, which make a constant translational velocity. Although the increased rotating frequency can make a faster velocity, the split chains dominate predominantly.

Tuneable Trapping Forces of VPNSs

The majority of particles will be constrained inside the core of VPNS since they are restricted by the fluidic trapping forces generated by VPNS. Therefore, the movement of the swarm can be considered as the motion of entire swarm. Moreover, it is required to investigate the fluidic trapping forces, because they affect the input parameters which influence the morphology of the swarm during locomotion. Multiple polystyrene marker microparticles are introduced to illustrate the tuneable trapping forces of VPNSs. Figure 8.15 shows the results. As shown in Fig. 8.15a1, b1, c1 and d1, the propelled VPNSs approach and trap the polystyrene marker microparticles which are randomly distributed. Due to the fluidic interaction, the VPNS will attract the microparticles. Figure 8.15a2, b2, c2 and d2 shows that the microparticles are trapped into the VPNSs' core. The parameters of propelling magnetic field used to collect microparticles in four cases are equal: the field strength is 6 Hz, the rotating frequency is 8 Hz, and the pitch angle is 5° . Figure 8.15a1–a3 demonstrates a successful trapping and transporting of multiple microparticles. The parameters of magnetic field in the transportation process are equal to those parameter during the collecting process. Since the VPNS maintains stable state, all cargos are successfully trapped by the VPNS during the motion. Then the input rotating frequency is decreased to 4 Hz and the other parameters remain having the same value. Figure 8.15b3 indicates that the inward vortex forces is reduced. This is because two microparticles leak from the core while three microparticles are initially trapped into the core. Increasing rotating frequency can enhance the inward trapping forces based on the comparisons of Fig. 8.15a1–a3 and b1–b3.

To increase the motion velocity of VPNS, the pitch angle is increased to 5° . Meanwhile, the field strength and rotating frequency remain the equal value in the case of Fig. 8.15a2, a3. However, it is incapable to trap all microparticles. Two microparticles eject from the core of vortex, which is depicted in Fig. 8.15c3. Comparing

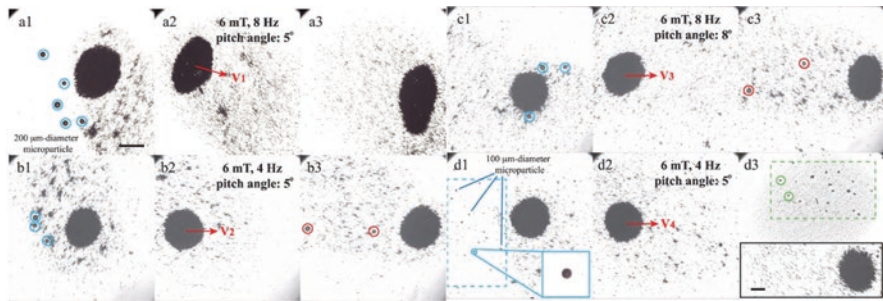


Fig. 8.15 Investigating the behaviours of non-magnetic marker microparticles under different conditions of magnetic fields with experiments to validate the trapping forces of VPNSs. The blue circles show the randomly distributed microparticles, red circles denote the leaking microparticles from the VPNS core, and the green circles are the trapped microparticles by the VPNS. The red arrows represent the velocity of VPNSs. The scale bar is $800\ \mu\text{m}$ and the scale bar of the inset is $500\ \mu\text{m}$

Fig. 8.15c1–c3 with a1–a3, the trapping capability of the VPNS is affected by the motion velocity of the background flow, and the stability of the vortical structure is weakened by a high velocity of the flow.

Furthermore, Fig. 8.15d1–d3 shows that microparticles with different inertia are applied. All the parameters of input magnetic field are equal to those parameters in the case of Fig. 8.15b3–b4 after collecting all smaller microparticles. As a result, the mobile velocity of VPNSs is equal ($V_4 = V_2$). Figure 8.15d3 illustrates that no microparticles eject from the core of VPNS. It is difficult to identify these small microparticles since nanoparticle swarm exists. It is necessary to apply a uniform magnetic field which is perpendicular to the experimental plane if we require an improvement of observation, shown in Fig. 8.15d3. The microparticles still remain inside the swarm. The microparticles with smaller inertial coefficients have a higher tendency to be trapped by the same VPNS by analysing Fig. 8.15d1–d3 and b1–b3. The experimental results closely match the results presented by mathematically analytical model and simulation. Therefore, the synchronized locomotion of VPNS can be ensured by higher input frequencies, smaller moving velocities and nanoscale of building blocks of the nanoparticle swarm.

Locomotion in a Channel

The VPNS can easily penetrate through a branched channel because of the morphology stability of a mobile VPNS. This process is illustrated in Fig. 8.16. A VPNS navigates from the left reservoir to the target one. As demonstrated in Fig. 8.16a1, it first locates at the entrance of a semicircle-shaped channel with two branches. Then, Fig. 8.16a2–a5 shows that it penetrates through the channel. The green spots in Fig. 8.16b1–b5 show the real-time locations of the VPNS in the channel. Furthermore, it is required for a VPNS to penetrate through an angled channel,

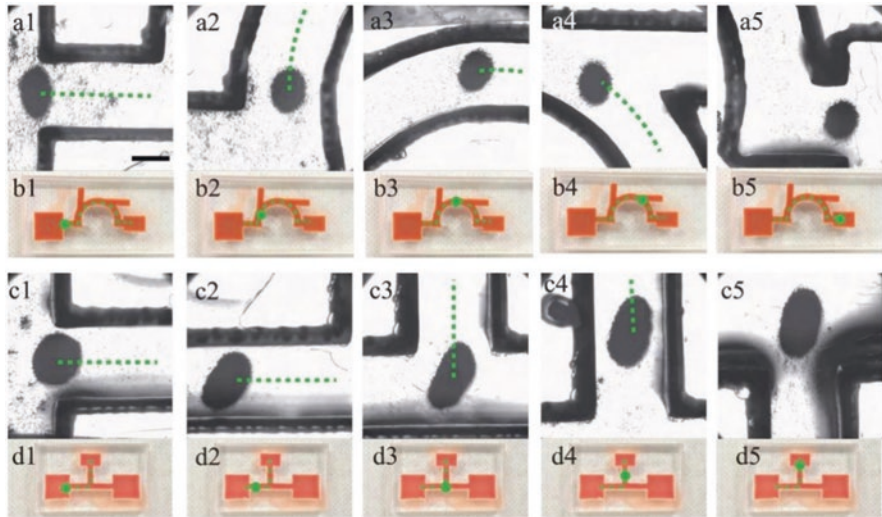


Fig. 8.16 Illustrations of propelling swarms to penetrate through two different microchannels. The VPNSs in semicircle-shaped and angled channels are shown by (a1)–(a5) and (c1)–(c5), respectively. (b1)–(b5) and (d1)–(d2) indicate an overall view of the semicircle-shaped and angled branched channels. The corresponding real-time locations of swarms are represented by green spots with an 800 μm scale bar

which is shown in Fig. 8.16c1–c5, and Fig. 8.16d1–d5 shows the channel. According to the figures proposed, the majority of nanoparticles can successfully reach the targeted reservoir although there are few fragments left inside the channel. An image processing application is utilized to compute the access rate of VPNS. We compare the areas of particle clusters reaching the target and those left inside the channel. Consequently, the particle swarm which can be regarded as a vortex-like entity has an extremely high accessing rate. It can, respectively, reach 91.6% and 96.8% for different cases in the semi-circular and angled channels.

We apply tumbling magnetic fields to propel the nanoparticle chains, during which the swarms elongate remarkably. The branches of channels cause extremely low access rate. Thus, few particles can reach target reservoir. Moreover, the access rate is lower than 10% in semi-circular channels, while it reaches 50% in the angled channel. These results show that the generation of dynamically balanced vortex-like swarm can ensure a high accuracy and precision of drug delivery for the target delivery applications.

Discussion on Imaging Modality

The proposed model can be used for imaging applications. Clinical MRI systems have following advantages, such as visualization of soft tissues and reduction of ionizing radiation exposure. In vivo particle tracking can be implemented due to its

high resolution. However, it also presents some drawbacks. For example, the rotation and translation of the particle swarm will be obstructed by its strong magnetic field. Thus, performing imaging of the motion is difficult. Practically, integration of additional coils is necessary to generate a rotating field with a constant field strength. Similarly, X-ray imaging can also cause some challenges for tracking VPNSs in vivo. The electromagnetic coils should be placed between the X-ray generator and receiver. However, the magnetic field will cause the distortion of the coils, which deteriorates the performance of X-ray imaging [47]. Moreover, although X-ray imaging can guarantee a milli-scale resolution, the long-time radiation exposure may be detrimental to patients. Hence, ultrasound imaging is regarded as an alternative approach for in vivo imaging. Ultrasound imaging uses two-dimensional ultrasound feedback to track the trajectory of objects by planning and steering the path to avoid dynamic obstacles [48]. Its resolution can reach 1–2 mm. It also has some merits such as low cost and avoidance of ionizing radiation. The approach for generating VPNS may be used to improve the imaging performance of ultrasound imaging. This is because the swarm size is capable to reach the tracking limitation by enlarging the amount of particles or applying particles with larger size.

8.7 Conclusion

This paper has discussed pattern generation, reversible merging, VPNSs splitting and navigated locomotion. The particles in VPNS chains make the swarm move as a dynamic entity because they perform synchronized motions. The models of generation process, the responses of the VPNS to the input frequency of the rotating magnetic fields and the spread state are independently illustrated. Notably, the corresponding experimental results closely match the models. The change of VPNS patterns such as the reversible merging process has been demonstrated. They can be flexibly controlled by applying magnetic field. Moreover, if the magnetic field has a small pitch angle, a VPNS can be actuated as a dynamic entity with a stable pattern. The trapping forces are illustrated with analysis and simulation of non-magnetic spheres' behaviour. It will critically affect the synchronized locomotion of the particle swarm. Finally, this paper demonstrates the penetration of VPNSs through the different channels with high accessing rates. The exploration of VPNS enables a fundamental investigation of microrobotic swarm behaviours. It can also be used for in vivo targeted drug delivery.

References

1. Nelson, B. J., Kaliakatsos, I. K., & Abbott, J. J. (2010). Microrobots for minimally invasive medicine. *Annual Review of Biomedical Engineering*, 12, 55–85.
2. Sitti, M., Ceylan, H., Hu, W., Giltinan, J., Turan, M., Yim, S., & Diller, E. (2015). Biomedical applications of untethered mobile milli/microrobots. *Proceedings of the IEEE*, 103(2), 205–224.

3. Zhang, L., Abbott, J. J., Dong, L., Kratochvil, B. E., Bell, D., & Nelson, B. J. (2009). Artificial bacterial flagella: Fabrication and magnetic control. *Applied Physics Letters*, *94*(6), 064107.
4. Peyer, K. E., Zhang, L., Kratochvil, B. E., & Nelson, B. J. (2010, May). Non-ideal swimming of artificial bacterial flagella near a surface. In *2010 IEEE international conference on robotics and automation* (pp. 96–101). IEEE.
5. Zhang, L., Abbott, J. J., Dong, L., Peyer, K. E., Kratochvil, B. E., Zhang, H., Bergeles, C., & Nelson, B. J. (2009). Characterizing the swimming properties of artificial bacterial flagella. *Nano Letters*, *9*(10), 3663–3667.
6. Petit, T., Zhang, L., Peyer, K. E., Kratochvil, B. E., & Nelson, B. J. (2012). Selective trapping and manipulation of microscale objects using mobile microvortices. *Nano Letters*, *12*(1), 156–160.
7. Folio, D., & Ferreira, A. (2017). Two-dimensional robust magnetic resonance navigation of a ferromagnetic microrobot using pareto optimality. *IEEE Transactions on Robotics*, *33*(3), 583–593.
8. Sadelli, L., Fruchard, M., & Ferreira, A. (2016). 2D observer-based control of a vascular microrobot. *IEEE Transactions on Automatic Control*, *62*(5), 2194–2206.
9. De Lanauze, D., Felfoul, O., Turcot, J. P., Mohammadi, M., & Martel, S. (2014). Three-dimensional remote aggregation and steering of magnetotactic bacteria microrobots for drug delivery applications. *The International Journal of Robotics Research*, *33*(3), 359–374.
10. Snezhko, A., & Aranson, I. S. (2011). Magnetic manipulation of self-assembled colloidal asters. *Nature Materials*, *10*(9), 698–703.
11. Servant, A., Qiu, F., Mazza, M., Kostarelos, K., & Nelson, B. J. (2015). Controlled in vivo swimming of a swarm of bacteria-like microrobotic flagella. *Advanced Materials*, *27*(19), 2981–2988.
12. Li, J., de Ávila, B. E. F., Gao, W., Zhang, L., & Wang, J. (2017). Micro/nanorobots for biomedicine: Delivery, surgery, sensing, and detoxification. *Science Robotics*, *2*(4), eaam6431.
13. Becker, A., Onyuksel, C., Bretl, T., & McLurkin, J. (2014). Controlling many differential-drive robots with uniform control inputs. *The International Journal of Robotics Research*, *33*(13), 1626–1644.
14. Donald, B. R., Levey, C. G., Paprotny, I., & Rus, D. (2013). Planning and control for microassembly of structures composed of stress-engineered MEMS microrobots. *The International Journal of Robotics Research*, *32*(2), 218–246.
15. Martel, S., & Mohammadi, M. (2010, May). Using a swarm of self-propelled natural microrobots in the form of flagellated bacteria to perform complex micro-assembly tasks. In *2010 IEEE international conference on robotics and automation* (pp. 500–505). IEEE.
16. Vach, P. J., Walker, D., Fischer, P., Fratzl, P., & Faivre, D. (2017). Pattern formation and collective effects in populations of magnetic microswimmers. *Journal of Physics D: Applied Physics*, *50*(11), 11LT03.
17. Chen, Q., Bae, S. C., & Granick, S. (2011). Directed self-assembly of a colloidal kagome lattice. *Nature*, *469*(7330), 381–384.
18. Mao, X., Chen, Q., & Granick, S. (2013). Entropy favours open colloidal lattices. *Nature Materials*, *12*(3), 217–222.
19. Yan, J., Bloom, M., Bae, S. C., Luijten, E., & Granick, S. (2012). Linking synchronization to self-assembly using magnetic Janus colloids. *Nature*, *491*(7425), 578–581.
20. Yan, J., Chaudhary, K., Bae, S. C., Lewis, J. A., & Granick, S. (2013). Colloidal ribbons and rings from Janus magnetic rods. *Nature Communications*, *4*(1), 1–9.
21. Hong, Y., Diaz, M., Córdova-Figueroa, U. M., & Sen, A. (2010). Light-driven titanium-dioxide-based reversible microfireworks and micromotor/micropump systems. *Advanced Functional Materials*, *20*(10), 1568–1576.
22. Palacci, J., Sacanna, S., Steinberg, A. P., Pine, D. J., & Chaikin, P. M. (2013). Living crystals of light-activated colloidal surfers. *Science*, *339*(6122), 936–940.
23. Xu, T., Soto, F., Gao, W., Dong, R., Garcia-Gradilla, V., Magaña, E., Zhang, X., & Wang, J. (2015). Reversible swarming and separation of self-propelled chemically powered nanomotors under acoustic fields. *Journal of the American Chemical Society*, *137*(6), 2163–2166.

24. Diller, E., Pawashe, C., Floyd, S., & Sitti, M. (2011). Assembly and disassembly of magnetic mobile micro-robots towards deterministic 2-D reconfigurable micro-systems. *The International Journal of Robotics Research*, 30(14), 1667–1680.
25. Miyashita, S., Diller, E., & Sitti, M. (2013). Two-dimensional magnetic micro-module reconfigurations based on inter-modular interactions. *The International Journal of Robotics Research*, 32(5), 591–613.
26. Kagan, D., Balasubramanian, S., & Wang, J. (2011). Chemically triggered swarming of gold microparticles. *Angewandte Chemie*, 123(2), 523–526.
27. Snezhko, A., Belkin, M., Aranson, I.S. & Kwok, W.K. (2009). Self-assembled magnetic surface swimmers. *Physical Review Letters*, 102(11), 118103.
28. Yu, J., Wang, B., Du, X., Wang, Q. & Zhang, L. (2018). Ultra-extensible ribbon-like magnetic microswarm. *Nature Communications*, 9(1), 1–9.
29. Yu, J., Jin, D., Chan, K.F., Wang, Q., Yuan, K. & Zhang, L. (2019). Active generation and magnetic actuation of microrobotic swarms in bio-fluids. *Nature Communications*, 10(1), 1–12.
30. Yu, J., Yang, L., & Zhang, L. (2018). Pattern generation and motion control of a vortex-like paramagnetic nanoparticle swarm. *The International Journal of Robotics Research*, 37(8), 912–930.
31. Chaluvadi, B., Stewart, K.M., Sperry, A.J., Fu, H.C. & Abbott, J.J. (2020). Kinematic model of a magnetic-microrobot swarm in a rotating magnetic dipole field. *IEEE Robotics and Automation Letters*, 5(2), 2419–2426.
32. Felfoul, O., Mohammadi, M., Taherkhani, S., De Lanaude, D., Xu, Y.Z., Loghin, D., Essa, S., Jancik, S., Houle, D., Lafleur, M. & Gaboury, L. (2016). Magneto-aerotactic bacteria deliver drug-containing nanoliposomes to tumour hypoxic regions. *Nature Nanotechnology*, 11(11), 941–947.
33. Wang, B., Chan, K.F., Yu, J., Wang, Q., Yang, L., Chiu, P.W.Y. & Zhang, L. (2018). Reconfigurable swarms of ferromagnetic colloids for enhanced local hyperthermia. *Advanced Functional Materials*, 28(25), 1705701.
34. Dong, X., & Sitti, M. (2020). Controlling two-dimensional collective formation and cooperative behavior of magnetic microrobot swarms. *The International Journal of Robotics Research*, 39(5), 617–638.
35. Yan, J., Han, M., Zhang, J., Xu, C., Luijten, E. & Granick, S. (2016). Reconfiguring active particles by electrostatic imbalance. *Nature Materials*, 15(10), 1095–1099.
36. Zhang, B., Sokolov, A., & Snezhko, A. (2020). Reconfigurable emergent patterns in active chiral fluids. *Nature Communications*, 11(1), 1–9.
37. Leunissen, M. E., Vutukuri, H. R., & van Blaaderen, A. (2009). Directing colloidal self-assembly with biaxial electric fields. *Advanced Materials*, 21(30), 3116–3120.
38. Singh, D.P., Choudhury, U., Fischer, P. & Mark, A.G. (2017). Non-equilibrium assembly of light-activated colloidal mixtures. *Advanced Materials*, 29(32), 1701328.
39. Klajn, R., Wesson, P.J., Bishop, K.J. & Grzybowski, B.A. (2009). Writing self-erasing images using metastable nanoparticle “inks”. *Angewandte Chemie International Edition*, 48(38), 7035–7039.
40. Liu, W., Chen, X., Lu, X., Wang, J., Zhang, Y. & Gu, Z. (2020). From passive inorganic oxides to active matters of micro/nanomotors. *Advanced Functional Materials*, 30(39), 2003195.
41. Melde, K., Mark, A.G., Qiu, T. & Fischer, P. (2016). Holograms for acoustics. *Nature*, 537(7621), 518–522.
42. Ahmed, D., Baasch, T., Blondel, N., Läubli, N., Dual, J. & Nelson, B.J. (2017). Neutrophil-inspired propulsion in a combined acoustic and magnetic field. *Nature Communications*, 8(1), 1–8.
43. Chen, Y., Ding, X., Steven Lin, S.C., Yang, S., Huang, P.H., Nama, N., Zhao, Y., Nawaz, A.A., Guo, F., Wang, W. & Gu, Y. (2013). Tunable nanowire patterning using standing surface acoustic waves. *ACS Nano*, 7(4), 3306–3314.

44. Keya, J.J., Suzuki, R., Kabir, A.M.R., Inoue, D., Asanuma, H., Sada, K., Hess, H., Kuzuya, A. & Kakugo, A. (2018). DNA-assisted swarm control in a biomolecular motor system. *Nature Communications*, 9(1), 1–8.
45. Theurkauff, I., Cottin-Bizonne, C., Palacci, J., Ybert, C. & Bocquet, L. (2012). Dynamic clustering in active colloidal suspensions with chemical signaling. *Physical Review Letters*, 108(26), 268–303.
46. Van Reenen, A., de Jong, A.M., den Toonder, J.M. & Prins, M.W. (2014). Integrated lab-on-chip biosensing systems based on magnetic particle actuation—a comprehensive review. *Lab on a Chip*, 14(12), 1966–1986.
47. Choi, J., Jeong, S., Cha, K., Qin, L., Li, J., Park, J. & Park, S. (2010). Positioning of micro-robot in a pulsating flow using EMA system. In *2010 3rd IEEE RAS & EMBS International Conference on Biomedical Robotics and Biomechatronics* (pp. 588–593). IEEE.
48. Vrooijink, G.J., Abayazid, M., Patil, S., Alterovitz, R. & Misra, S. (2014). Needle path planning and steering in a three-dimensional non-static environment using two-dimensional ultrasound images. *The International Journal of Robotics Research*, 33(10), 1361–1374.

Chapter 9

Shape-Programmable Magnetic Miniature Robots: A Critical Review



Chelsea Shan Xian Ng, Changyu Xu, Zilin Yang, and Guo Zhan Lum

9.1 Introduction

Shape-programmable robots are a new generation of soft machines that can produce desirable time-varying deformations upon command [1, 2]. A significant advantage of these robots is that they possess considerably higher degrees-of-freedom, agility, and adaptability than their traditional rigid counterparts [3–5]. As a result, shape-programmable robots have great potential to realize unprecedented mechanical functionalities [6–10], attracting substantial attention in the robotics community.

The shape-programmable robots are especially desirable at micro-/millimeter length scales because they can be much more dexterous and functional than traditional rigid miniature robots [6, 7, 11, 12]. For instance, shape-programmable miniature robots can be programmed to produce various modes of untethered soft-bodied locomotion, which allow them to negotiate across highly unstructured terrains [7, 11]. Such dexterity is therefore significantly higher than those of the untethered, rigid miniature robots, which have difficulties operating in such complicated environments [11, 12]. Likewise, these soft miniature robots are also able to realize mechanical functions that are unattainable by their rigid counterparts, and this has in turn enhanced their manipulation capabilities significantly [13, 14]. Examples of such functions include but are not limited to active gripping [15–17], reversible anchoring mechanisms [18], controllable cargo delivery mechanisms [19], and highly efficient fluid manipulations [6, 20]. It is highly desirable to create small-scale, shape-programmable robots because such devices can perform a wide range of small-scale manipulation tasks in highly confined and enclosed spaces [7, 15]. Due to this unique ability, scientists and engineers have hypothesized that such robots will have the potential to revolutionize biomedical applications such as

C. S. X. Ng · C. Xu · Z. Yang · G. Z. Lum (✉)

School of Mechanical and Aerospace Engineering, Nanyang Technological University, Singapore, Singapore

e-mail: gulum@ntu.edu.sg

minimally invasive surgery [21, 22] and targeted drug delivery [19, 23–25]. These miniature soft devices can also enable unprecedented bioengineering [14] and lab-on-chip applications [15, 26].

In general, shape-programmable miniature robots can be actuated by various stimuli such as magnetic fields [6, 7, 15, 27, 28], light [29–32], heat [17, 33–36], electric fields [37–39], chemicals [40–43], or pressure [44–46]. Magnetic actuation is especially promising among these methods because it offers more control parameters to the small robots [6, 47]. Unlike actuation methods such as heat, pressure, and chemicals, the actuating magnetic fields can be specified not only in magnitude but also in their directions and spatial gradients [5, 47–49]. Due to having more control parameters, the shape-programmable magnetic miniature robots have shown to be the most functional among the small-scale soft robots [6, 7]. Furthermore, since the actuating magnetic fields can harmlessly penetrate most biological materials [21, 22, 50], this type of robots is especially promising and compatible for biomedical applications [21, 22].

To create shape-programmable miniature robots that can be magnetically actuated, it is essential to first endow a desired magnetization profile into their bodies. A magnetization profile can be approximated as a collection of magnetic dipoles that are embedded in the robots' body. Based on the prescribed magnetization profile, the robots will experience a distribution of magnetic torques and forces along their bodies when actuating magnetic fields are applied. These induced torques and forces will in turn produce a spatially varying stress in the robots' body, allowing them to deform into another shape. By temporally varying the actuating magnetic field, shape-programmable magnetic miniature robots can therefore generate a series of time-varying shapes to enable their desired functionalities. In this chapter, we will review the fundamental actuation principles of shape-programmable magnetic robots that are in the micro-/millimeter length scales. A few notable shape-programmable robots in the centimeter length scale will also be included for a more complete discussion. We will also provide critical analyses on the key advancements and challenges in this technology. As we give an in-depth and detailed analysis of shape-programmable magnetic miniature robots, the contents here are therefore different from existing reviews that provide general discussions across a broad range of soft robots [3, 4, 11, 13, 51–53]. Our discussions are also significantly different from reviews that focus specifically on the applications or actuation principles of small-scale robots [5, 14, 21, 22, 54].

The organization of this book chapter is as follows: we first discuss the fundamental theory of shape-programmable magnetic miniature robots in Sect. 9.2. Subsequently, we highlight the key advancements of these robots in terms of their programming and fabrication methods in Sect. 9.3. This will be followed by Sect. 9.4, in which we discuss their achievable locomotion and mechanical functionalities. Additional discussions will be provided in Sect. 9.5, and Sect. 9.6 will conclude this chapter.

9.2 Theory

When shape-programmable robots are endowed with a desired magnetization profile, they will be able to produce a series of time-varying shapes when temporal actuating magnetic fields are applied. To allow scientists and engineers to better design and control these robots, it is essential to understand their physics. Hence, the fundamental actuation principles of shape-programmable magnetic miniature robots are derived, discussed, and explained in this section.

9.2.1 General Deformation Mechanics

When an external magnetic field (\vec{B}) is applied to the shape-programmable magnetic miniature robots, these robots will be able to deform and adopt another shape. Here we will analyze such phenomenon under quasi-static conditions, and the presented analysis will be general and applicable for shape-programmable robots that can produce 2D/3D deformations. Practical constraints will also be incorporated in our derivations. For instance, we assume that \vec{B} and its spatial gradients can be specified independently while obeying Gauss's law and Ampere's law [48, 49]. Unless specified otherwise, actuating magnetic fields will refer to both \vec{B} and its spatial gradients in the subsequent discussions. We also assume that the actuating magnetic fields are uniform across the robots' body as it will be difficult to create spatially variant fields at small-scale [48, 49].

To facilitate our discussions, we first explicitly express the magnetic field as $\vec{B} = (B_x \ B_y \ B_z)^T$, where the subscripts x , y , and z represent the Cartesian spatial coordinates of the global frame (Fig. 9.1a). Due to Gauss's law, the divergence of \vec{B} is always zero, and this implies that [48, 55]:

$$\frac{\partial B_x}{\partial x} + \frac{\partial B_y}{\partial y} + \frac{\partial B_z}{\partial z} = 0. \quad (9.1)$$

Similarly, Ampere's law dictates that when the workspace of the robot has no electrical current flowing through and if there is no rate of change of electric field with respect to time, the curl of \vec{B} will be a null vector [48, 56]. This implies that:

$$\frac{\partial B_z}{\partial y} = \frac{\partial B_y}{\partial z}, \quad \frac{\partial B_x}{\partial z} = \frac{\partial B_z}{\partial x}, \quad \frac{\partial B_y}{\partial x} = \frac{\partial B_x}{\partial y}. \quad (9.2)$$

The constraints by Eqs. 9.1 and 9.2 indicate that only five out of nine spatial gradients of \vec{B} are independent. By having these five independent spatial gradients and the three components of \vec{B} , the actuating magnetic fields are able to provide a total of eight independent control parameters [48, 49]. This is a significant

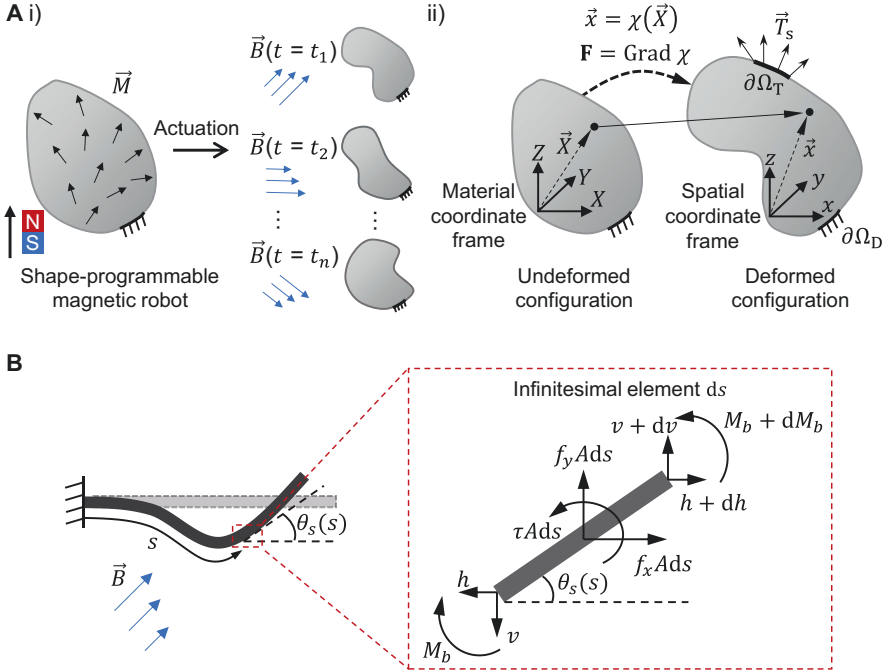


Fig. 9.1 Actuating principles of shape-programmable magnetic miniature robots. (a) (i) By applying temporally varying, actuating magnetic fields, the shape-programmable robot with a desired magnetization profile (\vec{M}) will generate a series of time-varying shapes. (ii) The deformation kinematics of the robot subjected to traction and displacement boundary conditions. (b) Analysis of a fix-free beam when it is under magnetic actuation

advantage over other actuation methods such as heat, pressure, and chemicals because they can only tune the intensity of their actuating signals [5]. By having more control parameters, magnetic actuation will be able to offer higher degrees-of-freedom to their shape-programmable robots, potentially allowing them to realize more sophisticated mechanical functionalities [6, 7, 15].

Once the actuating magnetic fields are applied in the workspace, they will interact with the robot’s magnetization profile (\vec{M}) to produce spatially varying stress along the robot’s body, allowing the robot to deform into another shape. By subjecting the robot to a time-varying, actuating magnetic field, the robot will therefore be able to generate a series of shapes across time (t), e.g., when $t = t_1, t_2, \dots, t_n$ (Fig. 9.1a-i). To understand the interaction between the actuating magnetic fields and \vec{M} , we first assign a material coordinate frame (\vec{X}) to the robot so that \vec{M} can be defined as a function of \vec{X} (Fig. 9.1a). When the robot undergoes deformation, each material point of the robot will be mapped to a corresponding point in the spatial coordinates of the global frame (\vec{x}) (Fig. 9.1a-i). The mathematical relationship between \vec{X} and \vec{x} can be represented by a smooth deformation mapping function (χ):

$$\bar{x} = \chi(\bar{X}). \quad (9.3)$$

Using the definition of χ , the deformation gradient tensor \mathbf{F} can be defined as [6]:

$$\mathbf{F} = \text{Grad } \chi, \quad (9.4)$$

where the operator, Grad, represents the gradient operator with respect to \bar{X} . Based on the deformation gradient tensor, the robot's magnetization profile in its deformed configuration, $\bar{M}_c(\bar{X})$, can be computed as [6, 57]:

$$\bar{M}_c = J^{-1} \mathbf{F} \bar{M}, \quad (9.5)$$

where J is the Jacobian of deformation gradient and it can be expressed as $J = \det(\mathbf{F})$. Using Eq. 9.5, the potential magnetic energy (per volume) of the deformed robot with reference to its material coordinate configuration, $W_{r, \text{magnetic}}$, can be computed as [56, 57]:

$$W_{r, \text{magnetic}} = -\bar{M}_c \cdot \bar{B} J = -\mathbf{F} \bar{M} \cdot \bar{B}. \quad (9.6)$$

Without any loss of generality, here we will assume that the shape-programmable robot has hard magnetic properties, and thus its magnetization is independent of \bar{B} . It is noteworthy that Eq. 9.6 is also applicable for robots with soft magnetic properties, but \bar{M} will be a function of \bar{B} in such scenarios.

In addition to $W_{r, \text{magnetic}}$, the deformed shape-programmable robot will also be able to store elastic potential energy. Such elastic energy (per volume) will be a function of \mathbf{F} , and it can be represented by $W_{r, \text{elastic}}$ with reference to the robot's material coordinate configuration. Depending on the material of the robot, $W_{r, \text{elastic}}$ can be computed by hyperelastic models such as the neo-Hookean [57, 58], Ogden [59], or Mooney–Rivlin models [60]. The summation of $W_{r, \text{magnetic}}$ and $W_{r, \text{elastic}}$ will form the Helmholtz free energy density (W_r) [56–58, 61]:

$$W_r = W_{r, \text{magnetic}} + W_{r, \text{elastic}}. \quad (9.7)$$

The robot's first Piola–Kirchhoff stress tensor, \mathbf{P} , can therefore be computed by partial differentiating the Helmholtz free energy density with respect to \mathbf{F} [57, 61]:

$$\begin{aligned} \mathbf{P} &= \frac{\partial W_r}{\partial \mathbf{F}} \\ &= \frac{\partial W_{r, \text{elastic}}}{\partial \mathbf{F}} - \bar{B} \otimes \bar{M}, \end{aligned} \quad (9.8)$$

where the operator \otimes denotes the dyadic product. The stress tensor, \mathbf{P} , is the stress experienced by the robot, expressed in the spatial coordinate frame but based on the robot's undeformed configuration. Because it will be more intuitive to analyze the

constitutive model with respect to the deformed configuration of the robot, the first Piola–Kirchhoff stress tensor will be converted into the Cauchy stress tensor ($\boldsymbol{\sigma}$) via the following mapping:

$$\begin{aligned}\boldsymbol{\sigma} &= \frac{1}{J} \mathbf{P} \mathbf{F}^T \\ &= \frac{1}{J} \frac{\partial W_{r,\text{elastic}}}{\partial \mathbf{F}} \mathbf{F}^T - \frac{1}{J} \vec{\mathbf{B}} \otimes \mathbf{F} \vec{\mathbf{M}}.\end{aligned}\quad (9.9)$$

If there are other body forces such as gravity acting on the robot, these forces and $\boldsymbol{\sigma}$ will have to satisfy the following quasi-static conditions:

$$\text{div } \boldsymbol{\sigma} + \vec{\mathbf{f}}_b = 0, \quad (9.10)$$

where $\vec{\mathbf{f}}_b$ denotes the body force (per unit volume), expressed in the spatial coordinate frame and based on the robot's deformed configuration. Note that $\vec{\mathbf{f}}_b$ will not include the distributed magnetic forces that are applied to the robot since the effects of these magnetic forces have already been accounted for by the divergence of $\boldsymbol{\sigma}$ [57].

Equation 9.10 represents the governing equation of the shape-programmable magnetic robot in which \mathbf{F} and χ can be solved based on the boundary conditions of the robot. In general, the robot can be subjected to displacement and traction boundary conditions [56, 57]:

$$\begin{aligned}\boldsymbol{\sigma} \cdot \vec{\mathbf{n}} &= \vec{\mathbf{T}}_s \quad \text{at } \partial\Omega_T \\ \text{and } \vec{\mathbf{u}} &= \hat{\vec{\mathbf{u}}} \quad \text{at } \partial\Omega_D,\end{aligned}\quad (9.11)$$

where $\partial\Omega_T$ and $\partial\Omega_D$ represent the boundaries where the traction and displacement boundary conditions are implemented, respectively (Fig. 9.1a-ii). The vector $\vec{\mathbf{n}}$ is the normal vector of the surface, and the vector $\vec{\mathbf{u}}$ represents the displacement vector induced by the deformation of the robot. The remaining vectors in Eq. 9.11, $\vec{\mathbf{T}}_s$ and $\hat{\vec{\mathbf{u}}}$, represent the required traction forces and displacements at their respective boundaries. Equations 9.10 and 9.11 form the general boundary value problem for shape-programmable magnetic miniature robots. Once \mathbf{F} and χ are solved from this boundary value problem, the shape of the deformed robot will be revealed. In general, it will be difficult to analytically solve this boundary value problem with a given set of $\vec{\mathbf{M}}$ and actuating magnetic fields. Hence, numerical methods are typically employed to solve such boundary value problems. As an example, Zhao et al. have proposed a nonlinear finite element analysis to solve this boundary value problem [57]. Specifically, they have adopted the neo-Hookean model to compute $W_{r,\text{elastic}}$ and assume that their robots have hard magnetic properties. By repeatedly solving the boundary value problem of Eqs. 9.10 and 9.11 with a $\vec{\mathbf{B}}$ discretized in small time steps, the numerical solution of Zhao et al. is able to reveal the time-varying shapes of their robots [57]. The simulation results of Zhao et al. are promising as

they agree well with experimental data [57]. Therefore, this suggests that the physics of shape-programmable magnetic robots can be modeled well, and it has the potential to guide scientists and engineers in designing and controlling such devices [57].

9.2.2 Deformation Mechanics of Shape-Programmable Magnetic Robots with Beam-Like Configurations

While the derivations in Sect. 9.2.1 are general, they can be further simplified in various scenarios. Here we will discuss how such simplifications can be accomplished when the shape-programmable robots assume beam-like configurations, since such highly functional devices have been very popular in recent years [6, 7, 62–64]. To make the discussions general, our analysis will be on beams with large deflections. In order to simplify our discussions, we will replace the tensor notations with simpler matrices and vectors in the subsequent derivations. Furthermore, instead of deriving the physics via the energy approach, we will use the more intuitive Newton-Euler approach here. Without any loss of generality, we will use a fix-free beam and a global spatial coordinate frame to explain the physics of such devices (Fig. 9.1b). We will also assume that the beam has a uniform width and its total length is L to further simplify this discussion.

The deformations of a large-deflection, magnetic beam can be fully described by its angular deflections, $\theta_s(s)$, where s is a spatial variable along the beam's length (Fig. 9.1b). In the undeformed configuration, the robot's magnetization profile can be expressed as $\vec{M}(s)$ in its material coordinate frame. Since bending is the dominant deformation of the beam, the robot will experience negligible stretch. Thus, this implies that the deformation gradient of the robot can be simplified into:

$$\mathbf{F} \approx \mathbf{R}_z = \begin{pmatrix} \cos \theta_s & -\sin \theta_s & 0 \\ \sin \theta_s & \cos \theta_s & 0 \\ 0 & 0 & 1 \end{pmatrix}, \text{ and } J = 1, \quad (9.12)$$

where \mathbf{R}_z represents the standard rotational matrix about the global coordinate frame's z-axis. When the robot undergoes a deformation, its magnetization profile in the deformed configuration, $\vec{M}_c(s)$, can be computed as [6]:

$$\vec{M}_c = \mathbf{R}_z(\theta_s) \vec{M}. \quad (9.13)$$

When the actuating magnetic fields are applied, an arbitrary infinitesimal element of the deformed robot will experience the following magnetic wrench (Fig. 9.1b):

$$\begin{aligned}
\tau &= [0 \ 0 \ 1](\vec{M}_c \times \vec{B}) = [0 \ 0 \ 1](\mathbf{R}\vec{M} \times \vec{B}), \\
f_x &= [1 \ 0 \ 0](\vec{M}_c \cdot \nabla)\vec{B} = [1 \ 0 \ 0]\{(\mathbf{R}\vec{M} \cdot \nabla)\vec{B}\}, \\
f_y &= [0 \ 1 \ 0](\vec{M}_c \cdot \nabla)\vec{B} = [0 \ 1 \ 0]\{(\mathbf{R}\vec{M} \cdot \nabla)\vec{B}\}.
\end{aligned} \tag{9.14}$$

The variable τ represents the induced magnetic torque (per volume), while f_x and f_y represent the x -axis and y -axis components of the magnetic force (per volume), respectively. In quasi-static conditions, the force balance equation for the infinitesimal element can be expressed as:

$$f_x = -\frac{1}{A} \frac{dh}{ds}, \quad f_y = -\frac{1}{A} \frac{dv}{ds}, \tag{9.15}$$

where A represents the cross-sectional area of the beam, while $v(s)$ and $h(s)$ represent the internal horizontal and vertical forces within the beam, respectively. Using the free end boundary conditions, Eq. 9.15 can therefore be rewritten as:

$$h = A \int_L^s f_x ds, \quad v = A \int_L^s f_y ds. \tag{9.16}$$

In a similar fashion, the torque balance equation for the infinitesimal element can be expressed as:

$$\tau A + v \cos \theta_s - h \sin \theta_s = -\frac{dM_b}{ds}, \tag{9.17}$$

where M_b represents the bending moment of the beam. Based on the Euler–Bernoulli beam theory, the mathematical relationship between the beam’s deformation and bending moment can be expressed as:

$$M_b = EI \frac{d\theta_s}{ds}, \tag{9.18}$$

where E and I represent the beam’s Young’s modulus and second moment of area, respectively. By substituting Eqs. 9.16 and 9.18 into Eq. 9.17, the governing equation for the magnetic beam can therefore be rearranged as [6]:

$$\tau + \left[\int_L^s f_y ds \right] \cos \theta_s - \left[\int_L^s f_x ds \right] \sin \theta_s = -\frac{EI}{A} \frac{d^2 \theta_s}{ds^2}. \tag{9.19}$$

The deformation of the robot, θ_s , can be determined by solving Eq. 9.19 with the fix-free boundary conditions:

$$\begin{aligned} \frac{d\theta_s}{ds} &= 0 \quad \text{at } s = L, \\ \theta_s &= 0 \quad \text{at } s = 0. \end{aligned} \quad (9.20)$$

Equations 9.19 and 9.20 form the boundary value problem for shape-programmable magnetic beams with fix-free boundary conditions. Similar to the general deformation mechanism, the time-varying shapes of such shape-programmable magnetic beams can be determined by repeatedly solving the boundary value problem of Eqs. 9.19 and 9.20 numerically with an actuating magnetic field discretized with small time steps. As demonstrated in various works [6, 7, 62], the physics indicated by Eqs. 9.19 and 9.20 is able to accurately predict the time-varying shapes of various shape-programmable magnetic miniature robots with beam-like configurations. A critical advantage of the boundary value problem of Eqs. 9.19 and 9.20 over the general one in Eqs. 9.10 and 9.11 is that the simpler beam mechanics can be solved much quicker because the numerical solution can converge easier. Although we have only presented the deformation mechanics of shape-programmable magnetic beams with fix-free boundary conditions, the boundary value problem of such robots can be derived similarly when they have different boundary conditions.

9.2.3 Rigid-Body Motion

If a shape-programmable magnetic miniature robot is untethered, it is also able to execute rigid-body motions in its deformed configuration. For instance, it will be possible to apply a magnetic torque (\vec{T}) to rotate the deformed robot:

$$\vec{T} = \iiint_V J^{-1} \mathbf{F} \vec{M} \times \vec{B} dV = \left(\iiint_V J^{-1} \mathbf{F} \vec{M} dV \right) \times \vec{B} = \vec{m} \times \vec{B}, \quad (9.21)$$

where \vec{m} and V are the net magnetic moment and volume of the deformed robot, respectively. In general, the deformed robot will rotate continuously until its net magnetic moment is aligned with the external \vec{B} [48, 49]. By exploiting this phenomenon, the deformed robot can therefore be rotated into its desired orientation via controlling the direction of \vec{B} . Likewise, magnetic forces (\vec{F}) can also be applied to translate the shape-programmable miniature robot:

$$\vec{F} = \iiint_V (J^{-1} \mathbf{F} \vec{M} \cdot \nabla) \vec{B} dV = \left[\frac{\partial \vec{B}}{\partial x} \frac{\partial \vec{B}}{\partial y} \frac{\partial \vec{B}}{\partial z} \right]^T \left(\iiint_V J^{-1} \mathbf{F} \vec{M} dV \right) = (\vec{m} \cdot \nabla) \vec{B}. \quad (9.22)$$

Applying \vec{T} and \vec{F} to the shape-programmable magnetic miniature robots can potentially be highly advantageous because this can enhance the robots' agility significantly. For example, shape-programmable magnetic robots, which can execute

jumping locomotion, can potentially jump higher and further after \vec{F} is applied [7]. Indeed, by allowing shape-programmable magnetic miniature robots to execute rigid-body motions, these soft machines are able to develop highly dexterous locomotive strategies, which can negotiate across various unstructured environments [7].

9.3 Programming and Fabrication Methods

Shape-programmable magnetic miniature robots have made tremendous progress in the last decade, especially in terms of their programming and fabrication methods. While programming conventionally involves the fabrication process in the literature [12, 65], here programming only refers to the process of identifying the required \vec{M} and actuating magnetic fields of the robots. We have distinguished fabrication from programming so as to make our discussions clearer. In this section, we discuss the key advancements of shape-programmable magnetic miniature robots in their programming and fabrication methods.

9.3.1 Programming Methods

To successfully realize the desired functionalities of shape-programmable magnetic miniature robots, it is critical to program their magnetization profiles and actuating magnetic fields correctly [6]. However, scientists and engineers are only able to rely solely on their intuition to approximate such programming processes before 2016 [65–74], because the physics of these machines is not well-understood then. As the programming process of such machines can be highly complicated, scientists and engineers have thus tried to simplify this process by adopting simple magnetization profiles and actuating magnetic fields when they design and control these robots. For instance, majority of the shape-programmable magnetic miniature robots are endowed with either uniform magnetization profiles [69, 71, 72, 74, 75] or discrete profiles that are assembled by several magnets [16, 28], as it is difficult to deduce the effects of having continuous, non-uniform magnetization profiles. Likewise, their actuating magnetic fields are relatively simple with either 2D rotating fields [62, 66] or magnetic fields that are discretized with a few time steps [65]. Although such simplifications can indeed create feasible shape-programmable magnetic miniature robots, the generated time-varying shapes of these devices are relatively simple, and thus they can only achieve limited functionalities [28, 65–68, 74, 76]. One of the most notable shape-programmable magnetic miniature robots that is created via human intuition will be the Taylor swimming sheet constructed by Diller et al. in 2014 [62]. By endowing the swimming sheet with a continuous harmonic magnetization profile, this robot is able to realize an undulating travelling wave along its body when subjected to a rotating \vec{B} . This generated undulation can be exploited as

an effective swimming gait, which can enable the robot to maneuver on an air-water interface as well as on the bed of the reservoir [62]. It is of great significance to create the Taylor swimming sheet because the locomotion of this classical, hypothetical device is highly desirable but difficult to realize. To be more precise, scientists and engineers took 63 years to successfully construct this device after its theoretical inception [62, 77]. Although human intuition may have the potential to create functional devices such as the Taylor swimming sheet, it is challenging to rely on such unsystematic programming methods to expand the functionalities of shape-programmable magnetic miniature robots.

In 2016, the universal programming methodology of Lum et al. signifies a key advancement in this research area [6]. A critical advantage of this programming methodology is that it has significant potential to surpass the barriers of human intuition since it can allow computers to automatically generate the required \vec{M} and actuating magnetic fields of these robots (Fig. 9.2) [6]. The universal programming methodology of Lum et al. has made two major contributions for shape-programmable magnetic miniature robots. First, they lay the foundation for the physics of this class of robots by using a fix-free, large deflection beam to explain their actuation principles [6], i.e., the physics that is presented in Sect. 9.2.2. They have also provided the first step toward deriving the general deformation model of these robots, i.e., the physics formulated in Sect. 9.2.1 [6]. Second, based on their developed theoretical model, Lum et al. have also proposed a computational approach that can replace human intuition with machine intelligence in the programming process [6]. To implement this computational approach, the \vec{M} and actuating magnetic fields of the robots are first represented by corresponding sets of Fourier series. Based on this representation, a numerical optimization is then performed to determine the optimal Fourier coefficients, which can allow the robots to realize their desired time-varying shapes. During the optimization process, the generated time-varying shapes of the robots are predicted based on their theoretical

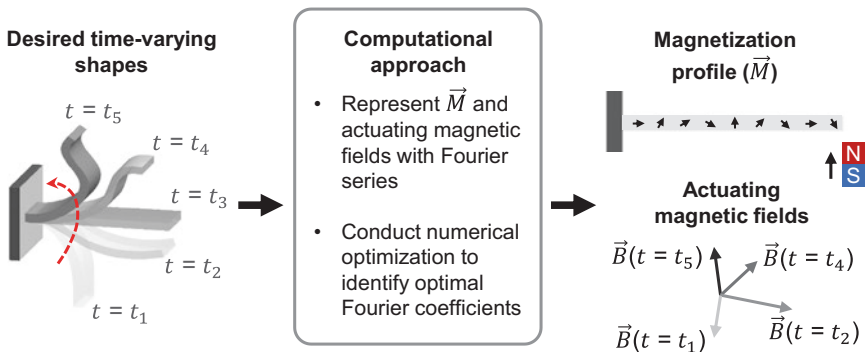


Fig. 9.2 The process of programming the magnetization profile and actuating magnetic fields of the robot (illustrated with a fix-free beam). The left shows an arbitrary beam with a series of desired time-varying shapes. By using the computational approach (center), the required magnetization profile and actuating magnetic fields (right) can be automatically generated

model. Once the Fourier coefficients are solved, the required \vec{M} and actuating magnetic fields will be automatically generated. A critical advantage of using the Fourier series representation is that it encompasses all possible mathematical functions, enabling the computational approach to be universal. Indeed, by using the universal programming methodology, Lum et al. are able to create a wide range of shape-programmable magnetic miniature robots such as a jellyfish-like robot, a sperm-like robot, and an artificial cilium [6]. Some of these robots have highly complicated \vec{M} and actuating magnetic fields, which are challenging to deduce via human intuition. While all the robots created by Lum et al. have assumed beam-shaped configurations [6], there is theoretically no loss of generality to use this universal programming methodology to deduce the required \vec{M} and actuating magnetic fields of such robots when they have 3D geometries. Since 2016, the work of Lum et al. has also inspired various other computational approaches [78, 79]. A notable example of such works will be the computational approach proposed by Wu et al. in which they explore the feasibility of representing the \vec{M} of the robots with discrete voxels [78].

While the universal programming methodology of Lum et al. is promising, it is unable to produce all types of time-varying shapes for their robots [6]. This is due to the assumption that the magnetization profiles and actuating magnetic fields of these shape-programmable robots are temporally and spatially invariant, respectively [6]. Since recent developments have shown that it is feasible to reprogram the magnetization profile of the robots under in situ conditions [80, 81], the universal programming methodology of Lum et al. can therefore be potentially enhanced by relaxing the constraints on the robots' \vec{M} . If this can be achieved, it will be possible to program this class of robots to realize a larger range of time-varying shapes, potentially allowing them to enhance their abilities significantly. Furthermore, depending on the complexity of the robots' time-varying shapes, the numerical solutions obtained via computational approaches may be trapped in a local optimum [6]. This is especially true if the desired time-varying shapes of the robots are very complicated as this will make the optimization process highly non-convex [6]. While Lum et al. have proposed a multi-step optimization process to mitigate such issues [6], it will be interesting to further investigate alternative numerical techniques in the future so as to increase the chances of identifying the global solution via such computational approaches.

The developments in theory and the introduction of computational approaches have significantly advanced the programming process of shape-programmable magnetic miniature robots. As a result, it is now possible to program a wide range of shape-programmable magnetic miniature robots. Nonetheless, the programming process of such robots can still potentially be improved by making the optimization processes more efficient and accounting for the effects of reprogrammable magnetization profiles in the future.

9.3.2 Fabrication Methods

Over the last two decades, various fabrication methods have been developed toward constructing shape-programmable magnetic miniature robots with their desired geometry and programmed magnetization profiles. In general, it is favorable to construct these robots with soft materials such as elastomers [6, 27, 62, 82] and hydrogels [65] because this can allow the robots to achieve their desired deformations more easily. To enable magnetic actuation, these soft materials are typically embedded with nano/micro magnetic particles. These magnetic particles can have either hard magnetic properties with high remanence or soft magnetic properties with low remanence [83, 84]. Robots embedded with hard magnetic particles are easier to analyze than those with soft magnetic properties because their magnetization profiles are independent of the actuating magnetic fields.

Molding is a popular method to construct shape-programmable robots with hard magnetic properties according to their desired planar geometries [6, 7, 27, 62]. Once the robots are molded, they are fitted into a jig before being magnetized by a strong, uniform magnetic field (1.1–1.7 T) [6, 7, 15, 62]. This magnetization process will allow the robots to obtain their desired direction-varying \vec{M} after they are removed from the jig. As an example, the harmonic magnetization profile of the Taylor swimming sheet is obtained after it is magnetized with a cylindrical jig [62]. Although most robots have been constructed with 2D direction-varying magnetization profile using this fabrication method, this method can also endow robots with 3D direction-varying magnetization profile [27]. In 2016, Lum et al. expand this fabrication method via a two-step, laser-based molding process, allowing robots with beam-shaped configurations to possess 2D direction- and magnitude-varying \vec{M} (Fig. 9.3a) [6]. Before these beams are magnetized in their jigs, the two-step molding process allows a heterogeneous distribution of magnetic and non-magnetic particles along the in-plane axis of their body. As a result, regions with a higher concentration of magnetic particles will have a larger magnetization magnitude after the robots are magnetized. This fabrication method is highly efficient as it allows Lum et al. to build a variety of highly functional shape-programmable robots with beam-shaped configurations [6]. While the two-step, laser-based molding process by Lum et al. is effective, this magnitude-varying method cannot be applied to robots that have 3D geometry as the distribution of magnetic particles along all axes of the robots cannot be tuned [6]. Therefore, it will be interesting to further enhance this fabrication method so that they can eventually create shape-programmable miniature robots that have 3D geometries and 3D magnetization profiles, which can vary in both direction and magnitude in the future.

The molding method can be further extended to shape-programmable magnetic miniature robots that can be decomposed into smaller discrete components [15, 16, 28]. These components can be molded and magnetized separately and thereafter assembled and bonded together to form a robot with 3D geometry and an overall 3D magnetization profile [16]. While this method has only been demonstrated to create robots with direction-varying magnetization profiles [15, 16, 28], there is no loss of

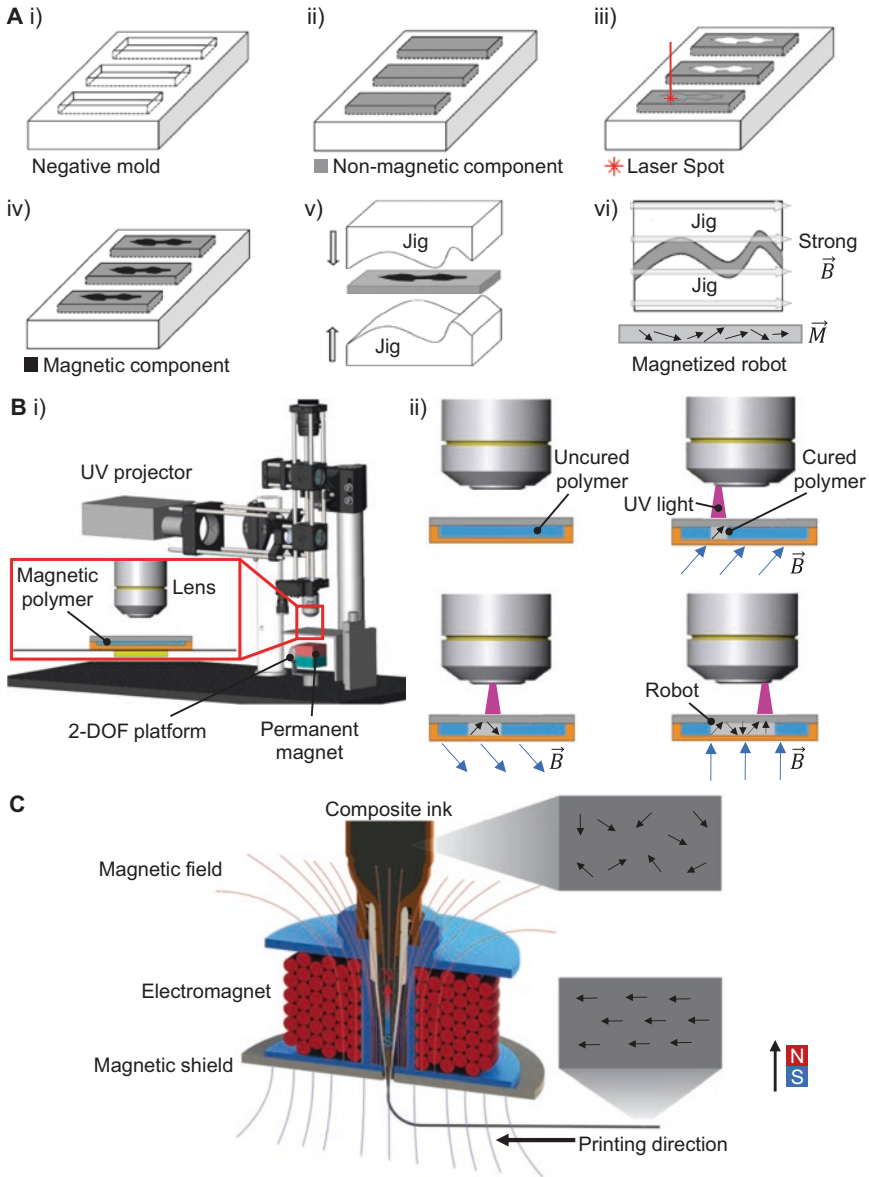


Fig. 9.3 Methods to fabricate shape-programmable magnetic miniature robots. (a) Creation of shape-programmable robots via the two-step, laser-based molding method. (b) Lithographic patterning of polymers containing hard magnetic particles using UV light to fabricate robots with 3D direction-varying magnetization. (c) 3D printing nozzle that magnetizes the magnetic material as it prints. ((a) Adapted with permission [6]. Copyright 2016, National Academy of Sciences. (b) Adapted with permission [12]. Copyright 2018, AAAS. (c) Adapted with permission [82]. Copyright 2018, Springer Nature)

generality to use this fabrication method to create robots with 3D geometry and 3D magnetization profiles that can vary in both direction and magnitude. A potential limitation of this fabrication method, however, is that the assembly process is typically performed manually [15, 16, 28]. As a result, it will become increasingly difficult to assemble the components at smaller scale. Indeed, robots fabricated via such methods are typically in the millimeter length scale [15, 16, 28], and it will be difficult to scale them down. In the future, it will be interesting to investigate the feasibility of automating the assembly process with high precision positioning stages [85–89], as this can potentially enhance such fabrication methods and allow them to construct smaller robots.

Sequential lithographic patterning is another efficient method to fabricate shape-programmable magnetic miniature robots (Fig. 9.3b) [12, 65, 90]. A unique characteristic of this method is that it can produce complex 3D direction-varying magnetization profiles in planar geometries at micrometer-scale [12, 65]. This type of fabrication method is first proposed by Kim et al. in 2011 [65]. To construct the robots, superparamagnetic nanoparticles (particles with soft magnetic properties) are first immersed into a solution of photocurable polymer. Before the solution undergoes polymerization, the superparamagnetic nanoparticles are aligned with external magnetic fields to define their preferred magnetic axis. Subsequently, UV light is shone on selective regions in the solution, inducing photopolymerization and fixing the alignment of the nanoparticles in these regions. This photopolymerization process is repeated until all the selected regions in the solution are endowed with a corresponding preferred magnetic axis. Eventually, all these polymerized regions will form a shape-programmable robot, which has an effective, direction-varying magnetization profile. In 2018, Xu et al. have investigated the feasibility of using the lithographic patterning method to create shape-programmable miniature robots with hard magnetic properties [12]. By replacing the superparamagnetic particles with NdFeB microparticles during the fabrication process (Fig. 9.3b), Xu et al. are able to create various shape-programmable robots with hard magnetic properties, including, but not limited to, a crawling robot, a swimmer, and a mobile gripper [12]. A significant advantage of having hard magnetic particles is that they allow the robots to be more deterministic than their counterparts with embedded soft magnetic particles. In general, while sequential lithographic patterning can endow 3D direction-varying magnetization profiles to the robots, they cannot create magnitude-varying profiles since the immersed magnetic particles are uniformly distributed before polymerization. Furthermore, it remains a great challenge to extend such fabrication methods to construct shape-programmable magnetic robots with 3D geometries. This fabrication method is also unable to achieve high resolution of 2D magnetization profiles. As an example, the smallest magnetization feature size achievable by the robots of Xu et al. are reported to be $250\ \mu\text{m} \times 250\ \mu\text{m}$ in the polymerized plane [12].

In contrast to sequential lithographic patterning, fabrication methods based on 3D printing technology is an effective strategy to construct shape-programmable magnetic miniature robots with 3D geometries [79, 82, 91]. In 2018, Kim et al. use direct ink writing to 3D-print shape-programmable miniature robots with an elastomer

composite embedded with ferromagnetic microparticles [82]. During the printing process, the microparticles are aligned according to the direction of an external magnetic field near the dispensing nozzle (Fig. 9.3c). Based on this fabrication method, Kim et al. have created various shape-programmable miniature robots with 3D geometries and 2D direction-varying magnetization profiles. However, the resolution of these robots is limited by the diameter of the dispensing nozzle, which is reported to be 410 μm [82]. In 2020, Wu et al. have further improved this 3D printing method such that it can be used to construct robots with 2D direction- and magnitude-varying profiles [78]. Although the magnetization direction of this 3D printing method is limited in the nozzle-moving plane, it can potentially be extended to print 3D direction-varying magnetization profiles by changing the applied magnetic field during printing. While 3D printing arguably possesses the most flexibility in the constructing shape-programmable magnetic miniature robots, the challenge remains to improve the printing resolution such that this fabrication method can create smaller robots.

While current fabrication methods can construct a wide range of shape-programmable magnetic miniature robots, it is still an open challenge to create robots with 3D geometries and 3D magnetization profiles (both direction- and magnitude-varying) at high resolution. If this critical challenge can be resolved in the future, shape-programmable robots can potentially be fabricated with far less constraints, allowing scientists and engineers to fully capitalize this technology.

9.4 Locomotion and Mechanical Functionalities

Due to the advancement in programming and fabrication methods, a wide range of shape-programmable magnetic miniature robots have been created over the last decade. In this section, we discuss the key advancements of such robots in terms of their untethered soft-bodied locomotion and mechanical functionalities.

9.4.1 Locomotion

To execute medical treatments such as minimally invasive surgery and targeted drug delivery, it is essential for untethered miniature robots to have the abilities to navigate in the highly unstructured environments within the human body [11]. Due to this critical requirement, many shape-programmable magnetic miniature robots have been programmed to produce time-varying shapes, which can enable various types of untethered soft-bodied locomotion to significantly enhance their dexterity [92]. While the effectiveness of these soft-bodied locomotion can be enhanced with magnetic gradient-based pulling forces, using such forces exclusively will be detrimental as the dynamics of such actuation method is inherently unstable [7, 48]. Here we highlight the key terrestrial, aquatic, and amphibious locomotive gaits producible by shape-programmable magnetic miniature robots.

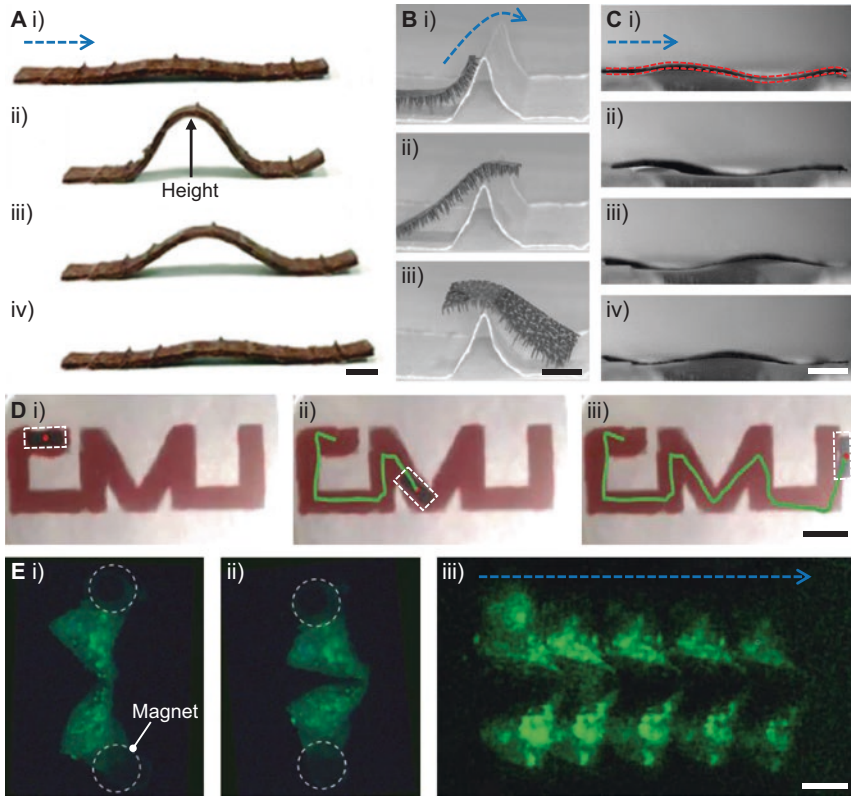


Fig. 9.4 Terrestrial and aquatic locomotive gaits of shape-programmable magnetic robots. Blue dashed arrows indicate direction of motion. (a) A magnetically actuated robot with a two-anchor crawling gait. Scale bar: 5 mm. (b) A legged magnetic robot overcomes an obstacle much taller than itself. Scale bar: 5 mm. (c) A miniature robot that performs undulatory motions to swim on the water surface. Scale bar: 1 mm. (d) An undulating magnetic robot that can swim on the water surface to follow a planar trajectory and trace a “CMU” logo. Scale bar: 5 mm. (e) A magnetic miniature robot that can perform scallop-like motion by varying the magnitude of \vec{B} . (i) At a low \vec{B} , the scallop robot opens. (ii) The scallop robot closes when a high \vec{B} is applied. (iii) The robot swims in non-Newtonian fluid with a reciprocal gait. Scale bar: 200 μm . ((a) Adapted under CC BY 4.0 [78]. (b) Adapted under CC BY 4.0 [94]. (c, d) Adapted with permission [62]. Copyright 2014, AIP Publishing. (e) Adapted under CC BY 4.0 [28])

Two-anchor crawling is a simple but effective soft locomotive gait, which can allow inchworms and caterpillars to cross uneven terrains or move up inclined surfaces [30, 93]. Inspired by this mode of locomotion, Wu et al. have programmed a beam-shaped robot to mimic such a crawling gait [78]. Under a strong \vec{B} (150 mT), the robot bends its middle segment to a height while anchoring its front and rear ends to the ground [78]. Because the frictional forces at the rear end is higher than the front end, the robot can produce a net displacement forward when \vec{B} is gradually switched off to allow the robot to recover its original shape (Fig. 9.4a). By repeating these time-varying shapes, the robot can execute an effective two-anchor

crawling locomotion (approximately 5 mm s^{-1} or 0.2 body length per second) [78]. Although the robot of Wu et al. is in the centimeter-scale (25 mm in length), in theory this two-anchor crawling gait can potentially be applied to smaller robots. While the two-anchor crawling gait is promising, its effectiveness is highly dependent on the surface properties of the terrain that the robot moves on [7]. In certain scenarios where the terrain is unable to provide sufficient friction to the robot, undesirable effects such as slipping may occur, which in turn will reduce the net displacement produced per stride and therefore lower the robot's crawling speed [7].

In contrast to two-anchor crawling, walking via legs will be a more reliable terrestrial locomotion as such gaits are less sensitive toward the surface properties of the terrain [12, 20, 94]. Seeing the potential of such locomotion, Lu et al. have programmed a shape-programmable magnetic miniature robot that can walk and steer itself across various dry and wet terrains [94]. This soft robot has numerous tapered legs that are connected to a body. These soft legs are programmed to deform and swing like a pendulum and thereby advance their contact points on the ground. Repeating these swinging motions allows the robot to enable a walking locomotion [94]. One notable advantage of the robot is that the compliance of its legs can drastically enhance its robustness, enabling it to overcome various obstacles, such as walking over steep barriers that are eightfold of its height (Fig. 9.4b) [94]. Furthermore, the superhydrophobic property of the legs helps to reduce the adhesion between the robot and the substrate, allowing the robot to move across wet surfaces effectively [94, 95]. While the work of Lu et al. is promising, the performance of their walking robot is not optimized yet as the time-varying shapes generated by the legs are coupled with one another. In the future, if each soft leg of the robot can be controlled independently, walking robots can potentially improve their robustness and adaptability to their terrestrial environments. In addition, the walking robot of Lu et al. is relatively large in size (17 mm in length) [94], and thus it will be interesting to apply this walking gait to smaller robots that in the future.

Due to scaling laws, miniature robots generally have to operate in low Reynolds number regimes when they are immersed within aqueous environments [28, 50, 77, 96, 97]. Under such regimes, the inertia effects of the robots are negligible compared to the viscous forces induced by the fluids [28, 50, 77, 96, 97]. As a result, many shape-programmable magnetic miniature robots have obeyed the scallop theorem and adopted non-reciprocal gaits to generate propulsion [62, 77, 96, 97]. In general, non-reciprocal gaits refer to a series of motions that are non-identical when reversed. One notable non-reciprocal swimming gait of shape-programmable magnetic miniature robots will be undulating swimming. By generating a travelling wave along the body, various robots such as the sperm-like robot or the Taylor swimming sheets [6, 62], are able to produce an effective undulating swimming gait that can navigate across aqueous environments. Such swimming locomotion is highly efficient. For instance, a Taylor swimming sheet of 5.9 mm in length can swim up to 17 body lengths per second on the water surface (Fig. 9.4c) [62]. Furthermore, this locomotive gait can be controlled well as the robots are able to track complex, planar paths (Fig. 9.4d). However, miniature robots with undulatory swimming gaits have not demonstrated the ability to precisely track 3D paths in the fluid bulk yet.

Roboticians have also explored alternative modes of swimming for shape-programmable magnetic miniature robots. For example, Qiu et al. have enabled their millimeter-scale robot to swim with a reciprocal, scallop-like gait by exploiting the shear-thinning or shear-thickening effects of non-Newtonian fluids (Fig. 9.4e) [28]. This is a highly significant demonstration because it shows that small robots can potentially exploit the unique rheological properties of non-Newtonian bodily fluids (such as blood [98, 99] and mucus [100–102]) and swim in the human body with reciprocal gaits. In addition, some shape-programmable magnetic miniature robots have also adopted reciprocal pulsatile gaits to swim in aqueous media like a jellyfish [6, 7]. By periodically ingesting and discharging fluids, these robots can achieve high momentum and generate sufficient inertial effects to propel themselves in an aqueous medium [6, 7]. The robots can reach high velocities of 2.7–18.1 body lengths per second in water, effectively allowing them to swim in moderate Reynolds number regimes (39–421) [7]. However, as sufficient inertial effects are required for enabling this pulsatile swimming gait, it is difficult to shrink the size of the robot down as this can further reduce their inertial effects [28, 50, 77, 96, 97].

A miniature robot that can transit reversibly between terrestrial and aquatic environments will be highly desirable for various biomedical applications as the robot will be able to navigate well in the human body. Heading along this direction, Hu et al. have created amphibious miniature robots, which can execute various modes of soft-bodied locomotion [7]. These millimeter-scale robots are programmed to be able to roll, perform two-anchor and undulating crawling, jump over large obstacles, and swim on the water surface and within the fluid bulk with their undulatory and pulsatile gaits, respectively (Fig. 9.5). It is favorable for miniature soft robots to adopt a rolling locomotion due to its fast speed and relative ease of actuation [103–105]. By applying a strong \vec{B} of 20 mT, the robots of Hu et al. can adopt a “C”-shape configuration while possessing a net magnetic moment. Thereafter, rotating \vec{B} will induce a rigid-body rotation that will make the deformed robots roll (approximately 150–213 mm s⁻¹) (Fig. 9.5a) [7]. However, rolling may not be ideal for moving on highly complex and unstructured terrain. To move across uneven terrains, these robots can instead choose to move with a two-anchor crawling gait, although at a slower speed (approximately 8–65.5 mm s⁻¹) (Fig. 9.5b) [7]. The robots can also jump over obstacles that are larger than themselves. By generating a fast shape-change from a flat configuration into an inverted “C”-shape, the two free ends of the robots can strike the ground with a large impulsive force and therefore allow them to gain sufficient vertical momentum and jump up. Based on these time-varying shapes, a 5-mm-long robot will be able to jump up to 12.2 mm (Fig. 9.5c) [7]. To achieve directional jumping, the robots can first adopt a “C”-shape configuration under an external \vec{B} . When \vec{B} is quickly changed to another direction, the robots can simultaneously undergo rigid-body rotation and deformation such that they can strike the ground and gain horizontal and vertical momentum for the jumping locomotion (Fig. 9.5d). When the robots encounter narrow channels, they can perform undulatory motion to crawl through these obstacles. For instance, a 5-mm-long robot can crawl through a tunnel that has a cross-sectional area of 0.645 mm × 2.55 mm at a high speed of approximately 4

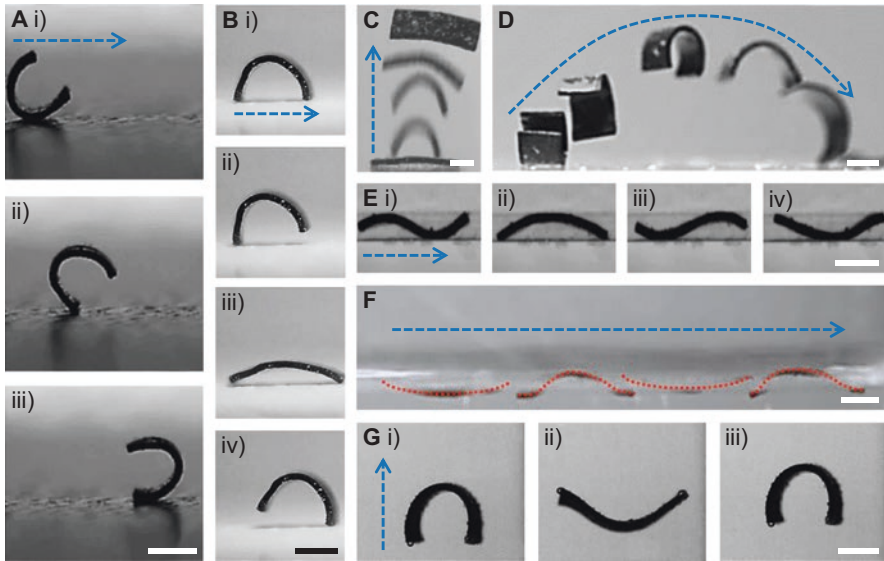


Fig. 9.5 An amphibious, magnetic miniature robot with multimodal locomotive gaits. Blue dashed arrows indicate direction of motion. **(a)** Rolling locomotion facilitated by the deformed “C”-shape of the robot. **(b)** The sequence of time-varying shapes and orientation control to achieve two-anchor crawling. **(c)** A magnetic miniature robot jumps straight up by quickly deforming into an inverted “C”-shape. **(d)** Directional jumping of a magnetic miniature robot. **(e)** Undulatory crawling through a narrow channel. **(f)** Undulatory swimming along the water surface. **(g)** Jellyfish-like, periodic swimming in the fluid bulk. Scale bars: 1 mm. ((a–g) Adapted with permission [7]. Copyright 2018, Springer Nature)

body lengths per second (Fig. 9.5e) [7]. The same undulatory motion can also be used to swim on the water surface (Fig. 9.5f) [7]. In addition, these robot can immerse themselves into the fluid bulk and swim with a periodic, jellyfish-like motion at moderate Reynolds number regimes (39–421) (Fig. 9.5g) [7]. The performance of some soft locomotive gaits, such as jumping, may be further enhanced by applying appropriate magnetic spatial gradients. For example, the jumping height of a 3.7-mm-long robot can be increased to approximately 2.2-fold once a magnetic force is applied against gravity [7]. These soft locomotive gaits have proven to be very effective as the robots can successfully negotiate across the liquid-solid environment of a stomach phantom with ease, and this signifies the robots’ high dexterity and potential for biomedical applications [7].

While the amphibious robots proposed by Hu et al. can perform multiple soft locomotive gaits, each gait is still not optimized [7]. For instance, it is difficult to control the robots at high rolling speed because the free ends of the robots may strike the ground too hard and produce undesired jumping motions [7]. The lateral and vertical jumping distance can also be better controlled [7]. In the future, if each of the soft locomotive gaits can be optimized, these amphibious robots can become much more dexterous and robust, and this can potentially be a significant step toward revolutionizing minimally invasive medical treatments.

9.4.2 *Mechanical Functionalities*

In addition to having soft-bodied locomotion, shape-programmable magnetic miniature robots have also developed various critical mechanical functionalities that are essential for biomedical applications [6, 15, 18, 19]. For instance, the shape-programmable magnetic miniature robot of Miyashita et al. shows great potential in administering treatments for internal stomach wounds [106]. The millimeter-scale robot of Miyashita et al. is made with drug-containing layers, and it can be folded up from a planar configuration like an origami. To enter the human body, a patient can ingest this biodegradable robot after it is encapsulated in an ice cube. Upon reaching the stomach, the ice melts, and the robot regains its mobility to perform soft-bodied, stick-slip locomotion. The mobile robot can be commanded to move toward the wound in the stomach and assume its planar configuration to patch the wound. As the robot's drug-containing layer degrades, drugs are released to the wound. After the drugs are transferred and the treatment is completed, this robot can then be fully dissolved by the stomach acid to end its mission. While the experiments of Miyashita et al. are conducted with an *in vitro* stomach phantom [106], their shape-programmable magnetic miniature robot illustrates the feasibility of using such robotic technologies for medical treatments. In recent developments, Wang et al. have also created a shape-programmable magnetic miniature robot that has an effective anchoring mechanism [18]. It is advantageous to develop such anchoring mechanism as various minimally invasive medical treatments may require the small robots to stay within the human body over a prolonged period of time. Examples of such treatments would include the administration of drugs to an intestinal infection or cancer site, as well as the facilitation of effective physical contraception in the fallopian tube [107]. The robot of Wang et al. is programmed and fabricated in such a way that it is able to move in highly confined spaces in its original configuration [18]. Once the robot reaches the desired anchoring location, it can actively expand its cross-sectional area and press against the surroundings to create a self-locking mechanism. Using such an anchoring mechanism, the robot is able to stay in static equilibrium and maintain its position at the desired location. Upon command, the robot can also reversibly reduce its cross-sectional area and disengage from the surroundings. While the robot of Wang et al. has introduced a valuable function for small-scale robotic technologies, it has a relatively large size (17.8 mm in length), and this may hinder its deployment for medical applications [18]. In the future, it will be interesting to construct such robots at smaller scales.

Shape-programmable magnetic miniature robots can also function as active, immobile scaffolds that can transfer drugs or cells to their surroundings via magnetic actuation [19, 108, 109]. The efficiency of such active scaffolds is significantly higher than traditional porous scaffolds, which can only perform such mass transfers via passive molecular diffusion, material degradation, and cell migration [19]. A notable example of such active scaffolds is shown by Zhao et al., where their immobile scaffolds can be controlled to reduce their volume by 70% via compression (Fig. 9.6a, b) [19]. By continuously alternating the volume of the scaffolds

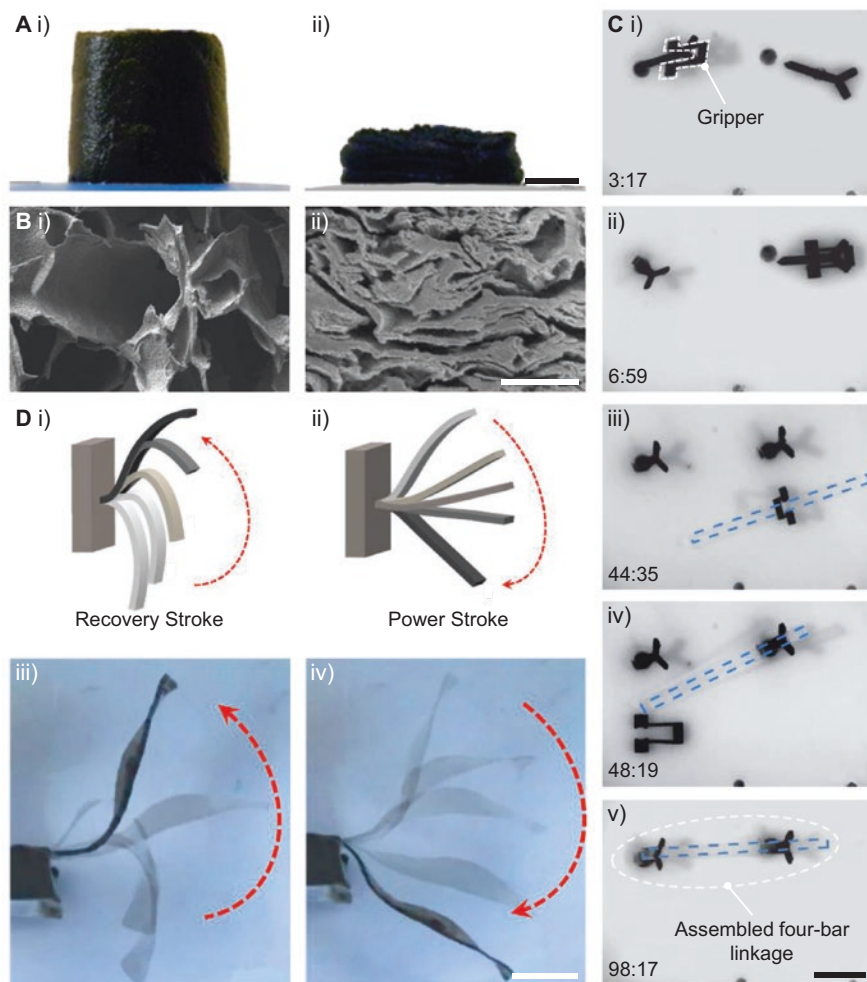


Fig. 9.6 Mechanical functions of shape-programmable magnetic miniature robots. (a) An active scaffold that can be compressed when subjected to magnetic field actuation. Scale bar: 5 mm. (b) The scaffold structure in its undeformed (i) and deformed (ii) configurations seen under a scanning electron microscope. Scale bar: 500 μm . (c) A gripper, outlined with a white dashed line, carrying out 3D-assembly of a four-bar linkage device. Scale bar: 1 mm. (d) (i–ii) The desired time-varying shapes for a magnetic artificial cilium. (iii–iv) A magnetic beam undergoing the programmed time-varying shapes to mimic the recovery and power strokes of a biological cilium. Scale bar: 2 mm. ((a, b) Adapted with permission [19]. Copyright 2011, National Academy of Sciences. (c) Adapted with permission [15]. Copyright 2014, John Wiley & Sons Inc. (d) Adapted with permission [6]. Copyright 2016, National Academy of Sciences)

between their compressed and original configurations, these devices are able to enhance their mass transfers considerably. For example, these active scaffolds are able to increase the amount of released drugs (mitoxantrone) by sevenfold over a period of 3 h when they undergo 120 cycles of such periodic deformations in every

30-min interval [19]. Similar benefits have also been observed when the scaffolds perform such time-varying deformations to transfer plasmid DNA and chemokine (SDF-1 α) [19]. The high mass transfer efficiency of such scaffolds therefore demonstrates the potential of deploying shape-programmable magnetic miniature robots for both biomedical and bioengineering applications.

Having the ability to perform 3D pick-and-place operations can be highly advantageous for shape-programmable magnetic miniature robots. Using such abilities, these shape-programmable robots can potentially enable a vast range of lab-on-chip applications that require 3D assembly of heterogeneous metamaterials, and they can potentially also construct medical devices inside the human body [15]. To allow shape-programmable magnetic miniature robots to perform 3D pick-and-place operations, Diller and Sitti have programmed a mobile gripper, which can actively grab 3D objects and transport them to their desired destinations via stick-slip locomotion or magnetic gradient-based pulling [15]. By exploiting such mechanical functionalities, this mobile gripper is able to accomplish various 3D pick-and-place operations, such as assembling a spatial four-bar linkage device (Fig. 9.6c). The demonstrations of Diller and Sitti mark a significant advancement for small-scale robotic technologies as previous miniature robots can at most perform 2D assembly tasks [110–114]. Despite the advancements of the mobile gripper, this device has two critical limitations [15]. First, the assembly speed is very slow as the mobile gripper requires 98 min to assemble the four-bar linkage device [15]. As a result, it will be necessary to increase the dexterity of such mobile grippers so that their manipulation capabilities can be further enhanced in the future. Second, the gripping surfaces of this mobile gripper are not optimized in terms of their geometries and stiffness [15]. Hence, it can only grasp a limited range of objects. To address this limitation, various other types of mobile grippers have been developed over the past few years such that their gripping surfaces can establish better contact with their manipulated objects and enhance their grasping performances [26, 115]. Nonetheless, as such enhancements are done via human intuition, it is still possible to further optimize the geometries and stiffness of such gripping surfaces in the future via numerical optimization methods. If such optimization can be performed successfully, this can potentially allow mobile grippers to better conform to the geometries of their manipulated objects, establish better contact, and enhance their grasping functionalities considerably.

Inspired by the motions of natural cilia, various shape-programmable magnetic miniature robots have been programmed to adopt similar time-varying shapes as this can allow them to operate as microfluidic pumps for a diverse range of lab-on-chip applications [6, 20, 116, 117]. It is highly desirable to adopt such motions because natural cilia are highly efficient in transporting biological fluids at small-scale, i.e., in low Reynolds number regimes [20, 116–118]. In 2016, the immobile artificial cilium created by Lum et al. represents a key advancement for such devices as this robot is able to generate a series of time-varying shapes that closely mimic the non-reciprocal power and recovery strokes of its biological counterpart (Fig. 9.6d) [6]. Since the work of Lum et al., Gu et al. have recently created an array of immobile artificial cilia, where each cilium is also able to generate similar,

non-reciprocal power and recovery strokes [20]. As the \vec{M} of each cilium is programmed to be different, the array of artificial cilia is able to coordinate with one another and produce effective metachronal waves when they are actuated by a rotating \vec{B} . The creation of such metachronal waves is highly critical because they can enable the artificial cilia array to significantly enhance its pumping efficiency [20, 116, 117]. While the artificial cilia array of Gu et al. shows great promise, its overall size is relatively large (about 8 cm in length). As a result, it will be interesting to explore the feasibility of reducing the size of such devices in the future. If this can be accomplished, shape-programmable magnetic miniature robots will have significant impact in microfluidic devices as they show great potential to mix or transport biological fluids at low Reynolds number regimes [118].

9.5 Discussion

Due to the advancements in theory and programming methods [6, 57], it is theoretically possible to program miniature soft robots with high resolution of 3D geometry and 3D direction- and magnitude-varying magnetization profiles. It will be highly desirable to make such robots because they would have the potential to realize a much more diverse range of locomotive gaits and functionalities compared to the existing miniature robots. Despite the potential benefits of such 3D robots, it remains a great challenge to use the available fabrication methods to successfully construct such complicated machines [6, 12, 82], especially if their desired geometry and magnetization profile are highly complex. To fully capitalize on the potential of shape-programmable magnetic miniature robots, it is therefore essential to explore novel fabrication methods.

Having the ability to control a swarm of untethered, shape-programmable magnetic miniature robots can potentially enhance their efficiency and enable new mechanical functionalities [119–121]. For instance, a swarm of collaborative robots will be able to deliver a much higher quantity of drugs to a disease area compared to an individual robot, and this can potentially enhance the efficiency of drug delivery significantly [122]. Despite the desirable features of swarm control, it is very difficult to implement such control strategies for shape-programmable magnetic miniature robots. One notable challenge in implementing swarm control is that the actuating magnetic fields are uniform across all the robots in the workspace [48, 49]. As a result, it will be difficult to independently control each individual robot in a swarm using such global control signals. In view of this challenge, Zhang and Diller have created two shape-programmable swimmers that have distinct \vec{M} [76]. Due to having different magnetization profiles, each swimmer responds differently to the actuating magnetic fields and thus exhibits distinct swimming patterns on the water surface [76]. While such strategies allow Zhang and Diller to effectively control two shape-programmable robots, they have not demonstrated independent control for a larger team of robots [76]. In the future, it will be interesting to investigate

the feasibility of using a combination of actuation methods to control shape-programmable miniature robots so that a larger number of such devices can collaborate with one another to achieve higher functionality [22, 47, 123].

A key requirement for shape-programmable magnetic miniature robots to realize their targeted biomedical applications is to have an effective visual feedback system, which can track the robots' position and orientation when they are operating in enclosed spaces [7, 21]. Such feedback is critical because it ensures that the untethered robots are performing the treatments at the correct location in the human body [21]. Of the available visual systems, ultrasound medical imaging systems have been shown to be a promising solution for providing such feedback [7, 21]. A significant advantage of the ultrasound medical imaging systems is that they are very compatible with shape-programmable magnetic miniature robots as there is minimal interference between the actuating magnetic fields and ultrasound feedback [7, 124, 125]. Indeed, Hu et al. have shown that their shape-programmable magnetic miniature robots can be tracked well in real-time when it executes multimodal soft-bodied locomotion in an enclosed ex vivo biological phantom [7]. The demonstration of Hu et al. is therefore highly significant as it represents a substantial advancement toward using shape-programmable robotic technologies for biomedical applications. We envision that with further advancements in actuation and visual feedback systems, shape-programmable magnetic miniature robots will have significant potential to transform a vast range of minimally invasive medical treatments in the future.

9.6 Conclusion

This chapter reviews the key advancements and challenges for shape-programmable magnetic miniature robots. To make our discussions complete, we have analyzed different aspects of such machines, including their fundamental actuation principles, programming and fabrication methods, locomotive gaits, and mechanical functionalities. It is highly desirable to advance the science of shape-programmable magnetic miniature robots as these machines can be programmed to be much more dexterous and functional than their rigid counterparts [6, 7, 11, 12]. Due to these unique advantages, shape-programmable magnetic miniature robots have significant potential to create a paradigm shift across a broad range of applications pertaining to biomedicine, bioengineering, and lab-on-chip technology [14, 15, 21, 22]. We envision that the analyses and discussion here will be able to inspire scientists and engineers to make shape-programmable magnetic miniature robots much more capable in the future.

Acknowledgments G.Z.L. was funded by the startup grant awarded by Nanyang Technological University. C.S.X.N. and C.X. contributed equally to this work.

References

1. Hawkes, E., An, B., Benbernou, N. M., Tanaka, H., Kim, S., Demaine, E. D., Rus, D., & Wood, R. J. (2010). *Proceedings National Academy of Sciences United States of America*, 107, 12441.
2. Felton, S., Tolley, M., Demaine, E., Rus, D., & Wood, R. (2014). A method for building self-folding machines. *Science*, 345, 644..
3. Rus, D., & Tolley, M. T. (2015). Design, fabrication and control of soft robots. *Nature*, 521, 467.
4. Rich, S. I., Wood, R. J., & Majidi, C. (2018). Untethered soft robotics. *Nature Electronics*, 1, 102.
5. Hines, L., Petersen, K., Lum, G. Z., & Sitti, M. (2017). Soft actuators for small-scale robotics. *Advanced Materials*, 29, 1603483
6. Lum, G. Z., Ye, Z., Dong, X., Marvi, H., Erin, O., Hu, W., & Sitti, M. (2016). Shape-programmable magnetic soft matter. *Proceedings National Academy of Sciences United States of America*, 113, E6007.
7. Hu, W., Lum, G. Z., Mastrangeli, M., & Sitti, M. (2018). Small-scale soft-bodied robot with multimodal locomotion. *Nature*, 554, 81.
8. Brown, E., Rodenberg, N., Amend, J., Mozeika, A., Steltz, E., Zakin, M. R., Lipson, H., & Jaeger, H. M. (2010). Universal robotic gripper based on the jamming of granular material. *Proceedings National Academy of Sciences United States of America*, 107, 18809.
9. Song, S., & Sitti, M. (2014). Soft grippers using micro-fibrillar adhesives for transfer printing. *Advanced Materials*, 26, 4901.
10. Song, S., Drotlef, D.-M., Majidi, C., & Sitti, M. (2017). Controllable load sharing for soft adhesive interfaces on three-dimensional surfaces. *Proceedings National Academy of Sciences United States of America*, 114, E4344.
11. Ng, C. S. X., Tan, M. W. M., Xu, C., Yang, Z., Lee, P. S., & Lum, G. Z. (2021). Locomotion of miniature soft robots. *Advanced Materials*. <https://doi.org/10.1002/adma.202003558>
12. Xu, T., Zhang, J., Salehizadeh, M., Onaizah, O., & Diller, E. (2019). Millimeter-scale flexible robots with programmable three-dimensional magnetization and motions. *Science Robotics*, 4, eaav4494.
13. Hu, C., Pané, S., & Nelson, B. J. (2018). Soft micro- and nanorobotics. *Annual Review of Control, Robotics, and Autonomous Systems*, 1, 53.
14. Ceylan, H., Giltinan, J., Kozielski, K., & Sitti, M. (2017). Mobile microrobots for bioengineering applications. *Lab on a Chip*, 17, 1705.
15. Diller, E., & Sitti, M. (2014). Three-dimensional programmable assembly by untethered magnetic robotic micro-grippers. *Advanced Functional Materials*, 24, 4397.
16. Zhang, J., Onaizah, O., Middleton, K., You, L., & Diller, E. (2017). Reliable grasping of three-dimensional untethered mobile magnetic microgripper for autonomous pick-and-place. *IEEE Robotics and Automation Letters*, 2, 835.
17. Gultepe, E., Randhawa, J. S., Kadam, S., Yamanaka, S., Selaru, F. M., Shin, E. J., Kalloo, A. N., & Gracias, D. H. (2013). Biopsy with thermally-responsive untethered microtools. *Advanced Materials*, 25, 514.
18. Wang, T., Hu, W., Ren, Z., & Sitti, M. (2020). Ultrasound-guided wireless tubular robotic anchoring system. *IEEE Robotics and Automation Letters*, 5, 4859.
19. Zhao, X., Kim, J., Cezar, C. A., Huebsch, N., Lee, K., Bouhadir, K., & Mooney, D. J. (2011). Active scaffolds for on-demand drug and cell delivery. *Proceedings National Academy of Sciences United States of America*, 108, 67.
20. Gu, H., Boehler, Q., Cui, H., Secchi, E., Savorana, G., Marco, C. D., Gervasoni, S., Peyron, Q., Huang, T.-Y., Pane, S., Hirt, A. M., Ahmed, D., & Nelson, B. J. (2020). Magnetic cilia carpets with programmable metachronal waves. *Nature Communications*, 11, 2637.
21. Nelson, B. J., Kaliakatsos, I. K., & Abbott, J. J. (2010). Microrobots for minimally invasive medicine. *Annual Review of Biomedical Engineering*, 12, 55.

22. Sitti, M., Ceylan, H., Hu, W., Giltinan, J., Turan, M., Yim, S., & Diller, E. (2015). Biomedical applications of untethered mobile milli/microrobots. *Proceedings of the IEEE*, 103, 205.
23. Fusco, S., Sakar, M. S., Kennedy, S., Peters, C., Bottani, R., Starsich, F., Mao, A., Sotiriou, G. A., Pané, S., Pratsinis, S. E., Mooney, D., & Nelson, B. J. (2013). An integrated micro-robotic platform for on-demand, targeted therapeutic interventions. *Advanced Materials*, 26, 952.
24. Erkoc, P., Yasa, I. C., Ceylan, H., Yasa, O., Alapan, Y., & Sitti, M. (2018). Mobile microrobots for active therapeutic delivery. *Advances in Therapy*, 2, 1800064.
25. Fusco, S., Huang, H. W., Peyser, K. E., Peters, C., Häberli, M., Ulbers, A., Spyrogiani, A., Pellicer, E., Sort, J., Pratsinis, S. E., & Nelson, B. J. (2015). Shape-switching microrobots for medical applications: The influence of shape in drug delivery and locomotion. *ACS Applied Materials & Interfaces*, 7, 6803.
26. Chung, S. E., Dong, X., & Sitti, M. (2015). Three-dimensional heterogeneous assembly of coded microgels using an untethered mobile microgripper. *Lab on a Chip*, 15, 1667.
27. Ren, Z., Hu, W., Dong, X., & Sitti, M. (2019). Multi-functional soft-bodied jellyfish-like swimming. *Nature Communications*, 10, 2703.
28. Qiu, T., Lee, T.-C., Mark, A. G., Morozov, K. I., Münster, R., Mierka, O., Turek, S., Leshansky, A. M., & Fischer, P. (2014). Swimming by reciprocal motion at low Reynolds number. *Nature Communications*, 5, 1.
29. Palagi, S., Mark, A. G., Reigh, S. Y., Melde, K., Qiu, T., Zeng, H., Parmeggiani, C., Martella, D., Sanchez-Castillo, A., Kapernaum, N., & Giesselmann, F. (2016). Structured light enables biomimetic swimming and versatile locomotion of photoresponsive soft microrobots. *Nature Materials*, 15, 647.
30. Zeng, H., Wani, O. M., Wasylczyk, P., & Priimagi, A. (2017). Light-driven, caterpillar-inspired miniature inching robot. *Macromolecular Rapid Communications*, 39, 1700224.
31. Na, J. H., Evans, A. A., Bae, J., Chiappelli, M. C., Santangelo, C. D., Lang, R. J., Hull, T. C., & Hayward, R. C. (2015). Programming reversibly self-folding origami with micropatterned photo-crosslinkable polymer trilayers. *Advanced Materials*, 27, 79.
32. Taccola, S., Greco, F., Sinibaldi, E., Mondini, A., Mazzolai, B., & Mattoli, V. (2015). Toward a new generation of electrically controllable hygromorphic soft actuators. *Advanced Materials*, 27, 1668.
33. Mourran, A., Zhang, H., Vinokur, R., & Möller, M. (2017). Soft microrobots employing non-equilibrium actuation via plasmonic heating. *Advanced Materials*, 29, 1604825.
34. Leong, T. G., Randall, C. L., Benson, B. R., Bassik, N., Stern, G. M., & Gracias, D. H. (2009). Tetherless thermobiochemically actuated microgrippers. *Proceedings National Academy of Sciences United States of America*, 106, 703.
35. Jiang, S., Liu, F., Lerch, A., Ionov, L., & Agarwal, S. (2015). Unusual and superfast temperature-triggered actuators. *Advanced Materials*, 27, 4865.
36. Lendlein, A., & Langer, R. (2002). Biodegradable, elastic shape-memory polymers for potential biomedical applications. *Science*, 296, 1673.
37. Kwon, G. H., Park, J. Y., Kim, J. Y., Frisk, M. L., Beebe, D. J., & Lee, S. H. (2008). Biomimetic soft multifunctional miniature aquabots. *Small*, 4, 2148.
38. Yang, C., Wang, W., Yao, C., Xie, R., Ju, X.-J., Liu, Z., & Chu, L.-Y. (2015). Hydrogel walkers with electro-driven motility for cargo transport. *Scientific Reports*, 5, 13622.
39. Gupta, B., Goudeau, B., Garrigue, P., & Kuhn, A. (2018). Bipolar conducting polymer crawlers based on triple symmetry breaking. *Advanced Functional Materials*, 28, 1705825.
40. Lee, H., Xia, C., & Fang, N. X. (2010). First jump of microgel; actuation speed enhancement by elastic instability. *Soft Matter*, 6, 4342.
41. Maeda, S., Hara, Y., Sakai, T., Yoshida, R., & Hashimoto, S. (2007). Self-walking gel. *Advanced Materials*, 19, 3480.
42. Stoychev, G., Zakharchenko, S., Turcaud, S., Dunlop, J. W. C., & Ionov, L. (2012). Shape-programmed folding of stimuli-responsive polymer bilayers. *ACS Nano*, 6, 3925.
43. Zhao, Q., Dunlop, J. W. C., Qiu, X., Huang, F., Zhang, Z., Heyda, J., Dzubiella, J., Antonietti, M., & Yuan, J. (2014). An instant multi-responsive porous polymer actuator driven by solvent molecule sorption. *Nature Communications*, 5, 4293.

44. Paek, J., Cho, I., & Kim, J. (2015). Microrobotic tentacles with spiral bending capability based on shape-engineered elastomeric microtubes. *Scientific Reports*, 5, 10768.
45. Gorissen, B., de Volder, M., & Reynaerts, D. (2015). Pneumatically-actuated artificial cilia array for biomimetic fluid propulsion. *Lab on a Chip*, 15, 4348.
46. Gorissen, B., Chishiro, T., Shimomura, S., Reynaerts, D., Volder, M. D., & Konishi, S. (2014). Flexible pneumatic twisting actuators and their application to tilting micromirrors. *Sensors and Actuators A: Physical*, 216, 426.
47. Sitti, M., & Wiersma, D. S. (2020). Pros and cons: Magnetic versus optical microrobots. *Advanced Materials*, 32, 1906766.
48. Kummer, M. P., Abbott, J. J., Kratochvil, B. E., Borer, R., Sengul, A., & Nelson, B. J. (2010). OctoMag: An electromagnetic system for 5-DOF wireless micromanipulation. *IEEE Transactions on Robotics*, 26, 1006.
49. Diller, E., Giltinan, J., Lum, G. Z., Ye, Z., & Sitti, M. (2016). Six-degree-of-freedom magnetic actuation for wireless microrobotics. *International Journal of Robotics Research*, 35, 114.
50. Peyer, K. E., Zhang, L., & Nelson, B. J. (2013). Bio-inspired magnetic swimming microrobots for biomedical applications. *Nanoscale*, 5, 1259.
51. Palagi, S., & Fischer, P. (2018). Bioinspired microrobots. *Nature Reviews Materials*, 3, 113.
52. Shen, Z., Chen, F., Zhu, X., Yong, K.-T., & Gu, G. (2020). Stimuli-responsive functional materials for soft robotics. *Journal of Materials Chemistry B*. <https://doi.org/10.1039/D0TB01585G>
53. Kuang, X., Roach, D., Hamel, C., Yu, K., & Qi, J. (2020). Materials, design and fabrication of shape programmable polymers. *Multifunctional Materials*. <https://doi.org/10.1088/2399-7532/aba1d9>
54. Yang, Z., & Zhang, L. (2020). Magnetic actuation systems for miniature robots: A review. *Advanced Intelligent Systems*, 2, 2000082.
55. Chow, T. L. (2006). *Introduction to electromagnetic theory: A modern perspective*. Jones & Bartlett Learning.
56. Kankanala, S. V., & Triantafyllidis, N. (2004). On finitely strained magnetorheological elastomers. *Journal of the Mechanics and Physics of Solids*, 52, 2869.
57. Zhao, R., Kim, Y., Chester, S. A., Sharma, P., & Zhao, X. (2019). Mechanics of hard-magnetic soft materials. *Journal of the Mechanics and Physics of Solids*, 124, 244.
58. Danas, K., Kankanala, S. V., & Triantafyllidis, N. (2012). Experiments and modeling of iron-particle-filled magnetorheological elastomers. *Journal of the Mechanics and Physics of Solids*, 60, 120.
59. Ogden, R. W. (1972). Large deformation isotropic elasticity – On the correlation of theory and experiment for incompressible rubberlike solids. *Proceedings of the Royal Society A*, 326, 565.
60. Mooney, M. (1940). A theory of large elastic deformation. *Journal of Applied Physics*, 11, 582.
61. Dorfmann, A., & Ogden, R. W. (2003). Magnetoelastic modelling of elastomers. *European Journal of Mechanics - A/Solids*, 22, 497.
62. Diller, E., Zhuang, J., Lum, G. Z., Edwards, M. R., & Sitti, M. (2014). Continuously distributed magnetization profile for millimeter-scale elastomeric undulatory swimming. *Applied Physics Letters*, 104, 174101.
63. Kim, Y., Parada, G. A., Liu, S., & Zhao, X. (2019). Ferromagnetic soft continuum robots. *Science Robotics*, 4, eaax7329.
64. Wang, L., Kim, Y., Guo, C. F., & Zhao, X. (2020). Hard-magnetic elastica. *Journal of the Mechanics and Physics of Solids*, 142, 104045.
65. Kim, J., Chung, S. E., Choi, S.-E., Lee, H., Kim, J., & Kwon, S. (2011). Programming magnetic anisotropy in polymeric microactuators. *Nature Materials*, 10, 747.
66. Garstecki, P., Tierno, P., Weibel, D. B., Sagués, F., & Whitesides, G. M. (2009). Propulsion of flexible polymer structures in a rotating magnetic field. *Journal of Physics Condensed Matter*, 21, 204110.

67. Dreyfus, R., Baudry, J., Roper, M. L., Fermigier, M., Stone, H. A., & Bibette, J. (2005). Microscopic artificial swimmers. *Nature*, *437*, 862.
68. Jang, B., Gutman, E., Stucki, N., Seitz, B. F., Wendel-García, P. D., Newton, T., Pokki, J., Egeneman, O., Pané, S., Or, Y., & Nelson, B. J. (2015). Undulatory locomotion of magnetic multilink nanoswimmers. *Nano Letters*, *15*, 4829.
69. Khoo, M., & Liu, C. (2001). Micro magnetic silicone elastomer membrane actuator. *Sensors and Actuators A: Physical*, *89*, 259.
70. Olsson, R. T., Samir, M. A. S. A., Salazar-Alvarez, G., Belova, L., Ström, V., Berglund, L. A., Ikkala, O., Nogués, J., & Gedde, U. W. (2010). Making flexible magnetic aerogels and stiff magnetic nanopaper using cellulose nanofibrils as templates. *Nature Nanotechnology*, *5*, 584.
71. Zrínyi, M., Barsi, L., & Büki, A. (1997). Ferrogel: A new magneto-controlled elastic medium. *Polymer Gels and Networks*, *5*, 415.
72. Zrínyi, M., Szabó, D., & Kilian, H.-G. (1998). Kinetics of the shape change of magnetic field sensitive polymer gels. *Polymer Gels and Networks*, *6*, 441.
73. Fuhrer, R., Schumacher, C. M., Zeltner, M., & Stark, W. J. (2013). Soft iron/silicon composite tubes for magnetic peristaltic pumping: Frequency-dependent pressure and volume flow. *Advanced Functional Materials*, *23*, 3845.
74. Nguyen, V. Q., Ahmed, A. S., & Ramanujan, R. V. (2012). Morphing soft magnetic composites. *Advanced Materials*, *24*, 4041.
75. Mitsumata, T., Horikoshi, Y., & Negami, K. (2008). High-power actuators made of two-phase magnetic gels. *Japanese Journal of Applied Physics*, *47*, 7257.
76. Zhang, J., & Diller, E. (2015). Millimeter-scale magnetic swimmers using elastomeric undulations. Presented at *IEEE/RSJ international conference on intelligent robots and systems*, Hamburg, Germany, September, 2015.
77. Taylor, G. I. (1951). Analysis of the swimming of microscopic organisms. *Proceedings of the Royal Society A*, *209*, 447.
78. Wu, S., Hamel, C. M., Ze, Q., Yang, F., Qi, H. J., & Zhao, R. (2020). Evolutionary algorithm-guided voxel-encoding printing of functional hard-magnetic soft active materials. *Advanced Intelligent Systems*, *2*, 2000060.
79. Qi, S., Guo, H., Fu, J., Xie, Y., Zhu, M., & Yu, M. (2020). 3D printed shape-programmable magneto-active soft matter for biomimetic applications. *Composites Science and Technology*, *188*, 107973.
80. Alapan, Y., Karacakol, A. C., Guzelhan, S. N., Isik, I., & Sitti, M. (2020). Reprogrammable shape morphing of magnetic soft machines. *Science Advances*, *6*, eabc6414.
81. Cui, J., Huang, T.-Y., Luo, Z., Testa, P., Gu, H., Chen, X.-Z., Nelson, B. J., & Heyderman, L. J. (2019). Nanomagnetic encoding of shape-morphing micromachines. *Nature*, *575*, 164.
82. Kim, Y., Yuk, H., Zhao, R., Chester, S. A., & Zhao, X. (2018). Printing ferromagnetic domains for untethered fast-transforming soft materials. *Nature*, *558*, 274.
83. Bertotti, G. (1998). *Hysteresis in magnetism: For physicists, materials scientists, and engineers*. Academic.
84. Ginder, J. M., Nichols, M. E., Elie, L. D., & Tardiff, J. L. (1999). Magnetorheological elastomers: Properties and applications. *Smart Materials and Structures*, *3675*, 131.
85. Lum, G.Z., Pham, M.T., Teo, T.J., Yang, G., Yeo, S.H., & Sitti, M. (2017). An XY θ z flexure mechanism with optimal stiffness properties. Presented at *IEEE international conference on advanced intelligent mechatronics*, Munich, Germany, July, 2017.
86. Lum, G.Z., Teo, T.J., Yang, G., Yeo, S.H., & Sitti, M. (2013). A hybrid topological and structural optimization method to design a 3-DOF planar motion compliant mechanism. Presented at *IEEE/ASME international conference on advanced intelligent mechatronics*, Wollongong, NSW, Australia, July, 2013.
87. Lum, G. Z., Teo, T. J., Yeo, S. H., Yang, G., & Sitti, M. (2015). Structural optimization for flexure-based parallel mechanisms – Towards achieving optimal dynamic and stiffness properties. *Precision Engineering*, *42*, 195.

88. Lum, G. Z., Teo, T. J., Yang, G., Yeo, S. H., & Sitti, M. (2015). Integrating mechanism synthesis and topological optimization technique for stiffness-oriented design of a three degrees-of-freedom flexure-based parallel mechanism. *Precision Engineering*, *39*, 125.
89. Pham, M. T., Teo, T. J., & Yeo, S. H. (2017). Synthesis of multiple degrees-of-freedom spatial-motion compliant parallel mechanisms with desired stiffness and dynamics characteristics. *Precision Engineering*, *47*, 131.
90. Huang, H.-W., Sakar, M. S., Petruska, A. J., Pané, S., & Nelson, B. J. (2016). Soft micromachines with programmable motility and morphology. *Nature Communications*, *7*, 1.
91. Ma, C., Wu, S., Ze, Q., Kuang, X., Zhang, R., Qi, H. J., & Zhao, R. (2021). Magnetic multimaterial printing for multimodal shape transformation with tunable properties and shiftable mechanical behaviors. *ACS Applied Materials & Interfaces*. <https://doi.org/10.1021/acsami.0c13863>
92. Abbott, J. J., Peyer, K. E., Lagomarsino, M. C., Zhang, L., Dong, L., Kaliakatsos, I. K., & Nelson, B. J. (2009). How should microrobots swim? *International Journal of Robotics Research*, *28*, 1434.
93. Ge, F., Yang, R., Tong, X., Camerel, F., & Zhao, Y. (2018). A multifunctional dye-doped liquid crystal polymer actuator: Light-guided transportation, turning in locomotion, and autonomous motion. *Angewandte Chemie*, *130*, 11932.
94. Lu, H., Zhang, M., Yang, Y., Huang, Q., Fukuda, T., Wang, Z., & Shen, Y. (2018). A bio-inspired multilegged soft millirobot that functions in both dry and wet conditions. *Nature Communications*, *9*, 3944.
95. Zhao, J., Zhang, X., Chen, N., & Pan, Q. (2012). Why superhydrophobicity is crucial for a water-jumping microrobot? Experimental and theoretical investigations. *ACS Applied Materials & Interfaces*, *4*, 3706.
96. Purcell, E. M. (1977). Life at low Reynolds number. *American Journal of Physics*, *45*, 3.
97. Lighthill, J. (1976). Flagellar hydrodynamics. *SIAM Review*, *18*, 161.
98. Brust, M., Schaefer, C., Pan, L., Garcia, M., Arratia, P., & Wagner, C. (2013). Rheology of human blood plasma: Viscoelastic versus Newtonian behavior. *Physical Review Letters*, *110*, 078305.
99. Baskurt, O. K., & Meiselman, H. J. (2003). Blood rheology and hemodynamics. *Seminars in Thrombosis and Hemostasis*, *29*, 435.
100. Lai, S. K., Wang, Y.-Y., Wirtz, D., & Hanes, J. (2009). Micro- and macrorheology of mucus. *Advanced Drug Delivery Reviews*, *61*, 86.
101. Curt, J. R. N., & Pringle, R. (1969). Viscosity of gastric mucus in duodenal ulceration. *Gut*, *10*, 931.
102. Cone, R. A. (2009). Barrier properties of mucus. *Advanced Drug Delivery Reviews*, *61*, 75.
103. Brackenbury, J. (1997). Caterpillar kinematics. *Nature*, *390*, 453.
104. Jäger, P. (2014). Cebrennus Simon, 1880 (Araneae: Sparassidae): A revisionary up-date with the description of four new species and an updated identification key for all species. *Zootaxa*, *3790*, 319.
105. Armour, R. H., & Vincent, J. F. V. (2006). Rolling in nature and robotics: A review. *Journal of Bionic Engineering*, *3*, 195.
106. Miyashita, S., Guitron, S., Yoshida, K., Li, S., Damian, D.D., & Rus, D. (2016). Ingestible, controllable, and degradable origami robot for patching stomach wounds. Presented at *IEEE international conference on robotics and automation*, Stockholm, Sweden, May, 2016.
107. Munoz, F., Alici, G., & Li, W. (2014). A review of drug delivery systems for capsule endoscopy. *Advanced Drug Delivery Reviews*, *71*, 77.
108. Yim, S., Goyal, K., & Sitti, M. (2013). Magnetically actuated soft capsule with the multimodal drug release function. *IEEE/ASME Transactions on Mechatronics*, *18*, 1413.
109. Kim, C., Kim, H., Park, H., & Lee, K. Y. (2019). Controlling the porous structure of alginate ferrogel for anticancer drug delivery under magnetic stimulation. *Carbohydrate Polymers*, *223*, 115045.

110. Tasoglu, S., Diller, E., Guven, S., Sitti, M., & Demirci, U. (2014). Untethered micro-robotic coding of three-dimensional material composition. *Nature Communications*, 5, 1.
111. Tasoglu, S., Kavaz, D., Gurkan, U. A., Guven, S., Chen, P., Zheng, R., & Demirci, U. (2013). Paramagnetic levitational assembly of hydrogels. *Advanced Materials*, 25, 1137.
112. Floyd, S., Pawashe, C., & Sitti, M. (2009). Two-dimensional contact and noncontact micro-manipulation in liquid using an untethered mobile magnetic microrobot. *IEEE Transactions on Robotics*, 25, 1332.
113. Pawashe, C., Floyd, S., Diller, E., & Sitti, M. (2012). Two-dimensional autonomous microparticle manipulation strategies for magnetic microrobots in fluidic environments. *IEEE Transactions on Robotics*, 28, 467.
114. Giltinan, J., Diller, E., & Sitti, M. (2016). Programmable assembly of heterogeneous microparts by an untethered mobile capillary microgripper. *Lab on a Chip*, 22, 4445.
115. Zhang, J., Salehizadeh, M., & Diller, E. (2018). Parallel pick and place using two independent untethered mobile magnetic microgrippers. Presented at *IEEE intertaional conference on robotics and automation*, Brisbane, QLD, Australia, May, 2018.
116. Khaderi, S. N., Craus, C. B., Hussong, J., Schorr, N., Belardi, J., Westerweel, J., Prucker, O., Rhe, J., den Toonder, J. M. J., & Onck, P. R. (2011). Magnetically-actuated artificial cilia for microfluidic propulsion. *Lab on a Chip*, 11, 2002.
117. Hanasoge, S., Hesketh, P. J., & Alexeev, A. (2018). Microfluidic pumping using artificial magnetic cilia. *Microsystems & Nanoengineering*, 4, 11.
118. Shields, A. R., Fiser, B. L., Evans, B. A., Falvo, M. R., Washburn, S., & Superfine, R. (2010). Biomimetic cilia arrays generate simultaneous pumping and mixing regimes. *Proceedings National Academy of Sciences United States of America*, 107, 15670.
119. Sitti, M. (2019). Robotic collectives inspired by biological cells. *Nature*, 567, 314.
120. Alapan, Y., Yasa, O., Schauer, O., Giltinan, J., Tabak, A. F., Sourjik, V., & Sitti, M. (2018). Soft erythrocyte-based bacterial microswimmers for cargo delivery. *Science Robotics*, 3, eaar4423.
121. Wang, B., Chan, K. F., Yu, J., Wang, Q., Yang, L., Chiu, P. W. Y., & Zhang, L. (2018). Reconfigurable swarms of ferromagnetic colloids for enhanced local hyperthermia. *Advanced Functional Materials*, 28, 1705701.
122. Servant, A., Qiu, F., Mazza, M., Kostarelos, K., & Nelson, B. J. (2015). Controlled in vivo swimming of a swarm of bacteria-like microrobotic flagella. *Advanced Materials*, 27, 2981.
123. Yigit, B., Alapan, Y., & Sitti, M. (2019). Programmable collective behavior in dynamically self-assembled mobile microrobotic swarms. *Advancement of Science*, 6, 1801837.
124. Tognarelli, S., Castelli, V., Ciuti, G., Natali, C. D., Sinibaldi, E., Dario, P., & Menciassi, A. (2012). Magnetic propulsion and ultrasound tracking of endovascular devices. *Journal of Robotic Surgery*, 6, 5.
125. Singh, A. V., Ansari, M. H. D., Dayan, C. B., Giltinan, J., Wang, S., Yu, Y., Kishore, V., Laux, P., Luch, A., & Sitti, M. (2019). Multifunctional magnetic hairbot for untethered osteogenesis, ultrasound contrast imaging and drug delivery. *Biomaterials*, 219, 119394.



Chelsea Shan Xian Ng received her B.Eng. in Aerospace Engineering from Nanyang Technological University, Singapore, in 2019. She is currently a Ph.D. student at the School of Mechanical and Aerospace Engineering at Nanyang Technological University, Singapore. Her research interest is in the area of miniature soft robotics and bioinspired design.



Changyu Xu received his bachelor's degree in Mechanical Engineering from Dalian University of Technology, China, in 2017. He is currently pursuing his Ph.D. in robotics, Nanyang Technological University, Singapore. His research interests include magnetic miniature robots, soft robots, and bioinspired robots.



Guo Zhan Lum received his B.Eng. from Nanyang Technological University in 2010. He went on to pursue his post-graduate studies under the dual Ph.D. program of Nanyang Technological University and Carnegie Mellon University. He received his M.Sc. degree from Carnegie Mellon University in 2015 and dual Ph.D. degrees in 2016. From 2016 to 2017, he was a post-doctoral researcher at the Max Planck Institute for Intelligent Systems. Since 2018, he is an Assistant Professor at Nanyang Technological University, and his research interests include soft robots, miniature robots, and biomedical devices.

Chapter 10

In Vitro Biosensing Using Micro-/Nanomachines



Jinhong Gao, Ke Yuan, and Li Zhang

10.1 Introduction

The concept of biosensing involves a large mixture of research endeavor and many practical applications [1]. In this chapter, we focus on in vitro biosensing whose application realms are limited to outside of living body of human and animals [2]. With the progress of globalization, the widely expanded industrialization and trans-oceanic transportation of human and goods have dramatically posed many tough challenges to the living standards of human as well as the high-performance and cost-/time-efficient biosensing technologies [3]. The industry has produced a large amount of hazardous pollutants (as by-products of industry and farming), such as heavy metal ions, toxins, pesticides, and biohazardous matters. Those substances are highly toxic and making serious threats to the ecosystem of earth and our health when accumulated in human bodies [4]. On the other hand, the rapid communication of human and goods have inevitably elevated the risk of the arise and spread of new diseases (in the worst case, a pandemic may spark). In 2019, COVID-19 broke out and spread across the world in a short time. The outbreak of this fatal virus has caused hundreds of thousands of infections and thousands of deaths and trillions of economic losses, threatening the health of human and economy of whole world [5].

J. Gao (✉) · K. Yuan

Department of Mechanical and Automation Engineering, The Chinese University of Hong Kong, Hong Kong, SAR, China
e-mail: jinhonggao@cuhk.edu.hk

L. Zhang

Department of Mechanical and Automation Engineering, The Chinese University of Hong Kong, Hong Kong, SAR, China

CUHK T Stone Robotics Institute, The Chinese University of Hong Kong, Hong Kong, SAR, China

Chow Yuk Ho Technology Centre for Innovative Medicine, The Chinese University of Hong Kong, Hong Kong, SAR, China

The quick detection of viruses and determination of infection have rapidly become a hot topic and drawn lots of attention in terms of biosensing [6]. Traditional *in vitro* biosensing methods usually include mass spectrum (MS), nuclear magnetic resonance (NMR), polymerase chain reaction (PCR), and high-performance liquid chromatography (HPLC) to directly evaluate toxic substances or indirectly probe the presence of those toxic substances and their changes [7]. These methods are powerful and highly reproducible and have low limit of detection (LOD), but need tedious preparation and purification of sample, sophisticated and expensive instruments, costly probes, and qualified personnel operation. In the past decades, many researchers have been endeavoring to address above issues by developing various devices or systems and low-cost electrochemical and optical probes that are able to sense and monitor these toxic compounds and pathogen [8]. Among those methods, the micro-/nanomachine-based methods have significantly impacted the field of *in vitro* biosensing due to not only the excellent selectivity and sensitivity but also the enhanced detection resolution and miniaturized detection devices [9].

Inspired by the natural micro-/nanomachines (such as sperms or kinesins), artificial micro-/nanomachines, a type of micro-/nanoscale robots or devices, have been developed due to vigorous advances in micro-/nanofabrication and microelectronics [10]. These artificial micro/nanomachines can swim in different fluids by converting diverse types of energies into mechanical motion or directly harnessing living microorganisms [11]. Due to their ultra-small dimensions and active motile property, these mimicked micro-/micromachines have proven their advantages in various tasks and applications when compared to their passive counterparts [12]. These tasks and applications include targeted drug delivery [9a, 13], cancer bioimaging and therapy, [14] manipulation and isolation of cells [13a, 14b, 15], micro-/nanosurgery [16], and *in vitro* biosensing [11c, 17]. In the past decades, various types of micro-/nanomachines (ranging from 1D wire structures and tubular structures to Janus spherical structures to delicate 3D structures [18]) with different fabrication strategies, materials, and mechanisms of propulsion (i.e., chemical energies, hydrogen peroxide, urea; energies from external fields, light, magnetic field, ultrasound) have been forged and used in above fields [19]. Moreover, by tailoring the surface functionalization of micro-/nanomachines, the motion behaviors and multiple properties of these intricately devices can be further tuned to meet their various application requirements. Particularly, in the field of *in vitro* biosensing, the controllable and efficient motions of the artificial micro-/nanomachines can greatly enhance fluid transport and accelerate recognition process in these bioassays, which is dramatically fitted with the requirement of real-time *in situ* identification and monitoring of analytes, and on-demand transport and separation of analytical targets in the realm of biosensing [9a, c, d, 10a].

The objective of this chapter is to highlight recent progress and future possibilities and challenges in developing advanced micro-/nanomachines for *in vitro* biosensing applications. Particular interests would be given to the main fields of *in vitro* biosensing: (1) *in vitro* detection and monitoring of hazardous or important chemical and biological components, (2) intracellular monitoring of life-important properties and molecules, and (3) pathogens and biomarker discrimination based on

micro-/nanomachines. The recent proof-of-concept studies exemplify the versatility of micro-/nanomachines and are indicative of their wide range potential in in vitro applications. In the next section of this chapter, we would first review propulsion and functionalization strategies of micro-/nanomachines, along which the manufacturing and micro-/nanofabrication of these intricately devices would also be covered. Next, the sensing mechanisms of these functional micro-/nanomachines would be systematically summarized, and the in vitro biosensing of these versatile micro-/nanomachines in three main fields as mentioned above would be presented to illustrate how the controllable and efficient movement of functional micro-/nanomachines add a new and powerful dimension to monitoring and sensing of analytes by providing fast or even real-time response, location-confined or in situ monitoring, as well as high accuracy and selectivity to analytes. Finally, existing challenges and perspectives of micro-/nanomachines would be further discussed before a brief conclusion.

10.2 Propulsion, Function of Micro-/Nanomachines

10.2.1 Propulsion of Micro-/Nanomachines

Similar to their macroscale counterparts, micro/nanomachines work by converting other forms of energy into mechanical motion. However, constrained by the time reversal symmetry that applies in the low Reynolds number regime, synthetic micro-/nanomachines typically cannot mimic their macroscale partners directly and have not moving parts [20]. Additionally, due to the inherent Brownian motion coming from the scaling-down effect, it is no an easy task to precisely control the motion of micro-/nanomachines [21]. A wide range of micro-/nanomachines based on different propulsion mechanisms have been developed in past years. The potential mechanism harnessed for the movement can be divided into three major classifications: (1) chemically catalytic propulsion [9a, 11b, 17b], (2) actuation by external fields [13b, 19a, b, e], and (3) propulsions based on biohybrid designs [13c, 22]. The first two ways involve exposing the synthetic micro-/nanomachines to a field or gradient, either chemical gradient or external sound or magnetic field to break time-reversal symmetry and power micro-/nanomachines. The third method, on the other hand, takes advantages of biological motors (i.e., sperm, flagella bacteria) to steer biohybrid micro-/nanomachines, which would combine the outstanding properties of artificial materials and high mobility and biocompatibility of these natural motors. Compared with the hybridized synthetic micro-/nanomachines, the propulsion motion of pure artificial micro-/nanomachines is more stable and less affected by external conditions such as temperature and solvent conditions due to the characteristic mechanism of propulsion.

The first method is based on the generation of local gradients of chemical/electrical potential or gas bubbles. The local gradients of chemical/electrical potential or

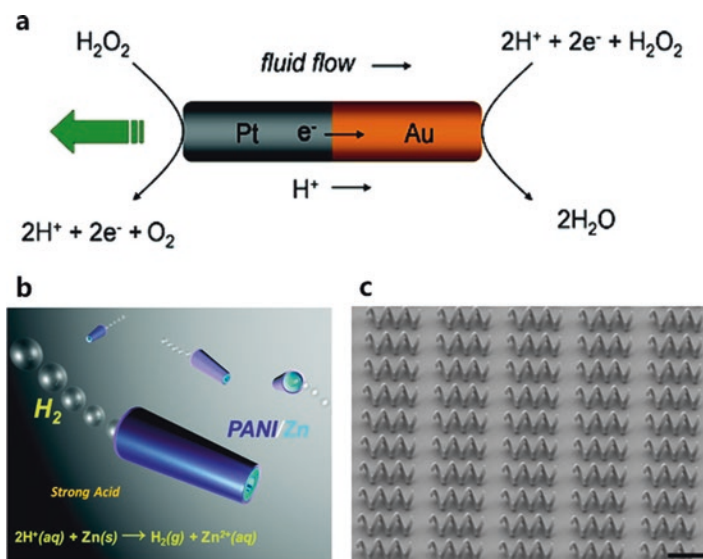


Fig. 10.1 Different propulsion mechanisms of micro-/nanomachines. (a) A schematic illustrating self-electrophoresis propulsion of bimetallic Pt-Au nanorods in H_2O_2 solution, reproduced with permission, Copyright 2016, American Chemical Society [24]; (b) schematic of motion hydrogen-driven PANI-Zn micro-rocket in an acidic environment, reproduced with permission, Copyright 2012, American Chemical Society [26]; (c) SEM image of artificial bacterial flagella array (the scale-bar: 10 μm) reproduced with permission [29]

bubbles can be obtained (1) by the catalytic decomposition of fuel/medium molecules on the surface of micro-/nanomachines and (2) spontaneous and irreversible chemical reactions between medium and composition of micro-/nanomachines. Such a propulsion mechanism requires some specific pairs of fuel or medium and specific composition of the outer layer of micro-/nanomachines. The typical pairs of fuel (or substrate) and catalysts include hydrogen peroxide (H_2O_2) and their catalyst (i.e., noble metal or catalase) as well as glucose/urea and their respective enzymes. Two independent early research established that bimetallic metal microrods moved autonomously in hydrogen peroxide solutions [23]. As shown in Fig. 10.1a, the mechanism by which these micromachines are propelled was verified, using both experimental and simulation methods, as to be self-electrophoresis [24]. The key-point of the mechanism is that micromachine particles generate chemical gradients of ions through bipolar electrochemical reactions at the two ends of the rods, resulting in an electric field between two ends and inducing motion of the micromachine through electrophoresis. Although micro-/nanomachines based on hydrogen peroxide fuel can move at a quite high speed and perform different types of motion, they are limited to some application fields due to the inherent toxicity of this toxic peroxide, and all of them are limited by access to fuel in the medium.

Second, the spontaneous and irreversible chemical reaction pair of medium and composition may include acid or water and active metal (i.e., zinc and magnesium).

Such design not only circumvents the need for external fuel and is more bio-friendly but also provides selective micro-/nanomachines activation only in particular environments [25]. Inspired by the aforementioned reaction pairs, Wang and co-workers developed novel motile micro-/nanomachines based on zinc (Zn) or magnesium (Mg) chemical reaction with acid [16a, 26]. Also, Gao et al. prepared a polyaniline (PANI)/Zn double-layer hollow tubular motor, which shows good motion in the gastric acid environment (Fig. 10.1b).

Third, the biohybrid artificial micro-/nanomachine could harness various types of flagellated organisms and show great flexibility. Moreover, the motile cells integrated in the biohybrid systems do not need to be cultivated and are able to swim in highly viscous media and are completely bio-friendly [22]. Magdanz et al. had combined magnetic microtube and sperm to develop sperm-flagella-driven micro-biorobot [27]. Nevertheless, both chemical- and biohybrid-based artificial micro-/nanomachines can only move in a quasi-random manner, and the inherent lack of a defined trajectory can only be alleviated by including a magnetic component (e.g., nickel) in their structures and under the guidance of an external magnetic field [28].

In order to circumvent the hindrances of lack of defined trajectory and need for fuel from circumstance, actuation with energies from external fields shows considerable promise for remote navigation in complex biological fluids and hard-to-access locations [14c, 19b, e]. These externally powered micro-/nanomachines, using mainly magnetic, ultrasound, and light energies to drive their motion, have gained great interest in biomedical applications due to their independence of the chemical compositions of the medium. Thus, higher biocompatibility and easy-to-steer and defined trajectory under the control of external fields can be realized. As the magnetic fields can penetrate the human body to wirelessly control these micro-devices without harming cells and tissues, micro-/nanomachines powered and actuated by magnetic fields have gained particular interest. In a pioneered work, a special type of magnetic helical microswimmer (artificial bacterial flagella, ABF), which can perform micrometer precision movement for 3D navigation, has been proposed (Fig. 10.1c) [29]. Under low-strength rotating magnetic fields (much lower than that of MRI setup), these tiny micromachines would translate rotational movement into linear motion in a controlled manner [30]. Furthermore, Felfoul *et al.* demonstrated that significantly improved delivery efficiency of drug nanocarriers to tumor hypoxic regions of limited accessibility can be achieved by harnessing the magneto-aerotactic behavior of selected bacteria swarms [31]. Similar to magnetic propulsion, acoustic forces propulsion has also shown high biocompatibility, deep tissue penetration, and easy-to-program properties, and micro/nanomachines actuated by acoustic forces have been widely utilized in various biomedical applications, including biosensing and drug delivery. Mallouk and colleagues at Penn State University demonstrated for the first time that ultrasound (US) propelled nanomachine made of gold nanowire can move in a directional manner and spin inside HeLa cells without leading to any damage [32]. These US-powered NW nanomachines show great promises for payload delivery in a single cellular level and biosensing in living cell which will be discussed in the following sections [13b, 33]. However, both magnetic actuation and US actuation are equipment dependent,

and the strengths of these propulsions are limited, compared to the bubble or chemical potential-based method.

In short, various propulsion mechanisms have been developed and utilized to actuate micro-/nanomachines for different applications. To further widen practical applications of micro-/nanomachines, more endeavors should be devoted to overcoming their disadvantages and further exploring and exploiting their respective advantages.

10.2.2 Chemical-, Biological-, and Self-Functionalization of Micro-/Nanomachines

Besides the different propulsion methods, the artificial micro-/nanomachines can further be classified according to their building block materials and shapes. In the past years, much efforts have been devoted to developing various types of micro-/nanomachines with diverse shapes (from the simplest 1D structure to Janus spherical structure and tubular micro-/nanostructures) [18] and different materials, for example, noble metal species (Au, Ag), inorganic materials (SiO_2 , Fe_3O_4), polymers (poly(3,4-ethylenedioxythiophene), polyaniline, and polypyrrole), and metal-organic frameworks (MOFs) [9d, 25b, 30, 34]. The prototype of micro-/nanomachines with different structures and shapes can only accomplish simple moving function; to make these micro-/nanostructures complete more complicated tasks, additional functionalization is indispensable. The purpose for functionalization of micro-/nanomachines can be categorized as follows: (1) to improve biocompatibility of synthetical micro-/nanomachines for their biomedical applications [25b]; (2) to label these stuffs, for example, fluorescent markers so that they can be traced in their working environment [14a, 17b, 25b]; (3) to endow specific functions to these tiny machines, especially to interact with or bind to analytes [9d, 13b, 16a, 17b]; (4) to improve the controllability or steer function of these tiny machines [28a, 30, 32]; and (5) to load cargo onto these transporters, such as delivery of drugs to target to cancer or infection area [11c, 13c, 15–16]. To meet such diverse purpose of functionalization, various kinds of functionalization methods have been developed during recent years and can be classified as follows: (1) chemical modification, (2) biological modification, and (3) self-functionalization.

Chemical modification or functionalization is the most convenient and widely used technology in the field of micro-/nanomachines for applications of cargo delivery, drug release, bioimaging, and environmental remediation. A majority of chemical modifications is targeted to change the surface properties of micro-/nanomachines, for example, to make these stuff more hydrophilic (more biocompatible) or more slippery to easily pass viscous environment [34b]. In 2018, Wu et al. demonstrated their slippery, helical magnetic micropropellers, that can be actively propelled through the vitreous humor to reach the retina for intravitreal delivery [35]. These novel microvehicles are equipped with a liquefied layer coating of perfluorocarbon

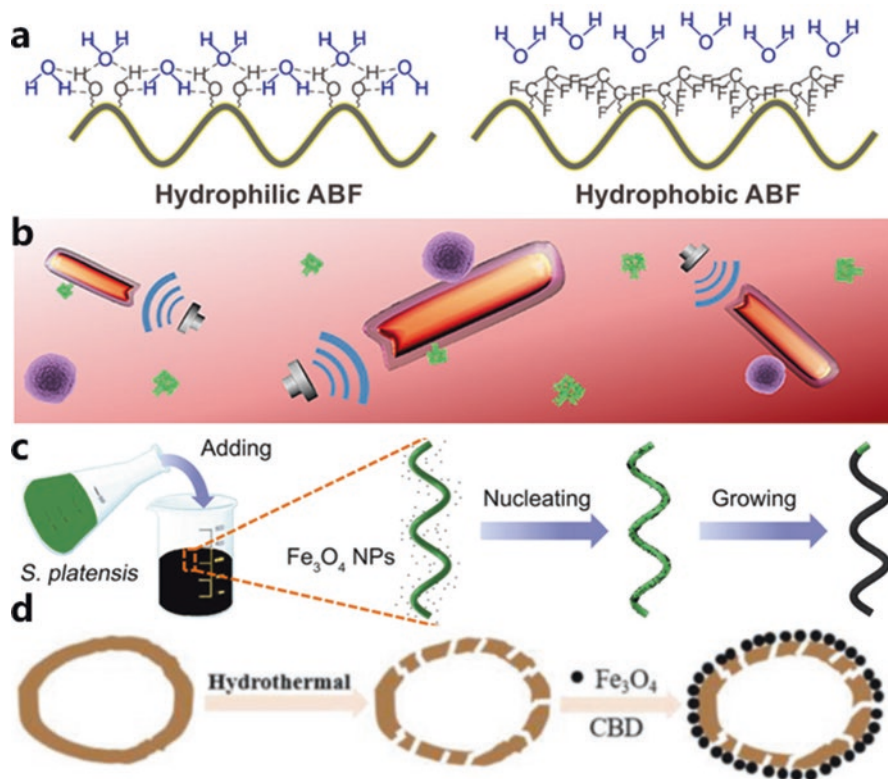


Fig. 10.2 Functionalization of micro-/nanomachines. (a) Schematic of the interaction between water and ABFs with different surface wettabilities, reproduced with permission, Copyright 2018, American Chemical Society [36]; (b) Illustration of hybrid bio-membrane functionalized nanorobots for removal of hazardous biological agents, reproduced with permission, Copyright 2018, American Association for the Advancement of Science [42]; (c) Schematic of fabrication of multifunctional biohybrid microrobots comprised of *Spirulina* microalgae and Fe_3O_4 nanoparticles, reproduced with permission, Copyright 2017, American Association for the Advancement of Science [14a]; (d) Schematic of the fabrication of biohybrid adsorbents comprised of fungi spores and Fe_3O_4 nanoparticles, reproduced with permission, Copyright 2018, Wiley-VCH [45]

molecules to minimize adhesion to the surrounding biopolymeric network. To endow the ABFs with different wettabilities, Wang *et al.* modified magnetic helical microswimmers with a series of thiols/thioethers with different hydrophilic/hydrophobic moieties, and they found that surface wettability has a huge effect on the swimming behavior of ABFs in aqueous media (deionized water and biologically relevant solutions) (Fig. 10.2a). [36]. Furthermore, Gao *et al.* and Wang *et al.*, respectively, demonstrated Janus micromotors and functionalized microtube-based micromachines for capture and removal of oil droplets from contaminated water, both utilizing long-chain alkanethiols to tune the hydrophobicity of their artificial micro-/nanomachines [36, 37]. To be able to see and track the micro-/

nanomachines, especially in vivo, some tracer agents like red light emitting dyes (Nile red), positron, or gamma emitters have been modified into micro-/nanomachines. Vilela et al. labeled their catalytic self-propelled, gold surface micromotors with positron-emitting isotope iodine-124 via chemisorption with a radio-chemical yield of $76 \pm 4\%$ and quantitatively tracked the swarms of such micromotors inside the phantom tubes using a positron-emission tomography (PET) in combination with X-ray computed tomography (CT) [38].

However, chemical functionalization is generally limited by the toxicity of chemical agents, the vulnerability of interference from the actual environment, and the lack of specific interaction with biomolecules or organisms. To alleviate the lack of specific interaction with biomolecules or organisms, various biorecognition motifs with high affinity and specificity including aptamers, lectins, and antibodies have been widely employed for the functionalization of the micro-/nanomachines, especially in the field of biomolecules biosensing and hazardous cargo or pollutant removal [25b, 33, 39]. Interestingly, the function of biomacromolecules immobilized on the surface of micro-/nanomachines can be altered and even enhanced when these micro-/nanomachines move in solution. Maria-Hormigos et al. developed magnetically propelled micromachines functionalized with β -galactosidase to degrade lactose in raw milk samples [40]. Compared to static counterparts and free enzymes, actively moving micromotors showed improved removal efficiency of lactose in raw milk samples, which should be contributed to the produced dynamic movement and the associated fluid mixing. The micromotor/enzyme hybrid can be reused, with only $\sim 11\%$ loss of enzyme activity in two successive cycles, showing their competitiveness in the biochemical process acceleration. To further improve their biocompatibility and avoid recognition by the immune system, Wang's team first proposed a biocompatible erythrocyte membrane-coated gold nanomotor activated and driven under ultrasound operations [41]. These red blood cells (RBCs) membrane-coated gold nanomotors could navigate effectively in diluted whole blood with high stability and biocompatibility. Furthermore, these membrane-coated nanomotor have been used to absorb membrane targeted toxins, which are defined as "motor sponges." The motor sponges under ultrasound propelled have shown $\sim 30\%$ more effective than the regular toxin sponges without motion indicated in quantitative hemolysis analysis, highlighting the application of neutralization of membrane-damaging toxins accelerated by large-scale collective motion of RBC membrane-coated nanomotors. In addition, Zhang et al. recently reported an ultrasound-propelled nanomachines coated with dual-cell membranes (including erythrocyte and platelet membranes), showing higher efficiency in targeting platelet-adhering pathogens and neutralization of toxins [42] (Fig. 10.2b).

The aforementioned chemical and biological strategies for functionalization of micro-/nanomachines are general bottom-up and require expensive chemical and biological reagents, elaborate organic synthetic technique, as well as cumbersome and dangerous post-treatment procedures [43]. Furthermore, multiple steps of functionalization are needed on the same micro-/nanomachines to achieve multiple surface functionalities, dramatically limiting the large-scale manufacturing micro-/nanomachines for practical applications. Various natural biological materials with

abundant functional groups would endow micro-/nanomachines with multiple functionalities and make the batch fabrication of high versatile micro-/nanomachine possible [44]. For the first time, our group has prepared multifunctional microrobots by exploiting the inherent functionality of *Spirulina* microalgae, a natural multifunctional organism with innate autofluorescence microalgae and intrinsic cytotoxicity to cancer cells [14a]. Using a biohybrid process with magnetite suspensions, these multifunctional microrobots would be propelled in the external magnetic field. Their strong red autofluorescence under green light illumination could be employed for in vivo fluorescence imaging in the subcutaneous tissue and the intraperitoneal cavity of nude mice. The biohybrid *Spirulina*-templated microrobots can induce apoptosis of SiHa and HepG2 cancer cell, which can be contributed to cytotoxic phycocyanin released from the *Spirulina* matter under ultrasonication-induced degradation (Fig. 10.2c). Thereafter, we developed a kind of magnetically propelled biohybrid microrobot based on the hydrothermally treated fungi spores as adsorbent and Fe₃O₄ nanoparticles as magnetic component. The obtained biohybrid adsorbents can effectively adsorb and remove heavy metal ions due to rich functional groups and porous structure on biological components [45] (Fig. 10.2d). Under the stimulation of external magnetic fields, these biohybrid adsorbents can swarm controllably and conduct efficient adsorption and rapid removal of various heavy metal ions from the contaminated water. We believe that the self-functionalization of micro-/nanomachines by further exploring more available and novel biological sources would be a highly promising way to bridge the gap between the micro-/nanomachines and real-world applications.

10.3 Micro-/Nanomachines for Sensing

10.3.1 Sensing Mechanisms of Micro-/Nanomachines

The emerging utilization of micro-/nanomachines has greatly impacted various biosensing applications and even precise diagnosis of diseases, providing a new paradigm for modern analytic chemistry. Combined with autonomous motion and effective recognition and capture of target analytes through various functionalizations aforementioned, these synthetic micro-/nanomachines realize “on-the-fly”-specific biomolecular sensing in the sample of complex biological media [9, 10b, 11a, 21b]. The continuous movement of the synthetic micro-/nanomachines can lead to efficient solution mixing in clinical samples with microliter volume, achieving greatly enhanced binding efficiency of targets and remarkable improvements in the sensitivity and speed of biological assays for heavy metal ions, proteins, nucleic acids, and even cancer cells. Furthermore, these artificial micro-/nanomachines are capable of in situ detection of untreated samples, which shows great advantage and benefit to the practical detection in the field by eliminating the need for cumbersome sample preparation (such as sample cleaning and component separation). The

sensing strategies of versatile micro-/nanomachines can be categorized as (1) motion or velocity change induced by binding of analytes target to micro/nanomachines [17b, 46] and (2) external signal change, in most cases fluorescence turn-on or turn-off, of micro-/nanomachines due to targeted recognition [33, 39a, 47]. The concept of motion-based sensing using micro-/nanomachines was first introduced by Wang and co-workers in 2009 for detection of silver ions which would be further discussed in the later section of this chapter [46]. Besides, the accelerated micro-mixing from the motion of micro-/nanomachines, which favors chemical reaction rate and enhances receptor and analytes binding, would benefit traditional sensing setups, such as immunoassay and electro-chemiluminescent assay.

Currently, a large number of micro-/nanomachines with different morphologies, including Janus spherical, rod-like, tubular, and helical shape, and propelled by various powers, including chemical, ultrasound, and magnetic energies, have been prepared as sensors. These high-performance biosensors based on well-designed micro-/nanomachines have been used for diverse analyte targets with different recognition methods or units, like antibodies [48], aptamers [39], and lectins [49] decorated on their surface. Here, we emphasize their applications in three fields: (1) *in vitro* detection for chemical and biological agents, including hazardous heavy metal ions, dangerous organic pollutants, and some toxins released from microbes; (2) intracellular monitoring of life-important properties and molecules, like viscosity inside the cell and expression level of key micro-RNAs (miRNAs); and (3) pathogen and biomarker discrimination based on micro-/nanomachines. For all three fields, several examples are demonstrated and discussed.

10.3.2 In Vitro Detection for Chemical and Biological Agent

As by-products of the rapid industrialization and globalization, toxic chemicals especially inorganic heavy metal ions and organic molecules have posed great threats to both environment and human health. In the past years, a number of artificial micro-/nanomachines using motion-based sensing as a transduction mechanism have been developed to determine many types of hazardous heavy metal ions. Such detection was based on the changes in the swimming behavior (i.e., speeds and trajectories) in the presence of analytes. The first work that used this strategy was developed by Wang and his co-workers in 2009 [46]. In this work, they observed a fivefold increase in speed of catalytic bimetallic Au-Pt nanorods upon Ag^+ addition when navigating in H_2O_2 solution containing (Fig. 10.3a) and found that other heavy metal analytes, such as Pb^{2+} and Cd^{2+} , have an adverse effect on the speeds due to the poisoning effects. The authors attributed this acceleration of micromotors to the superficial reduction of Ag^+ and subsequent deposition onto the nanomotors due to reduction effect of H_2O_2 . The deposition of silver on the surface of micromachines would enhance their catalytic properties. To prove their hypothesis, they compared the dynamics of passive and active nanowires (gold nanowires and Au-Pt nanomotors, respectively) in a silver ion gradient with experiments and Brownian dynamics

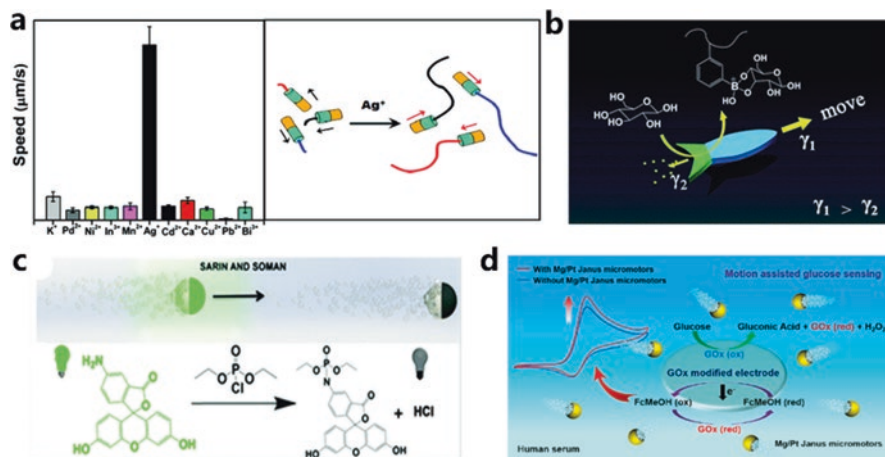


Fig. 10.3 In vitro detection of chemical and biological agents by micro-/nanomachines. (a) left, the average speed of Au-Pt nanomotor in the present of different metal ions; right, schematics of Ag^+ ion induced enhancement of Au-Pt nanomotor speed, Reproduced with permission, Copyright 2009, American Chemical Society [46]; (b) Schematic of the fish-like motor and its autonomous movement triggered by glucose, Reproduced with permission, Copyright 2017, Royal Society of Chemistry [51c]; (c) Schematic for “on-the-fly” fluorescent detection of nerve agent DCP based on Janus micromotor and corresponding detection mechanism of the reaction between fluorescein-amine and DCP, Reproduced with permission, Copyright 2015, Royal Society of Chemistry [53]; (d) Schematic of Mg/Pt Janus micromotor-assisted enhanced electrochemical detection of glucose in human serum, Reproduced with permission, Copyright 2019, American Chemical Society [55]

simulations, respectively. Based on these results, they elucidated the diffusion-phoretic motion mechanism of acceleration of the active micromotors in the presence of silver ion, providing a reliable Langevin model for analyzing the accelerated detection. Similarly, by exploiting the negative effect of Pb^{2+} on the motion of artificial inorganic tubular microrobots, Pumera and co-workers probed the presence of Pb^{2+} in water with a good specificity [50].

Utilizing the release of the surfactant and the resultant Marangoni effect, Liu et al. have demonstrated the successful fabrication of micro-/nanomachines for pH and glucose sensing [51]. In the first case, they developed a spindle-like micromachine for motion-based pH sensing using biodegradable polycaprolactone material [51a, b]. These environment-friendly micromachines can move autonomously on water surface for up to 40 min and exhibit motion-based pH sensing in response to variations of surface tension triggered by pH-dependent surfactant release. In the second case, they reported a fish-like micromachine capable of motion-based glucose sensing [51c]. Using boronic acid as glucose binding component, a correlation between the moving velocity of the micromotor and the glucose concentration was established. Such a motion-based pH or glucose detection may find their applications in the monitoring of reflux of gastric acid and diabetes (Fig. 10.3b).

The motion behavior of micro-/nanomachines can also be regulated by controlling the catalytical activity of inorganic catalysts or enzymes [51b, 52]. Su et al.

proposed motion-based pH sensing using cartridge-case-like micromotor by exploiting the accessibility of substrate to catalyst [51 b]. The micromachine consisted of a swellable gelatin shell and platinum NPs decorated on the shell's inner surface. These micromachines can autonomously move in the aqueous solution with H_2O_2 fuel. The pH-dependent "open and close" feature of gelatin material in micromachines impacted the catalytic activity of platinum NPs by regulating the accessibility of H_2O_2 to platinum NPs. An increase in the pH of the solution would lead to a monotonic increase in velocity of the micromachine. Similarly, by utilizing the inhibition effect of nerve-agent on catalase activity (resulting in lower bubble-generation frequency), Singh et al. developed a catalase-based micromotor for motion-based sensing of nerve-agent vapor plumes, sarin simulant diethyl chlorophosphate (DCP) [52]. The motion-based vapor detection strategy shows high promise for combating chemical warfare agents (CWA).

Micro-/nanomotors can also be further functionalized with external signal motifs, mainly fluorescent molecules for the effective and sensitive sensing of target analytes [53]. In 2015, Wang's group reported the first fluorescent "on-off" micromotor strategy for the detection of sarin and soman simulants as nerve agent models [53]. The two faces of Janus silica microparticle can realize different functions: the sensing face functionalized with a dye (fluoresceinamine, FLA) and the catalytic face with Pt for producing bubbles in H_2O_2 solution to propel the micromachine. The propelled motion can strongly accelerate the reaction between phosphoryl halides of sarin and soman simulants and amino moieties of the FLA molecules. The resulting fluorescence quench can sensitively and selectively probe the existence of such chemicals (Fig. 10.3c).

To further explore the capacity of "on-off" or "off-on" strategies, more types of recognition molecules (such as aptamers, antibodies) and fluorescent probes (like carbon dots) have been integrated into micro-/nanomachines [39a, 54]. Esteban-Fernandez et al. developed a membrane-template electrodeposited graphene/Pt tubular micromotors and used them for "off-on" selective sensing of toxins (ricin) [39a]. The fluorophore-labeled ricin aptamer can attach on their surface due to π -stacking interactions between graphene and nucleotide bases of aptamer, leading to fluorescence quench of the fluorophore. Upon the presence of ricin in the solution, fluorescence would recover due to ricin-induced distance between fluorophore and graphene. Similarly, graphene/Pt [54a] and graphene/Ni/Pt [54b] micromotors with fluorescent-labeled aptamers absorbed on surface have been utilized for the fast, simultaneous, and quantitation of two mycotoxins (fumonisin B1 (FB1) and ochratoxin A (OTA)) as contaminants in food samples, respectively.

The "on-off" or "off-on" strategies based on micro-/nanomachines could also be utilized to sense complex biomacromolecules, such as endotoxin [47, 54c]. In 2017, Jurado-Sanchez et al. have demonstrated an "on-off" detection strategy for bacterial endotoxins based on Janus micromotor [54c]. To synthesize these Janus micromotors, a 10% SDS water solution containing fluorescent graphene quantum dots (GQDs) and chloroform containing a polymer, Pt NPs, and Fe_3O_4 NPs were mixed under vigorous stirring. During the evaporation of organic solvent to yield solidified polymer-based microparticles, the immiscibility of metal NPs with the polymer led

to the accumulation of metal NPs on one hemisphere of the obtained microparticles. As these Janus micromachines bore a number of mesoporous pores, the endotoxins released from the bacteria could diffuse to the interior of the micromotors and quench the fluorescence of QDs. The active mixing function of Janus micromotors played an important role to improve the speed and sensitivity of endotoxins sensing. This approach was further modified and improved for the quantification of endotoxins from *Salmonella enterica* in food-contaminated samples, such as egg yolk/white, mayonnaise, and milk. The fluorescence emitted from the modified quantum dots in the Janus micromotor would quench upon interaction with endotoxin.

Micro-/nanomachines also can be used for improving the performance of traditional sensing and detection systems [55, 56]. For instance, Esteban-Fernández et al. developed a tubular micromotor-based cortisol immunoassays with a huge acceleration of detection speed and enhanced sensitivity. The dynamic movement and corresponding bubble generation of antibody functionalized micromotors led to enhanced fluid intermixing, likelihood of antibody-cortisol interaction in microliter samples, and horseradish peroxidase (HRP) catalysis effect on the tetramethylbenzidine (TMB)/H₂O₂ system, thus enabling rapid naked-eye detection of cortisol [56a]. Furthermore, the simple Mg-Au Janus micromachines can be exploited for the simultaneous detection and decomposition of persistent organic pollutants phthalates (DPP) in food and biological samples [56b]. The Mg-Au micromotors placed in proximity to screen-printed electrode would react with water producing (1) H₂ bubbles to swim and (2) hydroxyl ions (OH⁻) to degrade phthalates. Phenol molecules, the degradation of phthalates product, were electrochemically active at lower potentials than phthalates, producing strong and specific electrochemical signals. The synergy of the localized OH⁻ ions generation and an enhancement of the fluid mixing within a microliter sample droplet from the autonomous Mg-Au micromachine movement provided an improved analytical performance for DPP. Similarly, Kong et al. have developed a micromotor-assisted electrochemical platform for human serum glucose biosensing (Fig. 10.3d) [55]. The micromotor was propelled at a high speed by localized oxygen bubble generation, which could induce enhanced mass transfer in the solution, ultimately leading to improved performance on electrochemical detection of glucose in serum sample.

10.3.3 *Intracellular Monitoring of Life-Important Properties and Molecules*

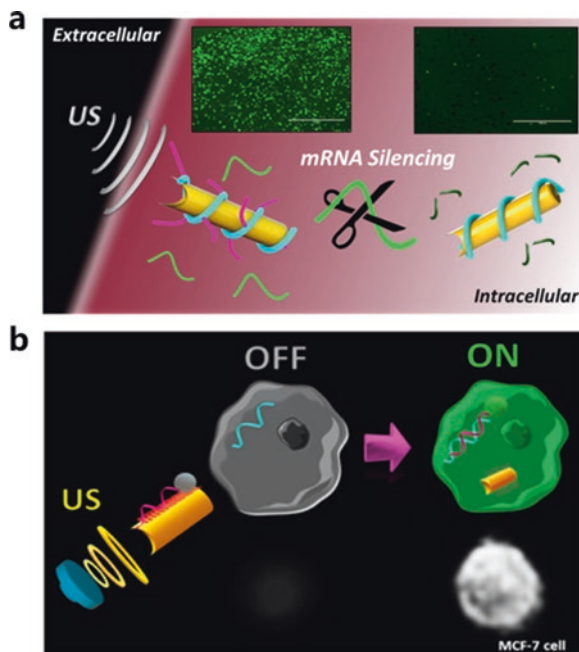
It would be of great value in the research area to be able to dynamically probe intracellular processes and monitor key molecules in individual cells [57]. However, traditional analytical methods for cell biology, such as Western blot (WB), cell staining, and quantitative flow cytometry (QFCM), can only be applied for probing cell processes in an ensemble manner or even in dead cells. Due to the vast heterogeneity of (1) cells in tissues/culture and (2) components/compartments within cells

and highly dynamics nature of metabolism in cells, the abovementioned methods could not fulfill the demands [58]. To investigate cell metabolism and understand the mechanisms of abnormal cells (such as tumor and senescence cells) in a comprehensive way, a large number of methods and toolkits have been developed to dynamically probe intracellular processes and monitor key molecules in a spatio-temporally controlled manner. These methods harness either chemical groups capable of cell compartment specified location to achieve spatial detection or activable motif (e.g., light, pH, temperature, etc.) to achieve spatiotemporal controllable probing of intracellular properties and molecules [59]. Despite enormous progress achieved in past decades, these methods are still suffering from some significant drawbacks: (1) need to eliminate the excessive chemical probe to avoid high signal background, (2) need for exquisite chemical synthesis or molecule designation to afford the location-controllable chemical probe or activable motif respectively, (3) low flexibility due to their static nature, and (4) need for elaborate equipment to activate the probe.

On the other hand, the micro-/nanomotors have shown their potential in intracellular applications, such as delivery of a variety of cargoes into cells. For example, Qiu et al. proposed ABFs functionalized with complexes of cationic lipids and plasmid DNA for *in vitro* gene delivery targeted to a single cell (human embryonic kidney cells HEK 293) [30]. Similarly, an effective gene silencing strategy using intracellular nanomachines was proposed by Wang's group. These nanomachines comprised acoustically propelled AuNWs, a rolling circle amplification (RCA)-derived DNA strand wrapped around AuNWs, and effective small interfering RNAs (siRNAs, specifically for green fluorescence protein sequence, siGFP) hybridized with DNA on the surface. This strategy can achieve about 94% silencing of the GFP expression in two different cell lines (HEK-293 and MCF-7, both pre-transfected with GFP sequence) after 5 min treatment with the siGFP/RCA-wrapped AuNWs [13b] (Fig. 10.4a). Recently, the same group has demonstrated the application of US-propelled nanomachines coated with pH-responsive polymer to induce apoptosis in human gastric adenocarcinoma cells by intracellular delivery of functional caspase-3 (CASP-3). This nanomachine strategy achieves a high apoptosis efficiency (> 80%) with significantly smaller amounts of CASP-3 and shorter time. More importantly, in all the examples, most of the cells remained alive after empty nanomotor treatment with a high nanomotor concentration, suggesting that such nanomachines can constitute powerful and biocompatible tools [13a]. Furthermore, the strong energy of the magnetic or acoustic fields can be exploited to facilitate internalization and movement of nanomotors inside living cells to tackle abovementioned challenges.

The first illustrative example was reported by Wang's group at 2015 by exploiting the efficient movement of US-powered nanomachine for rapid intracellular sensing of microRNA (miRNA) at the single-cell level [33]. They constructed the US-propelled nanomachine for attractive intracellular "off-on" fluorescence biosensing by combination of dye-labeled single-stranded DNA (ssDNA) and graphene-oxide (GO)-coated gold NWs, with fluorescence of the dye-labeled ssDNA quenched by the p-p interaction between GO and dye. After cell

Fig. 10.4 Intracellular monitoring of cell properties and molecules by micro-/nanomachines. (a) Schematic of the nanomotor-based gene silencing approach including fluorescence images and optical images of the acoustic movement of the motors inside living cells, Reproduced with permission, Copyright 2016, American Chemical Society [13b]; (b) Intracellular sensing of miRNA-21 using US-propelled gold nanomotors functionalized ssDNA(dye-label)@GO, Reproduced with permission, Copyright 2015, American Chemical Society [33]



internalization under US-propulsion, the fluorescence signal from the dye-labeled ssDNA is recovered due to the detachment of the dye-ssDNA probe from the GO nanomachine surface after hybridization with intracellular miRNA. They tested the US-propelled ssDNA@GO functionalized nanomotors by measuring the endogenous level of miRNA-21 in two kinds of intact cancer cells (MCF-7 and HeLa) of significantly different expression levels of miRNA21 (Fig. 10.4b). Their experiment results showed that in a few minutes (~ 5 min), 60% recovery of the fluorescence intensity can be obtained by applying US at 9 V, comparing to 30 min, 50% recovery of the fluorescence intensity under static conditions. The authors attributed major improvements in the sensitivity and sensing speed to the fast cell internalization process of the nanomotors and their rapid intracellular movement under the acoustic field, highlighting the capability of nanomotors for the determination of other important endogenous biomarkers, such as siRNAs, piRNAs, or proteins merely by using probe-modified nanomotors labeled with different dyes [60].

Besides gene silencing applications and miRNA molecule detection, spatiotemporally controlled active manipulation of external micro-/nanomachines with transducer components inside living cells can greatly contribute to development of real-time mechanical mapping of the intracellular environment, studying cellular response to local stress, and many more [14b, 61]. In the research field, Ambarish Ghosh's group has developed a number of versatile micro-/nanomachine-based innovative biomedical technologies for fundamental studies of various biophysical phenomena [61b, 62]. For the first time, they demonstrated cellular internalization and subsequent intracellular manipulation of a system of helical magnetically

propelled nanomachines with no adverse effect on the cellular viability and the utilization of such system to probe some important mechanical properties of an individual cell. In contrast to US- or chemical-propelled methods that perturb the entire experimental volume and external fluorescent probes that suffer from uncontrolled location and further washing process, the remotely driven and guided by small rotating magnetic field have limited and even harmless effect on cells. They prepared two kinds of micromachines with different sizes, with their width and length, corresponding to $250 \text{ nm} \times 2.4 \text{ }\mu\text{m}$ and $400 \text{ nm} \times 2.8 \text{ }\mu\text{m}$, respectively [62a]. They tested these two types of helical propellers in three cell types, including both cancerous and noncancerous types, and analyzed and engineered the motion of magnetic micromotors through the crowded intracellular space. They found that the ration of maneuverable to the total number of internalized helical nanomachines was significantly higher in the case of the smaller ($250 \text{ nm} \times 2.4 \text{ }\mu\text{m}$) nanomotors compared to the larger counterparts ($400 \text{ nm} \times 2.8 \text{ }\mu\text{m}$). They related these observations to the more consistency of porosity of the cytoskeleton and the size of nanomachines (thus smaller nanomotors showed enhanced propulsion in porous biological matrix). Furthermore, the speed of the helical nanomachines showed strong dependence on the position inside cells, and this strong position dependence of the speed should be largely attributed to the crowded and highly dynamic nature of the cellular interior. Both types of cells used in their experiments (HeLa and BAEC cells) remained completely viable even after the nanomachines were actuated within the cell for more than 1 h. In summary, their studies provided evidence for the strong heterogeneity, anisotropy, and spatiotemporal variability of the cellular interior and demonstrated the capability of helical magnetic nanomachines as promising tool for further cellular investigations and applications.

After demonstrating the suitability of helical magnetic nanomachines for intracellular investigations, the same group further disclosed their studies on how the tumbling-to-wobbling transition of helical magnetic nanomachines can be exploited to quantify the liquid viscosity of the local environment in real time [62b, 63]. They prepared helical magnetic nanomachines with their width and length similar to their previous studies. They first tested their tiny nanoprobe in both Newtonian and shear thinning media, and the obtained viscosity results showed a good match with measurements taken with a bulk rheometer and further supported by analytical and numerical studies. The dynamic range of viscosity measurements was about 100 cP that is comparable to most existing microrheological techniques. They undertook intracellular viscosity measurements in cells derived from human patients (HeLa cell) and demonstrated the “fluid phase” cytoplasmic viscosity of HeLa cell to ~ 200 cP. This novel technique has shown its strength in scenarios that require fast mechanical changes such as gelation and coagulation studies, especially in characterization of materials with mechanical heterogeneities [63]. Furthermore, since the helical magnetic nanomachine can be driven through the interface of two miscible fluids, they can be further explored and exploited to answer fundamental questions about local rheological changes happening in tandem inside cells or their environments due to various bio-physiochemical processes.

10.3.4 Pathogens and Biomarker Discrimination Based on Micro-/Nanomachines

In this section, we will review the application of versatile micro-/nanomachines with different propulsion methods and various types of functionalization in the field of pathogens and biomarkers discriminations, with emphasis on detection and diagnostics of bacteria, viruses, cancer cells, and their critical biomarkers.

It is imperative to develop highly sensitive and selective biosensing methods for bacterial detection, because the infections and pollutions have dramatical impacts on human welfare, for example, food safety and severe infection by hazardous microbe [64]. Traditional detection methods, such as enzyme-linked immunosorbent assay (ELISA), polymerase chain reaction, and chemiluminescence, are tedious, expensive, and time-consuming [65]. The development of micro-/nanomachines for quickly and sensitively identifying and detecting bacteria has shown great promise to tackle the drawbacks of traditional methods. Zhao et al. proposed the “motion-capture-lighting” strategy for visual, rapid, and real-time detection of *E. coli* without complicated sample pretreatment, expensive apparatus, and trained operators via integration of motion-enhanced capture of bacteria and capture-induced fluorescence turn-on of micromotors [66]. The flexible fiber rod-based micromotors could have less steric hindrance compared to the commonly used microtubes and microparticles, thus enabling multiple interactions with the bacterial surface. The flexible fiber rod-based micromotors are prepared by cryo-cutting of aligned fibers fabricated by side-by-side electrospinning (Fig. 10.5a). Catalase was further functionalized on one side of micromachines for propulsion of micromotors by producing oxygen bubbles, and mannose is grafted on the other side for specific recognition of FimH proteins from fimbriae on the bacterial surface, affording Janus-shaped micromachines (be referred as JMs, Janus micromotors). They fabricated different JMs with aspect ratios of 0.5, 1, 2, and 4 and found that the aspect ratios of JMs showed significant effects on the tracking trajectories and motion speed with the aspect ratio of 2 exhibiting significantly higher magnitudes of mean square displacement (MSD) with a directional motion trajectory. The fluorescence spectra of JMs would shift upon the bacteria capture by mannose on micromachine surface due to the aggregation-induced emission (AIE) effect of tetraphenylethylene (TPE) derivatives. Under ultraviolet irradiation, the fluorescence color change of JMs suspensions from blue to bluish-green and to green after incubation with *E. coli* of 10^2 and 10^5 CFU mL⁻¹, respectively, can be observed with naked eyes. The limit of detection (LOD) was around 45 CFU mL⁻¹ within 1 min using fluorescence intensity change of JM suspensions. Similarly, Campuzano et al. demonstrated Au/Ni/PANI/Pt microtubular motor with surface functionalized lectins ConA for identifying and isolating bacteria by exploiting the specific interaction between monosaccharides and oligosaccharides on the surface of Gram-negative bacteria and lectin ConA [49]. The functionalized micromachines were used as a sensor for the identification of *E. coli* in human urine samples with good selectivity and repeatability. Afterward, with a similar strategy, Garcia-Gradilla et al.

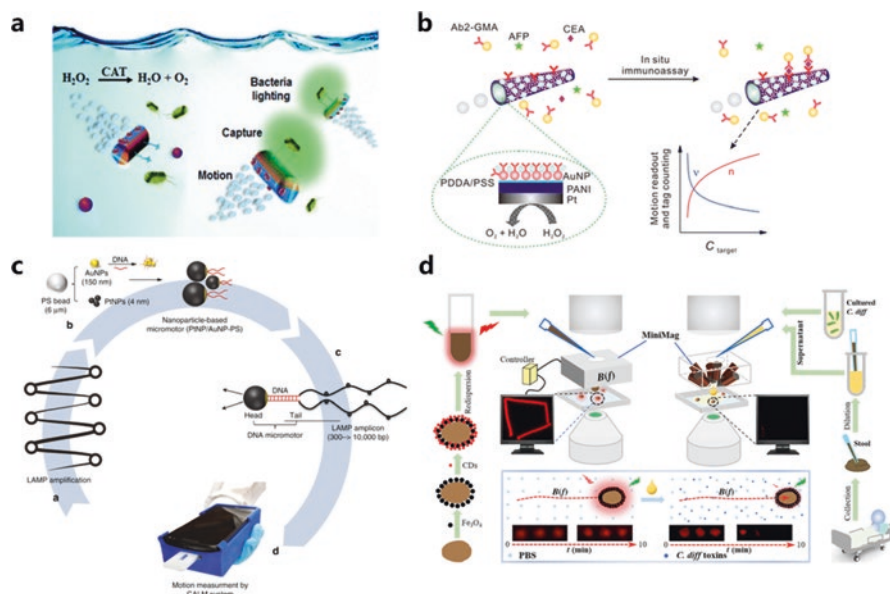


Fig. 10.5 Pathogens and biomarkers discrimination based on micro-/nanomachines. (a) Schematic showing “motion-capture-lighting” strategy for visual, rapid, and real-time detection of *E. coli* using JM, Reproduced with permission, Copyright 2019, Royal Society of Chemistry [66]; (b) In situ motion-based immunoassay for protein biomarker using micromachines, Reproduced with permission, Copyright 2014, American Chemical Society [48b]; (c) Schematic illustration of motion based cellphone diagnostics strategy for HIV-1 detection using DNA engineered micromotors, Reproduced with permission, Copyright 2018, Springer Nature Ltd. [17b]; (d) Schematic illustration of the preparation and *C. difficile* toxins detection application of fluorescent magnetic micromachines, Copyright 2019, American Association for the Advancement of Science [47]

fabricated a US-driven nanomachine-based sensor comprising ultrasonic-sensitive Au-Ni-Au nanomachine to overcome the limits of H_2O_2 fuels in biological systems. Those nanomachines could rapidly identify the bacteria in actual serum and saliva samples using US propulsion and guided by the external magnetic fields [67].

The rapid development and wide utilization of micro-/nanomachines have provided a new opportunity for miniaturizing and automating immunosensors for important biomarkers and cancer cells detection. Yu et al. have demonstrated PANI/Pt double-layer micromachines modified with gold nanoparticles and capturing antibodies for biomarker analysis (in this case, Alpha-fetoprotein (AFP) and Carcinoembryonic antigen (CEA)) without any washing and separation step, which shows considerable promise for diagnostic applications [48b] (Fig. 10.5b). The fast and selective capture of the protein analytes and subsequent binding of the secondary-antibody-modified glycidyl methacrylate microspheres (GMA) can be achieved under the autonomous movement of the micromachines in the fuel-contained sample mixture, leading to slowing down the movement of the moving microsensors. The velocity of the micromachines and the number of GMA loaded

on the micromachines can be easily observed with optical microscopy, which are negatively and positively dependent on the biomarker concentration, respectively. The dynamic detection range of these micromachines for carcinoembryonic antigen can be about 1–1000 ng/mL, and the time needed for protein targets detection can be reduced to ~5 min. Furthermore, the motor-based micromachines can be conveniently manufactured in batches. In addition, the use of the immunosensor for the detection of tumor markers in actual samples (such as human serum solutions) still maintained good specificity and detection performance, exhibiting broad application prospects in the field. In another case, Ma and co-authors developed a type of light-powered matchlike nanomachines for SERS sensing of MCF-7 breast cancer cells. These matchlike nanomachines are comprised of silica-coated silver nanowires (AgNW@SiO₂) and rough spherical AgCl tails and can be self-propelled via a self-diffusiophoresis mechanism. Combined with crystal violet dye as SERS agent, MCF-7 breast cancer cells can be easily detected through SERS signal. Their work showed great promises that micro-/nanomachines can be further exploited for highly sensitive light-guided sensing by combination with other sensing techniques [34a].

More recently, micro-/nanomachines have demonstrated their sensing ability in real clinical samples. HIV-1 infection has become a major health threat in both developed and developing countries [68]. By integration of mobile cellphone application and bioengineered catalytic nanomotors, Mohamed Shehata Draz and co-workers have proposed a sensitive and portable technology for HIV-1 management [17b]. Their technique relies on the average motion velocity change, merely using an optical attachment and a customized tracking cellphone application, to quantitatively probe the HIV-1 virus concentration in the sample based on simple cellphone (Fig. 10.5c). The HIV-1 RNA molecules were firstly amplified using loop-mediated isothermal DNA amplification to afford large-sized amplicons before nanomachines were added for motion-based molecular detection of amplified DNA signals. The velocity reduction of the nanomachine motion due to interaction and hindrance exerted by large-sized amplicons can be accurately measured using a cellphone system and positively correlated to the concentration of target nucleic acid in the sample. The easy-to-construct platform shows excellent specificity (99.1%) and sensitivity (94.6%) and could reach the LOD of 1000 virus particles/ml, the clinically relevant threshold value. After that, the same group further developed a similar Pt-modified nanomachine for motion-based immunological detection of Zika virus (ZIKV) using the same cellphone platform [69]. The detection system contains H₂O₂ energy doped sample, anti-Zika virus monoclonal antibody (anti-ZIKV mAb) modified Pt nanoparticles, and 3 μm polystyrene (PS) beads with anti-ZIKV mAb modified in a similar way. In the presence of ZIKV, 3D immunocomplex (beads-virus-motors) forms due to binding of Pt nanomotors to the surface of the beads. 3D immunocomplex would move by Pt nanomotor H₂O₂-induced decomposition, and the velocity of bead could be measured based on cellphone platform. The developed cellphone-based system could meet the World Health Organization's ASSURED criteria (affordable, sensitive, specific, user-friendly, rapid, equipment-free, and delivered) and hold the potential for the timely management of infectious diseases

in less developed countries where equipment is poor and operators are not well trained. However, the H_2O_2 used in detection would induce sample denatured, and motion-based detection manner would be highly sensitive to disturbance, which would cumulatively lead to an adverse false negative diagnosis.

To tackle current weakness of chemical-propelled, motion-based sensing with micro-/nanomachines (sample deterioration, less controllability, and less quantitative) in biological samples, our group recently developed fluorescent magnetic micromachines to serve as highly efficient mobile-sensing platform based on fluorescent quenching techniques [47]. The fluorescent magnetic micromachines were fabricated with simple steps: (1) pretreatment of natural spores from *Ganoderma lucidum* for easy functionalization, (2) depositing magnetic nanoparticles (Fe_3O_4 nanomaterials) onto surface of spores, and (3) covalent conjugation of functionalized carbon dots (as probes for the *Clostridium difficile* secreted toxins) onto spores (Fig. 10.5d). The obtained micromachines showed a continuous and controllable movement under magnetic stimulation, which was beneficial for interaction between analytes (*C. difficile* toxins) and carbon dots on the micromachines by accelerating the diffusion and mass transport. These magnetic micromachines had the capability for real-time fluorescent tracking for *C. difficile* toxins, in bacterial supernatant of *C. difficile* and even in clinical stool samples. The method showed good selectivity and sensitivity and can complete detection within tens of minutes (~15 min). We believe that this novel detection platform would hold the great promises for the sensing application of micro-/nanomachines for various analytes, pathogens, and biomarkers owing to its biocompatible actuation, simple functionalization, and reliable sensing strategy.

10.4 Conclusion and Perspective

Since the first report on self-propelled nanomotors in 2004 [23a], micro-/nanorobotics has achieved tremendous progress by integrating the advantages of nanotechnologies and robotic sciences. Thus far, researchers in this field have endeavored to explore and exploit a diverse set of design principles, advanced materials, sophisticated fabrication techniques, and propulsion mechanisms, ultimately promoting the micro-/nanomachines as a novel and versatile platform for various real applications [9–11]. Based on these endeavors and achievements, the chapter highlights the present progress on the micro-/nanomachines for in vitro biosensing. We have covered propulsion mechanisms and the functionalization of these micro-/nanomachines and emphasized on three promising subtopics, including (1) in vitro detection for chemical and biological agents; (2) pathogens and biomarkers discrimination based on micro-/nanomachines; and (3) intracellular monitoring of life-important properties and molecules. With the aids of proper functionalization, the versatile, dynamic motile micro-/nanomachines demonstrate enhanced performances such as improved sensitivity and higher selectivity and, more importantly, fast response rates or even real-time sensing owing to “on-the-fly” properties compared to the passive

counterparts. In addition, the small dimension and appealing controllable motion enable micro-/nanomachines to work precisely in narrow space, e.g., solution of microliters level, microfluidic chips, and even intracellular compartments. Such favorable capability to access hard-to-reach sites makes it possible for development of miniaturized devices for in situ detection of toxic chemicals and pathogens [25b].

The development of micro-/nanomachines for in vitro biosensing is still at its infant stage. To further expand and explore micro-/nanomotors for more realistic applications, some of the key challenges need to be addressed including propulsion strategies, fabrication issues, sensing mechanisms, and collective/cooperative behaviors. In the past decade, a number of strategies have been developed to propel micro-/nanomachines for in vitro biosensing. However, most of micro-/nanomotors in applications are bubble-propelled; and surfactants (e.g., sodium dodecyl sulfate, SDS) are required to ease the release of the bubble for micro/nanoagents propulsion; otherwise they would move slowly without surfactants [9a, 11b]. The chemical-fuels (in most cases, H_2O_2) are also indispensable and required to be doped into samples together with surfactants. Both additives would exert harmful effects on biosensing setup, due to their high chemical reactivity or denature ability on sensitive sample or living cells, thus limiting micro-/nanorobots applications. Among the developed propulsion, like magnetic field, ultrasonic stimulus, and light irradiation, magnetic actuation would show their advantage, gather more intensive research interest, and find more biosensing and biomedical applications, due to its excellent biocompatibility, the appealing remote propulsion and accurate motion control capabilities [10c, 14b, 19a, b, 25b].

Currently, one of the grand challenges for a new generation of versatile and efficient micro-/nanorobots is the development of new materials and fabrication schemes [70]. Current fabrication schemes involve expensive facilities, for instance, lithography platforms, electrochemical stations, and clean rooms to afford micro-/nanomachines with complex and multi-tile micro-/nanostructures, and often require expensive noble metals (Au, Ag, Pb, and Pt). More research endeavors have been devoted to alleviate the drawbacks in the fabrication schemes of micro-/nanomachines and direct toward the development of robust, affordable, and versatile micro-/nanorobots. For instance, this field has witnessed a noticeable transition in the composition of micro-/nanomachines from expensive noble metals (Au and Pt) to more economical metal oxides, such as Mn-based oxides and Co and Fe ferrites. In this realm, further exploration and exploitation of natural resource hold great promises, including biohybrid micro-/nanomachines that take advantage of biological entities such as bacteria or sperm cells as power providers and self-functionalized micro-/nanorobots which utilize abundant natural materials as both scaffold and functional motifs, thus avoiding tedious modification process [14a, 45, 47]. We speculate the nature offer enough room in biological materials with various interesting and useful function for our communities to further exploration and engineering.

Currently, most micro-/nanomachine-based biosensing methods rely on either motion-based or fluorescence-based signal mechanism. The motion-based strategy has shown its merits, like easy to setup, straightforward signal generation and low-cost, but suffer from unstable detection output as well as semiquantitative or even

qualitative results. In contrast, fluorescent signal is highly quantitative and general selective for analytes, but often require elaborate organic synthesis and cumbersome manufactures. Therefore, it is highly desired to explore and exploit more alternative and convenient signal transduction techniques for micro-/nanomachine-based biosensing realm [17b, 34a, 56a]. We envision that under intensive research efforts in our communities, more and more signal transduction methods with higher robustness, sensitivity, and selectivity would be introduced and integrated well into micro-/nanomachines, and eventually leading to their applications in more realistic scenarios.

The aforementioned micro-/nanomachine-based biosensing is limited to individual navigation and signal generation. However, collective behaviors of micro-/nanorobots have rarely been explored. More sophisticated tasks (e.g., behavior-based signal transduction and signal amplification under cooperation of many micro-/nanoagents) would not be possible using individual micro-/nanomachine. Recently, our group has achieved controllable assembly and disassembly behaviors by manipulating a swarm of magnetic nanoparticles with a time-varying magnetic field [71]. To further develop more collective and cooperative behaviors of micro-/nanomachines swarm and expand their potential applications, both scientists and engineers in different fields should endeavor in tight cooperation toward both fundamental understanding of quantitative control theory in micro-/nano-size scale and mimicking or taking advantage of communication and synchronized coordination within natural intelligent swarms [9d]. Hopefully, we expect to develop collective and cooperative behaviors of swarm comprising of micro-/nanomachines with different functions to achieve more integrated applications in biosensing field, namely, the integration of conventionally tedious, time-consuming sample collection, preparations, and signal generation or even data presentation into a single and easy-to-operate platform.

Acknowledgment This work was partially supported by the Hong Kong RGC Joint Laboratory Funding Scheme (JLFS) with Project No. JLFS/E-402/18, the projects funded by the Hong Kong ITC with Project Numbers MRP/036/18X and ITS/374/18FP, the projects from CUHK internal grants, and the support from SIAT-CUHK Joint Laboratory of Robotics and Intelligent Systems. J.H. Gao would like to thank the financial support from the Impact Postdoctoral Fellowship Scheme from the Chinese University of Hong Kong.

References

1. (a) Laing, S., Jamieson, L. E., Faulds, K., & Graham, D. (2017). *Nature Reviews Chemistry*, 1; (b) Bolotsky, A., Butler, D., Dong, C. Y., Gerace, K., Glayin, N. R., Muratore, C., Robinson, J. A., & Ebrahimi, A. (2019). *ACS Nano*, 13, 9781–9810.
2. Lee, K. H., & Kim, D. M. (2019). *Frontiers in Pharmacology*, 10.
3. (a) Padro-Miquel, A., & Candas-Estebanez, B. (2015). *Clinical Chemistry and Laboratory Medicine*, 53, 199–204; (b) Gruson, A., & Middleware, G. T. (2012). *Annales de Biologie Clinique*, 70, S1–S64; (c) Ndofor, H. A., Sirmon, D. G., & He, X. M. (2011). *Strategic*

- Management Journal*, 32, 640–657; (d) Sun, X. M., Wan, J. J., & Qian, K. (2017). *Small Methods*, 1.
4. (a) Singh, N., Gupta, V. K., Kumar, A., & Sharma, B. (2017). *Frontiers in Chemistry*, 5; (b) Uwizeyimana, H., Wang, M. I., Chen, W. P., & Khan, K. (2017). *Environmental Toxicology and Pharmacology*, 55, 20–29.
 5. (a) Hung, J. C. H. and Li, K. K. W. (2020). *Eye*; (b) Chen, Y., Guo, Y., Pan, Y. H., & Zhao, Z. J. (2020). *Biochemical and Biophysical Research Communications*, 525, 135–140; (c) Wrapp, D., Wang, N. S., Corbett, K. S., Goldsmith, J. A., Hsieh, C. L., Abiona, O., Graham, B. S., & McLellan, J. S. (2020). *Science*, 367, 1260–+; (d) Zhang, C. X., Zheng, W., Huang, X. Q., Bell, E. W., Zhou, X. G., & Zhang, Y. (2020). *Journal of Proteome Research*, 19, 1351–1360; (e) Letko, M., Marzi, A., & Munster, V. (2020). *Nature Microbiology*; (f) Mu, J. F., Xu, J. Y., Zhang, L. K., Shu, T., Wu, D., Huang, M. H., Ren, Y. J., Li, X. F., Geng, Q., Xu, Y., Qiu, Y., & Zhou, X. (2020). *Science China-Life Sciences*.
 6. (a) Halliday, J. E. B., Hampson, K., Hanley, N., Lembo, T., Sharp, J. P., Haydon, D. T., & Cleaveland, S. (2017). *Science*, 357, 146–148; (b) Kumar, A. A., Hennek, J. W., Smith, B. S., Kumar, S., Beattie, P., Jain, S., Rolland, J. P., Stossel, T. P., Chunda-Liyoka, C., & Whitesides, G. M. (2015). *Angewandte Chemie-International Edition*, 54, 5835–5852; (c) Abou Tayoun, A. N., Burchard, P. R., Malik, I., Scherer, A., & Tsongalis, G. J. (2014). *American Journal of Clinical Pathology*, 141, 17–24.
 7. (a) Cantwell, K., Bryant, J., & Frederick, K. (2016). *Abstracts of Papers of the American Chemical Society*, 251; (b) Lanaspá, M., Madrid, L., & Bassat, Q. (2014). *Biomarkers in Medicine*, 8, 1057–1060.
 8. (a) Llorent-Martinez, E. J., Ortega-Barrales, P., Fernandez-de Cordova, M. L., & Ruiz-Medina, A. (2011). *Analytica Chimica Acta*, 684, 30–39; (b) Albuquerque, T. G., Costa, H. S., Castilho, M. C., & Sanches-Silva, A. (2011). *Trends in Food Science & Technology*, 22, 543–560; (c) Karrman, A., & Lindstrom, G. (2013). *Trac-Trends in Analytical Chemistry*, 46, 118–128.
 9. (a) Zarei, M., & Zarei, M. (2018). *Small*, 14; (b) Chalupniak, A., Morales-Narvaez, E., & Merkoci, A. (2015). *Advanced Drug Delivery Reviews*, 95, 104–116; (c) Parmar, J., Vilela, D., Villa, K., Wang, J., & Sanchez, S. (2018). *Journal of the American Chemical Society*, 140, 9317–9331; (d) Li, J. X., de Avila, B. E. F., Gao, W., Zhang, L. F., & Wang, J. (2017). *Science Robotics*, 2.
 10. (a) Campuzano, S., de Avila, B. E. F., Yanez-Sedeno, P., Pingarron, J. M., & Wang, J. (2017). *Chemical Science*, 8, 6750–6763; (b) Zhang, Y. B., Yuan, K., & Zhang, L. (2019). *Advanced Materials Technologies*, 4; (c) Peng, F., Tu, Y. F., & Wilson, D. A. (2017). *Chemical Society Reviews*, 46, 5289–5310.
 11. (a) Wong, F., Dey, K. K., & Sen, A. (2016). *Annual Review of Materials Research*, 46, 407–432; (b) Illien, P., Golestanian, R., & Sen, A. (2017). *Chemical Society Reviews*, 46, 5508–5518; (c) Maier, A. M., Weig, C., Oswald, P., Frey, E., Fischer, P., & Liedl, T. (2016). *Nano Letters*, 16, 906–910.
 12. Zhang, L., Peyer, K. E., & Nelson, B. J. (2010). *Lab on a Chip*, 10, 2203–2215.
 13. (a) de Avila, B. E. F., Ramirez-Herrera, D. E., Campuzano, S., Angsantikul, P., Zhang, L. F., & Wang, J. (2017). *ACS Nano*, 11, 5367–5374; (b) de Avila, B. E. F., Angell, C., Soto, F., Lopez-Ramirez, M. A., Baez, D. F., Xie, S. B., Wang, J., & Chen, Y. (2016). *ACS Nano*, 10, 4997–5005; (c) Medina-Sanchez, M., Schwarz, L., Meyer, A. K., Hebenstreit, F., & Schmidt, O. G. (2016). *Nano Letters*, 16, 555–561.
 14. (a) Yan, X. H., Zhou, Q., Vincent, M., Deng, Y., Yu, J. F., Xu, J. B., Xu, T. T., Tang, T., Bian, L. M., Wang, Y. X. J., Kostarelos, K., & Zhang, L. (2017). *Science Robotics*, 2; (b) Srivastava, S. K., Medina-Sanchez, M., Koch, B., & Schmidt, O. G. (2016). *Advanced Materials*, 28, 832–837; (c) Soto, F., Martin, A., Ibsen, S., Vaidyanathan, M., Garcia-Gradilla, V., Levin, Y., Escarpa, A., Esener, S. C., & Wang, J. (2016). *ACS Nano*, 10, 1522–1528.
 15. Peng, F., Tu, Y. F., van Hest, J. C. M., & Wilson, D. A. (2015). *Angewandte Chemie-International Edition*, 54, 11662–11665.

16. (a) Gao, W., Dong, R. F., Thamphiwatana, S., Li, J. X., Gao, W. W., Zhang, L. F., & Wang, J. (2015). *ACS Nano*, *9*, 117–123; (b) Tu, Y. F., Peng, F., Andre, A. A. M., Men, Y. J., Srinivas, M., & Wilson, D. A. (2017). *ACS Nano*, *11*, 1957–1963.
17. (a) Wu, J., Balasubramanian, S., Kagan, D., Manesh, K. M., Campuzano, S., & Wang, J. (2010). *Nature Communications*, *1*; (b) Draz, M. S., Kochehyok, K. M., Vasari, A., Battalappalli, D., Sreeram, A., Kanakasabapathy, M. K., Kallakuri, S., Tsibris, A., Kuritzkes, D. R., & Shafiee, H. (2018). *Nature Communications*, *9*.
18. (a) Laocharoensuk, R., Burdick, J., & Wang, J. (2008). *ACS Nano*, *2*, 1069–1075; (b) Fan, D. L., Yin, Z. Z., Cheong, R., Zhu, F. Q., Cammarata, R. C., Chien, C. L., & Levchenko, A. (2010). *Nature Nanotechnology*, *5*, 545–551.
19. (a) Xu, L. L., Mou, F. Z., Gong, H. T., Luo, M., & Guan, J. G. (2017). *Chemical Society Reviews*, *46*, 6905–6926; (b) Chen, X. Z., Hoop, M., Mushtaq, F., Siringil, E., Hu, C. Z., Nelson, B. J., & Pane, S. (2017). *Applied Materials Today*, *9*, 37–46; (c) Wu, Z. G., Si, T. Y., Gao, W., Lin, X. K., Wang, J., & He, Q. (2016). *Small*, *12*, 577–582; (d) Abid, J. P., Frigoli, M., Pansu, R., Szeftel, J., Zyss, J., Larpent, C., & Brasselet, S. (2011). *Langmuir*, *27*, 7967–7971; (e) Li, W., Wu, X. R., Qin, H., Zhao, Z. Q., & Liu, H. W. (2016). *Advanced Functional Materials*, *26*, 3164–3171.
20. (a) Kapral, R. (2013). *Journal of Chemical Physics*, *138*; (b) Abbott, J. J., Peyer, K. E., Dong, L. X. X., & Nelson, B. J. (2010). *Robotics Research*, *66*, 157–167.
21. (a) Purcell, E. M. (1977). *American Journal of Physics*, *45*, 3–11; (b) Duan, W. T., Wang, W., Das, S., Yadav, V., Mallouk, T. E., & Sen, A. (2015). *Annual Review of Analytical Chemistry*, *8*, 311–333.
22. (a) Palagi, S., & Fischer, P. (2018). *Nature Reviews Materials*, *3*, 113–124; (b) Sun, Z. Y., Popp, P. F., Loderer, C., & Revilla-Guarinos, A. (2020). *Sensors*, *20*; (c) Bastos-Arrieta, J., Revilla-Guarinos, A., Uspal, W. E., & Simmchen, J. (2018). *Frontiers in Robotics and AI*, *5*.
23. (a) Paxton, W. F., Kistler, K. C., Olmeda, C. C., Sen, Y. Y., St Angelo, S. K., Cao, Y. Y., Mallouk, T. E., Lammert, P. E., & Crespi, V. H. (2004). *Journal of the American Chemical Society*, *126*, 13424–13431; (b) Fournier-Bidoz, S., Arsenault, A. C., Manners, I., & Ozin, G. A. (2005). *Chemical Communications*, 441–443.
24. Paxton, W. F., Baker, P. T., Kline, T. R., Wang, Y., Mallouk, T. E., & Sen, A. (2006). *Journal of the American Chemical Society*, *128*, 14881–14888.
25. (a) Wang, S. N., Liu, X. J., Wang, Y., Xu, D. D., Liang, C. Y., Guo, J. H., & Ma, X. (2019). *Nanoscale*, *11*, 14099–14112; (b) Ou, J., Liu, K., Jiang, J., Wilson, D. A., Liu, L., Wang, F., Wang, S., Tu, Y., & Peng, F. (2020). *Small*, e1906184.
26. Gao, W., Uygun, A., & Wang, J. (2012). *Journal of the American Chemical Society*, *134*, 897–900.
27. Magdanz, V., Sanchez, S., & Schmidt, O. G. (2013). *Advanced Materials*, *25*, 6581–6588.
28. (a) Magdanz, V., Medina-Sanchez, M., Chen, Y., Guix, M., & Schmidt, O. G. (2015). *Advanced Functional Materials*, *25*, 2763–2770; (b) Xu, H. F., Medina-Sanchez, M., Magdanz, V., Schwarz, L., Hebenstreit, F., & Schmidt, O. G. (2018). *ACS Nano*, *12*, 327–337.
29. Qiu, F. M., Mhanna, R., Zhang, L., Ding, Y., Fujita, S., & Nelson, B. J. (2014). *Sensors and Actuators B-Chemical*, *196*, 676–681.
30. Qiu, F. M., Fujita, S., Mhanna, R., Zhang, L., Simona, B. R., & Nelson, B. J. (2015). *Advanced Functional Materials*, *25*, 1666–1671.
31. Felfoul, O., Mohammadi, M., Taherkhani, S., de Lanauze, D., Xu, Y. Z., Loghin, D., Essa, S., Jancik, S., Houle, D., Lafleur, M., Gaboury, L., Tabrizian, M., Kaou, N., Atkin, M., Vuong, T., Batist, G., Beauchemin, N., Radzioch, D., & Martel, S. (2016). *Nature Nanotechnology*, *11*, 941–947.
32. Wang, W., Li, S. X., Mair, L., Ahmed, S., Huang, T. J., & Mallouk, T. E. (2014). *Angewandte Chemie-International Edition*, *53*, 3201–3204.
33. de Avila, B. E. F., Martin, A., Soto, F., Lopez-Ramirez, M. A., Campuzano, S., Vasquez-Machado, G. M., Gao, W. W., Zhang, L. F., & Wang, J. (2015). *ACS Nano*, *9*, 6756–6764.

34. (a) Wang, Y., Zhou, C., Wang, W., Xu, D. D., Zeng, F. Y., Zhan, C., Gu, J. H., Li, M. Y., Zhao, W. W., Zhang, J. H., Guo, J. H., Feng, H. H., & Ma, X. (2018). *Angewandte Chemie-International Edition*, 57, 13110–13113; (b) Guix, M., Orozco, J., Garcia, M., Gao, W., Sattayasamitsathit, S., Merkoci, A., Escarpa, A., & Wang, J. (2012). *ACS Nano*, 6, 4445–4451.
35. Wu, Z. G., Troll, J., Jeong, H. H., Wei, Q., Stang, M., Ziemssen, F., Wang, Z. G., Dong, M. D., Schnichels, S., Qiu, T., & Fischer, P. (2018). *Science Advances*, 4.
36. Wang, X. P., Hu, C. Z., Schurz, L., De Marco, C., Chen, X. Z., Pane, S., & Nelson, B. J. (2018). *ACS Nano*, 12, 6210–6217.
37. Gao, W., Feng, X. M., Pei, A., Gu, Y. E., Li, J. X., & Wang, J. (2013). *Nanoscale*, 5, 4696–4700.
38. Vilela, D., Cossio, U., Parmar, J., Martinez-Villacorta, A. M., Gomez-Vallejo, V., Llop, J., & Sanchez, S. (2018). *ACS Nano*, 12, 1220–1227.
39. (a) de Avila, B. E. F., Lopez-Ramirez, M. A., Baez, D. F., Jodra, A., Singh, V. V., Kaufmann, K., & Wang, J. (2016). *ACS Sensors*, 1, 217–221; (b) Orozco, J., Campuzano, S., Kagan, D., Zhou, M., Gao, W., & Wang, J. (2011). *Analytical Chemistry*, 83, 7962–7969.
40. Maria-Hormigos, R., Jurado-Sanchez, B., & Escarpa, A. (2018). *Advanced Functional Materials*, 28.
41. Wu, Z. G., Li, T. L., Gao, W., Xu, T. L., Jurado-Sanchez, B., Li, J. X., Gao, W. W., He, Q., Zhang, L. F., & Wang, J. (2015). *Advanced Functional Materials*, 25, 3881–3887.
42. de Avila, B. E. F., Angsantikul, P., Ramirez-Herrera, D. E., Soto, F., Teymourian, H., Dehaini, D., Chen, Y. J., Zhang, L. F., & Wang, J. (2018). *Science Robotics*, 3.
43. (a) Schliephake, H., & Scharnweber, D. (2008). *Journal of Materials Chemistry*, 18, 2404–2414; (b) Tallawi, M., Rosellini, E., Barbani, N., Cascone, M. G., Rai, R., Saint-Pierre, G., & Boccaccini, A. R. (2015). *Journal of the Royal Society Interface*, 12.
44. (a) Yasa, O., Erkok, P., Alapan, Y., & Sitti, M. (2018). *Advanced Materials*, 30; (b) Park, B. W., Zhuang, J., Yasa, O., & Sitti, M. (2017). *ACS Nano*, 11, 8910–8923.
45. Zhang, Y. B., Yan, K., Ji, F. T., & Zhang, L. (2018). *Advanced Functional Materials*, 28.
46. Kagan, D., Calvo-Marzal, P., Balasubramanian, S., Sattayasamitsathit, S., Manesh, K. M., Flechsig, G. U., & Wang, J. (2009). *Journal of the American Chemical Society*, 131, 12082–+.
47. Zhang, Y. B., Zhang, L., Yang, L. D., Vong, C. I., Chan, K. F., Wu, W. K. K., Kwong, T. N. Y., Lo, N. W. S., Ip, M., Wong, S. H., Sung, J. J. Y., Chiu, P. W. Y., & Zhang, L. (2019). *Science Advances*, 5.
48. (a) Vilela, D., Orozco, J., Cheng, G., Sattayasamitsathit, S., Galarnyk, M., Kan, C., Wang, J., & Escarpa, A. (2014). *Lab on a Chip*, 14, 3505–3509; (b) Yu, X. P., Li, Y. N., Wu, J., & Ju, H. X. (2014). *Analytical Chemistry*, 86, 4501–4507.
49. Campuzano, S., Orozco, J., Kagan, D., Guix, M., Gao, W., Sattayasamitsathit, S., Claussen, J. C., Merkoci, A., & Wang, J. (2012). *Nano Letters*, 12, 396–401.
50. Moo, J. G. S., Wang, H., Zhao, G. J., & Pumera, M. (2014). *Chemistry—A European Journal*, 20, 4292–4296.
51. (a) Liu, L. M., Dong, Y. G., Sun, Y. Y., Liu, M., Su, Y. J., Zhang, H., & Dong, B. (2016). *Nano Research*, 9, 1310–1318; (b) Su, Y. J., Ge, Y., Liu, L. M., Zhang, L. N., Liu, M., Sun, Y. Y., Zhang, H., & Dong, B. (2016). *ACS Applied Materials & Interfaces*, 8, 4250–4257; (c) Li, M. T., Zhang, H., Liu, M., & Dong, B. (2017). *Journal of Materials Chemistry C*, 5, 4400–4407.
52. Singh, V. V., Jurado-Sanchez, B., Sattayasamitsathit, S., Orozco, J., Li, J. X., Galarnyk, M., Fedorak, Y., & Wang, J. (2015). *Advanced Functional Materials*, 25, 2147–2155.
53. Singh, V. V., Kaufmann, K., Orozco, J., Li, J. X., Galarnyk, M., Arya, G., & Wang, J. (2015). *Chemical Communications*, 51, 11190–11193.
54. (a) Molinero-Fernandez, A., Moreno-Guzman, M., Lopez, M. A., & Escarpa, A. (2017). *Analytical Chemistry*, 89, 10850–10857; (b) Molinero-Fernandez, A., Jodra, A., Moreno-Guzman, M., Lopez, M. A., & Escarpa, A. (2018). *Chemistry—A European Journal*, 24, 7172–7176; (c) Jurado-Sanchez, B., Pacheco, M., Rojo, J., & Escarpa, A. (2017). *Angewandte Chemie-International Edition*, 56, 6957–6961.
55. Kong, L., Rohaizad, N., Nasir, M. Z. M., Guan, J. G., & Pumera, M. (2019). *Analytical Chemistry*, 91, 5660–5666.

56. (a) de Avila, B. E. F., Zhao, M. J., Campuzano, S., Ricci, F., Pingarron, J. M., Mascini, M., & Wang, J. (2017). *Talanta*, *167*, 651–657; (b) Rojas, D., Jurado-Sanchez, B., & Escarpa, A. (2016). *Analytical Chemistry*, *88*, 4153–4160.
57. (a) Singh, H., Tiwari, K., Tiwari, R., Pramanik, S. K., & Das, A. (2019). *Chemical Reviews*, *119*, 11718–11760; (b) Chan, J., Dodani, S. C., & Chang, C. J. (2012). *Nature Chemistry*, *4*, 973–984.
58. (a) Spiller, D. G., Wood, C. D., Rand, D. A., & White, M. R. H. (2010). *Nature*, *465*, 736–745; (b) Zhang, C., Tu, H. L., Jia, G. J., Mukhtar, T., Taylor, V., Rzhetsky, A., & Tay, S. (2019). *Science Advances*, *5*; (c) Junkin, M., & Tay, S. (2014). *Lab on a Chip*, *14*, 1246–1260.
59. (a) Karimi, M., Ghasemi, A., Zangabad, P. S., Rahighi, R., Basri, S. M. M., Mirshekari, H., Amiri, M., Pishabad, Z. S., Aslani, A., Bozorgomid, M., Ghosh, D., Beyzavi, A., Vaseghi, A., Aref, A. R., Haghani, L., Bahrami, S., & Hamblin, M. R. (2016). *Chemical Society Reviews*, *45*, 1457–1501; (b) Galler, K., Brautigam, K., Grosse, C., Popp, J., & Neugebauer, U. (2014). *Analyst*, *139*, 1237–1273; (c) Li, M. Y., Zhao, J., Chu, H. Q., Mi, Y. S., Zhou, Z. H., Di, Z. H., Zhao, M. P., & Li, L. L. (2019). *Advanced Materials*, *31*; (d) Chambers, J. E., Kubankova, M., Huber, R. G., Lopez-Duarte, I., Avezov, E., Bond, P. J., Marciniak, S. J., & Kuimova, M. K. (2018). *ACS Nano*, *12*, 4398–4407.
60. (a) Wu, Z., Liu, G. Q., Yang, X. L., & Jiang, J. H. (2015). *Journal of the American Chemical Society*, *137*, 6829–6836; (b) Baez, D. F., Ramos, G., Corvalan, A., Cordero, M. L., Bollo, S., & Kogan, M. J. (2020). *Sensors and Actuators B-Chemical*, *310*.
61. (a) Maier, C. M., Huergo, M. A., Milosevic, S., Perpeintner, C., Li, M., Singh, D. P., Walker, D., Fischer, P., Feldmann, J., & Lohmuller, T. (2018). *Nano Letters*, *18*, 7935–7941; (b) Schamel, D., Mark, A. G., Gibbs, J. G., Miksch, C., Morozov, K. I., Leshansky, A. M., & Fischer, P. (2014). *ACS Nano*, *8*, 8794–8801.
62. (a) Pal, M., Somalwar, N., Singh, A., Bhat, R., Eswarappa, S. M., Saini, D. K., & Ghosh, A. (2018). *Advanced Materials*, *30*, e1800429; (b) Ghosh, A., Dasgupta, D., Pal, M., Morozov, K. I., Leshansky, A. M., & Ghosh, A. (2018). *Advanced Functional Materials*, *28*.
63. Pal, M., Dasgupta, D., Somalwar, N., Reshma, V. R., Tiwari, M., Teja, D., Narayana, S. M., Katke, A., Jayshree, R. S., Bhat, R., Saini, D. K., & Ghosh, A. (2020). *Journal of Physics-Condensed Matter*, *32*.
64. (a) van der Merwe, R. G., van Helden, P. D., Warren, R. M., Sampson, S. L., & Gey van Pittius, N. C. (2014). *Analyst*, *139*, 2617–2626; (b) Majors, C. E., Smith, C. A., Natoli, M. E., Kundrod, K. A., & Richards-Kortum, R. (2017). *Lab on a Chip*, *17*, 3351–3387.
65. (a) Varadi, L., Luo, J. L., Hibbs, D. E., Perry, J. D., Anderson, R. J., Orenga, S., & Groundwater, P. W. (2017). *Chemical Society Reviews*, *46*, 4818–4832; (b) Furst, A. L., & Francis, M. B. (2019). *Chemical Reviews*, *119*, 700–726; (c) Tang, Y. J., Ali, Z., Zou, J., Jin, G., Zhu, J. C., Yang, J., & Dai, J. G. (2017). *RSC Advances*, *7*, 51789–51800.
66. Zhao, L., Xie, S. Z., Liu, Y., Liu, Q. J., Song, X. J., & Li, X. H. (2019). *Nanoscale*, *11*, 17831–17840.
67. Garcia-Gradilla, V., Orozco, J., Sattayasamitsathit, S., Soto, F., Kuralay, F., Pourazary, A., Katzenberg, A., Gao, W., Shen, Y. F., & Wang, J. (2013). *ACS Nano*, *7*, 9232–9240.
68. (a) Pratt, M., & Lamarre, M. C. (2013). *Global Health Promotion*, *20*, 128–131; (b) Maartens, G., Celum, C., & Lewin, S. R. (2014). *Lancet*, *384*, 258–271; (c) Barre-Sinoussi, F., Ross, A. L., & Delfraissy, J. F. (2013). *Nature Reviews Microbiology*, *11*, 877–883.
69. Draz, M. S., Lakshminaraasimulu, N. K., Krishnakumar, S., Battalapalli, D., Vasan, A., Kanakasabaathy, M. K., Sreeram, A., Kallakuri, S., Thirumalaraju, P., Li, Y. D., Hua, S., Yu, X. G., Kuritzkes, D. R., & Shafee, H. (2018). *ACS Nano*, *12*, 5709–5718.
70. Yang, G. Z., Bellingham, J., Dupont, P. E., Fischer, P., Floridi, L., Full, R., Jacobstein, N., Kumar, V., McNutt, M., Merrifield, R., Nelson, B. J., Scassellati, B., Taddeo, M., Taylor, R., Veloso, M., Wang, Z. L., & Wood, R. (2018). *Science Robotics*, *3*.
71. (a) Yu, J. F., Wang, B., Du, X. Z., Wang, Q. Q., & Zhang, L. (2018). *Nature Communications*, *9*; (b) Yu, J. F., Jin, D. D., K. F. Chan, ., Wang, Q. Q., Yuan, K., & Zhang, L. (2019). *Nature Communications*, *10*.

Chapter 11

Biophysical Measurement of Cellular and Intracellular Structures Using Magnetic Tweezers



Xian Wang, Tiancong Wang, Zhuoran Zhang, and Yu Sun

11.1 Introduction

From the 1920s, scientists have used magnetic fields to actuate magnetic microbeads to measure the viscosity of the fluidic medium. Then the magnetic field was applied to measure mechanical properties of cells and cellular structures [1]. To generate a strong magnetic field, permanent magnets or electromagnets with sharp pole tips were used, and the magnetic field generation system was named magnetic tweezers [2]. With advantages of large force output, non-contact actuation, and good biocompatibility, magnetic tweezers have soon been applied to biophysical measurement of various types of biological samples.

Within the human body, cells are subjected to multiple sources of mechanical stimulation (Fig. 11.1), such as fluidic shear from the body fluid (e.g., blood and cerebellum spinal fluid), stretching and compression from mussel movement, and compression from neighboring cells [3, 4]. Mechanical properties of cells and cellular structures become a center of understanding how cells sense and respond to mechanical stimulations [5, 6]. Researchers started to quantify the mechanical properties of cells and study how mechanical properties of cells are related to diseases since the 1930s [7]. It has been observed that cancer cells with high metastasis potential are softer than early-stage cancer cells [8]; abnormality of mechanics of cytoskeleton is associated with neurodegeneration, cancer invasion, and pulmonary fibrosis [9]; and altered cell nuclear mechanical properties are linked to many types of muscular dystrophy and heart failures [10].

Early magnetic tweezers utilized permanent magnets with sharp tips to exert forces on magnetic microbeads made from iron or iron oxide (Fig. 11.2a) [11]. However, force generation using the permanent magnet system is challenging

X. Wang · T. Wang · Z. Zhang · Y. Sun (✉)

Department of Mechanical and Industrial Engineering, University of Toronto,
Toronto, ON, Canada

e-mail: sun@mie.utoronto.ca

© Springer Nature Switzerland AG 2022

Y. Sun et al. (eds.), *Field-Driven Micro and Nanorobots for Biology and Medicine*, https://doi.org/10.1007/978-3-030-80197-7_11

269

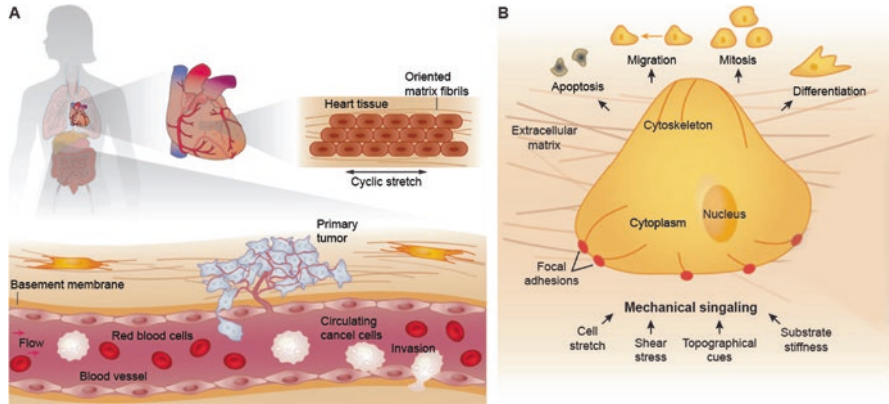


Fig. 11.1 Mechanical environment of a cell. (a) Multiple sources of mechanical stimulation exist in the human body [6]. (b) Biophysical cues inducing cell responses [6]. Reproduced with permission. 2009, Annual Reviews

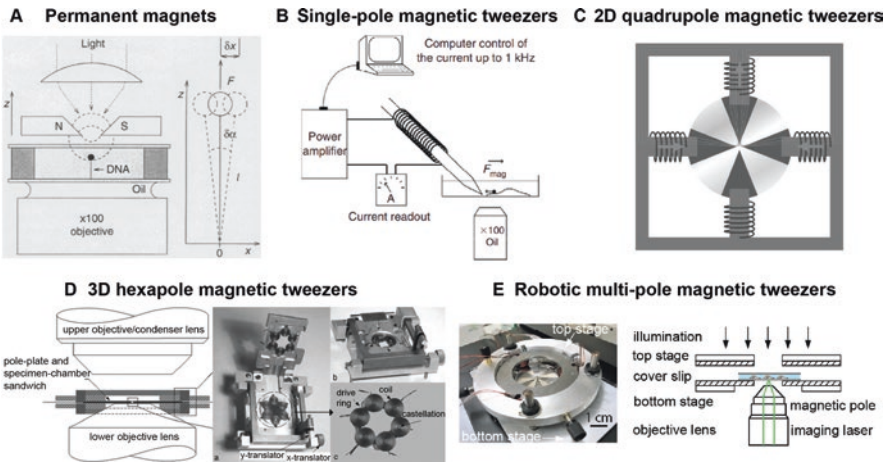


Fig. 11.2 Development of magnetic tweezers. (a) Magnetic tweezers using permanent magnets [11]. Reproduced with permission. 1996, AAAS. (b) Single-pole magnetic tweezers [13]. Reproduced with permission. 2005, AIP. (c) 2D quadrupole magnetic tweezers [17]. Reproduced with permission. 2005, Cell Press. (d) 3D hexapole magnetic tweezers [18]. Reproduced with permission. 2006, AIP. (e) Robotic multi-pole magnetic tweezers [20]. Reproduced with permission. 2019, AAAS

because magnetic force depends on many factors, including position, the material type, lifetime, and shape of the magnets [12]. To address these issues, an electromagnetic coil on a ferromagnetic core with a sharp tip was developed (Fig. 11.2b) [13, 14]. When current is supplied to the magnetic coil, a controllable magnetic field is generated, and the magnetic field has a high magnetic-field gradient near the sharp tip of the magnetic pole [15]. The generated gradient is then used to generate

a controllable force on the magnetic microbead attached to the structure of interest. For example, a microbead was functionalized with antibodies to attach to integrin on the cell surface for cell stiffness measurement [16]. However, the single-pole magnetic tweezers only apply one-directional attractive forces, thus cannot be used to control/navigate the bead position.

Multipole magnetic tweezers utilizing multiple magnetic poles for applying forces on a magnetic microbead in multiple directions were developed in 2005 (Fig. 11.2c, d) [17]. With the capability of applying forces in different directions to navigate a freely moving microbead, the multipole magnetic tweezers enabled the measurement of intracellular viscosity [18]. However, microbead navigation was controlled in an open-loop manner because the small inertia and fast dynamics of magnetic microbeads pose difficulties for position control; and force application was through empirically applying current to each of the coil due to the lack of guidance from a force control model [19]. In 2019, a magnetic model relating magnetic force to electric current applied to each magnetic coil and the bead position within the workspace was developed, and the control of bead position and force inside a single cell was achieved in 3D (Fig. 11.2e) [20].

Despite the developments and wide applications of magnetic tweezers for actuating magnetic beads to perform measurements of biological samples, there are still several challenges that await to be addressed. For instance, force output needs to be increased for manipulation and measurement at the cell and intracellular scales; cytotoxicity and long-term fate of the microbeads need to be further studied.

This chapter introduces the principles of magnetic tweezers and then discusses the applications of magnetic tweezers to the measurement and stimulation of cellular and intracellular structures. Prospects for the development of magnetic tweezers for biomedical applications are also discussed.

11.2 Principles of Magnetic Micromanipulation

11.2.1 *Magnetic Microbead*

Magnetic beads are commonly used for cellular and intracellular measurement and stimulation with a size range from a few nanometers to tens of microns. The wide range allows beads to attach to a variety of targets, including proteins, intracellular organelles, viruses, and cells [16, 21]. In mechanical measurement of cellular and intracellular structures, the bead size of hundreds of nanometers to several microns was most commonly used for generating sufficient forces in mechanical measurement.

The iron surface of iron-based magnetic beads has been shown to cause intracellular inflammation and increased oxidative stress, posing concerns to cell viability [22]. To avoid exposing iron on the bead surface, iron-based and iron oxide-based magnetic microbeads are usually encapsulated by biological matrix or dextran or

functionalized with carboxylic acid or amine groups, polyethylene glycol (PEG), and nitrilotriacetic acid (NTA) [20].

11.2.2 Magnetic Force and Magnetic Moment

For a magnetic bead within a magnetic field, the magnetic force exerted on the bead depends on the induced magnetic moment and the gradient of the magnetic field, namely,

$$\mathbf{F} = \mathbf{m}\nabla\mathbf{B} \quad (11.1)$$

where \mathbf{F} is the magnetic force, \mathbf{m} is the magnetic moment, and $\nabla\mathbf{B}$ is the gradient of the flux density of the magnetic field. The magnetic moment of the magnetic bead depends on the total bead volume, namely, $\mathbf{m} = \iiint\mathbf{M} dV$. When the size of the object scales down, the magnetic moment \mathbf{m} scales down with the volume. Thus, magnetic force scales down to the length by the factor of three.

The magnetic torque exerted on the magnetic bead is

$$\mathbf{T} = \mathbf{m} \times \mathbf{B} = |\mathbf{m}||\mathbf{B}|\sin\theta \quad (11.2)$$

where θ is the angle between \mathbf{m} and \mathbf{B} and $\sin\theta$ reaches the maximum when \mathbf{m} and \mathbf{B} are perpendicular and reaches the minimum when \mathbf{m} and \mathbf{B} are aligned.

When the direction of the magnetic flux density \mathbf{B} changes, the direction of the magnetic moment always aligns toward the direction of magnetic flux density due to the effects of the magnetic torque. When a rotatory magnetic field is applied to the magnetic bead, it rotates with the direction of magnetic field direction (direction of \mathbf{B}) and applies a torque to the structure to which the bead is attached. A magnetic rod has the magnetic moment direction (the direction of \mathbf{m}) aligned with its long axis, thus rotating with a rotatory magnetic field when its long axis has a different direction than the direction of the magnetic field flux density. When it freely rotates in the medium environment, the rotation of a magnetic rod within the magnetic field has been used to measure the viscosity and viscoelastic properties of biological samples [23].

11.2.3 Magnetic Bead Dynamics

The contact mechanics model based on Hertz model was commonly used to relate magnetic force and cell deformation [24]. The Hertz model for the microbead in contact with a cell is

$$F_{\text{elastic}} = \frac{4}{3} \frac{E}{1-\nu_s^2} R^{\frac{1}{2}} d^{\frac{3}{2}} \quad (11.3)$$

where E is the Young's modulus of the sample, ν_s is the Poisson's ratio of the sample, R is the radius of the microbead, and d is the displacement of the microbead after application of the magnetic force.

In addition to elastic properties, cells and intracellular organelles are usually modeled as viscoelastic materials [3, 25]. The viscoelastic model uses springs and dashpots to describe the elastic and viscous properties. For a viscoelastic material, the stress-strain relationship in the K-V model is

$$\sigma = E\varepsilon + \eta \frac{d\varepsilon}{dt} \quad (11.4)$$

where σ is stress, ε is strain, $\frac{d\varepsilon}{dt}$ is strain rate, E is the elastic modulus, and η is the viscosity of the sample. The K-V model combines the elastic portion and the viscous portion as

$$F = F_{\text{elastic}} + F_{\text{viscous}} \quad (11.5)$$

Combining the elastic portion and the viscous portion in the K-V model, the relationship between force, displacement, and speed is

$$F_{\text{mag}} = F_{\text{elastic}} + F_{\text{viscous}} = \frac{4}{3} ER^{1/2} d^{3/2} + \eta \frac{v}{l} \pi R d \quad (11.6)$$

When the microbead is introduced into the cell medium or intracellular environment, the bead subjects to a magnetic force and the random thermal force that induces Brownian motion. The bead dynamics is

$$\mathbf{F}_{\text{mag}} - \mathbf{F}_{\text{thermal}} = m \ddot{\mathbf{P}} + 6\pi\eta r \dot{\mathbf{P}} \quad (11.7)$$

where $\mathbf{F}_{\text{thermal}}$ is the random thermal force depending on bead size and environmental temperature, \mathbf{P} is the bead position in 3D, and $m\ddot{\mathbf{P}}$ is the inertia of the bead, which is negligible due to the microbead's small mass [20].

11.2.4 Magnetic Tweezers Based on Gradient Force

Direct force application is the most commonly used method in cellular and intracellular stimulation (Fig. 11.3a–c) [26]. In a magnetic gradient field, magnetic beads are subjected to a magnetic force, and the force is controlled by changing the distance between permanent magnets and the beads or by controlling the current

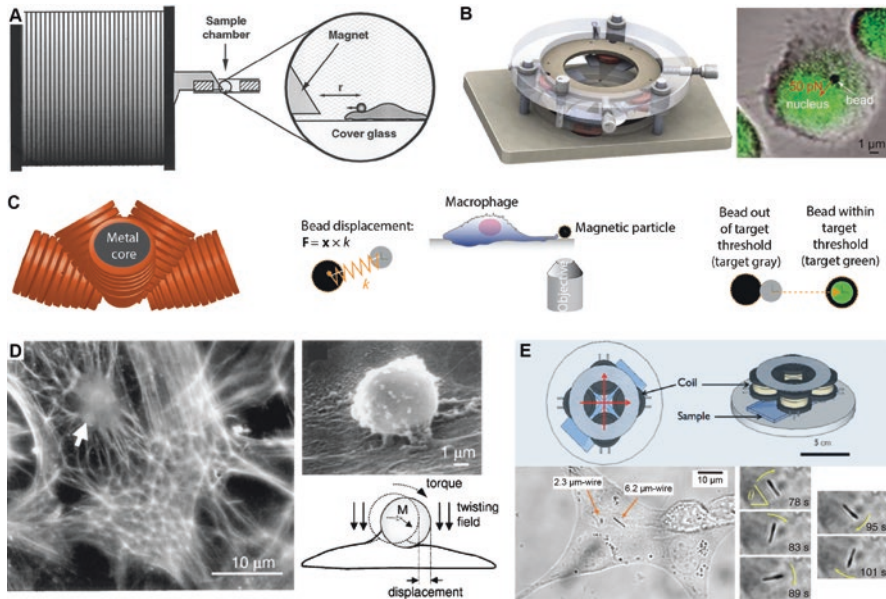


Fig. 11.3 Magnetic tweezers using magnetic gradient and torque. (a) Single-pole magnetic tweezers [25]. Reproduced with permission. 1998, Cell Press. (b) Multi-pole magnetic tweezers [20]. Reproduced with permission. 2019, AAAS. (c) MiniMag system utilizes magnetic field gradient to generate forces on magnetic microbeads [35]. Reproduced with permission. 2017, AAAS. (d and e) Magnetic tweezers cytometry for generating magnetic torque for microbead displacement and micro rod rotation [23, 29]. Reproduced with permission. 2016, Springer Nature and 2001, APS Physics

applied to the electromagnetic coils. Permanent magnets generate a large magnetic field without producing heat in the workspace [27]. However, the magnetic field generated by permanent magnets degrades with the life-time of the permanent magnets, and controlling the field strength by controlling the distance between the bead and the permanent magnets is sometimes infeasible for integration with microscopes. Additionally, controlling the rotation of the permanent magnets to control the frequency of the rotatory field can only reach a maximum of around tens of Hertz.

Compared with magnetic tweezers made from permanent magnets, the electromagnetic magnetic tweezers were used for generating more complex field profiles (e.g., rotating magnetic field and time-invariant magnetic field) and fast dynamics of the alternating field, by controlling the current applied to the coils. The generated controllable force on the magnetic bead can be used for measuring the mechanical properties (viscoelasticity, plasticity, etc.) by relating the force and the resulting deformation using a contact mechanics model [28]. The limitation of using the gradient field is that the magnetic gradient decays with the distance from the electromagnetic pole to the target by a factor of four. Thus, a close distance between the tip and the magnetic bead is required to generate a sub-nanoNewton force.

11.2.5 Magnetic Tweezers Based on Torque

Exerting a torque through the rotation of a magnetic bead or magnetic rod attached to cellular and intracellular structures was used to measure cell mechanics and intracellular cytoplasm viscosity [29]. When subjected to a magnetic field, the magnetic bead or rod aligns the direction of its magnetic moment with the direction of the magnetic field strength. With the capability of generating a large magnetic torque on a microbead coated with antibodies, magnetic twisting cytometry has been used for characterizing the mechanotransduction signaling pathways both on the cell surface and inside the cell (Fig. 11.3d, e).

In magnetic twisting cytometry, the model relating the torque and the local elastic properties of the cell was developed using the generated magnetic torque, T , and local stress caused by the torque. The ratio of the torque T to the resulting bead displacement d defines a complex elastic modulus of the cell $g = T/d$ in the unit of Pa/nm . For each bead, mechanical properties of the elastic modulus g' (the real part of g), the loss modulus g'' (the imaginary part of g), and the loss tangent η (the ratio g'/g'') can be calculated [30]. These results can also be used to relate the elastic and loss moduli by a geometric factor α that depends on the shape and thickness of the cell and the degree of bead embedded within the cellular structures, i.e.,

$$g = \alpha g' \quad (11.8)$$

The geometric factor α serves as an approximation and is model-independent. The quantification of the geometric factor can be achieved by using finite element analysis of cell deformation for a representative bead-cell geometry. For example, assuming 10% of the bead diameter embedded in a cell is 5 μm , the geometric factor α was quantified to be 6.8 μm [30].

After internalized into the cell through endocytosis, the intracellular rod was rotated within the magnetic field to measure cytoplasm viscosity. Actuated by a low-frequency (lower than the step-out frequency) magnetic field, the rods rotate at the same angular speed as the field, whereas at a higher frequency their motion becomes back-and-forth oscillations. The mechanical properties including viscosity, elastic modulus, and relaxation time of the cytoplasm can be calculated from the motion of these rods through fitting to rheological models.

Assuming the cytoplasm is a liquid environment with a viscosity η , a rod subjected to a rotating field experiences a restoring torque that slows down its rotation. As a result, the motion undergoes a transition between a synchronous and an asynchronous rotation. The critical frequency ω_c between these two regimes is

$$\omega_c = \frac{3}{4} \frac{\mu_0 \Delta\chi}{G} g \left(\frac{L}{D} \right) \frac{D^2}{L^2} H^2 \quad (11.9)$$

where μ_0 is the permeability in vacuum, L and D the length and diameter of the wire, H the amplitude of the magnetic excitation, and $g \left(\frac{L}{D} \right)$ is a dimensionless function

of the anisotropy ratio. Additionally, $\Delta\chi = \chi^2/(2 + \chi)$, where χ denotes the magnetic susceptibility [23]. Experimentally quantifying the critical frequency ω_c is used to quantify the shear elastic modulus.

When the cytoplasm is modeled as viscoelastic fluid, the Maxwell model (a spring and dashpot in series) is used to describe the viscoelastic response of the cytoplasm. A rotating rod immersed in such a medium experiences a restoring torque with both viscous and elastic components, and the torque opposes the applied magnetic torque. With increasing ω , the magnetic rod undergoes the same type of transition as the one described above, and the critical frequency ω_c is also as expressed in Eq. (11.9) [23]. From the amplitude of the oscillations $\theta_B(\omega)$ within a Newtonian fluid in the asynchronous regime, the shear elastic modulus G can be determined from

$$\lim_{\omega \rightarrow \infty} \theta_B(\omega) = \frac{3}{4} \frac{\mu_0 \Delta\chi}{G} g \left(\frac{L}{D} \right) \frac{D^2}{L^2} H^2 \quad (11.10)$$

11.3 Mechanical Measurement of Single Cells Using Magnetic Tweezers

11.3.1 Measurements of Cell Mechanics

Biophysical properties of a cell play important roles in regulating cell behaviors such as migration and mitosis and in adapting to the mechanical microenvironment including local stiffness and mechanical stimulation [31–34]. Understanding the biophysical properties of a cell helps better understand how cells interact with its mechanical microenvironment and potentially generate new therapeutic approaches. Within the magnetic field generated by magnetic tweezers, a magnetic bead is controlled to generate forces to deform cellular or intracellular structures for mechanical measurement, including cell stiffness, cytoplasm viscosity, and viscoelasticity of intracellular structures (Fig. 11.4) [35].

To measure mechanical properties at the single-cell level using magnetic tweezers, magnetic microbeads are functionalized with integrin or fibronectin for the beads to attach to the cell surface and to apply a force or torque on the cell surface, which is transmitted through the cytoskeleton. When subjected to a mechanical force or torque, living cells undergo viscoelastic deformations. Bausch et al. characterized the viscoelastic properties of cells by using 4.5 μm magnetic beads attached to the cell membrane and pulled by a single-pole magnetic tweezer to apply a nanoNewton force as a step pulse [36]. During force application, the creep response of the cell was recorded and used to calculate the viscoelastic properties (shear modulus and viscosity) of the cell. In addition to viscoelastic properties, the incomplete shape recovery on the cell after force application was observed and was believed due to plastic deformation of the cell. Using large alternating step-force

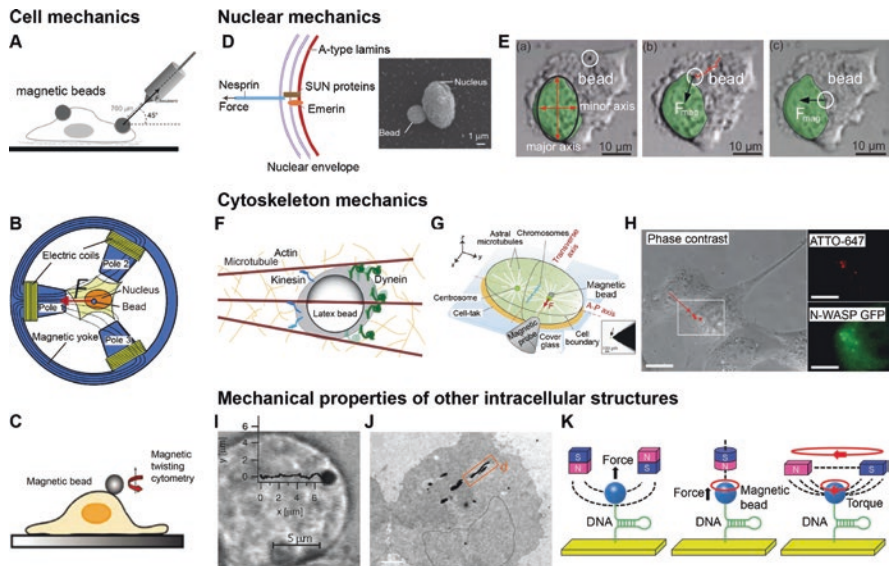


Fig. 11.4 Mechanical measurement on cells (a–c), 32–34 nucleus (d and e), 20, 41 cytoskeleton (f–h), 43–45, and other structures (i–k) 23, 36, 47. Reproduced with permission. 2018 Wiley; 2007, ACS Publications; 2014 SAGE Journals; 2014, Springer Nature; 2019, AAAS. 2012, PNAS; 2016, AAAS; 2013, Springer Nature; 1999, Cell Press; 2015, Springer Nature; 2017, Royal Society of Chemistry

pulses (e.g., 10 nN) applied to the cell with a 4 μm magnetic bead on the cell membrane, cell plasticity was quantified by measuring the irreversible deformation after force application [37].

Magnetic twisting cytometry was also used to quantify cell mechanics with a static torque and has been used to apply cyclic stress and study the frequency response of the cell. In experiments, ferromagnetic beads attached to the cell surface were magnetized with a strong external magnetic field (Fig. 11.4c). Then a sinusoidal magnetic field applied perpendicularly to the original field was used for cyclic loading on the cell. Butler et al. extended the actuation from 2D to 3D by developing a magnetic twisting device, which allowed rotation control three dimensionally. The study revealed the anisotropy of cell mechanics by twisting the magnetic bead and cytoskeleton along different axes and different angles.

With the advantage of high precision, large force output, and superb biocompatibility of magnetic measurement and manipulation, the application of magnetic tweezers to cell mechanics measurement was further extended to the measurement of long-term cell mechanics change during cell migration and mitosis and in cancer progression and stem cell maturation. For example, Osborne et al. characterized the stiffness change during TGF-β-induced EMT (epithelial-to-mesenchymal transition) over time and revealed a functional connection between the reduction in stiffness and the increase of the invasion capacity of the cells [38].

11.3.2 Measurement of Cellular Rheological Properties

After introduced into the cell through either microinjection or endocytosis, magnetic microbead can be controlled to navigate inside the cytoplasm by magnetic forces. Due to the small mass and small inertia, the magnetic force on the magnetic bead quickly balances with the fluidic drag force. According to magnetic field models, the magnetic force depends on the magnetic field gradient and magnetic moment of the microbead, and the magnetic force can be calibrated beforehand in an environment with known viscosity (e.g., silicone oil) [15]. By calculating the fluidic drag force from the balancing magnetic force, the viscosity of the local liquid environment in cytoplasm is calculated. A 1.3 μm microbead was moved in a macrophage to measure the viscoelastic of the cytoplasm by tracking the bead's moving speed under a constant magnetic force; the viscosity of the cytoplasm was measured to be 2–7 mPa·s (Fig. 11.4i) [36]. However, studies on measuring intracellular cytoplasm viscosity showed that a large portion of the magnetic microbeads was trapped in the cytoskeleton network, which must be taken into account for cytoplasm viscosity quantification.

Using the magnetic torque-based method, the rotation of magnetic wires within the magnetic field was recorded inside the cell to quantify the viscosity or viscoelastic properties of the cytoplasm. A magnetic micro wire was used for rotational magnetic spectroscopy to measure the shear viscosity of the cytoplasm inside living cells by relating the magnetic torque applied to the magnetic wire and the resulting rotation speed (Fig. 11.4j). Unlike the translational movement of magnetic beads inside the cell, the rotating wire can differentiate liquid-like (viscosity) from gel-like (viscoelasticity) behaviors by observing transient frequencies between a synchronous and an asynchronous regime of rotation. It was found that the cytoplasm behaved as viscoelastic fluid [23].

11.4 Mechanical Measurement of Intracellular Structures

11.4.1 Measurement of Cell Nucleus and Cytoskeleton

The cell nucleus is the largest organelle and the major DNA storage inside the cell [39]. Abnormal mechanical properties of the cell nucleus have been observed in cancers and muscular dystrophy [40]. With the small size and large force output of the magnetic bead within the magnetic gradient field, magnetic tweezers have become a powerful tool for studying nuclear mechanics. By attaching an antibody-coated magnetic bead onto Nesprin and applying an oscillating force (35 pN) on isolated nuclei, Guilluy et al. found that mechanotransduction existed on the nuclear envelope rather than only limited on the cell surface (Fig. 11.4d) [41]. However, the nucleus isolation process (either mechanically or chemically) disrupts the local cytoplasmic environment that the nucleus lies in, where the nucleus is closely

integrated with the cytoskeleton within the cytoplasm and the activities that occur within the nucleus are regulated by ions within the cytoplasmic environment. To study the mechanical properties of the cell nucleus inside a living cell, robotic multiple magnetic tweezers were developed to control a $0.7\ \mu\text{m}$ magnetic bead for measuring the nuclear mechanics inside the living cell without nucleus isolation (Fig. 11.4e) [20]. For studying intra-nucleus properties, Subramaniam et al. injected a single magnetic bead ($1\ \mu\text{m}$) into the nucleus a living cell and measured the viscoelasticity within the nucleus, proving the feasibility of intracellular measurement and manipulation of chromatin using magnetic microbeads [42].

11.4.2 Measurement of Cytoskeleton, DNA Strands, and Intracellular Motor Proteins

Magnetic measurement using magnetic tweezers has also enabled the study of properties of the cytoskeleton, DNA strands, and motor proteins [43–45]. With the small size of the magnetic microbead accessing small space in living cells, mechanical measurements were conducted on cytoskeleton to understand how molecular forces applied on the cytoskeleton regulate cell mitosis. Garzon-Coralin et al. measured the forces for a cell to maintain the position and orientation of the spindle during cell division (Fig. 11.4g) [44]. To measure mitotic forces in vivo, a $1.0\ \mu\text{m}$ magnetic bead was injected into the cell of a *C. elegans* embryo, and single-pole magnetic tweezers were used to exert forces up to $200\ \text{pN}$ to mitotic spindles. The results showed that a force-generating centration apparatus with spring-like properties maintained the spindle at the cell center. To further increase the force output for manipulating the cytoskeleton, the single-pole magnetic tweezers built by Tanimoto et al. with strong neodymium super magnets were capable of applying a force up to $1500\ \text{pN}$ to move the microtubule asters in a fertilized sea urchin egg [46]. With the ability to slow down or even move against the asters centering motion, they directly measured the force associated with the migration and centering of the aster, which also quantified the number of motor proteins involved in the process.

Since the early invention of magnetic tweezers, mechanical measurements were made on DNA strands using magnetic tweezers to study the unwinding force and DNA binding force to adhesion molecules. Through mechanical stretching (force application) or twisting (torque application) of the DNA strand, the force needed for unwinding or re-zipping DNA, the molecular force in DNA replication, and the force on torsional constraints have been studied. For example, Ebright et al. used magnetic tweezers to twist a single DNA molecule to create a super-coiled state and revealed the different transcription activity of RNA polymerase on different super-coiled states of DNA (Fig. 11.4k) [47, 48].

Through controlling the magnetic force or torque applied to balance the active force applied by the motor, magnetic actuation was used to estimate the driving force/torque of an isolated motor protein, such as kinesin, dynein, and rotary motor

protein. For example, a 2.8 μm magnetic bead was attached at the positive end of an isolated microtubule with intracellular motors kinesin on the substrate [49]. When the magnetic force was scaled by the average number of motors, the force-velocity relationships for multiple kinesin motors and single kinesin motor were quantified, for studying the kinesin motor's movement on microtubules. The results showed that *Drosophila* kinesin-1 motors moved a microtubule at 200–700 $\mu\text{m/s}$ against a 0–31 pN load at saturating ATP supply [49].

11.5 Summary and Outlook

The development of magnetic tweezers has enabled a multitude of applications for cellular and intracellular measurement. Different configurations of magnetic tweezers generating magnetic force or torque were developed to control a magnetic microbead, wire, or rod to apply a force on cellular/intracellular structures for measurement. Magnetic microbeads have been controlled by an external magnetic field to exert forces/torques and perform mechanical measurements on the cell membrane, cytoplasm, cytoskeleton, nucleus, and intracellular motors. Magnetic tweezers have become an important tool for cell biophysical measurement and will continue to be used widely for further exploration of cellular/intracellular structures and their functions.

Different from using specific target antibodies toward integrin for binding the magnetic microbead to the cell surface, existing magnetic tweezers are ineffective for controlling the microbead's position in a cell with sufficient resolution for targeting small intracellular structures (e.g., mitochondria, endosome, lysosome) [50]. The limitation was imposed by poor magnetic force scaling and by lacking the capability of applying an accurately controlled force due to thermal fluctuations [26]. Because gradient-generated force scales down with the bead size by a factor of three, the magnetic force exerted on a 1 μm magnetic bead is usually less than 1 pN, which is insufficient to deform cellular structures for mechanical measurement. Further increasing the magnetic field gradient to increase the magnetic force would pose limitations on workspace, as the magnetic gradient decays by the factor of four with space. Controlling the microbead position within the region with nonlinear magnetic field gradient can potentially increase the workspace, while a nonlinear magnetic force model is required to position control using magnetic tweezers.

The position control accuracy of microbead controlled by magnetic tweezers is also limited by the imaging resolution and sampling frequency of a microscope. The future development of magnetic tweezers could be integrated with more advanced imaging techniques, such as super-resolution microscopy (e.g., STED) for a higher imaging resolution and a higher sampling frequency for position control.

Measurements performed on intracellular structures require the microbeads to be internalized into the cell. It was shown that the internalization process was affected by the size, shape, surface charge, coating, and hydrophobicity of the microbeads.

After internalization, the microbeads are degraded in lysosomes by a number of enzymes such as the lysosomal Cathepsin L. The release of reactive iron species during degradation can be a source of cytotoxicity [51]. The cytotoxicity effect from the microbeads can affect measurement on cellular structures especially during time-lapsed measurement in the course of cell migration and mitosis, which are known to be related to the coordination of biophysical properties of nuclear mechanics, cytoskeleton organization, and hydraulic pressure [52].

How the degradation of the magnetic beads affects cell metabolism and what is the long-term intracellular fate of these beads require further studies [22]. Surface functionalization with biocompatible materials (e.g., carbon and gold) and the encapsulation of magnetic materials with biopolymers can potentially reduce the cytotoxic effect to the cells.

When used together with biophysical measurements, biochemical measurements have also been explored through functionalizing magnetic microbeads with various types of fluorescent dyes. Compared with traditional dye treatment, the use of dye-functionalized microbeads for measuring intracellular biochemical signals has the advantage of a high surface-area-to-volume ratio. Using magnetic tweezers, dye-functionalized magnetic microbeads can be controlled to form a swarm through on-demand magnetic aggregation and de-aggregation control. Through magnetic swarm/aggregate control using magnetic tweezers, fluorescent-dye-coated magnetic nanoparticles can form a swarm/aggregate of a controllable size to locally enrich the concentration of fluorescent dyes for a higher signal-to-noise ratio (SNR). Using a swarm of magnetic microbeads for biochemical measurement, only a small amount of dyes needs to be introduced into a cell, resulting in reduced toxicity to the cell, which can potentially become a tool for intracellular biochemical measurement with increased SNR and decreased toxicity.

References

1. Squires, T. M., & Mason, T. G. (2010). Fluid mechanics of microrheology. *Annual Review of Fluid Mechanics*, 42, 413–438.
2. De Vlaminck, I., & Dekker, C. (2012). Recent advances in magnetic tweezers. *Annual Review of Biophysics*, 41, 453–472.
3. Lim, C. T., Zhou, E. H., & Quek, S. T. (2006). Mechanical models for living cells – A review. *Journal of Biomechanics*, 39(2), 195–216.
4. Fletcher, D. A., & Mullins, R. D. (2010). Cell mechanics and the cytoskeleton. *Nature*, 463(7280), 485–492.
5. Wang, X., Liu, H., Zhu, M., Cao, C., Xu, Z., Tsatskis, Y., Lau, K., Kuok, C., Filleter, T., McNeill, H., & Simmons, C. A. (2018). Mechanical stability of the cell nucleus—roles played by the cytoskeleton in nuclear deformation and strain recovery. *Journal of Cell Science*, 131, 13.
6. Kim, D. H., Wong, P. K., Park, J., Levchenko, A., & Sun, Y. (2009). Microengineered platforms for cell mechanobiology. *Annual Review of Biomedical Engineering*, 11, 203–233.
7. Pelling, A. E., & Horton, M. A. (2008). An historical perspective on cell mechanics. *Pflügers Archiv-European Journal of Physiology*, 456(1), 3–12.

8. Goldmann, W. H., Auernheimer, V., Thievesten, I., & Fabry, B. (2013). Vinculin, cell mechanics and tumour cell invasion. *Cell Biology International*, 37(5), 397–405.
9. Ramaekers, F. C., & Bosman, F. T. (2004). The cytoskeleton and disease. *The Journal of Pathology: A Journal of the Pathological Society of Great Britain and Ireland*, 204(4), 351–354.
10. Davidson, P. M., & Lammerding, J. (2014). Broken nuclei–lamins, nuclear mechanics, and disease. *Trends in Cell Biology*, 24(4), 247–256.
11. Strick, T. R., Allemand, J. F., Bensimon, D., Bensimon, A., & Croquette, V. (1996). The elasticity of a single supercoiled DNA molecule. *Science*, 271(5257), 1835–1837.
12. Wang, X., Law, J., Luo, M., Gong, Z., Yu, J., Tang, W., Zhang, Z., Mei, X., Huang, Z., You, L., & Sun, Y. (2020). Magnetic measurement and stimulation of cellular and intracellular structures. *ACS Nano*, 14(4), 3805–3821.
13. Fisher, J. K., Cummings, J. R., Desai, K. V., Vicci, L., Wilde, B., Keller, K., Weigle, C., Bishop, G., Taylor, R. M., Davis, C. W., & Boucher, R. C. (2005). Three-dimensional force microscope: A nanometric optical tracking and magnetic manipulation system for the biomedical sciences. *Review of Scientific Instruments*, 76(5), 053711.
14. Schuerle, S., Erni, S., Flink, M., Kratochvil, B. E., & Nelson, B. J. (2012). Three-dimensional magnetic manipulation of micro- and nanostructures for applications in life sciences. *IEEE Transactions on Magnetics*, 49(1), 321–330.
15. Wang, X., Luo, M., Wu, H., Zhang, Z., Liu, J., Xu, Z., Johnson, W., & Sun, Y. (2017). A three-dimensional magnetic tweezer system for intraembryonic navigation and measurement. *IEEE Transactions on Robotics*, 34(1), 240–247.
16. Alenghat, F. J., Fabry, B., Tsai, K. Y., Goldmann, W. H., & Ingber, D. E. (2000). Analysis of cell mechanics in single vinculin-deficient cells using a magnetic tweezer. *Biochemical and Biophysical Research Communications*, 277(1), 93–99.
17. De Vries, A. H., Krenn, B. E., van Driel, R., & Kanger, J. S. (2005). Micro magnetic tweezers for nanomanipulation inside live cells. *Biophysical Journal*, 88(3), 2137–2144.
18. Fisher, J. K., Cribb, J., Desai, K. V., Vicci, L., Wilde, B., Keller, K., Taylor, R. M., Haase, J., Bloom, K., O'Brien, E. T., & Superfine, R. (2006). Thin-foil magnetic force system for high-numerical-aperture microscopy. *Review of Scientific Instruments*, 77(2), 023702.
19. Zhang, Z., Huang, K., & Menq, C. H. (2009). Design, implementation, and force modeling of quadrupole magnetic tweezers. *IEEE/ASME Transactions on Mechatronics*, 15(5), 704–713.
20. Wang, X., Ho, C., Tsatskis, Y., Law, J., Zhang, Z., Zhu, M., Dai, C., Wang, F., Tan, M., Hopyan, S., & McNeill, H. (2019). Intracellular manipulation and measurement with multipole magnetic tweezers. *Science Robotics*, 4, 28.
21. Tajik, A., Zhang, Y., Wei, F., Sun, J., Jia, Q., Zhou, W., Singh, R., Khanna, N., Belmont, A. S., & Wang, N. (2016). Transcription upregulation via force-induced direct stretching of chromatin. *Nature Materials*, 15(12), 1287–1296.
22. Cochran, D. B., Wattamwar, P. P., Wydra, R., Hilt, J. Z., Anderson, K. W., Eitel, R. E., & Dziubla, T. D. (2013). Suppressing iron oxide nanoparticle toxicity by vascular targeted antioxidant polymer nanoparticles. *Biomaterials*, 34(37), 9615–9622.
23. Berret, J. F. (2016). Local viscoelasticity of living cells measured by rotational magnetic spectroscopy. *Nature Communications*, 7(1), 1–9.
24. Harris, A. R., & Charras, G. T. (2011). Experimental validation of atomic force microscopy-based cell elasticity measurements. *Nanotechnology*, 22(34), 345102.
25. Bausch, A. R., Ziemann, F., Boulbitch, A. A., Jacobson, K., & Sackmann, E. (1998). Local measurements of viscoelastic parameters of adherent cell surfaces by magnetic bead microrheometry. *Biophysical Journal*, 75(4), 2038–2049.
26. Zhang, Z., Wang, X., Liu, J., Dai, C., & Sun, Y. (2019). Robotic micromanipulation: Fundamentals and applications. *Annual Review of Control, Robotics, and Autonomous Systems*, 2, 181–203.
27. Ryan, P., & Diller, E. (2017). Magnetic actuation for full dexterity microrobotic control using rotating permanent magnets. *IEEE Transactions on Robotics*, 33(6), 1398–1409.

28. Wang, X., Zhang, Z., Tao, H., Liu, J., Hopyan, S., & Sun, Y. (2018). Characterizing inner pressure and stiffness of trophoblast and inner cell mass of blastocysts. *Biophysical Journal*, *115*(12), 2443–2450.
29. Na, S., Collin, O., Chowdhury, F., Tay, B., Ouyang, M., Wang, Y., & Wang, N. (2008). Rapid signal transduction in living cells is a unique feature of mechanotransduction. *Proceedings of the National Academy of Sciences*, *105*(18), 6626–6631.
30. Fabry, B., Maksym, G. N., Butler, J. P., Glogauer, M., Navajas, D., & Fredberg, J. J. (2001). Scaling the microrheology of living cells. *Physical Review Letters*, *87*(14), 148102.
31. Miller, C. J., & Davidson, L. A. (2013). The interplay between cell signalling and mechanics in developmental processes. *Nature Reviews Genetics*, *14*(10), 733–744.
32. Charrier, E. E., Montel, L., Asnacios, A., Delort, F., Vicart, P., Gallet, F., Batonnet-Pichon, S., & Hénon, S. (2018). The desmin network is a determinant of the cytoplasmic stiffness of myoblasts. *Biology of the Cell*, *110*(4), 77–90.
33. de Vries, A. H., Krenn, B. E., van Driel, R., Subramaniam, V., & Kanger, J. S. (2007). Direct observation of nanomechanical properties of chromatin in living cells. *Nano Letters*, *7*(5), 1424–1427.
34. Unal, M., Alapan, Y., Jia, H., Varga, A. G., Angelino, K., Aslan, M., Sayin, I., Han, C., Jiang, Y., Zhang, Z., & Gurkan, U. A. (2014). Micro and nano-scale technologies for cell mechanics. *Nanobiomedicine*, *1*(Godište 2014), 1–5.
35. Schuerle, S., Vizcarra, I. A., Moeller, J., Sakar, M. S., Özkale, B., Lindo, A. M., Mushtaq, F., Schoen, I., Pané, S., Vogel, V., & Nelson, B. J. (2017). Robotically controlled microprey to resolve initial attack modes preceding phagocytosis. *Science Robotics*, *2*, 2.
36. Bausch, A. R., Möller, W., & Sackmann, E. (1999). Measurement of local viscoelasticity and forces in living cells by magnetic tweezers. *Biophysical Journal*, *76*(1), 573–579.
37. Bonakdar, N., Gerum, R., Kuhn, M., Spörner, M., Lippert, A., Schneider, W., Aifantis, K. E., & Fabry, B. (2016). Mechanical plasticity of cells. *Nature Materials*, *15*(10), 1090–1094.
38. Osborne, L. D., Li, G. Z., How, T., O'Brien, E. T., Blobe, G. C., Superfine, R., & Myhre, K. (2014). TGF- β regulates LARG and GEF-H1 during EMT to affect stiffening response to force and cell invasion. *Molecular Biology of the Cell*, *25*(22), 3528–3540.
39. Osmanagic-Myers, S., Dechat, T., & Foisner, R. (2015). Lamins at the crossroads of mechano-signaling. *Genes & Development*, *29*(3), 225–237.
40. Zwerger, M., Ho, C. Y., & Lammerding, J. (2011). Nuclear mechanics in disease. *Annual Review of Biomedical Engineering*, *13*, 397–428.
41. Guilluy, C., Osborne, L. D., Van Landeghem, L., Sharek, L., Superfine, R., Garcia-Mata, R., & Burridge, K. (2014). Isolated nuclei adapt to force and reveal a mechanotransduction pathway in the nucleus. *Nature Cell Biology*, *16*(4), 376–381.
42. Kanger, J. S., Subramaniam, V., & van Driel, R. (2008). Intracellular manipulation of chromatin using magnetic nanoparticles. *Chromosome Research*, *16*(3), 511.
43. Hendricks, A. G., Holzbaur, E. L., & Goldman, Y. E. (2012). Force measurements on cargoes in living cells reveal collective dynamics of microtubule motors. *Proceedings of the National Academy of Sciences*, *109*(45), 18447–18452.
44. Garzon-Coral, C., Fantana, H. A., & Howard, J. (2016). A force-generating machinery maintains the spindle at the cell center during mitosis. *Science*, *352*(6289), 1124–1127.
45. Etoc, F., Lisse, D., Bellaiche, Y., Piehler, J., Coppey, M., & Dahan, M. (2013). Subcellular control of Rac-GTPase signalling by magnetogenetic manipulation inside living cells. *Nature Nanotechnology*, *8*(3), 193.
46. Tanimoto, H., Sallé, J., Dodin, L., & Minc, N. (2018). Physical forces determining the persistence and centring precision of microtubule asters. *Nature Physics*, *14*(8), 848–854.
47. Xin, Q., Li, P., He, Y., Shi, C., Qiao, Y., Bian, X., Su, J., Qiao, R., Zhou, X., & Zhong, J. (2017). Magnetic tweezers for the mechanical research of DNA at the single molecule level. *Analytical Methods*, *9*(39), 5720–5730.

48. Revyakin, A., Ebright, R. H., & Strick, T. R. (2004). Promoter unwinding and promoter clearance by RNA polymerase: Detection by single-molecule DNA nanomanipulation. *Proceedings of the National Academy of Sciences*, *101*(14), 4776–4780.
49. Fallesen, T. L., Macosko, J. C., & Holzwarth, G. (2011). Force–velocity relationship for multiple kinesin motors pulling a magnetic bead. *European Biophysics Journal*, *40*(9), 1071–1079.
50. Liu, J., Wen, J., Zhang, Z., Liu, H., & Sun, Y. (2015). Voyage inside the cell: Microsystems and nanoengineering for intracellular measurement and manipulation. *Microsystems & Nanoengineering*, *1*(1), 1–5.
51. Feng, Q., Liu, Y., Huang, J., Chen, K., Huang, J., & Xiao, K. (2018). Uptake, distribution, clearance, and toxicity of iron oxide nanoparticles with different sizes and coatings. *Scientific Reports*, *8*(1), 1–3.
52. Fletcher, D. A., & Mullins, R. D. (2010 Jan). Cell mechanics and the cytoskeleton. *Nature*, *463*(7280), 485–492.

Chapter 12

Hepatic Vascular Network Construction Using Magnetic Fields



Eunhye Kim, Masaru Takeuchi, and Toshio Fukuda

Without perfusable vascular networks, three-dimensional tissues populated with cells cannot maintain a living condition. To construct 3D tissues, a well-organized vascular network is required. In this work, a method for constructing a hepatic lobule-like vascular network in 3D cellular structure by using magnetic fields is employed. To realize channel networks that mimic the hepatic lobule, steel rods and magnetic fibers were utilized as a sacrificial mold in fibrin gel. The network is simply constructed by three types of veins, a central vein, portal vein, and sinusoids. To realize two types of veins, the central vein and the portal vein, two different sizes of steel rods were utilized. In addition, magnetic fibers connected the central vein and the portal vein for delivering nutrients in 3D cellular structure. The steel rods and fibers were connected by magnetic fields using magnetic tweezers. The proposed tweezers were designed based on 3D simulation data to generate high magnetic fields to attract magnetic fibers. In addition, a tissue with 3D channel network was cultured for a week. To verify that the channel network can supply the nutrients to the cells in tissues, the viability of the cells located on the structure was analyzed. The cells close to the channel network show a higher cell viability than the cells far from the channel network.

12.1 Introduction

Recently, in vitro three-dimensional (3D) tissue fabrication has been one of the significant research issues for transplantation. To develop a substitute for real tissue and organs, construction of an artificial tissue is necessary. First, to build avascular and thin tissues, such as skin and cartilage, various methods have been

E. Kim (✉) · M. Takeuchi · T. Fukuda

Department of Mechatronics Engineering, Meijo University, Nagoya, Aichi, Japan

Department of Micro-Nano Systems Engineering, Nagoya University, Nagoya, Aichi, Japan

e-mail: kim@meijo-u.ac.jp

proposed – for example, cell sheet engineering and 3D bioprinting [1, 2]. However, because the diffusion of nutrients and oxygen in cell-dense tissues is limited, 3D cell-dense tissues thicker than 200 μm find it difficult to maintain cells in a living condition [3]. To avoid necrosis of the cells in 3D tissues, construction of well-organized vascular networks that can spread nutrients and oxygen to cells in 3D tissue is indispensable [4, 5]. Generally, vascularized tissues in the human body include a range of branching vessels from millimeter-sized veins to a micrometer-sized capillary network. Thus, a branching vascular network is essential for attaining perfusable tissues.

Many approaches have been addressed to construct vascular structure in 3D artificial tissues [6]. To fabricate a large tissue applying cell sheet engineering, simple vascular networks have been designed by sandwiching endothelial cells between two cell sheets [7]. Another approach is the assembly of small blocks made by hydrogel embedding cells for building vascular-like microtubes [8, 9]. For example, Takeuchi et al. proposed a self-assembly method of magnetized toroidal microstructures [9]. However, the constructed vascular-like structures made by cell sheets and the assembly of microstructures show simple patterns.

To fabricate various patterns of vascular networks in 3D tissues, 3D printing methods have been proposed. For example, Miller et al. printed rigid 3D filament networks of carbohydrate glass as a lattice structure and deposited it into cell-loaded matrices [10]. Subsequently, the glass skeleton was dissolved to create a vascular network in 3D tissue containing living cells. Bertassoni et al. printed agarose fibers and then constructed linear, branching, and lattice architectures of vascular structures in cell-laden methacrylated gelatin (GelMA) hydrogels [11]. Lee et al. constructed large perfused vascular channels [12]. They fabricated larger (more than 1-mm) vascular channels using gelatin and connected them by printing the adjacent capillary network for seeding endothelial cells.

Although the 3D printing method offers highly precise positioning and high control of speed, resolution, and diameter of the vessels, it is difficult to construct a 3D vascular network having a branching structure. There are several problems. First, because the assembly speed of tissues is decided by the size of the target and the printing speed, a longer assembly time corresponds to a larger size of the tissue. Second, the printing materials are restricted to printable and biocompatible elements. Third, the underlying layers tend to collapse as additional layers are printed on top of them, and so, the construction of the multilayered structure is still challenging.

The final goal of this research is to construct liver by assembling hepatic lobule-like structure. Liver is an important organ because of its many functions such as detoxification of blood, helping fighting infection, and aiding in digestion. In addition, it is an ideal cellular model for drug test and screening and cell behavior study. For this, as the first step, many researchers have constructed hepatic lobule-like structure. D. R. Albrecht et al. patterned cells and microspheres by dielectrophoresis (DEP) manipulation [13]. C. T. Ho et al. patterned hepatic and endothelial cells via an enhanced field-induced dielectrophoresis (DEP) trap [14]. G. S. Jeong et al. culture cells using honeycomb structures made by natural extracellular matrix (ECM)

[15]. However, they constructed only two-dimensional structure due to the lack of spatial organization techniques. To realize similar models with hepatic lobule, fabrication of 3D hepatic lobule-like structure with high similarity is necessary. 3D hepatic lobule-like structures have been constructed by using several approaches. V. L. Tsang et al. fabricated 3D cellular structure by multilayered photo patterning platform for embedding cells in hydrogels of complex structure [16]. X. Ma et al. made 3D hydrogel-based triculture model by 3D printing [17]. C. Ma et al. culture cell-laden hydrogel by pneumatic-aided micro-molding [18]. Although they construct 3D hepatic tissue, the depth of the structure is less than 200 μm . To construct large-sized hepatic lobule tissue, perfusable vascular network to supply nutrients and oxygen is required.

Recently, assembly of hepatic lobule-shaped microtissue containing liver cells for constructing multiple layered tissues has been proposed. Z. Liu et al. fabricated hepatic lobule tissues based on Ca-alginate cell sheets and assembly them by using glass micropipette [19]. J. Cui et al. utilized a gelatin methacryloyl (GelMA) hydrogel as a matrix to construct 3D lobule-like microtissues for co-culture and assembled them using micro bubbles [20]. Although they achieved multilayered structure, the vascular networks are too simple compare to real things.

In this research, magnetic fields were used to construct a 3D vascular network in a cell-dense structure. The magnetic fields make it possible to exert forces at a distance, without damage to the target materials, which makes it possible to increase the construction speed, regardless of the target size, and to maintain the biocompatible condition of the cells. Owing to these benefits, magnetic fields have been applied to various biological applications.

To manipulate a single particle including magnetic beads and biological cells, magnetic tweezers have been implemented for generating magnetic fields 13–20 [21–28]. The magnetic tweezers are able to concentrate magnetic fields into a small space. Bonakdar et al. precisely controlled a 4.5–5- μm microbead attached to a living cell for measurement of cell mechanical properties [22]. Robert et al. manipulated 5–100- μm magnetic objects and stem cells in a porous scaffold to probe the local physical properties for enhancing cell seeding [23]. Tweezers with two poles were utilized for characterizing intracellular properties of cells and for analyzing DNA molecules by manipulating micro objects [24, 25]. A quadrupole magnetic tweezers were reported [26]. Quadrupoles having sharp tips were employed to trap a magnetic particle in a 2D direction. A hexapole electromagnetic system was designed to generate magnetic force onto a microbead in the 3D direction [27, 28]. As mentioned above, the applications of the tweezers actuated by coils were limited as manipulation of microbeads on the cells for analyzing cell properties.

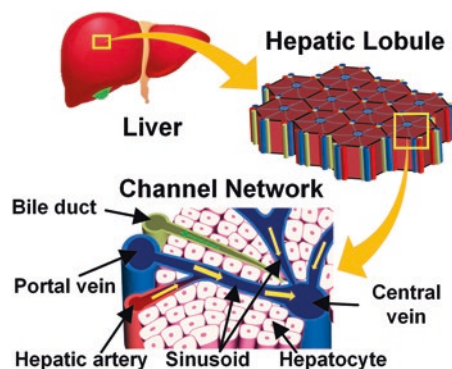
Recently, novel hybrid alginate microfibers by embedding magnetic particles have been proposed. Hu et al. fabricated magnetic hydrogel fibers with magnetic particles and living cells [29]. Sun et al. improved the fabricated magnetic fibers by encapsulating magnetic oil micro-droplets with uniform distribution to measure the magnetic forces on the magnetic fibers [30]. The magnetic hydrogel fibers showed high controllability, flexibility, and cell viability. These fibers were directly

manipulated using a magnetic tweezer, and then it was verified that cellular structures with diverse forms, such as a microscale helical microstructure and dome-shaped structure, can be constructed by assembling magnetic fibers [31, 32]. These results show that the magnetic hydrogel fiber is a suitable material for constructing vascular networks because of the flexibility provided by the hydrogel and the controllability provided by magnetic fields.

In this chapter, magnetic hydrogel fibers were manipulated by using magnetic tweezers for constructing a 3D vascular network. The magnetic hydrogel fibers were utilized as a sacrificial mold in cell-laden hydrogel, which makes a 3D channel network having a complex structure. A hepatic lobule that is a small division of the liver was realized, because the liver is an important organ that performs a multitude of functions, such as detoxification of blood and production of albumin.

Figure 12.1 shows the structure of the hepatic lobule and its vascular network. On the edge of the lobule, portal triads containing three vessels (bile duct, portal vein, and hepatic artery) are arranged, and a central vein is placed on the center of the lobule. In addition, the sinusoids connect portal triads and the central vein. The blood is transferred from portal triads to the central vein. To achieve the channel network of different sizes of veins, as at the bottom of Fig. 12.1, magnetic fibers were utilized for capillary networks and steel rods for the portal triads and the central vein. Moreover, fibrin gel with living cells concretes the shape of network and helps to construct a multilayer structure. This chapter focuses on designing magnetic tweezers by analyzing magnetic fields and constructing 3D tissue by the culturing of cells in the proposed structure. The main achievement in this work are (1) analysis of magnetic fields by a 3D simulator, (2) design of the magnetic tweezers with seven poles based on 3D simulation results to generate higher magnetic fields than the early version, (3) construction of a multilayered hepatic lobule-like vascular network with three times larger size than the real thing, and (4) verification of the constructed structure in a biocompatible condition by culturing it for 7 days.

Fig. 12.1 Structure of a hepatic lobule and its channel network



12.2 Concept of Research

The method of constructing a vascular network similar to a hepatic lobule is described in this section. The hepatic lobule is 1.0–1.3 mm in diameter and 1.5–2.0 mm in depth [33]. The structure of the vascular network of the hepatic lobule is given in Fig. 12.2a. In the figure, one can see a variety of veins, such as the bile duct, portal vein, hepatic artery, central vein, and sinusoids. To simplify the vascular network of the hepatic lobule, the focus was on three vessels: a central vein, portal vein, and sinusoid. They have different diameters provided by the dosimetry model in previous work [34]. The diameters of the central vein, portal vein, and sinusoid were 70, 30, and 7 μm , respectively. To mimic the hepatic lobule-like vascular network, the ratio among the diameters of the three veins were calculated and followed. Figure 12.2b indicates the structure of the proposed system. The central vein, the thickest vein among three veins, is made by a 1.5-mm steel rod. For the portal veins, 1-mm steel rods were substituted, and the sinusoids that deliver blood containing nutrients were replaced by 400- μm microfibers. The channel network is constructed within fibrin gel embedding rat liver cells (RLC-18).

The fabrication strategies for in vitro 3D tissue with a channel network are shown in Fig. 12.3. First, alginate gel fibers embedding ferrite particles were fabricated, and subsequently, the microfiber was cut and magnetized to make magnetic fibers. Next, magnetic fibers were manipulated by magnetic tweezers for making a 3D structure, and then the hydrogel with cells was deposited to the 3D structure. After solidification of the hydrogel, magnetic fibers were melted to be a channel network. Finally, the culture medium for supplying nutrients to living cells was injected, and the 3D cellular structure was cultured in an incubator. After several days, it was possible to fabricate in vitro 3D tissue. To follow this strategy, it was necessary to fulfill a few requirements: (1) manipulation of magnetic fibers at high magnetic fields, (2) seeding cells in a biocompatible hydrogel, and (3) making a channel network that can transfer nutrients to the cells in a biocompatible condition.

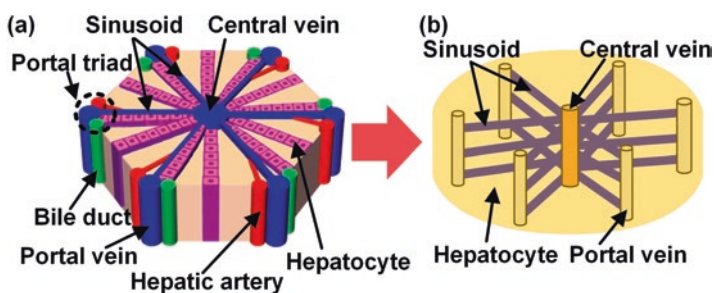


Fig. 12.2 Concept of the research. (a) Hexagonal shape of a hepatic lobule with a vascular network. (b) Proposed concept for constructing a hepatic lobule

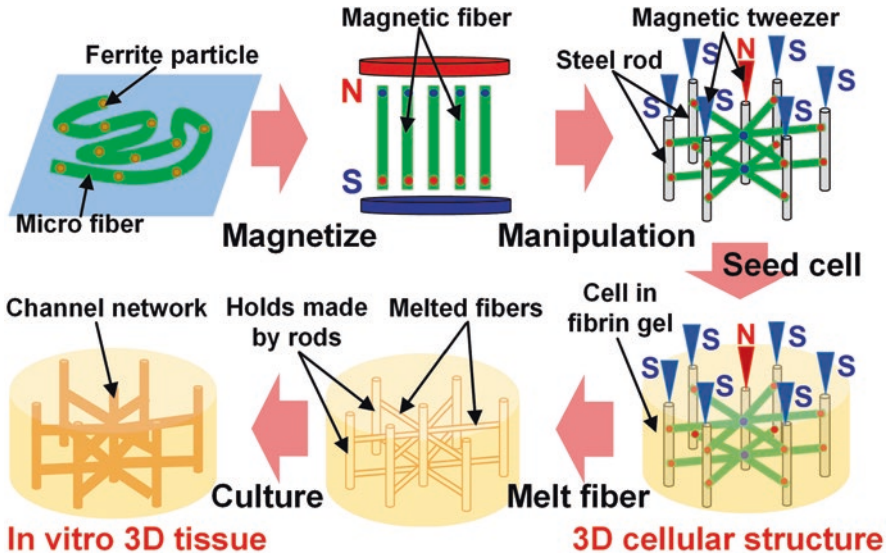


Fig. 12.3 Fabrication strategies for 3D tissue having a channel network

12.3 System of Magnetic Tweezers

12.3.1 Overall System of Manipulator

For constructing a hepatic lobule-like channel network in a 3D cellular structure, there are three required conditions. The first is generation of enough magnetic force to attract magnetic fibers to make capillary networks between two veins. For this, the magnetic tweezers were simulated with steel rods, and the shape of the tweezers was decided. In addition, the lower part of the tweezers was added to increase the magnetic fields on the steel rods. The second requirement is magnetic tweezers with a special structure to magnetize one central vein and six portal veins for making the hexagonal structure. Thus, magnetic tweezers with seven poles were proposed. Third, precision position control on a microscale was necessary to construct a millimeter-sized structure. For this, an XYZ motorized stage with 1- μm resolution was utilized.

The proposed magnetic-tweezer system is shown in Fig. 12.4. Because a single electromagnetic pole can only magnetize a single steel rod, seven electromagnetic poles were utilized to realize a hexagonal structure having one central vein and six portal veins. Each pole consisted of a copper coil of wire wrapped around a cylindrical soft iron core with a tapered tip. The diameter and length of the iron core were 5 mm and 120 mm, respectively. The tip diameter of the pole was the same as the diameter of the steel rod to concentrate the magnetic fields on the steel rod. The shape of the tweezer is elucidated in the left side of Fig. 12.4. Each pole connects to a steel rod to magnetize it. The seven steel rods have a 25-mm length. The rod that

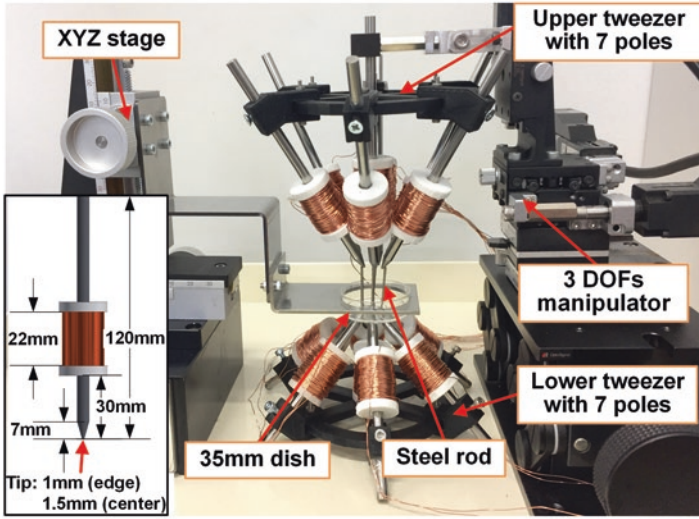


Fig. 12.4 System of magnetic tweezers

plays a role as the central vein has a 1.5-mm diameter; the rest of the six poles for making portal veins had a 1-mm diameter to realize the ratio of the hepatic lobule. The angle between the center of the pole and the edge of the poles is 30° . To increase the magnetic fields on the steel rods, a lower part of the tweezers with seven poles was added under the dish. The length of the iron core was 80 mm, and the angle between the center and edge of the poles was 45° . To increase the contact area between steel rods and tips of tweezers, we cut off the end of steels rods obliquely. The cut angles of the end of rods that magnetized by edge of the poles were the same as the angles between the center and the edge of the poles. Since the upper tweezer is 30° and lower tweezer is 45° , the cut angle of the top and bottom of the rods were 30° and 45° , respectively. A manipulation process was performed in a petri dish with a 10-mm depth and a 35-mm diameter. The XYZ-movement of the dish was generated by a manual stage (TAR-34805L).

The control system was composed of a magnetic field control and a position control. A PC managed the overall system that communicated with Arduino (Mega 2560) via an RS232 communication. Each power supply (ESP10-15-12, switching power supply) was connected to each relay (ALQ112, Panasonic) to supply 0.6 A of electrical current. Because magnetic poles always occur in pairs, a pair of magnetic poles was generated by switching relays. In this system, the center of the pole was magnetized N-pole, while the edge of the poles was magnetized S-pole to attract opposite ends of the fibers. Thus, electrical current was applied to two coils placed on the center and one of the edges of the pole. To be specific, the relay connected to the center of the pole was activated continuously, whereas the relays attached on the edge of the poles were switched on and off selectively. The magnetic coils were 0.4-mm enameled copper wires wound and 600 turns each.

A motorized stage (TSD-405SL) manipulates the upper tweezers in the XYZ-axis. It could generate motion at a high speed (1 mm/s) by actuating three stepping motors (SGSP-13ACT-B0) that could be moved up to 13 mm with a resolution of 1 μm . The velocity of the motors could be controlled by pulse width modulation through three motor drivers (MC-S0514ZU).

12.3.2 Simulation of Magnetic Tweezers

To generate high magnetic fields that can attract magnetic fibers on the steel rods, we redesigned magnetic tweezers based on the 3D simulation data. Magnetic fields were analyzed by utilizing EMWorks in SolidWorks. To increase the magnetic fields on the steel rods, first it was analyzed by changing the contact area between the steel rod and the tip of the tweezer. Figure 12.5 displays the simulation results by comparing two types of tips, a sharp tip with less than 1-mm radius curvature, as in Fig. 12.5a, and a flat tip with 1-mm diameter, as in Fig. 12.5b. Each pole consists of a solenoid (600 turns of a 0.4-mm diameter copper wire, 0.6 A of electric current) with a 5-mm diameter iron core (SS400). The geometry of each electromagnetic pole is the same as the computer-aided design (CAD) model on the left side of Fig. 12.4. The steel rod was attached on the bottom of the tip. The length and the diameter of the rod were 25 mm and 1 mm, respectively. To compare two types of tips, the magnetic flux density on the center of the steel rod was measured from the contact point with the tip to the bottom of the rod. The measurement points are marked as dotted arrows in Fig. 12.5a, b. The results are plotted in Fig. 12.5c. From the graph, it can be understood that the magnetic flux density on the steel rod increases as the contact area between the tip and the rod increases. Therefore, the tip of the tweezer was designed as a flat tip 1 mm in diameter that is the same as the diameter of the steel rod.

Figure 12.6 displays the simulation results of the magnetic tweezers with and without the lower parts. Figure 12.6a, b shows the cross-sectional area of the magnitude of magnetic flux density in the vertical plane. Without the lower parts as in Fig. 12.6a, the magnetic flux density on the bottom of the steel rod is too small to attract the fibers. To generate sufficient magnetic fields on the steel rod, supplementary tweezers were added to the bottom of the steel rods as in Fig. 12.6b. However, a space between the steel rods and the additional tweezers should be set as 1 mm, because a petri dish with 35-mm diameter and 1-mm thickness of bottom arranged.

In addition, electrical current was subsequently applied to two coils placed on the center and one on the edge of the pole, because magnetic poles always occur in pairs. The electrical current was applied to the coils on Pole 1 and Pole 2 in a different magnetic direction. Although the same currents were applied to two coils in Pole 1 and 2, the magnetic flux densities were not equal because of the different diameters of the steel rods; the center of the rod was 1.5 mm in diameter and the edges of the rods were 1 mm in diameter to realize the ratio of the veins. Figure 12.6c shows the results of the magnetic flux density with and without the lower parts of the

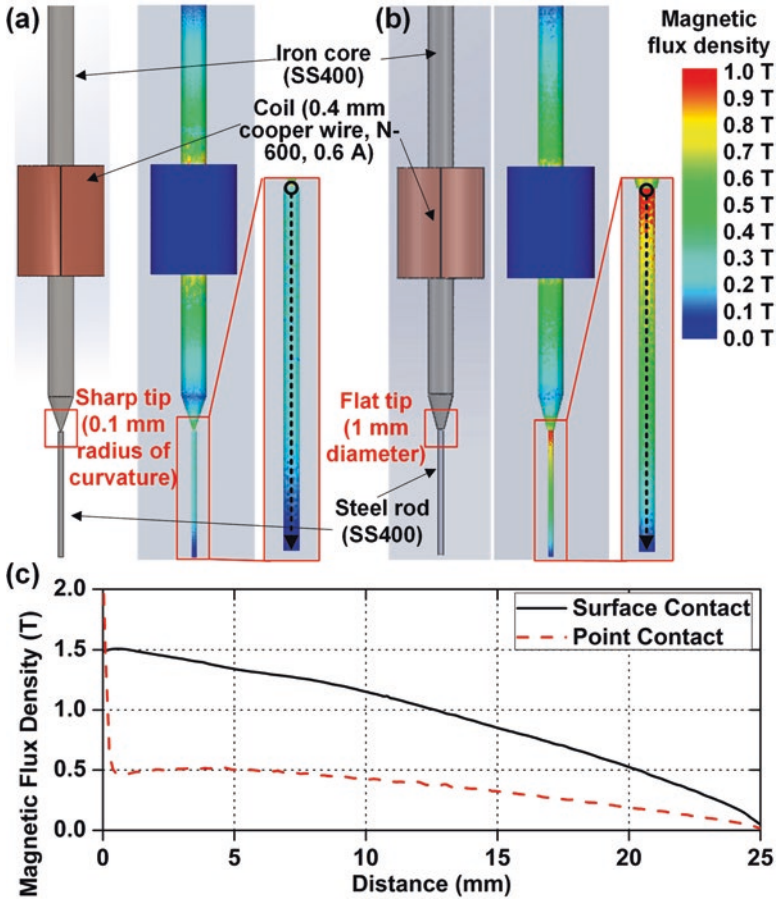


Fig. 12.5 Simulation of two types of tips. (a) Point contact by a sharp tip. (b) Surface contact by a flat tip. (c) Comparison of magnetic flux density of two types of tips

tweezers. The magnetic flux density of the central axis of the steel rods connected to Poles 1 and 2 were measured. The measurement points are marked as black dotted arrows in the right side of Fig. 12.6a, b. The results were plotted from the top of the rods that make the tip of tweezers contact the bottom of the rods. With the addition of the lower parts, the magnetic flux density on the bottom of the steel rods was increased more than twice.

From the simulation results that change the tip from sharp tip to flat tip and add lower parts of tweezers, the model of the tweezers was decided upon, as in Fig. 12.7. Figure 12.7a shows the CAD model and its boundary conditions. To analyze the magnetic fields on the steel rods and the iron cores, they were densely meshed, as in Fig. 12.7b. Vectors of magnetic flux density around the steel rods are plotted in Fig. 12.7c, d. Because the directions of the input current of Coils 1 and 2 are clockwise and counterclockwise, respectively, on the XZ-plane, the vectors between steel

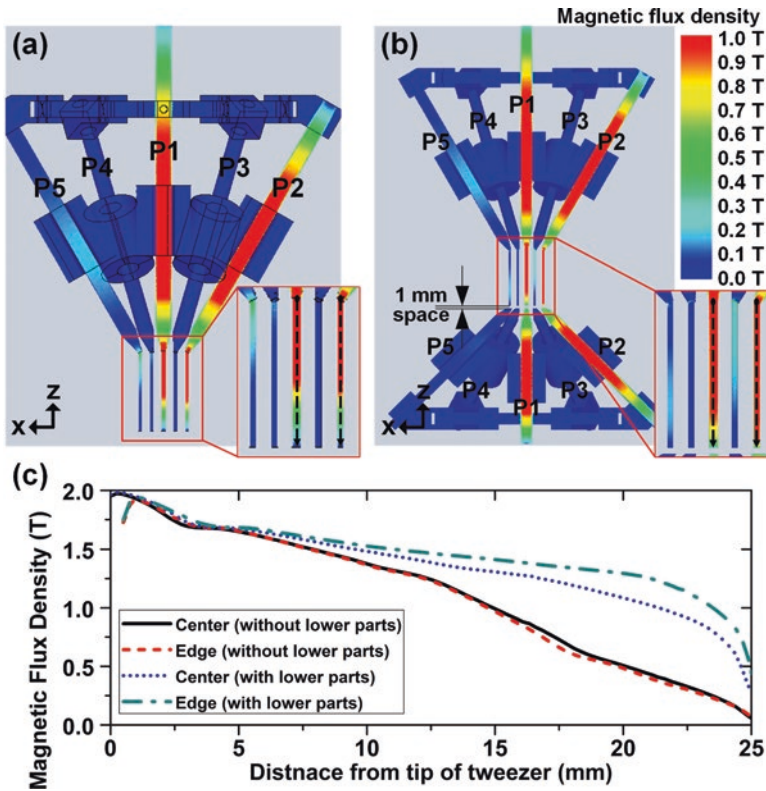


Fig. 12.6 Magnitude of magnetic flux density of tweezers (a) without lower parts and (b) with lower parts. (c) Comparison of the magnetic flux density of steel rods with the distance from the tip

rods connected on Poles 1 and 2 point to the rod attached to Pole 2. Figure 12.7d indicates the cross section of the black line in Fig. 12.7c. Two steel rods are magnetized in opposite directions, and then they can attract the opposite ends of the magnetic fibers by high magnetic fields.

As a result, we generated high magnetic fields on the steel by changing the tips of the tweezers from a sharpen tip to a flat tip and applying a switching system.

12.4 Method and Materials

12.4.1 Assembly Method of Multilayered Structure

Figure 12.8 illustrates the fabrication procedure of a 3D vascular network in a cellular structure. Alginate gel fibers were used as an alternative to sinusoids that form capillary networks by connecting two veins. Steel rods of 1.5-mm and 1-mm

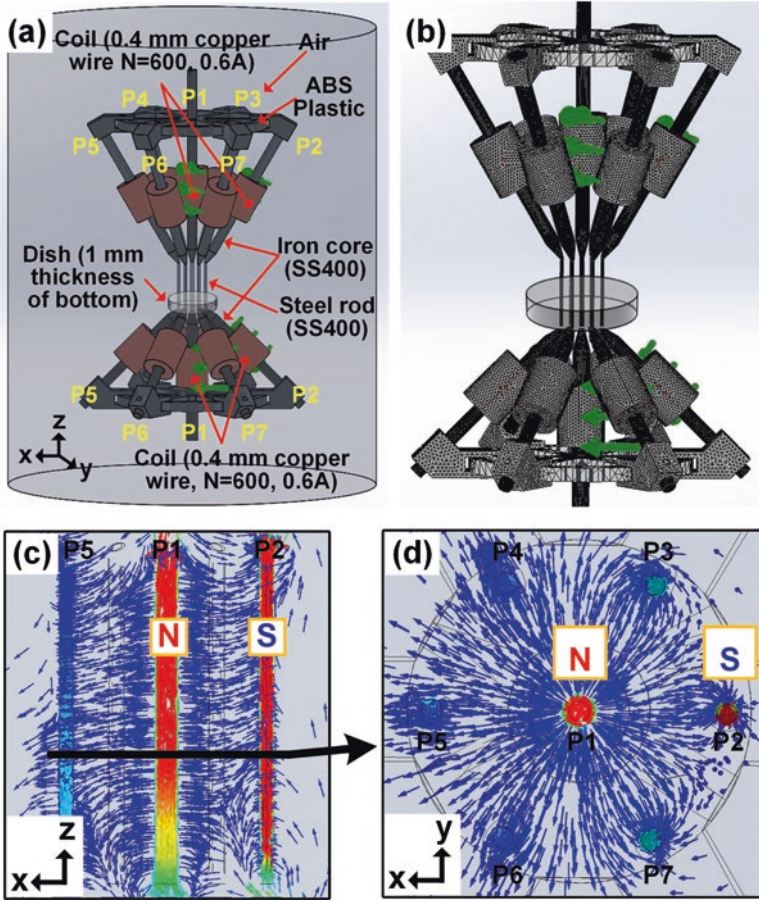


Fig. 12.7 Simulation of magnetic tweezers with seven poles by EMworks in SolidWorks. (a) CAD model. (b) Mesh of tweezers. Vectors of magnetic flux density (c) in the vertical plane and (d) in the horizontal plane

diameter realize a central vein and portal vein, respectively. First, the magnetic fibers shown in Fig. 12.8a were fabricated. Of the ferrite particles (SF-H470), 0.1 g were dissolved into 1 mL of 1.0% w/v sodium alginate solution. The alginate solution embedding ferrite particles was loaded into a 1 mL syringe with a 0.4-mm diameter needle, and then they were injected into a 2.0% w/v calcium chloride (CaCl_2) solution. To fabricate fibers with uniform diameter, a syringe pump delivered a flow rate of 0.7 mL/min. It became calcium alginate gel, and 0.4 mm of microfibers were formed with ferrite particles. Subsequently, the fiber was regularly cut by scissors. Because the fibers connect two veins (central vein and portal vein), the length of the fiber was set by the distance between the 1.5-mm steel rod and 1-mm steel rod. In this experiment, the distance was approximately 4 mm, and then

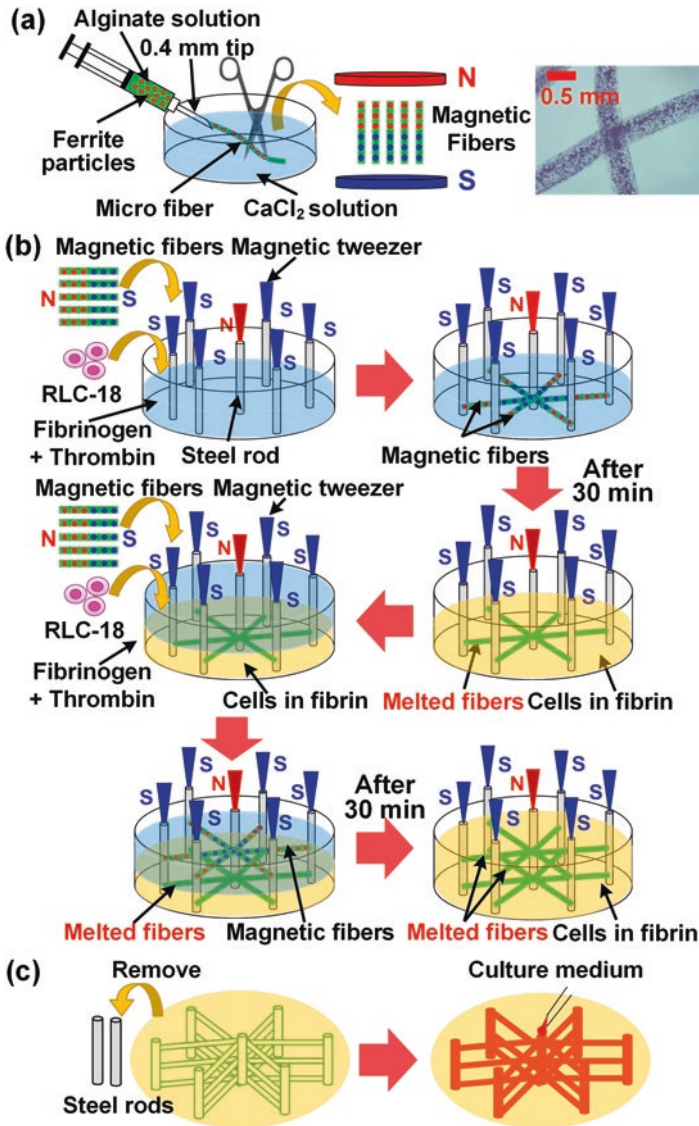


Fig. 12.8 Fabrication procedure of a 3D vascular network in a cellular structure. **(a)** Fabrication of magnetic fibers. **(b)** Construction of a multilayered structure in fibrin gel. **(c)** Verification of a 3D vascular network in a cellular structure

the fibers were cut to 5-mm length. Fibers having uniform length and thickness were magnetized at 3 T using a magnetizer (IMC-1050, IMS Co., Ltd.). Then, magnetic fibers were produced with different magnetic poles at the end of the fiber, as in Fig. 12.8a. The magnetic particles were dispersed embedded in the fibers. The fibers were washed three times with a 0.9% sodium chloride (NaCl) solution.

For attracting magnetic fibers into steel rods, magnetic fields were applied to seven steel rods, six 1-mm steel rods, and a 1.5-mm steel rod by using magnetic tweezers with seven poles. Two steel rods with different diameters were magnetized as contrary magnetic poles; hence, the magnetized steel rods attracted both ends of the fibers. For example, the 1-mm steel rods positioned on the outside of the hexagonal structure were magnetized to the South Pole, while the 1.5-mm steel rod located at the center of the structure were magnetized to the North Pole. In this case, because the two steel rods with different poles attract each other, the steel rods were fixed on 35 mm of petri dish by concreting 1 mL of polydimethylsiloxane. Next, 0.3 mL of thrombin solution (10 units/mL in distilled water) were prepared on the dish, and the living cells (RLC-18) and magnetic fibers were deposited in it. Simultaneously, the magnetic fibers were automatically attracted to two types of steel rod. In addition, 3 mL of fibrinogen solution (10 mg/mL fibrinogen, 20-mM HEPES, and 0.9% w/v NaCl in 10% PBS) were deposited into the dish to concrete the mixed solution. After 40 min, the fibrinogen and thrombin solution were changed into fibrin gel; simultaneously, the magnetic fibers were melted, which caused the fibers to be a channel between the two rods. As a result, a first-layered structure was constructed. To construct second-layered structure, the fibrinogen and the thrombin solution were deposited on the dish, and living cells and fibers were added one more time. After the solidification of the mixed solution, the second-layered structure was fabricated by melting the fibers. This process is shown in Fig. 12.8b.

After repeating the process for constructing the multilayered structure, the steel rods were removed from the fibrin gel. The holes made by steel rods realized a central vein and portal veins. To dissolve the inner calcein-alginate fibers, 55-mM citrate solution containing 0.45% NaCl was injected into the center of the hole for 5 min and then removed. Then, the culture medium was injected into the center of the hole fabricated by the steel rods for supplying the culture medium to the living cells close to the channel network, as shown in Fig. 12.8c. Figure 12.9 displays the experimental process of the multilayered structure. After the gelation of the fibrinogen solution, the channel can maintain the structure and can build the upper layers without collapse of the gel structure.

12.4.2 Method of Cell Culture and Viability Test

In the previous section, the fabrication process of the 3D vascular network in cellular structure was addressed. To verify whether the proposed process is conducted in a biocompatible condition or not, in this section, how to culture the cells in fibrin gel with more than 2 mm of thickness is explained, and their viability is analyzed. In addition, the survival rate of cells cultured in fibrin gel is analyzed according to the distance from the surface to prove that the cells close to the surface, contacting the culture medium, show a high survival rate compared with the cells far from the surface. For this, rat liver cells (RLC-18) were cultured in fibrin gel, and cell viability from the top to the bottom of the gel was analyzed.

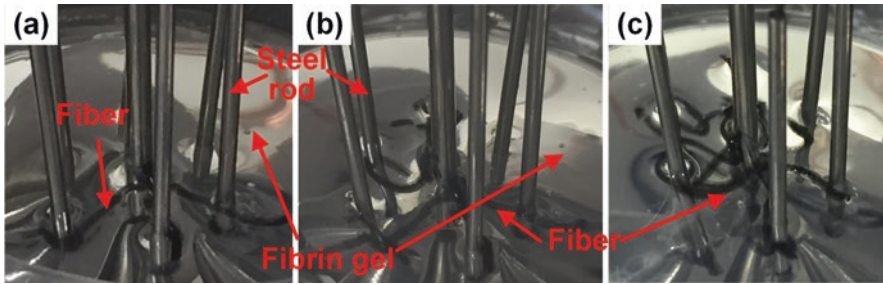


Fig. 12.9 Experimental process of a multilayered structure. (a) First-layered structure. (b) Second-layered structure. (c) Multilayered structure

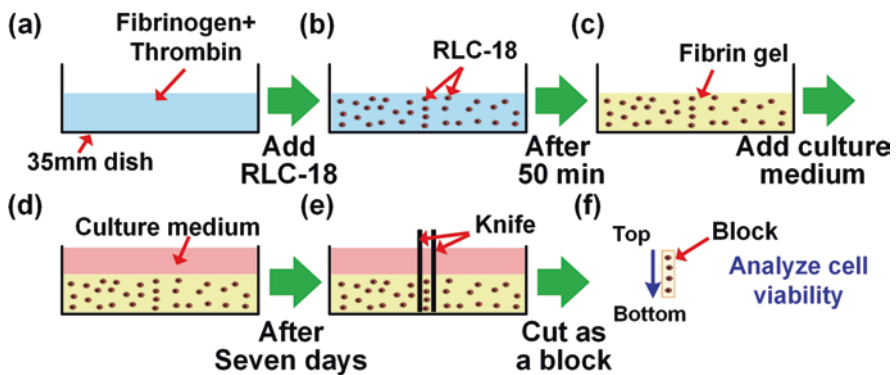


Fig. 12.10 Experiment procedure for analyzing cell viability

Figure 12.10 illustrates the fabrication process for analyzing cell viability in fibrin gel. First, 3 mL of fibrinogen (10-mg/mL fibrinogen, 20-mM HEPES, and 0.9% w/v NaCl in 10% PBS) and 300 μ L of thrombin solution (10 units/mL) were deposited on the 35-mm petri dish as in Fig. 12.10a. Subsequently, 230 μ L of rat liver cells (RLC-18, 1.8×10^7 cells/mL) cultured in Dulbecco's Modified Eagle's Medium (Sigma Aldrich) with 10% fetal bovine serum (Sigma Aldrich) and 270 μ L of aprotinin solution (500 KIU/mL, Wako) were dropped into the dish, as in Fig. 12.10b. To solidify the mixed solution in a biocompatible condition, the samples were held in an incubator (5% CO₂ at 37 °C) for 50 min, as shown in Fig. 12.10c. Afterward, the culture medium was deposited on top of the fibrin gel, and then the sample was incubated in 5% CO₂ at 37 °C for 7 days – see Fig. 12.10d. The culture medium and aprotinin solution were changed every day to maintain their environmental condition.

After incubation, the fibrin gel with cells was cut as a small block by a sharpened knife, and it was removed – Fig. 12.10e. Finally, the viability of the cellular block from the top, contacting the culture medium, to the bottom of the block, contacting the bottom of the dish, was analyzed as shown in Fig. 12.10f. The cells in the block were stained with calcein-AM and propidium iodide (PI). Then, 2 μ L of calcein-AM

solution (1 mg/mL DMSO) was dissolved in 10 ml of culture medium and cultured for 15 min in the incubator. Next, 25 μ L of PI solution (1 mg/mL H₂O) were mixed in 10 mL of the culture medium and cultured for 5 min.

To find a better environmental condition for living cells, two samples were tested in different conditions. Sample 1 was constructed with the same methods as in Fig. 12.10. For Sample 2, thrombin solution was added more than two times (600 μ L) than in Sample 1 (300 μ L) to reduce the solidification time. The time was reduced from 50 min to 25 min.

12.5 Results and Discussion

12.5.1 Hepatic Lobule-Like Vascular Network in Fibrin Gel

As shown in Fig. 12.11, a vascular network that mimics a hepatic lobule structure was constructed. The capillary network was formed as the alginate gel fibers embedding ferrite particles were melted by the fibrinogen solution. After the fibers were melted, the ferrite particles that were bonded in fibers were detached and then moved outside of the fibers, as in Fig. 12.11a. Figure 12.11b, c shows the top and bottom of the constructed structure. However, magnetic particles were separated, and therefore, the shape of the constructed structure is not clear. To verify the shape of the structure, solution dyed with Congo red was inserted in the center of the hole made by the 1.5-mm steel rod. The dyed solution was dispersed from the central vein to the portal veins through the capillary networks fabricated by the melted fibers. The results are displayed in Fig. 12.11d–f. In this experiment, a four-layered structure, as in Fig. 12.11d, having a hexagonal shape, as in Fig. 12.11e, f, was

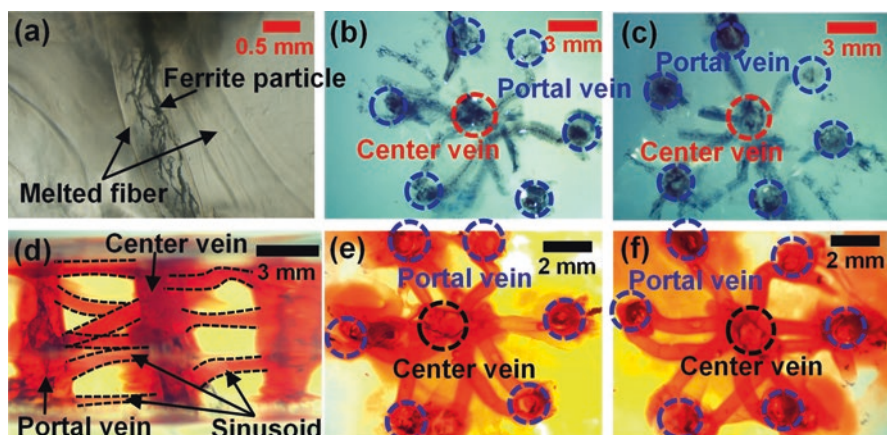


Fig. 12.11 Constructed 3D vascular network within fibrin gel

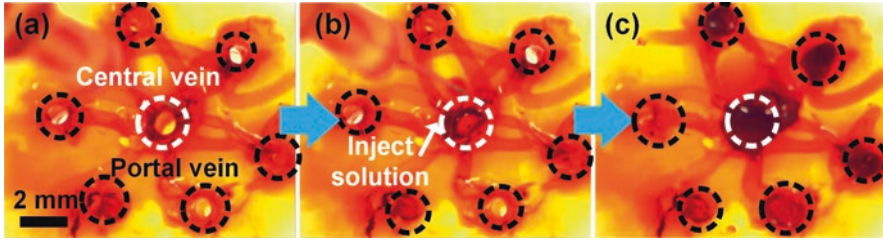


Fig. 12.12 Verification of the 3D channel network by injecting dyed solution

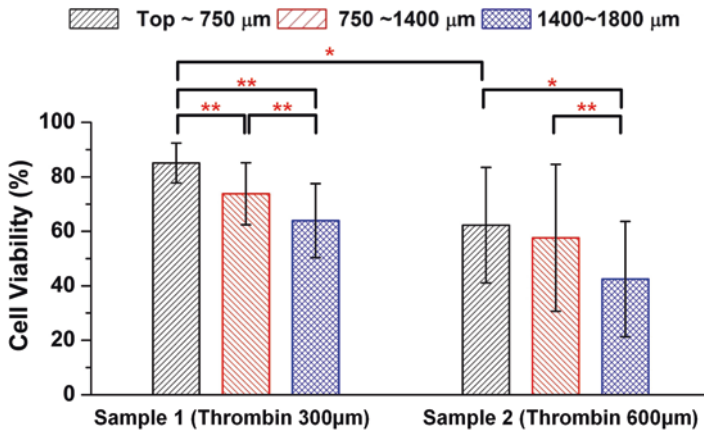


Fig. 12.13 Results of the cell viability test in different conditions. (*T*-test: * $p < 0.05$, ** $p < 0.01$, $n = 7$)

constructed. As a result, a hepatic lobule-like vascular network with four layers was fabricated. It had an approximately 8-mm diameter and 9-mm depth.

Figure 12.12 shows the dyed solution injected into the center vein, as in Fig. 12.12b, to verify the flow from the central vein to the portal vein via the channel network. Before injecting the dyed solution, the black dotted circles in Fig. 12.12b were empty. After the solution was transferred by sinusoid, the black dotted circles in Fig. 12.12c were filled. Thus, we were able to verify that the solution was moved from the central vein to the portal veins.

12.5.2 Cell Viability in 3D Cellular Structure with Channels

The results of the cell viability test in two different conditions are displayed in Fig. 12.13. In the graph, the area is allocated by the distance from the top of the gel, in contact with the culture medium. The result shows that the cell viability decreased as the cells were located away from the culture medium. To be specific, for Sample

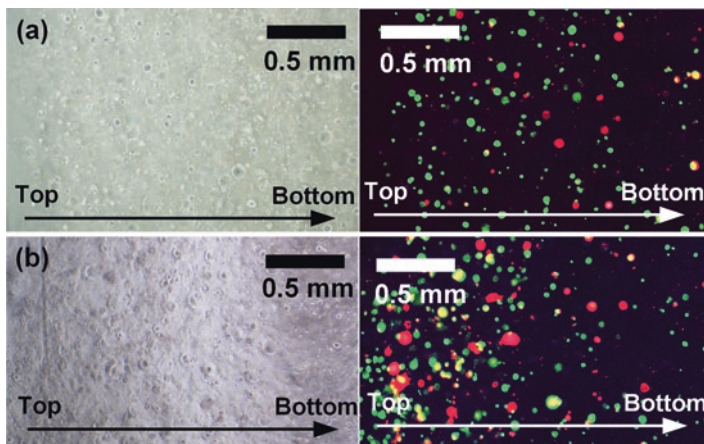


Fig. 12.14 Images of a cellular block from top to bottom of the fibrin gel. Cell viability test of (a) Sample 1 and (b) Sample 2

1, the cell viability was approximately 86% at the area (top – 750 μ m), whereas the cell viability decreased to 64% in the area (1400–1800 μ m). In addition, Sample 2, with decrease in the time to gelate, shows a lower cell viability than the case that does not change any environmental condition (Sample 1). The cell viability is approximately 62.3% in the area (top–750 μ m) and 42.4% in the area (1400–1800 μ m). Figure 12.14 shows the bright field image and fluorescent image after the live/dead staining of cells in the block. From this image, the living and dead cells can be observed from top of the gel to the bottom of the gel. Here, living cells decrease toward the bottom of the gel. Moreover, the cells in Sample 1 show higher cell viability than the cells in Sample 2.

Based on the result, it was assumed that the fabricated vascular network can improve the cell viability to supply the culture medium to the cells placed close to the network. To verify this assumption, the vascular network was cultured in a 3D cellular structure for 7 days. The procedure of the fabrication of the channel network in a cell cultured fibrin gel was explained in a previous section. A different thing is to add fibers for constructing a channel network. Before the depositing of the fibers, the fiber was washed with 0.9% NaCl three times. Next, the steel rods were arranged on the dish and magnetized using the tweezers. In addition, the mixed solution, thrombin, aprotinin solution, and living cells (RLC-18, 1.8×10^7 cells/mL) were injected into the dish. The washed fibers were deposited in the solution, and then the steel rods attract the fibers. When the fibers were attached to the rods, the fibrinogen solution was added to solidify them. After the mixed solution was transformed to gel, a vascular network was completed. To dissolve the inner alginate fibers, sodium citrate solution (2 mL, 55 mM, 0.45% NaCl) was injected into the center of the hole for 5 min. The cellular structure was cultured in an incubator for 7 days. During the culturing of the cells, the culture medium and aprotinin solution

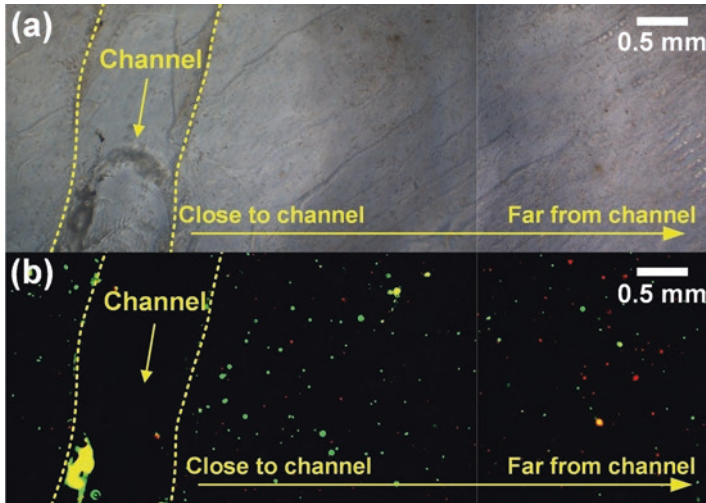


Fig. 12.15 Images of a 3D cellular structure with a channel network. (a) Bright field image of the cells. (b) Fluorescent image after the live/dead staining of cells

were refreshed daily to supply nutrients and oxygen to the cells. Figure 12.15 shows the cell viability result of the cells in the constructed structure. To analyze the efficiency of the channel network, the cell viability of the cells in fibrin gel was measured according to the distance from the channel. Figure 12.15a displays the bright field image of the cells according to the distance from the channel. Figure 12.15b shows the fluorescent image after the live/dead staining of cells according to the distance from the channel. In the area from the contact with the channel to $750\mu\text{m}$ from the channel, the viability of the cells was approximately 83.7%. In addition, the cell viabilities in the area $750\mu\text{m}$ to $1800\mu\text{m}$ from the channel and in the area $1800\mu\text{m}$ to $4000\mu\text{m}$ from the channel were approximately 68.6% and 52%, respectively. The results are similar to the cell viability of Sample 1 in Fig. 12.14. From the result, it was verified that the channel can supply nutrients by transferring the culture medium to the cells and then can help the cell to keep the living condition.

In the future, construction of the 3D vascular network as a true size of hepatic lobule is planned. In addition, the constructed structure will be cultured for a long time (more than 2 weeks). Finally, the hepatic lobule structure will be constructed in a biocompatible condition.

12.6 Conclusion

In this chapter, a hepatic lobule-like vascular network was successfully constructed in a 3D cellular structure by applying magnetic fields. The use of magnetic tweezers with seven poles made the manipulation of magnetic fibers possible and the fibers

constructed channel networks in a tissue. To construct well-organized vascular network, several aspects were achieved. First, magnetic tweezers were designed based on the 3D simulation results, and then we generated the enough magnetic fields to attract magnetic fibers on the steel rods. Second, we constructed a four-layered hepatic lobule-like vascular network which was fabricated in fibrin gel embedding rat liver cells (RLC-18). Third, the cell viability close to the channel network in 3D cellular structure was analyzed to verify the efficiency of the channel. As a result, the cells close to the channel network show a higher survival rate than the cells far from the channel. The results indicate that the channel network can transfer the nutriment and oxygen to the cells, which causes the cell to maintain a living condition.

Acknowledgments Research supported by Grant-in-Aid Scientific Research (A) (JP16H02322) from the Ministry of Education, Culture, Sports, Science and Technology of Japan.

References

1. Nishida, K., Yamato, M., Hayashida, Y., Watanabe, K., Maeda, N., Watanabe, H., Yamamoto, K., Nagai, S., Kikuchi, A., Tano, Y., & Okano, T. (2004). *Transplantation*. <https://doi.org/10.1097/01.TP.0000110320.45678.30>.
2. Lee, W., Debasitis, J. C., Lee, V. K., Lee, J. H., Fischer, K., Edminster, K., Park, J. K., & Yoo, S. S. (2009). *Biomaterials*. <https://doi.org/10.1016/j.biomaterials.2008.12.009>.
3. Griffith, L. G., & Naughton, G. (2002). *Science*, 80. <https://doi.org/10.1126/science.1069210>.
4. Dunn, J. C. Y., Chan, W. Y., Cristini, V., Kim, J. S., Lowengrub, J., Singh, S., & Wu, B. M. (2006). *Tissue Engineering*. <https://doi.org/10.1089/ten.2006.12.705>.
5. Langer, R. S., & Vacanti, J. P. (1999). *Scientific American*. <https://doi.org/10.1038/scientificamerican0499-86>.
6. Lee, V., Dai, G., Lee, V., & Dai, G. (2014). *Tissue and organ regeneration: Advances in micro- and nanotechnology*.
7. Asakawa, N., Shimizu, T., Tsuda, Y., Sekiya, S., Sasagawa, T., Yamato, M., Fukai, F., & Okano, T. (2010). *Biomaterials*. <https://doi.org/10.1016/j.biomaterials.2010.01.105>.
8. Liu, X., Shi, Q., Wang, H., Sun, T., Yu, N., Huang, Q., & Fukuda, T. (2018). *IEEE/ASME Transactions on Mechatronics*. <https://doi.org/10.1109/TMECH.2018.2796182>.
9. Takeuchi, M., Iriguchi, M., Hattori, M., Kim, E., Ichikawa, A., Hasegawa, Y., Huang, Q., & Fukuda, T. (2020). *Biomedical Materials*. <https://doi.org/10.1088/1748-605X/ab8487>.
10. Miller, J. S., Stevens, K. R., Yang, M. T., Baker, B. M., Nguyen, D. H. T., Cohen, D. M., Toro, E., Chen, A. A., Galie, P. A., Yu, X., Chaturvedi, R., Bhatia, S. N., & Chen, C. S. (2012). *Nature Materials*. <https://doi.org/10.1038/nmat3357>.
11. Bertassoni, L. E., Cecconi, M., Manoharan, V., Nikkhah, M., Hjortnaes, J., Cristino, A. L., Barabaschi, G., Demarchi, D., Dokmeci, M. R., Yang, Y., & Khademhosseini, A. (2014). *Lab on a Chip*. <https://doi.org/10.1039/c4lc00030g>.
12. Lee, V. K., Lanzi, A. M., Ngo, H., Yoo, S. S., Vincent, P. A., & Dai, G. (2014). *Cellular and Molecular Bioengineering*. <https://doi.org/10.1007/s12195-014-0340-0>.
13. Albrecht, D. R., Underhill, G. H., Wassermann, T. B., Sah, R. L., & Bhatia, S. N. (2006). *Nature Methods*. <https://doi.org/10.1038/nmeth873>.
14. Ho, C. T., Lin, R. Z., Chen, R. J., Chin, C. K., Gong, S. E., Chang, H. Y., Peng, H. L., Hsu, L., Yew, T. R., Chang, S. F., & Liu, C. H. (2013). *Lab on a Chip*. <https://doi.org/10.1039/c3lc50402f>.

15. Jeong, G. S., No, D. Y., Lee, J., Yoon, J., Chung, S., & Lee, S. H. (2016). *Nature Communications*. <https://doi.org/10.1038/ncomms11269>.
16. Tsang, V. L., Chen, A. A., Cho, L. M., Jadin, K. D., Sah, R. L., DeLong, S., West, J. L., & Bhatia, S. N. (2007). *The FASEB Journal*. <https://doi.org/10.1096/fj.06-7117com>.
17. Ma, X., Qu, X., Zhu, W., Li, Y. S., Yuan, S., Zhang, H., Liu, J., Wang, P., Lai, C. S. E., Zanella, F., Feng, G. S., Sheikh, F., Chien, S., & Chen, S. (2016). *Proceedings of the National Academy of Sciences of the United States of America*. <https://doi.org/10.1073/pnas.1524510113>.
18. Ma, C., Tian, C., Zhao, L., & Wang, J. (2016). *Lab on a Chip*. <https://doi.org/10.1039/c6lc00540c>.
19. Liu, Z., Takeuchi, M., Nakajima, M., Hu, C., Hasegawa, Y., Huang, Q., & Fukuda, T. (2017). *Acta Biomaterialia*. <https://doi.org/10.1016/j.actbio.2016.12.020>.
20. Cui, J., Wang, H., Shi, Q., Sun, T., Huang, Q., & Fukuda, T. (2019). *Molecules*. <https://doi.org/10.3390/molecules24091762>.
21. Zhang, X., Le, T. A., Hoshier, A. K., & Yoon, J. (2018). *IEEE/ASME Transactions on Mechatronics*. <https://doi.org/10.1109/TMECH.2018.2843820>.
22. Bonakdar, N., Luczak, J., Lautscham, L., Czonstke, M., Koch, T. M., Mainka, A., Jungbauer, T., Goldmann, W. H., Schröder, R., & Fabry, B. (2012). *Biochemical and Biophysical Research Communications*. <https://doi.org/10.1016/j.bbrc.2012.02.083>.
23. Robert, D., Fayol, D., Le Visage, C., Frasca, G., Brulé, S., Ménager, C., Gazeau, F., Letourneur, D., & Wilhelm, C. (2010). *Biomaterials*. <https://doi.org/10.1016/j.biomaterials.2009.11.014>.
24. Hosu, B. G., Jakab, K., Bánki, P., Tóth, F. I., & Forgacs, G. (2003). *The Review of Scientific Instruments*. <https://doi.org/10.1063/1.1599066>.
25. Haber, C., & Wirtz, D. (2000). *The Review of Scientific Instruments*. <https://doi.org/10.1063/1.1326056>.
26. Zhang, Z., Huang, K., & Menq, C. H. (2010). *IEEE/ASME Transactions on Mechatronics*. <https://doi.org/10.1109/TMECH.2009.2032179>.
27. Long, F., Matsuura, D., & Menq, C. H. (2016). *IEEE/ASME Transactions on Mechatronics*. <https://doi.org/10.1109/TMECH.2015.2503274>.
28. Zhang, Z., & Menq, C. H. (2011). *IEEE/ASME Transactions on Mechatronics*. <https://doi.org/10.1109/TMECH.2011.2105500>.
29. Hu, C., Nakajima, M., Yue, T., Takeuchi, M., Seki, M., Huang, Q., & Fukuda, T. (2014). *Microfluidics and Nanofluidics*. <https://doi.org/10.1007/s10404-013-1325-3>.
30. Sun, T., Hu, C., Nakajima, M., Takeuchi, M., Seki, M., Yue, T., Shi, Q., Fukuda, T., & Huang, Q. (2015). *Microfluidics and Nanofluidics*. <https://doi.org/10.1007/s10404-014-1511-y>.
31. Sun, T., Huang, Q., Shi, Q., Wang, H., Hu, C., Li, P., Nakajima, M., & Fukuda, T. (2016). *Journal of Micromechanics and Microengineering*. <https://doi.org/10.1088/0960-1317/26/10/105017>.
32. Sun, T., Huang, Q., Shi, Q., Wang, H., Liu, X., Seki, M., Nakajima, M., & Fukuda, T. (2015). *Microfluidics and Nanofluidics*. <https://doi.org/10.1007/s10404-015-1633-x>.
33. Kuntz, E., Kuntz, H.-D., Kuntz, E., & Kuntz, H.-D. (2002). *Hepatology*.
34. Stenvall, A., Larsson, E., Strand, S. E., & Jönsson, B. A. (2014). *Physics in Medicine and Biology*. <https://doi.org/10.1088/0031-9155/59/13/3353>.

Chapter 13

Biohybrid Microrobots



Federica Iberite, Lorenzo Vannozzi, and Leonardo Ricotti

13.1 Introduction

The development of robots at small scales raises peculiar needs and sets several constraints for the design and the choice of robot components. On this matter, two key aspects must be taken into account. Conventionally, a robot perceives and learns through on-board sensing and computational abilities, so that it can decide an appropriate response (e.g., movement) in given environmental conditions. It must be taken into account that the traditional sensor-actuator-control system paradigm typical of conventional robots must be abandoned at small scales: it is technologically unfeasible first to miniaturize and then to assemble nano-sensors, nano-controllers, and nano-actuators. Instead, programmable physical and chemical properties of microrobots, dynamically interacting with their surrounding world, provided with an intrinsic capability of sensing and adapting to the changes in the environment, can enable robust design routes for making sophisticated systems at the microscale.

The second key aspect concerns scaling issues: at small scales, the relative importance of the physical laws changes considerably. Volumetric quantities such as inertia, weight, heat capacity, and body forces scale as L^3 , while surface quantities such as friction, heat transfer, and surface forces scale as L^2 . Furthermore, intermolecular van der Waals forces scale as $\sim L$, if only the radius of the object scales, or even as $\sim L^{-1}$, if both the object radius and its distance from the target scale [1]. This has a twofold implication: first, the life “at low Reynolds numbers” is very different from the one at the macroscale [2]: as inertia plays an insignificant role at low Reynolds numbers, reciprocal motion does not lead to displacement. Thus, the movement due to the forward component of the motion will be canceled out by the

F. Iberite · L. Vannozzi · L. Ricotti (✉)

The BioRobotics Institute, Scuola Superiore Sant’Anna, Pisa, Italy

Department of Excellence in Robotics & AI, Scuola Superiore Sant’Anna, Pisa, Italy

e-mail: leonardo.ricotti@santannapisa.it

backward component of the motion. Second, traditional actuators (e.g., electromagnetic motors) cannot be reduced much in size without exponentially losing the ability to produce detectable forces and torques. Only piezoelectric motors can be scaled relatively efficiently in the mini-domain (from a few millimeters to a few centimeters), and they just stay at the boundary of the micro-domain (below 1 mm) [3]. Nowadays, some highly miniaturized piezoelectric motors are available, such as the SQUIGGLE ($1.8 \times 1.8 \times 6 \text{ mm}^3$) or the PiezoWave ($14 \times 7.2 \times 4.4 \text{ mm}^3$). Few attempts to overcome the 10^{-2} cm^3 “barrier” have been pursued [4] but with limited success.

Biological systems comply with such physical requirements: microorganisms have evolved elaborated swimming strategies, such as continuous rotation of helical bacterial flagella and nonreciprocal beating of sperm tail and paramecium cilia, which are efficient at low Reynolds numbers. Furthermore, biological cells are intrinsically miniaturized objects, whose diameter ranges from $\sim 1 \mu\text{m}$ (for prokaryotic ones) to $\sim 20 \mu\text{m}$ (for eukaryotic ones) and whose functional elements (proteins, organelles, etc.) have nanometric dimensions. Thus, an intriguing research direction in micro-/nanorobotics deals with harnessing the unique features of biological elements, optimized by millions of years of natural evolution, adapting and interfacing them with artificial technologies toward the development of biohybrid systems [5]. In this chapter, biohybrid robots based on different cell types will be described, highlighting their advantages over other fully synthetic strategies (e.g., based on magnetic, ultrasonic, or light-based locomotion and catalysis) and the challenges related to their harvesting, use, and maintenance. First, biohybrid robots based on bacteria and other single motile cells will be analyzed. Then, multicellular systems based on contractile muscle cells will be described.

13.2 The Biological Motors of Motile Cells

Several prokaryotic microorganisms, as well as several mammalian cells, have the intrinsic capability of moving thanks to extremely efficient biological motors. The biological tool that bacteria typically exploit for their locomotion is the flagellum, which is rotated to generate propulsion [7, 8]. The flagellum is a passive polymeric organelle attached to the cell body via the hook-basal body complex and rotated by the bacterial rotary motor. Such a motor is a “molecular engine” that exerts a torque on the flagella. The torque applied determines a rotation of the flagella, thus resulting in propulsion. Flagella are approximately 20 nm in diameter, consisting of approximately 30 proteins, and their architecture can be divided into the basal body and the exterior hook, the hook-filament junction, and filament structures (Fig. 13.1a). The basal body hosts two proteins (MotA and MotB – 12 copies of each) that form a proton channel through the membrane and constitute the “stator” of the molecular motor. The cytoplasmic part of the basal body is called the C(cytoplasmic)-ring, and it is composed of three proteins (FliM, FliN, and FliG). This structure is essential for transducing chemosensory signals into torque

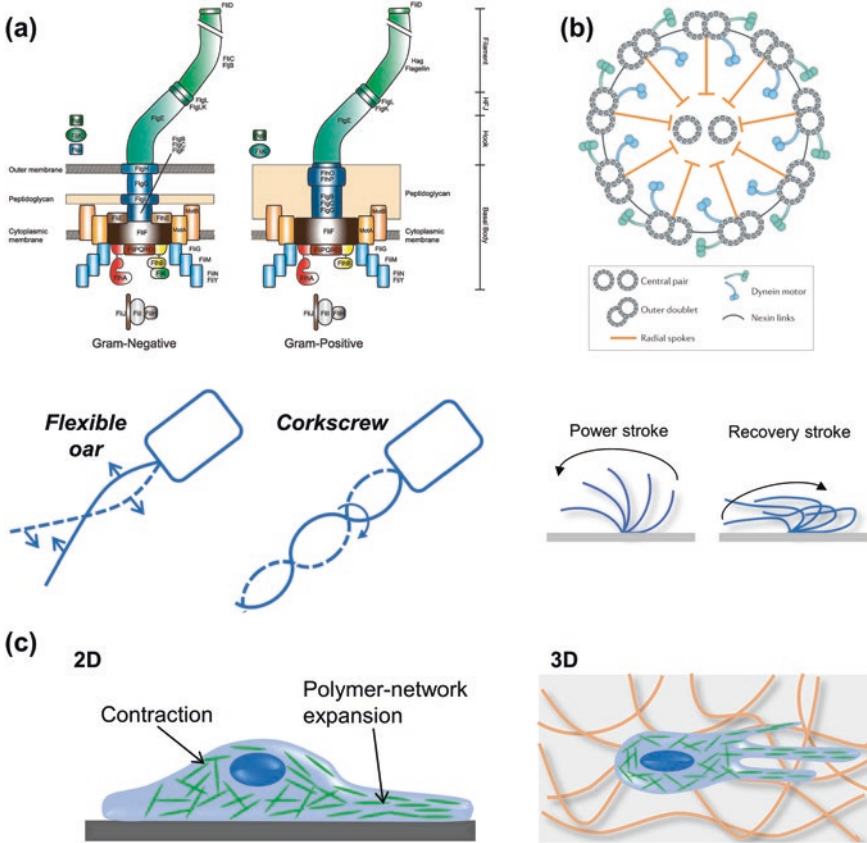


Fig. 13.1 (a) Top, structure of bacteria flagella. Image reproduced from [9]. Copyright: Taylor & Francis; bottom, two possible locomotion strategies of flagellated bacteria. (b) Top, structure of cilia. Image reproduced from [13]. Copyright: Springer Nature; bottom, depiction of the key phases enabling cilia-based locomotion. (c) Examples of ameboid locomotion through cytoskeleton reorganization in 2D and 3D environments, by non-flagellated eukaryotic cells

generation. FliG determines the connection between the C-ring (the rotor) and the stator. The diameter of the C-ring is approximately 40–45 nm. The hook is approximately 55 nm in length and acts as a universal joint, connecting rod and filament. The filament is the largest part of the bacterial flagellum and consists of more than 20,000 copies of the flagellin protein, which assembles in a helical pattern of 11 subunits per turn.

From a biochemistry/bioenergetics viewpoint, the engine powering strategy grounds on the protonmotive force, namely, the proton electrochemical potential across the cell membrane, in contrast to the ATP-hydrolyzing mechanisms of muscle, eukaryotic flagella, or ameboid motility (see next sections). How the protonmotive force is precisely used to provide energy for torque generation is still poorly understood, but it is a fantastic example of natural complexity and efficiency at the

same time. The number and position of the flagella vary across bacterial species: for example, *Monotrichous* bacteria have a single flagellum, while *Peritrichous* bacteria have many flagella randomly distributed over their bodies. Flagella enable flexible oar oscillation or corkscrew-type rotating propulsion.

From an engineering viewpoint, flagella guarantee outstanding performance: the thrust forces produced range from ~ 0.5 pN for *E. coli* and *S. marcescens* to ~ 4 pN for *Magnetospirillum marine coccus* (MC-1), determining high-speed motility (up to more than 100 body lengths per second) [10]. The design of such a molecular motor, relying on a rotor turning 360° stepwise inside a stator, has similarities with its counterpart macroscale electrical motor designed by engineers, except for the material and the energy source. Indeed, flagellated bacteria as self-powered actuators avoid the technical constraints related to the generation and storage of electrical energy, which make miniaturization of self-powered untethered artificial microsystems and microrobots so difficult. The proton flux generating torque for rotating the flagella has been reported to convert chemical into mechanical energy with near 100% efficiency [11], a fantastic achievement enabled by natural evolution.

Besides flagellated bacteria, also other microorganisms (although less frequently) have been explored for building biohybrid devices, such as strains of protozoa and certain strains of algae, which typically generate movements through long appendages extending from the cell body, named cilia. Cilia are featured by a radial pattern consisting of nine outer microtubule doublets that surround two centrally located microtubules (Fig. 13.1b). The ring of microtubule scaffolding is known as the axoneme and measures about 250 nm in diameter. At its base (where it attaches to the cell), the axoneme is attached to cylindrical structures known as basal bodies. The basal bodies measure about 400 nm in length and 200 nm in width. Apart from anchoring cilia in the cytoplasm, basal bodies also play an important role in the assembly of these structures. Similarly to muscle contraction, the movement of cilia is the result of protein filaments sliding. In particular, the dynein proteins on one microtubule slide past each other, while those on the other side do not. This results in the bending of the axoneme, while the switching of this system causes the structure to bend to the other side. The repetition of this mechanism causes cilia motility.

From a biochemistry/bioenergetics viewpoint, the attachment and release of dynein arms to adjacent microtubules is caused by the binding or hydrolysis of ATP.

From an engineering viewpoint, this mechanism is also very effective and allows cilia, which are essentially short flagella, to beat back (recovery stroke) and forth (effective stroke) at different rates transcribing what is known as a “polarized” beat. Cilia can be up to ~ 27 μm long (in *S. polymorphus*) and beat at a frequency of up to ~ 60 Hz [12]. Nowadays, experiments and models are starting to elucidate the inner workings of single cilia, which behave as complex nonlinear oscillators, enabling a variety of hydrodynamical phenomena resulting from beating dynamics [13].

Some eukaryotic cells (such as sperm cells or green microalga) are also provided with flagella that guarantee their motility, similarly to bacteria. However, the structure and the bioenergetics featuring eukaryotic flagella are similar to the cilia ones, shown in Fig. 13.1b. Indeed, they are grounded on the typical “9 + 2” architecture,

highly conserved across different eukaryotes, and are powered by binding or hydrolysis of ATP.

Non-flagellated eukaryotic cells also have the capability to move, but through a considerably different mechanism, based on cytoskeleton reorganization. This capability is called “ameboid locomotion” and consists of crawling on 2D surfaces or even navigating through 3D porous environments, such as the surrounding extracellular matrix (Fig. 13.1c). Such locomotion is enabled by large deformations of the compliant cell body and does not require specialized appendages, but rather an assembly and de-assembly of intracellular F-actin fibers [14].

13.3 Robots Based on Bacteria

As described in the previous section, bacteria have the intrinsic capability of moving thanks to extremely efficient biological motors. Often, such a capability is integrated with a series of chemico-physical sensors (mostly based on specialized proteins on the cell membrane). Such sensors provide the cells with the so-called *taxis* response, namely, the ability to move toward a specific environmental stimulus autonomously: chemical gradients in the case of chemotaxis, magnetic fields in the case of magnetotaxis, electric fields in the case of galvanotaxis, light in the case of phototaxis, temperature in the case of thermotaxis, and oxygen concentration in the case of aerotaxis. These features are exciting when the development of microscale robots is targeted. Thus, these cells are being the object of several efforts in the state-of-the-art.

The first example of biohybrid robot based on bacteria was proposed in 2004: *Serratia marcescens*, a peritrichously flagellated rod-shaped gram-negative bacterium, was used as an active cargo delivery agent for potential operations at the micron scale [6]. In the following years, many other studies focused on other bacterial cells as possible active components to bring a therapeutic molecule in the desired area (thus targeting drug delivery medical applications) or to carry out lab-on-a-chip micromanipulation or environmental monitoring applications. In the following sections, some of the most relevant examples of this technology will be described.

13.3.1 Bacterial Robots Based on Chemotaxis

Chemotaxis alone does not allow full control of biohybrid microrobots, but it is a form of environmental sensing that can determine the autonomous steering of the robot toward preprogrammed target stimuli. The signaling pathway that is involved in chemotaxis is one of the most well-understood physiological processes in biology [15]. The pathway is grounded on chemoreceptors, the histidine protein kinase chemotaxis protein (Che)A and two diffusible response regulators (CheY and

CheB). CheY controls flagellar motor switching, whereas CheB controls chemoreceptor adaptation (Fig. 13.2a). Thanks to this biomolecular architecture, together with other components that might be expressed under particular environmental conditions (thus allowing bacteria to tune their responses to a specific environment), these cells can respond to a change of just a few molecules of the target compound over background concentrations that can vary over five orders of magnitude.

In 2007, Akin et al. demonstrated that *Listeria monocytogenes* could be used to favor the delivery of nanoparticles and nucleic acid-based model drugs into cells, both in vitro and in vivo [16]. In 2008, Behkam and Sitti used *Serratia marcescens* conjugated to polystyrene microbeads and investigated the effect of quantity and configuration of the attached bacteria on the propulsion speed [17] experimentally. In 2011, Fernandes et al. proposed a robot based on *Escherichia coli*, selectively attached to a submicrometer-scale cargo through a two-antibody-based method, enabling a release of the cargo on-demand, thanks to not harmful chemicals [18]. In the mentioned studies, the chemotaxis ability of bacteria was not exploited but was claimed as a possible feature to be exploited in the future. Similar studies were proposed in that period, focusing on *Vibrio alginolyticus* [19], *Salmonella typhimurium* [20], and *Serratia marcescens* [21–23], without really exploiting bacterial chemosensors for targeting applications.

In 2013, “bacteriobots” were proposed by Park and colleagues: these biohybrid systems were based on attenuated *Salmonella typhimurium* adhered to polystyrene microbeads and were used to target solid tumors [24]. The bacteria strain used was featured by high motility (thanks to flagellar motors), and the bacteria were engineered to display biotin in their outer membrane proteins; this allowed to firmly attach rhodamine-containing fluorescent polystyrene microbeads to them by exploiting the high-affinity interaction between biotin and streptavidin (Fig. 13.2b, top images). The fluorophores were used by the authors to obtain a near-infrared fluorescence image for tracking purposes. *Salmonella typhimurium* alone, as well as the bacteriobots based on such a strain, showed significantly greater motility toward tumor cell lysates or spheroids than toward normal cell lysates or spheroids. This chemotaxis was an intrinsic feature of the bacterial strain used and enabled the biohybrid system to have an intrinsic and embedded microsensing ability toward tumoral environments. The bacteriobots were injected systemically into CT-26 tumor-bearing mice via tail veins, and through both fluorescence readings and histological immunofluorescence, the authors demonstrated successful tumor-targeting ability (Fig. 13.2b, bottom images).

In 2016, Nguyen et al. developed microrobots propelled by attenuated *Salmonella typhimurium* and provided with paclitaxel-encapsulated liposomes. Bacterial microrobots carrying drug-loaded liposomes showed a better tumor-killing ability compared to the bare liposomes, which were passively distributed due to Brownian motion. The chemotaxis of bacterial microrobots toward cancer cells was also assessed through a coculture system containing healthy and tumor cells [25].

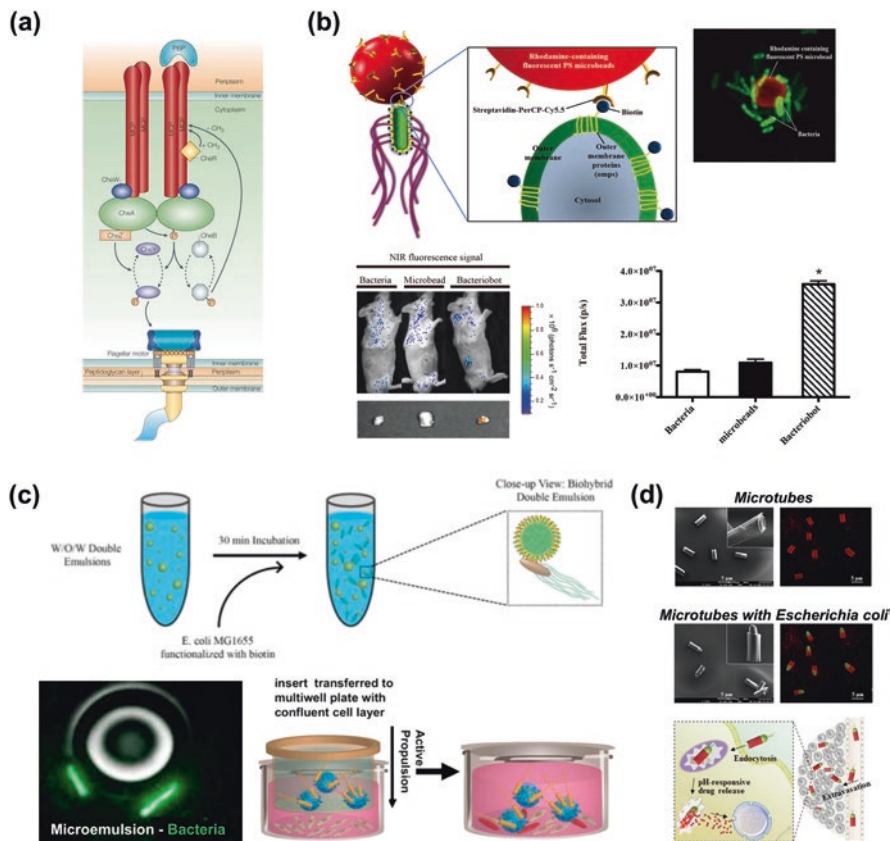


Fig. 13.2 Biological mechanism of bacterial chemotaxis and examples of bacteria-based chemotactic microrobots. **(a)** Chemosensory system of *Escherichia coli*. MCPs = methyl-accepting chemotaxis proteins (the chemoreceptors of the cell); PBP = periplasmic binding protein (a molecule activating the cell chemotactic response); CheW, CheA, CheR, CheZ = monomeric and dimeric proteins supporting and regulating the activity of MCPs and the transmission of the information to CheY and CheB; CheY = response regulator protein that, once phosphorylated, binds to the flagellar motor determining a change in direction; CheB = response regulator protein that, once phosphorylated, helps “resetting” the signaling state of the receptors, allowing them to adapt to the present concentration of attractant and to sense subsequent changes; P = phosphoryl group. Reproduced from [15]. Copyright: Springer Nature. **(b)** Bacteriobot based on *Salmonella typhimurium*, exploiting the chemotactic ability of this bacterium to target solid tumors and to favor the accumulation of the biohybrid robots at the tumor site. Images reproduced from [24]. Copyright: Springer Nature. **(c)** Biohybrid microsimmers based on *Escherichia coli*, attached to microemulsions, able to embed fluorescent dyes or therapeutic molecules: in vitro experiments using a Transwell membrane highlighted the ability of biohybrid robots to reach the target cells, steered by a glucose gradient. Images reproduced from [26]. Copyright: American Chemical Society. **(d)** Microrockets embedding doxorubicin and propelled by *Escherichia coli*, featured by high motility and ability to extravasate into tumor tissues. Images adapted from [29]. Copyright: Elsevier

Another interesting example of a chemotactic biohybrid microrobot was proposed in 2017 by the group of Prof. Sitti [26]. Here, biohybrid systems based on biotin-conjugated *Escherichia coli* attached to an outer oil shell functionalized with streptavidin were proposed (Fig. 13.2c, top images). The use of such microemulsions provided many advantages, such as soft and viscoelastic properties allowing better interaction with tissue cell membranes, the ability to encapsulate a wide range of hydrophilic and hydrophobic cargos and protect their payload against harsh environments, and the possibility for the free diffusion of the cargo at oil–water interface into the tissue cells. Researchers created a concentration gradient of glucose across a Transwell membrane, in vitro. Similar gradients are naturally present in the body: tumor environments possess higher local glucose and a lower oxygen concentration, with respect to normal tissues. They verified that the microswimmers actively swam through the Transwell's bottom membrane (pore size: 8 μm) and reached the cells at the bottom plate, guided and steered by the glucose gradient (Fig. 13.2c, bottom images). When fluorescent dyes were encapsulated in microemulsions, experiments showed the ability of microswimmers to efficiently deliver such dyes to the target cells, thus opening avenues for the possible delivery in vivo of therapeutic molecules such as drugs, imaging agents, siRNAs, etc.

In the same year, Mostaghaci et al. proposed a bacterial microrobot (based on *Escherichia coli*) that was able to attach to epithelial cells (expressing mannose on the membrane) thanks to a mannose–lectin interaction. This system was proposed for gastrointestinal and urinary delivery of therapeutics [27].

Still in 2017, Xie et al. directly attached drug molecules onto a probiotic bacterial species, *E. coli* Nissle 1917, via acid-labile linkers of cis-aconitic anhydride [28]. The resulting bacterial microrobots swam at a speed of 9 $\mu\text{m/s}$ and were able to accumulate the drug in the target tumor environment efficiently (12.9%, 3 h after intravenous injection), a value that is much higher than the one featuring the commonly used bare nanocarriers.

In 2020, Xie and colleagues proposed *Escherichia coli*-propelled microrockets [29]. Microtubes developed via layer-by-layer deposition of oxidized alginate and chitosan in sacrificial porous membranes were loaded with doxorubicin (DOX). A concentration gradient of L-aspartate as the chemoattractant was used to embed *Escherichia coli* into the microtubes. Bacterial chemotaxis was thus exploited in the fabrication process to build the assembled microrockets, which exhibited high motion velocities in both water and viscous media. After intravenous injection of bacteria-propelled microrockets, the DOX levels in mice tumors reach 6.1-fold higher than those of the bare microtubes, without bacteria embedded after 7 days, suggesting that the assembled structure promoted the extravasation from blood circulation and the retention in tumors (Fig. 13.2d).

13.3.2 *Bacterial Robots Based on Magnetotaxis or Embedding Paramagnetic Elements*

As highlighted by the numerous examples described in the previous section, the potential of bacterial strains as tumor-targeting vectors is high. However, relying only on chemotaxis implies adopting a sort of “nonrobotic” strategy in which the microswimmer can be directed to conduct a biased random walk. This can improve drug targeting with respect to passive nanocarriers, but remains rather far from being optimal. Besides, this drug delivery is normally systemic, raising issues of systemic toxicity and therapeutic index reduction (see Sect. 2.3). Such drawbacks can be mitigated through non-systemic delivery and robotic control approaches, e.g., with the use of magnetic field-based steering followed by a taxis. Responsivity to the magnetic field (and thus controllability) can be enabled in two ways: (1) using bacteria naturally showing a magnetotaxis and (2) providing the bacteria or the cargo they are attached to with magnetically responsive elements.

One of the first examples of the former case was the study of Felfoul et al. in 2011 [30]. Here the authors used *Magnetococcus* sp. (MC-1), a magnetotactic bacterial species, and navigated these vectors toward regions located inside a solid tumor using a computer-controlled set of magnetic coils. By the way, this bacterium type shows a speed of 200 $\mu\text{m/s}$ in human blood, resulting much faster than one species, e.g., the *S. marcescens*, which has a mean speed of 26 $\mu\text{m/s}$. The magnetotactic behavior of this species, similarly to other magnetotactic ones, is guaranteed by a chain of magnetosomes (organelles containing magnetic crystals) that is present in the cell, which respond to a directional magnetic field as low as the geomagnetic field. These organelles probably aid these organisms to reach regions with optimal oxygen concentrations, but can be actually exploited to force their alignment and to steer them toward the desired target, by applying an appropriate magnetic field. Over the last decades, many other examples of the use of magnetotactic bacteria for controlled locomotion have been reported, primarily by the group of Prof. Martel [31–34] (Fig. 13.3a).

Many examples of magnetically responsive elements attached to bacteria have also been proposed in recent years. Park et al. developed a microswimmer for targeted active drug delivery, where *Escherichia coli* was attached to the surface of drug-loaded polyelectrolyte multilayer microparticles with embedded magnetic nanoparticles, made of Fe_3O_4 (Fig. 13.3b). The microswimmer showed chemotactic ability toward tumor tissues, but it could also be steered remotely using external magnetic fields [35].

In another recent study, Alapan and colleagues developed bacterial microrobots exploiting red blood cells as cargos, attached to bioengineered bacteria (*E. coli* MG1655), used as actuators. The red blood cells were loaded with anticancer doxorubicin drug molecules and superparamagnetic iron oxide nanoparticles (SPIONs), which make the system responsive to external magnetic fields and thus steerable [36]. Doxorubicin release from the cargos was demonstrated at different pH conditions, as well as active deformation of the cargo when the bacteria’s own propulsive

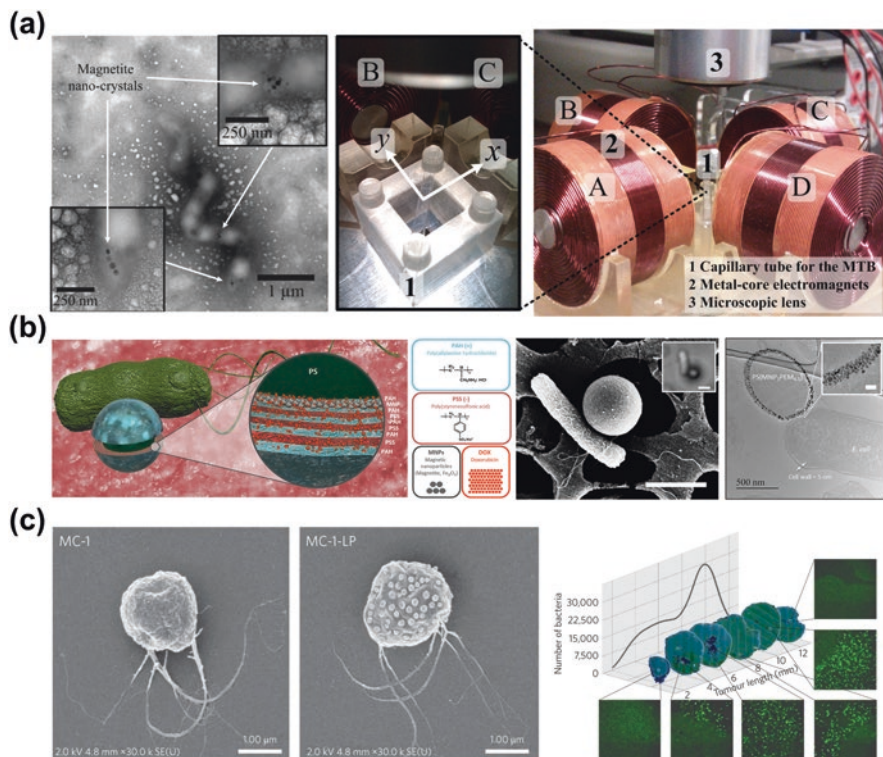


Fig. 13.3 Examples of biohybrid microrobots steered by magnetic fields. **(a)** Left: scanning electron microscope images of the magnetotactic bacterium *Magnetospirillum magnetotacticum* MS-1 and its chain of magnetite nanocrystals; right: manipulation system for the characterization and the closed-loop control of the magnetotactic bacterium. A, B, C, and D = metal-core electromagnets; 1 = manipulation arena; 2 = electromagnetic control system; 3 = microscopic vision system. Images reproduced from [33]. Copyright: SAGE Publications, Inc. **(b)** Artistic depiction (left) and scanning electron microscope/transmission electron microscope images (right) of *Escherichia coli* attached to a polystyrene (PS) microparticle, embedding magnetic nanoparticles in its external layer. PAH positively charged poly(allylamine hydrochloride), PSS negatively charged poly(sodium 4-styrenesulfonate), MNPs magnetic nanoparticles made of Fe_3O_4 , DOX doxorubicin. Images adapted from [35]. Copyright: American Chemical Society. **(c)** Left: scanning electron microscope images of MC-1 with and without liposomes (diameter, ~ 170 nm) attached to its surface; right: distribution of the loaded MC-1 cells throughout the tumor volume, showing a good accumulation in the internal regions. Images adapted from [41]. Copyright: Springer Nature

force drove the system through narrow pillars. This ability suggested the possibility to navigate effectively into narrow capillaries of the human body. Furthermore, a termination switch was integrated into the biohybrid system, to kill bacteria once the drug molecules were delivered to the site of action, thus reducing the risk of infections and toxicity.

Artificial magnetic elements to be embedded in microrobots to enhance their controllability are normally paramagnetic or superparamagnetic ones (similarly to the natural crystals available in magnetotactic bacteria, which show a paramagnetic behavior). Indeed, the ability of magnetic crystals to align with an imposed magnetic field can create a temporary magnetization of the robot that can be exploited for steering. Using ferromagnetic materials featured by a permanent magnetization could actually increase the magnetic link between external magnets and internal micro-objects but would also imply aggregation risks.

13.3.3 Other Taxis Abilities and Multifunctional Robots

Chemotaxis and magnetotaxis (or magnetic steerability enabled by embedded particles) have been often exploited in synergy, as highlighted in some examples reported in the previous section. However, different taxis abilities can also be exploited, alone or in synergy among them. Electric fields can steer bacteria in the case of galvanotaxis [37], light in the case of phototaxis [38], temperature in the case of thermotaxis [39], and oxygen concentration in the case of aerotaxis [40].

A great example of synergy between different taxis abilities was demonstrated in 2016 by Felfoul et al. The authors developed a biohybrid robot based on a magnetotactic bacterium (*Magnetococcus marinus* MC-1), loaded with liposomes containing an anticancer drug [41]. The system showed responsiveness to magnetic fields, but the microorganism used also showed aerotactic properties. A three-dimensional targeting magnetic field, slightly higher than the geomagnetic one, was used to induce a directional torque on the chain of bacterial magnetosomes in order to penetrate the tumor from the peritumoral regions. Then, the bacterium progressed autonomously, exploiting its aerotaxis to penetrate the hypoxic regions of the tumor, which typically occupy the core of the cancer tissue. The aerotaxis-based self-steering, together with remote magnetic steering, allowed a very efficient targeting of colorectal xenografts in mice, also in the internal regions that are usually not effectively targeted by traditional drugs and nanovectors (Fig. 13.3c).

In 2020, chemotaxis and phototaxis were combined in a system based on *E. coli* and micro cargo particles with the proteins PhyB and PIF6, binding to each other under red light and dissociating from each other under far-red light [42]. This strategy allowed the chemotactic bacteria to adhere and transport the cargo under red light and to release it on-demand upon far-red light illumination, adding a degree of freedom to the system. Other synergies among the mentioned bacterial abilities are under exploration in the scientific community and will hopefully bring significant steps ahead, especially in the field of cancer therapy (see Sect. 13.5).

13.4 Microrobots Based on Other Motile Cells

13.4.1 Robots Based on Non-bacterial Flagellated Cells

Besides bacteria, other flagellated motile cells can be found in nature and exploited as microswimmers for medical and non-medical applications.

Sperm cells are featured by high motility, thanks to their flagellum. They have been claimed as possible means to improve drug transfer to the target cells, thanks to their somatic cell-fusion ability [43]. In addition, the sperm membranes are also able to protect drugs from opsonization phenomena and consequent removal from the blood circulation. Sperms have been effectively used as carriers encapsulating Fe_3O_4 nanoparticles, providing them with magnetic steering ability in 2008 [43] and later, in 2014, with unilamellar lipid vesicles, for delivery into mouse oocytes [44]. In 2018, a sperm-driven microrobot was used for active drug delivery toward cervical cancer cells in vitro [45]. Here the authors loaded the cell with doxorubicin hydrochloride and guided it magnetically to an in vitro cultured tumor spheroid. They also designed the system to release the sperm cell from the structure in which it was embedded (showing a tetrapod-like shape) when the biohybrid micromotor hit the tumor walls, allowing it to swim into the tumor, activate membrane fusion, and deliver the drug in an effective way (Fig. 13.4a). Dr. Magdanz and colleagues proposed other studies in recent years, focused on sperm cells for biomedical applications (cancer therapy, but also in vitro fertilization), progressively evolving the features and performance of these biohybrid systems. One of the last examples of these efforts is the so-called IRONSperm, developed through electrostatic self-assembly of non-motile sperm cells and magnetic nanoparticles [46], featured by a swimming speed exceeding 0.2 body lengths ($6.8 \pm 4.1 \mu\text{m/s}$) at an actuation frequency of 8 Hz and precision angle of 45° . The incorporation of magnetite nanoparticles onto the cell surface enabled a distributed actuation by a rotating magnetic field while maintaining the flexibility of the swimmer. Furthermore, they also increased the acoustic impedance of the sperm cells, thus enabling the localization of microrobot clusters using ultrasound feedback. Overall, the authors claimed this solution as a biocompatible, controllable, and detectable biohybrid tool for in vivo targeted therapy.

The helical-shaped microalga *Spirulina platensis* is another flagellated eukaryotic cell that has been exploited to build biohybrid microswimmers. In 2015, Yan et al. coated these microorganisms with magnetite suspensions to enable their steering under a magnetic field [47]. In a recent evolution of this study, MRI was exploited to track in real-time a swarm of microswimmers based on the same microorganism inside a rodent stomach. The authors also demonstrated the ability of the microrobot to release overtime C-phycoerythrin, an abundant compound in *Spirulina* that was released upon degradation of the microalga and which showed cytotoxic effects on cancer cells [48] (Fig. 13.4b).

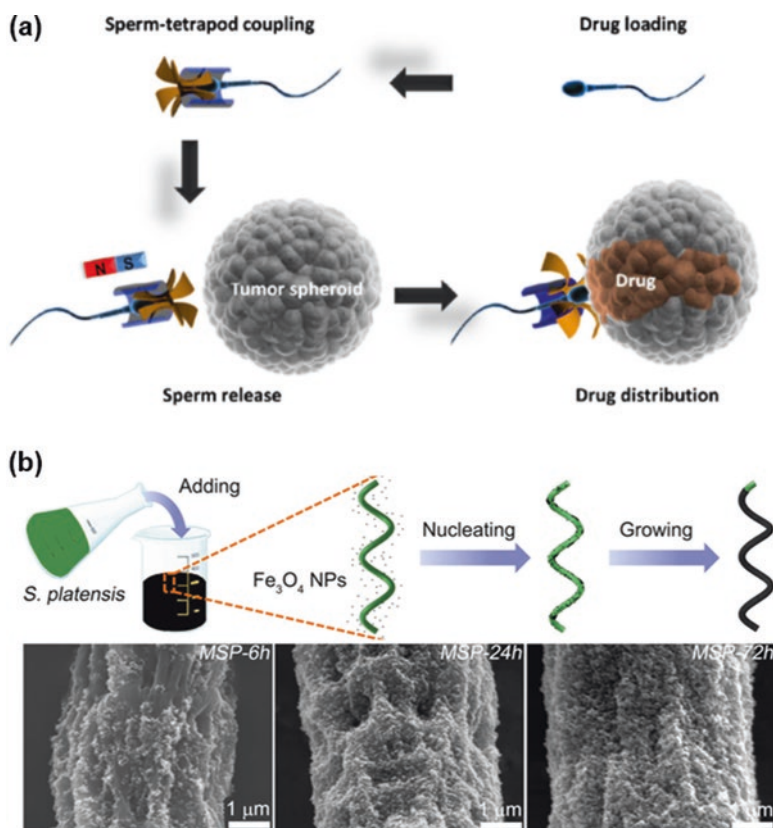


Fig. 13.4 Biohybrid microrobots based on sperm cells. (a) Depiction of the therapeutic strategy envisaged for a sperm-driven microrobot embedding doxorubicin and targeting a tumor spheroid, in vitro. Image reproduced from [45]. Copyright: American Chemical Society. (b) Dip-coating process to provide *S. platensis* with Fe_3O_4 nanoparticles and scanning electron microscope images of the microorganism subjected to 6, 24 and 72 h dip-coating treatment, respectively. As the dipping time increases, the amount of Fe_3O_4 nanoparticles, and thus the thickness of the Fe_3O_4 coating on the *S. platensis*, also increases. Image reproduced from [48]. Copyright: AAAS

13.4.2 Robots Based on Non-flagellated Cells

Eukaryotic non-flagellated cells move through the mechanisms described in Sect. 13.2 and depicted in Fig. 13.1. Among the cell types exploited in microrobotics, it is worth mentioning red blood cells and leukocytes.

Red blood cells are the most common type of blood cell and the vertebrate's principal means of delivering oxygen (O_2) to the body tissues. They are biconcave disk-shaped cells having a cytoplasm rich in hemoglobin (the iron-containing molecule able to bind oxygen) and without a nucleus, to maximize their cargo. Their membrane is composed of a peculiar combination of proteins and lipids that guarantees deformability and stability while passing through the capillary network (they

can repeatedly deform through capillaries that are half of their diameter). Their average lifetime in circulation is 120 days. These properties, together with the possibility to efficiently harvest the patient's cells, thus avoiding any rejection risk, have attracted interest in turning them into mobile microrobots.

In 2014, Wu and colleagues demonstrated the possibility to turn red blood cells in steerable carriers by loading them with iron oxide nanoparticles. The asymmetric nanoparticle distribution within the cell resulted in a net magnetization, enabling magnetic alignment and guidance under acoustic propulsion [49]. The authors reported a method for including the nanoparticles in the cell cytoplasm, based on a hypotonic dilution (Fig. 13.5a): immersing cells in a hypotonic lysing buffer, they underwent a hypotonic hemolysis process. Such a process created an influx of fluid, which in turn created pores in the red blood cell membrane with a diameter of ~ 100 nm. These nanopores allowed for inward diffusion of the magnetic nanoparticles from the surrounding medium into the cell, allowing at the same time the outward diffusion of the intracellular hemoglobin protein. After 1 h incubation at low temperature to reach equilibrium, the solution reached isotonicity, and the cell

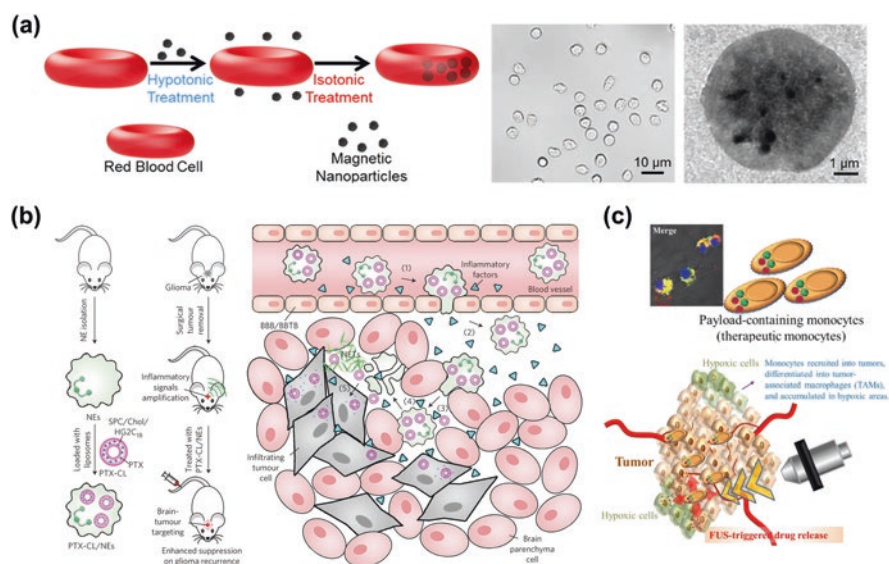


Fig. 13.5 Microrobots based on red blood cells and leukocytes. (a) Left: scheme of the hypotonic lysis process allowing encapsulation of iron oxide nanoparticles within red blood cells; right: optical and SEM images of the nanoparticle-loaded erythrocyte-based biohybrid robots. Images reproduced from [49]. Copyright: American Chemical Society. (b) Example of neutrophil-based biohybrid microrobot: the cells were encapsulated with paclitaxel-loaded liposomes and then injected intravenously. Cell chemotaxis was exploited to deliver the therapeutic cargo at the tumor site. *NE* neutrophils, *PTX* paclitaxel, *CL* cationic liposomes, *SPC* soy phosphatidylcholine, *Chol* cholesterol, *HG2C₁₈* 1,5-dioctadecyl-N-histidyl-L-glutamate, *NETs* neutrophil extracellular traps. Images reproduced from [55]. Copyright: Springer Nature. (c) Scheme of monocytes with embedded echogenic polymeric bubbles and drug release in the hypoxic regions of the tumor after focused ultrasound (FUS) triggering. Images adapted from [63]. Copyright: Elsevier

membrane was resealed by the restoration of osmolarity. This method has been extensively used in many studies for promoting the encapsulation of functional nanoparticles or therapeutic molecules into these cells.

In other studies, in addition to magnetic nanoparticles, also drug molecules or quantum dots were encapsulated for therapeutic and imaging applications [50]. The active release of drugs was demonstrated in 2015 by Sun et al., promoting remote heating of red blood cells using photosensitizers and triggering this phenomenon using near-infrared light [51]: light-induced photothermal heating determined cell membrane destruction and consequent drug release, on-demand. The surface of cells was also modified with a targeting peptide to allow cancer cell targeting. This biohybrid system resulted promising, enabling a possible combined photothermal-chemotherapy against cancer.

Another interesting approach was proposed by the group of Dr. Cinti [52, 53]: in this case, the therapeutic molecule (a monoclonal antibody) and superparamagnetic nanoparticles were embedded in the cell through a hypotonic treatment similar to the one shown in Fig. 13.5a. However, the drug release mechanism was not based on an external physical trigger, but on a cell-embedded biotechnological tool: the erythrocytes were engineered to present on their membrane a fusogenic protein, the filamentous hemagglutinin, which is a functional element of certain viruses and that promotes membrane fusion with the target cell, facilitating the release of entrapped material (nanoparticles and drug) to the target area. The magnetic properties of the vectors were exploited to accumulate them at the target through a static magnetic field and then relying on such a biotechnological modification for executing the drug release task in a “virus-like” fashion.

Leukocytes are the backbone of the innate and adaptive immune system. Their physiological concentration in the blood is from 4000 to 11,000 cells per μL of blood. They can be distinguished in neutrophils (54–62%), eosinophils (1–6%), basophils (< 1%), lymphocytes (28–33%), and monocytes (2–10%), in addition to a smaller number of macrophages and dendritic cells. Their diameter ranges from 7 to 8 μm of lymphocytes to $\sim 21 \mu\text{m}$ of macrophages. One of their more intriguing features is the ability to cross biological barriers actively, e.g., the tissue endothelium and the blood-brain barrier, once activated by local chemotactic factors, with the aim of fighting infections, inflammation, tumor growth, and other non-physiological conditions. This “directed migration” is based on cell chemotaxis. Due to this unique feature, they have been claimed as possible high-potential drug delivery systems, able to bring therapeutic molecules into otherwise inaccessible or difficult-to-access body parts [54].

Neutrophils are the “first line” of defense cells: they are rapidly recruited (within minutes) in an infection site, and they migrate to tumor sites upon chemokine release. Xue et al. exploited this property and developed a neutrophil-based therapeutic microrobot [55]. The system was based on mice neutrophils, provided with paclitaxel-loaded liposomes, aimed to suppress postoperative glioma recurrence. After intravenous administration, the neutrophils were primed by the chemoattractants and migrated along the chemotactic gradient toward the infiltrating tumor cells in the inflamed brain. The activating signals determined the release of neutrophil

extracellular traps and the concomitant release of paclitaxel (Fig. 13.5b). The drug was thus efficiently delivered into the tumor cells and induced cytotoxicity, thus inhibiting tumor recurrence. Remarkably, the toxic cargo did not affect the physiological properties of the neutrophils.

Other studies exploited neutrophils to deliver albumin nanoparticles to the lungs against lipopolysaccharide-induced acute inflammation and infection by *Pseudomonas aeruginosa* [56], to deliver drug-loaded mesoporous silica nanoparticles coated with a bacterial membrane (favoring the internalization by the neutrophils), exploiting in vitro chemotaxis with improved migration speed toward *Escherichia coli* [57].

Monocytes are the “second responders” of the immune system: they typically migrate to the region of inflammation within 12 h. They usually are highly recruited in necrotic and tumor hypoxic regions. Thus, they can be effectively used for the delivery of therapeutics into deep tumor microenvironments. Choi et al. utilized embedded gold nanoshells in macrophages and exploited cell chemotaxis and phagocytosis to deliver them into the hypoxic regions of tumor tissues. Once delivered, the nanoshells promoted tumor cell death through near-infrared irradiation [58]. Among the different approaches involving monocytes/macrophages, it is worth mentioning peptide-modified carbon nanotubes selectively engulfed by the cells, to enhance their accumulation into tumors [59] and hybrid devices with doxorubicin-containing liposomes attached to the cell surface as a backpack and enable sustained delivery in vitro [60]. A magnetic targeting approach was also proposed for biohybrid vectors based on this cell type: macrophages loaded with magnetic nanoparticles and an anticancer drug were effectively manipulated by magnetic intervention and directed to the tumor region [61]. Magnetic properties were also exploited by Nguyen and colleagues, who engineered macrophages engulfed with anticancer and magnetic liposomes. The authors demonstrated the possibility to control the system by electromagnetic fields, navigating it through blood vessels. The biohybrid robot proposed in this work was able to cross the blood barriers and infiltrate to tumors using macrophage’s chemotaxis. Once released from liposomes, the drug was finally able to simultaneously kill macrophages and tumor cells [62].

Similarly to other drug delivery systems, the possibility to selectively activate on-demand the release of therapeutics by an external user would dramatically increase the efficacy of the paradigm and, overall, the therapeutic index (TI). This attempt was pursued by some authors in recent years, who added a degree of freedom to these systems, through a triggering strategy. Huang et al. reported biohybrid robots based on monocytes/macrophages and provided with a drug release triggering mechanism grounded on echogenic polymeric bubbles (embedded in the cells, via phagocytosis) and used to create inertial cavitation through focused ultrasound, thus triggering the release of doxorubicin, also encapsulated in the cell body [63] (Fig. 13.5c).

T lymphocytes have also been proposed for the development of biohybrid robots: Stephan et al. showed a stable conjugation of lipidic/polymeric nanoparticles to the surface of a T-cell surface, demonstrating a good accumulation performance of such

nanoparticle-decorated cells into the tumor microenvironment, by transmigrating the endothelial barrier in tumor-bearing mice [64]. The group of Prof. Irvine also developed a system based on nanocapsules covalently conjugated to the membranes of autologous T-cells and demonstrated that, by reinfusing them into tumor-bearing mice, effective drug delivery at the target site was achieved by extravasation into lymphoma-infiltrated organs [65].

13.5 Challenges and Perspectives of Robots Based on Bacteria and Other Motile Cells

As it emerges from the previous sections, biohybrid robots falling into this category are featured by small dimensions (typically 1–3 μm in the case of bacteria and other microorganisms and 10–20 μm in the case of mammalian cells, which have anyhow flexible and adaptable/squeezable bodies). This makes them compatible with the dimensions of human capillary networks and interstitial spaces, thus encouraging the application of these robots in the vascular network as drug delivery systems [5, 10, 31]. Table 13.1 summarizes some ongoing clinical trials, at present, involving bacterial agents for cancer therapy.

This preferential application raises the need for carefully considering the concept of the TI. Indeed, similarly to machines whose efficiency can be expressed as the ratio between the power produced as the output over the power used as the input, the efficiency of a therapeutic agent can be computed as follows:

$$\text{TI} = \frac{\text{TD}_{50}}{\text{ED}_{50}} \quad (13.1)$$

where TD_{50} is the drug dose producing undesired toxicity in 50% of the population and ED_{50} is the minimum drug dose that is effective for the desired therapy for 50% of the population [67]. Bacteria and other living cells, especially if controlled by exploiting a combination of taxis abilities, can considerably increase the TI, mostly guaranteeing a better targeting (a high number of functional systems hits the cancer cells, while a low number results off-target). However, the intrinsic safety of the carrier and its final fate must also be considered: indeed, if it is highly toxic, it lowers the TD_{50} value. The efficacy of therapies, including the ones based on biohybrid robots, depends on this trade-off.

Despite exciting results, there are still many open challenges, such as motility performance, control, and immunogenicity of the biological segment of the microswimmers, which should be overcome before their successful transition to the clinic.

To address immunogenicity (especially of bacteria), many efforts are ongoing. Researchers are looking for as many inert as possible microorganism strains; other ones aim to “mask” foreign bodies with molecules derived from patient’s cells. For example, Buss et al. recently proposed biohybrid microrobots propelled by a

Table 13.1 Ongoing clinical trials assessing the safety and therapeutic efficacy of bacteria-based systems for cancer therapy. Adapted from [66]

Bacterium type	Drugs or genes delivered	Tumor model	Phase	Observation	NCT number
<i>Salmonella typhimurium</i> (VNP20009)	HSV-TK gene	B16F10 melanomas	I	Dose-dependent suppression of tumor growth and prolonged survival	NCT00004988
<i>Listeria monocytogenes</i> (JNJ-64041809)	JNJ-64041809	CT26 colon tumor, prostate cancer	I	Breaking of self-tolerance and prolonged survival	NCT02625857
<i>Clostridium novyi-NT</i>	<i>Clostridium novyi-NT</i> spores	Solid tumor	I	Reduced tumor size	NCT01924689
<i>Salmonella typhimurium</i> (VNP20009)	VNP20009	Metastatic melanoma, metastatic renal cell carcinoma	I	VNP20009 induced a dose-related increase in the circulation of proinflammatory cytokines, such as interleukin (IL)-1 β , tumor necrosis factor-alpha, IL-6, and IL-12	NCT00006254
<i>Salmonella typhimurium</i> γ 4550.	IL-2	Hepatoma, liver neoplasms	I	Consistent reduction in the mean number of hepatic metastases in animals fed γ 4550 (pIL-2)	NCT01099631
<i>Listeria monocytogenes</i> (CRS-207)	GVAX+ CRS-207	Metastatic pancreatic cancer	II	Extended survival for patients with pancreatic cancer, with minimal toxicity	NCT01417000

genetically engineered peritrichously flagellated *Escherichia coli* species, integrated with red blood cell-derived nanoliposomes, called nanoerythroosomes, by using non-covalent streptavidin interaction [68]. The interaction of microrobots with immune cells is a hot topic, which is being extensively investigated also on entirely artificial counterparts [69, 70].

Concerning control, besides chemotaxis, which is interesting but it only allows a partial controllability degree, electric steering, obtained through galvanotaxis or electrophoresis, is currently rather limited to lab-on-a-chip applications and other *in vitro* scenarios. Optical control methods, enabled, for example, by phototactic bacteria and algae, are effective, but they face the intrinsic limitation of the low transparency of body tissues. Thus, *in vivo* applications of these methods are not straightforward, especially in deep regions of the body. Ultrasound has also been proposed as a control means, but its low reliability and reversibility have limited its success so far. Magnetic control enabled by natural cell magnetotaxis or by the inclusion of paramagnetic nanoparticles into biohybrid systems seems the most promising approach, at present. Indeed, magnetic fields can efficiently and safely penetrate body tissues. Some open challenges concern the hardware used to generate magnetic fields. In fact, the input current can be used to precisely generate magnetic fields in electromagnets. However, currents can heat the system and the whole workspace, with the risk of interference with the therapy or even affecting cell and tissue viability. Permanent magnets avoid this problem, but they are bulky, and they need to be moved, to properly modulate a field.

As highlighted in the previous section, the “passive” steering ability guaranteed by chemotaxis, as well as similar ones enabled by thermotaxis and aerotaxis, is attractive only in combination with other “active” strategies, such as magnetic steering. The combination of long-range active “robotic” control strategies and short-range passive “biological” reactivity may represent the most promising paradigm, in the next years [5, 71].

Red blood cells and leukocytes possess numerous attractive features. However, there are still many challenges to overcome before translation into the clinic. One issue concerns the conjugation of the cells to synthetic or live actuators, which may imply damages to the cell membrane. This event can compromise the key properties of the biological cargo, such as the ability to be “transparent” to the immune cells, thus avoiding the opsonization of therapeutic molecules, and the high deformability enabling passage into small capillaries. Furthermore, red blood cells do not possess intrinsic sensing capabilities and are limited in their ability to cross biological barriers, differently from leukocytes.

Leukocytes have indeed the advantage of intrinsic sensing and barrier crossing, which make them promising as autologous biohybrid robots. However, it is important to highlight the short lifespan of neutrophils, with an average of 5 days in circulation and few hours after isolation, which is an important limiting factor. Monocytes, once differentiated in macrophages, have a longer lifespan. However, they are affected by other possible issues; among them, the risk of untimely degradation (e.g., due to the embedded drugs) and uncontrolled release of payloads, which would considerably reduce the TI. Furthermore, better strategies to selectively and remotely control cell-based microrobots are still needed. Effective on-demand strategies for the release of drugs are still scarce in the state-of-the-art, concerning these cell types, and their integration would further extend the potential of microrobotic cell-based delivery approaches. Furthermore, another critical challenge that cannot be neglected concerns the standardization of protocols and safety

issues regarding the biological material, which must be carefully addressed before reaching the clinical and commercial reality.

Finally, the lack of safe and reliable imaging to track microswimmers *in vivo* is broadly recognized as one of the most critical bottlenecks limiting the clinical translation of biohybrid microrobots, but even micro-/nano-scale robots in general [48, 72, 73].

13.6 Muscle Cells as Biological Motors

Natural muscle is considered an attractive source of inspiration by many engineers, being considered an optimized mechanism evolved over millions of years. Indeed, muscles are a noticeable example of linear actuators, capable of large displacements (up to 40%) and high power/force-to-weight ratio while preserving an excellent stiffness control [74].

Muscles are generally subdivided into skeletal, cardiac, and smooth, even if our sections are going to deepen only the striated types of muscles (skeletal and cardiac), which are the most investigated ones for biohybrid microrobots. From a functional and structural point of view, cardiac and skeletal muscle (SM) tissues present several differences and similarities.

SM is the tissue responsible for the voluntary movement in vertebrates, holding a highly versatile nature to dynamically adapt to different signals and damages. SM shows an organized and hierarchical structure, starting from its building block: SM cells (also called myotubes or myofibers) are tightly compacted in a strictly ordered environment, forming the SM itself (Fig. 13.6a).

Cylindrically shaped, SM cells usually have a diameter from 10 to 100 μm , they can be several centimeters long, and they can each generate a contraction force in the range of 1 μN [76]. Due to the high metabolic demand of the tissue, a rich capillary network surrounds each fiber, providing it with the appropriate nutrition.

During embryonic development, proliferating mononucleated muscle cells (myoblasts) fuse together forming multinucleated postmitotic myofibers. This process is called myogenesis. The myofiber's plasma membrane is called the sarcolemma. It encloses the sarcoplasm (namely, the muscle cell cytoplasm) and has several invaginations toward the center of the cells, called transverse tubules (T tubules). Inside every myofiber, the cytoskeleton is organized in the specialized functional unit, the sarcomere, composed of parallel thick myofilaments (myosin) and thin myofilaments (actin) (Fig. 13.6b). Sarcomeres are arranged one next to the other, forming the myofibrils and the typical striation of SM tissue. A thick network of tubules, the sarcoplasmic reticulum (SR), surrounds each myofibril, coming in contact with each T tubule and thus forming a triad. The high content of Ca^{2+} inside the SR is crucial to trigger SM contraction, also regulated by the amount of ATP produced by the mitochondria scattering the sarcoplasm.

SM contraction is voluntarily activated by the electrical triggering of motor neurons. Motor neurons directly contact the myofibers on the sarcolemma at the level

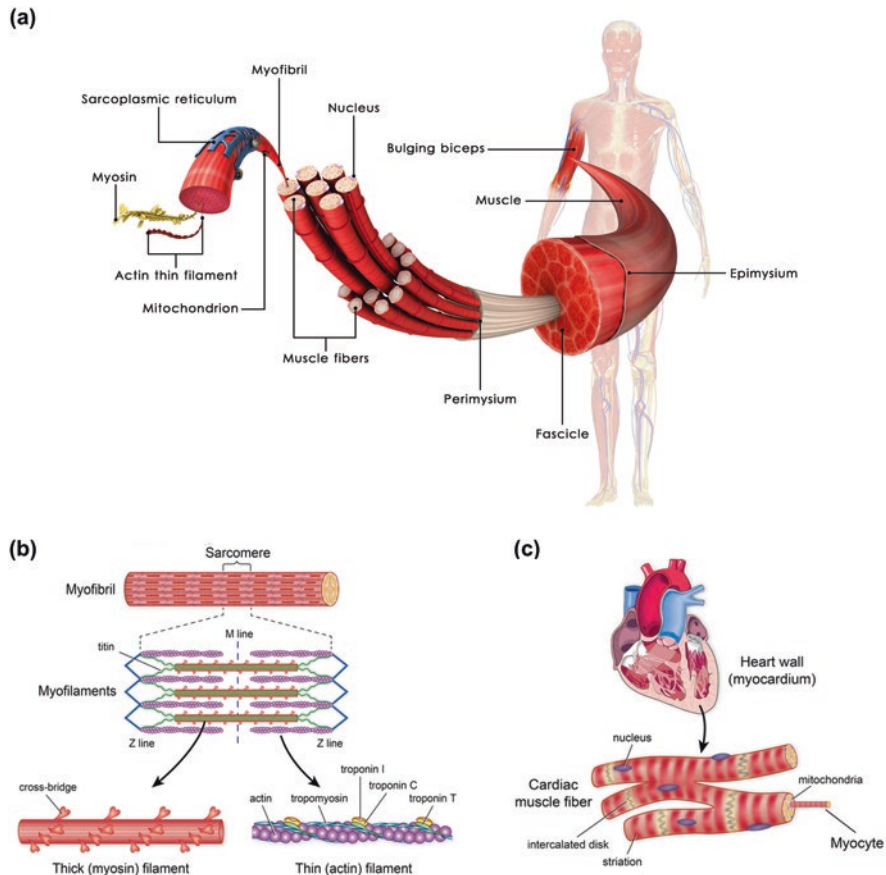


Fig. 13.6 Mammalian skeletal and cardiac muscle organization, organelles, and cell structures. (a) Skeletal muscle tissue structure. Image reproduced with permission from sciencepics/Shutterstock.com. (b) Molecular composition of the sarcomere. (c) Cardiac muscle tissue structure. Images adapted from [75]. Copyright: Springer Nature

of the neuromuscular junctions (NMJ): chemical synapses where the action potential is transmitted as a depolarization wave from the nerve to the muscle. The depolarization is then propagated along the T tubules, activating the release of Ca^{2+} from the SR. SM contraction depends on sarcomere shortening, thanks to the slide of actin myofilaments toward the center of the sarcomere. This is possible thanks to the conformational changes of the myosin's heads, which are bound to the actin filaments when the muscle is at rest [77]. In the presence of ATP, Ca^{2+} release from SR activates the myofilament sliding, triggering muscle contraction. All the events, starting with the electrical impulse and ending with the cell contraction, are known as excitation-contraction coupling.

On the other hand, cardiomyocytes are striated cylindrical muscle cells ($\sim 10 \mu\text{m}$ in diameter and about $100 \mu\text{m}$ in length, each generating a contraction force in the

range of 10 μN [78]) showing essential differences compared to SM cells (Fig. 13.6c). Cardiomyocytes and SM share the same contraction mechanism, based on T tubules, electrically controlled Ca^{2+} release from SR, and sarcomere shortening. However, individual cardiomyocytes are tightly connected at the level of intercalated discs: connection site allowing the rapid movement of ions involved in the contraction mechanism, creating an electrically integrated syncytium. They allow rapid transmission of the action potential between the cells, which can contract simultaneously. Cardiomyocytes are usually mononucleated, branched, and with shorter myofibrils than SM ones. One of the main differences is that cardiomyocyte contraction is not driven by voluntary control, and it is sustained autonomously over time.

Muscle cells' inherent modular and scalable nature (from the mesoscale down to the microscale) and their responsiveness to electrical stimulation make them a suitable component to be used for building general-purpose controllable biohybrid actuators.

Cardiomyocytes and SM cells have been exploited as biological drivers with a bottom-up approach, based on the assembly of multiple contractile cells in more complex and functional devices. The resultant actuator can be therefore tailorable in size and architecture, opening a broad panorama of applications.

It is worth mentioning that the use of contractile tissues derived from insects that have been investigated in this field broadens the choice of contractile elements for the actuation of biohybrid devices. Contractile tissues from insects possess remarkable features compared to mammalian cells. Small insects live and locomote in a wide range of temperatures (from values below 0 $^{\circ}\text{C}$ to approximately 55 $^{\circ}\text{C}$), more extreme than those tolerated by mammalian cells, and can resist to changes of pH due to the variation of the external environment.

Implanted tissues from insects, usually dorsal vessel tissue (DVT), show self-contractile properties similar to cardiomyocytes. Moreover, their robustness to extreme and rapid variations of external conditions enhances their potential and usability, making them valid candidates in extra-corporeal applications.

From an engineering viewpoint, the natural muscle has enormous potential with respect to artificial actuators. It holds a maximum efficiency of 40% [79], defined as the ratio of work generated to input energy spent; it can exert a maximum force of <1 kN, considerably greater than most artificial actuators' performances [80]. By far, biohybrid actuators are struggling to reach these performances, with the cardiomyocyte-based robots showing better performances than SM-based or insect-derived ones, in terms of exerted stroke and stress (respectively 10–10⁻¹ m and approximately 10⁻² MPa for cardiomyocytes, approximately an order of magnitude higher than other actuators [5]). They are still outperformed by artificial actuators, and several challenges still need to be faced.

From a fabrication viewpoint, biohybrid actuators are usually composed of a soft scaffold with cells growing on top of it or cells embedded in a 3D soft hydrogel. The efficiency of the actuation is highly dependent on the profound synergy and link between the living component and the substrate in terms of cell adhesion, scaffold

biocompatibility, compliance, and microarchitecture (that can enhance muscle differentiation and maintenance). All these components may strongly affect the actuation performance of the biohybrid actuator, as extensively analyzed in 2014 by Duffy and Feinberg [81].

The elastic modulus of muscle tissue, depending on the type, has been reported to be approximately 10–40 kPa [82]. Therefore biocompatible soft materials able to be compliant by reaching this range of rigidity became ideal candidates, such as polydimethylsiloxane (PDMS), polylactic acid, poly(ethylene glycol) diacrylate (PEGDA), and different hydrogels based on extracellular matrix (ECM) proteins (e.g., collagen, laminin). More specifically, the presence of proteins belonging to the muscle *in vivo* microenvironment and the spatial organization of these biochemical cues is indeed crucial to give cell instructive inputs to engineer muscle tissue. In this view, different groups explored the micropatterning of substrate surfaces by physical or biochemical techniques to direct myotube organization and differentiation. The anisotropic cell alignment can be pushed either by physically modifying a material with a specific pattern (e.g., alternated grooves and ridges), by transferring anisotropic repetitive protein designs on the substrate surface, or even by using aligned micro-fibrous substrates.

Starting from 2000, different studies have been carried out, resulting in the fabrication of different biohybrid microrobots able to grip, pump, walk, swim, and crawl.

13.6.1 Robots Based on Cardiomyocytes

Cardiomyocytes are attractive actuating elements, being part of the most important and stronger muscular tissue of animals. This cell type can generate a higher force than SM cells, without the need for long differentiation protocols. Despite such advantages, the controllability of cardiac cells remains an unsolved issue since their spontaneous contraction can only be paced (electrically, optically, or chemically), thus not representing an “on/off” biological motor. Furthermore, cardiomyocytes, usually derived from explanted tissues of animals, raise possible ethical issues for their supply.

Being almost “ready-to-use” biological motors, proper contractile systems based on cardiomyocytes have been tested earlier than SM cell-based devices. Starting from 2005 [83], cardiomyocytes were investigated as actuating elements in organic/inorganic robots (length, 138 μm ; width, 40 μm ; thickness of the Au/Cr layer, 20 nm/300 nm) built through microelectromechanical system (MEMS) technology, able to walk with a maximum speed of 38 $\mu\text{m/s}$. At that time, this cardiomyocyte-driven device revealed the enormous potentialities behind the deployment of cardiac cells for actuating micro-/nanodevices. The first example of completely organic microrobot was investigated by Kim et al. [84]. The crab-like robot was able to walk up to 10 days, with an average velocity of 100 $\mu\text{m/s}$.

After these promising studies, the possibility of finely engineer muscle tissue controlling its hierarchical architecture has been pursued by investigating two-dimensional (2D) systems based on free-standing polymeric micro-/nanofilms. These systems allow modifying the chosen substrate surface and, consequently, the muscle cell growth and disposition on top of it. This bottom-up approach is interesting since it allows providing a single biohybrid device with different areas, in which cells are differently organized, thus achieving articulated actuation possibilities and, if adequately controlled, multiple degrees of freedom.

Park et al. proposed a micropumping system based on an $800 \times 800 \mu\text{m}^2$ -sized membrane, made of PDMS, actuated by cardiomyocytes, directly seeded onto that surface [85]. The actuating frequency of the membrane was found in the order of 0.2–0.4 Hz, while the detected vertical movement was about $8 \mu\text{m}$. The micropump achieved a net flow rate of 0.226 nL/min, with potential applications in the biomedical field as a local drug delivery system.

Muscular robots made from thin films were proposed in 2007, when Feinberg and colleagues [86] demonstrated the potential of cardiomyocyte-powered muscular thin PDMS films (MTFs) (Fig. 13.7a). MTFs (maximum size: $5 \text{ mm} \times 5 \text{ mm}$) showed a broad versatility for multiple purposes (gripping, pumping, working, and swimming). Such MTFs worked for at least 16 days post cardiomyocyte seeding, showing superior performance than previous studies (i.e., walking at $133 \mu\text{m/s}$ and swimming up to $400 \mu\text{m/s}$) upon electrical stimulation (10 V, 10 ms square wave at pacing rates from 0.1 to 10 Hz). Despite those exciting results, MTFs were almost poorly scalable because of the need for a manual procedure to shape the film in the desired form, even if such results paved the way to further investigations on this topic.

A newer generation of walking “bio-bot” was proposed by Chan et al. in 2012 [87, 88]. Using stereolithography, micro-thick “bio-bot” (width: 2 mm; length: from 7 to 10 mm; the thickness varied from 156 to $326 \mu\text{m}$) made of PEGDA was moved by the contraction of cardiomyocytes, seeded on one of its sides to promote an asymmetric movement of the whole “bio-bot” (Fig. 13.7d). This behavior promoted a linear motion of the bot upon the bending of the layer actuated by cardiac cells, with a maximum recorded velocity of $\sim 236 \mu\text{m/s}$. The “bio-bots” performed optimally for 3–5 days, after which the contraction force decreased significantly.

These works were also the premises on the investigation of more bioinspired devices, concurrently with more extensive use of PDMS as structural and conformable material. Nawroth et al. [89] developed an interesting hybrid microrobot inspired by the jellyfish. A tissue-engineered PDMS structure (thickness, $20 \mu\text{m}$; diameter, $\sim 10 \text{ mm}$) was fabricated, replicating the organization of the muscle fibers of the jellyfish by patterning muscle cells using the microcontact printing technique. This prototype of microrobot imitated the propulsion mechanism of this marine animal (Fig. 13.7b). Paced by electrical stimuli (1 Hz, 2.5 V/cm, 10 ms pulse width), the microrobot was able to achieve a maximum velocity of 2.4 mm/s , outperforming all previous prototypes. Another self-propelled swimmer driven by cardiomyocytes was investigated by Williams et al. [90]. The swimmer (length, 2 mm; width, $100 \mu\text{m}$), made in PDMS, could swim for 3–4 days at a velocity up to $9.7 \mu\text{m/s}$ with

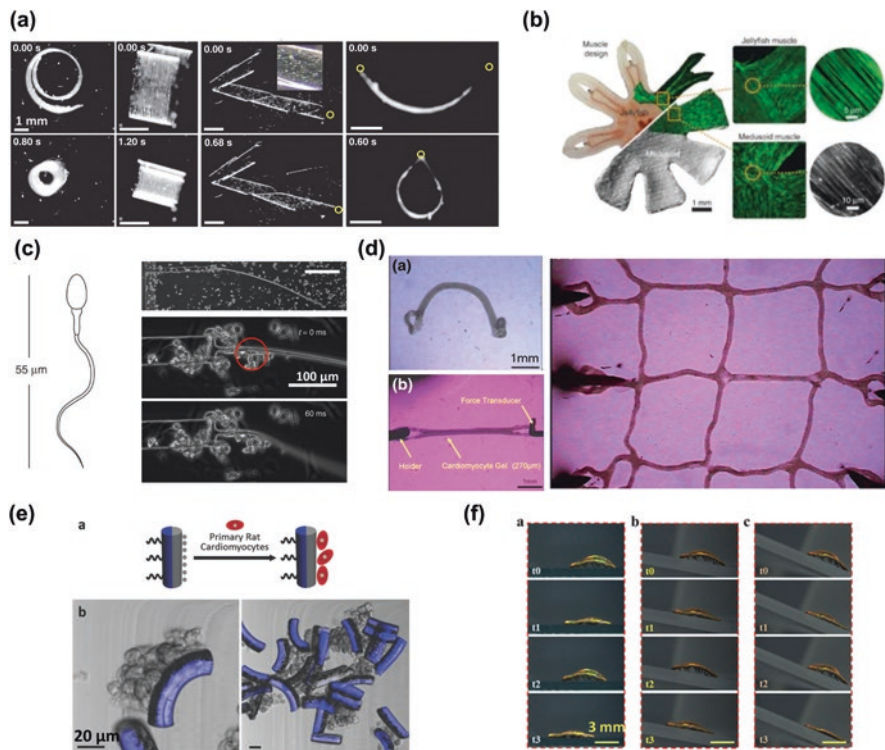


Fig. 13.7 (a) Thin elastomeric films actuated by aligned cardiomyocytes with customized shape/function. Adapted from [86]. Copyright: AAAS. (b) Body design of the tissue-engineered jellyfish and a magnification of the engineered Jellyfish 2D muscle. Reproduced from [89]. Copyright: Springer Nature. (c) Sperm-like biohybrid swimmer, consisting of an elastic filament with a rigid head and a compliant tail and a small cluster of contractile cardiomyocytes which deform the filament during a complete contraction cycle. Reproduced from [90]. Copyright: Springer Nature. (d) Freely moving gel actuated by cardiomyocyte gel and an example of a lattice nine-node cardiomyocyte gel network. Reprinted from [92]. Copyright: Springer Nature. (e) Microcylinders powered by cardiomyocytes. Reprinted from [95]. Copyright: John Wiley and Sons. (f) The crawling of cardiomyocyte-driven soft robot at different inclinations. Reprinted from [96]. Copyright: John Wiley and Sons

a propulsive force of around $0.4 \mu\text{N}$. The PDMS was also adopted by Vannozzi et al. [91] for the fabrication of customizable linear actuators (PDMS thickness, from 10 to $25 \mu\text{m}$; length, 10 mm) obtained through the rolling of 2D micro-membranes thanks to the generation of internal mechanical stresses by coupling layers at different stress levels. The authors evaluated the linear displacement generated by the cardiomyocyte contraction force, highlighting the interplay between cardiomyocyte force and material properties.

On the other hand, the use of softer substrates, as hydrogels, has been investigated in order to maximize the performance of cardiomyocyte-driven robots, making the microrobot skeleton softer and more compliant to cell contraction. For

example, Hoshino et al. explored the performance, upon chemical stimulation with adrenaline, of the so-called gel robots. These devices were made of cardiomyocyte gel filaments composed of collagen and Matrigel (width ranging between 50 and 200 μm ; length, ~ 5 mm) and showed a life expectancy of at least 7 days (Fig. 13.7c) [92]. Further studies have involved even hydrogels doped with carbon-based nanomaterials for engineering bioactuators with superior performance thanks to the presence of conductive elements [93, 94]. Cardiomyocytes were also used to actuate swimmers based on a microcylinder-shaped body, fabricated by electrohydrodynamic co-jetting and thermoplastic materials (Fig. 13.7d) [95]. A group of cells was attached to one side of the microcylinders (60–70 μm length, 10 μm diameter) in order to get the movement of such linear cylinder through bending, thanks to a total force of 191 ± 12 μN exerted by the spontaneous contraction of cardiomyocytes.

Recently, further efforts have been directed to the investigation of bioinspired platforms for cardiomyocyte-driven robots. In this study of Chen et al. [96], the cardiomyocytes were seeded on the parallel nanoridges of the butterfly wings. Thus they can align thanks to the wing topography, optimizing their contraction performance. Another bioinspired platform was proposed by Sun et al. [97]. The authors developed bioinspired soft caterpillar made of 100 μm -thick hydrogels actuated by cardiomyocytes (Fig. 13.7e). Such prototypes mimic the crawling behavior of caterpillars, achieving a maximum speed of 20 $\mu\text{m}/\text{s}$.

In recent years, other control strategies have also been optimized because of the need for more controllable cardiomyocyte-driven devices, activated and steered by light. Optogenetics is an approach well investigated in neuroscience [98]; it relies on engineering living cells to express light-responsive proteins on their membranes. After such modification, the exposure of cells to specific light wavelengths enables fast, localized, and minimally invasive contraction activation. At this purpose, a recent work [99] proposed the phototactic guidance of a biomimetic soft robot actuated upon cardiomyocyte contraction. Speed (up to 3.2 mm/s) and direction were controlled by modulating light frequency (470 nm, 10 ms pulses, from 1 to 3 Hz) and by independently eliciting the fin, making the robot steerable. Despite the macroscale of such a robot (size: 10 mm), this example showed the enormous progress made in the control of cardiomyocytes, making them still an intriguing option to pursue a somehow controllable actuation of microrobots.

Lately, an interesting work was proposed by Xu et al. [100] on multifunctional microrobots. Despite the macro size of the robot (centimeter-scale), such a concept is interesting because it combines the cellular engine based on the contractile properties of cardiomyocytes, emulating the swimming of whales, with a second degree of freedom due to the presence of thermoresponsive wings. The robot achieved a maximum velocity of 0.6 mm/s and could be sustained within 3 weeks without the need for external power supplies. If scaled at smaller scales, this concept could be potentially used as a cargo carrier for programmed and localized delivery of drugs.

13.6.2 Robots Based on Skeletal Muscle Cells

Preliminary studies on SM-powered systems grounded on densely packed worm-like structures, composed of differentiated myotubes and proteins derived from the ECM. These studies exploited the inherent driving force of muscle cells to self-assemble in a functional tissue. A seminal work in this field was proposed in 2000 by Dennis and colleagues [101], with the fabrication of the so-called myooids: elongated muscle constructs with a diameter ranging from 0.1 to 1 mm, and a twitch force of 215 μN under electrical stimulation (Fig. 13.8a).

However, relying only on the muscle cell ability to self-assemble in a contractile tissue strongly limits the possible actuator designs. This first study represented a proof-of-concept of SM cells potential as motors for bio-integrated systems. In the

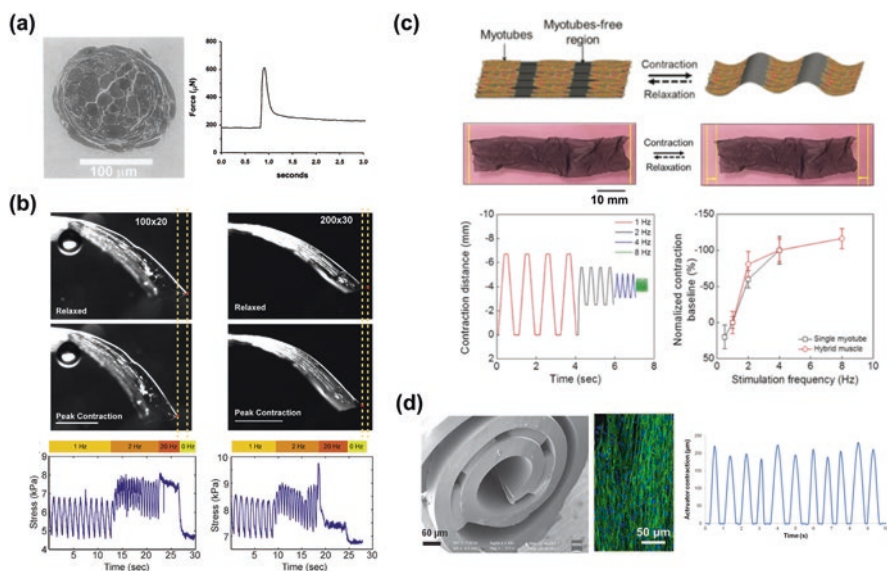


Fig. 13.8 (a) Left: cross section of a “myooid”; right: peak twitch force of a single myoid (electrical paced 70 V, 4-ms pulse). Images adapted from [101]. Copyright: Springer Nature. (b) Top: contraction behavior of the films with different fibronectin pattern at peak contraction; bottom: stress vs. time plot of the thin films stimulated at different frequencies. Images adapted from [102] Copyright: Elsevier. (c) Top, representation and photographs of the electrical-stimulated hybrid muscle (left, relaxation state; right, contraction state); bottom, frequency-contraction distance relationship of the hybrid muscle in response to varying stimulation frequencies. Images adapted from [103]. Copyright: Springer Nature. (d) Top, scanning electron microscope image of the three-dimensional rolled polydimethylsiloxane structure; middle, fluorescence images of C2C12 cells at day 7 of differentiation growing on the structure; bottom, contraction behavior of the bioactuator. Images adapted from [91]. Copyright: IOP Publishing

following years, other solutions were explored to engineer more tailorable and multifunctional biohybrid actuators.

Concerning 2D systems, Sun and co-authors [102] fabricated thin films made of PDMS (1.5 mm × 4.5 mm, 15- μ m thick), optimizing cell alignment with fibronectin patterning and obtaining a peak twitch stress of 10 kPa upon electrical stimulation (1–20 Hz, 0.4 V/mm, 10 ms pulse width) (Fig. 13.8b). In 2016 Kim and colleagues [103] fabricated an example of an interesting synergy between the living component and the substrate features, in view of maximizing SM contraction efficiency and force transmission (Fig. 13.8c). The nano-fibrous structure of the multiwalled carbon nanotubes (MWCNT) sheet, stabilized in solution thanks to a poly(3,4-ethylenedioxythiophene) (PEDOT) coating, helped cell alignment, while the mechanical features of the PEDOT/MWCNT film (60 mm × 10 mm, approximately 47 nm thick) were able to assist cell relaxation. Furthermore, MWCNT electrical conductivity helped in SM cell electrical stimulation (1–8 Hz), even if quantification of the contraction force was missing. In the same year, an exciting solution to avoid additional substrate processing to foster cell adhesion and differentiation was proposed by Webster and colleagues [104] with an electrocompacted and aligned collagen scaffold seeded with SM cells able to produce locomotion of approximately 77.6 ± 86.4 μ m/min, 1.16 of its body length per hour.

A good compromise between the advantages of the 2D and those of the 3D systems was proposed by Vannozzi and colleagues [91], who developed a 3D rolled PDMS structure (25- μ m thick) contracting up to 0.12% of its length in the presence of differentiated SM cells (Fig. 13.8b). The authors also built a finite element model simulation to predict the contraction behavior by varying some fabrication parameters. In silico simulations played an interesting role also in the work of Hasebe et al. [105]. Such a bioactuator was made of a thermoplastic elastomer (poly(styrene-*block*-butadiene-*block*-styrene)) and consisted of a micro-grooved thin film (3 mm × 10 mm, 2.7- μ m thick), powered by contractile, aligned SM cells. The low flexural rigidity of the material allowed the contraction of the self-standing biohybrid thin film, and this performance matched with the in silico results with a small error of 5%. In a recent work carried out by Vannozzi et al. [106], a novel computational approach coupling finite element modeling and smooth particle hydrodynamics was proposed for the estimation of the contractile capabilities of skeletal muscle cell-powered biohybrid systems. These results highlighted the possibility to create more accurate models of 2D biohybrid systems based on thin films and to create real “design tools.”

In parallel to 2D systems, some research groups are focusing on scaling up biohybrid systems in the third dimension, envisioning multiple applications. Li et al. [107] developed a “pump-bot,” a millimetric ring-like system controlled by electrical stimulation (1–4 Hz, 0.45 V/mm, 10 ms pulse width), able to generate a flow rate in the order of ~ 20 μ L/min. The micropump (12-mm outer diameter, 5–6-mm inner diameter, 3-mm depth) exhibited a relevant difference with previous pumping biohybrid robots, usually showing a pumping capacity estimated around a few nL/min [85, 108], with potential applications in the lab-on-a-chip domain or as a drug delivery system.

In 2012, Sakar and colleagues [109] developed a 3D SM microtissue auto-assembled around two PDMS pillars, used to indirectly register the construct contraction behavior. The system was composed of a suspension of differentiated SM cells in a collagen/Matrigel hydrogel. While all the abovementioned biohybrid actuators were controlled through electrical stimulation, in this work the use of light stimulation and optogenetically modified muscle cells was explored. The authors were able to selectively activate specific regions of the actuator, triggering a directional torsion of the construct and introducing a second degree of freedom in the actuator control (excitation wavelength: 473 nm). Despite this considerable innovation, the contraction behavior of this construct still needed improvements, being able to generate a passive tension force of 10.8 μN and an active contraction force of only 1.41 μN after 14 days of differentiation (stress: ~ 1.12 kPa). The overall size of this 3D construct was less than 100 μm width, with a length of approximately 400 μm (Fig. 13.9a).

Nevertheless, this work kicked off a new approach that was then optimized in the following years. In 2014, Cvetkovic et al. [110] focused on creating a self-standing crawling “bio-bot,” with the cell-matrix solution grown around two pillars (artificial tendons) joined by a flexible beam (artificial joint) (overall dimensions, 6 mm \times 3 mm; pillars height, ~ 3 mm, Fig. 13.9b). Notably, the design optimization of the scaffold and the addition of insulin-like growth factor-1 (IGF-1) to enhance SM differentiation for functional output, brought to a generation of a system with a passive tension force of 1 mN (0.84 kPa), an active tension force 200 μN (0.17 kPa), and a speed of ~ 156 $\mu\text{m}/\text{s}$, meaning ~ 0.025 body length per second.

Two years later, Raman and colleagues [111] slightly modified this design, ending with the cell-matrix solution shaped in a muscle ring of ~ 1 mm width and ~ 5 mm length. Interestingly, the authors exploited the SM innate adaptability to optimize the actuator performance, by applying different mechanical and optical stimulations to exercise the differentiating muscle, causing a $\sim 550\%$ greater force in exercised muscle rings compared with non-stimulated ones. Even if the design concept presented in the last works cannot be up- or downscaled in dimension per se, a smart combination of the muscle rings with the fabricated skeleton in a modular and additional approach may have several applications. Raman et al. leveraged this modular concept creating a two-legged symmetrical bot powered by two muscle rings. The use of electric stimulation and in combination with localized light stimulation resulted in the steering of the bot in different directions with net locomotion of ~ 312 $\mu\text{m}/\text{s}$ (Fig. 13.9c).

Recently, Pagan-Diaz and co-authors [112] modified the living junction geometry with the aid of computer simulations and fabricated different prototypes of walking biohybrid machines, ending with a high force produced (passive tension force up to ~ 8 mN, peak force up to 0.97 mN), demonstrating once more the power of in silico design tools.

Starting from these studies, Morimoto et al. [113] made a relevant leap forward in the integration of living components in an engineering setting, achieving the fabrication of a centimeter-scale biohybrid robot. The use of an antagonistic pair of contractile elements under electrical stimulation control enabled the

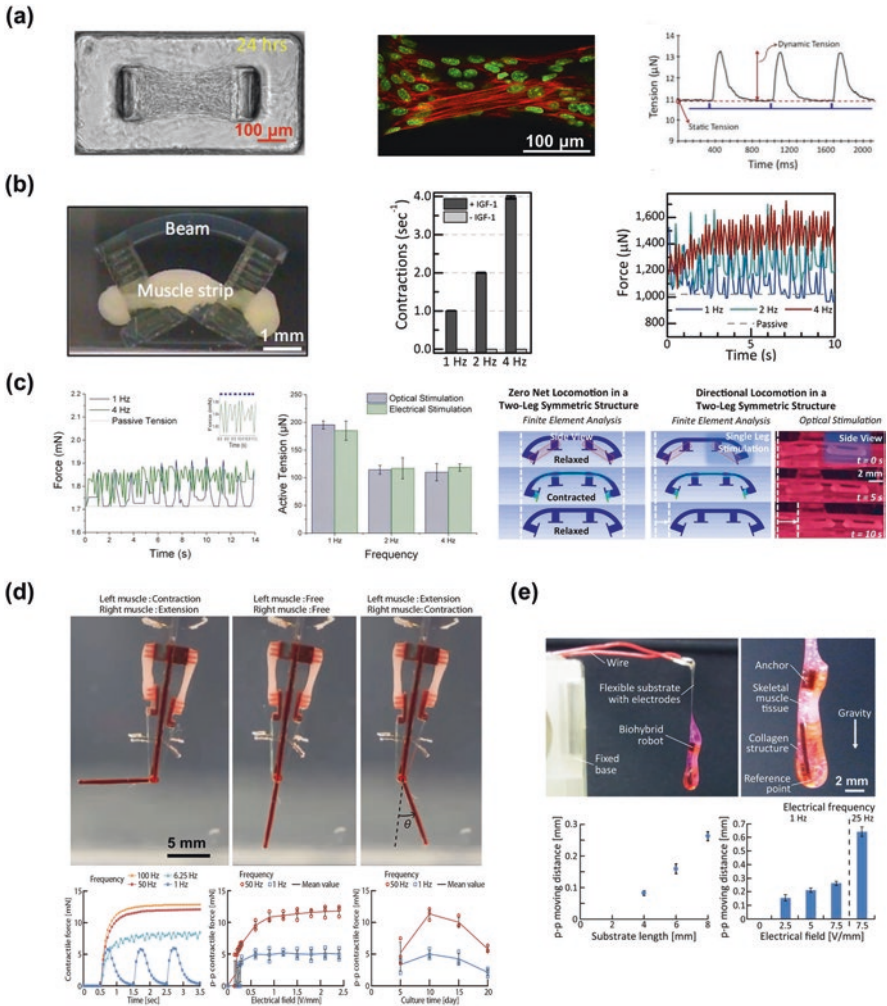


Fig. 13.9 (a) Left, top view of the fabricated “bio-bot”; middle, top view with fluorescent staining for actin (red) and cell nuclei (DAPI), green; right, representative recording of the static and dynamic tension of an SMT on day 15. The microtissue is stimulated with a brief blue light pulse series (indicated by blue bars). Images adapted from [109]. Copyright: Royal Society of Chemistry. (b) Left, photograph of optogenetic muscle ring-powered “bio-bot”; middle, contraction behavior of muscle ring with or without insulin-like growth factor-1 stimulation; right, active tension force for a representative muscle ring. Images adapted from [110]. Copyright: National Academy of Sciences. (c) Right, active tension produced by the optically-stimulated muscle strip; left, locomotion and steering of the two-leg “bio bot.” Images adapted from [111]. Copyright: PNAS. (d) Top, motions of the biohybrid robot powered by the antagonistic pair of skeletal muscle tissues (electrically paced: 1.5 V/mm, 50 Hz, 2 ms); bottom, actuator contractile force in relation to time, electrical stimulation, and culture time, depending on the different electrical frequencies applied (1.5 V/mm, 2 ms). Images adapted from [113]. Copyright: AAAS. (e) Actuations of the biohybrid robot in air powered by the skeletal muscle tissue. Images adapted from [114]. Copyright: AIP Publishing

implementation of the engineering part, creating a robot capable of object manipulation, achieving $\sim 90^\circ$ rotation of the joint, and able to survive for 20 days (Fig. 13.9d). The encapsulation of the actuator in a collagen shell allowed the motion at room temperature for 60 min [114], keeping the appropriate culture conditions for long-term usability and actuation, and giving exciting hints for the applications in real-world scenarios (Fig. 13.9e).

Following a biomimetic approach, a possible evolution in this field is the coculture of SM cells and motor neurons to recreate an *in vivo*-like neuromuscular junction. This would help to boost SM differentiation and actuator force functional output and may lay the foundations for a new type of control [115, 116]. In this view, Aydin et al. [117] have recently proposed a hybrid swimmer actuated by motor neuronal activation of muscle contraction, showing a locomotion velocity of $0.7 \mu\text{m/s}$.

13.6.3 Robots Based on Insect-Derived Cells

The use of contractile insect-derived cells has raised an enormous interest recently, because of their remarkable properties. These cells, in fact, are extremely robust and featured by a high resistance outside the culture medium, with respect to mammalian and human cells [118]. As shown by Akiyama et al. [119], the excised tissue from self-contractile DVT (corresponding to the mammalian cardiac tissue) of different types of lepidopteran larvae (*Bombyx mori*, *Thysanoplusia intermixta*, or *Ctenoplusia agnata*) can beat spontaneously for more than 25 days without medium replacement at 25°C , a condition that is non-sustainable for other cell types (e.g., skeletal and cardiac cells). This makes insect-derived cells optimal candidates for building microrobots featured by a high life expectancy in environmental conditions.

It must be noticed that, in the absence of external stimulation, the contraction frequency might decrease over time, leading to an overall decrease of the actuation performance (e.g., average frequency of about 0.15 Hz), which could be no less than that of conventional mechanical actuators [120]. As shown by Akiyama et al. in a PDMS-based squared device (lateral dimension, $\sim 3 \text{ mm}$), their controllability can only be achieved by pacing the contraction by means of electrical stimulation, as for cardiac cells (Fig. 13.10a).

Two examples of insect cell-powered microrobots were proposed in 2012. In the first case [121], the insect muscle-powered autonomous microrobot was able to achieve an average velocity of $38 \mu\text{m/s}$ (Fig. 13.10b), while in the second case [122], the so-called polypod microrobot arrived at a speed of $3.5 \mu\text{m/s}$, an order of magnitude less the previous prototype. Such a difference might be due to the different type of larva deployed by the authors (tissue from the larvae of the *Thysanoplusia intermixta* moth and tissue from lepidopteran larvae *Ctenoplusia agnata* inchworm, respectively), as well as the configuration of the robot skeleton, based in both cases on PDMS. Despite the actual macro size of both robots (length, 12.5 mm ; width, 0.90 mm), it is worth mentioning that the optimization of the robot structure and of

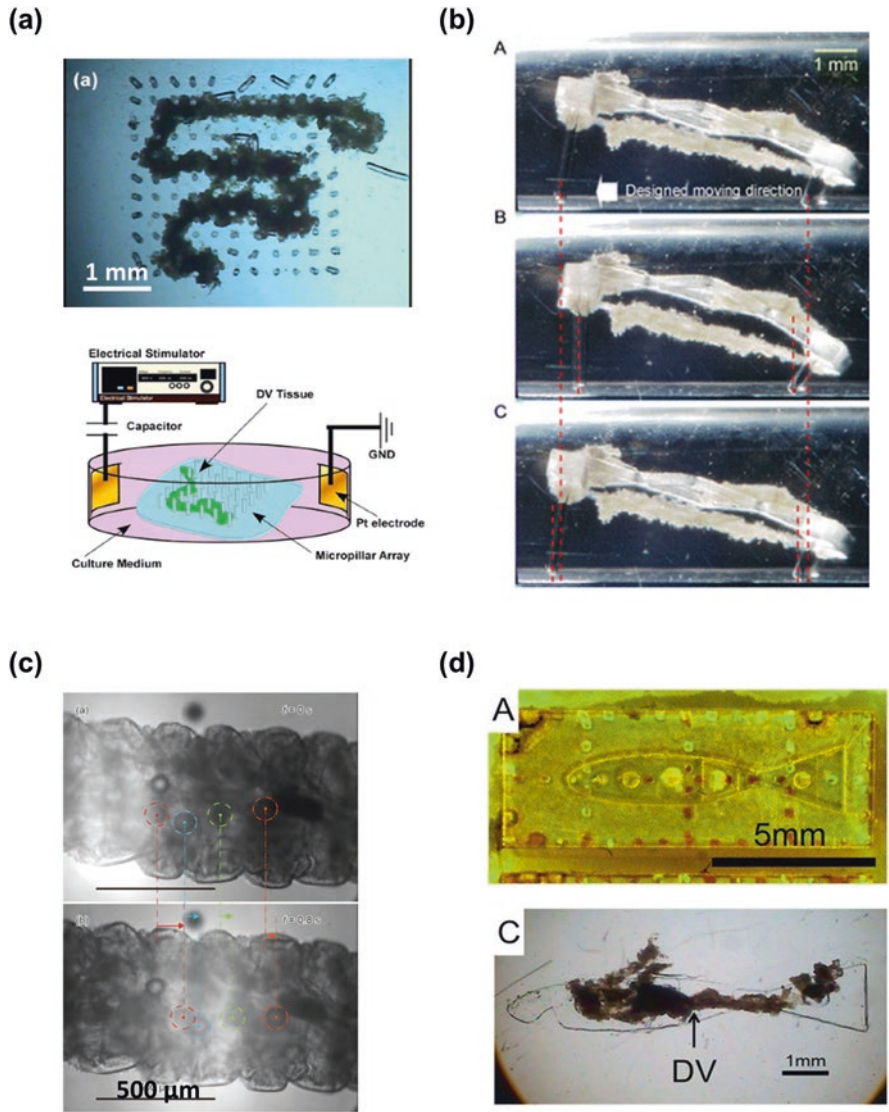


Fig. 13.10 (a) A dorsal vessel-derived tissue assembled on the micropillar array and the experimental setup for electrical stimulation. Images adapted from [120]. Copyright: Springer Nature. (b) Image analysis of the contraction of the insect muscle-powered autonomous microrobot (iPAM). Images adapted from [121]. Copyright: Springer Nature. (c) Time-lapse images of the micropump actuated by insect cells when transporting microbeads. Images adapted from [126]. Copyright: Creative Commons. (d) The mold fabricated by the stereolithography method and the swimming PDMS robot with the attached dorsal vessel tissue. Images adapted from [128]. Copyright: Creative Commons

the tissue organization might guarantee a certain degree of miniaturization. Akiyama et al. [123] proposed a relevant work in 2013, reporting the possibility of exploiting the DVT from the final stage larvae of the *Thysanoplusia intermixta* inchworm for actuating a pair of tweezers in the air. The system remained operative for more than 5 days at room temperature, out of the incubator. This work added a noticeable insight into the adoption of insect cells in real-world scenarios.

Subsequently, Baryshian and colleagues [124] evaluated the performance of a bioactuator built from embryonic *Manduca sexta* muscle stem cells. The authors analyzed the stress generated by such a device (up to 2 kPa) and checked that cells remained functional for more than 2 months in culture without media replacement.

Various stimulation strategies have been evaluated for the regulation of cell insect activity. Uesugi et al. [125] investigated the use of electrical stimulation (square pulses of 3, 5, 10, 15, and 20 V with 1 s duration and 1 Hz frequency), thermal stimulation (the temperature was changed by 5 °C in 1 min), and chemical stimulation (cardioactive neuropeptide at a concentration of 10⁻¹⁰, 10⁻⁹, 10⁻⁸, 10⁻⁷, 10⁻⁶, or 10⁻⁵ M) on insect cells harvested from moth larva. On the one hand, the thermal stimulus can modulate the contractile force and contractile frequency without thermal damage up to 35 °C. On the other hand, the electrical stimulation allows controlling the contractile force, while the chemical stimulation regulates only the contractile frequency. This study confirmed the possibility of adopting a wide choice of stimulation strategies for controlling the contractile properties of insect-derived cells, depending on the specific needs.

More recently, these cells have been analyzed for building microvalves, enabling pumping functions. Yamatsuta and colleagues [126] proposed an optically controllable micro-peristaltic pump with an internal diameter of the tubular structure of about 400 μm, actuated by cells from *Drosophila melanogaster* (wild-type strain, Canton-S third instar) larvae (Fig. 13.10c). In this case, *D. melanogaster* larvae were modified in order to express channelrhodopsin-2 (ChR2) on the cell membrane, thus being optically controllable with the use of blue light (power density, 2 mW/mm²). The pump was able to transport microbeads at a speed of 120 μm/s, demonstrating relatively good performance for being applied in a smart biomachine. From a technological viewpoint, Uesugi et al. [127] tried to tackle the scalability of such a bioactuator by exploiting the cell sheet technique using the NIASAeAl-2 insect-cell line (AeAl2 cells) derived from pieces of larval bodies of *Aedes mosquito*. Through this approach, cells were able to survive at least 13 days and made possible further steps ahead to customize the bioactuator.

Ultimately, a unique example of a swimming robot actuated by insect cells (cells from the final stage larvae of lepidopteran inchworms) was proposed by Yalikul et al. [128]. The body was made of PDMS with a thickness of about 50 μm, even if the other sizes were above the microscale (Fig. 13.10d). Such a robot was able to achieve an average velocity of 11.7 μm/s. This prototype may be scaled by adopting proper microfabrication techniques for potential application in the microscale domain.

13.7 Challenges and Perspectives of Robots Based on Muscle Cells

As discussed in Sect. 13.5, there are still many open challenges to be tackled before multicellular muscle cell-powered biohybrid robots can find applications in the clinic or other scenarios. The key issues are scalability to small dimensions, the lifetime of the biohybrid constructs, efficient in situ control, and possible immunogenicity.

Despite their inherent scalability, multicellular muscle cell-powered biohybrid robots are currently featured by considerably larger dimensions than biohybrid robots based on bacteria and other single cells. This is mainly due, at present, to the difficulty in precisely controlling the fabrication process at the microscale: building millimeter- or even centimeter-scale substrates on top of which culturing cells is much easier than controlling cell positioning and orientation on the substrate one-by-one. However, in theory, such a cell-level control is possible and would enable a bottom-up design of biohybrid microrobots based on muscle cells and working at the microscale. Here the struggle would concern the trade-off between miniaturizing these systems, yet keeping a detectable contraction force enabling their movement or other actions (reducing the size means reducing the number of cells and thus the force produced).

Actuator dimensions can also be influenced by the need to create a multifunctional system. Most of the multicellular actuators described in the state-of-the-art so far show only one degree of freedom. The fabrication of a system with more degrees of freedom should rely on the presence of different cell types, or the same cell types but organized in different ways, over the device surface/volume. This process, which would broaden the possible application of biohybrid microrobots, would add further challenges in the device scalability. It seems inevitable that this challenge should be faced in future years by taking advantage of advanced computer simulations, relying less and less on trial-and-error approaches, which are typical of the tissue engineering field. Smart design tools for miniaturized biohybrid systems should rely on a careful prediction of the force produced and thus, on the efficiency guaranteed, given specific geometries, mechanical features, cell differentiation level, and features of the surrounding environment in which the biohybrid robot is thought to operate [106].

In any case, it is unlikely that muscle-based biohybrid devices will be directly used to navigate and transport cargos or drugs through narrow capillary networks. In fact, although advanced simulation tools may help the miniaturization of these devices, they will probably remain too big to fit the lumen of capillaries ($\sim 2 \mu\text{m}$). Navigation in tiny vessels, included capillaries, for targeted drug delivery of other therapies, will probably be the “killer application” only of biohybrid microrobots based on single motile cells described in Sects. 13.3 and 13.4, relying on a complete and autonomous organism showing various and sophisticated sensing abilities. Multicellular systems, instead, need engineering modifications to provide them with on-board specific sensing. Most of the described works are mainly focused on

the implementation of the contraction ability of the muscle unit. On the other hand, multicellular muscle-based systems have the advantage of enabling a bottom-up design of biohybrid devices, with almost infinite possibilities and without the need to manage an entire autonomous organism (that necessarily implies less flexibility in the design). The possible applications of muscle-based biohybrid devices in the clinic may concern millimeter or centimeter-scale devices for surgical operations or other types of therapy, or more miniaturized systems (down to the microscale), but used as components of biohybrid implantable devices or biohybrid small therapeutic medical tools, rather than autonomous robots navigating in the capillary network. Besides the clinic scenario, many other possible applications can be envisaged for muscle-based biohybrid robots, from lab-on-a-chip systems to environmental monitoring, up to large-scale robotics, which would enormously benefit from a new generation of actuators with the features of natural muscles [5].

However, the combination of microfabrication technologies and muscle tissue engineering techniques are not at a fully mature stage, yet. More efforts are needed in this field, especially concerning a deep understanding of the biological mechanisms underlying the development and maintenance of mature and functional muscle tissue, starting from precursor cells.

SM-based bioactuators may be dynamically responsive to environmental changes and resistant to mechanical damages through inherent healing strategies. Raman et al. [129] showed that a complete functional recovery was possible within 2 days, after tissue damage. This implies that biohybrid robots can accomplish a complete remodeling of the SM tissue, potentially recovering the muscle force production post-damage. This aspect would dramatically increase the life expectancy of muscle-based robots, once the other challenges on long-term cell culture is solved, widening the possible applications of these systems. On the other hand, mammalian cardiac tissue has a minimal regeneration capability, so in this case, other approaches should be developed to guarantee a long-term operation.

Longevity and actuator stability over time are challenges that have been scarcely addressed so far in the state-of-the-art, but they strongly affect the system usability. By far, insect-derived contractile tissues have been demonstrated to be the most resilient solutions. However, insect cells can raise biocompatibility issues in the case of clinical applications. Most mammalian cell-based devices are viable for 2–3 weeks, but no extensive studies have been done to evaluate the longevity and functionality over a more extended period of time.

Concerning the controllability of muscle-cell based device contraction, multicellular systems are divided into two main groups: self-contractile cardiomyocytes or insect-derived cells and electrically or optically paced SM tissues. Electrical stimulation has been extensively used over the years as a control means, but other options and combinations can also be envisioned, such as optical control. The use of light as a trigger is a smart solution because of its low invasiveness and precision. However, when light is used other issues arise, especially in clinical scenarios, due to light absorption by tissues, which makes it difficult to reach deep regions of the body.

From an engineering viewpoint, a key factor in favor of using biohybrid microrobots in the clinics regards their energy source. In fact, to correctly operate, these

systems need glucose and oxygen. Thus, in-body environments can guarantee the presence of these nutrients, without the need to provide them through complex bioreactors. Obviously, this advantage becomes a limitation when out-of-body applications are targeted: in this case, biohybrid devices must be kept at 37 °C (or a wider range of temperature in the case of insect cells) and provided with nutrients, periodically.

Another critical factor for possible applications in the clinic is the safety of these systems in terms of biocompatibility and immunogenicity. This is an aspect that concerns all biohybrid robots: muscle-based but also bacteria-based and other motile cell-based ones. In the state-of-the-art, mainly immortalized and primary cells from mouse or rat have been used. If using a biocompatible material could overcome the safety issue regarding the scaffold, concerning the cell source, two possibilities can be envisioned: (1) using primary human muscle cells, directly derived from the patient, or (2) using muscle cells differentiated from stem cells, such as induced pluripotent stem cells (iPSCs), also derived from the patient. In the second case, to avoid the long process of reprogramming of patient-derived cells and the approval for clinical application, a solution can be envisioned. It is desirable for the scientific community to gather and push to create a shared database of a limited number of allogenic iPSCs grade for clinical trials. The iPSC lines could be derived from different human leukocyte antigen-homozygous donors, matching a large part of the population, and in this way easing many processes [130].

References

1. Abbott, L. J. J., et al. (2007). Robotics in the small. *IEEE Robotics and Automation Magazine*, 14, 92.
2. Purcell. (1976). *Life at low Reynolds numbers*.
3. Pons, J. L. (2005). *Emerging actuator technologies: A micromechatronic approach*. Wiley.
4. Liu, D. K.-C., Friend, J., & Yeo, L. (2010). A brief review of actuation at the micro-scale using electrostatics, electromagnetics and piezoelectric ultrasonics. *Acoustical Science and Technology*, 31, 115–123.
5. Ricotti, L., Trimmer, B., Feinberg, A. W., Raman, R., Parker, K. K., Bashir, R., ... Menciassi, A. (2017). Biohybrid actuators for robotics: A review of devices actuated by living cells. *Science Robotics*, 2(12).
6. Darnton, N., Turner, L., Breuer, K., & Berg, H. C. (2004). Moving fluid with bacterial carpets. *Biophysical Journal*, 86(3), 1863–1870.
7. Berg, H. C. (1975). How bacteria swim. *Scientific American*, 233(2), 36–45.
8. Macnab, R. M. (1979). How do flagella propel bacteria? *Trends in Biochemical Sciences*, 4(1), N10–N13.
9. Altegoer, F., Schuhmacher, J., Pausch, P., & Bange, G. (2014). From molecular evolution to biobricks and synthetic modules: A lesson by the bacterial flagellum. *Biotechnology and Genetic Engineering Reviews*, 30(1), 49–64.
10. Carlsen, R. W., & Sitti, M. (2014). Bio-hybrid cell-based actuators for microsystems. *Small*, 10(19), 3831–3851.
11. Yasuda, R., Noji, H., Kinosita, K., Jr., & Yoshida, M. (1998). F1-ATPase is a highly efficient molecular motor that rotates with discrete 120 steps. *Cell*, 93(7), 1117–1124.

12. Brennen, C., & Winet, H. (1977). Fluid mechanics of propulsion by cilia and flagella. *Annual Review of Fluid Mechanics*, 9(1), 339–398.
13. Gilpin, W., Bull, M. S., & Prakash, M. (2020). The multiscale physics of cilia and flagella. *Nature Reviews Physics*, 1–15.
14. Bershadsky, A. D., & Kozlov, M. M. (2011). Crawling cell locomotion revisited. *Proceedings of the National Academy of Sciences*, 108(51), 20275–20276.
15. Wadhams, G. H., & Armitage, J. P. (2004). Making sense of it all: Bacterial chemotaxis. *Nature Reviews Molecular Cell Biology*, 5(12), 1024–1037.
16. Akin, D., Sturgis, J., Ragheb, K., Sherman, D., Burkholder, K., Robinson, J. P., ... Bashir, R. (2007). Bacteria-mediated delivery of nanoparticles and cargo into cells. *Nature Nanotechnology*, 2(7), 441–449.
17. Behkam, B., & Sitti, M. (2008). Effect of quantity and configuration of attached bacteria on bacterial propulsion of microbeads. *Applied Physics Letters*, 93(22), 223901.
18. Fernandes, R., Zuniga, M., Sassine, F. R., Karakoy, M., & Gracias, D. H. (2011). Enabling cargo-carrying bacteria via surface attachment and triggered release. *Small*, 7(5), 588–592.
19. Nogawa, K., Kojima, M., Nakajima, M., Homma, M., Arai, F., & Fukuda, T. (2011, November). *Improvement of motility of bacterium-driven microobject fabricated by optical tweezers*. In 2011 international symposium on micro-nanomechanics and human science (pp. 482–485). IEEE.
20. Park, S. J., Bae, H., Ko, S. Y., Min, J. J., Park, J. O., & Park, S. (2013). Selective bacterial patterning using the submerged properties of microbeads on agarose gel. *Biomedical Microdevices*, 15(5), 793–799.
21. Park, S. J., Bae, H., Kim, J., Lim, B., Park, J., & Park, S. (2010). Motility enhancement of bacteria actuated microstructures using selective bacteria adhesion. *Lab on a Chip*, 10(13), 1706–1711.
22. Traoré, M. A., Sahari, A., & Behkam, B. (2011). Computational and experimental study of chemotaxis of an ensemble of bacteria attached to a microbead. *Physical Review E*, 84(6), 061908.
23. Edwards, M. R., Carlsen, R. W., & Sitti, M. (2013). Three dimensional motion analysis of bacteria-driven microbeads near and away from walls. *Applied Physics Letters*, 102(14), 143701.
24. Park, S. J., Park, S. H., Cho, S., Kim, D. M., Lee, Y., Ko, S. Y., ... Park, S. (2013). New paradigm for tumor theranostic methodology using bacteria-based microrobot. *Scientific Reports*, 3(1), 1–8.
25. Han, J. W., Choi, Y. J., Cho, S., Zheng, S., Ko, S. Y., Park, J. O., & Park, S. (2016). Active tumor-therapeutic liposomal bacteriobot combining a drug (paclitaxel)-encapsulated liposome with targeting bacteria (*Salmonella Typhimurium*). *Sensors and Actuators B: Chemical*, 224, 217–224.
26. Singh, A. V., Hosseindoust, Z., Park, B. W., Yasa, O., & Sitti, M. (2017). Microemulsion-based soft bacteria-driven microswimmers for active cargo delivery. *ACS Nano*, 11(10), 9759–9769.
27. Mostaghaci, B., Yasa, O., Zhuang, J., & Sitti, M. (2017). Bioadhesive bacterial microswimmers for targeted drug delivery in the urinary and gastrointestinal tracts. *Advanced Science*, 4(6), 1700058.
28. Xie, S., Zhao, L., Song, X., Tang, M., Mo, C., & Li, X. (2017). Doxorubicin-conjugated *Escherichia coli* Nissle 1917 swimmers to achieve tumor targeting and responsive drug release. *Journal of Controlled Release*, 268, 390–399.
29. Xie, S., Xia, T., Li, S., Mo, C., Chen, M., & Li, X. (2020). Bacteria-propelled microrockets to promote the tumor accumulation and intracellular drug uptake. *Chemical Engineering Journal*, 392, 123786.
30. Felfoul, O., Mohammadi, M., Gaboury, L., & Martel, S. (2011, September). *Tumor targeting by computer controlled guidance of magnetotactic bacteria acting like autonomous*

- microrobots*. In 2011 IEEE/RSJ international conference on intelligent robots and systems (pp. 1304–1308). IEEE.
31. Martel, S., Mohammadi, M., Felfoul, O., Lu, Z., & Pouponneau, P. (2009). Flagellated magnetotactic bacteria as controlled MRI-trackable propulsion and steering systems for medical nanorobots operating in the human microvasculature. *The International Journal of Robotics Research*, 28(4), 571–582.
 32. Martel, S., & Mohammadi, M. (2009, October). *A robotic micro-assembly process inspired by the construction of the ancient pyramids and relying on several thousand flagellated bacteria acting as micro-workers*. In 2009 IEEE/RSJ international conference on intelligent robots and systems (pp. 426–427). IEEE.
 33. Khalil, I. S., Pichel, M. P., Abelman, L., & Misra, S. (2013). Closed-loop control of magnetotactic bacteria. *The International Journal of Robotics Research*, 32(6), 637–649.
 34. Taherkhani, S., Mohammadi, M., Daoud, J., Martel, S., & Tabrizian, M. (2014). Covalent binding of nanoliposomes to the surface of magnetotactic bacteria for the synthesis of self-propelled therapeutic agents. *ACS Nano*, 8(5), 5049–5060.
 35. Park, B. W., Zhuang, J., Yasa, O., & Sitti, M. (2017). Multifunctional bacteria-driven microswimmers for targeted active drug delivery. *ACS Nano*, 11(9), 8910–8923.
 36. Alapan, Y., Yasa, O., Schauer, O., Giltinan, J., Tabak, A. F., Sourjik, V., & Sitti, M. (2018). Soft erythrocyte-based bacterial microswimmers for cargo delivery. *Science robotics*, 3(17).
 37. Adler, J., & Shi, W. (1988, January). *Galvanotaxis in bacteria*. In Cold Spring Harbor Symposia on quantitative biology (Vol. 53, pp. 23–25). Cold Spring Harbor Laboratory Press.
 38. Clayton, R. K. (1964). Phototaxis in microorganisms. *Photophysiology*, 2, 51–77.
 39. Paulick, A., Jakovljevic, V., Zhang, S., Erickstad, M., Groisman, A., Meir, Y., ... Sourjik, V. (2017). Mechanism of bidirectional thermotaxis in *Escherichia coli*. *eLife*, 6, e26607.
 40. Taylor, B. L., Zhulin, I. B., & Johnson, M. S. (1999). Aerotaxis and other energy-sensing behavior in bacteria. *Annual Reviews in Microbiology*, 53(1), 103–128.
 41. Felfoul, O., Mohammadi, M., Taherkhani, S., De Lanauze, D., Xu, Y. Z., Loghin, D., ... Gaboury, L. (2016). Magneto-aerotactic bacteria deliver drug-containing nanoliposomes to tumour hypoxic regions. *Nature Nanotechnology*, 11(11), 941–947.
 42. Sentürk, O. I., Schauer, O., Chen, F., Sourjik, V., & Wegner, S. V. (2020). Red/far-red light switchable cargo attachment and release in bacteria-driven microswimmers. *Advanced Healthcare Materials*, 9(1), 1900956.
 43. Makhluaf, S. B. D., Abu-Mukh, R., Rubinstein, S., Breitbart, H., & Gedanken, A. (2008). Modified PVA–Fe₃O₄ nanoparticles as protein carriers into sperm cells. *Small*, 4(9), 1453–1458.
 44. Geerts, N., McGrath, J., Stronk, J. N., Vanderlick, T. K., & Huszar, G. (2014). Spermatozoa as a transport system of large unilamellar lipid vesicles into the oocyte. *Reproductive Biomedicine Online*, 28(4), 451–461.
 45. Xu, H., Medina-Sánchez, M., Magdanz, V., Schwarz, L., Hebenstreit, F., & Schmidt, O. G. (2018). Sperm-hybrid micromotor for targeted drug delivery. *ACS Nano*, 12(1), 327–337.
 46. Magdanz, V., Khalil, I. S., Simmchen, J., Furtado, G. P., Mohanty, S., Gebauer, J., ... Schmidt, O. G. (2020). IRONSperm: Sperm-templated soft magnetic microrobots. *Science Advances*, 6(28), eaba5855.
 47. Yan, X., Zhou, Q., Yu, J., Xu, T., Deng, Y., Tang, T., ... Zhang, L. (2015). Magnetite nanostructured porous hollow helical microswimmers for targeted delivery. *Advanced Functional Materials*, 25(33), 5333–5342.
 48. Yan, X., Zhou, Q., Vincent, M., Deng, Y., Yu, J., Xu, J., ... Kostarelos, K. (2017). Multifunctional biohybrid magnetite microrobots for imaging-guided therapy. *Science Robotics*, 2(12).
 49. Wu, Z., Li, T., Li, J., Gao, W., Xu, T., Christianson, C., ... Wang, J. (2014). Turning erythrocytes into functional micromotors. *ACS Nano*, 8(12), 12041–12048.

50. Villa, C. H., Anselmo, A. C., Mitragotri, S., & Muzykantov, V. (2016). Red blood cells: Supercarriers for drugs, biologicals, and nanoparticles and inspiration for advanced delivery systems. *Advanced Drug Delivery Reviews*, *106*, 88–103.
51. Sun, X., Wang, C., Gao, M., Hu, A., & Liu, Z. (2015). Remotely controlled red blood cell carriers for cancer targeting and near-infrared light-triggered drug release in combined Photothermal–chemotherapy. *Advanced Functional Materials*, *25*(16), 2386–2394.
52. Cinti, C., Taranta, M., Naldi, I., & Grimaldi, S. (2011). Newly engineered magnetic erythrocytes for sustained and targeted delivery of anti-cancer therapeutic compounds. *PLoS One*, *6*(2), e17132.
53. Grifantini, R., Taranta, M., Gherardini, L., Naldi, I., Parri, M., Grandi, A., ... Campagnoli, S. (2018). Magnetically driven drug delivery systems improving targeted immunotherapy for colon-rectal cancer. *Journal of Controlled Release*, *280*, 76–86.
54. Erkoc, P., Yasa, I. C., Ceylan, H., Yasa, O., Alapan, Y., & Sitti, M. (2019). Mobile microrobots for active therapeutic delivery. *Advanced Therapeutics*, *2*(1), 1800064.
55. Xue, J., Zhao, Z., Zhang, L., Xue, L., Shen, S., Wen, Y., ... Ping, Q. (2017). Neutrophil-mediated anticancer drug delivery for suppression of postoperative malignant glioma recurrence. *Nature Nanotechnology*, *12*(7), 692.
56. Chu, D., Gao, J., & Wang, Z. (2015). Neutrophil-mediated delivery of therapeutic nanoparticles across blood vessel barrier for treatment of inflammation and infection. *ACS Nano*, *9*(12), 11800–11811.
57. Shao, J., Xuan, M., Zhang, H., Lin, X., Wu, Z., & He, Q. (2017). Chemotaxis-guided hybrid neutrophil micromotors for targeted drug transport. *Angewandte Chemie*, *129*(42), 13115–13119.
58. Choi, M. R., Stanton-Maxey, K. J., Stanley, J. K., Levin, C. S., Bardhan, R., Akin, D., ... Halas, N. J. (2007). A cellular Trojan horse for delivery of therapeutic nanoparticles into tumors. *Nano Letters*, *7*(12), 3759–3765.
59. Smith, B. R., Ghosn, E. E. B., Rallapalli, H., Prescher, J. A., Larson, T., Herzenberg, L. A., & Gambhir, S. S. (2014). Selective uptake of single-walled carbon nanotubes by circulating monocytes for enhanced tumour delivery. *Nature Nanotechnology*, *9*(6), 481.
60. Polak, R., Lim, R. M., Beppu, M. M., Pitombo, R. N. M., Cohen, R. E., & Rubner, M. F. (2015). *Advanced Healthcare Materials*, *4*, 2832.
61. Han, J., Zhen, J., Van Du Nguyen, G. G., Choi, Y., Ko, S. Y., Park, J. O., & Park, S. (2016). *Hybrid-actuating macrophage-based microrobots for active cancer therapy sci*.
62. Han, J., Go, G., Zhen, J., Zheng, S., Le, V. H., Park, J. O., & Park, S. (2017). Feasibility study of dual-targeting paclitaxel-loaded magnetic liposomes using electromagnetic actuation and macrophages. *Sensors and Actuators B: Chemical*, *240*, 1226–1236.
63. Huang, W. C., Chiang, W. H., Cheng, Y. H., Lin, W. C., Yu, C. F., Yen, C. Y., ... Chiu, H. C. (2015). Tumortropic monocyte-mediated delivery of echogenic polymer bubbles and therapeutic vesicles for chemotherapy of tumor hypoxia. *Biomaterials*, *71*, 71–83.
64. Stephan, M. T., Moon, J. J., Um, S. H., Bershteyn, A., & Irvine, D. J. (2010). Therapeutic cell engineering with surface-conjugated synthetic nanoparticles. *Nature Medicine*, *16*(9), 1035–1041.
65. Huang, B., Abraham, W. D., Zheng, Y., López, S. C. B., Luo, S. S., & Irvine, D. J. (2015). Active targeting of chemotherapy to disseminated tumors using nanoparticle-carrying T cells. *Science Translational Medicine*, *7*(291), 291ra94.
66. Alizadeh, S., Esmaeili, A., Barzegari, A., Rafi, M. A., & Omid, Y. (2020). Bioengineered smart bacterial carriers for combinational targeted therapy of solid tumours. *Journal of Drug Targeting*, 1–14.
67. Ricotti, L., Cafarelli, A., Iacovacci, V., Vannozzi, L., & Mencias, A. (2015). Advanced micro-nano-bio systems for future targeted therapies. *Current Nanoscience*, *11*(2), 144–160.
68. Buss, N., Yasa, O., Alapan, Y., Akolpoglu, M. B., & Sitti, M. (2020). Nanoerythrocyte-functionalized biohybrid microswimmers. *APL Bioengineering*, *4*(2), 026103.

69. Yasa, I. C., Ceylan, H., Bozuyuk, U., Wild, A. M., & Sitti, M. (2020). Elucidating the interaction dynamics between microswimmer body and immune system for medical microrobots. *Science Robotics*, 5(43).
70. Cabanach, P., Pena-Francesch, A., Sheehan, D., Bozuyuk, U., Yasa, O., Borros, S., & Sitti, M. (2020). Zwitterionic 3D-printed non-immunogenic stealth microrobots. *Advanced Materials*, 2003013.
71. Xing, J. et al. (2021). Sequential magneto-actuated and optics-triggered microrobots for targeted cancer therapy. *Adv. Funct. Mater.* 31(11): 2008262.
72. Iacovacci, V., Blanc, A., Huang, H., Ricotti, L., Schibli, R., Mencias, A., ... Nelson, B. J. (2019). High-resolution SPECT imaging of stimuli-responsive soft microrobots. *Small*, 15(34), 1900709.
73. Aziz, A., Holthof, J., Meyer, S., Schmidt, O., & Medina-Sanchez, M. (2020). *In vivo* imaging of swimming micromotors using hybrid high-frequency ultrasound and photoacoustic imaging. *bioRxiv*.
74. Liang, W., Liu, H., Wang, K., Qian, Z., Ren, L., & Ren, L. (2020). Comparative study of robotic artificial actuators and biological muscle. *Advances in Mechanical Engineering*, 12(6), 1687814020933409.
75. Golob, M., Moss, R. L., & Chesler, N. C. (2014). Cardiac tissue structure, properties, and performance: A materials science perspective. *Annals of Biomedical Engineering*, 42(10), 2003–2013.
76. Shimizu, K., Sasaki, H., Hida, H., Fujita, H., Obinata, K., Shikida, M., & Nagamori, E. (2010). Assembly of skeletal muscle cells on a Si-MEMS device and their generative force measurement. *Biomedical Microdevices*, 12(2), 247–252.
77. Karp, G. (2009). *Cell and molecular biology: Concepts and experiments*. Wiley.
78. Yin, S., Zhang, X., Zhan, C., Wu, J., Xu, J., & Cheung, J. (2005). Measuring single cardiac myocyte contractile force via moving a magnetic bead. *Biophysical Journal*, 88(2), 1489–1495.
79. Madden, J. D., Vandesteeg, N. A., Anquetil, P. A., Madden, P. G., Takshi, A., Pytel, R. Z., ... Hunter, I. W. (2004). Artificial muscle technology: Physical principles and naval prospects. *IEEE Journal of Oceanic Engineering*, 29(3), 706–728.
80. Zupan, M., Ashby, M. F., & Fleck, N. A. (2002). Actuator classification and selection – The development of a database. *Advanced Engineering Materials*, 4(12), 933–940.
81. Duffy, R. M., & Feinberg, A. W. (2014). Engineered skeletal muscle tissue for soft robotics: Fabrication strategies, current applications, and future challenges. *Wiley Interdisciplinary Reviews: Nanomedicine and Nanobiotechnology*, 6(2), 178–195.
82. Collinsworth, A. M., Zhang, S., Kraus, W. E., & Truskey, G. A. (2002). Apparent elastic modulus and hysteresis of skeletal muscle cells throughout differentiation. *American Journal of Physiology-Cell Physiology*, 283(4), C1219–C1227.
83. Xi, J., Schmidt, J. J., & Montemagno, C. D. (2005). Self-assembled microdevices driven by muscle. *Nature Materials*, 4(2), 180–184.
84. Kim, J., Park, J., Yang, S., Baek, J., Kim, B., Lee, S. H., ... Park, S. (2007). Establishment of a fabrication method for a long-term actuated hybrid cell robot. *Lab on a Chip*, 7(11), 1504–1508.
85. Park, J., Kim, I. C., Baek, J., Cha, M., Kim, J., Park, S., ... Kim, B. (2007). Micro pumping with cardiomyocyte–polymer hybrid. *Lab on a Chip*, 7(10), 1367–1370.
86. Feinberg, A. W., Feigel, A., Shevkoplyas, S. S., Sheehy, S., Whitesides, G. M., & Parker, K. K. (2007). Muscular thin films for building actuators and powering devices. *Science*, 317(5843), 1366–1370.
87. Chan, V., Park, K., Collens, M. B., Kong, H., Saif, T. A., & Bashir, R. (2012). Development of miniaturized walking biological machines. *Scientific Reports*, 2, 857.
88. Chan, V., Jeong, J. H., Bajaj, P., Collens, M., Saif, T., Kong, H., & Bashir, R. (2012). Multi-material bio-fabrication of hydrogel cantilevers and actuators with stereolithography. *Lab on a Chip*, 12(1), 88–98.

89. Nawroth, J. C., Lee, H., Feinberg, A. W., Ripplinger, C. M., McCain, M. L., Grosberg, A., ... Parker, K. K. (2012). A tissue-engineered jellyfish with biomimetic propulsion. *Nature Biotechnology*, *30*(8), 792–797.
90. Williams, B. J., Anand, S. V., Rajagopalan, J., & Saif, M. T. A. (2014). A self-propelled biohybrid swimmer at low Reynolds number. *Nature Communications*, *5*(1), 1–8.
91. Vannozi, L., Ricotti, L., Cianchetti, M., Bearzi, C., Gargioli, C., Rizzi, R., ... Menciasci, A. (2015). Self-assembly of polydimethylsiloxane structures from 2D to 3D for bio-hybrid actuation. *Bioinspiration & Biomimetics*, *10*(5), 056001.
92. Hoshino, T., Imagawa, K., Akiyama, Y., & Morishima, K. (2012). Cardiomyocyte-driven gel network for bio mechano-informatic wet robotics. *Biomedical Microdevices*, *14*(6), 969–977.
93. Shin, S. R., Jung, S. M., Zalabany, M., Kim, K., Zorlutuna, P., Kim, S. B., ... Wan, K. T. (2013). Carbon-nanotube-embedded hydrogel sheets for engineering cardiac constructs and bioactuators. *ACS Nano*, *7*(3), 2369–2380.
94. Shin, S. R., Shin, C., Memic, A., Shadmehr, S., Miscuglio, M., Jung, H. Y., ... Dokmeci, M. R. (2015). Aligned carbon nanotube-based flexible gel substrates for engineering biohybrid tissue actuators. *Advanced Functional Materials*, *25*(28), 4486–4495.
95. Yoon, J., Eyster, T. W., Misra, A. C., & Lahann, J. (2015). Cardiomyocyte-driven actuation in biohybrid microcylinders. *Advanced Materials*, *27*(30), 4509–4515.
96. Chen, Z., Fu, F., Yu, Y., Wang, H., Shang, Y., & Zhao, Y. (2019). Cardiomyocytes-actuated morpho butterfly wings. *Advanced Materials*, *31*(8), 1805431.
97. Sun, L., Chen, Z., Bian, F., & Zhao, Y. (2020). Bioinspired soft robotic caterpillar with cardiomyocyte drivers. *Advanced Functional Materials*, *30*(6), 1907820.
98. Fenno, L., Yizhar, O., & Deisseroth, K. (2011). The development and application of optogenetics. *Annual Review of Neuroscience*, *34*.
99. Park, S. J., Gazzola, M., Park, K. S., Park, S., Di Santo, V., Blevins, E. L., ... Pasqualini, F. S. (2016). Phototactic guidance of a tissue-engineered soft-robotic ray. *Science*, *353*(6295), 158–162.
100. Xu, B., Han, X., Hu, Y., Luo, Y., Chen, C. H., Chen, Z., & Shi, P. (2019). A remotely controlled transformable soft robot based on engineered cardiac tissue construct. *Small*, *15*(18), 1900006.
101. Dennis, R. G., & Kosnik, P. E. (2000). Excitability and isometric contractile properties of mammalian skeletal muscle constructs engineered in vitro. *In vitro Cellular & Developmental Biology-Animal*, *36*(5), 327–335.
102. Sun, Y., Duffy, R., Lee, A., & Feinberg, A. W. (2013). Optimizing the structure and contractility of engineered skeletal muscle thin films. *Acta Biomaterialia*, *9*(8), 7885–7894.
103. Kim, T. H., Kwon, C. H., Lee, C., An, J., Phuong, T. T. T., Park, S. H., ... Kim, S. J. (2016). Bio-inspired hybrid carbon nanotube muscles. *Scientific Reports*, *6*(1), 1–8.
104. Webster, V. A., Hawley, E. L., Akkus, O., Chiel, H. J., & Quinn, R. D. (2016). Effect of actuating cell source on locomotion of organic living machines with electrocompacted collagen skeleton. *Bioinspiration & Biomimetics*, *11*(3), 036012.
105. Hasebe, A., Suematsu, Y., Takeoka, S., Mazzocchi, T., Vannozi, L., Ricotti, L., & Fujie, T. (2019). Biohybrid actuators based on skeletal muscle-powered microgrooved ultrathin films consisting of poly (styrene-block-butadiene-block-styrene). *ACS Biomaterials Science & Engineering*, *5*(11), 5734–5743.
106. Vannozi, L., Mazzocchi, T., Hasebe, A., Takeoka, S., Fujie, T., & Ricotti, L. (2020). A coupled FEM-SPH modeling technique to investigate the contractility of biohybrid thin films. *Advanced Biosystems*, 1900306.
107. Li, Z., Seo, Y., Aydin, O., Elhebeary, M., Kamm, R. D., Kong, H., & Saif, M. T. A. (2019). Biohybrid valveless pump-bot powered by engineered skeletal muscle. *Proceedings of the National Academy of Sciences*, *116*(5), 1543–1548.
108. Tanaka, Y., Morishima, K., Shimizu, T., Kikuchi, A., Yamato, M., Okano, T., & Kitamori, T. (2006). An actuated pump on-chip powered by cultured cardiomyocytes. *Lab on a Chip*, *6*(3), 362–368.

109. Sakar, M. S., Neal, D., Boudou, T., Borochin, M. A., Li, Y., Weiss, R., ... Asada, H. H. (2012). Formation and optogenetic control of engineered 3D skeletal muscle bioactuators. *Lab on a Chip*, 12(23), 4976–4985.
110. Cvetkovic, C., Raman, R., Chan, V., Williams, B. J., Tolish, M., Bajaj, P., ... Bashir, R. (2014). Three-dimensionally printed biological machines powered by skeletal muscle. *Proceedings of the National Academy of Sciences*, 111(28), 10125–10130.
111. Raman, R., Cvetkovic, C., Uzel, S. G., Platt, R. J., Sengupta, P., Kamm, R. D., & Bashir, R. (2016). Optogenetic skeletal muscle-powered adaptive biological machines. *Proceedings of the National Academy of Sciences*, 113(13), 3497–3502.
112. Pagan-Diaz, G. J., Zhang, X., Grant, L., Kim, Y., Aydin, O., Cvetkovic, C., ... Saif, T. (2018). Simulation and fabrication of stronger, larger, and faster walking biohybrid machines. *Advanced Functional Materials*, 28(23), 1801145.
113. Morimoto, Y., Onoe, H., & Takeuchi, S. (2018). Biohybrid robot powered by an antagonistic pair of skeletal muscle tissues. *Science Robotics*, 3(18).
114. Morimoto, Y., Onoe, H., & Takeuchi, S. (2020). Biohybrid robot with skeletal muscle tissue covered with a collagen structure for moving in air. *APL Bioengineering*, 4(2), 026101.
115. Cvetkovic, C., Rich, M. H., Raman, R., Kong, H., & Bashir, R. (2017). A 3D-printed platform for modular neuromuscular motor units. *Microsystems & Nanoengineering*, 3(1), 1–9.
116. Aydin, O., Passaro, A. P., Elhebeary, M., Pagan-Diaz, G. J., Fan, A., Nuethong, S., ... Saif, M. T. A. (2020). Development of 3D neuromuscular bioactuators. *APL Bioengineering*, 4(1), 016107.
117. Aydin, O., Zhang, X., Nuethong, S., Pagan-Diaz, G. J., Bashir, R., Gazzola, M., & Saif, M. T. A. (2019). Neuromuscular actuation of biohybrid motile bots. *Proceedings of the National Academy of Sciences*, 116(40), 19841–19847.
118. Akiyama, Y., Iwabuchi, K., Furukawa, Y., & Morishima, K. (2008). Culture of insect cells contracting spontaneously; research moving toward an environmentally robust hybrid robotic system. *Journal of Biotechnology*, 133(2), 261–266.
119. Akiyama, Y., Iwabuchi, K., Furukawa, Y., & Morishima, K. (2009). Long-term and room temperature operable bioactuator powered by insect dorsal vessel tissue. *Lab on a Chip*, 9(1), 140–144.
120. Akiyama, Y., Iwabuchi, K., Furukawa, Y., & Morishima, K. (2010). Electrical stimulation of cultured lepidopteran dorsal vessel tissue: An experiment for development of bioactuators. *In vitro Cellular & Developmental Biology-Animal*, 46(5), 411–415.
121. Akiyama, Y., Odaira, K., Sakiyama, K., Hoshino, T., Iwabuchi, K., & Morishima, K. (2012). Rapidly-moving insect muscle-powered microrobot and its chemical acceleration. *Biomedical Microdevices*, 14(6), 979–986.
122. Akiyama, Y., Hoshino, T., Iwabuchi, K., & Morishima, K. (2012). Room temperature operable autonomously moving bio-microrobot powered by insect dorsal vessel tissue. *PLoS One*, 7(7), e38274.
123. Akiyama, Y., Sakuma, T., Funakoshi, K., Hoshino, T., Iwabuchi, K., & Morishima, K. (2013). Atmospheric-operable bioactuator powered by insect muscle packaged with medium. *Lab on a Chip*, 13(24), 4870–4880.
124. Baryshyan, A. L., Domigan, L. J., Hunt, B., Trimmer, B. A., & Kaplan, D. L. (2014). Self-assembled insect muscle bioactuators with long term function under a range of environmental conditions. *RSC Advances*, 4(75), 39962–39968.
125. Uesugi, K., Shimizu, K., Akiyama, Y., Hoshino, T., Iwabuchi, K., & Morishima, K. (2016). Contractile performance and controllability of insect muscle-powered bioactuator with different stimulation strategies for soft robotics. *Soft Robotics*, 3(1), 13–22.
126. Yamatsuta, E., Beh, S. P., Uesugi, K., Tsujimura, H., & Morishima, K. (2019). A micro peristaltic pump using an optically controllable bioactuator. *Engineering*, 5(3), 580–585.
127. Uesugi, K., Sakuma, Y., Akiyama, Y., Akiyama, Y., Iwabuchi, K., Okano, T., & Morishima, K. (2019). Temperature-responsive culture surfaces for insect cell sheets to fabricate a bioactuator. *Advanced Robotics*, 33(5), 219–231.

128. Yalikun, Y., Uesugi, K., Hiroki, M., Shen, Y., Tanaka, Y., Akiyama, Y., & Morishima, K. (2019, June). *Insect muscular tissue-powered swimming robot*. In *Actuators* (Vol. 8, no. 2, p. 30). Multidisciplinary Digital Publishing Institute.
129. Raman, R., Grant, L., Seo, Y., Cvetkovic, C., Gapinske, M., Palasz, A., ... Bashir, R. (2017). Damage, healing, and remodeling in optogenetic skeletal muscle bioactuators. *Advanced Healthcare Materials*, 6(12), 1700030.
130. Doss, M. X., & Sachinidis, A. (2019). Current challenges of iPSC-based disease modeling and therapeutic implications. *Cells*, 8(5), 403.

Chapter 14

Microrobots in the Gastrointestinal Tract



Ming You, Daniel Mukasa, and Wei Gao

14.1 Introduction

Robots are designed and manufactured to free human beings from hard and complicated work. Micro-/nanorobots, which are synthetic devices capable of harvesting energy for propulsion [1–4], aim to complete missions that are impossible for macroscale robots to complete. The first self-propelled millimeter-sized plate was reported by Whitesides's group in 2002 [5]. Since then, tremendous efforts have led to a number of innovative applications including microrobot-based assisted fertilization [6], water remediation [7–9], migrating against blood flow for targeted drug delivery [10], and multiple applications in gastrointestinal tract [11]. Among the many uses, *in vivo* applications like imaging, targeted drug delivery, and targeted therapy are particularly attractive since the autonomous motion of micro-/nanorobots enables incomparable advantages over conventional methods. Compared with traditional imaging agents and drug delivery systems based on passive diffusion, microrobot-based methods can complete missions more accurately and efficiently with less dosage.

Despite the great potential of microrobots in biomedical applications, there are a number of challenges that must be overcome, the greatest being propulsion in complex media [12]. Microrobots can either use self-propulsion, requiring a biocompatible fuel source [13, 14], or external propulsion, requiring large and complex equipment capable of producing an external field to propel *in vivo* [4]. Furthermore, the microrobots themselves must be capable of cargo loading, navigation in complex biological fluids, and biocompatible. Along with these requirements, micro-/nanorobots injected into blood vessels must be able to generate strong propulsive forces and navigate narrow blood vessels while in high flow rate environments to

M. You · D. Mukasa · W. Gao (✉)

Andrew and Peggy Cherng Department of Medical Engineering, California Institute of Technology, Pasadena, CA, USA

e-mail: weigao@caltech.edu

complete their tasks. In the case of those entering living bodies through oral administration, the hydrodynamic environment becomes much more moderate, but there is now an added difficulty in keeping the micro-/nanorobots mobile and active in the gastrointestinal tract. The gastrointestinal tract, including the stomach and intestines, which digests food, absorbs nutrients, and expels remaining waste, has one of the harshest chemical environments in vivo.

In this chapter, we will start with the environmental features of GI tract, followed by discussing the design strategy and propulsion of microrobots in such environment. Then representative works on microrobots propulsion and application in GI tract are highlighted and discussed and finally ends with conclusion and future prospects on the microrobots in GI tract and in other biomedical applications.

14.2 Microrobots in GI Tract: Environmental Features and Propulsion

After being chewed and swallowed, food passes through the esophagus and reaches the stomach, where it is mixed with acidic digestive juices and enzymes to break food into smaller molecules. Nutrients are then absorbed by the walls of the small intestines, and waste passes through the large intestine to be excreted out of the body [15]. As depicted in Fig. 14.1a, the pH value ranges between 1 and 3 in the presence of gastric acid and 6 and 7 in intestines [11]. In such acidic environment with multiple ion species, propulsion mechanisms based on diffusiophoresis and enzyme-assisted reactions are no longer suitable; however, those propelled by bubble-recoil mechanism can still move regardless of pH values and ionic species

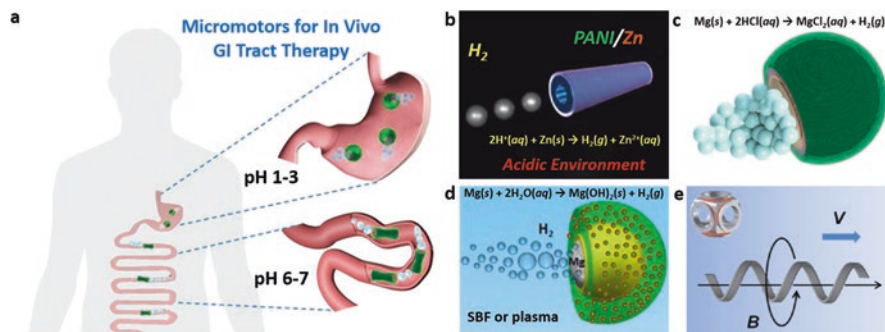
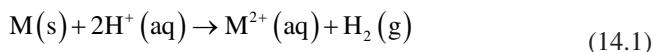


Fig. 14.1 Overview of the environmental features of GI tract and mechanisms suitable for propulsion in GI tract. (a) Schematic illustration of chemical environment in the stomach and intestines. Reproduced with permission from reference [11]. Microrobots powered by (b) zinc-acid reaction. (Reproduced with permission from reference [17]), (c) Mg-acid reaction. (Reproduced with permission from reference [18]) and (d) Mg-water reaction. (Reproduced with permission from reference [16]). (e) Magnetic microhelices powered by rotating magnetic field. Reproduced with permission from reference [27]

as long as bubbles can be generated and ejected, and the presence of ionic species may even facilitate bubble generation [16].

Thus, by taking advantages of the acidic environmental conditions, micro-/nanorobots that can propel in gastrointestinal tract have been developed. Figure 14.1b [17] and c [18] illustrates the propulsion mechanisms of metal-acid reaction-based microrobots. Metal-based microrobots use the acidic gastric acid as fuel; as Eq. (14.1) shows, reaction between acid and metal, mostly zinc and magnesium, results in generation of hydrogen bubbles; asymmetric structures allow bubble formation and ejection from one side/end of the microrobot, which propels the microrobot through bubble recoil. Besides acid corrosion, Mg-water reaction can also be used for bubble generation, as demonstrated in Fig. 14.1d [16]. Specific ionic species can facilitate the Mg-water reaction while also removing the $\text{Mg}(\text{OH})_2$ passivation layer, thus allowing the reaction to occur for a longer duration of time.



External fields including electric field [19, 20], acoustic field [21–23], light [24], and magnetic field [25, 26] can all be utilized to propel micro-/nanorobots. In the case of *in vivo* applications, noninvasive magnetic field, which can be applied from afar, has become one of the most attractive method to externally power and control micro-/nanorobots (Fig. 14.1e) [27]. The chirality of helices makes their axial rotational motion time-irreversible, thus generating net force and enabling efficient propulsion of microhelices.

14.3 Propulsion of Microrobots in GI Tract

The most intriguing feature of micro-/nanorobots is without a doubt their autonomous motion. Enhanced motion-induced mass transfer and interactions with surrounding environment endow micro-/nanorobots with incomparable advantages in applications such as targeted drug delivery and environmental remediation. Figure 14.2a shows the morphology of a zinc-based microtube with a length of $20\mu\text{m}$ and diameter of $5\mu\text{m}$. Upon immersion in simulated gastric acid (pH 1.2), the PEDOT layer protects outer zinc layer from reacting with acid. Spontaneous oxidation of the inner layer zinc component results in hydrogen bubble generation; the bubbles are ejected from one end of the microrobot, which propels the microrobot in opposite direction of bubble release (Fig. 14.2b). Figure 14.2c shows time-lapse images with 1 second interval, demonstrating the motion of a single PEDOT-Zn microrobot in gastric acid. It can be clearly observed that a bubble tail is released from one end of the microrobot, which propels it at a velocity calculated to be $60\mu\text{m/s}$ (3 body lengths/s) for ~ 10 min [28].

Janus particles are another class of microrobots that can efficiently propel through bubble recoil. Figure 14.2d is the schematic dissection of a Mg-based Janus microrobot which is designed for drug delivery in the stomach. As the figure shows,

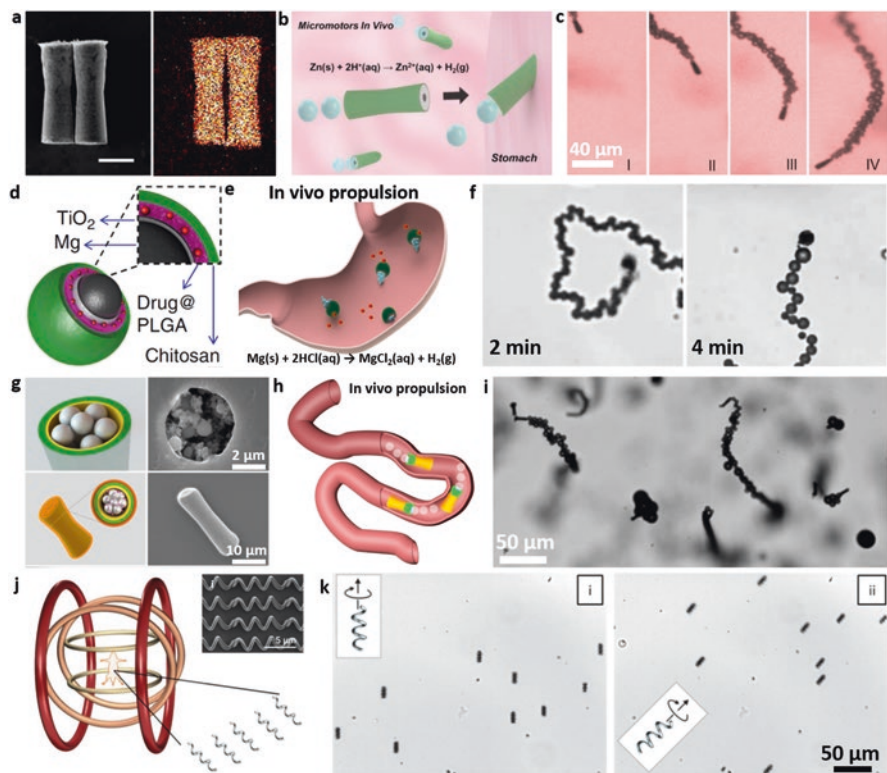


Fig. 14.2 Propulsion methods of microrobots in GI tract. (a) SEM image (left) and the corresponding EDX data (right) of elemental Zn in the PEDOT-Zn tubular microrobot, scale bar, 5 μm . (b) Schematic of the in vivo propulsion and tissue penetration of the zinc-based micromotors in mouse stomach. (c) Time-lapse images (1 s intervals, I–IV) of the propulsion of PEDOT/Zn micromotors in gastric acid under physiological temperature (37 $^{\circ}\text{C}$). (a–c) Reproduced with permission from reference [28]. (d) Schematic dissection of the Mg-based Janus microrobot with a TiO_2 shell coating, a drug-loaded PLGA layer, and a chitosan layer. (e) Schematic of in vivo propulsion in mouse stomach. (f) Time-lapse images (2 min intervals) of the propulsion of the drug-loaded Mg-based micromotors in simulated gastric fluid (pH \sim 1.3). (d–f) Reproduced with permission from reference [18]. (g) Schematic top view, side view, and corresponding SEM images of the enteric Mg microrobot. (h) Schematic of the propelling in intestines. (i) Propulsion snapshot of multiple enteric Mg microrobot in intestinal fluid. (g–i) Reproduced with permission from reference [29]. (j) Schematic of the in vivo experiment, inset: SEM image of the microhelices. (k) Snapshots of controlled swimming of the microhelices swarm in vitro under magnetic field of 9 mT and 90 Hz. (j, k) Reproduced with permission from reference [30]

the microrobot has a Mg core and is subsequently coated with TiO_2 , drug-loaded poly(lactic-co-glycolic acid) (PLGA) and chitosan layers. The TiO_2 layer acts as shell scaffold to maintain the spherical shape, while Mg is etched during propulsion. The PLGA film is loaded with drug molecules and coated onto the TiO_2 layer, which is subsequently coated by a chitosan layer to protect the PLGA layer and ensure efficient electrostatic adhesion to the mucosal layer of stomach wall. Figure 14.2e

depicts the propulsion and drug release in the stomach; reaction between Mg and gastric acid leads to hydrogen bubbles released from the opening, which propels the microrobot. The propulsion of the Mg-based microrobot is evaluated *in vitro* using simulated gastric fluid (pH 1.3); time-lapse images in Fig. 14.2f clearly show the bubble tail of the Janus microrobot and illustrate the prolonged propulsion with an average speed 120 $\mu\text{m/s}$ (6 body lengths/s). The lifetime is observed to be ~ 6 min, which is determined by the size of the opening [18].

As opposed to the stomach which has a pH between 1 and 3, intestinal fluid is much less acidic with pH between 6 and 7 creating a new set of conditions that must be considered in the microrobot fabrication process. Microrobots must however pass through stomach's acidic environment to reach the intestines and therefore must be protected from etching by gastric acid. In 2016, Wang's group demonstrated an enteric microrobot consisting of a Mg-based body with an enteric polymer coating that can pass through the stomach and arrive at predesigned location in intestines. Figure 14.2g shows the schematic and corresponding SEM images of the enteric Mg-based microrobot. During fabrication, Mg particles with a uniform diameter of 5 μm are loaded into the template-synthesized PEDOT-Au microtubes through infiltration technique, the Mg-loaded microtubes are then coated with methacrylate-based polymer Eudragit L100-55, which is used for protecting oral drug capsules from gastric acid. The polymer layer is quite stable in acidic environments, while in neutral or alkaline media, it gradually dissolves and exposes what's encapsulated. To evaluate the propulsion performance of the enteric Mg microrobot in intestines, they are immersed in intestinal fluid and observed under microscope, as shown in Fig. 14.2i. It can be seen that reaction between Mg particles in the PEDOT-Au microtubes and water in intestinal fluid results in hydrogen bubble release from one end, propelling the enteric microrobot with an average speed of 60 $\mu\text{m/s}$ for 1 min, demonstrating efficient propulsion of the microrobot via the Mg-water reaction [29].

Magnetic microswimmers have always been one of the most promising type for *in vivo* applications owing to the facts that magnetic fields are noninvasive and the motion performance of magnetic microswimmers can be controllable by adjusting external magnetic fields. Among the many types of magnetic microswimmers, microhelices attract the most attention because they can be fabricated in large scale with high quality through 3D direct laser writing (DLW) and glancing angle deposition (GLAD). Figure 14.2j illustrates the experimental setup for propelling magnetic microhelices *in vivo*. The size of the microhelices can be tailored by adjusting DLW parameters; after obtaining the microhelices, a 50-nm-thick Ni layer is coated to enable magnetic propulsion and control of the microrobot; and subsequently a 5 nm Ti layer is coated to improve biocompatibility. The microhelices dispersed in 5% dextrose are injected into the mouse, and then the anesthetized mouse is placed upside down with its lower abdominal at the center of the three-axial Helmholtz coils. Figure 14.2k demonstrates the controlled *in vitro* motion of the magnetic microhelices under rotational magnetic field generated by the Helmholtz coils. Chirality of the microhelices allows translational displacement from rotation, by alternating the magnetic field parameters such as strength, frequency, and direction;

motion behaviors of the microhelices are changed accordingly. At some circumstances, the microhelices can assemble and disassemble, which can further change their motion behaviors [30]. Tracking the in vivo motion of these microhelices requires fluorescence-based near-infrared imaging, which will be discussed in the following section.

14.4 In Vivo Imaging and Localization of Microrobots in GI Tract

Typically, microrobots must swim to some specified site and initiate a task upon arrival like releasing a drug. For this process to be effective, one must know when the microrobot is in this specified location. Tremendous efforts have been devoted to in vivo imaging to track the location of microrobots in real time. Said efforts broadly fall into two categories, molecular visualization techniques such as optical imaging (fluorescence and bioluminescence), positron emission tomography (PET), and single proton emission computed tomography (SPECT) and anatomical imaging including ultrasound imaging, magnetic resonance imaging (MRI), and computed tomography (CT). In this section, various in vivo imaging methods for tracking microrobots are introduced, which lays the foundation for their in vivo applications.

Optical imaging is a relatively simple method to locate a target in vivo since it does not require any complex devices or modifications of the target. Figure 14.3a illustrates a Mg-based microrobot powered by gastric acid neutralization. The microrobot has a Mg core which, when introduced into the stomach, rapidly consumes local protons for efficient bubble propulsion and neutralizes gastric acid. The Mg-based microrobot is coated with a pH-responsive polymer and loaded with fluorescent molecules (model drug). 20 minutes after entering the mouse stomach through oral administration, the stomach was excised and cut open for imaging. The results demonstrate simultaneous propulsion of the microrobot and efficient acid neutralization, thus yielding pH-responsive drug release within the entire stomach, as the superimposed fluorescence images shown in Fig. 14.3b [31].

The aforementioned method requires the subject be cut open, which is obviously impractical. Therefore, harmless methods have been investigated. In a paper published by Nelson's group in 2015, helical structures subsequently coated with Ni and Ti and then modified with NIR-emitting fluorophore to monitor their motion in vivo (Fig. 14.3c). A mouse injected with fluorescent helical microswimmers was anesthetized and placed inside the 3D magnetic coils, and a fluorescent signal was detected in the mouse body where the microswimmer swarms were injected. Then a rotational magnetic field was applied to actuate the microswimmers, and their location was recorded by capturing images every minute. The fluorescent images showed controlled motion under magnetic actuation [30].

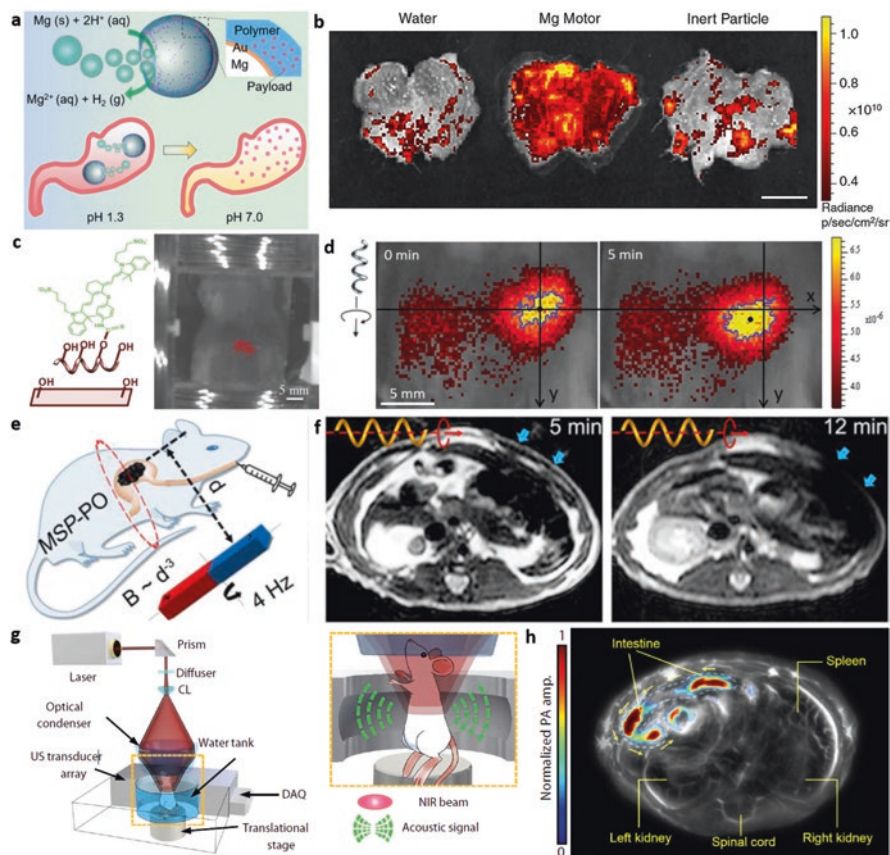


Fig. 14.3 In vivo imaging and localization of microrobots in GI tract. (a) Intragastric administration of magnetized *Spirulina platensis* (MSP) and schematic of magnetic actuation. (b) MR imaging across the rat's stomach of MSP swarm with the same concentration but subject to actuation and steering (with a rotating magnetic field) of different time periods. (a, b) Reproduced with permission from reference [31]. (c) Illustrations of an Mg-based micromotor powered by Mg-acid reaction and its acid neutralization mechanism. (d) Superimposed fluorescent images, of the whole stomach of mice, collected 20 min post administration of DI water, Mg micromotors, and inert PS microparticles. (c, d) Reproduced with permission from reference [30]. (e) Schematic of photoacoustic computed tomography (PACT) of the microcapsules in the GI tract in vivo. (f) PACT image of the microcapsules in intestines. (e, f) Reproduced with permission from reference [32]. (g) Microhelices coupled with NIR-797 molecule for NIR imaging and image of an anesthetized mouse inside the magnetic coils; red spots represent the fluorescent signal of modified microhelices. (h) Fluorescence images demonstrating the displacement of a swarm of microhelices in vivo. (g, h) Reproduced with permission from reference [33]

Another common noninvasive imaging method is magnetic resonance (MR) imaging. In the work by Zhang's group in 2017, *Spirulina platensis*, a microalgae subspecies with helical shapes, is bonded with Fe_3O_4 nanoparticles through dip-coating method. Fe_3O_4 nanoparticles are chosen due to their MR contrast and low

cytotoxicity. Figure 14.3e illustrates the experiment for *in vivo* propulsion of the microhelices. Intra-gastric administration is used to deliver the microhelices into the stomachs of rats, followed by magnetic actuation by a rotating permanent magnet for different time durations. Figure 14.3f shows the cross-sectional MR images of the rats after magnetic actuation of 5 and 12 min of the microhelices. Emergence of susceptibility artifacts close to the subcutaneous tissue is observed (indicated by blue arrows), which confirms the presence of the microhelices. The difference between susceptibility artifacts indicates that the microhelices prove that the microhelices were efficiently actuated toward desired direction [32].

Photoacoustic computed tomography (PACT) has advantages of high spatiotemporal resolution, noninvasiveness, molecular contrast, and deep penetration, which makes it attractive for locating and guiding microrobots *in vivo*. Gao's group demonstrated a PACT-guided microrobotic system for targeted navigation in intestines *in vivo*. The Mg-based Janus microrobots are encapsulated in enteric coating to form a microrobot capsule (MC). The MCs dispersed in water were orally administered into mice, which were then anesthetized and placed inside the PACT device for further imaging (Fig. 14.3g); the result is shown in Fig. 14.3h [33]. The blood vessels and background tissues are shown in gray, and the highlighted colors indicate MCs in intestines. In addition, PACT could distinguish the signals from the slowly migrating MCs in the intestines, indicating this method could effectively track the location of the MCs in deep tissues *in vivo*.

14.5 Enhanced Retention and Navigation of Microrobots in GI Tract

From the previous two sections, we now understand quite well the various environments microrobots must traverse in the GI tract. After ingestion, they enter the esophagus, then the acidic stomach, and finally the less acidic intestines. Along the way the epithelial tissues of GI tract produce large amount of mucin glycoprotein, which forms a viscoelastic gel (mucus) under acidic conditions. This mucus has dual functionality in that it both protects the GI tract from acid and pathogens which may attempt to penetrate the epithelial tissue. Consequentially however microrobots can also be trapped in this gel. This both offers the opportunity for microrobotic retention in mucus and necessitates modified propulsion mechanisms to navigate this complex media.

As Fig. 14.4a illustrates, bubble-propelled Zn tubular microrobots swim in the bulk and get trapped in mucus. Microscopic images in Fig. 14.4b then show retained microrobots in the stomach tissues 2 h after oral administration where inactive PEDOT/Pt microtubes that do not exhibit autonomous motion were used as the control. The microscopic images clearly indicate that the autonomous propulsion of PEDOT/Zn microrobot greatly improved their mucus penetration and thus retention in the stomach. Further experiments reveal the retention of PEDOT/Zn after 6 and

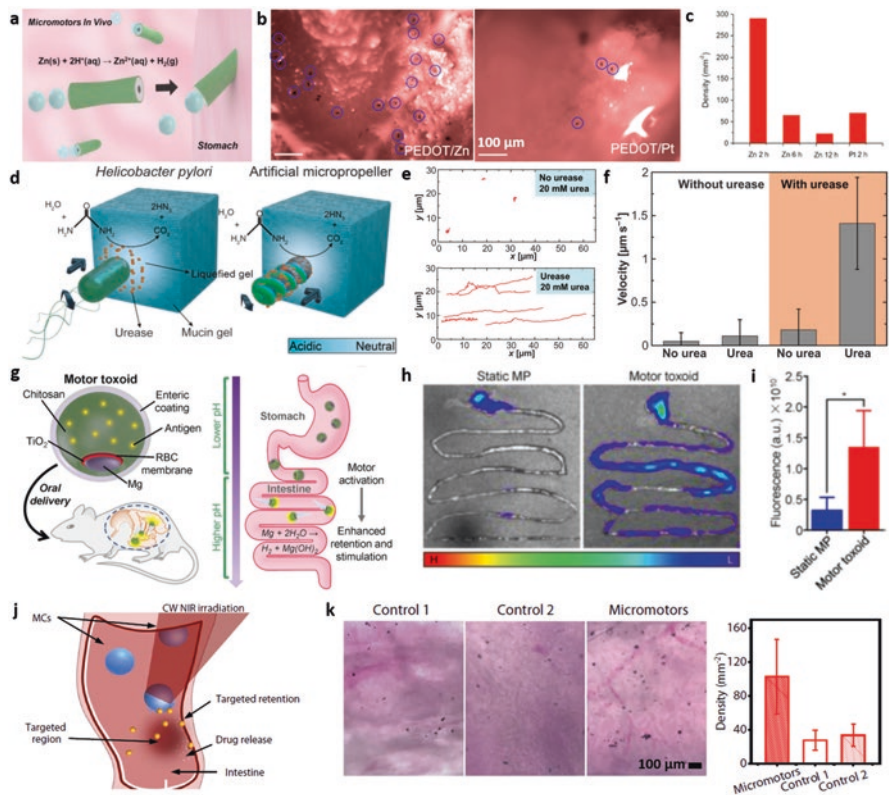


Fig. 14.4 Enhanced retention of microrobots in GI tract. **(a)** Schematic of the propulsion and tissue penetration of the Zn-based tubular robot. **(b)** Microscopic images of the stomach tissue 2 h after oral administration of PEDOT/Zn (left) and PEDOT/Pt (right) microrobots. **(c)** Enumeration of the density of PEDOT/Zn and PEDOT/Pt micromotors retained on the stomach tissues at the different times after the administration. **(a–c)** Reproduced with permission from reference [28]. **(d)** Schematic illustrating of the propulsion mechanism of *H. pylori* and the catalytically active magnetic micropropellers through mucin gels. **(e)** Trajectories of the helical microrobot propelling in an acidified 2% mucin gel with 20 mM urea with (lower panel) and without (upper panel) urease immobilized on the microrobot surface. **(f)** Average velocity of the helical microrobot of different surface modification and environmental conditions. **(d–f)** Reproduced with permission from reference [34]. **(g)** Schematic showing the composition and the behaviors of the microrobot toxinoids in GI tract after oral administration. **(h)** Fluorescence images of the GI tract of mice 6 h after oral administration of DiD-labeled static microparticles or microrobot toxinoids (*H* high fluorescence, *L* low fluorescence). **(i)** Quantification of the fluorescence from **(h)** ($n = 3$, mean + SD). **(g–i)** Reproduced with permission from reference [35]. **(j)** Schematic of the PACT-guided microrobotic system for targeted drug delivery in intestines. **(k)** Microscopic images showing the in vivo retention of the control microparticles and the micromotors in intestines (left) and the quantitative analysis of the particle retention in intestines (right). Control 1, paraffin-coated Mg; Control 2, Mg/Au microparticles. **(j, k)** Reproduced with permission from reference [33]

12 h demonstrating the microrobots retention capability even at 12 h after administration and indicating the motion-enhanced effective retention in the stomach (Fig. 14.4c) [28].

As it is well-known, there are pathogens in GI tract with the ability to overcome the mucus barrier. *H. pylori*, for example, a flagellated bacterium which can cause peptic ulcer disease and gastritis, can locally and reversibly manipulate mucus. The urease secreted by *H. pylori* can actively reduce local mucus viscosity to facilitate propulsion. Inspired by *H. pylori*, Fischer's group demonstrates an artificial magnetic microrobot system that can propel through gastric mucus. Figure 14.4d illustrates the design and propulsion mechanism of the microrobot system in gastric mucus. Urease immobilized on the microhelices catalyzes the hydrolysis of urea; the product ammonia results in a local pH rise, which subsequently induces the gel-sol transition of mucus; the liquefied mucus can no longer trap pathogens or microrobots, thus allowing enhanced local propulsion. Figure 14.4e shows the trajectories of the microhelices propelling in an acidified 2% mucin gel with 20 mM urea during a period of 25 s. Compared with microhelices without urease immobilized on the surface, those with urease exhibit apparent propulsion under the same condition, indicating the enhanced propulsion enabled by urease. Figure 14.4f shows the average velocity of the microhelices under different conditions, which further confirms that microhelices modified with urease can locally liquefy urea-containing mucus and thus propel in it [34].

Microhelices that can actively manipulate mucus offer a new strategy for improving drug delivery efficiency in GI tract. For instance, microrobots powered by external fields can be controlled to penetrate into mucus and then stay trapped by removing the external stimuli. The mucus protects the drug from gastric acid, and the liquefied mucus can improve drug diffusion process. There are also those with autonomous propulsion which can propel in all directions and subsequently penetrate into mucus, retaining their locations for further drug release and improving delivery efficiency.

The two systems discussed above detail microrobotic application in the stomach, but for intestinal application further considerations are needed. To protect the microrobots from extreme acidic environment in the stomach, enteric coating is an effective method. Figure 14.4g shows the composition of an enteric-coated Mg microrobot toxoids and how they pass through the stomach to reach intestines for antigen release. The enteric coating layer protects the Mg core until they reach intestines; the autonomous propulsion of activated microrobots enables penetration into intestinal walls; enhanced retention of the microrobot toxoids in intestines is illustrated in Fig. 14.4h. In the GI tract of the mouse administered with static microparticles, the fluorescence signal is mainly observed in the stomach, while in the case of the mouse with microrobot oral intake, fluorescence signal is highly present within the intestinal region. Figure 14.4i is the quantitative analysis of the total fluorescence within the gastrointestinal tract, which further confirms the enhanced retention of the motor toxoids in intestines [35].

Besides the enteric coating, another method to protect the microrobots is using a polymer layer that will collapse under external stimuli. Figure 14.4j illustrates the

PACT-guided microrobotic system for drug delivery in intestines. Once the microcapsules reached intestines and continuous wave near-infrared irradiation is turned on, the Au layer convert NIR energy into heat, which results in gel-sol transition of the gelatin-based capsule to release the microrobots trapped inside. Figure 14.4k shows microscopic images and quantitative analysis showing the retention of the microrobots and control particles; compared with passive particles, the PACT-guided microrobotic system exhibits apparent enhanced retention in intestines, which is promising for in vivo drug delivery [33].

14.6 In-Stomach Application of Microrobots: Cargo Delivery and Therapy

Autonomous motion of microrobots allows their penetration into mucus and thus enhanced retention in the stomach and intestinal walls, which is a distinct advantage of microrobot-based drug delivery. Following the in-stomach retention experiment in Fig. 14.4b, the drug delivery capacity of the PEDOT/Zn tubular microrobot is evaluated. As Fig. 14.5a shows, the tubular microrobot is loaded with Au nanoparticles as model drug, and no obvious difference is observed in the propulsion behaviors between the Au NP-loaded and unloaded ones. A group of mice are orally administered with Au NP-loaded microrobots; Au NPs and regular PEDOT/Zn microrobot are administered as control group. 2 hours post administration,

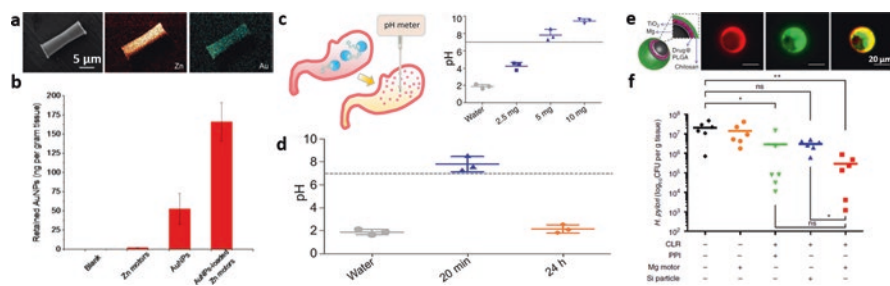


Fig. 14.5 In stomach applications of microrobots. (a) SEM image and EDX analysis of the PEDOT/Zn microrobot loaded with Au nanoparticles. (b) ICP-MS analysis of the amount of payload (Au NPs) on the stomach tissues. (a, b) Reproduced with permission from reference [28]. (c) Schematic illustration of in vivo gastric acid neutralization process by Mg-based microrobot. (d) In vivo gastric pH values of the stomachs of mice administered with different amounts of Mg microrobots. (c, d) Reproduced with permission from reference [31]. (e) Schematic dissection of the Mg-based microrobot and fluorescence images showing the dye-loaded micromotors in the DiD channel (Red, PLGA layer), j FITC channel (Green, chitosan layer), along with an overlay of the two channels (right panel). (f) Quantification of bacterial burden in the stomach of *H. pylori*-infected mice treated with DI water (black color), bare Mg-based microrobots (orange color), free CLR + PPI (green color), CLR-loaded silica microparticles (blue color), and CLR-loaded Mg-based microrobots (red color), respectively. (e, f) Reproduced with permission from reference [18]

inductively coupled plasma-mass spectrometry is used to quantify the amount of Au NPs retained on the stomach tissues. As Fig. 14.5b shows, on the stomach tissues of the mouse administered with Au NP-loaded microrobot, the Au NP retention is significantly larger than that of the mouse administered with equivalent amount of naked Au NPs. The results clearly indicate that autonomous motion-induced retention of microrobot in stomach tissues can effectively improve drug delivery. The model drug can be replaced by real drugs or imaging agents for practical application; what's more, the zinc-based microrobot can self-destroy after completing delivery task, leaving no residues to be dealt with [28].

The bubble propelled microrobots in stomach obtain propulsion force from metal-acid reactions; the reactions generate bubbles by consuming protons, which can lead to pH increase in the stomach. Figure 14.5c demonstrates the gastric acid neutralization by Mg-based microrobot. Different amounts of Mg microrobots are administered to four groups of mice; 20 min post oral administration, the mice were euthanized; and a microelectrode sensor coupled with a pH meter was used to measure their stomach pH values immediately. The results shown in the right panel of Fig. 14.5c clearly show a pH change which is dependent on the microrobot dosage. At the dosage of 5 mg, the consumption of protons in the stomach by microrobots results in about neutral pH 7.81 ± 0.38 ; the control group administered with DI water further confirms that the Mg microrobots can effectively consume protons in the stomach [31].

The stomach pH neutralization induced by microrobots can be utilized for in-stomach applications. In this paper, Mg microrobots are coated with a payload-encapsulated in a pH-responsive polymer layer which can survive the acidic environment and dissolves in media with pH > 5.5. Upon neutralization of gastric acid, the dissolution of the polymer layer leads to payload release. This microrobots' ability to transiently adjust local stomach pH offers a new strategy for controlled drug delivery and release in the stomach.

Work from the Wang group demonstrates antibiotic drug-loaded Mg microrobot for in vivo treatment of stomach infection. Left panel in Fig. 14.5e illustrates the composition of the Mg-based microrobot. A Mg core is covered by a thin TiO₂ layer, drug-loaded PLGA layer, and chitosan polymer layer, respectively, to obtain the Janus Mg microrobot. The chitosan layer is deposited to ensure efficient electrostatic adhesion to the mucosal layer of stomach walls and to protect the antibiotic drug clarithromycin (CLR, drug for *H. pylori* infection) from gastric acid. The fluorescence images indicate the polymer layers are successfully deposited. Autonomous propulsion of the Mg microrobot allows them to migrate in all directions, and the positively charged chitosan layer enables better adhesion of the stomach walls, facilitating the release of CLR from the PLGA coating.

Owing to the fact that gastric acid can weaken the effectiveness of antibiotics, antibiotic treatment is combined with proton pump inhibitors (PPIs) to reduce the production of gastric acid. But long-term use of PPIs can lead to multiple adverse effects. In the case of antibiotic-loaded Mg-based microrobot, the Mg-acid reaction could actively consume protons to increase local pH value, which can effectively protect the antibiotics from gastric acid. Quantification of the in vivo treatment

results of *H. pylori* infection with CLR-loaded Mg microrobot is shown in Fig. 14.5f. The bacterial burden in the mouse stomach is not statistically different from that observed in a mouse administered with DI water (2.1×10^7 CFU g⁻¹, black color), bare Mg-based microrobots (1.4×10^7 CFU g⁻¹, orange color), and CLR-loaded silica microparticles (3×10^6 CFU g⁻¹, blue color). In contrast, CLR-loaded Mg microparticles lead to a significant bacterial burden decrease (2.9×10^5 CFU g⁻¹, red color); compared with the group treated with free CLR + PPI (2.8×10^6 CFU g⁻¹, green color), the drug-loaded microrobot showed better efficacy [18]. The difference can be attributed to the autonomous motion of microrobots which can actively deliver antibiotics to the whole stomach. These findings indicate that the antibiotic-loaded Mg microrobots can actively deliver antibiotics to the stomach for infection treatment without using PPIs, which paves the way for practical application of microrobots active drug delivery for in vivo treatment of diseases.

Microrobots based on metal-acid reaction with autonomous propulsion can achieve enhanced retention in the stomach and have the ability to actively adjust local pH values without causing noticeable toxicity; compared with conventional methods, these types of microrobots provide new methods of in vivo drug delivery with advantages of enhanced efficiency and efficacy, which may inspire new generation of in vivo drug delivery system.

14.7 Intestinal Application of Microrobots: Cargo Delivery

The small intestine is a part of GI tract where over 90% of food digestion and absorption occurs. The main function of the small intestine is to absorb nutrients and minerals from food; thus intestinal disease may have severe consequences. Considering the function of intestines, targeted delivery of payload into intestines may significantly improve delivery efficiency. Figure 14.6a illustrates the targeted delivery of mineral into the intestine using Mg microrobot as carrier. Fe and Se are combined as a model mineral payload and loaded onto the Mg microrobot via a chitosan coating. The microrobot is further coated with a pH-responsive enteric coating to protect the inner layer from gastric acid. The mineral-loaded Mg microrobots pass through the stomach to reach intestines; enteric coating gradually dissolves in the weakly acidic intestinal fluid to allow mineral release into intestines. Figure 14.6b shows the release profiles of Fe and Se in the intestines from the Fe/Se-loaded Mg microrobots. After treated with the microrobots, the ⁵⁶Fe content in the blood increased to $391 \pm 23 \mu\text{g/g}$, which is significantly higher than the other control groups, including the free ion, unprotected motor, passive particle, and PBS groups (left panel); similar results can be obtained for the ⁷⁸Se content (right panel) [36]. The Mg microrobot platform shows no in vivo toxicity, which offers an attractive approach toward alleviating nutrition deficiencies and active drug delivery in the intestines.

In Fig. 14.3g, the DOX-loaded microrobots encapsulated in microcapsules can be guided by PACT to reach intestines for CW NIR-triggered controlled release, as

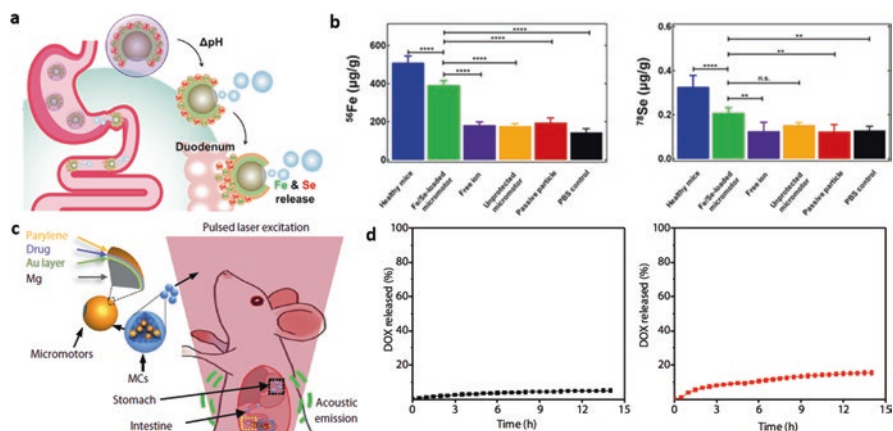


Fig. 14.6 In-intestine applications of microrobots. **(a)** Schematic of micromotor-based in vivo delivery and release of Fe and Se at the duodenum region. **(b)** Elemental ^{56}Fe ($\mu\text{g/g}$) (left) and ^{78}Se ($\mu\text{g/g}$) (right) content of whole blood for each group of mice. **(a, b)** Reproduced with permission from reference [37]. **(c)** Schematic illustration of the PACT-guided microrobotic system in the GI tract. **(d)** Profile of drug (DOX) release from the microcapsules (left) and the Mg microrobots (right). **(c, d)** Reproduced with permission from reference [33]

shown in Fig. 14.6c. After being released from the capsules, the DOX-loaded Mg microrobots are activated, and autonomous propulsion aids in obtaining enhanced retention of the microrobots in intestine walls for drug release. Figure 14.6d shows the release profiles of the DOX-loaded microcapsules (left panel) and DOX-loaded micromotors (right panel) [33], the higher release rate observed in the DOX-loaded microrobots indicates the potential of the system being used for controlled in vivo targeted drug delivery for treatment of intestinal diseases.

Compared with the stomach, the intestinal environment is much less acidic. By using responsive coatings, microrobots can be protected from gastric acid to reach intestines for further actions. The fact that intestines absorb over 90% of nutrients and minerals makes intestines the ideal location for targeted delivery of therapeutic drugs and essential minerals. Combined with the autonomous propulsion and enhanced retention of microrobots in the intestines, the payload delivery efficiency and efficacy can be significantly increased.

14.8 Biocompatible and Biodegradable

To complete tasks in vivo, the system must be biodegradable or biocompatible, or at least nontoxic to the organism. Tremendous efforts have been devoted into the biodegradability/biocompatibility of microrobots for in vivo use. Generally, Mg and Zn micro-/nanoparticles are used as core, and degradable materials are used to carry payloads or protect the metal core. In the case of microrobots propelling in GI tract,

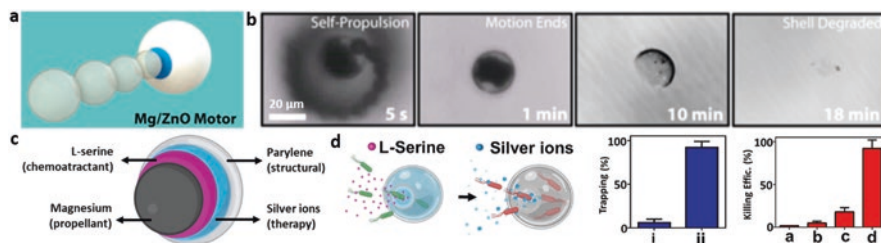


Fig. 14.7 Biodegradable/biocompatible microrobots. (a) Schematic of the Mg/ZnO Janus microrobot. (b) Time-lapse images of the motion and degradation of a typical Mg/ZnO Janus microrobot in 0.5 M NaHCO₃ solution. (a, b) Reproduced with permission from reference [37]. (c) Schematic of the Mg-based onion-like microrobot. (d) Schematic and statistical plots of the enhanced pathogen trapping and Ag⁺-driven killing of pathogens. (c, d) Reproduced with permission from reference [38]

usually metal cores are depleted within several or tens of minutes, and then the outer loading layer and/or protective layer is left to degrade in gastrointestinal fluid. Figure 14.7a illustrates the structure of a Mg microrobot with ZnO coating; its autonomous propulsion and degradation process in 0.5 M NaHCO₃ solution is shown in Fig. 14.7b. Mg-water reaction quickly depletes magnesium for bubble propulsion, and then the ZnO shell degraded after 18 min. OH⁻ in NaHCO₃ solution facilitates the degradation of ZnO; in the case of neutral or acidic media, the shell can also fully degrade [37]. This structure requires further functionalization for biomedical or environmental use, but the transient platform with fast self-destruction ability offers insight into future development of biocompatible and biodegradable drug carriers for in vivo applications.

On the basis of the transient Mg microrobots, an onion-like microrobot for trapping and killing pathogens is demonstrated. Figure 14.7c shows the composition of the onion-like microrobot. Mg core is subsequently coated with biodegradable transient EUDRAGIT S-100 and PVP layers which are loaded with L-serine and silver nitrate, respectively. Finally, a parylene layer is coated to protect the inner polymer layers. When exposed to gastric acid, depletion of Mg cores leaves the microrobots with hollow cavities which serve as traps with small openings. Subsequent dissolution of inner transient layers leads to release of the chemoattractant L-serine and Ag⁺ ions, which can attract motile pathogens to accumulate in the cavities and trapped inside and then killed by the Ag⁺ ions released (Fig. 14.7d). The microrobots loaded with chemoattractant presented 89% area occupied by pathogens, which is significantly higher than that of bare microtraps (7%). The killing efficiency of the pathogens is also evaluated, the chemoattractant and Ag⁺-loaded microrobots showed killed 94% of pathogens. After completing pathogen trapping and killing, the transient layers and the protective parylene layer can gradually degrade, leaving no residue to be cleaned [38].

This transient Mg microrobot platform that is capable of attracting, trapping, and killing pathogens presents a big step toward the communication between artificial microrobots and motile microorganism, which can be applied to fields such as

environmental remediation and infection treatment. For synthetic microrobots, material selection is important for improving biocompatibility and biodegradability. Mg or Zn cores can be used safely in the GI tract, but further consideration must be given to any external layers to assure both biocompatibility and biodegradability. Furthermore, for practical applications, one must consider the functionality, cost, and large-scale production of the microrobots as a whole.

14.9 Conclusion and Future Prospects

In this chapter, we have summarized and discussed the progress of microrobots for propulsion and application in GI tract. Both metal-acid reaction-based and external field-powered microrobots exhibit efficient propulsion in GI tract without requiring additional fuel, which allows penetration into mucus and thus enhanced retention in the gastrointestinal walls. In the case of the metal-based microrobots, after depletion of the metal core, the nontoxic residues are gradually degraded. Microhelices powered by magnetic field can be recollected after task completion if they do not easily degrade. Utilizing the medical imaging technologies, the location of ingested microrobots in GI tract can be tracked, by tracking the location of the microrobots, controlled release of drugs can be implemented more precisely for better efficacy. Microrobots with the ability to load, transport, and release payloads on demand make them ideal carriers for in vivo drug delivery. Combined with their autonomous propulsion, enhanced retention in gastrointestinal walls, and excellent biocompatibility/biodegradability, microrobots that are capable of operating in GI tract are considered promising for targeted payload delivery in GI tract for applications such as mineral supplement and disease treatment.

Despite their tremendous potential in active payload delivery in GI tract, there are still challenges to be addressed before large-scale application. In the case of metal-based microrobots toward GI tract applications, the most challenging one is the fabrication of microrobots, which is also a challenge all microrobots are confronted with. Current fabrication methods for microrobots involves multiple procedures, yet with low yield, consecutive coating of drug loading layer and protective layer onto the metal spheres can only be done in small batch. Simple fabrication and easy functionalization which allows customization according to different application scenarios will be the future direction of fabrication of microrobots.

Another challenge is the lifetime of the microrobots; the lifetime of microrobots based on metal-acid reaction ranges between several and tens of minutes, which is sufficient for applications in stomach, but for intestinal applications, the lifetime is too short considering the fact that the small intestine length of an adult is about 6.7 m; a balance between propulsion force and lifetime must be reached. There are more challenges current microrobots are facing, including higher cargo loading capability for enhancing efficacy, precise targeted release of cargo, and evaluation of long-term toxicity of the microrobots. Possible solutions are to use new biocompatible responsive materials for loading cargoes and combine with in vivo imaging

methods and external stimulus, which allows the microrobots to release cargo in response to external stimulus upon arriving target locations.

After confronting material selection and fabrication of metal-based microrobots, different propulsion mechanisms for the microrobot must be considered. One potential direction is to design biohybrid microrobots. By modifying motile microorganisms that already exist in GI tract, the natural part serves as power source and the artificial part for functionalization. The advantages are that no additional fuel is needed and the motile microorganisms can migrate toward their favorable regions, for example, the motile that *H. pylori* can liquefy and swim in mucus. Taking advantage of the biological chemotaxis, by selecting appropriate microorganism, the efficiency of targeted cargo delivery can be further increased. Modifying microorganisms can be a rather difficult and inefficient task. An alternative could be designing and fabricating functional microrobots with artificial chemotactic behaviors for application in GI tract. Although this alternative could be very intriguing, it too may be rather difficult.

Active cargo delivery in GI tract is only one potential application for microrobots. Their motion-induced advantages over conventional delivery systems based on passive diffusion makes them attractive for drug delivery to other parts of the body. Hereby we offer our humble opinions on the future prospects of microrobots for in vivo applications. Despite the fact that there are a lot of challenges to be addressed, we see great potential in microrobots for in vivo applications and hope this chapter will inspire new ideas and put microrobots into practical in vivo applications.

Acknowledgments This work was supported by grants from the National Science Foundation (Grant No. 1931214) and Caltech Space-Health Innovation Fund by Translational Research Institute for Space Health.

References

1. Sengupta, S., Ibele, M. E., & Sen, A. (2012). Fantastic voyage: Designing self-powered nanorobots. *Angewandte Chemie, International Edition*, *51*, 8434–8445.
2. Wang, J. (2013). *Nanomachines: Fundamentals and applications*. Wiley.
3. Sánchez, S., Soler, L., & Katuri, J. (2015). Chemically powered micro- and nanomotors. *Angewandte Chemie International Edition*, *54*, 1414–1444.
4. Xu, T., Gao, W., Xu, L. P., Zhang, X., & Wang, S. (2017). Fuel-free synthetic micro-/nanomachines. *Advanced Materials*, *29*, 1603250.
5. Ismagilov, R. F., Schwartz, A., Bowden, N., & Whitesides, G. M. (2002). Autonomous movement and self-assembly. *Angewandte Chemie International Edition*, *41*, 652–654.
6. Medina-Sánchez, M., Schwarz, L., Meyer, A. K., Hebenstreit, F., & Schmidt, O. G. (2016). Cellular cargo delivery: Toward assisted fertilization by sperm-carrying micromotors. *Nano Letters*, *16*, 555–561.
7. Gao, W., Feng, X., Pei, A., Gu, Y., Li, J., & Wang, J. (2013). Seawater-driven magnesium based Janus micromotors for environmental remediation. *Nanoscale*, *5*, 4696–4700.
8. Jurado-Sánchez, B., Sattayasamitsathit, S., Gao, W., Santos, L., Fedorak, Y., Singh, V. V., Orozco, J., Galarnyk, M., & Wang, J. (2015). Self-propelled activated carbon Janus micromotors for efficient water purification. *Small*, *11*, 499–506.

9. Pan, D., Mou, F., Li, X., Deng, Z., Sun, J., Xu, L., & Guan, J. (2016). Multifunctional magnetic oleic acid-coated MnFe_2O_4 /polystyrene Janus particles for water treatment. *Journal of Materials Chemistry A*, 4, 11768–11774.
10. Alapan, Y., Bozuyuk, U., Erkok, P., Karacakol, A. C., & Sitti, M. (2020). Multifunctional surface microrollers for targeted cargo delivery in physiological blood flow. *Science Robotics*, 5.
11. de Ávila, B. E. F., Angsantikul, P., Li, J., Gao, W., Zhang, L., & Wang, J. (2018). Micromotors go in vivo: from test tubes to live animals. *Advanced Functional Materials*, 28, 1705640.
12. Wu, Z., Chen, Y., Mukasa, D., Pak, O. S., & Gao, W. (2020). Medical micro/nanorobots in complex media. *Chemical Society Reviews*.
13. Gao, W., Pei, A., & Wang, J. (2012). Water-driven micromotors. *ACS Nano*, 6, 8432–8438.
14. Chen, C., Karshalev, E., Guan, J., & Wang, J. (2018). Magnesium-based micromotors: Water-powered propulsion, multifunctionality, and biomedical and environmental applications. *Small*, 14, 1704252.
15. Kong, F., & Singh, R. P. (2008). Disintegration of solid foods in human stomach. *Journal of Food Science*, 73, R67–R80.
16. Mou, F., Chen, C., Zhong, Q., Yin, Y., Ma, H., & Guan, J. (2014). Autonomous motion and temperature-controlled drug delivery of Mg/Pt-poly(N-isopropylacrylamide) Janus micromotors driven by simulated body fluid and blood plasma. *ACS Applied Materials & Interfaces*, 6, 9897–9903.
17. Gao, W., Uygun, A., & Wang, J. (2012). Hydrogen-bubble-propelled zinc-based microrockets in strongly acidic media. *Journal of the American Chemical Society*, 134, 897–900.
18. de Ávila, E.-F. B., Angsantikul, P., Li, J., Lopez-Ramirez, M. A., Ramirez-Herrera, D. E., Thamphiwatana, S., Chen, C., Delezuk, J., Samakapiruk, R., Ramez, V., Obonyo, M., Zhang, L., & Wang, J. (2017). Micromotor-enabled active drug delivery for in vivo treatment of stomach infection. *Nature Communication*, 8, 1–9.
19. Liang, Z., & Fan, D. (2018). Visible light-gated reconfigurable rotary actuation of electric nanomotors. *Science Advances*, 4, eaau0981.
20. Liang, X., Mou, F., Huang, Z., Zhang, J., You, M., Xu, L., Luo, M., & Guan, J. (2020). Hierarchical microswarms with leader-follower-like structures: Electrohydrodynamic self-organization and multimode collective Photoresponses. *Advanced Functional Materials*, 30, 1908602.
21. Wang, W., Castro, L. A., Hoyos, M., & Mallouk, T. E. (2012). Autonomous motion of metallic microrods propelled by ultrasound. *ACS Nano*, 6, 6122–6132.
22. Aghakhani, A., Yasa, O., Wrede, P., & Sitti, M. (2020). Acoustically powered surface-slipping mobile microrobots. *Proceedings of the National Academy of Science USA*, 117, 3469–3477.
23. Ren, L., Nama, N., McNeill, J. M., Soto, F., Yan, Z., Liu, W., Wang, W., Wang, J., & Mallouk, T. E. (2019). 3D steerable, acoustically powered microswimmers for single-particle manipulation. *Science Advances*, 5, eaax3084.
24. Xu, L., Mou, F., Gong, H., Luo, M., & Guan, J. (2017). Light-driven micro/nanomotors: From fundamentals to applications. *Chemical Society Reviews*, 46, 6905–6926.
25. Dreyfus, R., Baudry, J., Roper, M. L., Fermigier, M., Stone, H. A., & Bibette, J. (2005). Microscopic artificial swimmers. *Nature*, 437, 862–865.
26. Peyer, K. E., Zhang, L., & Nelson, B. J. (2013). Bio-inspired magnetic swimming microrobots for biomedical applications. *Nanoscale*, 5, 1259–1272.
27. Gao, W., Feng, X., Pei, A., Kane, C. R., Tam, R., Hennessy, C., & Wang, J. (2014). Bioinspired helical microswimmers based on vascular plants. *Nano Letters*, 14, 305–310.
28. Gao, W., Dong, R., Thamphiwatana, S., Li, J., Gao, W., Zhang, L., & Wang, J. (2015). Artificial micromotors in the mouse's stomach: A step toward in vivo use of synthetic motors. *ACS Nano*, 9, 117–123.
29. Li, J., Thamphiwatana, S., Liu, W., de Ávila, E.-F. B., Angsantikul, P., Sandraz, E., Wang, J., Xu, T., Soto, F., Ramez, V., Wang, X., Gao, W., Zhang, L., & Wang, J. (2016). Enteric micromotor can selectively position and spontaneously propel in the gastrointestinal tract. *ACS Nano*, 10, 9536–9542.

30. Servant, A., Qiu, F., Mazza, M., Kostarelos, K., & Nelson, B. J. (2015). Controlled in vivo swimming of a swarm of bacteria-like microrobotic flagella. *Advanced Materials*, *27*, 2981–2988.
31. Li, J., Angsantikul, P., Liu, W., de Ávila, E.-F. B., Thamphiwatana, S., Xu, M., Sandraz, E., Wang, X., Delezuk, J., Gao, W., Zhang, L., & Wang, J. (2017). Micromotors spontaneously neutralize gastric acid for pH-responsive payload release. *Angewandte Chemie International Edition*, *56*, 2156–2161.
32. Yan, X., Zhou, Q., Vincent, M., Deng, Y., Yu, J., Xu, J., Xu, T., Tang, T., Bian, L., Wang, Y. X. J., Kostarelos, K., & Zhang, L. (2017). Multifunctional biohybrid magnetite microrobots for imaging-guided therapy. *Science Robotics*, *2*.
33. Wu, Z., Li, L., Yang, Y., Hu, P., Li, Y., Yang, S. Y., Wang, L. V., & Gao, W. (2019). A microrobotic system guided by photoacoustic computed tomography for targeted navigation in intestines in vivo. *Science Robotics*, *4*.
34. Walker, D., Käsdorf, B. T., Jeong, H. H., Lieleg, O., & Fischer, P. (2015). Enzymatically active biomimetic micropropellers for the penetration of mucin gels. *Science Advances*, *1*, e1500501.
35. Wei, X., Beltrán-Gastélum, M., Karshalev, E., de Ávila, E.-F. B., Zhou, J., Ran, D., Angsantikul, P., Fang, R. H., Wang, J., & Zhang, L. (2019). Biomimetic micromotor enables active delivery of antigens for oral vaccination. *Nano Letters*, *19*, 1914–1921.
36. Karshalev, E., Zhang, Y., de Ávila, E.-F. B., Beltrán-Gastélum, M., Chen, Y., Mundaca-Uribe, R., Zhang, F., Nguyen, B., Tong, Y., Fang, R. H., Zhang, L., & Wang, J. (2019). Micromotors for active delivery of minerals toward the treatment of iron deficiency anemia. *Nano Letters*, *19*, 7816–7826.
37. Chen, C., Karshalev, E., Li, J., Soto, F., Castillo, R., Campos, I., Mou, F., Guan, J., & Wang, J. (2016). Transient micromotors that disappear when no longer needed. *ACS Nano*, *10*, 10389–10396.
38. Soto, F., Kupor, D., Lopez-Ramirez, M. A., Wei, F., Karshalev, E., Tang, S., Tehrani, F., & Wang, J. (2020). Onion-like multifunctional microtrap vehicles for attraction–trapping–destruction of biological threats. *Angewandte Chemie International Edition*, *59*, 3480–3485.

Chapter 15

Polymer-Based Swimming Nanorobots Driven by Chemical Fuels



Zhiguang Wu, Tingxin Yang, and Qiang He

15.1 Introduction

Chemically powered actuation through inputting chemical fuels and subsequent conversion into mechanical work are widely utilized in the world under microscope, ranging from vehicles to spacecraft. On the other hand, physicist Richard Feynman envisioned the era of micro-/nanomachines in 1959 – design and manufacture micro- and nanoscale devices that can perform multiple and complex operations. The fantastic idea inspired the scientists to visualize the development of micro-/nanoscale robots capable to swim toward previously inaccessible locations in the body. Now we have facilitated with nanotechnology to realize the fantasy. It also opens up new door with significant promises in biomedicine or other field, accompanying with challenges on the development of these swimming nanorobots. The promises lie in the navigation of the swimming nanorobots into hard-to-reach tissues for various biomedical utilizations [1]. However, the fantastic biomedical applications is also challenging simply scaling down macroscopic machines would not work. The actuations in micro-/nanoscale locomotion are different stories with that in macroscale world.

15.1.1 Challenges of Propulsion in Micro-/Nanoworld

In case of propulsion in fluids, inertial and viscous forces are two major forces encountered by robots to swim in fluids. The ratio of inertial to viscous forces is expressed by the Reynolds number, $Re = \rho UL/\mu$, where ρ is density, U is a

Z. Wu · T. Yang · Q. He (✉)

Key Laboratory of Micro-systems and Micro-structures Manufacturing
(Ministry of Education), Harbin Institute of Technology, Harbin, China
e-mail: qianghe@hit.edu.cn

characteristic velocity, L is a characteristic length, and μ is dynamic viscosity of the fluid, respectively. Locomotion of macroscale objects such as fishes, humans, and ships in fluid belongs to moderate to large Reynolds numbers, which inertial forces dominate over the viscous forces. In contrast, the propulsion of nanoscale synthetic swimming robots, natural motile microorganism, and biological motors occurs in fluid with low Reynolds number. Accounting the example of a swimming micro-robot with a size $L \approx 1 \mu\text{m}$ and swimming speed $U \approx 10 \mu\text{m s}^{-1}$ in water, the Reynolds number is on the order of $\text{Re} \approx 10^{-5}$. The effect of inertia is thus virtually absent, rendering inertia-based propulsion mechanisms at the macroscopic scale largely ineffective in the world under the microscope.

The absence of inertia at low Reynolds number leaves stringent constraints that is illustrated by Purcell's scallop theorem [2]. In case of propulsion at low Reynolds numbers, the scallop theorem excludes reciprocal motion due to kinematic reversibility, resulting in an ineffective propulsion with minor displacement in a Newtonian fluid when a "scallop" microstructure is opening and closing its shell periodically regardless of the opening and closing rates. Taken together, the absence of inertia leads to a fundamental challenge in the development of strategies for effective propulsion at the microscopic scale.

15.1.2 Lessons from Natural Nanoswimmers

Facing the challenges of propulsion in the micro-/nanoscale world, nature offers an unlimited source to inspire researchers for development of artificial swimming nanorobots though mimicking the geometry and function of biological systems. Among various motor-like biomolecule and organisms, biological molecular motors, including myosins, kinesins, and ATP synthase (ATPase) [3], are response for a significant number of biological processes ranging from intracellular cargo transportation to macroscopic muscle contractions. They perform the autonomous propulsion in various biofluids though the spontaneous hydrolysis of biological energy units such as adenosine triphosphate (ATP). Kinesin, for example, is a linear biological molecular motor consisting of two heavy chains and two light chains. It is responsible for intracellular transportation and mitosis though walking-motion along microtubules. Their motile function of biomolecular motors has led to the pursuit of engineering natural motor proteins into artificial systems [4]. But the integration of synthetic with natural motor proteins brings a number of experimental issues such as the extraction and purification from living cells and stability of the motor proteins in artificial environments.

15.1.3 From Natural Biomotors, Molecular Motors, Toward Swimming Nanorobots

To overcome this issue, the biomimetic efforts have shifted to the development of biomotor protein-mimicking molecules, so-called molecular machines. J. P. Sauvage, Sir J. F. Stoddart, and B. L. Feringa, who won the Nobel Prize because of their

contribution of molecular machine, demonstrated a significant number of chemically powered synthetic molecular machines such as molecular elevators and rotary motors. The actuation of molecular machine mainly involves the principle that one molecular or submolecular component behaves in a controllable manner. Beyond the molecular level actuation, the research of biomimic propulsion was transfer to imitate the function of biological motor proteins, the conversion of chemical energy into mechanical work. In 2004, the bimetal nanowire robots that are powered by decomposition of hydrogen peroxide were reported as the first synthetic swimming nanorobots. Over the past decade, substantial efforts was devoted toward the design of chemically powered swimming robots at the micro- and nanoscale, and these nanorobots have demonstrated the efficient propulsion in various biofluids though converting chemical energy into mechanic motion using the various chemical fuels. Among various chemically powered swimming nanorobots, the polymeric swimming nanorobots with defined structures can be constructed and functionalized in a versatile and simple manner and thus hold considerable promises in many fields of biotechnologies such as subcellular surgery, targeted cancer therapy, and genome editing.

15.2 Bottom-Up Fabrication of Polymer-Based Swimming Nanorobots

Following the idea of Feynman, who wondered the manipulation and control the atoms and molecules to fabricate the nanoscale robots, the chemists developed a series of polymeric swimming nanorobots by assembling various molecules into nanoscale architectures in a controllable manner. Since the He group and van Hest group initialized the controllable assembly-derived construction of polymer swimming nanorobots in 2012 [5]. A significant number of polymer swimming nanorobots have been developed over the past decade.

15.2.1 *Layer-by-Layer Assembly Technique*

LbL-assembled polyelectrolyte multilayers (PEM) can be easily prepared by continuous adsorption of alternating layers of polymers onto the sacrificial colloidal particles [6]. Multifunctional film is formed on solid substrate. Due to the resulting controllability of the LbL component structure, the LbL method is the most commonly used tool in nanoarchitecture [7]. The structural characteristics of LbL components, such as wall thickness, overall size, and shape, can be adjusted through the assembly process and the geometric characteristics of the template. Various components including polymers, nanoparticles, proteins, lipids, and even inorganic or organic functional molecules can be simply integrated into LbL-assembled capsules or nanotubes through noncovalent interactions [8]. These functional units enable LbL-assembled capsules or nanotubes to be multifunctional and responsive to chemical, physical, or biological stimuli.

In 2012, the He group, for the first time, reported Janus polymer multilayer hollow capsules swimming microrobots based on LbL assembly technique [9]. Silica particles with diameter of 8 μm were served as template; five bilayers of polystyrene sulfonate (PSS)/polyallylamine hydrochloride (PAH) were alternatively deposited on the template. The key step to effectively drive Janus capsule robots is the asymmetric modification of the catalyst to the surface of the capsule. Dendritic platinum nanoparticles (Pt NPs) with large specific surface area and high catalytic activity were used to realize high propulsion with the presence of chemical fuel. Dendritic Pt NPs was encapsulated by microprinting technique to produce an asymmetric capsule with controlled speckle. In detail, PDMS embossing with dendritic Pt NPs ink was placed on top of the LbL-assembled template. The single layer is then decomposed into water, and the spherical template is removed to form hollow asymmetric capsules modified with Pt NPs. The resulting Janus microcapsule robots were obtained after the dissolution of silica template using hydrofluoric acid. As a modified cargo, the Janus microcapsule robots retain considerable encapsulation capacity and enable the controllable release under the external stimuli such as light, ultrasound, and magnetic field, which make them to be candidates for smart delivery of various therapeutic agents. More importantly, using the hydrogen peroxide as fuel, Janus microcapsule robots display efficient propulsion that is driven by the thrust of oxygen bubbles from catalytic decomposition at the Pt NPs side. The maximum velocity of Janus microcapsule robots can reach 140 $\mu\text{m s}^{-1}$ upon hydrogen peroxide with concentration of 15% H_2O_2 . Such assembled Janus capsules robots can be served as combination of chemically powered swimming microrobots and multifunctional cargo. This makes them extremely attractive especially toward the design of more powerful nanomachines and diverse biomedical applications (Fig. 15.1).

Beside microprinting technology, the Pt catalyst can be coated on the upper part of the microcapsule by sputtering in a vacuum [10]. In this method, Ti or Ni intermediate metal layers are usually required as the bonding layer used to catalyze the strong connection between the metal layer and the polymer. The thickness of metal layers can be controlled through the manipulation of sputtering coating. Therefore, the polymer Janus microcapsule nanorobots with controllable thickness of metal layer can be produced by introducing Pt NPs or a layer with high catalytic capacity into LbL-assembled capsules. Tetra-substituted Ru^{IV} polymetallic oxalates, which catalyze the decomposition of H_2O_2 into water and oxygen, have also been introduced into PEM capsules as catalysts [11]. Calcium carbonate particles doped with dextran-rhodamine were used as sacrificial templates for capsule preparations. After removal of the template, dextran-rhodamine remains encapsulated in the capsule cavity and is used as a fluorescent label for motion observation. The nanorobot displays linear or circular trajectories with a maximum velocity of 25 $\mu\text{m}\cdot\text{s}^{-1}$. Due to oxygen released between the polymer layers, the stability of the sandwich structure is limited, causing some capsules to collapse irreversibly.

Compared with Janus micro-/nanosphere swimming micro-/nanorobots, chemically powered tubular swimming micro-/nanorobots (micro-/nanorockets) have exhibited high propulsion and controllable movement. However, the pioneering micro-/nanorockets based on metallic materials leaves drawbacks including poor

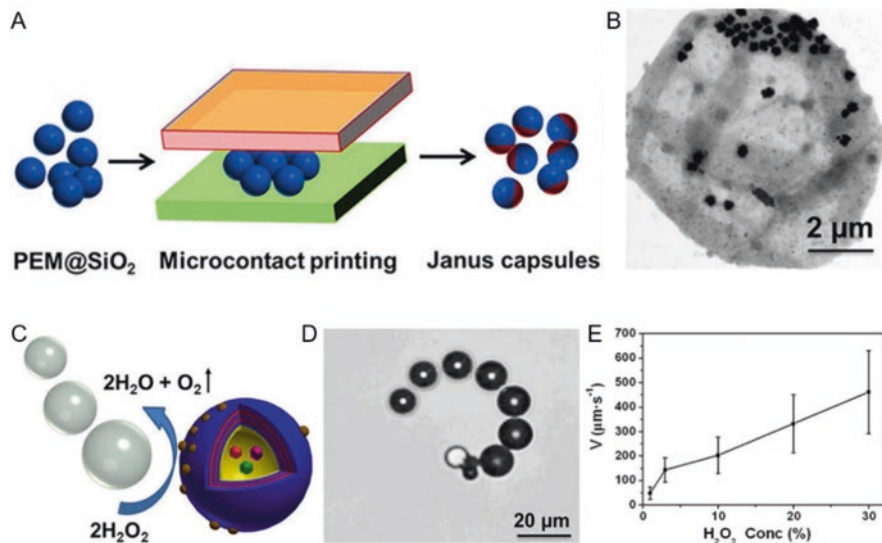


Fig. 15.1 Polymer Janus microcapsule swimming robots based on layer-by-layer assembly technique. (a) Schematic fabrication of dendritic Pt-NP-modified Janus microcapsule robots via LbL assembly and microprinting. (b) Transmission electron microscopy (TEM) image of the prepared capsule nanorobots. (c) Schematic bubble propulsion of Pt-NP-modified Janus microcapsule robots (d) Microscopic image illustrating the propulsion of Pt-NP-modified Janus microcapsule robots in the presence of hydrogen peroxide. (e) Dependence of velocity of Pt-NP-modified Janus microcapsule robots on the concentration of hydrogen peroxide. Reproduced with permission from Ref. [9]. Copyright 2012 ACS Publishing Group

biocompatibility or biodegradability, roughness for surface chemistry, and capability of drug loading and release. To address these challenges, the He group demonstrated polymer multilayer tubular nanorobots can be constructed with LbL technique using nanopore membrane as template [12]. Two biodegradable natural polysaccharides, positively charged chitosan (CHI) and negatively charged sodium alginate (ALG) as building blocks, were alternately assembled into the pores of template, followed by the functionalization with poly (diallyl dimethyl ammonium chloride)-stabilized Pt NPs into the pores of the template. The different pore sizes of template resulting in the LbL-assembled tubular structure possess an asymmetric geometry along its axis, which is beneficial to control the directivity of motion. The tubular swimming nanorobots have a conical shape with two openings of different diameters, which forces the resulting oxygen bubble to move back to the large opening and eventually to be released from the large back opening. The tubular structure exhibits efficient propulsion with a velocity of up to 74 $\mu\text{m}\cdot\text{s}^{-1}$. By analyzing the released bubble tails, the chemical propulsion of tubular nanorobots exhibit four typical trajectories including straight, circular, curved, and rotational motion.

Compared with the Janus sphere structure, the bubble propulsion of tubular swimming nanorobots possess different mass transportation and bubble formation process. Because the catalyst is loaded inside the tubular structure, the geometry

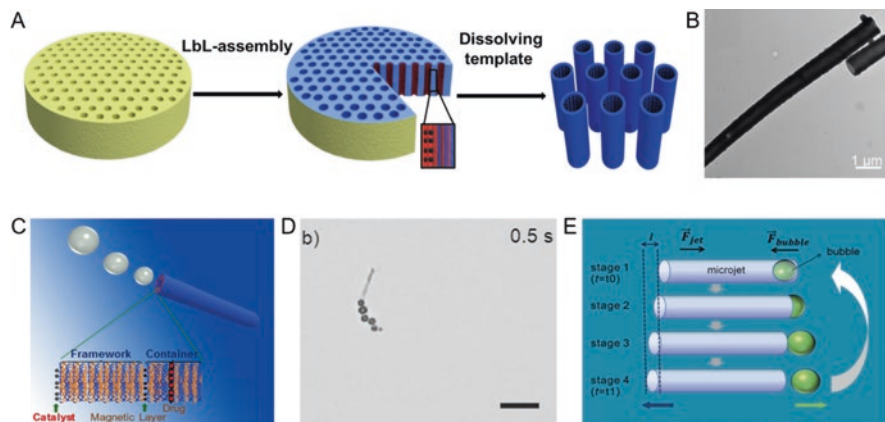


Fig. 15.2 Polymer tubular swimming nanorobots. (a) Schematic construction of polymer multilayer tubular swimming nanorobots. (b) TEM image showing the geometry of polymer multilayer tubular swimming nanorobots. (c) Schematic illustration showing the polymer tubular swimming nanorobots and its bubble propulsion using hydrogen peroxide as fuel. (d) Microscopic image showing the bubble propulsion of polymer multilayer tubular swimming nanorobots in the presence of hydrogen peroxide. Reproduced with permission from Ref. [12]. Copyright 2013 Wiley Publishing Group. (e) Schematic illustration showing the dynamic deformation process of the bubble nanorobot-bubble system within one moving step. Reproduced with permission from Ref. [13]. Copyright 2011 RSC Publishing Group

parameters, such as the asymmetry, diameter, length, and shape of tube openings, make impact on the fuel supplying process. Although the mechanism of bubble propulsion within tubular structure is still under discussion, the dynamics of the bubble-tubular structure systems in one motion cycle are basically acknowledged as several steps including bubble formation, bubble growth, bubble migration, and bubble ejection (Fig. 15.2e) [13]. Initially, the oxygen from catalytic decomposition of hydrogen peroxide accumulate and form bubble on the inner wall of tubular structure (stage 1). Although the oxygen production is hindered in the catalyst area that is covered by bubble, other area with catalyst can still generate oxygen and accumulate on the bubbles, resulting in the growth of bubbles (stage 2). When the size of bubble is beyond the inner diameter of tubular structure, the bubble is under the imbalance capillary forces from both sides due to the geometric asymmetry of the tubular structure, leading to the migration of bubble toward the opening of tube with larger size (step 3). Noted that the migration of bubble within the tube cannot generate the drive force of the tubular micro-/nanorobots along their axis, once the bubble come out from tubular structure from the opening, it generates a momentum transfer to the fluid. To compensate the transfer of the momentum, a jet force acts on the tubular micro-/nanorobots and thus drive their propulsion (stage 4). The bubble propulsion mechanism of tubular micro-/nanorobots is similar to that of the low Reynolds numbers natural microswimmers such as *E. coli*, which enable active motion in liquid though mechanical deformation of its body.

15.2.2 *Supramolecular Assembly*

The aim of supramolecular chemists is to synthesize the simplest molecular structure capable of forming supramolecular assemblies that cannot be achieved by a single molecule or a collection of molecules with a novel function. These supramolecular architectures produce a variety of functions, such as novel magnetic and optical properties, catalysis, molecular recognition, and transport processes. The term “self-assembly” is often used in supramolecular chemistry to refer to a highly rigid, organized synthetic structure promoted by molecular receptors using a bottom-up approach. In addition, from a material perspective, self-assembly technology allows the design of soft supramolecular structures with unique shapes that can facilitate better interfaces with biological systems. Thus, such structures could potentially be used for applications in biological media such as active drug delivery.

The Wilson group designed an asymmetric supramolecular bowl with narrow openings and placed a reactive catalyst (PtNPs) inside the structure (Fig. 15.3a) [14]. Dialysis of flexible polymer capsules assembled in the presence of organic solvents caused differences in osmotic pressure. The semipermeable membrane fails to balance the pressure and suddenly folds inward, leading to transforming the shape of the vesicle into oral cells. The catalytic nanoparticles were subsequently loaded into the structure, and the fuel diffuses inside the assembly to produce the propellant gas (Fig. 15.3b) [14]. Such supramolecular-based swimming nanorobots exhibit efficient propulsion using chemical fuel and represent the various advantages including administration toward diseased area with shorten period for drug delivery, offering considerable promises for future dynamic delivery systems.

15.2.3 *Biological Hybridization*

The pursuit of the effective movement of swimming micro-/nanorobots with the biological functions of natural cells simulate substitutional efforts on the integration and engineering of biological entities onto the micro-/nanorobots. These biohybrid swimming micro-/nanorobots provide efficient motion in complex biofluids, accomplishing prolonged propulsion without the contamination in biofluids, drug encapsulation and release strategies, and improved positioning and targeting of imaging and therapeutic reagents.

As a natural cargo over millions of years of evolution, red blood cells (RBCs) and their derivative have developed various unique mechanical and biological properties such as antifouling effect and avert from immune attack, which are desirable for systematic delivery. Therefore the transformation of RBCs into the swimming micro-/nanorobots provides considerable expectation for active delivery. The Wang and Zhang group reported a RBC membrane-coated and magnesium-powered (RBC-Mg) swimming microrobot that mimics the motile natural cells. The RBC-Mg with Janus geometry was fabricated with successively deposited (alginate/chitosan)

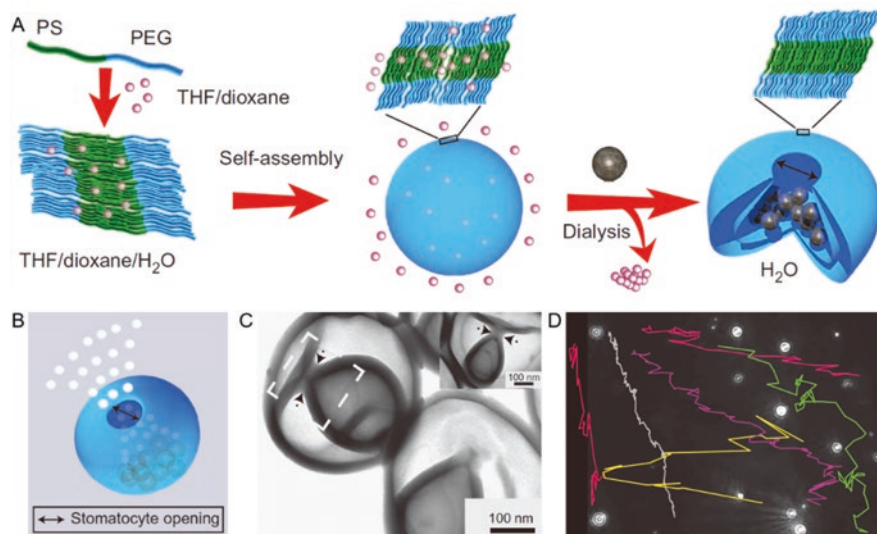


Fig. 15.3 Polymer stomatocytes swimming nanorobots based on supramolecular assembly. (a) Schematic supramolecular assembly of stomatocytes nanorobots. (b) Schematic propulsion of stomatocytes nanorobots driven by hydrogen peroxide as fuel. (c) TEM imaging of stomatocytes nanorobots. (d) Microscopic imaging showing the trajectories of chemically powered stomatocytes nanorobots. Reproduced with permission from Ref. [14]. Copyright 2012 Nature Publishing Group

multilayer, gold nanoparticles (AuNPs), and the (RBC) membranes, onto the magnesium particles which were partially embedded on the parafilm (Fig. 15.3a) [15]. The resulting RBC membrane-coated magnesium (RBC-Mg) Janus microrobots exhibited hydrogen bubble-driven propulsion in water containing sodium chloride. More importantly, the coating of RBC membrane onto the Mg-based swimming microrobots hold antifouling capability that bestow efficient propulsion with extend period when the swimming micro-/nanorobots were subjected to biological fluids (Fig. 15.3b).

Moreover, the He group developed a drug delivery system though coating the mesenchymal stem cell membrane onto the particles [16]. The resulting particles exhibited the biological function of natural stem cell membrane, which promotes remarkable stability and tumor-targeting capability *in vitro* and *in vivo*. Once intravenously injected, the stem cell membrane coating enhanced the accumulation of particles in tumor tissues and thus exhibited anti-tumor effect. H&E staining analysis of treated mice verified minor adverse effects in sensitive organ such as heart, liver, spleen, lung, and kidney tissues. Moreover, the He group switch the stem cell membrane coating toward upconversion particle for photodynamic therapy (PDT). Such biologically interfaced PDT system was achieved though the fusion of the upconversion particle-encapsulated mesoporous silica with the stem cell membrane [17]. Benefiting from the stem membrane coating, the resulting particles possess various merits such as extended circulation period, enhanced accumulation toward

targeted tumor, and evasion from immune attack. The above investigation indicates that the biological hybridization such as coating of natural cell membrane offer a board of unique functions and properties toward swimming micro-/nanorobots and thus make them hold potential promises in the field of biomedicines.

Besides the cell membrane, the biological hybridization also extends the entire motile microorganisms. The Wang group demonstrated a variety of freestyle functionalized sperm-hybrid microrobots though the integration of natural sperm with CdSe/ZnS quantum dots, iron oxide nanoparticles, and doxorubicin as model drug (Fig. 15.3c) [18]. Such sperm-based microrobots have shown effective self-propulsion ability in various biological and environmental media and have controllable swarm behavior after exposure to chemical attractants. The sperm-based microrobots enable the load, and release therapeutic payloads were demonstrated by placing it in an acidic environment where changes in sperm membrane permeability allow rapid DOX release. Furthermore, inheriting the capability of natural sperms, the sperm robots can be sensitive to the local environment and subsequently autonomously leave or approach a targeted site by changing the osmotic pressure of solution leading to different flagella lengths.

15.3 Motion Control

15.3.1 Navigation Using External Field

The precise spatiotemporal control of the swimming micro-/nanorobots can be manipulated though the operation of the catalytic activity of micro-/nanorobots or chemical fuels supply. Various approaches to modulate the direction and velocity of swimming micro-/nanorobots have been described. One of the most conventional strategies to achieve the directionality of swimming micro-/nanorobots is to functionalize micro-/nanorobots with magnetic materials and subsequently navigate their motion though manipulation of external magnetic field. For example, magnetic navigation of Janus polymer microcapsule robots can be accomplished though the assembly of citrate-stabilized magnetic nanoparticles with negative charge onto the positive charged polymer layer of the microcapsules robots [19]. The microcapsule robots enable the change of directionality along the magnetic field in the presence of 15% hydrogen peroxide. Another example from the He group indicated the magnetic guidance of tubular polymer swimming micro-/nanorobots toward targeted cancer cell. Upon the external magnetic field, the propulsion behavior of the tubular swimming nanorobots changed from random motion to directional movement which is aligned with the direction of magnetic field [12]. More interestingly, when the tubular attached toward the targeted cancer cells, it did not detach from the cells. Further characterization of the tubular nanorobot-attached cell indicated that it was partially penetrated into the membrane of cell.

The Sen group demonstrated directional control of nanorods in a free fluid using (Pt/Ni/Au/Ni/Au) rods [20]. Noted that the magnetic field did not contribute to the velocity of the swimming micro-/nanorobots, but only their direction through magnetic alignment. Moreover, the Wang group demonstrated the precise motion of Au/Ni/Au/Pt-CNT particles in complex microchannel systems [21]. In addition to direction control, a fast-moving magnetic field can be used to capture and release cargo. The microrobot system would be more versatile if the motion is controlled and regulated by a stimulus response valve equipped with molecules without changing the shape of the motor itself or affecting its catalytic activity. The Wilson group developed a stomatocytes microrobot reversibly controlled by a thermal responsive valve/brake [22]. The temperature change mechanism stimulates and controls the motion of the self-assembled stomatocytes microrobot. A temperature-sensitive polymer brush was employed to graft onto the stomatocyte microrobots, the resulting microrobots enable the controllable entry of hydrogen peroxide. Thus the microrobots can regulate movement by controlling the opening of oral cells to increase or decrease in temperature.

Furthermore, near-infrared (NIR) light is of particular interest in the field of biomedicine due to its minimum absorption and optimal penetration in tissues. The He group designed a controllable “on-off” motion of polymer micromotor using NIR light [23]. The tubular nanorobots were fabricated through nanoporous template-assisted LbL deposition of polymers and Pt NPs into the nanoporous template, followed by the functionalization of gold nanoshell. On the threshold concentration of hydrogen peroxide (0.1%) for propulsion, the swimming nanorobots remained immobile due to the slow formation of oxygen bubbles. Upon the illumination of NIR light, however, the swimming nanorobots were activated and displayed efficient chemical propulsion in the same concentration of hydrogen peroxide. Such NIR light-induced on and off motion is attributed to the increased kinetics of catalytic reaction and accelerated mass transport. These swimming nanorobots with the characteristics of near-infrared laser-controlled emission and self-propulsion can be further applied to highly specific cancer recognition and subsequent photothermal cancer treatment. Additionally, short heat pulses can be utilized to regulate the velocity of swimming nanorobots. It is found that Pt/Au nanowires traveled faster at high temperature than that at room temperature [24]. The enhanced velocity is attributed to the increase in the temperature of the electrochemical process and the decrease in the viscosity of the solution. Coupling with thermal and of magnetic guidance, advanced spatiotemporal navigation can be achieved.

Most of the reported inorganic artificial microswimmers are unable to change their shape [25], whereas stimulus-responsive polymers can make large changes in shape, size, and material composition. The Sanchez group reported a flexible, heat-responsive polymer microrobots that can be reversibly folded and unfolded by changing the temperature of the solution [26]. The catalytic swimming microrobots were of tubular geometry and consisting of Pt layer, polycaprolactone layer, and thermoresponsive poly(N-isopropylacrylamide) (PNIPAM) layer. The swimming microrobots preserved tubular structure and exhibited tube-based bubble propulsion using hydrogen peroxide as fuel at room temperature. In contrast, the elevation of

environment temperature above 288 °C triggered change of shape owing to the phase transition of PNIPAM, and tubular microrobot was bent to a minimum radius of about 45 μm , leading to the stop movement. When the temperature drops below 288 °C again, the tubular microrobot was bent to a minimum radius of about 45 μm ; the microrobot can self-propel itself again. A radius greater than 70 μm means the tube will unfold and show an open polymer film. During several cycles from 20 °C to 308 °C, the swimming microrobots exhibited reversible control of the movement. The radius of the tubular microinjector and the size of the bubble thus released greatly influence the velocity of the bubble-driven microrobots.

Different levels of pH maintain the activity of different enzymes and achieve various functions in human body. Scientists have taken advantage of these pH gradients to promote the motion of artificial motors. Recently, magnesium or zinc-based micro-/nanorobots can be degraded through the digestive tract and used for acid power drive. The main products of degradation are also important nutrients to the human body. Biocompatible calcium carbonate can also be used in the manufacture of microrobots in addition to inductive motion based on metal-acid reactions [27]. It has been reported that calcium carbonate Janus particles can be moved in situ in HeLa cells under very weak acid conditions (pH = 6.5). The strategy not only avoids the need for external fuels that may be harmful to biological systems but also achieves the controlled activation of micromotors in the presence of tumor cells. In addition to driving motion under acidic conditions, the motion control of microrobots can be further realized by adjusting the pH value of environmental conditions.

The Wang group reported electrochemical controlled movement of catalytic nanowire swimming robots [28]. The velocity of the nanowire robots were modulated by increasing the potential of the gold electrode near the nanowire from negative to positive in solution. The process was reversible and also could be induced by increasing negative potential. Such potential-induced motion control is due to local changes in oxygen levels. Although the methods described above can be used for precise direction and speed control, more complex motion patterns are required for advanced applications. By assigning asymmetric geometry to nanowires, rotational components of motion can be realized. The Mirkin group employed photolithography to coat the nanowires asymmetrically, exposing only one side of the catalytic surface and thus allowing the nanowires to spin in H_2O_2 [29]. The Sen group deposited additional layers of Cr, SiO_2 , Cr, Au, and Pt on one side of the Au/Ru bimetallic nanowires in the vapor phase and showed a rotation speed of up to 400 rpm in 15% of H_2O_2 , with an average rotation speed of 180 rpm (Fig. 15.4d).

15.3.2 Chemotaxis

In nature, swimming microorganisms approach or leave a targeted site through various biological behaviors such as chemotaxis, which sense chemical concentration gradients and move toward or away from certain chemicals around microorganisms. Learning from the natural chemotaxis behavior, the Sen and Velegol group reported

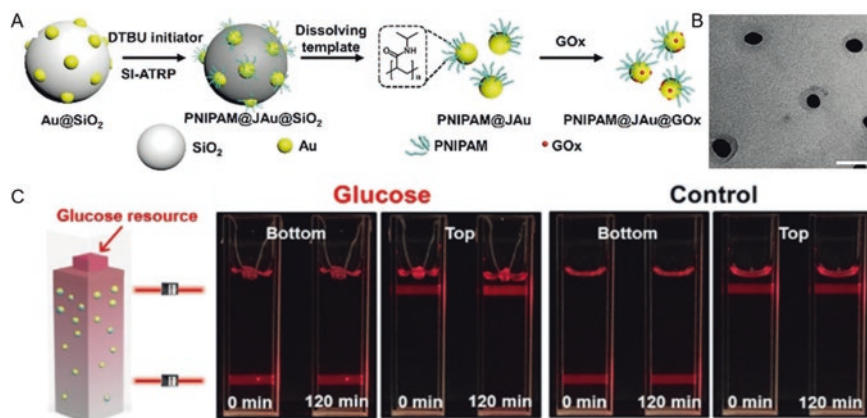


Fig. 15.4 Chemotaxis of polymer brush-grated swimming nanorobots. (a) Schematic fabrication of PNIPAM brush-grated glucose oxidase-functionalized Janus swimming nanorobots. (b) TEM image of the fabricated polymer brush-grated swimming nanorobots. (c) Schematic (left) and actual (right) chemotaxis of polymer brush-grated swimming nanorobots toward a gel containing glucose in a cuvette. Reproduced with permission from Ref. [30]. Copyright 2019 Wiley Publishing Group

an instance of chemotactic behavior in an abiotic artificial motion system, in which the 2.0-m-long platinum rod is shown to be oriented toward higher hydrogen peroxide concentrations through “active diffusion” [31]. These bimetallic microrods showed a directional movement toward a higher hydrogen peroxide fuel concentration gradient caused by a higher 30% fuel-soaked agarose hydrogel. After 110 h, more than 70% of the microrods gathered around the hydrogel, while at 38 h, the density of microrods was less than 30%. Chemotaxis of Janus spherical and tubular micromotors has also been implemented in microfluidic channels [32].

To extend the chemotaxis concept to biomedical applications, the Wilson group demonstrated that self-assembled stomatocyte nanorobots with soft interfaces produced higher hydrogen peroxide concentration gradients when moving to model cells [33]. The stomatocyte nanorobots enable the chemotaxis along the gradient of hydrogen peroxide secreting from neutrophils. To realize the chemotaxis toward inframammary factors, a neutrophil-hybrid swimming microrobots were developed by loading mesoporous silica nanoparticles with *E. coli* membranes, leading to the development of self-directed microrobots for targeted drug delivery [34]. The chemotactic behavior of neutrophils was studied by studying the movement of *E. coli* in response to chemotactic gradient, using *E. coli* as chemokine factor.

After having realized the chemotactic motion of individual polymer swimming nanorobots along the gradient of chemicals, the He group focus on the chemotaxis of nanorobots swarm, which is of importance to fulfill biomedical tasks. In nature, the *E. coli* swarm could perform collective migration chemotaxis toward the nutrition sources such as glucose. To realize the *E. coli* mimicking swarm chemotaxis, the polymer brush-grated, glucose oxidase (GOx)-functionalized Janus swimming

nanorobots with diameter of ~ 50 nm were developed [30]. With the catalytic decomposition of glucose fuels into gluconic acid, the Janus swimming nanorobots with GOx on one side of gold particles achieve the propulsion involving self-diffusiophoresis mechanism. As the scaling down to 50 nm, the directional motion of nanorobots were dramatically suffered from strong Brownian force and display rotation diffusion, which challenges the emergence of nanorobots swarm. To overcome this issue, the PNIPAM brush were grafted onto the Au side, considerably enhance the translation motion of Janus Au nanorobots. Such elevated propulsion accomplished the emergence of Janus nanorobots swarm and collective chemotaxis along the concentration gradient of glucose at the macroscale (Fig. 15.4).

15.3.3 Autonomous Sense and Act

Although effective in simple control under external field and chemotaxis to certain chemicals, it remains challenging in advanced intelligent navigation as natural micro-/nanoswimmers. For example, *E. coli* are able to sense the surrounding environments and autonomously leave or approach for survival. To this end, the He group carried out variable modulation of chemically powered swimming nanorobots though introducing polymer brush onto the polymer swimming nanorobots [35]. They firstly integrate the salt-responsive polymer brushes to realize the regulation of the velocity of bubble-propelled swimming nanorobots. Thanks to grafting with salt-responsive poly[2-(methacryloyloxy)ethyltrimethylammoniumchloride] (PMETAC) brushes, the bubble-propelled Janus sphere swimming microrobots facilitates the modulation velocity with the type and concentration of counterion in fluid. With the ion exchange with ClO_4^- and polyphosphate anions, the PMETAC brush grafted and LbL-assembled Janus microrobot endow the reversible transition of propulsion between low and high velocities. The results indicate that the integration of polymer brushes with precisely adjustable responsiveness allows for the manipulation of velocity in a predictable manner and an autonomous acknowledge and response to the salt concentration in local environment.

Moreover, the responsive-stimuli were shift toward more general item, temperature. To this end, a thermoresponsive polymer brush, PNIPAM, was decorated onto the Janus Au-Pt bimetallic swimming microrobot for sense the surrounding temperature and modulate the motion behavior [36]. Below the lower critical solution temperature (LCST) of PNIPAM brush, the PNIPAM-Au-Pt Janus microrobots performed hydrogen peroxide-driven locomotion at a velocity of $8.5 \mu\text{m s}^{-1}$ with an orientation of “Au-Pt” orientation. It is attributed to hydrophilic and swelled PNIPAM brush which rendered the transformation of electron and diffusion of proton on the Au side, resulting in the propulsion of PNIPAM-Au-Pt Janus microrobots with a self-electrophoretic mechanism. In contrast, the orientation of locomotion was reversed above the LCST as the PNIPAM brush was transformed to be hydrophobic and collapsed, and therefore the propulsion mechanism was transitioned to the self-diffusiophoresis. Such PNIPAM-functionalized Janus swimming microrobot

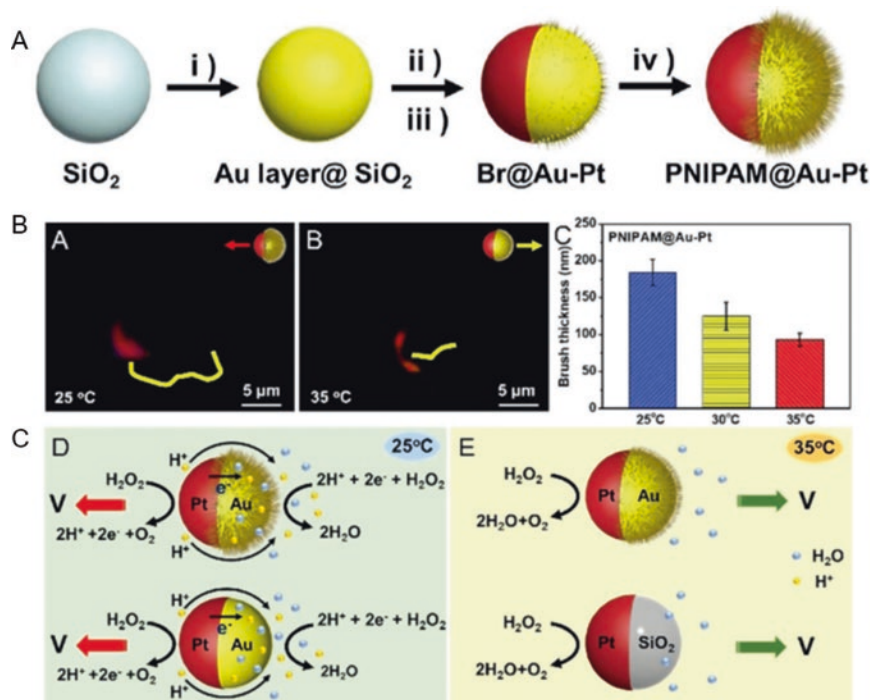


Fig. 15.5 Sense and act of polymer brush-grafted swimming micro-/nanorobots on surrounding temperature. (a) Schematic fabrication of the PNIPAM brush-grafted Janus swimming microrobots. (b) Movement behavior of PNIPAM brush-grafted Janus swimming microrobots. (c) Schematic mechanism of thermoresponsive polymer brush on the movement modulation of Janus swimming micro-/nanorobots. Reproduced with permission from Ref. [36]. Copyright 2019 Wiley Publishing Group

endows reversibly transition of motion orientation with the switch of PNIPAM between hydrophobic and hydrophilic states. These above investigations offer strategies to achieve the autonomous sense and act as the natural living microswimmers (Fig. 15.5).

15.4 Polymer Nanorobots In Vivo

15.4.1 Benefits of Propulsion Function in Active Therapy

The ultimate goal of scientists is to develop polymer nanobots that can directly enter diseased tissue for human treatment. Polymer nanobots are controlled nanomachines that can transport drug payloads to disease sites and skillfully use other forms of energy around them to autonomously move through the medium. The

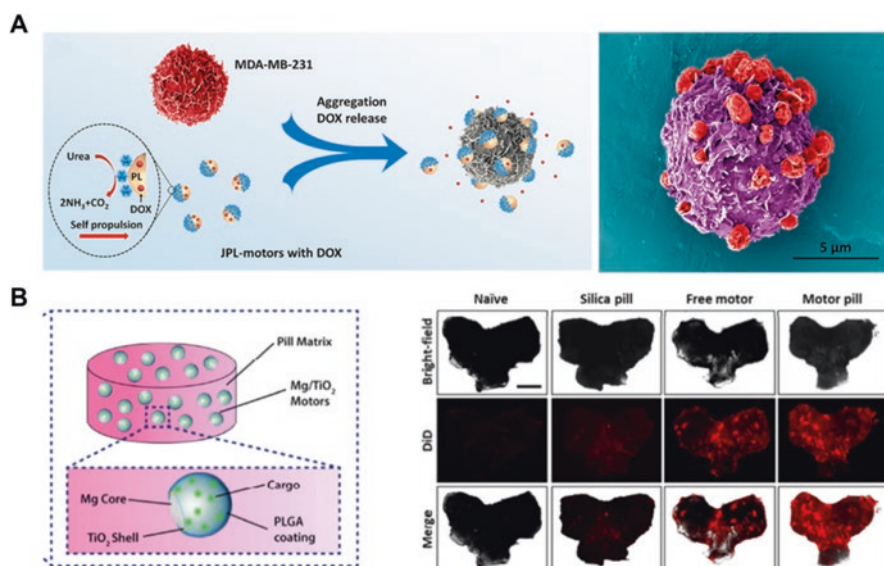


Fig. 15.6 Active therapy using polymer swimming micro-/nanobots. (a) Schematic of Janus platelet microrobots for targeted delivery (left) and actual Janus polymer microrobot (right). Reproduced with permission from Ref. [37]. Copyright 2020 Science Publishing Group. (b) Schematic of the microrobot pill composition consisting of a lactose/maltose pill matrix and the encapsulated swimming microrobots consisting of Mg, TiO₂ and PLGA (left) and merged images of the luminal lining of freshly excised mouse stomachs at 4 h after oral gavage of DI water (right). Reproduced with permission from Ref. [38]. Copyright 2018 RSC Publishing Group

Wang group reports an endogenous enzyme-driven Janus platelet microrobots that causes uneven breakdown of urea in biofluids, resulting in enhanced chemical electrophoretic motion (Fig. 15.6a). The effective propulsion of Janus platelet microrobots with urea as fuel greatly improves the combination efficiency and therapeutic effect with biological targets [37]. The Wang group synthesized biocompatible swimming microrobot pills by dispersing Mg-based micromotors in lactose/maltose pill matrix. In addition, these micromotor pills bestowed the cargos highly retained on the wall of stomach in animal experiments (Fig. 15.6b) [38].

15.4.2 Imaging and Control of Polymer Nanorobots In Vivo

In the biomedical applications of nanorobots, imaging of swimming micro-/nanorobots in vivo is the primary problem to achieve clinical translation [39]. The imaging technology needs to have high spatiotemporal resolution, noninvasive, and be able to penetrate deeply to produce accurate and reliable control and navigation. The use of radionuclides in nuclear imaging technology can improve the sensitivity in imaging research. According to the report, X-rays could be used to observe and power

tiny metal robots [40]. The Sanchez group successfully tracked the catalytic micro-robot by combining X-ray CT with positron emission tomography (PET) [41]. By modifying the gold surface with iodine isotopes, the movement of chemically driven tubular microrobots in the channel can be monitored in real time at the rate of 1 frame per minute for 15 min. Other clinical imaging techniques, such as ultrasound imaging and fluorescence imaging, exhibit limited resolution and contrast in tissues. To overcome these problems, targeted adjustments have been made to achieve real-time visualization of the range. In a recent study, ultrasound imaging was used to track microbots in biofluids. A population of tiny machines is much larger than a handful and therefore easier to image [42].

In addition to ultrasound imaging, photoacoustic tomography (PAT) detects photon-induced ultrasound and provides high-resolution images at depths of up to 7 cm. In order to achieve real-time imaging in deeper tissues within the body, a microrobotic system has been developed that enables real-time visualization in the gastrointestinal tract (Fig. 15.7a) [43]. A magnesium-based microrobot with a contrasting gold layer is encapsulated in enteric polymer-coated microcapsule. Once orally administered, the microcapsules serving as microrobot pills endow the protection from gastric acid, exhibition of strong photoacoustic signal for PAT imaging, and NIR-triggered activation of swimming microrobots. In addition, PAT imaging

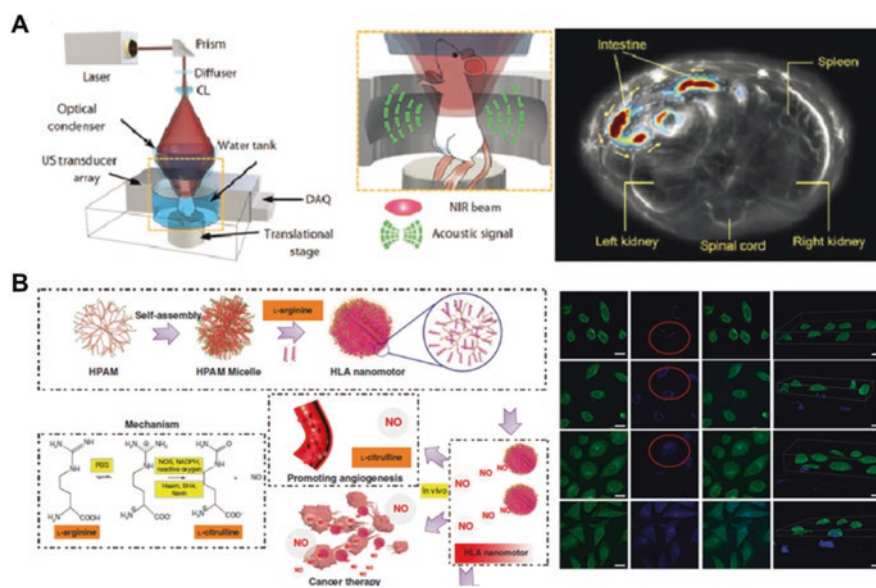


Fig. 15.7 Imaging of the polymer-based swimming micro-/nanorobots in vivo. (a) Schematic illustration and PAT image showing the imaging of swimming microcapsule microrobot in vivo. Reproduced with permission from Ref. [43]. Copyright 2019 Science Publishing Group. (b) Schematic illustration of fabrication and propulsion mechanism of zwitterion-based swimming nanorobots (left) and confocal laser scanning microscopy images of the HLA-based swimming nanorobots (right). Reproduced with permission from Ref. [44]. Copyright 2019 Springer Publishing Group

can separate sudden breathing movements from the position of the microrobot, allowing accurate real-time monitoring in deep tissue in the body. The Mao group proposed a NO-dissipated hyperbranched polyamide/L-arginine (HLA) swimming nanorobots that converts the amino acid L-arginine into nitric oxide (NO) through NO synthase (NOS) or reactive oxygen species [44]. HLA nanorobots with unique fluorescence characteristics can reflect its entry into the cell process (Fig. 15.7b). The HLA-based nanorobots, which requires no additional fluorescent dye, is expected to be tracked in vivo by fluorescence imaging.

15.4.3 Active Therapy of Nanorobots In Vivo

Various therapeutic studies have been conducted on nanorobots that can transport therapeutic agents to hard-to-reach tissues. One important issue is to overcome the upstream flow to controllable delivery. To this end, the Kastrup group reported the calcium carbonate-based swimming microrobots that enable self-propulsion through flowing blood. The swimming microrobots were consisted of carbonate and tranexamic acid. The propulsion is involved in a bubble propulsion from the chemical reaction between calcium carbonate with acid. The large number of bubbles produced by the mixture of CaCO_3 and XA-NH^+ has also been used in various cases for coagulase autoigniting transport systems [45]. In contrast to conventional surface modifications, chemically propelled microrobots enhanced their retention without the need for complex and precise surface designs for specific diseases. A zinc-based microrobot that can move autonomously in the gastrointestinal (GI) tract was evaluated in vivo using a mouse model [46]. Relying on the chemical propulsion from zinc and acid, the drug-loaded microrobot exhibited high bubble propulsion in GI tract. Such active and effective propulsion promoted the penetration of mucus in GI tract, resulting in the extended retention in vivo. Magnesium-based microrobots have been widely used for in vivo therapy due to their optimal propulsion in biological media while minimal toxicity toward the body [47]. A study of gastric therapy for *Helicobacter pylori* infection based on active delivery of magnesium-based micro-/nanobots has been reported.

The enteric polymer-coated swimming microrobotic system consists of a magnesium-based tubular micromotor coated with an enteric-coated polymer layer that accurately locates and maintains controllability in the required portion of the gastrointestinal tract [48]. The dissolution of their enteric coats activates their push toward local tissue penetration at the targeted site. Compared with the passive treatment vector, the active delivery efficiency of the in vivo drug carrying microrobot is enhanced, and the bacterial burden is reduced. Another therapeutic example of magnesium-based microrobots in the stomach is to regulate the local physiological conditions of gastric juices (such as neutralizing the pH of the stomach) to facilitate pH-triggered drug release. The reaction of magnesium and gastric acid with the local convective coupling caused by active motion leads to the rapid depletion of the

microrobot's protons without side effects and offers considerable promise for the habitation and controlled release of proton pumps [49].

Besides the targeted drug delivery, active vaccine delivery is another important therapeutic application. For example, a magnesium-based polymer robotic toxoid has been developed and used for oral vaccination. The toxification of the red cell membrane coating on the microrobot neutralizes the toxic antigen payload and induces mucosal immunity [50]. Then intestinal localization, made of mucosal adhesion and enteric-coated microbots, simulated invasive infections. High propulsion of microrobot in the gastrointestinal tract enhanced the retention and accelerated uptake of antigens *in vivo*.

The He group designed a self-moving particle composed of biocompatible gold and magnetite nanoparticles and biocompatible polyelectrolyte complexes that can be used to aid tissue welding with infrared lasers, thus effectively sealing mouse wounds *in vivo* [51]. The resulting Janus microrobots possess considerable photothermal property and thus can not only accomplish the thermophoretic motion under the exposure of NIR light but also exhibited sealing effect of swimming nanorobots through melting collagen fibers. This approach proves that temperature measurements at the level of individual particles demonstrated successful photothermal heating, while the mechanical properties of welded liver, skin, and meat confirmed the mechanical repair of welded biological samples.

15.5 Conclusion

In this chapter, we summarize the recent research efforts on chemically powered swimming polymeric nanorobots including the controllable construction, propulsion mechanisms, motion navigation, movement in complex media, and applications *in vivo*. Inspired by the Richard Feynman envisaged that the operation of atoms and molecules to fabricate the nanoscale robots, also the chemically powered motion from natural biomolecular motors. Inspired by them, a series of polymer swimming nanorobots capable of autonomous propulsion driven by chemical fuels have been developed by assembling various molecules into nanoscale architectures in a controllable manner. Benefiting from the "top-down" approaches, various functional materials including natural polymers, enzymes, and synthetic nanoparticles, could be utilized as building blocks to construct the polymer-based nanoarchitectures with controllable geometry and size. The robotic transformation of these nanoarchitecture results in the development of various polymer swimming nanorobots driven by chemical fuels. Such polymer nanorobots are able to be served as swimming robots and intelligent cargo, performing drug encapsulation, self-propulsion, navigation toward targeted area, controllable release, and active delivery toward diseases. With continuous chemistry and material innovations, we envision that the swimming micro-/nanorobots will prove to be of considerable importance for diverse biomedical applications and eventually realize the "Fantastic Voyage" vision in scientific story.

References

1. (a) Ozin, G. A., Manners, I., Fournier-Bidoz, S., & Arsenault, A. (2005). *Advanced Materials*, *17*, 3011–3018; (b) Wang, J. (2013). *Nanotechnology*; (c) Sitti, M. J. N. R. M. (2018). *Nature Reviews Materials*, *3*, 74–75; (d) Gao, C., Wang, Y., Ye, Z., Lin, Z., Ma, X., & He, Q. (2020). *Advanced Materials*, e2000512.
2. Purcell, E. M. (1977). *American Journal of Physics*, *45*, 3–11.
3. He, Q., Duan, L., Qi, W., Wang, K., Cui, Y., Yan, X., & Li, J. (2008). *Advanced Materials*, *20*, 2933–2937.
4. Wu, Z., Lin, X., Si, T., & He, Q. (2016). *Small*, *12*, 3080–3093.
5. Lin, X., Wu, Z., Wu, Y., Xuan, M., & He, Q. (2016). *Advanced Materials*, *28*, 1060–1072.
6. Ariga, K., Ji, Q., Hill, J. P., Bando, Y., & Aono, M. (2012). *NPG Asia Materials*, *4*, e17.
7. Ai, S., Lu, G., He, Q., & Li, J. (2003). *Journal of the American Chemical Society*, *125*, 11140.
8. Zhang, X., Chen, H., & Zhang, H. (2007). *Chemical Communications*, *14*, 1395–1405.
9. Wu, Y., Wu, Z., Lin, X., He, Q., & Li, J. (2012). *ACS Nano*, *6*, 10910–10916.
10. Wu, Y., Si, T., Lin, X., & He, Q. (2014). *Chemical Communications*, *51*, 511–514.
11. Del Mercato, L., Carraro, M., Zizzari, A., Bianco, M., Miglietta, R., Arima, V., Viola, I., Nobile, C., Sorarù, A., & Vilona, D. (2014). *Chemistry – A European Journal*, *20*, 10910–10914.
12. Wu, Z., Wu, Y., He, W., Lin, X., Sun, J., & He, Q. (2013). *Angewandte Chemie, International Edition*, *52*, 7000–7003.
13. Li, J., Huang, G., Ye, M., Li, M., Liu, R., & Mei, Y. (2011). *Nanoscale*, *3*, 5083–5089.
14. Wilson, D. A., Nolte, R. J. M., & van Hest, J. C. M. (2012). *Nature Chemistry*, *4*, 268–274.
15. Wu, Z., Li, J., Estebanfernandez De Avila, B., Li, T., Gao, W., He, Q., Zhang, L., & Wang, J. (2015). *Advanced Functional Materials*, *25*, 7497–7501.
16. Gao, C., Lin, Z., Jurado-Sánchez, B., Lin, X., Wu, Z., & He, Q. (2016). *Small*, *12*, 4056–4062.
17. Gao, C., Lin, Z., Wu, Z., Lin, X., & He, Q. (2016). *ACS Applied Materials & Interfaces*, *8*, 34252–34260.
18. Chen, C., Chang, X., Angsantikul, P., Li, J., Estebanfernandez De Avila, B., Karshalev, E., Liu, W., Mou, F., He, S., Castillo, R., Liang, Y., Guan, J., Zhang, L., & Wang, J. (2018). *Advanced Biosystems*, *2*, 1700160.
19. Deng, Z., Mou, F., Tang, S., Xu, L., Luo, M., & Guan, J. (2018). *Applied Materials Today*, *13*, 45–53.
20. Kline, T., Paxton, W., Mallouk, T., & Sen, A. (2004). *Angewandte Chemie, International Edition*, *44*, 744–746.
21. Burdick, J., Laocharoensuk, R., Wheat, P. M., Posner, J. D., Wang, J., & Am, J. (2008). *Chemical Society*, *130*, 8164–8165.
22. Tu, Y., Peng, F., Sui, X., Men, Y., White, P. B., van Hest, J. C. M., & Wilson, D. A. (2016). *Nature Chemistry*, *9*, 480–486.
23. Wu, Z., Lin, X., Wu, Y., Si, T., Sun, J., & He, Q. (2014). *ACS Nano*, *8*, 6097–6105.
24. Balasubramanian, S., Kagan, D., Manesh, K. M., Calvomarzal, P., Flechsig, G., & Wang, J. (2009). *Small*, *5*, 1569–1574.
25. Ionov, L. (2010). *Journal of Materials Chemistry*, *20*, 3382–3390.
26. Magdanz, V., Stoychev, G., Ionov, L., Sanchez, S., & Schmidt, O. (2014). *Angewandte Chemie, International Edition*, *53*, 2673–2677.
27. Gennes, P. G. D. (2010). *Angewandte Chemie, International Edition*, *104*, 856–859.
28. Calvomarzal, P., Manesh, K. M., Kagan, D., Balasubramanian, S., Cardona, M., Flechsig, G., Posner, J. D., & Wang, J. (2009). *Chemical Communications*, 4509–4511.
29. Qin, L., Banholzer, M. J., Xu, X., Huang, L., & Mirkin, C. A. (2007). *Journal of the American Chemical Society*, *129*, 14870–14871.
30. Ji, Y., Lin, X., Wu, Z., Wu, Y., Gao, W., & He, Q. (2019). *Angewandte Chemie, International Edition*, *58*, 12200–12205.
31. Hong, Y., Blackman, N. M. K., Kopp, N. D., Sen, A., & Velegol, D. (2007). *Physical Review Letters*, *99*, 178103.

32. Baraban, L., Harazim, S., Sanchez, S., & Schmidt, O. G. (2013). *Angewandte Chemie, International Edition*, 52, 5552–5556.
33. Peng, F., Tu, Y., van Hest, J. C. M., & Wilson, D. A. (2015). *Angewandte Chemie, International Edition*, 54, 11662–11665.
34. Shao, J., Xuan, M., Dai, L., Si, T., Li, J., & He, Q. (2015). *Angewandte Chemie, International Edition*, 54, 12782–12787.
35. Ji, Y., Lin, X., Wang, D., Zhou, C., Wu, Y., & He, Q. (2019). *Chemistry, an Asian Journal*, 14, 2450–2455.
36. Ji, Y., Lin, X., Zhang, H., Wu, Y., Li, J., & He, Q. (2019). *Angewandte Chemie, International Edition*, 58, 4184–4188.
37. Tang, S., Zhang, F., Gong, H., Wei, F., Zhuang, J., Karshalev, E., Ávila, B. E. F., Huang, C., Zhou, Z., Li, Z., Yin, L., Dong, H., Fang, R. H., Zhang, X., Zhang, L., & Wang, J. (2020). *Science Robotics*, 5, eaba6137.
38. Karshalev, E., Esteban-Fernández de Ávila, B., Beltrán-Gastélum, M., Angsantikul, P., Tang, S., Mundaca-Uribe, R., Zhang, F., Zhao, J., Zhang, L., & Wang, J. (2018). *ACS Nano*, 12, 8397–8405.
39. Li, J., Esteban-Fernández de Ávila, B., Gao, W., Zhang, L., & Wang, J. (2017). *Science Robotics*, 2, eaam6431.
40. Xu, Z., Chen, M., Lee, H., Feng, S., & Yeon, J. (2019). *ACS Applied Materials & Interfaces*, 11, 15727–15732.
41. Vilela, D., Cossío, U., Parmar, J., Gómez-Vallejo, V., Martínez, A. M., Llop, J., & Sanchez, S. (2018). *ACS Nano*, 12, 1220–1227.
42. Yu, J., Jin, D., Chan, K. F., Wang, Q., & Zhang, L. (2019). *Nature Communications*, 10, 5631.
43. Wu, Z., Li, L., Yang, Y., Hu, P., Li, Y., Yang, S.-Y., Wang, L. V., & Gao, W. (2019). *Science Robotics*, 4, eaax0613.
44. Wan, M., Chen, H., Wang, Q., Niu, Q., Xu, P., Yu, Y., Zhu, T., Mao, C., & Shen, J. (2019). *Nature Communications*, 10, 966.
45. Baylis, J. R., Yeon, J. H., Thomson, M. H., Kazerooni, A., Wang, X., John, A. E. S., Lim, E. B., Chien, D., Lee, A., Zhang, J. Q., Piret, J. M., Machan, L. S., Burke, T. F., White, N. J., & Kastrup, C. J. (2015). *Science Advances*, 1, e1500379.
46. Gao, W., Dong, R., Thamphiwatana, S., Li, J., & Wang, J. (2015). *ACS Nano*, 9, 117–123.
47. de Avila, B. E., Angsantikul, P., Li, J., Lopezramirez, M. A., Ramirezherrera, D. E., Thamphiwatana, S., Chen, C., Delezuk, J., Samakapiruk, R., Ramez, V., Obonyo, M., Zhang, L., & Wang, J. (2017). *Nature Communications*, 8, 272.
48. Li, J., Thamphiwatana, S., Liu, W., Estebanfernandez De Avila, B., Angsantikul, P., Sandraz, E., Wang, J., Xu, T., Soto, F., Ramez, V., Wang, X., Gao, W., Zhang, L., & Wang, J. (2016). *ACS Nano*, 10, 9536–9542.
49. Li, J., Angsantikul, P., Liu, W., De Avila, B. E., Thamphiwatana, S., Xu, M., Sandraz, E., Wang, X., Delezuk, J., & Gao, W. (2017). *Angewandte Chemie, International Edition*, 56, 2156–2161.
50. Wei, X., Beltrán-Gastélum, M., Karshalev, E., Esteban-Fernández de Ávila, B., Zhou, J., Ran, D., Angsantikul, P., Fang, R. H., Wang, J., & Zhang, L. (2019). *Nano Letters*, 19, 4760–4769.
51. He, W., Frueh, J., Hu, N., Liu, L., Gai, M., & He, Q. (2016). *Advancement of Science*, 3, 1600206.

Chapter 16

Magnetic Micro-/Nanopropellers for Biomedicine



Tian Qiu, Moonkwang Jeong, Rahul Goyal, Vincent M. Kadiri,
Johannes Sachs, and Peer Fischer

16.1 Introduction

The motion of micro- and nano-objects in a fluid is, in the most general case, described by the Navier-Stokes equation. However, biomedical applications benefit from propellers that are so small that the mass (inertia) becomes negligible in fluid media. In this case, the Navier-Stokes equation can be approximated with the Stokes equation, which is simpler and shows no explicit time dependence. Therefore, the propulsion behavior of externally powered micro- and nanopropellers, which are proposed to perform biomedical tasks such as targeted drug delivery or minimally invasive surgery in fluids and soft tissues, is determined by the Stokes equation. A common measure of the applicability of this approximation is the Reynolds (Re) number [1]:

$$\text{Re} = \frac{\text{inertial forces}}{\text{viscous forces}} \quad (16.1)$$

T. Qiu · M. Jeong

Micro Nano and Molecular Systems Lab, Max Planck Institute for Intelligent Systems,
Stuttgart, Germany

Cyber Valley Group Biomedical Microsystems, University of Stuttgart, Stuttgart, Germany

R. Goyal · V. M. Kadiri · J. Sachs

Micro Nano and Molecular Systems Lab, Max Planck Institute for Intelligent Systems,
Stuttgart, Germany

P. Fischer (✉)

Micro Nano and Molecular Systems Lab, Max Planck Institute for Intelligent Systems,
Stuttgart, Germany

Institute of Physical Chemistry, University of Stuttgart, Stuttgart, Germany

e-mail: fischer@is.mpg.de

If the inertial forces are small, which is the case for microswimmers and nanorobots, viscous fluid forces are dominant. This is the regime of low Reynolds numbers ($Re < 1$), where reciprocal movements cannot propel a swimmer. This complicates the number of effective propulsion mechanisms at low Re , a fact that is captured by the “scallop theorem” of Purcell [2]. A scallop that opens and closes its arms periodically cannot swim. It does not matter how fast or slow the scallop opens or closes its arms, as at the end of the opening and closing cycle, which is reciprocal, it experiences no net displacement. Thus, in Newtonian (incompressible) fluids, like water or glycerol, biological and artificial microswimmers (that are not pulled by an external force or torque) require more sophisticated propulsion strategies.

One possibility to overcome the problem of time-reversibility is demonstrated by flagellated bacteria that spin their flagella in a corkscrew-like stroke in order to swim. Here the continuous rotation is non-reciprocal, because of the chiral symmetry of the flagella. The propeller effect describes the translation of a helix due to rotation-translation coupling [3]. It is an efficient method for propulsion especially for very small microswimmers. The handedness of the (chiral) corkscrew and its rotation sense fixes the direction of the movement, e.g., a right-handed screw moves forward upon a clockwise rotation and backwards upon a counter-clockwise rotation. In contrast, the left-handed mirror-image structure will translate in the opposite direction.

It is also possible to build artificial corkscrew-shaped propellers that mimic this propulsion strategy. These have been experimentally demonstrated by utilizing rigid micro-screws that were actuated by means of an external magnetic field that is rotating (Fig. 16.1) [4–6]. The rotation of the propeller by an external torque (as opposed to the inherent internal motion provided by the bacterium) is also advantageous for actuation. The slender body of the corkscrew means that the structure can be used to efficiently navigate complex biofluids. Rotating magnetic fields can also be more easily established over larger volumes and at greater distance than magnetic gradient fields. The latter can only be used to pull a magnetic object, whereas the unidirectional motion of a screw-propeller ensures high maneuverability and

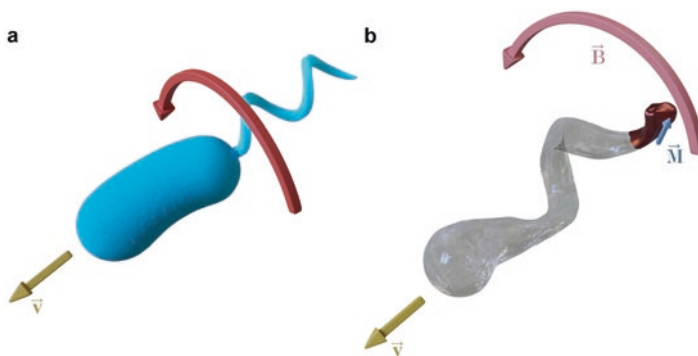


Fig. 16.1 Artificial micro-/nanopropellers (b) mimic bacteria flagella (a) to rotate and propel at small scale in fluids for biomedical applications

controllability, which is a highly desirable feature for externally powered biomedical devices.

In this book chapter, we review recent advances concerning artificial micro- and nanopropellers that are powered by magnetic fields and that can navigate through biological fluids and tissues for potential biomedical applications. Specifically, the chapter is organized as follows: In Sect. 16.2 we review the symmetry requirements for propulsion at low Re numbers by rotation-translation coupling; in Sect. 16.3 we describe the fabrication of micro-/nano-helices using physical vapor deposition; in Sect. 16.4 we review schemes to wirelessly actuate micro- and nanopropellers with magnetic fields. In Sect. 16.5 we discuss materials and, in particular, recent achievements in realizing propellers that are biocompatible, which is important for biomedical applications.

16.2 Theory of Micro-propulsion by Rotation-Translation Coupling

The propulsion force of the micro-/nanopropellers in fluids is generated by the coupling of the rotation to the translation of a helical shape. The rotation of the structures is generally driven by an external rotating magnetic field. We assume there is no field gradient and that no other external forces are present. The solution to the Stokes equation in low Re hydrodynamics reduces to two coupled equations [1]:

$$\begin{aligned} \mathbf{U} &= \mathbf{C}^{-1}\mathbf{L} \\ \mathbf{\Omega} &= \mathbf{B}^{-1}\mathbf{L} \end{aligned} \quad (16.2)$$

where \mathbf{U} is the translational velocity vector and $\mathbf{\Omega}$ the rotational (angular) velocity of the object, whereas \mathbf{L} is the torque exerted on the object by the external field. The coupling mobility tensor \mathbf{C} and the rotation resistance tensor \mathbf{B} relate the external torque to the objects' translational and rotational motion. Further, the equations show that, in general, the object's rotational motion is coupled to its translation, i.e., a translating body will always rotate and a rotating body will always translate, if the corresponding tensors are nonzero.

The exact form of the tensors \mathbf{B} and \mathbf{C} is determined by the geometry of the propellers' body, i.e., its symmetry. For example, a sphere, is an object with highest symmetry with three mutually perpendicular planes of mirror symmetry, has $\mathbf{C} = 0$ [1]. Consequently, a sphere cannot be propulsive by means of rotation-translation coupling at low Re. In contrast, a nonzero coupling tensor ($\mathbf{C} \neq 0$) is found for a chiral corkscrew shape. Thus, and because of the inspiration from biology, most experiments with artificial micro- and nanopropellers consider shapes with helical and thus chiral geometries in order to generate propulsion by means of an external rotating field. Chiral corkscrew shapes have been found to be optimal for propulsion [7]. It is generally assumed that chirality (handedness) is essential for efficient propulsion by means of an external rotating field and rotation-translation coupling.

This raises the question if chirality is strictly required for rotation-translation coupling or if a shape that is not chiral (achiral objects that possess mirror-image symmetry) can also translate when they are rotated by an applied magnetic field. This is not a purely academic question, as it is easier to synthesize or fabricate objects with high symmetry. Hence it is interesting to ask if such objects can also propel when magnetized and spun by a magnetic torque.

To shed light on this question, the fundamental symmetries that underlie rotation-translation coupling at low Re have recently been analyzed [8, 9]. Explicitly solving Eq. 16.2 for a magnetized and arbitrary shaped object [8, 9] that is subject to a rotating external field reveals that even objects that do not possess a chiral shape can propel at low Re . For instance, an achiral V-shaped body, which exhibits two mutually perpendicular planes of mirror symmetry, was shown to be able to propel under certain conditions. The V-shaped object was demonstrated to be propulsive as long as it does not rotate around one of its principal axes of rotation. However, theory and experiments proved that the orientation of the dipole moment with respect to the body of the V-shape plays a crucial role whether the V-shape can be propelled or not [9]. In the symmetry analysis, especially when determining if the object is chiral, it is essential that both the geometric shape and the object's magnetic dipole moment are considered [9]. If the symmetries of the whole object (shape and dipole) are considered, it is possible to correctly predict whether or not the object is propulsive and in this case if unidirectional or bidirectional propulsion will occur. The latter case means that the object has equal probability to move forward or backward, i.e., the rotation sense of the external field does not fix the propulsion direction. Note, however, that even the V-shape with its high geometrical symmetry can be designed to yield unidirectional propulsion if the V-shape is magnetized in a particular direction [9].

The mathematical definition of chirality is parity (spatial inversion), and hence, the V-shaped object's overall chirality is determined by executing the parity operator on both, the geometric shape and the dipole moment. Interestingly, in case of unidirectional propulsion, the object is necessarily chiral due to the orientation of the magnetic dipole moment it carries. On the other hand, one can design a magnetized chiral V-shaped object, which is non-propulsive upon rotation as is shown in Fig. 16.2. Therefore, chirality is certainly not a prerequisite for efficient propulsion via rotation-translation coupling, and in addition, parity alone does not fully explain the propulsion of such propellers. Instead, it becomes necessary to consider charge conjugation. Consequently, applying parity in conjunction with charge conjugation symmetry to a magnetized object is sufficient to fully predict whether the object will propel in a rotating magnetic field.

In practice, and in particular with a view of biomedical applications, magnetic fields applied to magnetized micro- and nanopropellers are used for externally driven propulsion, because it is easier to realize large torques. However, actuation of a V-shape by an external electric field is also possible and has recently been experimentally realized. Remarkably, because in this case the V-shape carries an electric dipole moment, and not a magnetic moment, its symmetry becomes achiral, and it therefore constitutes the first demonstration of an achiral propeller that propels by rotation-translation coupling in a fluid at low Re [9].

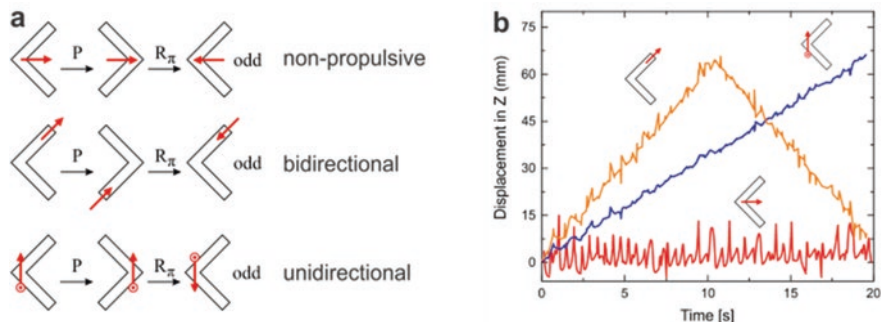


Fig. 16.2 Parity and charge conjugation symmetry need to be both taken into account to give a comprehensive prediction of low Re propulsion. (a) Three V-shaped objects that carry a magnetic dipole moment with different orientations (shown as the red arrows) with respect to the body shape. All three objects are parity-odd and therefore chiral but exhibit different propulsion gaits; (b) Experimental data show the propulsion gaits corresponding to the designs in a, including uni- and bidirectional, as well as a non-propulsive V-shaped object. (Reproduced with permission [61], 2020, University of Stuttgart)

It should be mentioned that not only rotating but also precessing external fields, i.e., the external field vector rotates on a cone due to a superposition of an in-plane rotating field with a constant component orthogonal to it, can be used to propel highly symmetric V-shaped objects. In this case, also propellers, which are non-propulsive in a rotating field, can exhibit unidirectional motion [10]. Extending the types of applied magnetic fields from purely rotational to precessing fields and at the same time to consider additional geometrical shapes promises to extend the design space of propulsive micro- and nanorobots for biomedicine.

Irrespective of the body shape or its symmetry, the velocity of external field-driven propellers always depends on the external field's rotation speed [6, 8, 9]. Beyond a certain rotation frequency, at the step-out frequency, the micro- or nanopropellers can no longer follow the external field any more. Therefore, they will not maintain a constant angular synchronous velocity for frequencies larger than the step-out frequency. Instead, an asynchronous slip-motion will occur, and the propulsion velocity will drop to zero. The step-out frequency depends on several parameters, e.g. the strength of the magnetic dipole moment, the amplitude of the external magnetic field, and the viscosity of the fluid.

The discussion in this section starts with the governing Stokes equation, which does not have any explicit time dependence, and thus a reciprocal motion does not lead to a net translation in Newtonian fluids. However, most biofluids are non-Newtonian (e.g., the vitreous, mucus, blood, and so on), and in such fluids the time-reversibility problem can also be overcome by exploiting the time-dependent properties of the fluid itself, i.e., a scallop can even with reciprocal motion generate a net translation in non-Newtonian media. For this, it has to open and close its arms with varying speeds, as has been demonstrated with an artificial micro-scallop that was actuated with an external oscillating magnetic field [11]. Utilizing the biofluids' non-Newtonian rheology, i.e., its shear rate-dependent viscosity, allows the small

robot to propel with a reciprocal motion. This significantly simplifies the robot design and allows most actuators to be used for swimming in most biological fluids, even though they are not propulsive in Newtonian fluids (water) due to the scallop theorem. This may lead to new designs of simpler artificial microswimmers that are especially designed to operate in biological media and tissues.

16.3 Fabrication of Micro- and Nanopropellers by Glancing Angle Deposition (GLAD)

A few microfabrication techniques exist to fabricate micron-sized corkscrew shapes, but we focus here on the technique known as glancing angle deposition (GLAD). This technique can be used to fabricate the smallest propellers as well as the highest number of propellers, and that allows a large number of materials to be used including the strongest magnetic materials, which as we shall show are nevertheless biocompatible. The complex helix-shaped micro- and nanopropellers mentioned in the previous section were all fabricated using GLAD. It is a physical vapor deposition (PVD) method where a solid source material is heated in a crucible, either thermally or by an electron beam, under high vacuum conditions until it starts to melt and evaporate. Due to the low background pressure, the evaporant forms a directed flux and coats a surface (substrate). The substrate, on which the propeller structures grow, is tilted and held into this flux. Thus, the incident atoms and molecules adsorb on the surface of the substrate. The micro- and nanopropellers are not grown under normal incidence as is customary in PVD, but with oblique angle deposition (OAD), a technique where the evaporant and the substrate are intentionally tilted with respect to each other. Due to the tilt, the flux is shadowed, especially if there are any seed particles, and columnar structures will grow. The tilt-angle is commonly denoted as α , as shown in Fig. 16.3a. The GLAD technique adds another degree of freedom by rotating the substrate during deposition around the surface normal. The corresponding angle is denoted by ϕ . Those two parameters can be either constant or dynamically adjusted to grow complex and low-symmetry-shaped bodies on the micro- and nanoscale. Usually α is constant and if ϕ is constant too, a tilted column will form. If this process is repeated after the ϕ angle was changed by 180° , another column tilted in the opposite direction grows on top, and hence results in the V-shaped zig-zag structure as shown in Fig. 16.3b. Sometimes it is useful to have columnar structures that form columns perpendicular to the substrate. This is possible if a constant α angle and a continuous and fast ϕ rotation is used during the deposition process. An example of such pillar structures is shown in Fig. 16.3c. In case the ϕ angle is varied continuously but with a slow rotation speed, a helical corkscrew shape will form. Thus, the GLAD technique is useful for the fabrication of complex three-dimensional micro- and nanostructures, sometimes also denoted sculptured thin films (STF). During the deposition, multiple materials can be combined or deposited sequentially, which results in a large number of possible shapes

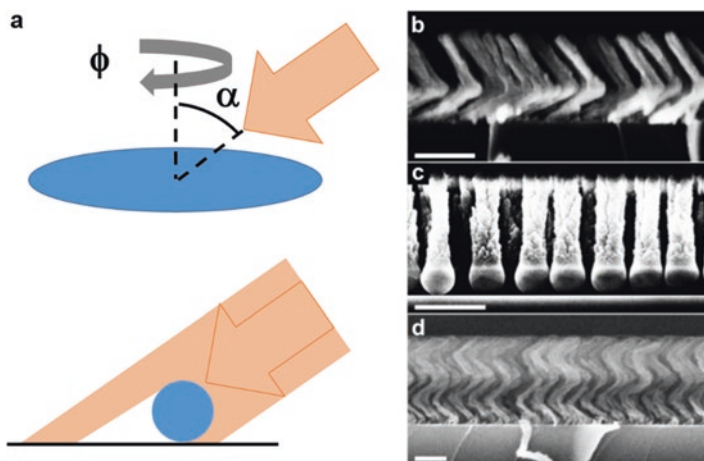


Fig. 16.3 Glancing angle deposition for the fabrication of micro-/nanopropellers. (a) Schematic visualization of the deposition process and the shadow effect. (b) SEM of nano-zigzags with one arm Ni and one arm SiO₂ grown on Au nanodots (scale bar 200 nm). (c) TiO₂ pillars grown perpendicular to the substrate on SiO₂ beads (scale bar 1 μ m). (d) Chiral corkscrew-shaped SiO₂ structures grown on Au nanodots (scale bar 200 nm). ((b), (c), and (d) are reproduced with permission [61]. 2020, University of Stuttgart)

and structures. Typically 10^9 – 10^{10} structures grow on a cm^2 of substrate area. The entire growth process only takes a few hours.

To further facilitate the shadow-effect pre-patterned substrates are used, which already have well-structured nucleation seed patterns. A common procedure is to create a monolayer of closed-packed silica beads with sizes between 0.1 μm and 5 μm on a silicon substrate [12]. The seed particles can be deposited on an entire wafer using the Langmuir-Blodgett method [6]. For this purpose, nanoparticles, such as silica beads, are first gently pipetted onto a water surface and then transferred to the wafer by dip coating. The vertical columnar structures seen in Fig. 16.3c were grown on top of a monolayer of Langmuir-Blodgett-deposited SiO₂ beads. Another method for pre-patterning the GLAD substrate is to use Block-Copolymer-Micelle-Nanolithography [13], a method that coats a wafer with a (non-closed-packed) hexagonal monolayer of ~ 10 nm gold nanoparticles. This method has been used to pattern the substrate on which the zig-zags and helices in Fig. 16.3b, d were grown. The pre-patterning improves the quality of the structures, as it prevents the fusion of particles during the deposition. Depending on the materials that are used, it is sometimes also advantageous to actively cool the substrate during evaporation, which means the thermal energy of the incident atoms is reduced and hence their ability to diffuse on the substrate after their adsorption. This can be an important feature as the high surface mobility of the adatoms facilitates the growth of highly symmetric (e.g., spherical) shapes rather than complex structures, such as helices [14].

Another advantage of GLAD is the wide choice of possible evaporation materials as well as the ability to alloy several elements by simultaneous evaporation of two or more source materials. Micro- and nanopropellers typically comprise a magnetic head, grown with a fast ϕ rotation of, e.g., Co, Fe, or Ni (but also see Sect. 16.5 for a discussion of biocompatible materials), followed by a helical structure made out of an oxide such as SiO_2 [6]. After the GLAD process, the propellers are magnetized in a strong external magnetic field while still attached to the substrate. For further applications, the individual structures are then transferred into solution via ultrasonication to obtain colloidal suspensions of magnetic propellers.

16.4 Magnetic Actuation Systems

Micro-/nanopropellers cannot use traditional powering and actuation mechanisms as in large-scale robotics, such as on-board batteries or electromagnetic motors, due to their small size. Moreover, tethers for power transfer, such as wires or tubing, would restrict the locomotion of small-scale robots; thus untethered power transmission is needed for minimally invasive biomedical applications. Magnetic fields are commonly used in the medical field for imaging as well as for wireless actuation [15], due to its large biological tissue penetration depth, high controllability, and reliability. The magnetic fields can exert relatively large forces and/or torques on small-scale magnetic robots [16].

The magnetic torque $\boldsymbol{\tau}$, which is generated in a magnetic material is:

$$\boldsymbol{\tau} = \boldsymbol{m} \times \boldsymbol{B} \quad (16.3)$$

where \boldsymbol{m} is the magnetic moment and \boldsymbol{B} is the external magnetic field vector. The torque applied on the magnetic material/structure can cause translation, for instance, via rotation of a micropropeller [17] or can induce an angular displacement of a magnetic rod [18].

Magnetic fields have also been widely applied to the actuation of micro-/nanorobots for potential biomedical applications both *in vitro* and *in vivo* [19–21], i.e., steering a micro-guidewire by a magnetic field gradient [22], propelling micro-/nanopropellers in biological fluids by a rotating magnetic field [23–25], conducting micro-rheological tests [18], and steering chemically powered micro-/nano-motors in the intestine [26–28].

The generation and control of the magnetic field is achieved either by a specific configuration of permanent magnets or by controlling the electric currents in electromagnetic coils. A few examples of magnetic actuation systems are summarized in Table 16.1. In this section, we discuss some typical magnetic actuation systems. These systems are often customized, and the details depend on the particular application, i.e., the required field strength, the working volume, and the frequency range in case of an oscillating field. The design of the magnetic actuation system therefore needs to consider particular applications and operating conditions. Two main categories, i.e., permanent magnet systems and electromagnetic systems, are discussed

Table 16.1 Comparison of published magnetic actuation systems

Types	DOF ^(a)	Field strength [mT]	Rotating frequency [Hz]	Working volume [cm ³]	Size of the robot [μ m]	Working media	No. of magnets/coils	Size of each magnet/coil [mm]	Ref.
Permanent magnet systems	1	105	20	8	$\Phi 10 \times 250$	Vitreous of porcine	4	$30 \times 30 \times 30$	[62]
	5	30	10	0.5	250	Silicone oil	8	$25.4 \times 25.4 \times 25.4$	[31]
	2	100	Manual rotation	–	$\Phi 30$	Dodecane	16 inside 8 outside	$\Phi 34 \times 19.5$ octagon	[33]
Electromagnetic systems	3	10	>1 kHz	0.125	$\Phi 0.5 \times 2$	Vitreous of porcine	6	$\Phi 40$ (inner), $\Phi 70$ (outer), 10 (height), largest coil	[63]
	–	Up to 400	100	~ 4000	20,000 In length	Pork fillet	18	~ $\Phi 350$, ~ $\Phi 450$	[38]
	5	50	–	4	2500 In length	Chick chorallantoic membrane	8	$\Phi 62 \times 210$	[37]
	6	100	–	–	$\Phi 1000 \times 1000$	Arteries of swine	Clinical MRI scanner		[22]

(a) Degree Of Freedom

Table 16.2 General comparison of magnetic actuation systems

Key parameters	Permanent magnet systems	Electromagnetic systems
Field strength	Strong	Weak
Working space	Large	Small
Controllability (on/off)	Low	High
Driving frequency	Low	High
Active cooling system	No	Yes
Mechanical motion, noise, and vibration	Yes	No
System total weight	Low	High
Cost	Low	High

in the following sections, respectively, and their advantages and disadvantages are compared in Table 16.2.

16.4.1 Permanent Magnet Actuation Systems

The basic concept of an actuation system based on permanent magnets is that several permanent magnets are distributed in space in a particular configuration to generate a superimposed magnetic field that is controllable in a defined volume. Compared to electromagnetic setups (Table 16.2), permanent magnet-based systems often offer higher field strength in a larger working volume. Moreover, permanent magnets do not require expensive ancillary equipment, such as electric amplifiers or active cooling systems. They are also less bulky, lighter, and generally cheaper. However, the trade-off is that the permanent magnet is always energized and that mechanical driving systems are required, in order to change the field amplitude or direction. Mechanically moving permanent magnets is also not suitable for high-frequency actuation.

Combining several permanent magnets that can be manipulated individually in their position and orientation provides a system with several degrees of freedom (DOF). For example, superimposing magnetic fields from a pair of magnets at an angle creates a small region of zero magnetic field strength, which can be used to push magnetic particles away from the permanent magnet [29].

To generate a time-varying magnetic field, a mechanical drive system is needed to rotate or translate the permanent magnets. As the permanent magnets cannot be “turned off” and since the magnetic attraction force between two magnets is inversely proportional to the distance square, the attractive force pulling a magnetic object toward the magnet can lead to very strong forces at short distance and can be a cause for safety concerns. A safer design does not rely on translation of magnets, but instead utilizes the rotation of the permanent magnets around a fixed support axis. Different approaches are listed in Table 16.1 and can be categorized according to three basic criteria:

1. The magnets are connected by a synchronizing mechanical drive mechanism (e.g., via a belt or gears) and are driven by one electrical motor (Fig. 16.4a) [18, 30]. Jeong et al. presented a magnetic actuation system using the synchronized rotation of four permanent magnets [18] (Fig. 16.4a). The magnets are firstly positioned in a desired direction and then connected using a timing belt-pulley to achieve a rotating magnetic field that is homogeneous at the center and that showed a strength of 105 mT. This system was designed for biomedical applications, with ample of space in between the magnets and access ports in all directions to accommodate medical imaging equipment, such as X-ray, ultrasound, and fluorescent imagers. These were used to localize the robots in the specimen. Although the system has only 1-DOF rotation, the addition of two sets of magnets provides two additional DOF, making the setup comparable to a 3-axis Helmholtz coil system.
2. Each magnet is individually driven and rotated by an electrical motor (Fig. 16.4b) [31, 32]. A permanent magnet system which has 5-DOF was reported by Ryan et al. using eight independent rotating magnets attached to eight servo motors. This system could generate a magnetic field of 30 mT and a magnetic gradient of $0.83 \text{ T} \cdot \text{m}^{-1}$ and no constraints on the direction of the magnetic fields [31]. This kind of system with multiple motors allows individual rotation of each magnet, which allows for the control of the magnetic gradient and the field direction [31, 32]. However, it requires several strong motors (that match the strong magnetic torque between the permanent magnets), and it requires a synchronized control of each of them.
3. The combination of a set of fixed magnets and a set of rotatable magnets (Fig. 16.4c) [33]. Baun et al. reported a system that is composed of an inner ring with 16 magnets and an outer ring with 8 magnets that can achieve a field strength of 100 mT and a gradient of $0.3 \text{ T} \cdot \text{m}^{-1}$ [33]. The magnets on the system are coaxially assembled along a specific direction to generate a dipolar magnetic field, a quadrupolar magnetic field, and the combination of both magnetic fields which defines the magnetic gradient to manipulate objects placed in the working volume. The movement direction is controlled by rotation of the outer ring (quadrupole). If particles are not placed in the center, they move slowly toward the rim due to the magnetic gradient.

16.4.2 Electromagnetic Actuation System

Many types of electromagnetic systems have been proposed and are commonly used to manipulate small-scale robots. Basically, magnetic fields are generated by controlling the electric current applied to a coil or to a pair of coils. One of the advantages of electromagnets is that the strength of the magnetic field is controllable even at high frequency.

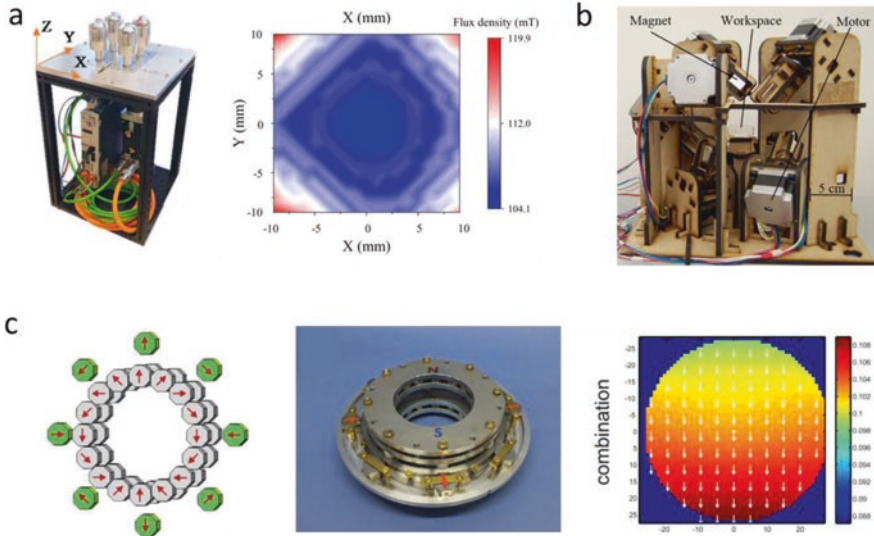


Fig. 16.4 Permanent magnet actuation systems. (a) Synchronized magnet rotating system; (b) Independent controllable magnet system; (c) Three cylinder Halbach system. (Reproduced with permission. (a) [18] 2019, IEEE; (b) [31] 2019, IEEE; (c) [33] 2017, Elsevier)

One of the commonly used types of electromagnetic actuation systems is a Helmholtz coil geometry. The Helmholtz coil is comprised of a set of identical coils aligned coaxially where the distance between the two coils equals the radius of coil. This particular configuration ensures a relatively homogeneous magnetic field in the central region between the two coils, which is beneficial for the study of micro-/nanopropellers that are actuated by a rotating magnetic field. This gradient-free system permits the study of magnetic torque-driven micro- and nanorobots. Assembling three pairs of (Helmholtz) coils (Fig. 16.5a) along three orthogonal directions can be used to generate relatively homogeneous fields that can point in any arbitrary direction. Wu et al. used a system of three pairs of coils that were arranged in an almost Helmholtz-like geometry to control the propulsion of helical magnetic micropropellers to move in the porcine vitreous to reach the optic disc region on the retina [25].

Electromagnetic actuation systems have also been widely used to generate gradient fields [23, 34–36]. For example, Kratochvil et al. demonstrated 5-DOF (3 translation, 2 rotation) electromagnetic actuation system, named OctoMag (Fig. 16.5c) [34]. This system consists of eight electromagnetic coils and generates magnetic field strength of 50 mT in a working space of 4 cm³. The magnetic field strength was strengthened by soft magnetic cores inside the coils. The OctoMag successfully demonstrated that the robot's movement could be controlled in a fluidic tank, and it

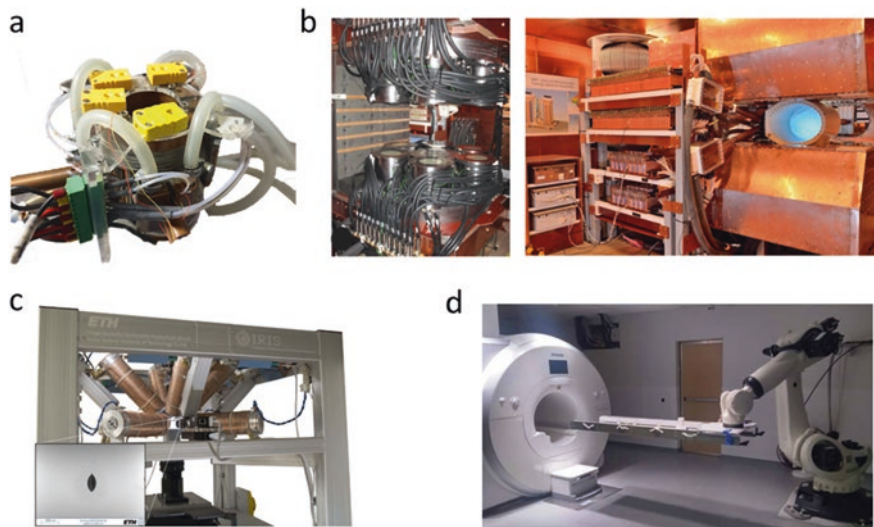


Fig. 16.5 Electromagnetic actuation systems. (a) A 3-axis Helmholtz coil with the cooling system; (b) A clinical-scale high-power system; (c) OctoMag system with 5-DOF; (d) The fringe field of an MRI scanner is used as the gradient field for magnetic manipulation. (Reproduced with permission. (b) [38] 2018, PLOS ONE; (c) [34] 2010, IEEE; (d) [22] 2019, Science Robotics)

also showed that it could be used to steer a needle tip to puncture tissue [37]. To extend these electromagnetic systems to accommodate a full human body, however, causes numerous engineering challenges. Rahmer et al. designed a clinical-scale magnetic field generator using 18 copper coils which have cylindrical soft magnetic iron-silicon cores to increase the field flux (Fig. 16.5b) [38]. The magnetic field strength from 30 to 90 mT at a frequency up to 10 Hz were applied for the experiment. The working space where the magnetic field is still homogeneous was reported to be spherical volume with a diameter of 200 mm. The resulting magnetic field was used to move a millimeter-scale helical robot to penetrate into a fillet of pork composed of muscle and connective tissue [38]. However, the system equipped with 100 kW cooling capacity uses more than 110 A per stack [38]. An alternate approach was presented by Azizi et al. who utilized the fringe fields of a superconducting magnetic resonance imaging (MRI) machine (Fig. 16.5c). A robotic arm was used to position a bed in the fringe field to navigate a guidewire in the blood vessels. The magnetic fringe field gradient (larger than $2 \text{ T} \cdot \text{m}^{-1}$) from the MRI scanner exerted a large pulling force to steer the tip of the micro-guidewire in the neck and brain arteries of a swine [22]. However, objects placed in the vicinity of an MRI magnet also compromise the quality of the field homogeneity necessary for nuclear magnetic imaging.

It is clear that electromagnetic actuation systems outperform permanent magnet systems in aspects of controllability and whenever time-varying fields are needed. They are in general also safer to operate. However, electromagnetic coils require cooling systems and expensive power supplies and are thus bulky and expensive. Regardless, whether electromagnetic or permanent magnets are used, the magnetic field strength always decays quickly over distance, which means it is difficult to realize high field strengths, which determines the magnetic driving force/torque on the robots, over a large volume (e.g., as is needed if it is to accommodate a human). Previous studies have shown that actuation based on homogeneous rotating magnetic fields scale better than gradient fields for a given distance [19]. Given the constraints in the magnet system, it is advantageous to optimize the micro-/nanopropeller design (helical geometry) and the magnetic materials, to increase the efficiency of converting the external driving magnetic field to actual locomotion inside biological fluids and tissues.

16.5 Biocompatible Magnetic Materials for Micro-/Nanorobots

Section 16.2 demonstrates the crucial role magnetic materials play in the maneuverability, reliability, and performance of magnetic propellers. Yet, as is to be expected in such a relatively young field, the fabrication and types of materials used for different propellers vary widely. While some materials can simply be deposited in a physical vapor deposition (PVD) chamber (e.g., Ni), others require more complicated solution processing or annealing steps ($Zn_xFe_{3-x}O_4$) [39]. In recent years, the use of nanopropellers has progressed from the first proof-of-concepts studies [4, 5] to the propulsion through biological media [24, 25, 40] as well as biomedical applications [41, 42]. This led to a closer inspection of the materials used in micro-/nanorobots [39, 43].

The following section will provide a few criteria which are helpful in evaluating the properties of magnetic materials and to judge their suitability toward specific, especially biomedical, applications. An overview of commonly used materials is provided. FePt in the $L1_0$ phase is identified as a particularly promising material for biomedical micro-/nanodevices.

16.5.1 Criteria for Magnetic Materials

Biocompatibility

Biocompatibility describes the absence of adverse biological effects (death, toxicity, oxidative stress) caused by the presence of a certain chemical or nanostructure. Determining cell viability is a common cell culture technique that can easily be

adopted for a rapid *in vitro* measure of biocompatibility. There are many types of ready-to-use commercial cell death assays. These are typically simple colorimetric assays, which are, for instance, based on calcein AM, a cell membrane permeable compound that is metabolized into a dye by live cells, and the ethidium homodimer-1, a membrane impermeable dye that only penetrates dead cells [44]. This in turn means that these dyes provide characteristic fluorescent readouts for dead versus live cells and hence biocompatibility that can be analyzed in a fluorescence microscope or via flow cytometry measurements. Assays like these can readily be performed *in vitro* with low cost. Compared to cell death assays, *in vivo* toxicity tests are as complicated, as they are varied due to the often complex interrelations between different cell types and organs. Regardless, *in vivo* biocompatibility testing is ultimately required for biomedical micro-/nanorobots to ascertain their long-term pharmacokinetics [42].

Magnetic Properties: Coercivity

The coercivity H_C describes the magnetic field necessary to re-magnetize a ferromagnetic material. The working principle of helical nanorobots, as depicted in Fig. 16.1, however, relies on reorienting a magnetized section thereby transferring torque τ – without re-magnetizing the robot. For this, low ~ 2 to 100 mT rotating fields are used. Soft magnetic materials that have coercivities in the \sim mT range are thus unsuitable as magnetic materials for nanopropellers. This, conversely, justifies the use of high coercivity (\sim T) materials – hard magnets – in nanopropeller applications, to avoid re-magnetization while allowing for the application of high magnetic fields.

Magnetic Properties: Remanence

The magnetic remanence M_R describes the residual magnetization in a ferromagnetic material in the absence of an external magnetic field. As Eq. 16.3 illustrates, the magnetic moment of a propeller determines the torque that can be applied to the robot. While keeping the driving magnetic field strength the same, a higher magnetic remanence allows for a higher torque, or inversely a smaller magnetic field strength B can achieve the same torque. The former could lead to higher propulsion velocities and the latter to a simplification of the magnetic setup.

Biodegradability

The biodegradability characterizes a materials' property to be digested via biological processes or decomposition in biological media such as blood or cell media. Biodegradation is a common feature of many macroscopic biomedical tools such as degradable sutures made from polylactic acid (PLA) and/or polyglycolic acid [45].

A major advantage of magnetic materials based on iron, for instance, is that they decompose easily inside the body. Their biocompatibility and rapid clearance are two major reasons why iron oxides have enjoyed increased popularity over the last years [46]. However, not every biodegradable material is necessarily biocompatible. In the case of nickel or cobalt, the products of the metals' dissociation are highly toxic toward cellular functions, making these materials rather undesirable for biomedical applications [47, 48].

The biodegradability of an entire microswimmer has been realized in coating helically shaped microorganisms (*Spirulina*) with biodegradable iron oxide nanoparticles [49–51]. Similarly, biodegradable polymers have been used to fabricate iron-oxide-containing artificial soft microswimmers by a number of methods [51–54]. The difficulty in all of these studies is that the magnetic loading is limited and the magnetic strength of the nanoparticles is also low, which results in weak magnetic moments and thus small torques. In contrast, FePt is a harder magnet with a far higher magnetization [43].

3D Nanostructuring

Section 16.2 introduces GLAD as a promising method of generating three-dimensional nanoswimmers. As discussed in the previous subsection, other methods such as 2-Photon polymerization are also capable of producing similar, if bigger, structures. The method of fabrication limits which materials can be used. For instance, the hard magnet NdFeB cannot be evaporated using an electron beam or thermal evaporation making it unsuitable for fabrication via GLAD. 2-Photon polymerization, while suitable for the fabrication of some biodegradable polymeric propellers, can only accommodate a relatively small loading of magnetic powders, such as FeO_x nanoparticles. Two photon polymerization cannot process more favorable metals with high magnetic remanence and coercivity. These typically have to be added in a subsequent processing step [55]. Direct incorporation of strong biocompatible magnetic materials is, however, possible with GLAD.

16.5.2 *Magnetic Materials for Biomedical Applications*

Nickel is cheap and has excellent deposition characteristics in PVD and has thus in the past been a material of choice for many early nanoswimmer applications [25, 55]. However, similarly to cobalt, it is not ideal for biomedical applications since it shows toxicity and is chemically unstable in biological media [48].

Iron, on the other hand, is similarly inexpensive and can also be nanostructured via GLAD [25]. Its corrosion and degradation products are biocompatible and iron typically exhibits a high saturation magnetization of 1.6 T. The remanent magnetization of pure iron is usually less impressive at the nanoscale (40 emu/cm³), and crucially iron's coercive field of ~0.2 mT is low when compared to other hard

magnets like NdFeB's 1.2 T [56, 57]. Iron oxides are typically soft magnets and are thus not ideal materials in order to realize large forces and torques. Additionally, FeO_x species are difficult to nanostructure via PVD since carefully controlled post-processing steps are usually required to obtain the correct phase [58].

Combinations of multiple magnetic materials are also possible, at the expense of a more involved fabrication process, as demonstrated by Venugopalan et al. Here Fe is first deposited via GLAD or PVD, and solution processed annealed zinc ferrite coatings are subsequently incorporated. This process yields multimodal non-agglomerating nanopropellers that could double as magnetic hyperthermia agents [39].

Finally, NdFeB is probably one of the most widely used hard magnets. Since NdFeB is not stable in moisture, it typically has to be coated with a protective layer. In addition, NdFeB cannot easily be nanostructured using physical vapor deposition. However, there is an attractive processable, biocompatible hard magnet that is suitable for nanopropeller fabrication: iron platinum (FePt).

FePt a Strong Magnetic Material for Nanodevices

The $L1_0$ phase of iron platinum has recently come into focus as a promising material for the construction of hard magnetic nanodevices due to a number of advantages over NdFeB [59]. $L1_0$ describes the face-centered tetragonal phase of a ~50:50 iron/platinum alloy where iron and platinum positions are arranged in an alternating ABA fashion (Fig. 16.6 center) as opposed to a face-centered cubic phase. FePt has the highest recorded magnetic energy products of up to ~70 MGOe – the maximum magnetic energy storable in a material – and coercivities of up to 7 T that easily rival those of other conventional, typically Nd- or Sm-based hard magnets [59]. What makes this comparison especially interesting is the fact that FePt is completely rare-earth free. Due to the addition of the platinum and its effect on the iron's electronic configuration, FePt also exhibits a significantly higher remanence than pure iron, despite exhibiting a lower saturation magnetization of $3.1 \mu_B$ ($2.7 \mu_B$ from Fe and $0.4 \mu_B$ from Pt) [59]. While the merits of iron as a material for biomedical applications were already discussed, there is also precedence of platinum being used in this capacity. In addition, FePt can be processed without the need for inert gases, and it is unreactive and thus does not need to be coated with a protective layer [43, 59]. FePt is thus uniquely positioned to be a next-generation magnetic material for micro- and nanorobotic devices. $L1_0$ FePt nanoparticles smaller than 10 nanometers are considered as superparamagnetic contrast agents for MRI. It is not cytotoxic and is therefore a prime candidate for applications in biomedical nano- and micro-devices that can leverage these hard magnets' unique combination of easy nanostructuring, biocompatibility, and high magnetic moments [60].

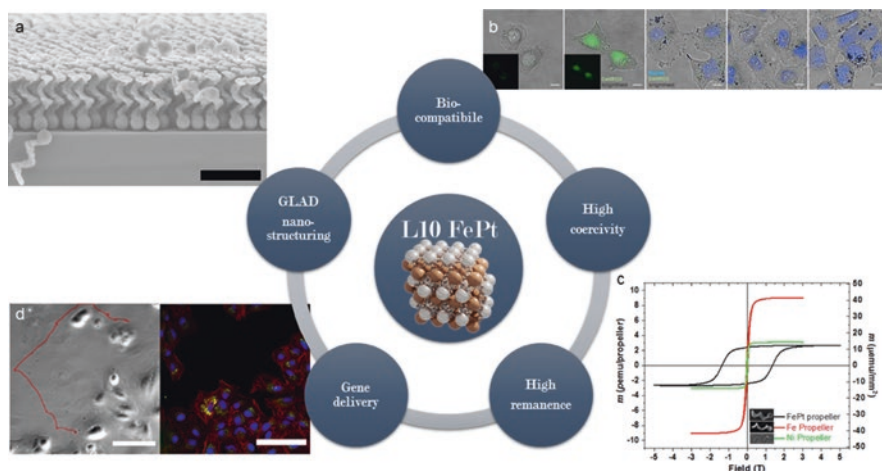


Fig. 16.6 $L1_0$ FePt (crystal structure in center) as a novel material for biomedical microswimmers. (a) The material can be 3D nanostructured via glancing angle deposition; (b) It is biocompatible (pictured are the results of a CellROX assay for reactive oxygen species.) and (c) It exhibits higher magnetic coercivity and remanence than previous materials Ni and Fe. (d) FePt-based microswimmers enable targeted active gene delivery in A549 cells. (Reproduced with permission [43]. 2020, Wiley VCH)

Fabrication and Characterization of FePt Nanopropellers

Using GLAD, nanopropellers that use FePt instead of the standard Ni or Fe can be fabricated via a co-deposition of iron and platinum followed by an annealing step at 680 °C to obtain the correct phase, fct $L1_0$. This phase transition can be observed both via XRD and SQUID magnetometry. The latter further reveals that $L1_0$ FePt as used in this shape exhibits a magnetic remanence of 333 emu/cm³, which rivals that of microstructured NdFeB (400 emu/cm³). Compared to Fe-based propellers of similar geometry, this is an eightfold increase in magnetic remanence [43].

Table 16.3 offers an overview of how nanostructured $L1_0$ FePt compares to other magnetic materials. The increased magnetic moments are also reflected in the maximum propulsion speeds for these propellers which reach up to 13 body lengths per second. Microswimmers' typical propulsion behavior increasing speeds for higher magnetic fields and frequencies is observed up to the respective step-out frequencies, where the propeller cannot follow the magnetic field.

Biocompatibility Tests and Gene Delivery

Despite both major components in the microswimmers (FePt and SiO₂) having individually been deemed biocompatible, it is important to note that their combination in the form of the microswimmer also shows no detectable toxicity. Upon

Table 16.3 Comparison of magnetic materials for micro-/nanopropellers

Material	Biocompatibility	Coercivity [T]	Magnetic remanence [emu/cm ³]	3D nanostructuring
Ni	No [47, 48]	0.01 [43]	11 [43]	PVD [41, 63]
Co	No [47, 48]	0.09 [64]	0.2 [65]	PVD [66]
Fe	Yes (concentration-dependent) [67]	0.028[43]	40 [43]	PVD [63]
FePt (680 °C)	Yes [43, 60]	1.3276 [43]	333 [43]	PVD [43]
NdFeB	–	1.2 (bulk) [57]	400 [43]	–
Fe ₃ O ₄	Yes [46]	~0 [68]	~0 [68]	2-Photon-polymerization [52, 53]

incubation with multiple cell lines (HEK and A549), both the cell viability and reactive oxygen species (ROS) assays confirmed that the FePt nanopropeller is fully biocompatible [43].

This in turn allowed for their biomedical application to deliver green fluorescent protein (GFP) encoding plasmids into A549 cells. FePt microswimmers enabled both the passive transport of the plasmids into the cell's cytoplasm, which after an incubation time of 24 h started expressing GFP, and the active, i.e., targeted delivery.

16.6 Conclusion

In this chapter, we summarize some of the recent advances of magnetically driven micro-/nanopropellers for biomedical applications. We emphasize the challenges and new developments in the geometrical design, nano-fabrication, wireless actuation, and the choice of biocompatible materials for these small-scale robots. Recent advances have focused on motility studies in organ models *in vitro* or *in ex vivo* animal organs. The next step is to test these micro-/nanorobotic systems *in vivo* and to demonstrate a useful biomedical application. The constraints given by the relatively low torques that can be realized in laboratory magnetic systems calls for shape-optimized structures, with large magnetic moments that can also slip through the complex matrices found in real tissues and organs. Nanopropellers are thus promising for a truly minimally invasive nanomedicine of the future.

Acknowledgments The work is partially funded by the Max Planck Society. T.Q. and V.K. acknowledge financial support from the Vector Foundation. T.Q. and M.J. acknowledge the support by the Stuttgart Center for Simulation Science (SimTech).

Received: 30th of March 2021

Revised: 24th August 2021

References

1. Happel, J., & Brenner, H. (1981). *Low Reynolds number hydrodynamics* (Vol. 1). Springer Netherlands.
2. Purcell, E. M. (1977, January). Life at low Reynolds number. *American Journal of Physics*, 45(1), 3. <https://doi.org/10.1119/1.10903>
3. Baranova, N. B., & Zel'dovich, B. Y. (1978, August). Separation of mirror isomeric molecules by radio-frequency electric field of rotating polarization. *Chemical Physics Letters*, 57(3), 435–437. [https://doi.org/10.1016/0009-2614\(78\)85543-2](https://doi.org/10.1016/0009-2614(78)85543-2)
4. Ghosh, A., & Fischer, P. (2009, June). Controlled propulsion of artificial magnetic nanostructured propellers. *Nano Letters*, 9(6), 2243–2245. <https://doi.org/10.1021/nl900186w>
5. Zhang, L., Abbott, J. J., Dong, L., Kratochvil, B. E., Bell, D., & Nelson, B. J. (2009, February). Artificial bacterial flagella: Fabrication and magnetic control. *Applied Physics Letters*, 94(6), 064107. <https://doi.org/10.1063/1.3079655>
6. Schamel, D., Pfeifer, M., Gibbs, J. G., Miksch, B., Mark, A. G., & Fischer, P. (2013, August). Chiral colloidal molecules and observation of the propeller effect terms of use. *Journal of the American Chemical Society*, 135(33), 12353–12359. <https://doi.org/10.1021/ja405705x>
7. Keaveny, E. E., Walker, S. W., & Shelley, M. J. (2013, February). Optimization of chiral structures for microscale propulsion. *Nano Letters*, 13(2), 531–537. <https://doi.org/10.1021/nl3040477>
8. Morozov, K. I., Mirzae, Y., Kenneth, O., & Leshansky, A. M. (2017, April). Dynamics of arbitrary shaped propellers driven by a rotating magnetic field. *Physical Review Fluids*, 2(4). <https://doi.org/10.1103/PhysRevFluids.2.044202>
9. Sachs, J., et al. (2018, December). Role of symmetry in driven propulsion at low Reynolds number. *Physical Review E*, 98(6). <https://doi.org/10.1103/PhysRevE.98.063105>
10. Cohen, K. J., Rubinstein, B. Y., Kenneth, O., & Leshansky, A. M. (2019, July). Unidirectional propulsion of planar magnetic nanomachines. *Physical Review Applied*, 12(1), 014025. <https://doi.org/10.1103/PhysRevApplied.12.014025>
11. Qiu, T., et al. (2014). Swimming by reciprocal motion at low Reynolds number. *Nature Communications*, 5. <https://doi.org/10.1038/ncomms6119>
12. Zhou, C. M., & Gall, D. (2006). The structure of Ta nanopillars grown by glancing angle deposition. *Thin Solid Films*, 515(3), 1223–1227. <https://doi.org/10.1016/j.tsf.2006.07.136>
13. Glass, R., Möller, M., & Spatz, J. P. (Oct. 2003). Block copolymer micelle nanolithography. *Nanotechnology*, 14(10), 1153–1160. <https://doi.org/10.1088/0957-4484/14/10/314>
14. Mark, A. G., Gibbs, J. G., Lee, T. C., & Fischer, P. (2013). Hybrid nanocolloids with programmed three-dimensional shape and material composition. *Nature Materials*, 12(9), 802–807. <https://doi.org/10.1038/nmat3685>
15. Sliker, L., Ciuti, G., Rentschler, M., & Menciassi, A. (2015, November 2). Magnetically driven medical devices: A review. *Expert Review of Medical Devices*, 12(6), 737–752. Taylor and Francis Ltd. <https://doi.org/10.1586/17434440.2015.1080120>
16. Li, D., et al. (2019). *Soft phantom for the training of renal calculi diagnostics and lithotripsy*. <https://doi.org/10.1109/EMBC.2019.8856426>
17. Li, D., Jeong, M., Oren, E., Yu, T., & Qiu, T. (2019, October). A helical microrobot with an optimized propeller-shape for propulsion in viscoelastic biological media. *Robotics*, 8(4), 87. <https://doi.org/10.3390/robotics8040087>
18. Jeong, M., Choi, E., Li, D., Palagi, S., Fischer, P., & Qiu, T. (2019, July). *A magnetic actuation system for the active microrheology in soft biomaterials*. <https://doi.org/10.1109/MARSS.2019.8860985>
19. Nelson, B. J., Kaliakatos, I. K., & Abbott, J. J. (2010, July). Microrobots for minimally invasive medicine. *Annual Review of Biomedical Engineering*, 12(1), 55–85. <https://doi.org/10.1146/annurev-bioeng-010510-103409>
20. Fischer, P., & Ghosh, A. (2011, February 10). Magnetically actuated propulsion at low Reynolds numbers: Towards nanoscale control. *Nanoscale*, 3(2), 557–563. The Royal Society of Chemistry. <https://doi.org/10.1039/c0nr00566e>.

21. Nacev, A., et al. (2012). Towards control of magnetic fluids in patients: Directing therapeutic nanoparticles to disease locations. *IEEE Control Systems*, 32(3), 32–74. <https://doi.org/10.1109/MCS.2012.2189052>
22. Azizi, A., Tremblay, C. C., Gagné, K., & Martel, S. (2019, November). Using the fringe field of a clinical MRI scanner enables robotic navigation of tethered instruments in deeper vascular regions. *Science Robotics*, 4(36), 7342. <https://doi.org/10.1126/scirobotics.aax7342>
23. Qiu, T., Schamel, D., Mark, A. G., & Fischer, P. (2014, September). Active microrheology of the vitreous of the eye applied to nanorobot propulsion. In *Proceedings – IEEE international conference on robotics and automation* (pp. 3801–3806). <https://doi.org/10.1109/ICRA.2014.6907410>
24. Walker, D., Käsdorf, B. T., Jeong, H. H., Lieleg, O., & Fischer, P. (2015, December). Biomolecules: Enzymatically active biomimetic micropropellers for the penetration of mucin gels. *Science Advances*, 1(11), e1500501. <https://doi.org/10.1126/sciadv.1500501>
25. Wu, Z., et al. (2018, November). A swarm of slippery micropropellers penetrates the vitreous body of the eye. *Science Advances*, 4(11), eaat4388. <https://doi.org/10.1126/sciadv.aat4388>
26. Li, J., et al. (2016, October). Enteric micromotor can selectively position and spontaneously propel in the gastrointestinal tract. *ACS Nano*, 10(10), 9536–9542. <https://doi.org/10.1021/acsnano.6b04795>
27. De Ávila, B. E. F., et al. (2017, December). Micromotor-enabled active drug delivery for in vivo treatment of stomach infection. *Nature Communications*, 8(1), 1–9. <https://doi.org/10.1038/s41467-017-00309-w>
28. Wu, Z., et al. (2019, July). A microrobotic system guided by photoacoustic computed tomography for targeted navigation in intestines in vivo. *Science Robotics*, 4(32). <https://doi.org/10.1126/scirobotics.aax0613>
29. Shapiro, B., Dormer, K., & Rutel, I. B. (2010). A two-magnet system to push therapeutic nanoparticles. *AIP Conference Proceedings*, 1311(1), 77–88. <https://doi.org/10.1063/1.3530064>
30. Zhang, W., Meng, Y., & Huang, P. (2008, October). A novel method of arraying permanent magnets circumferentially to generate a rotation magnetic field. *IEEE Transactions on Magnetics*, 44(10), 2367–2372. <https://doi.org/10.1109/TMAG.2008.2002505>
31. Ryan, P., & Diller, E. (2016, June). Five-degree-of-freedom magnetic control of micro-robots using rotating permanent magnets. In *Proceedings – IEEE international conference on robotics and automation* (Vol. 2016-June, pp. 1731–1736). <https://doi.org/10.1109/ICRA.2016.7487317>
32. Qiu, T., Palagi, S., Sachs, J., & Fischer, P. (2018, September). Soft miniaturized linear actuators wirelessly powered by rotating permanent magnets. In *Proceedings – IEEE international conference on robotics and automation* (pp. 3595–3600). <https://doi.org/10.1109/ICRA.2018.8461145>
33. Baun, O., & Blümler, P. (2017, October). Permanent magnet system to guide superparamagnetic particles. *Journal of Magnetism and Magnetic Materials*, 439, 294–304. <https://doi.org/10.1016/j.jmmm.2017.05.001>
34. Kummer, M. P., Abbott, J. J., Kratochvil, B. E., Borer, R., Sengul, A., & Nelson, B. J. (2010). OctoMag: An electromagnetic system for 5-DOF wireless micromanipulation. In *Proceedings – IEEE international conference on robotics and automation* (pp. 1610–1616). <https://doi.org/10.1109/ROBOT.2010.5509241>
35. Tasoglu, S., Diller, E., Guven, S., Sitti, M., & Demirci, U. (2014, January). Untethered micro-robotic coding of three-dimensional material composition. *Nature Communications*, 5(1), 1–9. <https://doi.org/10.1038/ncomms4124>
36. Wang, X., et al. (2018, February). A three-dimensional magnetic Tweezer system for Intraembryonic navigation and measurement. *IEEE Transactions on Robotics*, 34(1), 240–247. <https://doi.org/10.1109/TRO.2017.2765673>
37. Kratochvil, B. E., Kummer, M. P., Abbott, J. J., Borer, R., Ergeneman, O., & Nelson, B. J. (2010). OctoMag: An electromagnetic system for 5-DOF wireless micromanipulation. In *Proceedings – IEEE international conference on robotics and automation* (pp. 1080–1081). <https://doi.org/10.1109/ROBOT.2010.5509857>

38. Rahmer, J., Stehning, C., & Gleich, B. (2018, March). Remote magnetic actuation using a clinical scale system. *PLoS One*, *13*(3), e0193546. <https://doi.org/10.1371/journal.pone.0193546>
39. Venugopalan, P. L., Jain, S., Shivashankar, S., & Ghosh, A. (2018, February). Single coating of zinc ferrite renders magnetic nanomotors therapeutic and stable against agglomeration. *Nanoscale*, *10*(5), 2327–2332. <https://doi.org/10.1039/c7nr08291f>
40. Pal, M., et al. (2018, May). Maneuverability of magnetic nanomotors inside living cells. *Advanced Materials*, *30*(22), 1800429. <https://doi.org/10.1002/adma.201800429>
41. Mhanna, R., et al. (2014, May). Artificial bacterial flagella for remote-controlled targeted single-cell drug delivery. *Small*, *10*(10), 1953–1957. <https://doi.org/10.1002/smll.201303538>
42. Venugopalan, P. L., Esteban-Fernández De Ávila, B., Pal, M., Ghosh, A., & Wang, J. (2020, August 25). Fantastic voyage of nanomotors into the cell. *ACS Nano*, *14*(8), 9423–9439. American Chemical Society. <https://doi.org/10.1021/acsnano.0c05217>
43. Kadiri, V. M., et al. (2020, June). Biocompatible magnetic micro- and nanodevices: fabrication of FePt nanopropellers and cell transfection. *Advanced Materials*, *32*(25), 2001114. <https://doi.org/10.1002/adma.202001114>
44. Stoddart, M. J. (2011). Cell viability assays: Introduction. *Methods in Molecular Biology (Clifton, N.J.)*, *740*. Humana Press, 1–6. https://doi.org/10.1007/978-1-61779-108-6_1
45. Kopeček, J., & Ulbrich, K. (1983, January 1). Biodegradation of biomedical polymers. *Progress in Polymer Science*, *9*(1), 1–58. Pergamon. [https://doi.org/10.1016/0079-6700\(83\)90005-9](https://doi.org/10.1016/0079-6700(83)90005-9)
46. Jain, T. K., Reddy, M. K., Morales, M. A., Leslie-Pelecky, D. L., & Labhasetwar, V. (2008, March). Biodistribution, clearance, and biocompatibility of iron oxide magnetic nanoparticles in rats. *Molecular Pharmaceutics*, *5*(2), 316–327. <https://doi.org/10.1021/mp7001285>
47. Griffith, W. H., Pavcek, P. L., & Mulford, D. J. (1942). The relation of the sulphur amino acids to the toxicity of cobalt and nickel in the rat. *The Journal of Nutrition*, *23*(6), 603–612. <https://doi.org/10.1093/jn/23.6.603>
48. Ermolli, M., Menné, C., Pozzi, G., Serra, M. Á., & Clerici, L. A. (2001, February). Nickel, cobalt and chromium-induced cytotoxicity and intracellular accumulation in human haemat keratinocytes. *Toxicology*, *159*(1–2), 23–31. [https://doi.org/10.1016/S0300-483X\(00\)00373-5](https://doi.org/10.1016/S0300-483X(00)00373-5)
49. Yan, X., et al. (2015, September). Magnetite nanostructured porous hollow helical microswimmers for targeted delivery. *Advanced Functional Materials*, *25*(33), 5333–5342. <https://doi.org/10.1002/adfm.201502248>
50. Yan, X., et al. (2017, November). Multifunctional biohybrid magnetite microbots for imaging-guided therapy. *Science Robotics*, *2*(12), 22. <https://doi.org/10.1126/scirobotics.aaq1155>
51. Peters, C., Hoop, M., Pané, S., Nelson, B. J., & Hierold, C. (2016, January). Degradable magnetic composites for minimally invasive interventions: Device fabrication, targeted drug delivery, and cytotoxicity tests. *Advanced Materials*, *28*(3), 533–538. <https://doi.org/10.1002/adma.201503112>
52. Bozuyuk, U., Yasa, O., Yasa, I. C., Ceylan, H., Kizilel, S., & Sitti, M. (2018, September). Light-triggered drug release from 3D-printed magnetic chitosan microswimmers. *ACS Nano*, *12*(9), 9617–9625. <https://doi.org/10.1021/acsnano.8b05997>
53. Wang, X., et al. (2018, November). 3D printed enzymatically biodegradable soft helical microswimmers. *Advanced Functional Materials*, *28*(45), 1804107. <https://doi.org/10.1002/adfm.201804107>
54. Ceylan, H., Yasa, I. C., Yasa, O., Tabak, A. F., Giltinan, J., & Sitti, M. (2019, March). 3D-printed biodegradable microswimmer for theranostic cargo delivery and release. *ACS Nano*, *13*(3), 3353–3362. <https://doi.org/10.1021/acsnano.8b09233>
55. Qiu, F., Fujita, S., Mhanna, R., Zhang, L., Simona, B. R., & Nelson, B. J. (2015, January). Magnetic helical microswimmers functionalized with Lipoplexes for targeted gene delivery. *Advanced Functional Materials*, *25*(11), 1666–1671. <https://doi.org/10.1002/adfm.201403891>
56. Thompson, S. P. (1896). *Dynamo-electric machinery: A manual for students of electrotechnics*. American Technical Book Company.

57. Fuerst, C. D., & Brewer, E. G. (1993, May). High-remanence rapidly solidified Nd-Fe-B: Die-upset magnets (invited). *Journal of Applied Physics*, 73(10), 5751–5756. <https://doi.org/10.1063/1.353563>
58. Zhao, B. et al. (2007). *Iron oxide(III) nanoparticles fabricated by electron beam irradiation method*.
59. Son, K., et al. (2019, August). Superior magnetic performance in FePt L10 nanomaterials. *Small*, 15(34), 1902353. <https://doi.org/10.1002/sml.201902353>
60. Shi, Y., Lin, M., Jiang, X., & Liang, S. (2015). Recent advances in FePt nanoparticles for biomedicine. *Journal of Nanomaterials*, 2015. Hindawi Limited. <https://doi.org/10.1155/2015/467873>
61. Sachs, J. (2020). *Motion, symmetry & spectroscopy of chiral nanostructures*. University of Stuttgart.
62. Jeong, M., Choi, E., Li, D., Palagi, S., Fischer, P., & Qiu, T. (2019). *A magnetic actuation system for the active microrheology in soft biomaterials*. <https://doi.org/10.1109/MARSS.2019.8860985>
63. Wu, Z., et al. (2018, November). A swarm of slippery micropropellers penetrates the vitreous body of the eye. *Science Advances*, 4(11), eaat4388. <https://doi.org/10.1126/sciadv.aat4388>
64. Luo, H., Wang, D., He, J., & Lu, Y. (2005, February). Magnetic cobalt nanowire thin films. *The Journal of Physical Chemistry. B*, 109(5), 1919–1922. <https://doi.org/10.1021/jp045554t>
65. Wang, W., Giltinan, J., Zakharchenko, S., & Sitti, M. (2017, May). Dynamic and programmable self-assembly of micro-rafts at the air-water interface. *Science Advances*, 3(5), e1602522. <https://doi.org/10.1126/sciadv.1602522>
66. Ghosh, A., & Fischer, P. Controlled propulsion of artificial magnetic nanostructured propellers. <https://doi.org/10.1021/nl900186w>
67. Zhu, S., et al. (2009, June). Biocompatibility of pure iron: In vitro assessment of degradation kinetics and cytotoxicity on endothelial cells. *Materials Science and Engineering: C*, 29(5), 1589–1592. <https://doi.org/10.1016/j.msec.2008.12.019>
68. Maldonado-Camargo, L., Unni, M., & Rinaldi, C. (2017). Magnetic characterization of iron oxide nanoparticles for biomedical applications. *Methods in Molecular Biology*, 1570., Humana Press Inc., 47–71.

Index

A

- Acoustic
 - tweezing, 82
 - Bessel beams, 82
 - demonstration of, 85
 - Langevin transducers, 83
 - uses, 83
 - Acoustic air levitation, 72
 - Acoustic fields, 165, 180, 183
 - Acoustic force, 172
 - Acoustic jets, 53, 54
 - Acoustic propulsion, 318
 - Acoustic radiation force (ARF), 33, 34, 63
- Acoustics
 - acoustic radiation force (ARF), 63
 - acoustic streaming-induced drag forces, 67, 69
 - Bjerknes forces, 66
 - bulk acoustic waves (BAW), 69
 - design considerations, 71, 72
 - driven systems, 70
 - theory, 69
 - overview, 61
 - phenotypical assessments, 62
 - standing waves, 78
 - applications, 80
 - BAW systems, 79
 - gelatin methacryloyl, 81
 - one-cell-per-well (OCPW), 80
 - split-flow thin (SPLITT) fractionation, 79
 - SSAWs, 79
 - surface acoustic waves (SAW), 69, 72
 - Huygens-Fresnel principle, 75
 - interdigital transducers (IDTs), 73
 - leaky Rayleigh wave, 74
 - travelling waves, 75
 - travelling waves, 81
 - applications, 82
 - TSAW systems, 81
 - tweezing, 75
 - acoustic structures, 77
 - ultrasonic arrays, 77
 - ultrasonic beams, 76
- Acoustic streaming, 36, 37
- Acoustofluidics, 61
- Active drug delivery, 375
- Active therapy
 - polymer nanorobots in vivo, 385, 386
 - propulsion function benefits, 382, 383
- Active vaccine delivery, 386
- Actuating magnetic fields, 212–214, 216, 217, 219–223, 234, 235
- Actuation, 316
 - biohybrid devices, 326
 - biohybrid robot, 334
 - controllable, 330
 - efficiency, 326
 - performance, 335
- Adenosine triphosphate (ATP), 184
- Aerotaxis-based self-steering, 315
- Alginate gel fibers, 294
- Ameboid locomotion, 307, 309
- Anchoring mechanism, 231
- Antibody-antigen, 184
- Artificial micro-/nanopropellers, 390
- Artificial motors, 379
- Au/Ni/Au/Pt-CNT particles, 378
- Autonomous sense and act, 381, 382
- Axoneme, 308

B

Bacteria flagella, 307
 Bacterial chemotaxis, 312
 Bacteriobots, 310
 Biocompatibility, 402, 403
 Biocompatible magnetic materials, 396, 404, 407
 for biomedical application
 biocompatibility tests and gene delivery, 406, 407
 FePt, 405–407
 iron, 404
 NdFeB, 405
 nickel, 404
 for micro-/nanorobots
 biocompatibility, 402, 403
 biodegradability, 403, 404
 coercivity, 403
 remanence, 403
 3D nanostructuring, 404
 Biodegradability, 403
 Biodegradation, 403
 Biohybrid microrobots
 clinical application, 339, 340
 Biohybrid microswimmers, 311, 316
 Biohybrid robots
 autologous, 323
 based on bacteria
 chemotaxis, 309–312
 magnetotaxis/embedding paramagnetic elements, 313–315
 based on non-bacterial flagellated cells, 316
 based on non-flagellated cells, 317–321
 based on sperm cells, 317
 cell types, 306
 centimeter-scale, 333
 challenges, 321–324
 efficacy of therapies, 321
 macrophage's chemotaxis, 320
 micropump, 332
 multicellular muscle cell-powered, 338
 muscle-based, 339
 nanoparticle-loaded erythrocyte-based, 318
 SM tissue, 339
 smart design tools, 338
 T lymphocytes, 320
 Biological energy units, 370
 Biological hybridization, 375–377
 Biological motors, 306, 309, 327
 Biological systems, 306
 Biological tissue penetration depth, 396
 Biological tool, 306
 Biomedical applications, 369, 372, 380, 383, 386, 389
 Biomedical tasks, 389

Biomedicine, 369, 377, 378
 Biomotor protein-mimicking molecules, 370
 Biophysical cues, 270
 Biopolymers, 281
 Biosensing
 artificial micro-/nanomachines, 244
 in vitro detection and monitoring, 244
 intracellular monitoring, 244, 255–258
 low limit of detection (LOD), 244
 micro-/nanomachine-based methods, 244
 micro/nanomachines (*see* Micro/nanomachines)
 natural micro-/nanomachines, 244
 pathogens and biomarker discrimination, 244, 259–262
 Biosilica opto-plasmonic microsensor, 129
 Bjerknes forces, 66
 Bottom-up fabrication polymer-based
 swimming nanorobots
 biological hybridization, 375–377
 layer-by-layer assembly technique, 371, 373, 374
 supramolecular assembly, 375, 376
 Brownian motion, 138
 Bubble streamers, 47
 acoustic pressure, 50
 commercial Teflon tube, 48
 magnetic steering, 50
 mechanism, 46, 48
 practical considerations, 50, 51
 propulsion force, 49, 50
 3D laser printing, 49
 Bubble-tubular structure systems, 374

C

Cancer therapy, 322
 Cardiomyocyte-driven devices, 327, 330
 Cardiomyocyte-driven robots, 329, 330
 Cardiomyocytes, 327–330
 Cartesian coordinates, 185
 Catalytic nanowire swimming robots, 379
 Catalytic swimming microrobots, 378
 Cell-embedded biotechnological tool, 319
 Cell metabolism, 281
 CellIROX assay, 406
 Cell seeding, 287
 Cell sheet engineering, 286
 Cell viability, 300, 302
 Chemical functionalization, 250
 Chemical propulsion, 373, 378, 385
 Chemical signaling, 184
 Chemically catalytic propulsion, 245
 Chemico-physical sensors, 309
 Chemiluminescence, 259

- Chemoattractant, 312
 Chemosensory signals, 306
 Chemotaxis, 309–310, 379–381
 bacterial microrobots, 310
 directed migration, 319
 and magnetotaxis, 315
 “nonrobotic” strategy, 313
 and phagocytosis, 320
 and phototaxis, 315
 Chirality, 391, 392
 Cilia, 307, 308
 Clinical trials, 322
 Clinical-scale magnetic field generator, 401
 Coercivity, 403
 Collaborative robots, 234
 Colloidal systems, 180
 Combating chemical warfare agents (CWA), 254
 Contractile insect-derived cells, 335
 Control Lyapunov functions (CLF), 15
 Conventional robots, 305
 Corkscrew-type rotating propulsion, 308
 Cylinder Halbach system, 400
- D**
 Deformation mechanics, 213–216, 219
 Dendritic platinum nanoparticles (Pt NPs), 372
 Dielectrophoresis (DEP) manipulation, 116,
 184, 286
 Discrete Element Modeling (DEM), 11
 DNA-based binding, 184
 DNA-based linking, 184
 Drug delivery, 234, 313, 316, 319–321, 328,
 332, 338, 376
- E**
 Electric field-based methods
 adaptive control scheme, 136
 DEP force, 135
 EO-induced disturbances, 136
 EO modeling and optimization
 algorithms, 135
 integrated online adaptive manipulation
 scheme, 136
 microfabricated electrodes, 136
 motion planning strategies, 136
 pH values, 135
 Electric fields, 181
 Electric tweezers, 114
 AC electroosmosis, 119, 127
 Brownian motion, 120
 cargo delivery, 123
 combined DC and AC E-fields, 120
 cytokine molecule delivery, 122
 DC electroosmosis, 119
 dielectrophoretic (DEP) force, 116
 electric double layer (EDL), 115
 electrophoresis, 115
 Joule heating, 121
 QD-nanowires, 127
 Re[CM] value, 117
 Reynolds number (Re), 114
 SERS detection, 125
 spherical dielectric particle, 118
 superstructural Raman nanosensor, 126
 suspension medium properties, 121
 tunable release of biochemicals, 124
 Electrical stimulation, 326, 328, 331–337, 339
 Electromagnetic actuation system, 399, 401, 402
 Electromagnetic fields, 320
 Electroosmotic effect, 184
 Electrophoresis (EP)
 EP-based motion model
 adaptive control, 145–147
 adaptive tube model predictive control,
 147–151, 153 (*see also* EP-based
 motion model)
 nonlinear feedback control, 142, 143
 sequential particle control and
 assembly, 142, 144
 simultaneous particle control, 145, 146
 EP-based particle motion
 planning, 153–157
 micro- and nanoparticles, 158–160
 Electrostatic interactions and
 electrohydrodynamics, 181
 Embedded microsensing, 310
 Engineering natural motor proteins, 370
 Environmental sensing, 309
 Enzyme-linked immunosorbent assay
 (ELISA), 259
 EP-based motion model
 problem formulation, 140
 system configuration, 137, 138
 system inertial effects, 138
 Eukaryotic cells, 308
 Eukaryotic non-flagellated cells, 317
 Externally driven propulsion, 392
 External magnetic field, 213, 251
- F**
 Fabricated magnetic hydrogel fibers, 287
 Fabrication, 373
 micro-/nano-propellers by GLAD, 394
 corresponding angle, 394
 OAD, 394
 PVD method, 394
 V-shaped zig-zag structure, 394

Fabrication methods, 223, 225, 226, 234
 Fabrication process, 298
 Feedback, 235
 Feedback controller design, 145
 FePt microswimmers, 407
 FePt nanopropellers, 406, 407
 Fibrin gel, 297–299, 301
 Field-based manipulation methods, 134
 Field-based nanomanipulation, 134
 Field-induced agent-agent interactions, 184
 Flagella enable flexible oar oscillation, 308
 Flagellar streamers, 51–53
 Flagellated bacteria, 307, 308
 Focused ultrasound (FUS) triggering, 318, 320

G

Galvanotaxis, 309, 315, 323
 Gastric therapy, *Helicobacter pylori* infection, 385
 Gastrointestinal (GI) tract, 385
 applications, 349
 biocompatible and biodegradable, 362, 363
 cargo delivery and therapy, 359–362
 enhanced retention and navigation, 356–358
 environmental features, 350
 in vivo imaging and localization, 354, 355
 propulsion, 351–353
 Gelatin methacryloyl (GelMA) hydrogel, 287
 Gene delivery
 in A549 cells, 406
 and biocompatibility tests, 406–407
 Generalized predictive controller (GPC), 23
 Geomagnetic field, 313
 Geometric patterns, 146
 Geometrical shape, 392, 393
 Glancing angle deposition (GLAD), 353, 406
 advantage, 396
 complex helix-shaped micro- and nanopropellers, 394
 corresponding angle, 394
 description, 394
 for fabrication of micro-/nanopropellers, 394, 395
 nanopropellers, 406
 and PVD, 405
 three-dimensional nanoswimmers, 404
 Gold microparticle swarms, 182
 Green fluorescent protein (GFP), 407

H

Helical magnetic nanomachines, 258
 Helices, 395

Helmholtz coil geometry, 400
 Hepatic lobule
 central vein, portal vein, and sinusoid, 289
 in fibrin gel, 299, 301
 in vitro 3D tissue, 289
 vascular network of, 289
 Hertz model, 272
 Higher signal-to-noise ratio (SNR), 281
 HLA nanorobots, 385
 Hybrid micro-/nanorobots, 166
 Hydrazine, 184
 Hydrogen peroxide, 372

I

Imaging technology, 383
 In vitro three-dimensional (3D) tissue fabrication, 285
 In vivo applications, 396
 In vivo biocompatibility testing, 403
 In vivo toxicity tests, 403
 Independent controllable magnet system, 400
 Indium tin oxide (ITO)-coated coverslip, 137
 Inherent Brownian motion, 245
 Inorganic artificial microswimmers, 378
 Interdigital transducers (IDTs), 73
 chirped, 74
 design of, 73, 74
 finger spacing, 74
 focused or curved, 74
 Intermolecular van der Waals forces scale, 305
 Intracellular structures
 cell nucleus and cytoskeleton, 278, 279
 cytoskeleton, 279
 DNA strands, 279
 intracellular motor proteins, 279
 Iron, 404
 Iron oxide nanoparticle, 133
 IRONSperm, 316

J

Janus microcapsule robots, 372
 Janus micro-/nanosphere swimming micro-/nanorobots, 372

L

Lamb-Oseen vortex, 189
 Laser-based molding method, 224
 Laser-based molding process, 223
 Layer-by-layer assembly technique, 371, 373, 374
 LbL-assembled polyelectrolyte multilayers (PEM), 371

- Leukocytes, 317–319, 323
- Light-activated virtual electrodes, 96
- Light-based locomotion, 306
- Linear quadratic regulator (LQR), 19
- Lithographic patterning
 - feasibility, 225
 - of polymers, 224
 - sequential, 225
- Locomotion, 306, 307
- Low Re number, 390–392

- M**
- Macroscale objects, 370
- Magnesium-based microrobot, 384, 385
- Magnesium-based polymer robotic toxoid, 386
- Magnetic actuation, 167, 212
- Magnetic actuation systems, 396–400
- Magnetic bead, 4, 271
- Magnetic beam, 217
- Magnetic control, 323
- Magnetic fibers, 289, 296
- Magnetic field generation system, 269
- Magnetic fields, 165, 180, 269, 309, 313–316, 319, 323, 396
- Magnetic helical microswimmer, 247
- Magnetic hydrogel fibers, 288
- Magnetic micromanipulation
 - gradient force, 273, 274
 - magnetic bead dynamics, 272, 273
 - magnetic beads, 271
 - magnetic force and magnetic moment, 272
 - torque, 275, 276
- Magnetic micromotors, 258
- Magnetic microrobot, 166
- Magnetic navigation, Janus polymer microcapsule robots, 377
- Magnetic remanence, 403
- Magnetic resonance imaging (MRI), 1, 133, 401, 405
 - control strategies, 14
 - MRI-based backstepping control approach, 15
 - MRI-based optimal control approach, 19
 - MRI-based predictive control approach, 18
 - drug-loaded magnetic microrobot, 6
 - magnetic forces, 5
 - magnetic microrobot, 7
 - apparent height, 9
 - contact force, 11
 - gravitational force, 12
 - hydrodynamics, 7
 - magnetic force, 10
 - translational and rotational motions, 7
 - van der Waals forces, 12
- MRI-guided nanorobotic systems, 2
 - architecture, 4
 - clinical and preclinical list, 3
 - drug delivery and release, 2
 - enhanced diagnostics, 2
 - in vivo propulsion and navigation, 2
 - propulsion scheme, 4
 - pulsative blood's velocity, 21
 - robustness gains model, 21
 - state-space representation, 13–14
- Magnetic robots, 212
- Magnetic torque, 218
- Magnetic tweezers, 280, 287
 - cellular rheological properties, 278
 - control system, 291
 - development of, 270
 - developments and wide applications of, 271
 - magnetic microbeads, 269
 - measurements of cell mechanics, 276, 277
 - multipole magnetic tweezers, 271
 - requirement, 290
 - simulation of, 292, 293
- Magnetite suspensions, 251
- Magnetization profile, 212
- Magnetized *Spirulina platensis* (MSP), 355
- Magneto-acoustic neutrophil-inspired microrobots, 173
- Magnetotactic bacteria (MTB), 181
- Magnetotaxis, 309, 313, 315, 323
- Mammalian cardiac tissue, 335, 339
- Mammalian cell-based devices, 339
- Mammalian cells, 306, 321, 326
- Marangoni effect, 253
- Mechanical functionalities, 211, 212, 214, 226, 231–235
- Mechanical stimulation, 269
- Medium-based interactions, 184
- Metal-acid reaction, 361
- Micro/nanomachines
 - chemical and biological agent, 252–255
 - chemical, biological, and self-functionalization, 248–251
 - propulsion of, 245–247
 - sensing mechanisms, 251, 252
- Micro-/nano-propellers
 - biomedical applications, 392
 - external field vector, 393
 - microfabrication techniques (*see* Fabrication)
 - non-Newtonian, 393
 - parity and charge conjugation symmetry, 393
 - rotation-translation coupling, 391, 392

- Micro-/nanorobot, 29
 - Micro-/nanorobotics
 - biocompatible and versatile propulsion, 172
 - biocompatible energy sources, 165
 - biocompatible fuel-free propulsion mechanisms, 165
 - bi-segment configuration, 170
 - collective behavior, 170, 171
 - geometric parameters, 169
 - hybrid micro-/nanorobots, 166
 - magnetic and acoustic, 165, 168
 - magneto-acoustic hybrid nanomotor, 168, 174
 - polydimethylsiloxane (PDMS)-based microchannel, 173
 - practical biomedical applications, 170
 - propulsion performance, 170
 - Microfabrication techniques, 337, 339, 394
 - Microhelices, 358
 - Micromanipulation, 179
 - Microprinting technology, 372
 - Micro-propulsion, 389, 391–394
 - Microrobotic swarms
 - biomedical applications, 180
 - control strategies, 180
 - controllable and reversible process, 180
 - feedback signal, 180
 - field-driven microrobotic swarms, 181, 183, 184
 - imaging modality, 205
 - locomotion in channel, 204, 205
 - pattern control and motion control, 180
 - self-assembled magnetic asters, 182
 - synchronized fashion, 201, 202, 204
 - vortex-like swarms
 - characteristics of, 188–190
 - generating of, 195
 - minimum particle concentration, 186
 - vortices merging, 186
 - Microrobots, 305
 - external fields, 179
 - gastrointestinal tract (*see* Gastrointestinal tract)
 - microrobotic agents, 179
 - optical microrobot (*see* Optical microrobot)
 - opto-chemical microrobot, 103–105
 - opto-mechanical soft microrobot (*see* Opto-mechanical soft microrobot)
 - Microrod streamers, 37–46
 - basic sciences, 45
 - biomedical applications, 42, 44
 - dazzling speed, 37
 - mechanisms, 38, 40–42
 - operation, 38
 - practical considerations, 44
 - Microswimmers, 312, 313, 316, 321, 324, 406
 - biodegradability, 404
 - FePt and SiO₂, 406
 - and nanorobots, 390
 - Microswimmers' typical propulsion behavior, 406
 - Millimeter-scale helical robot, 401
 - Min-cost-max-flow (MCMF) problem, 154
 - Miniature soft devices, 212
 - Miniature soft robots, 229, 234
 - Minimally invasive nanomedicine, 407
 - Minimally invasive surgery, 389
 - Model predictive control (MPC), 147, 148
 - Modern fabrication techniques, 134
 - Molding, 223
 - Molecular engine, 306
 - Molecular machines, 370
 - Motion control problem, 140
 - Motion control, swimming nanorobots
 - autonomous sense and act, 381, 382
 - chemotaxis, 379–381
 - navigation using external field, 377–379
 - Motion gain matrix, 140
 - Motion planning problem, 140
 - MRI scanner, 401
 - Multicellular actuators, 338
 - Multicellular muscle cell-powered biohybrid robots, 338
 - Multicellular muscle-based systems, 339
 - Multicellular systems, 306, 338, 339
 - Multilayered structure
 - experimental process, 298
 - 3D vascular network, 294
 - Multistep electrodeposition techniques, 167–168
 - Muscle cells
 - as biological motors, 324
 - Muscle-based biohybrid devices, 338, 339
 - Muscle-based biohybrid robots, 339
 - Muscle-cell based device contraction, 339
 - Muscular robots, 328
 - Myofibers, 324
- N**
- Nanoerythroosomes, 322
 - Nano-fabrication, 407
 - Nanohelical magnetic segment, 168
 - Nano-helices, 391, 395
 - Nanorods, 378
 - Nanotechnology, 133

- Nanowire robots, 379
- Natural motor proteins, 370
- Natural muscle, 324, 326, 339
- Natural nanoswimmers, 370
- Navier-Stokes equation, 389
- Near-infrared (NIR) light, 378
- Network flow-based two-stage motion
 - planning algorithm, 154
- Newtonian (incompressible) fluids, 390
- Newtonian fluid, 370
- Nickel, 404
- Noncontact actuation techniques, 134
- Non-flagellated eukaryotic cells, 307, 309
- Noninvasive imaging method, 355
- Nonlinear feedback controller, 142, 143
- Non-uniform magnetization profiles, 220
- Nuclear imaging technology, 383

- O**
- Oblique angle deposition (OAD), 394
- OctoMag system, 400, 401
- On-board sensing, 305
- Optical control methods, 323
- Optical imaging, 354
- Optical microrobot
 - biological samples, 92
 - closed-loop feedback system, 95
 - indirect cell manipulation, 95
 - limitations, 96
 - optical gradient forces, 92
 - opto-mechanics hardware, 93
 - optothermal effect, 97, 98
 - photo-curable polymer materials, 93
 - two-photon polymerization techniques, 93
 - UV-curable polymer materials, 97
 - working mechanisms of, 93
- Opto-chemical microrobot, 103–105
- Optogenetics, 330
- Opto-mechanical soft microrobot
 - actuation mechanisms, 100
 - applications, 101
 - DMD projector, 100
 - LCP materials, 100
 - photomechanical dyes, 100
 - piezoelectric and piezoresistive responses, 102
- Organic microrobot, 327
- Oseen vortex, 189

- P**
- Paramagnetic nanoparticles, 184
- PAT imaging, 384
- PDMS-based squared device, 335
- Permanent magnet actuation systems,
 - 398–400
- Permanent magnets, 396, 398, 399
- Permanent magnet systems, 396–399, 402
- Photoacoustic computed tomography (PACT), 356
- Photoacoustic tomography (PAT) detects
 - photon-induced ultrasound, 384
- Photodynamic therapy (PDT), 376
- Photopolymerization process, 225
- Phototaxis, 183
- Physical vapor deposition (PVD)
 - chamber, 402
- Piezoelectric motors, 306
- Piola–Kirchhoff stress tensor, 215, 216
- PNIPAM-Au-Pt Janus microrobots, 381
- Poly(N-isopropylacrylamide) (PNIPAM),
 - 378, 380–382
- Polyallylamine hydrochloride (PAH), 372
- Polydimethylsiloxane (PDMS), 51, 327–329,
 - 332, 333, 335, 337
- Polyelectrolyte multilayers (PEM), 371
- Polymer Janus microcapsule nanorobots, 372
- Polymer Janus microcapsule swimming
 - robots, 373
- Polymer nanorobots in vivo
 - active therapy, 385, 386
 - propulsion function benefits, 382, 383
 - imaging and control, 383–385
- Polymer tubular swimming nanorobots, 374
- Polymerase chain reaction, 259
- Polymer-based swimming nanorobots
 - bottom-up fabrication (*see* Bottom-up fabrication, polymer-based swimming nanorobots)
- Polystyrene sulfonate (PSS), 372
- Positron-emission tomography (PET), 250
- Potential magnetic energy, 215
- Potential-induced motion control, 379
- Printed agarose fibers, 286
- Propeller effect, 390
- Propulsion, 306
- Propulsion force, 391
- Propulsion gaits, 393
- Propulsion mechanism, 328
- Propulsion speed, 310
- Propulsion, micro-/nanoworld, 369
- Proton pump inhibitors (PPIs), 360
- Protonmotive force, 307
- Pt/Au nanowires, 378
- Pt-NP-modified Janus microcapsule
 - robots, 373

Q

Quadrupole magnetic tweezers, 287
 Quincke rotation, 181

R

RBC membrane-coated and magnesium-powered (RBC-Mg), 375
 Reactive oxygen species (ROS), 406, 407
 Red blood cells (RBCs), 250, 313, 317–319, 322, 323, 375
 Reversible anchoring mechanisms, 211
 Reynolds (Re) number, 389, 390
 Reynolds numbers, 370, 374
 Robots
 based on cardiomyocytes, 327–330
 based on insect-derived cells, 335–337
 based on skeletal muscle (SM) cells, 331–335
 challenges, robot based on muscle cells, 338–340
 Rotating magnetic fields, 390–392, 396, 399, 400, 402
 Rotation-translation coupling, 390, 392

S

Sculptured thin films (STF), 394
 Self-assembled stomatocyte nanorobots, 380
 Self-assembly technology, 375
 Self-propulsion, 182
 Sensing, 305, 323, 338
 Sequential lithographic patterning, 225
 Shape-programmable magnetic miniature robots
 actuating principles, 214
 deformation mechanics, 213–217
 fabrication methods, 223–226
 locomotion functionalities, 226–230
 mechanical functionalities, 231–234
 programming methods, 220–222
 requirement, 235
 rigid-body motions, 219–220
 with beam-like configurations, deformation mechanics, 217–219
 Shape-programmable magnetic robots, 212, 216, 217
 Shape-programmable miniature robots
 actuation methods, 235
 magnetic forces, 219
 magnetization profile, 212
 stimuli, 212

3D geometries and magnetization profiles, 223
 3D-print, 225
 untethered soft-bodied locomotion, 211
 Shape-programmable robots
 advantage, 211
 micro-/millimeter length scales, 211
 Shape programming
 developments, 222
 and fabrication method, 220, 223–225
 functionalities, 220
 jellyfish-like robot, 222
 Taylor swimming sheet, 220, 221
 uniform magnetization profiles, 220
 universal methodology, 221, 222
 Silicon nanowires' zeta potentials, 141
 SM cell-based devices, 327
 SM contraction, 324, 325, 332
 Soft miniature robots, 211
 Sperm-based microrobots, 377
 Split-flow thin (SPLITT) fractionation, 79
 SSAW-assisted nanowire patterning technique, 182
 Standing surface acoustic wave (SSAW), 183
 Stomatocyte nanorobots, 380
 Superconducting MRI machine, 401
 Superparamagnetic microparticle swarms, 183
 Superparamagnetic microparticles, 183
 Supramolecular assembly, 375, 376
 Supramolecular-based swimming nanorobots, 375
 Swarm control, 234
 Swimming nanorobots
 bimetal nanowire robots, 371
 biomedical utilizations, 369
 biomimetic efforts, 370
 molecular machine, 371
 motion control (*see* Motion control, swimming nanorobots)
 polymer (*see* Polymer-based swimming nanorobots)
 Synchronized magnet rotating system, 400

T
 Targeted drug delivery, 212, 226, 351, 386, 389
 Target-oriented drug delivery, 133
 Tetra-substituted Ru^{IV} polymetallic oxalates, 372
 3D bioprinting, 286

3D cellular structure, 290
 3D direct laser writing (DLW), 353
 3D hepatic tissue, 287
 3D magnetization profiles, 223, 225
 3D pick-and-place operations, 233
 3D-printed surface profile, 167
 3D-printed transmission element, 183
 3D printing methods, 226, 286
 3D printing technology, 225
 3D robots, 234
 3D vascular network, 287, 296
 Tissue penetration, 396
 Tissue-engineered PDMS structure, 328
 Traditional actuators, 306
 Traditional rigid miniature robots, 211
 Tubular micromotor-based cortisol
 immunoassays, 255
 Tubular swimming nanorobots, 373, 377
 Tumor environments, 312
 Tumor-targeting vectors, 313
 Two-anchor crawling, 227–230

U

Ultrasonication-induced degradation, 251
 Ultrasound, 323
 Ultrasound feedback, 235
 Ultrasound imaging, 384
 Ultrasound micro-/nanorobots
 acoustic jets, 53, 55
 acoustic radiation forces, 31, 32, 34, 35
 acoustic streaming, 33, 37
 bubble streamers, 47
 acoustic pressure, 50
 commercial Teflon tube, 48
 magnetic steering, 50
 mechanism, 46, 48
 practical considerations, 50, 51
 propulsion force, 49, 50
 3D laser printing, 49

 flagella streamers, 51–53
 microrod streamers, 37
 basic sciences, 45
 biomedical applications, 42, 44
 dazzling speed, 37
 mechanisms, 38, 40–42
 operation, 38
 practical considerations, 44
 scientific and technological challenges, 55
 types of, 31, 32
 Ultrasound-powered micro-/nanorobots, 29
 Ultrasound-propelled nanomachines, 250
 Unidirectional/bidirectional propulsion, 392
 Universal programming methodology,
 221, 222
 Untether locomotion control, 211, 226,
 234, 235
 US-powered NW nanomachines, 247
 UV light, 224, 225

V

Visual feedback systems, 235
 Volumetric quantities, 305
 VPNS
 characteristics of, 188–191, 196, 197
 minimum particle concentration, 186
 pattern transformation of
 change of core size, 198
 core size modification, 191
 spread state, 192–194, 196, 199, 200

W

Wireless actuation, 134, 396, 407

Z

Zeta potentials, 145
 Zinc-based microrobot, 385